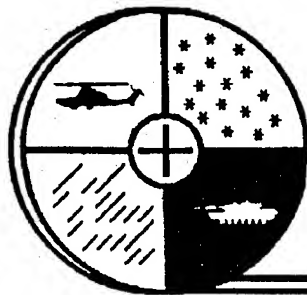


PROCEEDINGS of the



1991 BATTLEFIELD ATMOSPHERICS CONFERENCE

**Ft. Bliss, Texas
3-6 December 1991**

Conference Manager, Edward Creegan

Conference Chairman, Robert Lee



**ATMOSPHERIC SCIENCES LABORATORY
U.S. Army Laboratory Command**

**White Sands Missile Range
New Mexico**

Approved for public release; distribution is unlimited.

DTIC QUALITY INSPECTED 3

19971215 128

NOTICES

Disclaimers

The findings in this report are not to be construed as an official Department of the Army position, unless so designated by other authorized documents.

The citation of trade names and names of manufacturers in this report is not to be construed as official Government endorsement or approval of commercial products or services referenced herein.

DESTRUCTION NOTICE

When this document is no longer needed, destroy it by any method that will prevent disclosure of its contents or reconstruction of the document.

Proceedings
of the
1991 Battlefield Atmospherics Conference

3 - 6 December

Sponsor:
Atmospheric Sciences Laboratory
U.S. Army Laboratory Command
White Sands Missile Range, NM 88002-5501

Conference Manager:
Edward Creegan
Atmospheric Sciences Laboratory

Conference Chairman:
Robert Lee
Atmospheric Sciences Laboratory

Host:
Fort Bliss, El Paso, Texas

DMC QUALITY ASSURED

Program Committee

U.S. Army Atmospheric Sciences Laboratory

Conference Manager

Edward Creegan (505) 678-4684 or DSN 258-4684

Conference Chairman

Robert Lee (505) 678-4006 or DSN 258-4006

Conference Advisers

Dr. Franklin E. Niles (505) 678-3721 or DSN 258-3721

Dr. Bernard F. Engebos (505) 678-1489 or DSN 258-1489

Dr. Mary Ann Seagraves (505) 678-4200 or DSN 258-4200

Mr. Bob Rubio (505) 678-2926 or DSN 258-2926

Administrative Assistants

Mrs. Nancy Fudge (505) 678-4450 or DSN 258-4450

Ms. Millie Mead (505) 678-2926 or DSN 258-2926

Physical Science Laboratory/New Mexico State University

Conference Coordinator

Ms. Janet Vasiliadis (505) 522-9100

Conference Support

Mrs. Wilhelmina Goldsborough (505) 522-9100

CONTENTS

OPENING SESSION

Keynote Address	3
Col. William H. Campbell	

Session I: Electromagnetic and Acoustic Transmission

MODTRAN	7
L. W. Abreu, F. X. Kneizys, G. P. Anderson, J. H. Chetwynd, A. Berk, L. S. Bernstein, and D. C. Robertson	
XSCALE 92	15
Robert P. Fiegel	
A Theoretically Based Double Exponential Extinction Model for Very Low Stratus Clouds and Subcloud Regions: An Option for the Vertical Profile Model in XSCALE	25
Neal H. Kilmer and Henry Rachele	
Transformation of COMBIC to Dynamic Battlefield Environment Target Acquisition Model (DYBETA)	35
S. Grossman, A. Katz, and D. Elial	
Electro-Optical Climatology Microcomputer Version 2.0	36
R. L. Miller and B. T. Regan	
Theoretical and Measured Fractal Dimensions for Battlefield Aerosol Cloud Visualization and Transmission	46
Donald W. Hoock	
Visualization of Battlefield Obscurants	56
Geoffrey Y. Gardner and G. Michael Hardaway	
Acoustic Propagation in the Atmosphere using the Scanning Fast Field Program	66
John M. Noble	

Session II: Weather Decision Aids

Thermal Reversal Tactical Decision Aid Evaluation	75
Stephen W. Berrick and Patti S. Gillespie	
Target Acquisition Model Evaluation with Smoke Week Data	84
Brian A. Locke, Stephen W. Berrick, Lori Fuentes, Ronald A. Catherson, and Patti Gillespie	
Influence of Battlefield-Induced Obscurants and Atmospheric Effects on a High-Resolution Combat Simulation	94
Martin E. Lee and Steven J. LaMotte	
An Application of AAODL Meteorological and Nephelometer Field Test Data: Obscurant Plume Characterization	103
Roger E. Davis, John Crain, and Robert A. Sutherland	

Mesoscale Wind Variability in Germany: Comparison of Wind Profiles in Close Proximity from Four Pairs of Radiosonde Launch Sites Larry J. Levitt and Dorathy A. Stewart	113
The AirLand Battlefield Environment Program at ASL David Sauter	123

Session III: Battle Scale Weather

Research at the U.S. Army Center for Geosciences Related to Tactical Weather Intelligence T. H. Vonder Haar and J. L. Behunek	131
Directory of Atmospheric Transport and Diffusion Models, Equipment, and Projects Col. Floyd F. Hauth	141
Air Weather Service Battlefield Weather Programs J. D. Fink and P. B. Roohr	142
Source Strength Terms for Winter Dispersion Models A. Hogan and D. Leggett	149
An Assessment of the Potential of the UK Met Office Mesoscale Model for Predicting Anomalous Radiowave Propagation Conditions Keith S. Groves, Ian D. Todd, and Jonathan D. Turton	156
Variation of Cloud Base by Season and Climate Zone Oskar Essenwanger	166
Forecasting Convective Precipitation and Severe Weather by Applying Artificial Intelligence Approaches Robert E. Dumais, Jr., and Jeffrey E. Passner	176
Results of Man-Made Fog Experiments Robert A. Sutherland, Young P. Yee, Frank D. Eaton, William A. Peterson, Miklos Z. Kiss, and Craig E. Foster	185

Session IV: Remote Sensing

Fog Microphysics Information from Multispectral Reflectance Data J. L. Behunek and T. H. Vonder Haar	197
Rapid Deployment Imagery Terminal (RDIT) using DMSP Special Sensor Data Thomas L. Harris and Jimmy A. Jensen	202
PC-Based Rainfall Estimation from Infrared Geostationary Satellite Imagery D. L. Reinke, C. L. Combs, and T. H. Vonder Haar	212
A Comparison of Measured and Differential Corrected Global Positioning Systems Data Thelma Chenault, John Fox, and Don Foiani	217
Testing a Microwave Radiometer in Arctic, Temperate, and Tropical Climates Edward M. Measure, Teddy L. Barber, Randall J. Hulsey, and Dick R. Larson	223

Improving Atmospheric Characterizations at HELSTF:	228
Winds and Humidity	
Gail Tirrell Vaucher and Robert W. Endlich	

Session V: PBL Energy Budget

Estimating Effects of Temperature and Moisture on C_n^2 in the Damp, Unstable Boundary Layer for Visible, Infrared, Radio, and Millimeter Wavelengths	241
Arnold Tunick and Henry Rachele	
Energy Balance Model for Imagery and Electromagnetic Propagation	251
Henry Rachele and Arnold Tunick	
Boundary Layer Illumination Radiation Balance Model: BLIRB	261
Andrew Zardecki and Alan E. Wetmore	
Tactical Correction of Near Surface Atmospheric Refraction	268
David H. Tofsted and James B. Gillespie	

Session VI: BEST TWO

BEST TWO: An Overview of the Test, the Simulation of	281
Artillery-Produced Dust, and the Target Vehicles Tracking	
Jacques Vesque	
Meteorological Conditions and Data for the BEST TWO Field Trial	282
Robert W. Smith and Ted Corbin	
Obscurant Measurements during BEST TWO by Means of MPTR	292
A. N. de Jong	
Multispectral Transmission through Dust, (Infrared) Signatures of	302
Target Vehicles and Target Boards	
J. Rogge	
MISL Measurements at the NATO BEST TWO (Best Paper Award)	303
Wendell R. Watkins, Samuel B. Crow, Daniel R. Billingsley, Fernando R. Palacios, and Richard W. Dutro	
Operational Efficiency of Different Lasers through Battlefield Effects	313
-- BEST TWO -- July/August '90, France	
Alain Le Dortz	
Reliability of Observer Responses using Inventory Thermal Imagers	314
J. Rogge and LCol D. M. Vonhof	
CCD-Camera Measurements during BEST TWO	315
J. A. Boden and R. J. L. Lerou	
A Simple Transmission Model of Infrared Laser Beam in Low	316
Troposphere: TRANSMIR	
Philippe Bataille	
BEST TWO: The Influence of Cues on the Observer Performance	317
Mogens Caspersen	
Measurements during BEST TWO with a CO ₂ Laser System	318
R. J. L. Lerou	

British Aerospace Acoustic Experiments during the BEST 2 Field Trial 1990 A. R. Tooth	319
Observer Performance Experiments with BEST TWO Thermal Images J. M. Valetton and P. Bijl	328

POSTER AND DEMONSTRATION SESSIONS

Electromagnetic and Acoustic Transmission Posters and Demonstrations

Differences in the LOWTRAN-7 and XSCALE Calculations of Infrared Aerosol Extinction James Williams, Robert Fiegel, and Alan Wetmore	331
Near Infrared Transmittance Variability Edward D. Creegan	341
Illustration of FITTE/FGLOW 4-D Model Output Dorothy Bruce	349
A Novel Approach to Reducing Atmospheric Obscuration Effects on Neural Network Pattern Recognition Donald W. Hooch and John C. Giever	350
Cloud Information Reference Library and Archive (CIRLA) Ronald J. Nelson and Kenneth P. Freeman	360
Spectrally Resolved Transmittance Measurements at Smoke Week XIII (Best Poster) William A. Peterson, Dennis M. Garvey, and William M. Gutman	361
A Synoptic Tactical Smoke Combat Model W. Michael Farmer, Bruce W. Kennedy, and Van R. Jones	371
Visualization and Quantitative Measures of Smoke Plume Intermittency Charles L. Medler and Maureen E. Cianciolo	380
UVTRAN Demonstration James B. Gillespie and Edward M. Patterson	381
COMBIC 92: New and Improved Scarlett D. Ayres	382
Electro-Optical Climatology Version 2.0 Maj. Robert L. Miller	392

Weather Decision Aids Posters and Demonstrations

A Multiple Meteorological Station Version of the BRL General Trajectory Model Abel J. Blanco and Sherrill J. H. Edwards	395
Integrating Battlefield Weather and Terrain Data for IPB through Automated Techniques Gary McWilliams	405

Meteorological Observations, Interpolation, and Tactical Decision Aids Robert R. Lee, Philip Raihl, and Sylvia Cossio	411
TARGAC Demonstration Patti Gillespie	421
PC-Based Beta Site System for AAODL Applications Young P. Yee, Robert A. Sutherland, John Crain, and Liam McDaid	422
WADIF: A Prototype Software System for Fusing Weather and Doctrinal Information Stephen Kirby	431
Tactical Decision Aid Software Design on the ALBE Testbed Computer John B. Spalding and Danforth C. Weems	435

Battle Scale Weather Posters and Demonstrations

Micrometeorological Surface Layer Measurements for Characterization and Model Evaluation Ronald M. Cionco	447
Evaluation of a Coupled Knowledge-Based Nowcasting System for U. S. Army Field Operations Montie Orgill, Robert Sutherland, and John Kincheloe	459
Nowcasting Airflows and Temperature over Complex Terrain by Four-Dimensional Data Assimilation Teizi Henmi	467
Implementation of the Army/Navy Mesoscale Forecast Model on the Integrated Meteorological System James E. Harris and Ronald E. Meyers	476
On the Characterization of Army-Scale Surface Layer Micrometeorology using Field Measurements Brian L. Orndorff and Ronald M. Cionco	486
GIS Mapping of Winter Surface Conditions at Camp Grayling, Michigan Richard K. Haugen, Roy E. Bates, and Andrew J. Bruzewicz	496

Remote Sensing Posters and Demonstrations

A Survey of Artificial Intelligence Techniques used in Processing Meteorological Satellite Data Donald D. Bustamante and Arthur W. Dudenhoeffer	499
A Preliminary Method for Computing Infrared Transmittances in the Troposphere using Satellite Values of Precipitable Water James Cogan	509

Ground Truth Facilities at the U. S. Army Atmospheric Sciences Laboratory for Satellite Environmental Sensors James Cogan, Richard Szymer, and Edward Measure	518
Visioceilometer: A Prototype System to Map Atmospheric Aerosols and Determine Slant Range Visibility R. G. Steinhoff, A. E. Wade, and R. G. Trujillo	525
Cloud Mapping and the Determination of Aerosol Densities along a Line of Sight Ralph G. Steinhoff	535
Statistical Inversion of Temperature Profiles from Microwave Radiometry Measurements when There Are Instrument Errors Dick Larson	536
Personal Computer-Based Codes for Identification by Fluorescence Signature David Rosen, James Klett, and James Gillespie	546
Improving Atmospheric Characterization at the High-Energy Laser Systems Test Facility Kenneth P. Freeman and Robert W. Endlich	554
An In Situ Soil Moisture Sensor for Soil Sensing and Modeling Applications Robert Olsen, René Klein, Harold Ballard, Claude Tate, Robert Hootman, Ronald Atkins, and Roy Bates	562
An Algorithm for the Retrieval of Atmospheric Constituent Concentrations Frank T. Kantrowitz, Daniel R. Billingsley, Fernando R. Palacios, and Wendell R. Watkins	563
Portable Weather Testbed John R. Elrick	573
The Kuwait Smoke Plume as a Source of Battlefield Obscuration Howard Holt, Robert Sutherland, John Grace, S. A. Luces, William Ohmstede, John Barnes, and Kenneth Chin-Purcell	576
Rapid Deployment Imagery Terminal (RDIT) using DMSP Special Sensor Data Thomas L. Harris	587

PBL Energy Budget Posters and Demonstrations

Evapotranspiration and Latent Heat Flux in the Surface Boundary Layer Frank V. Hansen, Henry Rachele, and Arnold Tunick	591
Prediction of Surface and Subsurface Temperatures using a Two-Dimensional Model of Coupled Surface Energy Balance Michael D. DeAntonio	605

BEST TWO Poster

The Battlefield Emissive Source Trials (BEST) Database: Status and Update Roger E. Davis and Patti S. Gillespie	619
---	-----

Attendees	629
------------------	------------

Index by First Author	643
------------------------------	------------

Opening Session

KEYNOTE ADDRESS

**Tuesday Morning
3 December 1991**

**Keynote Speaker
Colonel William H. Campbell**

(The text of the Keynote Address was unavailable at press time.)

Session I

ELECTROMAGNETIC AND ACOUSTIC TRANSMISSION

**Tuesday
3 December 1991**

**Chairperson
Mr. Bob Rubio**

MODTRAN

L.W. Abreu, F.X. Kneizys, G.P. Anderson
and J.H. Chetwynd
Geophysics Directorate
Phillips Laboratory
Hanscom AFB, MA 01731-5000

A. Berk, L.S. Bernstein and D.C. Robertson
Spectral Sciences Inc.
99 South Bedford St.
Burlington, MA 01803

ABSTRACT

MODTRAN is a moderate resolution model and computer code which calculates atmospheric transmittance and background radiance in the microwave, infrared, visible and near ultra-violet spectral regions (0 to 50,000 cm^{-1} or 0.2 μm to infinity). The MODTRAN code was designed to maintain complete compatibility with the LOWTRAN 7 model. Specifically, both codes contain the same model atmospheres, aerosol and particulate models, rain attenuation, spherical refractive geometry routines, clouds (water and ice), and similar routines for calculation of single scattered solar/lunar radiance and irradiance as well as multiply scattered thermal and solar radiance.

1. THE MODTRAN MODEL

The MODTRAN model¹ and computer code is used to predict atmospheric transmittance and background radiance in the microwave, infrared, visible and near ultraviolet spectral regions (0 to 50,000 cm^{-1} or 0.2 μm to infinity). The model is designed to maintain complete compatibility with LOWTRAN 7². Specifically, both codes contain the same six built-in model atmospheres, they utilize identical spherical refractive geometry routines as well as identical interpolation routines. All of the aerosol models, clouds (water and ice), rain attenuation and the single scattered solar/lunar radiance/irradiance options are available. Multiple scattered solar and thermal radiance algorithms^{3,4} are treated in a similar manner in both codes.

The MODTRAN code contains a ten-fold improvement of the standard LOWTRAN spectral resolution; from 20 cm^{-1} to 2 cm^{-1} , full width/half maximum (fwhm) with an option to vary the spectral resolution between 2 and 50 cm^{-1} (fwhm), utilizing a built-in triangular slit function. The band model parameters were formulated from the HITRAN⁵ line atlas for twelve atmospheric gases: H_2O , CO_2 , O_3 , N_2O , CO , CH_4 , O_2 , NO , SO_2 , NO_2 , NH_3 and HNO_3 .

These parameters were calculated for 1 cm^{-1} spectral intervals from $0\text{--}17900\text{ cm}^{-1}$ at 5 temperatures from $200\text{--}300\text{ K}$, all stored on an external data file accessed by the program. This procedure is similar to an earlier effort which created a 5 cm^{-1} option^{6,7} for LOWTRAN 5⁸. Since the 1 cm^{-1} bins are square and non-overlapping, the ideal spectral resolution of MODTRAN is 2 cm^{-1} (fwhm). At larger wavenumbers (beyond the 1986 HITRAN line atlas, over $17,900\text{ cm}^{-1}$) the calculations are performed at the standard LOWTRAN spectral resolution of 20 cm^{-1} .

The molecular transmittance calculation for each bin is performed with an equivalent-width formulation which accounts for the finite spectral width of each interval and the number of lines contained within each 1 cm^{-1} bin. LOWTRAN 7 uses a one parameter band model (absorption coefficient) plus molecular density scaling functions. The MODTRAN approach relies on three temperature-dependent parameters; an absorption coefficient, a line density parameter and an average line width.

The absorption due to line centers, within the 1 cm^{-1} bins, is modeled separately from the absorption due to the line tails. The absorption due to lines within each bin is calculated by integrating over a Voigt line shape⁹. The line tail parameters consist of tail contributions from lines within $\pm 25\text{ cm}^{-1}$. The line tail absorption coefficient band model parameters are determined by integrating over all the Lorentzian line tails contributing to a bin.

The Curtis-Godson^{10,11} approximation, considered accurate for moderate temperature variations existing within the earth's atmosphere, is used to replace the multi-layered paths by an equivalent homogeneous one.

The k- distribution method from the LOWTRAN 7 multiple scattering algorithms (used for averaging over large spectral intervals), is not required in the MODTRAN code. Three monochromatic k-values are used for the 5 cm^{-1} averages of LOWTRAN 7, while the 1 cm^{-1} MODTRAN steps produce an equivalent accuracy within the multiple scattering calculations.

2. COMPARISONS WITH FASCOD3 AND SHARC-2

A comprehensive comparison between FASCOD3¹² and MODTRAN has been completed. The two codes were compared at the same resolution in 500 cm^{-1} segments at various altitudes for horizontal paths of widely varying ranges. Table 1 is representative of the data in this comparison. The mean transmittance, mean difference and standard deviation for each altitude at various temperatures in 500 cm^{-1} segments is displayed. These calculations were made in the spectral range of $0\text{--}17900\text{ cm}^{-1}$ (the extent of the 1986 HITRAN Data Base).

The spectra displayed in Figure 1 is calculated for $1400\text{--}2600\text{ cm}^{-1}$ for a path from 10 to 20Km looking straight up. The MODTRAN resolution is 2 cm^{-1} (fwhm) while the LOWTRAN 7 resolution is 20 cm^{-1} (fwhm).

Figure 2 is a comparison among LOWTRAN 7, MODTRAN and FASCOD3 for the same path as shown in Figure 1. The spectral range is reduced to between 2000-2100 cm^{-1} . LOWTRAN 7 and MODTRAN are at the same resolution as in Figure 1 while FASCOD3 is calculated monochromatically.

Radiation from the H_2O pure rotational spectra from 400-500 cm^{-1} along a 60 Km limb path is shown in Figure 3. This comparison is between MODTRAN and SHARC-2¹³. The SHARC-2 calculations are normally performed for NLTE (non-local thermodynamic equilibrium) from 50-300 Km. However, this spectral region is essentially LTE and H_2O rotations are treated as LTE in SHARC-2, hence the excellent comparison for the two calculations.

Figure 4 shows a calculation performed at the nominal LOWTRAN 7 resolution of 20 cm^{-1} (fwhm) for an 8 Km range at the surface with 20 gm/m^3 of H_2O . The three codes, LOWTRAN 7, FASCOD3 and MODTRAN are run for the spectral range of 2500-3000 cm^{-1} .

Figure 5 depicts MODTRAN predictions for the single and multiple scattered solar radiance in the spectral region from 0.3 to 0.7 μm . The line of sight path for this calculation is 20 Km to the surface with the surface albedo set to 0.4 and the solar zenith angle set equal to 60.

3. AVAILABILITY

The MODTRAN computer code is available through the:

National Climatic Data Center, NOAA
Federal Building
Asheville, NC 28801

DoD organizations and other government agencies may apply directly to:

L.W. Abreu
Phillips Laboratory/GPOS
Hanscom AFB, MA 01731-5000

The MODTRAN package contains the Source Code, data base file, sample input and output files as well as a filter function package and a scanning function package (each containing source code and sample input & output files).

4. FUTURE MODIFICATIONS

An improved multiple scattering algorithm based on the Discrete-Ordinate-Method is presently being implemented in MODTRAN. This will improve the accuracy of the calculations for low sun angles, specifically for cloudy atmospheres. A world-wide data base of vertical atmospheric profiles for 10 degree latitude/longitude blocks will be accessible to the code.

In a separate effort, MODTRAN will be integrated with another code; APART¹⁴, Atmospheric Propagation and Radiative Transfer Computer Code (version 7.00). The result of this integration will produce a code with spectrally dependent backgrounds, numerous modeled background materials and the inclusion of variable amounts of cloud cover. In this same effort the geometry routines will be modified to correct for some machine dependent errors found on various 32 bit machines.

5. REFERENCES

1. Berk, A., Bernstein, L.S., and Robertson, D.C. (1989) MODTRAN: A Moderate Resolution Model for LOWTRAN 7, GL-TR-89-0122, AD A214337
2. Kneizys, F.X., Shettle, E.P., Abreu, L.W., Anderson, G.P., Chetwynd, J.H., Gallery, W.O., Selby, J.E.A., and Clough, S.A. (1988) Users Guide to LOWTRAN 7 AFGL-TR-880177, AD A206773
3. Isaacs, R.G., Wang, W-C., Worsham, R.D., and Goldenberg, S. (1986) Multiple Scattering Treatment for use in the LOWTRAN and FASCODE Models, AFGL-TR-86-0073, AD A173990
4. Isaacs, R.G., Wang, W-C., Worsham, R.D., and Goldenberg, S. (1987) Multiple Scattering LOWTRAN and FASCODE Models, Appl. Opt. 26: 1272-1281.
5. Rothman, L.S., Gamache, R.R., Goldman, A., Brown, L.R., Toth, R.A., Pickett, H.M., Poynter, R.L., Flaud, J.M., Camy-Peyret, C., Barbe, A., Husson, N., Rinsland, C.P., and Smith, M.A.H., The HITRAN Database: 1986 Edition, Appl. Opt., 26: 4058 (1987)
6. Robertson, D.C., Bernstein, L.S., and Haimes, R., Addition of a 5 cm⁻¹ Spectral Resolution Band Model Option to LOWTRAN 5, ARI-RR-232, Aerodyne Research Inc., Billerica, MA (1980)
7. Robertson, D.C., Bernstein, L.S., Haimes, R., Wunderlich, J., and Vega, L., 5 Cm⁻¹ Band Model Option to LOWTRAN 5, Appl. Opt., 20, 3218 (1981)
8. Kneizys, F.X., Shettle, E.P., Gallery, W.O., Chetwynd, J.H., Abreu, L.W., Selby, J.E.A., Fenn, R.W., and McClatchey, R.A., Atmospheric Transmittance/Radiance: Computer Code LOWTRAN5, AFGL-TR-80-0067, (1980), AD A088215
9. Ludwig, C.B., Malkmus, W., Reardon, J.E., and Thomson, J.A.L., Handbook of Infrared Radiation from Combustion Gases, NASA Report SP-3080 (1973)
10. Curtis, A.R., Q.J.R. Meteorol. Soc., 78, 165 (1952)

11. Godson, W.L., J. Meteorol., 12, 123 (1955)
12. Clough, S.A., Kneizys, F.X., Anderson, G.P., Shettle, E.P., Chetwynd, J.H., Abreu, L.W., Hall, L.A., and Worsham, R.D. FASCOD3: Spectral Simulation, IRS 88 Lenoble and Geleyn (Eds.) Proc. of the Inter. Radiation Symposium, Lille, France, 372 (1988)
13. Sharma, R.D., Sundberg, R.L., Bernstein, L.S., Healey, R.J., Gruninger, J.H., Duff, J.W., and Robertson, D.C. Description of SHARC-2, The Strategic High-Altitude Atmospheric Radiance Code, PL-TR-91-2071, AD A239008
14. Cornette, W.M., Atmospheric Propagation and Radiative Transfer (APART) Computer Code (version 7.00), R-024-90, Photon Research Associates Inc., San Diego, CA (1990)

Table 1. A Comparison between MODTRAN and FASCOD3 for horizontal paths at various altitudes and temperatures of 200-300 K.

		MODTRAN		FASCOD3			
FREQ(CM ⁻¹)	ALT(KM)	T (K)	RANGE(KM)	MEAN TR	MEAN TR	MEAN DIF	STAND DEV
0-500	45	200	500000	.61717	.71211	.09494	4.93700E-3
	30	200	5000	.63104	.65932	.01228	5.05750E-4
	30	300	5000	.71573	.71211	.00457	2.69319E-5
	15	300	10	.83113	.83315	.00003	6.04105E-5
	15	275	10	.87833	.87309	.00033	2.61406E-5
	15	250	10	.87291	.87207	.00084	2.77936E-5
	15	225	10	.86576	.86513	.00063	4.90320E-5
	15	200	10	.85955	.85537	.00278	1.14533E-4
	0	300	.005	.44175	.44270	.00095	2.78843E-4
	0	275	.005	.43219	.42703	.00315	1.83705E-5
	0	250	.005	.42247	.41373	.00859	3.15083E-4
	0	225	.005	.41293	.39513	.01581	5.35519E-4
	0	200	.005	.40193	.37459	.02724	6.52214E-4
500-1000	60	300	5000000	.72815	.65373	.07443	8.56086E-3
	45	300	500000	.59773	.53755	.05818	3.29788E-3
	30	300	5000	.62821	.58147	.04674	4.59872E-3
	30	260	5000	.65704	.61793	.03905	6.05537E-3
	15	300	500	.53123	.51777	.01326	3.53059E-3
	15	300	10	.79876	.78273	.01573	4.57932E-4
	15	260	500	.57125	.56230	.00844	4.04507E-3
	15	260	10	.81105	.80050	.01055	2.67364E-4
	0	300	1	.51721	.51560	.00151	4.55383E-4
	0	260	1	.49037	.48749	.00319	3.36036E-4

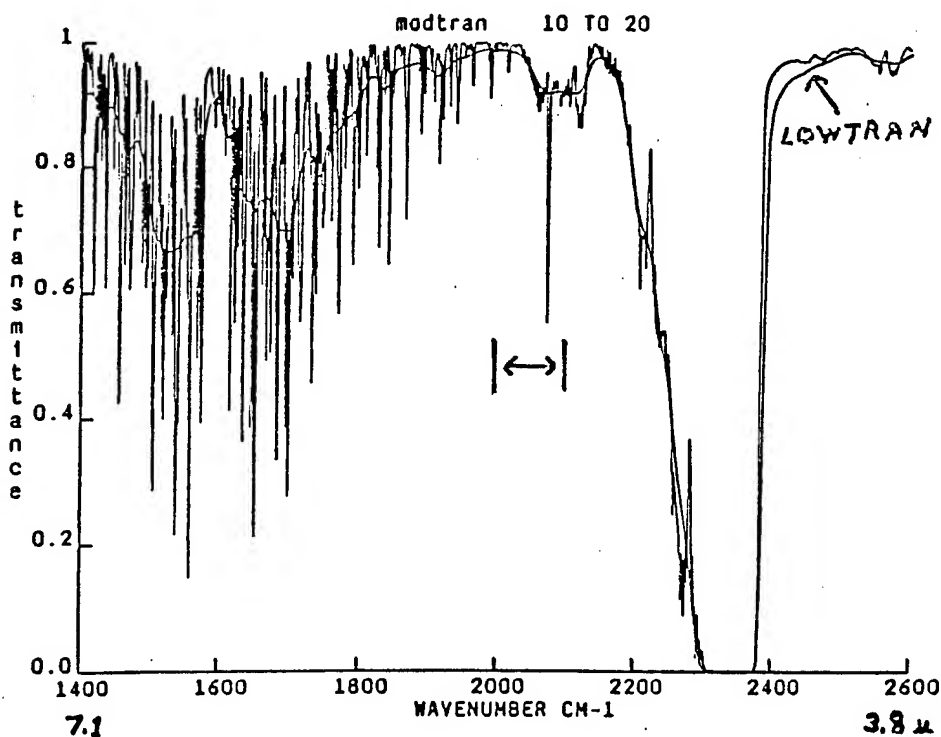


Figure 1. Transmittance calculated by MODTRAN and LOWTRAN 7 for a vertical path from 10 to 20 Km at 2 cm⁻¹ and 20 cm⁻¹ resolution respectively.

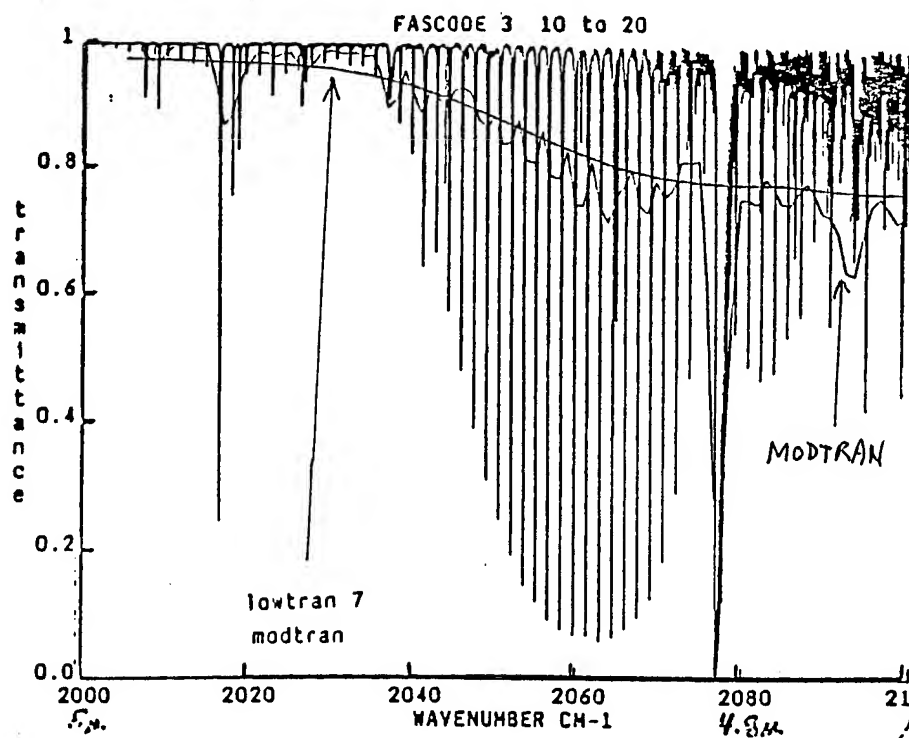


Figure 2. A reduced spectral range of Figure 1 (2000-2100 cm^{-1}) with the addition of a FAS-COD3 run. each code is calculating transmittance at its prime resolution.

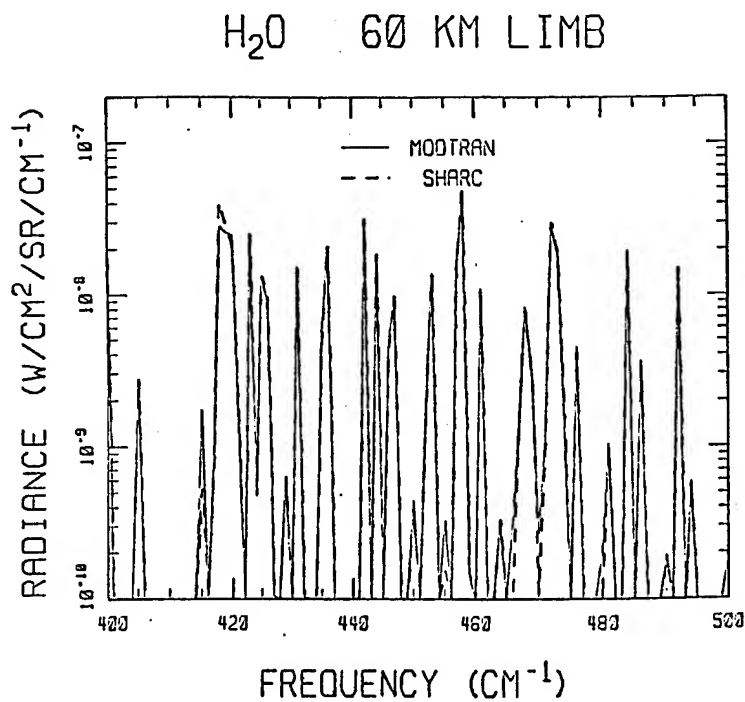
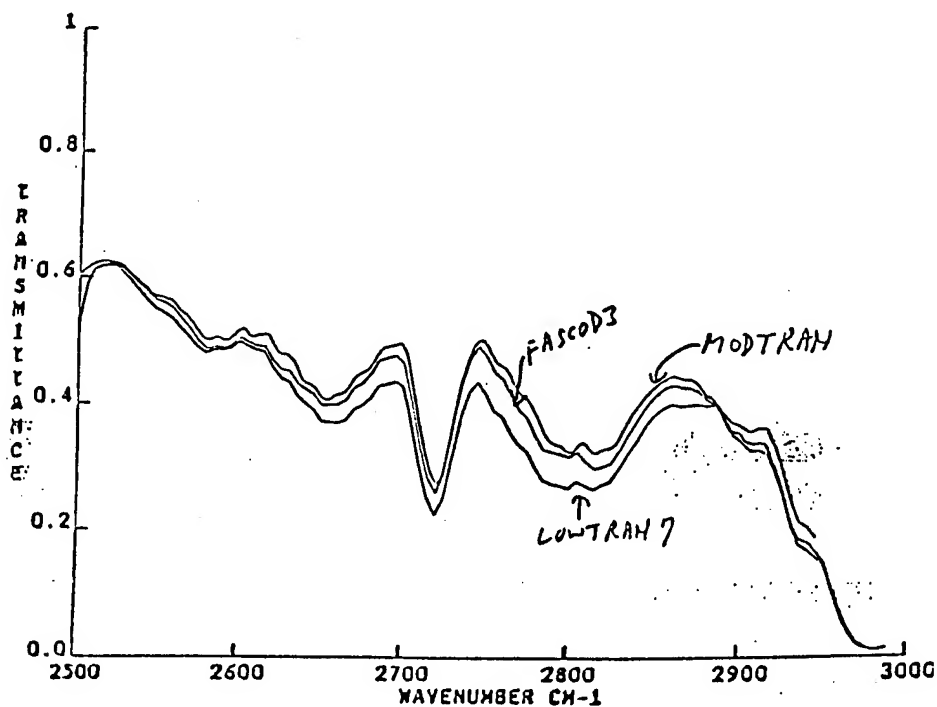


Figure 3. Calculations from MODTRAN and SHARC-2 for a 60 Km limb path of H_2O rotations.



Range 8km at SFC 20 gm/m³ H₂O

Figure 4. A horizontal path at the surface with a range of 8 km and 20 gm/m³ of H₂O. The calculations of each code are performed for the standard LOWTRAN 7 resolution of 20 cm⁻¹ (fwhm).

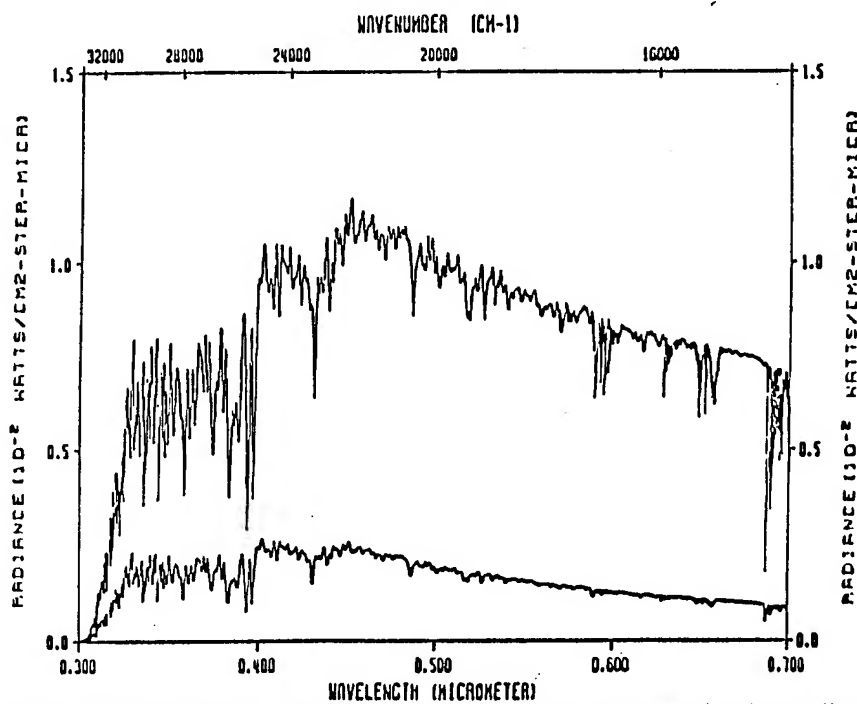


Figure 5. MODTRAN predictions of single and multiple scattered solar radiance. The path for this calculation is from 20 Km, the surface albedo is 0.4 and the solar zenith angle is 60. The upper line is the total multiple scattered radiance and the lower line shows the single scattered solar radiance contribution.

XSCALE 92

Robert P. Fiegel
U.S. Army Atmospheric Sciences Laboratory
White Sands Missile Range, NM 88002-5501 USA

ABSTRACT

The XSCALE 92 module contains the following enhancements over XSCALE 87: a vertical profile for blowing snow, a desert aerosol model, and an allowance for transmission path endpoints above the surface for the rural, urban, maritime, fog, and blowing snow aerosols that have a vertical profile calculation. XSCALE has been tested against measurements of fogs and the rural, urban, and maritime hazes; along horizontal paths for visible and infrared (IR) wavelengths; and along slant paths for 0.55 μm . The snow model has been independently tested along horizontal paths. XSCALE successfully predicts measured values for the above cases. XSCALE predictions are marginal for combined aerosols such as fog and haze or haze and rain, and for the IR profile within a cloud. Untested aerosol models are the desert aerosol, rain, ice fog, and blowing snow. These tests show that the single most important input value is the visibility, a quantity very difficult to measure precisely. This in turn leads to the caveat that the 0.55- μm extinction depends on the visibility through the Kochmeider relation, and further that the IR extinction is scaled by the 0.55- μm extinction. The XSCALE FORTRAN program has also been improved. Nearly all the variables have default values assigned, only the wavelength of interest and the visibility need to be input. All the input values are checked for impossible values, some cross-checking is done. The user is notified of the unacceptable values and the acceptable range. The input/output statements have been gathered into a separate subroutine. We believe this makes the code more accessible to users. The XSCALE program can also be easily called as a subroutine from another program, the I/O subroutine can be bypassed and its code dropped in this case.

1. INTRODUCTION

XSCALE 92 contains one new model, the desert aerosol model, and an extension of the blowing snow model to include an altitude dependence. A user may specify path endpoints above ground level for any aerosol model that includes a vertical dependence calculation.

Since its inception XSCALE predictions of extinction and transmittance have been compared to corresponding measurements in the visible and IR for horizontal paths through hazes, fogs, rain, and snow. Slant path predictions for visible wavelengths have been compared to measurements taken below, within, and above stratus clouds. A few visible measurements have been taken within and above inversion layers. Comparisons with slant path IR extinction (or transmittance) measurements are few for any type of aerosol. Aside from the empirical measurements on which the models are based, the desert, icefog, and blowing snow aerosols are essentially untested. As discussed below, XSCALE predictions are usually quite good. Disagreement between a model and a measurement can often be traced to an attempt to use XSCALE to model a situation that it is not designed for. Such situations include mixed aerosols like fog and rain or multiple cloud layers.

The value of the surface visibility has the greatest impact of any input value on the predictions of all the aerosol models. This is because the visible extinction depends on the visibility, and in turn the IR extinction depends on the visible extinction. Of course, the transmittance over a path depends on the extinction along the path. The visibility is the most difficult input value to measure accurately and consistently.

The FORTRAN code for XSCALE 92 has also been improved. All the input values have an associated default value, except for visibility and wavelength. These two come to XSCALE from the EOSAEL executive program. XSCALE checks that each input value is within an acceptable range. A few values are checked against one

another. The user is notified and program execution halts when an inappropriate input value is found. All input values that the program uses are written to output, default values are labeled as such. All input and output statements have been gathered into a single subroutine. This will allow the easy elimination of unwanted I/O statements if XSCALE is used as a subroutine in a user written program.

2. ENHANCEMENTS

The desert aerosol model of Longtin, Shettle, Hummel, and Pryce (1988) has been incorporated as aerosol index 6. As with the other XSCALE models, the predictions correspond to a generic desert aerosol. Many possible variations of composition, shape, and particle size distribution are neglected to provide a model acceptable for most situations and dependent on easily observed parameters. A complete description of the XSCALE implementation can be found in the 1992 XSCALE User's Guide (Fiegel, 1991).

The XSCALE desert air mass is made up of three components, each having a different log-normal particle size distribution and indices of refraction. The three components are carbonaceous particles, water soluble particles, and sand. The sand itself has two components. Half the sand by number is particles of pure quartz, and half is quartz contaminated by 10% hematite. The sand component alone depends on windspeed. The XSCALE inputs for this model are the aerosol index (6.0), visibility, wavelength, windspeed, and horizontal path length. Although in reality the particle sizes depend on humidity, the Longtin model does not, and so the XSCALE model does not.

The desert aerosol model is implemented in the same manner as the hazes and fogs. A data statement loads the extinction and absorption values at 31 wavelengths and 4 windspeeds into two arrays. Linear interpolation is used to find the relative extinction (and absorption) at the specified wavelength and windspeed. The relative extinction is then scaled by the visible extinction (obtained from the visibility) to give the prediction value.

The XSCALE 87 User's Guide (Duncan *et al.*, 1987) contains a description for the vertical dependence of blowing snow. This is an extension of the blowing snow model at ground level. The ground level extinction depends on the detection wavelength, the detector radius, the path length, the surface temperature, and the windspeed. A power law of the altitude, in the form of Z^{-a} , scales the surface value of the extinction to that at height Z . The exponent a depends on constants and the surface windspeed. The expression for extinction as a function of altitude can be integrated analytically. The analytic expression is programmed within XSCALE, a numerical integration is unnecessary. Consequently the vertical profile is not calculated and thus cannot be printed out. The input values needed for an inclined path through blowing snow are: aerosol index (10.0), wavelength, visibility, detector radius, surface temperature, windspeed, path length, and elevation of one or both path endpoints.

The XSCALE 87 program is only capable of computing a slant path if one of the path ends lies at the surface, and a horizontal path only at the surface. XSCALE 92 allows both endpoints to be elevated, even by the same amount, for any aerosol model that includes a vertical dependence. The input values that specify the path are horizontal distance, altitude of one endpoint, slant distance, and path elevation angle (positive or negative). The use of these values is described in chapter 4 of the XSCALE 92 User's Guide (Fiegel, 1991).

3. MEASUREMENTS

Details of the XSCALE tests are given in chapter 3 of the XSCALE 92 User's Guide (Fiegel, 1991). The following is a brief description of the XSCALE models tested and the primary results. XSCALE is for the most part based on empirical models, as such each model has been developed to mimic closely at least one set of real world data. Tests independent of the empirical basis are discussed in this section.

3.1 PREVIOUS TESTS

Avara's (1985) study compared the climatological average transmittance to the transmittance calculated by XSCALE using the climatological meteorology as inputs. Since only average visible transmittance was

considered, not transmittance for specific cases, this was not a very strict test.

Burlbaw (1985) compared measurements of the visible transmittance along a slant path to XSCALE predictions. XSCALE predictions are sensitive to the cloud ceiling height and surface visibility. Both values depended on a human observer, they were not instrumental measurements in this test.

Hoidale (1985) compared tower-based visibility measurements to XSCALE slant path transmittances in the visible. For the sub-cloud case modeled by XSCALE, agreement was very good. Several occurrences were noted in which the extinction decreases, these were primarily for "high" clouds. XSCALE does not model this situation.

Schulze (1986) examined the Sprakensehl data set (the same used by Hoidale, (1985)) for the frequency of occurrence of episodes of decreasing visible extinction with height. Such episodes predominate for high ceiling, moderate (2 to 6 km) surface visibility situations. Such episodes should serve to remind the user that XSCALE (as any model) will not model all real world situations. The Sprakensehl data suggests that often a thin haze layer may occur under a cloud layer. Such an occurrence would result in constant extinction near the surface, then decreasing extinction above the haze (near the tower top), and finally increasing extinction as the cloud is approached.

Shirkey and Hutt (1985) and Hutt and Shirkey (1987) compared visible measurements of transmittance through snow and fog with XSCALE calculations. The agreement at visible wavelengths was very good, but less so at IR wavelengths. An adjustment to the model was suggested, but such an adjustment has not yet been implemented in XSCALE 92.

Gillespie (1987) compared XSCALE horizontal path calculations to visible and IR transmissometer measurements through fog, haze, and rain during the BEST-ONE test. Agreement was spotty, occasionally good, and often poor. There are three reasons for the disagreement.

1. Many trials were modeled as an advection fog; only one trial had a visibility that XSCALE recognizes as advection fog. For visibility greater than 0.55 km, a radiation fog model should be used.
2. In only one trial does the human estimate of visibility agree with the transmissometer measured visibility. The transmissometer always measured a higher visibility than that recorded by the observer. If the transmissometer visibility were used as the XSCALE input, the agreement would improve.
3. IR extinction is sensitive to the air mass; and which air mass to employ was uncertain. All the BEST-ONE trials used in this comparison were composed of multiple aerosols: fog, drizzle, maritime, and urban haze. XSCALE does not deal with multiple aerosols.

3.2 TESTS SINCE 1987

3.2.1 Vertical profile model and Sprakensehl visible extinction

All the extinction profiles and any associated data from one measurement program will be termed a data set. The data making up a single measured extinction profile will be termed a data block, or a measured profile.

Fiegel (1990a) compared the XSCALE visible vertical profile model to tower measurements made at Sprakensehl, Germany. This data set has been classified into different types of episodes (Hoidale, 1986). An episode is a continuous span of time during which low visibility was recorded at the tower. Episodes showing low visibility (less than 1 km) at the surface and high visibility at the top of the tower were studied. These episodes were selected so that the tower would span the entire low visibility region and the air just above. These thus provide a test of the model in the overlaying clear air region as well as a test of the model in the low visibility region. These episodes ranged in duration from 2 to 40 hours (Hoidale, 1986); the low visibility region was from 9 to 225 m thick.

The vertical extinction profile depends on the ceiling height, cloud thickness, inversion height, and on the value of the surface extinction. During analysis of these data, the clear air extinction value above the low visibility region was also a model input. The ceiling height is calculated by linear interpolation between the data points to find the altitude at which the extinction is 7 km^{-1} or greater. Measured surface extinction

and the "upper-air" extinction are taken to be the extinctions at 2 m and 300 m, respectively. The reduced chi-square, χ_r^2 , was computed to measure the agreement between model and measurement. The cloud top or inversion layer heights were determined to minimize the subsequent χ_r^2 value of the model profile and data block.

In this study a block was said to represent an inversion layer (for instance) if the reduced chi-square was less than that for the low cloud/fog case. The Atmospheric Aerosol and Optic Data Library (AAODL) has 1066 blocks of data for 17 different episodes of this type. The ceilometer recorded an average ceiling less than 300 m for 733 of these blocks, the remaining blocks were not considered in this study. Of the 733 low ceiling blocks, 293 represent the XSCALE low cloud/advection fog profile and 119 represent the inversion/radiation fog profile. The remaining 321 blocks included 127 blocks with missing data that were considered, and 194 profiles that were not well modeled by XSCALE 92.

Low clouds/fogs gave the following results. For these data blocks the most common thickness is only 80 m, many blocks (~50) evidence a cloud less than 30 m thick. The previous XSCALE default was 200 m. The default has been changed to 100 m. This frequency distribution highlights the danger of using the model default value for all runs.

XSCALE employs clear air extinction above clouds, the model default is 0.030 km^{-1} . The most commonly measured extinction was 0.075 km^{-1} , this is the limit of the visibility meters used for the measurements. A very broad range of greater extinctions were measured at a significant frequency of occurrence, suggesting that clear air is not always immediately above fogs or cloud tops.

For many applications the most important question is whether XSCALE calculates a reasonable transmittance. Figure 1 shows the path transmittance (from 2 to 300 m) calculated from the measured visibilities compared to the path transmittance determined by the XSCALE extinction profile at the tower stations. In almost every case the transmittance agrees to within the measurement uncertainty, as shown by the error bars overlapping the slope 1 line. The most frequent transmittance was about 10%.

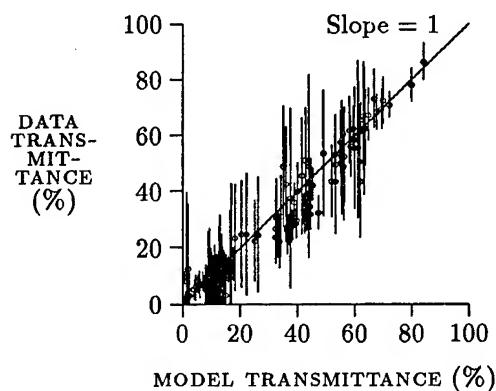


Figure 1. Low cloud/fog measured versus calculated transmittances. Transmittances determined from the measured visibilities (y -axis) versus transmittance calculated from the model extinction (x -axis). The line has slope 1.

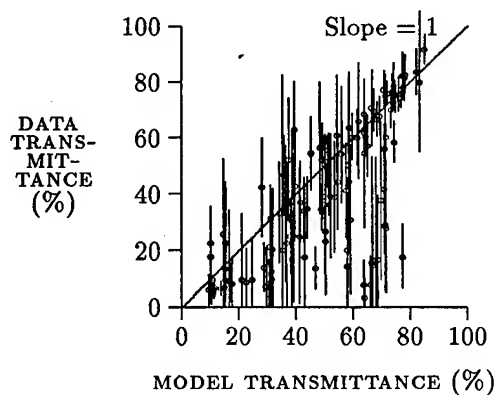


Figure 2. Inversion measured versus calculated transmittances. Transmittances determined from the measured visibilities (y -axis) versus transmittance calculated from the model extinctions (x -axis). The line has slope 1.

Two representative data blocks are shown – one demonstrating good agreement ($\chi_r^2 = 1.0$) (fig. 3), and one marginal agreement ($\chi_r^2 = 2.0$) (fig. 4). Both figures illustrate a difficulty in the data, the calculation of z_C and the selection of z_T places a cloud between two of the observation levels. Since both the data and model transmittance are calculated from extinction at the six tower platforms, they agree with each other. However, had XSCALE been run for these parameters along a continuous path, a much lower transmittance would have been found. The few measurement altitudes in each data block severely restrict any conclusions that may be drawn from this data.

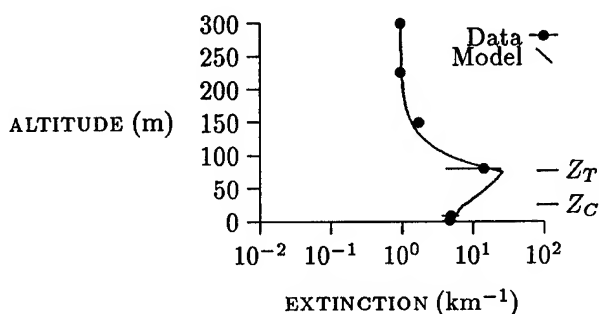


Figure 3. Low cloud profile, $\chi_r^2 = 1.0$, transmittance calculated from the data is $23 \pm 19\%$, from the model 18% . The measured ceiling is 35 ± 8 m, the calculated ceiling is 25 m, the cloud top is at 76 m.

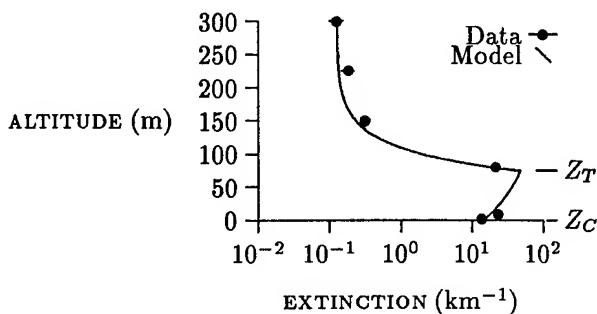


Figure 4. Advection fog profile, $\chi_r^2 = 2.0$, transmittance calculated from the data is $8 \pm 3\%$, from the model 11% . The measured ceiling is 10 ± 8 m, the calculated ceiling is 0 m, the cloud top is at 75 m.

Radiation fogs/inversion layers gave the following results. Figure 5 shows the frequency distribution the extinction at 300 m in 0.025 km^{-1} steps. The most common extinction is 0.075 km^{-1} , the upper limit of the visibility meters. Again, higher extinction values were found suggesting other than clear air above this layer.

The most likely inversion height found was approximately 170 m, although other heights were quite common. The XSCALE default height was 200 m, underestimating transmittance by approximately 15% . Thin layers, of heights less than 100 m, are also quite common. The XSCALE default has been changed to 100 m, again no one default should be used always.

Figure 2 compares the transmittance calculated from the measured visibilities with that calculated from the XSCALE profile. Most of the points lay along the slope 1 line; however, many points show that XSCALE overestimates the transmittance.

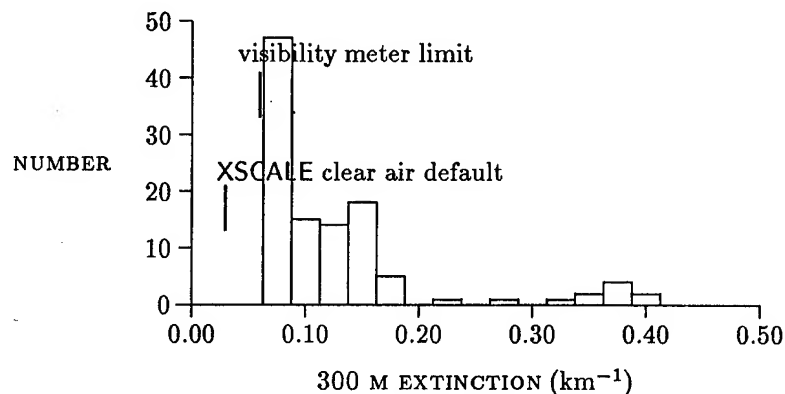


Figure 5. Frequency distribution of the upper air extinction in steps of 0.025 km^{-1} for inversion layer cases.

3.2.2 Vertical profile model and Meppen, Cardington, Sprakensehl visible extinction

Fiegel (1990b) compared data from three separate measurement programs to the XSCALE vertical profile model visible extinction predictions. The earliest set is from the Meppen 1980 measurement program (Lindberg *et al.*, 1984). A tethered balloon carried particle counters between the surface and approximately 750 m. The flights occurred during November and December. The Cardington set is from tethered balloon flights near Cardington, England, in January and February 1983 (Lindberg, 1984). The Sprakensehl data

(1983–1985) was described in section 3.2.1.

As a measure of the agreement between the model and measurements, the reduced chi-squared, χ_r^2 , was computed. Unlike the previous study, the clear air extinction value was not adjusted to minimize χ_r^2 . Also only very poor or incomplete data blocks were discounted, all others were modeled. Thus, the χ_r^2 values are higher. Figure 6 shows the frequency distribution of χ_r^2 for the fog/low cloud data sets. Note that, the Meppen data result in values less than or near 10.0, while the Sprakensehl data show values of approximately 30. The reason for the large Sprakensehl values can be traced to the visibility meters used. The upper limit of these meters is 50 km; the XSCALE profile above a cloud quickly approaches a value of 100 km. One or two points out of six with this much difference will easily result in a χ_r^2 value of 30. The Cardington set results in high χ_r^2 due to multiple layers found in the larger altitude range (~ 1300 m) covered.

Figure 7 shows a similar frequency distribution for the haze layer data sets. Here the Meppen data also show large χ_r^2 . Above a haze layer the particle counters frequently obtained a particle size distribution reflecting clearer air, but not as clear as that measured above clouds.

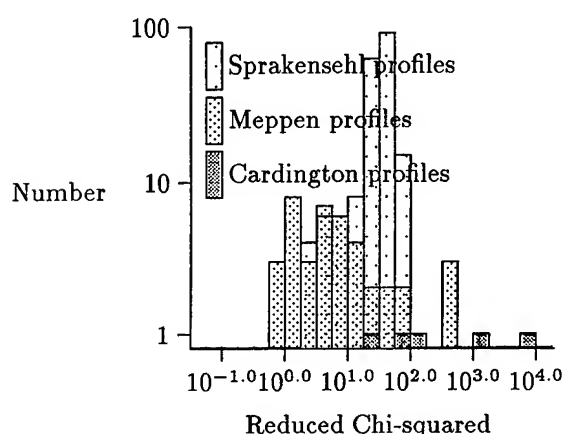


Figure 6. Frequency distribution of χ_r^2 between measured and XSCALE cloud profiles.

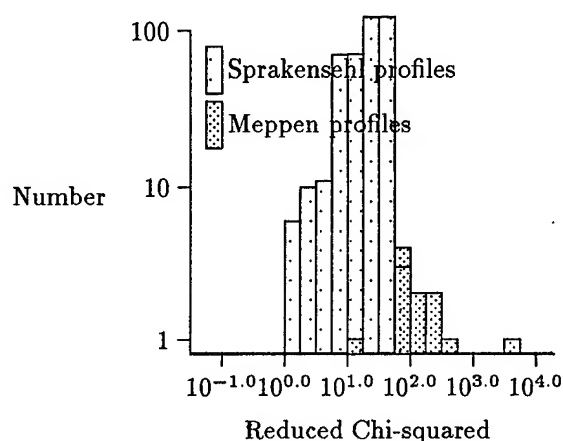


Figure 7. Frequency distribution of χ_r^2 between measured and XSCALE inversion profiles.

Figures 8 through 17 show representative data sets and XSCALE calculated profiles that contributed to the above χ_r^2 frequency distributions. Data sets reflecting both low and high χ_r^2 values are shown from the Meppen, Cardington, and Sprakensehl measurement programs. Figures 8 through 13 show fog/low cloud occurrences; figs. 14 through 17 show inversion samples. While at any particular altitude the agreement between the measured and the XSCALE profile may be poor, overall the agreement is quite good as reflected by the transmissions, noted on the graphs by T_{data} and T_{xscale} for transmission calculated directly from the data and from the XSCALE profile for each data block. Even the very high χ_r^2 of fig. 9 appears to be a quite reasonable fit. This large χ_r^2 value arises from low uncertainty in the points, a cloud profile not quite identical with that of XSCALE, and above cloud extinction greater than that of the clear air profile.

As noted above, the predictions depend critically on surface visibility, cloud ceiling height, and cloud thickness. Approximately one-fourth of the Sprakensehl profiles exhibited structure that is not modeled by XSCALE. These structures appear to be multiple layers such as a ground haze under clear air under a cloud or a low cloud under a haze layer under clear air. The Sprakensehl data are not spatially dense enough to be certain of this however.

3.2.3 Vertical profile model and Meppen IR extinction

Rachele and Kilmer (1990) compared the IR extinction calculated from the particle size distributions taken during three balloon flights of the Project Meppen 80 with the XSCALE vertical structure algorithm and their own similarity theory model. Reasonable agreement was found for visible and 3 to 5 μm transmittance;

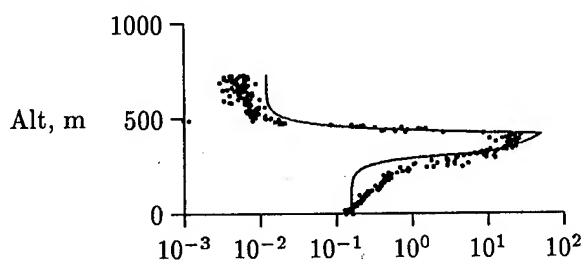


Figure 8. Meppen flight 1 and XSCALE profile. $T_{data} = 9 \pm 4\%$, $T_{xscale} = 4\%$, and $\chi_r^2 = 360$.

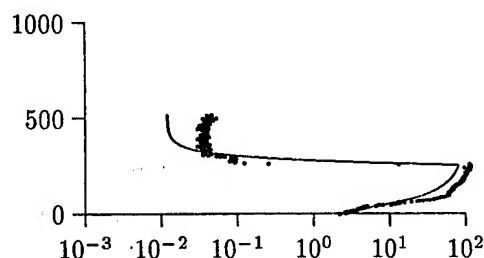


Figure 9. Meppen flight 7 and XSCALE profile. $T_{data} = (9 \pm 6) \times 10^{-6}\%$, $T_{xscale} = 2 \times 10^{-3}\%$, and $\chi_r^2 = 16000$.

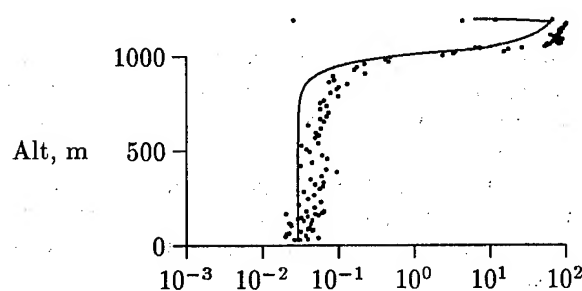


Figure 10. Cardington flight 5 and XSCALE profile. $T_{data} = (0.9 \pm 1.4) \times 10^{-3}\%$, $T_{xscale} = 0.38\%$, and $\chi_r^2 = 82$.

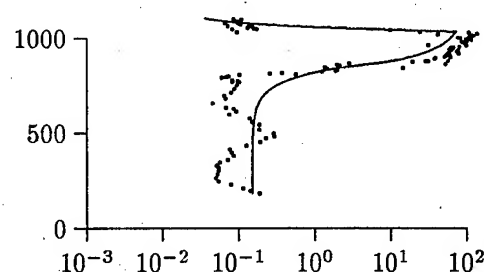


Figure 11. Cardington flight 27 and XSCALE profile. $T_{data} = (4 \pm 9) \times 10^{-4}\%$, $T_{xscale} = 0.07\%$, and $\chi_r^2 = 1500$.

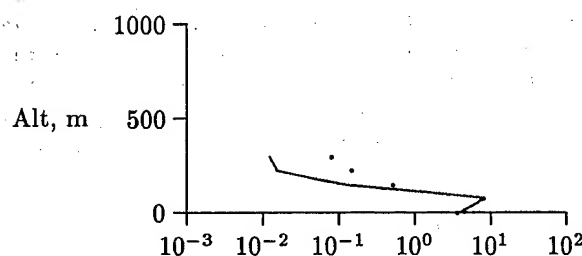


Figure 12. Sprakensehl block 14 and XSCALE profile. $T_{data} = 44 \pm 13\%$, $T_{xscale} = 46\%$, and $\chi_r^2 = 3$.

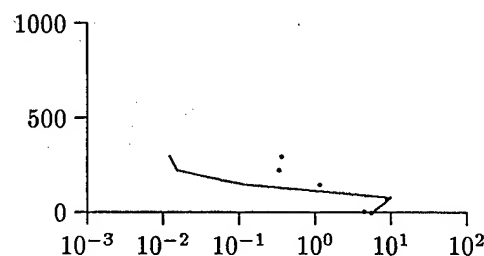


Figure 13. Sprakensehl block 926 and XSCALE profile. $T_{data} = 39 \pm 20\%$, $T_{xscale} = 38\%$, and $\chi_r^2 = 35$.

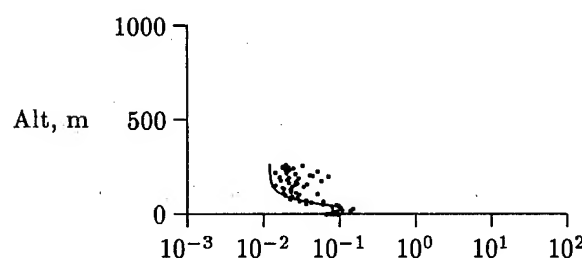


Figure 14. Meppen flight 89 and XSCALE profile. $T_{data} = 99 \pm 0.2\%$, $T_{xscale} = 99\%$, and $\chi_r^2 = 16$.

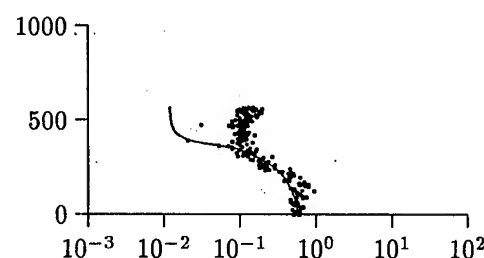


Figure 15. Meppen flight 53 and XSCALE profile. $T_{data} = 83 \pm 2\%$, $T_{xscale} = 87\%$, and $\chi_r^2 = 150$.

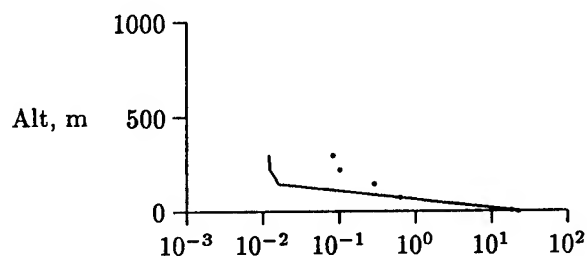


Figure 16. Sprakensehl block 735 and XSCALE profile. $T_{data} = 41 \pm 10\%$, $T_{xscale} = 38\%$, and $\chi_r^2 = 16$.

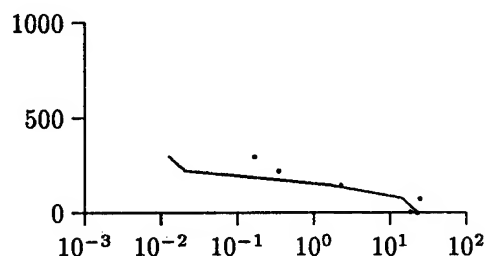


Figure 17. Sprakensehl block 790 and XSCALE profile. $T_{data} = 6 \pm 3\%$, $T_{xscale} = 12\%$, and $\chi_r^2 = 30$.

however, XSCALE greatly overestimated the 8 to 12 μm transmittance for these three profiles. These three flights make for a very limited test of the IR profile.

The Project Meppen 80 balloon flight data sets were reviewed. Thirty-three data blocks, each representing one flight and representative of low stratus or fog conditions were examined. These data are measured particle size distributions that have been reduced and tabulated for extinction at 0.55, 1.06, and 10.6 μm as a function of altitude. XSCALE calculations were made for these profiles at these three wavelengths. The reduced data and XSCALE results in the cloud layer were plotted for comparison; the visible and 1.06 μm profiles show very good agreement. The 10.6 μm in-cloud profiles show agreement that varies, often XSCALE overestimates the extinction, although sometimes it underestimates or gives good agreement. Figures 18, 19, and 20 consolidate all 3×33 comparisons onto three histograms.

An average measured-to-modeled extinction ratio was calculated for each profile and wavelength by finding the ratio at each altitude within the cloud and then averaging for each profile. The histograms show the number distribution of these profile averages at the three wavelengths—fig. 18 at 0.55 μm ; fig. 19 at 1.06 μm ; and fig. 20 at 10.6 μm . This ratio is centered on 1.0 for the 0.55 and 1.06 μm distributions, suggesting that the model and data agree. The 10.6 μm distribution, however, shows a larger spread of values. The mean and standard deviation is 0.68 and 0.46, the median is 0.62. This suggests that XSCALE generally overestimates the 10.6 μm extinction. This is a limited data set made up of low, wintertime, German stratus clouds. The distribution is broad; it includes 1.0 and shows no clear peak. Since the data are limited and the disagreement neither well-defined nor very bad, XSCALE will not be changed at this time. A broader data base or a particle size distribution specifically designed for stratus clouds are needed to justify a change.

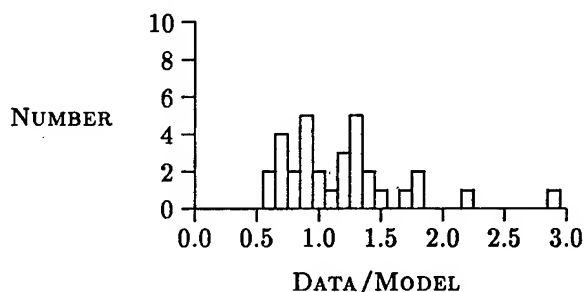


Figure 18. Data to model extinction ratio at 0.55 μm . Frequency distribution of the ratios of 33 profiles. The data to model ratio of each profile is average of the ratios at each altitude of measurement.

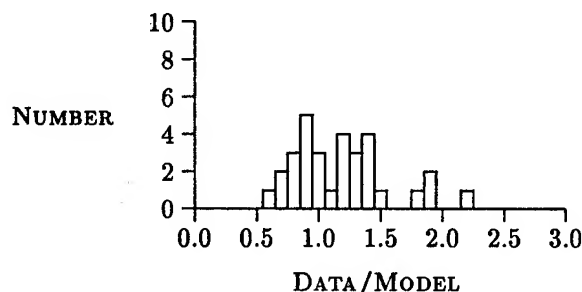


Figure 19. Data to model extinction ratio at 1.06 μm . Frequency distribution of the ratios of 33 profiles. The data to model ratio of each profile is average of the ratios at each altitude of measurement.

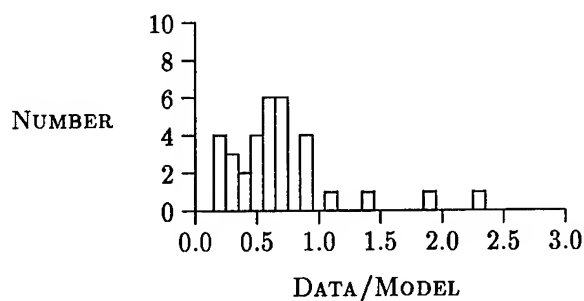


Figure 20. Data to model extinction ratio at $10.6 \mu\text{m}$. Frequency distribution of the ratios of 33 profiles. The data to model ratio of each profile is average of the ratios at each altitude of measurement.

4. SURFACE VISIBILITY

XSCALE predicts the IR extinction, absorption, and backscattering based on the input visibility. The visibility is converted to extinction at $0.55 \mu\text{m}$ by the Kochmeider relation. This $0.55 \mu\text{m}$ extinction is then scaled to the IR wavelength of interest by the formulas encoded within XSCALE. The accuracy of the XSCALE predictions will be improved if similar devices are used to measure visibility and IR extinction. Since this is often impossible effort must be made to better define the correlation between visibility observations and the $0.55 \mu\text{m}$ extinction.

5. CODE

All input values are checked to ensure that they fall in a physically possible range. Any value not explicitly input is assigned a default value. The visibility and wavelength are not assigned a value since these are passed from the EOSAEL executive program. If a selected option uses this default value it is flagged during output. If a value is outside the acceptable range, it is printed to the output file along with the acceptable range. A limited amount of cross-checking of the input values is performed. For instance, no slant path is allowed for desert aerosol, rain, or icefog.

A subroutine has been created to handle all standard input and output. This subroutine stands between the EOSAEL executive program and the XSCALE computation programs. Programs that call XSCALE as a subroutine can bypass this I/O subroutine to avoid unwanted processing and output messages. This reduces program size and execution time.

6. CONCLUSIONS

XSCALE 92 includes a desert aerosol model. The slant path is no longer tied to ground level. Many tests of XSCALE predictions have been performed. These tests show that the XSCALE predictions are reasonable and realistic. They also show that XSCALE does not model every real world situation, and that default values are not always correct values. Certainly improvements are possible; at this time they will be driven by the needs of the user community. The single most important input value to XSCALE is the visibility. Better predictions depend on accurately observing the visibility. The XSCALE program now checks for physically plausible input values and assigns default values to variables not explicitly entered. We hope this will prove to be less aggravating than an unsuccessful run due to an inappropriate or forgotten input value. Those users who wish to use XSCALE as a subroutine should be able to do so easier and with greater assurance of success.

REFERENCES

- Avara, Elton P., 1985: Comparison of Estimates of Average Transmission. In *Proceedings of the Sixth Annual EOSAEL Conference*. U.S. Army Atmospheric Sciences Laboratory, White Sands Missile Range, NM 88002-5501.
- Burlbaw, Edward J., 1985: Slant-Path Transmittance in the Visible: Sensitivity and Comparison of Methods. In *Proceedings of the Sixth Annual EOSAEL Conference*. U.S. Army Atmospheric Sciences Laboratory, White Sands Missile Range, NM 88002-5501.
- Duncan, Louis D., Mary Ann Seagraves, and Melvin G. Heaps, 1987: *EOSAEL 87 Volume 7 Natural Aerosol Extinction Module XSCALE*. Technical Report ASL-TR-0221-7, U.S. Army Atmospheric Sciences Laboratory, White Sands Missile Range, NM 88002-5501.
- Fiegel, Robert P., 1990a: Comparison of XSCALE 89 Vertical Structure Algorithm with Sprakensehl Measurements. In Shettle, E. P. and Kneizys, F. X., Eds., *Proceedings of the Thirteenth Annual Review Conference on Atmospheric Transmission Models*, Hanscom Air Force Base, MA 01731. Geophysics Laboratory.
- Fiegel, Robert P., 1990b: XSCALE Vertical Structure Algorithm Comparison with Field Data. In *Proceedings of the Eleventh Annual EOSAEL Conference*, White Sands Missile Range, NM 88002-5501.
- Fiegel, Robert P., 1991: *Natural Aerosol Extinction Module XSCALE 92 User's Guide*. Technical report, U.S. Army Atmospheric Sciences Laboratory, White Sands Missile Range, NM 88002-5501. In preparation.
- Gillespie, Patti S., 1987: *BEST-ONE Data Analysis and Comparison*. Technical Report OMI-237, Optometrics, Inc., 106 Idaho, Las Cruces, NM 88005.
- Hoidale, Glenn B., 1985: XSCALE Visits Sprakensehl, West Germany. In *Proceedings of the Sixth Annual EOSAEL Conference*: U.S. Army Atmospheric Sciences Laboratory, White Sands Missile Range, NM 88002-5501.
- Hoidale, Glenn B., 1986: *Classification Guide for the Development and Dissipation of Low Visibilities, Sprakensehl, West Germany, Surface to 300 M, 1989 - 1985*. Technical Report ASL-DR-86-0003, U.S. Army Atmospheric Sciences Laboratory, White Sands Missile Range, NM 88002-5501.
- Hutt, Dan and Richard Shirkey, 1987: *Verification of EOSAEL Snow Transmittance Predictions*. DREV Report 4423/87, Defence Research Establishment, Valcartier, Québec, Canada.
- Lindberg, James D., Radon B. Loveland, Louis D. Duncan, and M. B. Richardson, 1984: *Vertical Profiles of Extinction and Partical Size Distribution Measurements Made in European Wintertime Fog and Haze*. Technical Report ASL-TR-0151, U.S. Army Atmospheric Sciences Laboratory, White Sands Missile Range, NM 88002-5501.
- Lindberg, James D., 1984: *Final Report on the European Vertical Structure Experiment at Cardington, England*. Technical Report ASL-TR-0153, U.S. Army Atmospheric Sciences Laboratory, White Sands Missile Range, NM 88002-5501.
- Longtin, David R., Eric P. Shettle, John R. Hummel, and James D. Pryce, 1988: *A Wind Dependent Desert Aerosol Model: Radiative Properties*. Technical Report AFGL-TR-88-0112, Air Force Geophysics Laboratory, Hanscom Air Force Base, MA 01731.
- Rachele, Henry and Neal H. Kilmer, 1990: Comparison of Estimates of Vertical Extinction Profiles in Very Low Stratus Clouds and Subcloud Regions. In *Proceedings of the Eleventh Annual EOSAEL Conference*. U.S. Army Atmospheric Sciences Laboratory, White Sands Missile Range, NM 88002-5501.
- Schulze, Beth, 1986: A Proposed Modification to XSCALE. In *Proceedings of the Seventh Annual EOSAEL Conference*. U.S. Army Atmospheric Sciences Laboratory, White Sands Missile Range, NM 88002-5501.
- Shirkey, Richard and Dan Hutt, 1985: Verification of the Snow Algorithm in EOSAEL Module XSCALE. In *Proceedings of the Sixth Annual EOSAEL Conference*. U.S. Army Atmospheric Sciences Laboratory, White Sands Missile Range, NM 88002-5501.

**A THEORETICALLY BASED DOUBLE EXPONENTIAL EXTINCTION MODEL
FOR VERY LOW STRATUS CLOUDS AND SUBCLOUD REGIONS:
AN OPTION FOR THE VERTICAL PROFILE MODEL IN XSCALE**

Neal H. Kilmer
Physical Science Laboratory, New Mexico State University
Las Cruces, NM 88003-0002, U.S.A.

Henry Rachele
U.S. Army Atmospheric Sciences Laboratory
White Sands Missile Range, NM 88002-5501, U.S.A.

This paper is dedicated to the memory of Dr. Louis D. Duncan of the U.S. Army Atmospheric Sciences Laboratory.

ABSTRACT

A theoretically based microphysics model developed by the authors was used to simulate a large number of vertical drop size distribution profiles in very low stratus clouds and subcloud regions. These drop size distributions were used with Mie calculations to simulate vertical profiles of extinction at wavelengths of 0.55, 1.06, 4.0, and 10.6 μm . These extinction profiles were combined to structure a theoretical equivalent of a portion of XSCALE, an empirically derived model in the U.S. Army Atmospheric Sciences Laboratory (ASL) Electro-Optical Systems Atmospheric Effects Library (EOSAEL). That portion of XSCALE includes a vertical profile model for very low stratus clouds based largely on drop size distribution data collected in the vicinity of Meppen, Germany. Double exponential equation parameter values determined from fitting simulated data are presented. It is proposed that simulated parameter values be used to augment the XSCALE model set for possible worldwide application.

1. BACKGROUND AND INTRODUCTION

To optimize the design and operational capability of electro-optical systems for use in the lower atmosphere, it is necessary to have quantitative knowledge of the vertical structure of extinction, backscatter, and absorption. Furthermore, this understanding is needed for sensors operating at different transmission wavelengths. Limited knowledge of vertical drop size distributions, extinction, backscatter, and absorption was documented prior to 1980. This knowledge was based largely on 18 vertical profiles of drop size and number data collected by the U.S. Army ASL at Graffenwöhr and Meppen, Germany (Duncan et al., 1980). It was concluded that additional data and research were needed to adequately address electro-optical problems in Europe, especially Germany. To expedite this research, it was decided that data should be collected in the field and analyzed from an electro-optical viewpoint. Consequently, the U.S. Army ASL conducted additional field experiments at Meppen, Germany, in 1980 (see Lindberg, 1982). These field experiments, which were included in Project Meppen 80, were designed to measure drop sizes and number with height in conditions of moist haze, fog, and very low stratus clouds. These measurements were made with Knollenberg FSSP-100C aerosol spectrometers suspended from a

tethered balloon that was allowed to descend, often through a cloud. The overall nominal size range of drops that could be counted was from a $0.25 \mu\text{m}$ radius to a $23.5 \mu\text{m}$ radius. These vertical profiles of drop size distributions were then used as input (assuming the drops were pure water) for Mie calculations (Miller, 1983) resulting in vertical profiles of extinction, backscatter, and absorption coefficients for wavelengths of 0.55, 1.06, 4.0, and $10.6 \mu\text{m}$ (see Lindberg et al., 1984). From these data, the early empirical vertical profile model was evaluated and modified.

The first "basic" empirical model (Duncan et al., 1980) was developed using the data from Graffenwöhr and Meppen as follows. The logarithm of liquid water content (LWC) or extinction coefficient (σ_e) at each height $z + 20 \text{ m}$ was plotted against the logarithm of LWC or σ_e at height z for all profiles. This produced a scattergram of points to which two lines were determined (see dashed lines in fig. 1), producing the relationships shown by Duncan et al. (1980). A discrete mathematical representation of these relationships is

$$\begin{aligned} x(z + 20 \text{ m}) &= a'x(z) + b' \\ \text{where } x(z + 20 \text{ m}) &= \ln \text{ LWC or } \sigma_e \text{ at height } z + 20 \text{ m} \\ x(z) &= \ln \text{ LWC or } \sigma_e \text{ at } z \end{aligned} \quad (1)$$

a' and b' are constants. This model is very appealing to the user, since it is simple, very easy to execute and requires only a single value of LWC or σ_e near the surface as input.

Heaps (1982) and Rachele and Kilmer (1991), in addition, showed that eq. (1) can be expressed in continuous form as double exponential, i.e.,

$$\text{LWC or } \sigma_e = A \cdot \exp \{ B \exp Cz \} \quad (2)$$

where A , B , and C are constants that can be calculated from a' , b' , a reference or "hinge" height z_r , and y_r , the LWC or σ_e at that height as follows.

$$A = \exp \left[\frac{b'}{1 - a'} \right] \quad (3)$$

$$B = \left(\ln y_r + \frac{b'}{a' - 1} \right) (a')^{-z_r/k} \quad (4)$$

$$C = \frac{1}{k} \ln a' \quad (5)$$

The LWC and extinction models of Duncan and Heaps are basically empirical models representing the "average" profiles for the locales where the data were collected. The Heaps version of an empirical model (the double exponential form) was coupled with a U.S. Air Force model, the Shettle-Fenn (1979) drop size distribution expression, resulting in the vertical extinction profile model currently in the XSCALE module of EOSAEL (Duncan et al., 1987).

In addition to the empirically developed electro-optical models, U.S. Army ASL opted to develop a theoretically based microphysical model which together with Mie theory would produce extinction, backscatter, and absorption coefficients. The evolution of the Rachele-Kilmer microphysics model (hereafter designated the RK model) has been documented in several papers (Kilmer and Rachele, 1991a and 1991b). Two equations — a lapse rate equation and a mass (moisture) conservation equation — have been modified since the most recent (Kilmer and Rachele, 1991b) of those papers was written. The modified equations are given below. The current RK model is based on the concept that a cluster of drops embedded in a mass of moist air rises from a reference height to the top of a cloud. The initial drops of the cluster are characterized by the reference level drop size distribution, but as the cluster rises the drop sizes change. The physical and

thermodynamical changes of the drops and their environment are computed as though a hypothetical completely permeable sphere envelops the drops and their environment.

The currently used cluster sphere lapse rate equation is

$$\frac{L_e}{C_p^*} \frac{dW_v}{dz} + \frac{dT}{dz} = \left\{ -\frac{gT(1+W_v')}{C_p^* T'} - \left[\frac{L_e(W_v - W_v')}{C_p^*} + \frac{C_p''}{C_p^*} (T - T') \right] \left[\frac{3\alpha_e T}{4RT'} \right] \right\} \times \left\{ \frac{1+W_v/\epsilon}{1+W_v'/\epsilon} \right\} + \frac{be^{-c(z_\tau - z)^2}}{C_p^*} + a(z - z_\tau) \quad (6)$$

$$C_p^* = C_p + C_p' W_v + S_L W_L + \sum_i S_{si} W_{si} \quad (7)$$

$$C_p' = C_p + C_p' W_v' \quad (8)$$

- α_e = entrainment coefficient
- R = radius of sphere
- W_v = grams of water vapor per gram of dry air in sphere
- W_v' = grams of water vapor per gram of dry air in ambient air
- z = height above ground level
- b = an adjustable parameter
- c = an adjustable parameter
- ϵ = ratio of molecular weight (MW) of water to mean MW of dry air = 0.621972
- T' = temperature of the ambient air in kelvins
- T = sphere temperature in kelvins
- W_L = mass loading (liquid water plus dry material) mixing ratio inside the sphere
- z_τ = height above ground at top of cloud
- L_e = specific enthalpy of vaporization of water at temperature of sphere
- a = temperature radiation constant
- C_p = specific heat of dry air at constant pressure
- C_p' = specific heat of water vapor at constant pressure
- S_L = specific heat of liquid water
- S_{si} = specific heat of solid or dissolved substance i
- W_{si} = grams of solid or dissolved substance i per gram of dry air

(In this study, the $\sum_i S_{si} W_{si}$ term is set equal to zero.)

The currently used mass (moisture) conservation equation is

$$4\pi \left(\frac{R_r}{R} \right)^3 \rho_w \sum_{i=1}^{N_{sc}} N_{ir} r_i^2 \frac{dr_i}{dz} + \rho_a \frac{dW_v}{dz} = -\frac{3\alpha_e}{4R} \rho_a' (W_v - W_v') \quad (9)$$

- N_{ir} = N_i (number of drops of size class i per cubic centimeter) at reference height
- N_{sc} = number of drop size classes
- r_i = radius of drop in size class i ($i = 1, 2, \dots$)
- R_r = radius of cluster sphere at reference height
- ρ_a = density of dry air in cluster sphere
- ρ_a' = density of dry air in ambient environment
- ρ_w = density of pure water

The primary products of this model include vertical profiles of drop size distribution, relative humidity, temperature, drop concentration, and liquid water content. Drop size distributions simulated using the microphysics model have been used with Mie formulations

to compute vertical profiles of extinction, backscatter, and absorption coefficients (Kilmer and Rachele, 1991a and 1991b). In the present work, complex indices of refraction of pure water are used when calculating vertical profiles of these coefficients.

The primary purpose of this study was to determine the feasibility of using the RK microphysics model to generate double exponential constants A, B, and C that in turn could be used to generate vertical profiles of extinction in very low stratus clouds and subcloud regions for various combinations of surface level temperature, pressure, relative humidity, visibility, and air mass. If this procedure were found to be valid, then the model could be used to generate double exponential constants needed for worldwide applications.

2. SIMULATED PROFILES

To compute the extinction and backscatter profiles using the RK model, the drop size distribution is computed first as it varies with height according to the RK microphysics model. Mie theory then is applied to the drop size distributions.

To execute the RK microphysics model, a number of input values are required. Also required are values of certain physical constants (such as the exponential mass increase coefficient at infinite dilution) that affect growth of individual drops and depend upon the chemistry of the dry particles upon which moisture condenses to form the drops and the air mass type (urban, rural, or maritime). The RK microphysics model uses physical constants reported by Hänel and Lehmann (1981).

The reference level drop size distribution is defined using a Shettle-Fenn (1979) bimodal lognormal distribution. It was found necessary to truncate the Shettle-Fenn distribution to omit drops that would form from condensation nuclei having radii less than a certain cutoff value. This truncation is in line with the Kelvin cutoff and also is qualitatively consistent with losses due to scavenging by larger drops. The exact cutoff value to be used is an input parameter to be specified as input to the RK model. In the present work, $0.004 \mu\text{m}$ is used as the cutoff value.

3. MODEL CONCEPT

Execution of the RK microphysics model requires an estimate of the cloud top height; dry particle chemistry; air mass type (maritime, rural, or urban); and reference level (2 m above ground level) values of temperature, pressure, relative humidity, and visibility. The relative humidity and visibility are required to define the Shettle-Fenn drop size distributions. Our approach is to compute Shettle-Fenn drop size distributions at the reference level for different combinations of relative humidity, visibility, and air mass type. For systematically selected combinations of these, we vary the reference level temperature (0, 15, and 30 °C) and estimated cloud top height (300 or 500 m above ground level). The pressure at the reference level is always set at 1000 millibars (1 millibar = 1 hectopascal), since the drop size distribution is not sensitive to pressure changes. However, we have found that the distribution in the cloud varies with the liquid water content of the cloud. Hence, we also vary input parameters to make the maximum liquid water content approximately 50%, 75%, and 100% of the quasi-adiabatic values. (In this work, a "quasi-adiabatic" simulation differs from a truly adiabatic one by allowing minimal entrainment. For a quasi-adiabatic simulation, the term containing the "a" coefficient in the cluster lapse rate equation is set equal to zero to correspond with that term's absence in a truly adiabatic case.) Therefore, for each reference level combination of Shettle-Fenn parameters, we vary the cloud top height, liquid water content, and temperature, giving $2 \times 3 \times 3 = 18$ drop size profiles. Applying Mie theory, we then obtain 18 extinction profiles for each of four wavelengths. The method indicated below is used to determine the two sets of double exponential constants A, B, and C for each combination used.

4. BEHAVIOR AND DETERMINATION OF FUNCTION

Extinction simulated using the RK model typically increases more rapidly with increasing height in the subcloud region; therefore, a vertical profile plotted in the usual fashion (with height on the vertical axis) appears concave downward in this region (see fig. 2). Such a plot exhibits an inflection point somewhere in the vicinity of the base of the cloud and then appears concave upward in the cloud up to a region near the top of the cloud, where simulated vertical entrainment of warmer air from an inversion layer above the cloud eventually causes extinction to decrease with height. (This region of decreasing extinction is beyond the scope of the double exponential model addressed in this work.) The extinction coefficient profile in the region below the inflection point (generally the subcloud region) is approximated using eq. (2) with all positive values for A, B, and C. Such a function would increase without bound with increasing height. However, above the inflection point, a form of eq. (2) having a positive value for A and negative values for B and C is used. This form behaves somewhat like a cumulative distribution function (with height as the independent variable) multiplied by A. At a sufficiently great height, this form of eq. (2) approaches an asymptotic value equal to A, because large negative values of Cz cause B exp (Cz) to approach zero and therefore cause exp [B exp (Cz)] to approach one. For much of the region of interest in modeling, it is desired that the double exponential function not be very close to either zero or the asymptotic value of A. This suggests that B exp (Cz) be of about the same order of magnitude as -1, which in turn suggests that |B| be of about the same order of magnitude as exp (-Cz). Since z is expressed in meters and this work simulates clouds having tops around 300 and 500 m, there is some chance that some values of C appropriate for fitting extinction profiles might lead to really huge values of |B|. Although many combinations led to values of B that appeared quite reasonable, this problem surfaced with several profiles, for which C values of about -0.23 or -0.24 led to values of B as huge as -6×10^{25} . This behavior seems undesirable, although a measure of fractional error (double exponential vs. RK model extinction) was reasonable: around 10%.

A few early estimates of A, B, and C were calculated using eqs. (3), (4), and (5). It was found that calculated double exponential extinction profiles were extremely sensitive to variations in a' and b' . Therefore, it was decided to bypass eqs. (3), (4), and (5) and calculate A, B, and C by requiring that the right-hand side of eq. (2) produce the exact extinction coefficient values at three heights. An attempt to solve the three resulting simultaneous equations algebraically led to

$$e^{C(z_3 - z_1)} \ln \left(\frac{\sigma_{e2}}{\sigma_{e1}} \right) - e^{C(z_2 - z_1)} \ln \left(\frac{\sigma_{e3}}{\sigma_{e1}} \right) + \ln \left(\frac{\sigma_{e3}}{\sigma_{e2}} \right) = 0 \quad (10)$$

where (z_1, σ_{e1}) , (z_2, σ_{e2}) , and (z_3, σ_{e3}) are the three points (height, extinction) at which this equation is exact. Two rearranged forms of this equation form the basis for iterative calculation of C. After C is determined, B and A are calculated in turn by

$$B = \frac{\ln \left(\frac{\sigma_{e2}}{\sigma_{e1}} \right)}{e^{Cz_2} - e^{Cz_1}} \quad (11)$$

$$A = \sigma_{e1} \exp \left(-B e^{Cz_1} \right) \quad (12)$$

The inflection point that occurs somewhere in the vicinity of the base of the cloud is chosen as a "hinge" at which both sets of A, B, and C must satisfy eq. (2). Also, the double exponential function for the lower piece must equal the extinction when evaluated at the reference height, and that for the upper piece must equal the maximum extinction when evaluated at whatever height level this maximum occurs. The other point for each piece

is chosen to be the one that, when used with the other two points, leads to the minimum residual sum of squares at all height levels between the other two points.

5. RESULTS

Although the RK model has been used to generate vertical profiles of extinction for other studies, as indicated in Section 1, we had not previously presented simulations of the Duncan type \ln/\ln plots. We present in this paper a sample of our simulated results (solid line in fig. 1) that are similar to those of Duncan (dashed line in fig. 1) based on measured data. Recall, however, that Duncan's plots are the result of fitting straight line segments to the \ln/\ln plots of a composite of several (18) extinction profiles. Hence, his straight lines are an "average" of the profiles used. However, our \ln/\ln plots, such as the one represented in fig. 1, are of individual profiles. Note, in particular, that our curve is somewhat nonlinear, but has strong linear trends in each of the subcloud and cloud portions.

Considering the linear trends, we felt strongly justified in structuring our simulated theoretically based extinction profiles in discrete linear or double exponential forms. However, much to our surprise, we found that we could not efficiently determine the straight line coefficients a' and b' needed for the discrete equations, probably due to nonlinearities in the \ln/\ln plots. The extinction profiles produced from the linear equations were much too sensitive to the estimates of a' and b' , and hence would not reproduce extinction profiles that matched the original profiles acceptably. This was the most startling find of this research. However, we still felt that a double exponential fit to extinction profiles was viable. We found, in fact, that we could quite successfully determine the double exponential constants if we used simulated extinction values directly and were gratified to find that we could match simulated profiles to within 10% (root mean square of the residuals divided by mean extinction coefficient, where both quantities are taken from 2 m above ground level to the height of maximum extinction) for 85% of our tries. Figure 2 shows a typical example, which was selected because it is very close to the fiftieth percentile in goodness of fit ranking.

Because of the large number of combinations involved, A, B, and C results for this study were determined for only five selected relative humidity-visibility pairs with only one air mass type (maritime). Eighteen different combinations of temperature, cloud top height, and maximum liquid water content were used with each of those pairs. Of all the possible combinations, we selected only a few, given in tables 1-4, to show the wide variations of A, B, and C for four wavelength (λ) values. Effects on calculated double exponential extinction profiles from varying the maximum liquid water content and reference level relative humidity are shown in figs. 3 and 4.

SUMMARY AND CONCLUSIONS

The empirically developed extinction profile part of the XSCALE module of EOSAEL has several desirable features — it is simple, easy to execute, and requires only very limited input. The most significant limitation of this module is due to the limited amount of data used to define the double exponential relationships.

To nullify the limitations of the empirical model for very low cloud cases, the authors developed a theoretically based very low stratus cloud/subcloud model (documented in other reports, except for refinements presented in this paper) that simulates vertical profiles of extinction for a variety of atmospheric conditions that can occur worldwide. This model was used for this study to generate extinction profiles that vary with reference level values of temperature, relative humidity, and visibility for a given air mass.

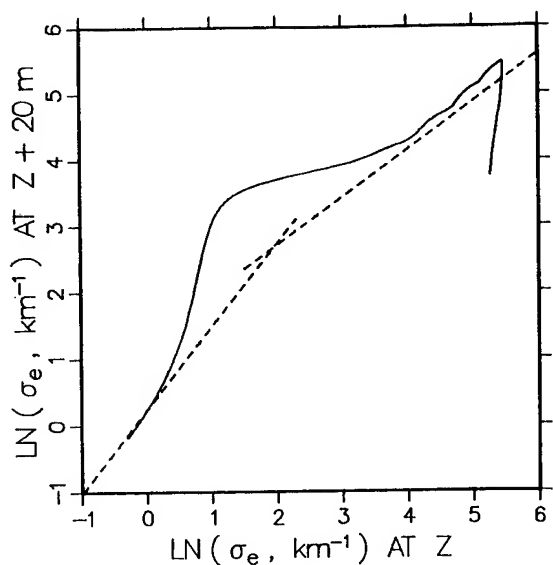


Figure 1. Relationships from one RK model simulation (solid line) and composite of observed data (Duncan et al., 1980) (dashed lines), all for $\lambda = 0.55 \mu\text{m}$.

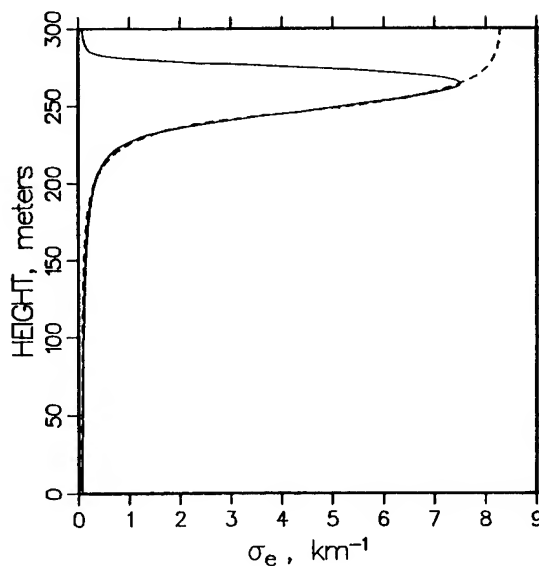


Figure 2. Extinction profiles from RK model (solid line) and double exponential calculation (dashed line) for $\lambda = 10.6 \mu\text{m}$.

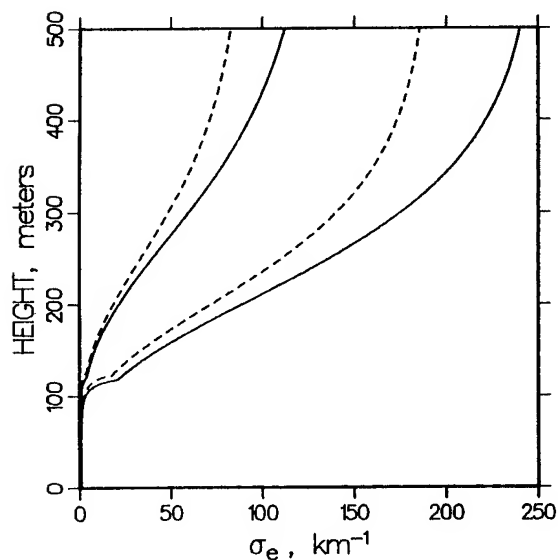


Figure 3. Effect of maximum LWC (quasi-adiabatic for solid lines; 75% of quasi-adiabatic for dashed lines) on extinction for $\lambda = 10.6 \mu\text{m}$ (left) and $0.55 \mu\text{m}$ (right)

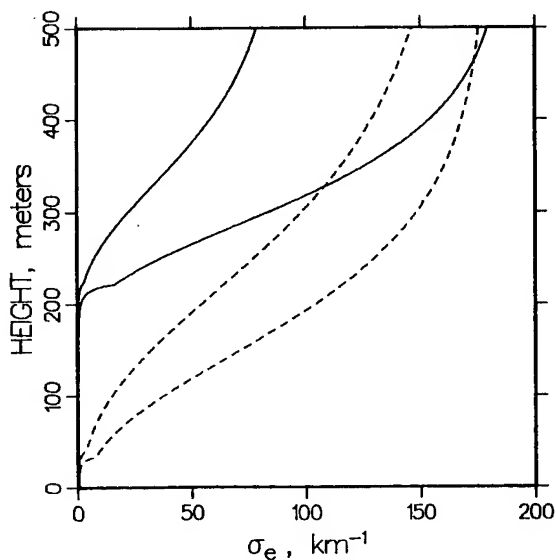


Figure 4. Effect of reference level relative humidity (0.90 for solid lines; 0.99 for dashed lines) on extinction for $\lambda = 10.6 \mu\text{m}$ (left) and $0.55 \mu\text{m}$ (right).

TABLE 1. A, B, AND C AS FUNCTIONS OF WAVELENGTH AND REFERENCE HEIGHT TEMPERATURE

The estimated cloud top height is 500 m, maximum LWC is quasi-adiabatic, and the reference height values of relative humidity and visibility are 0.95 and 5 km, respectively.

λ (μm)	Subcloud Region			In Cloud		
	A	B	C	A	B	C
Reference height temperature = 0 °C						
0.55	0.722	3.031E-02	0.0438543	194.675	-7.353E + 00	-0.0104415
1.06	0.678	8.281E-03	0.0575220	231.089	-6.819E + 00	-0.0088808
4.00	0.503	5.914E-02	0.0367735	310.006	-1.144E + 01	-0.0123053
10.60	0.153	8.239E-02	0.0327618	87.364	-8.184E + 00	-0.0080016
Reference height temperature = 15 °C						
0.55	0.736	1.274E-02	0.0471859	250.584	-8.768E + 00	-0.0106532
1.06	0.682	3.749E-03	0.0587265	247.175	-1.074E + 01	-0.0120716
4.00	0.522	2.400E-02	0.0413470	342.876	-1.845E + 01	-0.0155592
10.60	0.158	4.745E-02	0.0347375	129.265	-9.808E + 00	-0.0084441

TABLE 2. A, B, AND C AS FUNCTIONS OF WAVELENGTH AND MAXIMUM LWC

The estimated cloud top height is 500 m, and the reference height values of relative humidity, visibility, and temperature are 0.95, 5 km, and 15 °C, respectively. (Resulting extinction profiles for 0.55 and 10.6 μm are plotted in fig. 3.)

λ (μm)	Subcloud Region			In Cloud		
	A	B	C	A	B	C
Maximum LWC = 75% of quasi-adiabatic						
0.55	0.733	1.655E-02	0.0427292	191.285	-9.873E + 00	-0.0115246
1.06	0.680	6.950E-03	0.0506520	196.402	-1.060E + 01	-0.0120134
4.00	0.518	3.179E-02	0.0371543	268.636	-1.994E + 01	-0.0160506
10.60	0.155	7.049E-02	0.0300579	91.089	-1.035E + 01	-0.0093070
Maximum LWC = 100% of quasi-adiabatic						
0.55	0.736	1.274E-02	0.0471859	250.584	-8.768E + 00	-0.0106532
1.06	0.682	3.749E-03	0.0587265	247.175	-1.074E + 01	-0.0120716
4.00	0.522	2.400E-02	0.0413470	342.876	-1.845E + 01	-0.0155592
10.60	0.158	4.745E-02	0.0347375	129.265	-9.808E + 00	-0.0084441

TABLE 3. A, B, AND C AS FUNCTIONS OF WAVELENGTH AND REFERENCE HEIGHT
RELATIVE HUMIDITY

The estimated cloud top height is 500 m, maximum LWC is quasi-adiabatic, and the reference height values of visibility and temperature are 10 km and 15 °C, respectively. (Resulting extinction profiles for 0.55 and 10.6 μm are plotted in fig. 4.)

λ (μm)	Subcloud Region			In Cloud		
	A	B	C	A	B	C
Relative humidity at reference height = 0.90						
0.55	0.361	1.637E-04	0.0452904	188.226	-5.564E + 01	-0.0140685
1.06	0.324	3.410E-05	0.0528367	191.574	-6.856E + 01	-0.0149210
4.00	0.227	4.682E-04	0.0405062	260.673	-2.409E + 02	-0.0200106
10.60	0.064	2.185E-03	0.0332388	90.043	-4.646E + 01	-0.0116490
Relative humidity at reference height = 0.99						
0.55	0.324	1.188E-01	0.0993516	179.596	-4.477E + 00	-0.0105095
1.06	0.333	5.373E-02	0.1277945	175.683	-4.982E + 00	-0.0119005
4.00	0.196	4.939E-01	0.0581411	232.006	-3.351E + 00	-0.0069252
10.60	0.062	7.630E-01	0.0410789	162.729	-5.173E + 00	-0.0077372

TABLE 4. A, B, AND C AS FUNCTIONS OF WAVELENGTH AND REFERENCE HEIGHT
VISIBILITY

The estimated cloud top height is 500 m, maximum LWC is quasi-adiabatic, and the reference height values of relative humidity and temperature are 0.99 and 15 °C, respectively.

λ (μm)	Subcloud Region			In Cloud		
	A	B	C	A	B	C
Reference height visibility = 2 km						
0.55	1.487	2.216E-01	0.0688225	255.544	-3.729E + 00	-0.0094215
1.06	1.587	1.192E-01	0.0896080	293.263	-3.860E + 00	-0.0083949
4.00	1.109	4.133E-01	0.0498145	281.385	-5.074E + 00	-0.0176466
10.60	0.533	2.744E-01	0.0529644	162.802	-4.811E + 00	-0.0071380
Reference height visibility = 10 km						
0.55	0.324	1.188E-01	0.0993516	179.596	-4.477E + 00	-0.0105095
1.06	0.333	5.373E-02	0.1277945	175.683	-4.982E + 00	-0.0119005
4.00	0.196	4.939E-01	0.0581411	232.006	-3.351E + 00	-0.0069252
10.60	0.062	7.630E-01	0.0410789	162.729	-5.173E + 00	-0.0077372

The double exponential constants A, B, and C were determined for 358 simulated extinction profiles. The values of A, B, and C varied considerably for different inputs, suggesting that extinction profiles vary geographically and by season. (To our knowledge this approach does not appear in the literature.) Because of the page limitation of this paper we presented only selected sets of values of A, B, and C showing their variability with input. A more complete set will appear in a U.S. Army ASL technical report.

Because of the encouraging results of the ongoing research we propose that theoretically generated values of A, B, and C be considered for the EOSAEL XSCALE vertical structure module.

REFERENCES

- Duncan, L. D., J. D. Lindberg, and R. B. Loveland, 1980: An Empirical Model of the Vertical Structure of German Fogs, ASL Technical Report ASL-TR-0071, U.S. Army Atmospheric Sciences Laboratory, White Sands Missile Range, NM 88002.
- Duncan, L. D., M. A. Seagraves, and M. G. Heaps, 1987: Natural Aerosol Extinction Module XSCALE, EOSAEL 87, Vol. 7, ASL Technical Report ASL-TR-0221-7, U.S. Army Atmospheric Sciences Laboratory, White Sands Missile Range, NM 88002.
- Hänel, G., and M. Lehmann, 1981: Equilibrium Size of Aerosol Particles and Relative Humidity: New Experimental Data from Various Aerosol Types and Their Treatment for Cloud Physics Application, Contributions to Atmospheric Physics (Beiträge zur Physik der Atmosphäre), 54(1), 57-71.
- Heaps, M. G., 1982: A Vertical Structure Algorithm For Low Visibility/Low Stratus Conditions, ASL Technical Report ASL-TR-0111, U.S. Army Atmospheric Sciences Laboratory, White Sands Missile Range, NM.
- Kilmer, N. H., and H. Rachele, 1991a: Comparison of Estimates of Vertical Extinction Profiles in Very Low Stratus Clouds and Subcloud Regions. In Proceedings of the Eleventh Annual EOSAEL/TWI Conference, 722-731, U.S. Army Atmospheric Sciences Laboratory, White Sands Missile Range, NM. Also references therein.
- Kilmer, N. H., and H. Rachele, 1991b: Simulation of Vertical Profiles of Extinction and Backscatter Coefficients in Very Low Stratus Clouds and Subcloud Regions. In Propagation Engineering: Fourth in a Series, Luc R. Bissonnette and Walter B. Miller, eds., Proc. SPIE, 1487, 109-122. Also reference therein.
- Lindberg, J. D., 1982: Early Wintertime European Fog and Haze, Report on Project Meppen 80, ASL Technical Report ASL-TR-0108, U.S. Army Atmospheric Sciences Laboratory, White Sands Missile Range, NM 88002.
- Lindberg, J. D., R. B. Loveland, L. D. Duncan, M. B. Richardson, and J. Esparza, 1984: Vertical Profiles of Extinction and Particle Size Distribution Measurements Made in European Wintertime Fog and Haze, ASL Technical Report ASL-TR-0151, U.S. Army Atmospheric Sciences Laboratory, White Sands Missile Range, NM 88002.
- Miller, A., 1983: Mie Code Agaus 82, ASL-CR-83-0100-3, New Mexico State University, Department of Physics, Las Cruces, NM 88003.
- Rachele, H., and N. H. Kilmer, 1991: A Derivation for Determining Double Exponential Liquid Water Content and Extinction Profiles from Discrete Data, ASL Technical Report ASL-TR-0290, U.S. Army Atmospheric Sciences Laboratory, White Sands Missile Range, NM.
- Shettle, E. P., and R. W. Fenn, 1979: Models for the Aerosols of the Lower Atmosphere and the Effects of Humidity Variations on Their Optical Properties, AFGL Technical Report AFGL-TR-79-0214, Air Force Geophy. Lab., Hanscom AFB, MA 01731.

TRANSFORMATION OF COMBIC TO DYNAMIC BATTLEFIELD ENVIRONMENT
TARGET ACQUISITION MODEL (DYBETA)

S. Grossman, A. Katz, D. Elial
Hancal System Engineering
Israel Military Industries Ltd.
Ramat Hasharon, 47100, Israel

ABSTRACT

When predicting target acquisition performance, one has to consider the various degradations of the initial contrast of targets and then compare the apparent contrast to thresholds corresponding to desired acquisition level and device used.

COMBIC program scenario management and smoke transmission results were combined with target acquisition and contrast transmission algorithms to form a single comprehensive model for target acquisition.

In the model, contrast transmission thresholds are computed for each line of sight, according to target size and initial contrast, device used, observer target range and various acquisition levels.

Contrast transmission thresholds are then translated using lookup tables, into various smoke transmission thresholds, which are directly compared to COMBIC results.

The lookup tables are based on CONTRAST and LOWTRAN programs, and are computed for different smoke types, visibilities, wavelengths, target observer ranges and sun positions.

The resulting model enables one to produce a dynamic evaluation of target acquisition for various observation devices and positions in a given battlefield scenario.

The full text of this paper is for LIMITED DISTRIBUTION.

To request a reprint of this paper, write to

S. Grossman
Hancal Systems Engineering
Israeli Military Industries
P. O. Box 1044/45
Ramat Hashazom 47100
ISRAEL

03-5484265/252

ELECTRO-OPTICAL CLIMATOLOGY

MICROCOMPUTER VERSION 2.0

R. L. Miller and B. T. Regan
USAF Environmental Technical Applications Center
Scott AFB, IL 62225-5008, USA

ABSTRACT

Electro-optical Climatology (EOCLIMO) Ver 2.0 was developed to enhance employment of precision guided munitions and target acquisition systems. This paper explains how EOCLIMO was produced, and interpretation of each output type. Guidance is provided on EOCLIMO 2.0 program manipulation, station/data comparisons, geographical map/narrative display, and transmittance versus ceiling output.

1. INTRODUCTION

1.1 PURPOSE of the STUDY

The use of precision guided munitions and target acquisition systems (PGMs/TASS) by armed forces makes weather and its adverse effects a critical factor in planning and contingency support. To ensure optimal employment of these "smart" weapon systems operators must know the impact of atmospheric conditions on electro-optical sensors. This program focuses on the infrared (IR) portion of the electromagnetic spectrum within the 8-12 micron band. EOCLIMO 2.0 provides climatological transmittance, conventional weather, narratives, and maps. This allows planners to gauge how well a PGM/TAS should perform in an area of interest for different months and time of day.

1.2 TRANSMITTANCE DEFINED

The term transmittance is defined as a measure of the amount of radiation propagated through a given medium; defined as the ratio of transmitted radiation to the total radiation incident

upon the medium. Some hold transmittance and transmissivity as interchangeable, others do not. To avoid confusion, the term "transmittance" will be used. A more complete discussion on radiative transfer principles and electromagnetic propagation can be found in Liou (1980).

1.3 The MODEL

Using measured transmittance data would be the best way to study weather effects on E-O systems, but atmospheric transmittance and aerosol data are not routinely available. In lieu of "real" measurements, one can use a model to compute transmittance values from standard meteorological data (see Seagraves and Avara (1991); Edson et al. (1987); Tooth (1987); or Soliz and Davis (1981)). The use of such a study depends on both the ability of the model to reproduce the physics of the atmosphere and how well the meteorological data can be translated into model input.

LOWTRAN7 (Kneizys et al., 1988) was selected for this study for several reasons. It is easy to run, and has found wide acceptance in both the military and scientific communities. LOWTRAN7 is used by the USAF and the USA for transmittance calculations for IR Tactical Decision Aids (TDAs). Because the USAF IR TDA provides an estimated 4 km transmittance, results from this study are comparable to USAF IR TDA computations. Condray (1990) did comparisons between LOWTRAN6 and LOWTRAN7. LOWTRAN7 provides a better account of water vapor absorption and handles desert conditions (dust, sand, and particulate matter) better than its predecessors.

2. METHODOLOGY

The methodology used for this study was largely based on Edson et al. (1987), which showed the strengths and weaknesses of basing climatological transmittance studies on modeled data. Another technique demonstrated in Edson et al. (1987) and used extensively in Condray and Edson (1988) was grouping stations with similar climatological features into distinct regions. EOCLIMO Ver 2.0 differs significantly because it provides site-specific data and information for every station within the area of interest with a sufficient period of record. It is much more comprehensive than similar efforts (i.e. Seagraves and Avara, 1991).

2.1 MODEL INPUT

Each weather observation was processed by LOWTRAN7 to build three hourly, site specific, transmittance climatologies. Data was

obtained from USAFETAC's surface DATSAV2 database. The data was derived from 4- to 14-year period of record (POR) data sets. DATSAV2 data is more quality controlled than standard DATSAV data used in previously released studies.

The stations were selected based on a sufficient number of observations and period of record (POR) for an adequate statistical analysis. Each month/hour combination should contain at least 150 observations to provide a robust climatological analysis.

LOWTRAN7 requires several meteorological variables (such as aerosol type and precipitation rate) not available in routine surface observations. Extensive computer code was developed to set input values such as temperature, dewpoint, visibility, and pressure from a variety of surface observation formats including Airways, METAR, and synoptic. The LOWTRAN7 code itself was not altered.

For the low altitude slant path used in this study, surface data were interpolated from the surface to the sensor height to create a vertical profile. A standard atmosphere with a lapse rate of 6.5 degrees C per kilometer was assumed for both temperature and dewpoint. Variables such as temperature, dewpoint, and pressure were used as direct inputs into LOWTRAN7. Present weather was used to set other LOWTRAN7 inputs such as aerosol type and precipitation rate.

2.2 GEOMETRY and WAVELENGTH

Variables such as wavelength and geometry, were set for the entire POR. The standard geometry and wavelength (shown below) for these studies were selected to provide a typical low-level scenario for an air-to-ground E-O weapons system. The range, assumed to be cloud free, is set to 4 km to make the results comparable to the USAF IR TDA transmittance results.

<u>VARIABLE</u>	<u>STANDARD</u>
Wavelength	8.0 to 12.0 microns
Wave # Interval	830 to 1250 cm-1 at
Spectral Resolution	20 cm-1
Height of Sensor	125 m (410 ft) AGL
Height of Target	0.0 m AGL
Slant Range	4 km (2.16 NM)

2.3 AEROSOL SELECTION

The most difficult LOWTRAN7 input variable to set, based on standard surface observations, is the aerosol type. Although coastal and maritime regions have been successfully modeled

(Gathman, 1983), and although LOWTRAN7 contains both rural and urban aerosol models, it is not easy to decide which model (if any) is most appropriate. The actual aerosol present is usually some mixture of the different categories (urban and rural, maritime and rural, etc.). Generally, except for fog or very low visibilities due to other types of obscurants such as dust, smoke, or haze, aerosol selection has less influence than absolute humidity. The criteria used to select the aerosol model for EOCLIMO Ver 2.0 are shown below:

TYPE	DESCRIPTION
------	-------------

Rural:	Unobscured or haze conditions with no blowing dust reported, and not affected by maritime influence. Also used for precipitation observations, unless fog with 1km or less visibility was also reported.
--------	--

Maritime:	Used for stations subject to maritime influence (within 50 km of the ocean, no coastal mountain ranges, onshore flow greater than 5 kts). Also used for fog with visibility greater than 1km but less than 7 km.
-----------	--

Desert:	Default for stations located in or near deserts; used for any observation reporting blowing sand or dust as an obscuration.
---------	---

Fog-Advection:	Advection fog (visibility less than or equal to 1km with BKN/OVC ceilings or wind greater than or equal to 7 kts). Also selected for observations that report both fog and precipitation with visibility less than or equal to 1km.
----------------	---

Fog-Radiative:	Radiation fog (visibility less than or equal to 1 km and wind less than 7 kts).
----------------	---

Fog selection was challenging. Fog is often reported as an obscurant under current Air Weather Service (AWS) procedures when visibilities are less than 4-6 miles (7-10 km). Only fog reports with visibilities less than or equal to 1 km were accepted. For fog reported with visibility greater than 1 km and less than 7 km, and dewpoint depression less than 3C, we selected the maritime aerosol based on PL guidance. If the dewpoint depression was greater than 3C (and visibility between 1km and 7km), the observation was categorized as haze. Fog reports with visibilities greater than or equal to 7km and less than 10 km were redefined as haze. To distinguish between advection and radiation fog, present weather, visibility, and windspeed were used to choose fog type. Reports of shallow fog were classified as radiation fog, otherwise, windspeed and cloud cover were used to select the appropriate fog type.

If blowing dust or sand was observed, the desert aerosol was used. If no fog, precipitation, or dust were present, wind direction and distance to either a seacoast or a desert were used to distinguish between maritime, desert, and rural aerosols. A

maritime aerosol was only selected for those stations within 50 km of the coast with no intervening ridges or mountain ranges, and with a 5 kt or greater onshore breeze. Similar logic was used for stations near deserts to use the desert aerosol model.

2.4 STATIONS

Visibility reporting was critical to aerosol selection and had a significant influence on the results. Some reporting locations rarely recorded visibilities greater than 10 km (7 miles). This was especially true when observations were taken in METAR and values greater than 10 km were not indicated. Visibilities recorded in DATSAV2 also may be unrealistically low due to the observing bias of choosing known distances to local visibility markers. For example, if an object used as a 5km visibility marker is visible and one used as a 10km marker is not, reported visibility tends to cluster at 5km even though the real visibility is somewhere between 5 and 10km. Although there is no scientific way to correct for this problem, the authors of LOWTRAN7 suggested multiplying the reported value by a value near 1.3. This approach was used in all observations where no obscurant was reported. Another consideration was in both fog and haze reporting. In many locations, fog and haze were often reported with uncharacteristically high visibilities. To be consistent with AWS observing practices, all haze reports with visibilities greater than 10 km (7 miles) were treated as unobscured observations. This did not affect the way the LOWTRAN model was run.

3. RESULTS and OUTPUT

3.1 GENERAL

Each stations' graphs and tables are available in month/3-hourly combinations which provide a total of 96 month/hour combinations for analysis. Side-by-side station comparisons can be made in the EGA version. Comparing month/hourly data provides a picture of how transmittance changes during the day/year. Each type of output can be enlarged to full screen display, and downloaded to a printer.

Some station month/hour combinations contain less than 150 observations in data sparse regions. These sites are flagged with the title block (station name and month/hour combination) appearing in yellow (EGA version), or with an asterisk (*) by their name (CGA) version. Stations for a particular country are accessed via selection of the "Stations" option from the main menu label.

3.2 CONVENTIONAL WEATHER DATA

Certain weather conditions have consistent and significant effects on IR sensors, directly affecting IR transmittance, the thermal contrast of the target and its background, and PGM delivery method. To account for such effects, the frequency of occurrence for several types of weather variables are included to provide a more complete description of IR working conditions than the transmittance alone provides. The following types of conventional weather data can be viewed:

3.2.1 Percent Occurrence of Ceiling: The presence of cloud ceilings is an important consideration when employing air-to-ground or ground-to-air EO systems. Transmittance is effectively zero through all but the thinnest clouds. A cloud layer between the sensor and the target will block the line of sight in the IR and the visible wavelengths. The vertical bars on these histograms give the percent frequency of occurrence for 13 ceiling categories. The curve shows the cumulative percent frequency of occurrence.

3.2.2 Ceiling Criteria (Menu output option "L"): Allows the user to display the percent frequency of ceiling at a selected height. The horizontal axis displays the time in GMT, by month, while the vertical axis depicts the percent frequency of occurrence. Similar to other output graphs, the histograms represent the percent frequency of occurrence, while the curve displays the cumulative percent frequency of occurrence.

3.2.3 Percent Occurrence of Precipitation: Precipitation has a varying effect on working conditions in the IR, depending on the intensity of the precipitation and the absolute humidity of the atmosphere. Moderate to heavy rain or snow usually reduces IR transmittance to zero, which makes IR systems useless. Even light rain or drizzle can severely reduce transmittance, but sensitive systems will retain some capability in such conditions.

The vertical axis shows the percent frequency of occurrence, while the horizontal axis shows time in GMT. Light rain (ra-) and light snow (sn-) are shown separately from moderate to heavy rain or snow because the different impacts of light and heavy precipitation on IR transmittance. The precipitation chart is logarithmic to allow for more clear analysis.

3.2.4 Percent Occurrence of Fog: Fog is a severe problem for systems using the 8-12 micron band because the condensed water vapor in the fog both absorbs and emits IR radiation. As noted in the "Aerosol Selection" (2.3) discussion, calculated

transmittance with fog conditions was accomplished three ways. High visibility fog significantly reduces the 4 km transmittance. As the visibility decreases, the IR transmittance drops as well. The percent frequencies of radiative and advective fog are combined because they have almost identical transmittance results (approximately zero). High visibility fog, fog with visibility 1 km or less, and the combined frequency of occurrence, are plotted for each month. Similar to the precipitation graph, the fog chart is logarithmic for quick identification of percent frequency of occurrence.

3.2.5 Absolute Humidity: Absolute humidity graphs provide a quick reference, by month and hour, of selected station mean absolute humidity values in grams per cubic meter. The horizontal axis displays time in GMT, while the vertical axis displays absolute humidity values. Absolute humidity values greater than 12 grams per cubic meter significantly degrade transmittance.

3.3 TRANSMITTANCE DATA

3.3.1 Mean Transmittance: Mean transmittance values (times 100) are read on the vertical axis, while months are shown on the horizontal axis. Mean monthly values of transmittance are plotted for each three-hourly time period. These plots enable the user to identify both the annual and diurnal variations of mean transmittance for each station of interest. Often the diurnal changes of mean transmittance are greater than the annual change.

3.3.2 Percent Occurrence of Transmittance: The distribution of transmittance in 0.05 increments for each station's month/hour combination is provided for analysis. The histograms give the percent frequency of occurrence for each of the 20 intervals of transmittance, while the curve provides the cumulative percent frequency of occurrence. If some threshold transmittance is known for the system being supported, you may determine how often transmittance falls below the threshold value. With the aid of the weather category tables (see 3.3.3) the influence and relative frequency of the various weather elements can be interpreted.

3.3.3 Weather Category Tables: The frequency of occurrence for weather elements for a given month/hour combination and the associated transmittance are provided in these tables to help interpret the data. Each observation is binned in only one weather category. Observations are binned in a cloud category ONLY if there is not a restriction to visibility. For instance, a cloud category will not be listed if there was also a

restricted visibility. The summary category presents calculations for the total number of observations used for a particular station's month/hour of interest. The summary line also provides the total number of observations used to generate the data in the table. Each listing gives the frequency of observations for that month/hour period, plus mean values of temperature, dew point, relative humidity, absolute humidity, visibility, wind speed, and transmittance. Transmittance values are further divided into 10 "Frequency of Transmittance" intervals to show the correlation of transmittance and weather categories.

3.3.4 Ceiling versus Transmittance Tables: Similar to weather category tables, these tables provide 10 transmittance values in association with 13 ceiling heights. The user can identify most (least) likely transmittance and ceiling combinations.

3.3.5 Electro-Optical Criteria (EOCRIT): EOCRIT allows the user to select a transmittance threshold value, ceiling threshold height, and two percent frequency of occurrence thresholds. A map is displayed of station circles each colored red (unfavorable), yellow (marginal), or green (favorable). The user can readily associate locations and E-O conditions. The EOCRIT utility can be used in a planning, training, or contingency mode to determine the climatologically best and worst locations.

3.4 STATION NARRATIVES

Narratives address a given stations' POR, synoptic influences, and transmittance values associated with climatological weather conditions. They were developed using EOCLIMO Ver 2.0 output and literature sources such as Miers et al. (1985), Vojtesak et al., (1990, 1991a, 1991b), and Walters et al. (1991). The narratives serve as a quick reference summary of a given site.

3.5 GEOGRAPHICAL MAP DISPLAY

This subprogram displays a geographical map of the stations loaded in the (sub)directory. The chosen station (centered on the map) and surrounding stations are displayed. A similar map display is used for the EOCRIT subprogram mentioned above.

4. CONCLUSIONS

LOWTRAN7 was used to compute climatologies of atmospheric transmittance in the 8-12 micron band using 4- to 14-year periods of record. USAFETAC surface DATSAV2 was used to provide input

data for the transmittance calculation, and to assemble statistics on the frequency of conventional weather elements (cloud ceilings, precipitation, and fog) that have a significant impact on electro-optical weapon employment. Results show the importance of absolute humidity in determining the IR transmittance (which is consistent with previously published reports). Without obscuring weather, this relationship drives both the seasonal and diurnal variation of IR transmittance. Because these data are derived from a model, users should familiarize themselves with the obvious (and some not so obvious) limitations inherent to the model. Any suggestions, comments, and criticisms that will help USAFETAC refine this format into the best operational tool are welcome. Your suggested improvements to the program may be included in the next release of EOCLIMO. Our objective is to create a product that can be applied, understood, and used throughout the EO community.

5. DISTRIBUTION

Distribution authorized to U.S. Government agencies and their contractors, critical technology, Sep 1991. Other requests for this software and data shall be referred to USAFETAC/LD, Scott AFB, IL 62225-5438. EOCLIMO Ver 2.0 will be available by geographical region through USAFETAC/LD, Scott AFB, IL 62225. A listing of the geographical regions is found in AWS/TC-FY/001, the Catalog of Air Weather Service Technical Documents. Data disks will contain EOCLIMO 2.0 data for 13-14 stations (3.5 inch floppy) grouped by block station number. Data sets will not be updated until an additional 5-year period of record has been established.

6. BIBLIOGRAPHY

- Condray, P. M., 1990: A LOWTRAN7 Sensitivity Study in the 8-12 and 3-5 Micron Bands. USAFETAC TN-90/002, USAF Environmental Technical Applications Center, Scott AFB, IL 62225.
- Condray, P. M. and R. T. Edson, 1988: Persian Gulf Transmittance Study in the 8-12 Micron Band. USAFETAC TN-88/003, USAF Environmental Technical Applications Center, Scott AFB, IL 62225.
- Edson R. T., R. H. Grumm, and J. G. Miller, 1987: Global Transmissivity Study for Electro-optical Weapon Systems in the 8-12 and 3-5 Micron Bands. USAFETAC PR-87/002, USAF Environmental Technical Applications Center, Scott AFB, IL 62225.
- Gathman, S. G., 1983: Optical Properties of the Marine Aerosol as Predicted by the Navy Aerosol Model. Optical Engineering, 22: 57-62.

- Kneizys, F. X., E. P. Shettle, W. O. Gallery, J. H. Chetwynd, L. W. Abreu, J. E. A. Selby, S. A. Clough, and G. P. Anderson, 1988: Users Guide to LOWTRAN 7. AFGL-TR-88-0177, Air Force Geophysics Laboratory, Hanscom AFB, MA 01731.
- Liou, K. N.: An Introduction to Atmospheric Radiation. International Geophysics Series, Volume 26, Academic Press, CA, pp 392.
- Miers, T. B., E. P. Avara, and L. D. Duncan, 1985: Global Electro-Optical Systems Environmental (GEOSEM) Climatology for Mideast and Southwest Asia. ASL-TR-0172, U.S. Army Atmospheric Sciences Laboratory, White Sands Missile Range, NM, 88002-5501.
- Seagraves, M. A. and E. P. Avara, 1991: Weather Effects on Smart Weapons Performance: A Climatological Study. ASL-TR-0295, U.S. Army Atmospheric Sciences Laboratory, White Sands Missile Range, NM, 88002-5501.
- Soliz, P. and J. S. Davis, 1981: Electro-Optical Systems Performance Climatology: An Alternative to Weather Statistics. Avionics Laboratory, AF Wright Aeronautical Laboratories, unpublished project report, 1981.
- Tooth, A. R., 1987: Atmospheric Modeling Studies. Postprints of 8th Annual EOSAEL/TWI Conference, U.S. Army Atmospheric Sciences Laboratory, White Sands Missile Range, NM 88002-5501.
- Vojtesak, M. J., K. P. Marten, and G. Myles, 1990: SWANEA (Southwest Asia-Northeast Africa)-A Climatological Study, Volume I: The Horn of Africa. USAFETAC/TN-90/004, USAF Environmental Technical Applications Center, Scott AFB, IL 62225.
- Vojtesak, M. J., K. P. Marten, G. Myles, and M. Gilford, 1991: SWANEA (Southwest Asia-Northeast Africa)-A Climatological Study, Volume II: The Middle East Peninsula. USAFETAC/TN-91/002, USAF Environmental Technical Application Center, Scott AFB, IL 62225.
- Vojtesak, M. J., K. M. Traxler, M. T. Gilford, K. P. Marten, and G. Hepburn, 1991: SWANEA (Southwest Asia-Northeast Africa)-A Climatological Study, Volume IV-The Mediterranean Coast and Northeast Africa. USAFETAC/TN-91/005, USAF Environmental Technical Application Center, Scott AFB, IL 62225.
- Walters, K. R., M. J. Vojtesak, K. P. Marten, G. Myles, M. T. Gilford, and K. M. Traxler, 1991: SWANEA (Southwest Asia-Northeast Africa)-A Climatological Study, Volume III: The Near East Mountains. USAFETAC/TN-91/003, USAF Environmental Technical Applications Center, Scott AFB, IL 62225.

THEORETICAL AND MEASURED FRACTAL DIMENSIONS FOR BATTLEFIELD AEROSOL CLOUD VISUALIZATION AND TRANSMISSION

**Donald W. Hoock
U. S. Army Atmospheric Sciences Laboratory
White Sands Missile Range, NM 88002-5501, USA**

ABSTRACT

The Hurst parameter and the related fractal dimension for the structure function and variance of obscuration through individual battlefield aerosol clouds are theoretically derived and compared to field measurements. The derivation assumes that the underlying atmospheric turbulent eddy structure follows a Kolmogorov scaling. With this assumption it is shown that as two lines of sight are separated more in space (or as obscuration differences over one line of sight are compared for increasing time differences), the Hurst parameter should decrease monotonically from a value of $5/6$ to a value of $1/3$. For time dependent obscuration this corresponds to the fractal dimension of transmittance increasing monotonically from 1.17 to 1.67. Although the fractal dimension is not a constant, obscuration through battlefield aerosols can still be characterized as a multi-fractal process. Its importance to target acquisition and protective aerosol screening is that large "holes" in the obscuration should be relatively more frequent than small "holes" in a statistically quantifiable way. Predictions are shown to compare favorably with measured transmission data through actual smoke and dust clouds. The implications of these results to physically correct scene visualization of battlefield clouds are demonstrated.

1. INTRODUCTION

Atmospheric turbulence induces concentration fluctuations in clouds of smoke and dust that are evident as variations in line of sight (LOS) obscuration and as rough, meandering, inhomogeneous clouds in images. The frequency and magnitude of "thick" and "thin" regions through obscurant plumes obviously impact target acquisition and tracking, laser ranging and designation, protective screening from EO systems, and detection of clouds themselves. Plume statistics are also important to obscuration simulation modeling and to scene visualization requiring realistic atmospheric effects.

These statistics have their origins in the dynamic cascade of energy from larger structures or eddies to smaller eddies, eventually to be consumed in the heat of dissipative friction. The process is maintained by changes in horizontal wind velocity with height, terrain coupling and mesoscale weather. Within the atmospheric boundary layer, over a range of sizes from a few hundred meters down to a few tenths of millimeters, the energy spectrum exhibits a striking linear fall off in the log of the Fourier transform power (squared velocity amplitude) when plotted versus log wavenumber (inverse length scale). If the turbulence is homogeneous (space filling) and isotropic (independent of direction), then this slope has the well-known value of $-5/3$, and the spectrum is named for Kolmogorov (Kolmogorov, 1941; 1962).

This paper connects homogeneous turbulence to transmittance fluctuations in smoke and dust plumes. First, it is shown theoretically that transmittance fluctuations are not a pure fractal. The Hurst parameter, which is related to the fractal dimension, is derived for transmittance over pairs of parallel LOS separated in space and for transmittance varying over a single LOS in time. This theoretical Hurst parameter is shown to vary with the ratio of LOS separation to length of the LOS through a plume. Next, measured transmittance is analyzed to support the theory. Finally, a visualization method is described that can induce these statistics on to Gaussian concentration models. The methods used are similar to those of a previous paper (Hoock, 1991), but the theory is new and greater control is provided in the current visualization technique.

2. THEORY

A Brownian time series $V(t)$ can be produced by adding at each time step an independent, Gaussian-distributed random number X_i from a population of variance σ^2 (Barnsley, 1988):

$$V(t_i) = V(t_{i-1}) + X_i \quad (1)$$

Over a time difference Δt , the mean squared variance in $V(t)$ will then be

$$\langle |V(t + \Delta t) - V(t)|^2 \rangle = (\Delta t)^{2H} \sigma^2 \quad (2)$$

H is called the Hurst parameter and is, for example, one-half for Brownian processes. For a Brownian process in particular, Eq. 2 is easily verified from the fact that the variance of a sum of independent random numbers is the sum of the population variances. More generally, however, Eq. 2 must apply over all time intervals and magnifications for a fractal process. Thus, the following functions must be statistically indistinguishable:

$$[V(t_0 + \Delta t) - V(t_0)] \quad \text{and} \quad r^{-H} [V(t_0 + r\Delta t) - V(t_0)] \quad (3)$$

The fact that $V(t)$ changes with a power law in magnification r is called self-affinity. It is the basis for many fractal generation schemes that add together such statistically indistinguishable functions over many scales. Equation 3 defines how much variance must be imposed at each scale for the result to be fractal.

Next, consider that a smooth line has a Euclidean dimension $E = 1$. If the line fluctuates on a sheet of paper in certain ways, however, then its fractal dimension D is said to exceed its Euclidean dimension $E = 1$. As the fluctuations are made larger, the line could begin to totally cover the paper as the fractal dimension D approached that of a surface $E = 2$. Fractal lines must have properties such that the lines remain equally "dense" at all magnifications (self-similarity) or at least that they follow some power law in scale magnification like Eq. 3 (self-affinity) at all magnifications. The Hurst parameter is related to the fractal dimension D and the Euclidean dimension E in which a fractal line, surface or volume lies by

$$D = E - H \quad (4)$$

The smoothness of the time series (or similar spatial distribution) thus increases as the Hurst parameter varies from zero to one. A Hurst parameter between zero and one-half has more pronounced fluctuations than those of Brownian motion and a negative correlation or anti-persistence over time in the chosen X_i . A Hurst parameter between one-half and one implies a positive correlation or persistence between X_i , and fluctuations are smoother than those of Brownian motion.

Homogeneous Kolmogorov turbulence follows a similar power law for components of wind velocity and for conservative scalars such as concentration. H has a value of one-third. The spatial version of the variance over time lags is called the structure function:

$$(\Delta x)^{-2H} \langle |v(x + \Delta x) - v(x)|^2 \rangle = \text{Const.} \quad (5)$$

If the time series (or similarly the spatial curve) is Fourier transformed, then the power per unit frequency (or per spatial wavenumber) will thus fall off in scale as $-(2H + 1)$. For velocity components or concentrations in Kolmogorov turbulence with $H = 1/3$, this will be the familiar $-5/3$ fall off in power spectral density.

Path-integrated concentration is also called the concentration-length (CL). To estimate the effects of concentration fluctuations on CL, a fluctuation factor f_T can be used to relate the instantaneous, fluctuating CL to the local mean $\langle CL \rangle$ as

$$CL(\rho) = \langle CL(\rho) \rangle [1 + f_T(\rho)] \quad (6)$$

where ρ is a position in the plane perpendicular to the LOS. The effect on transmittance T can be written in terms of α , the smoke mass extinction coefficient, and approximated:

$$\begin{aligned} T(\rho) &= e^{-\alpha CL} = e^{-\alpha \langle CL \rangle [1 + f_T(\rho)]} = \langle T(\rho) \rangle e^{-\alpha \langle CL \rangle f_T(\rho)} \\ &\approx \langle T(\rho) \rangle [1 + f_T(\rho) \ln \langle T(\rho) \rangle] \end{aligned} \quad (7)$$

Fluctuations across an image depend on correlations between separated LOS and the structure function for the CL fluctuation f_T . Assume two parallel LOS separated by a distance ρ . Each LOS passes through an aerosol cloud over a length x . Using H of $1/3$ for concentration fluctuations, the theoretical structure function for CL is:

$$\begin{aligned} &\langle |f_T(x, \rho) - f_T(x, 0)|^2 \rangle \\ &= \left(\frac{C_{cf}}{x}\right)^2 \int_0^x ds \int_0^x ds' \{ [(s-s')^2 + \rho^2]^{\frac{1}{3}} - (s-s')^{\frac{2}{3}} \} \\ &= 3.82 \left(\frac{x}{L_o}\right)^{\frac{2}{3}} \sigma_c^2 \int_0^1 dw (1-w) \{ [w^2 + (\frac{\rho}{x})^2]^{\frac{1}{3}} - w^{\frac{2}{3}} \} \end{aligned} \quad (8)$$

where the fluctuation strength C_{cf} can be estimated in terms of the local mean gradient in concentration and the outer scale of turbulence (largest eddy in the inertial range) L_o :

$$C_{cf}^2 = 2.8 L_o^{\frac{4}{3}} \left| \frac{\nabla \langle c \rangle}{\langle c \rangle} \right|^2 = 1.91 L_o^{-\frac{2}{3}} \sigma_c^2 \quad (9)$$

where σ_c is the (dimensionless) concentration fluctuation standard deviation.

For optical turbulence an integral like that in Eq. 8 is also performed. However, in that case one confines the LOS path separations to small distances on the order of the sensor lens or effective aperture and, applying appropriate approximations, one obtains analytic results. Here, however, the LOS separations of interest can be very large, even exceeding

the length of the LOS itself. The integral in Eq. 8 can easily be performed numerically, however, without resorting to approximations. Values for the integral are shown in Fig. 1 for various ratios of the LOS separation ρ to the path length through the aerosol x .

Of particular interest is the slope of the log of the integral plotted in Fig. 1 with respect to the log of the ratio of path separation to path length. The Hurst parameter H is one-half this slope. H is plotted in Fig. 2 for the integral plotted in Fig. 1.

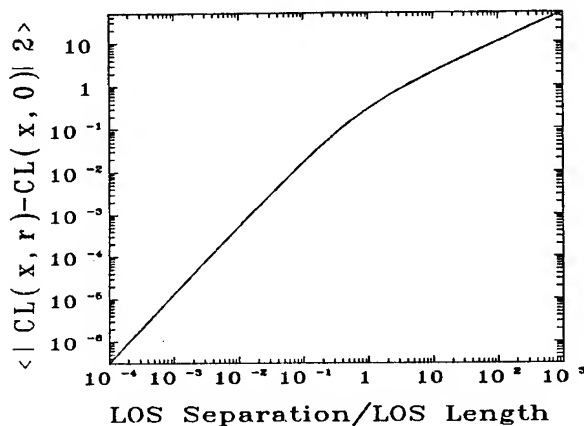


Figure 1. CL Structure Function for LOS Separation ρ with Each LOS of Length x .

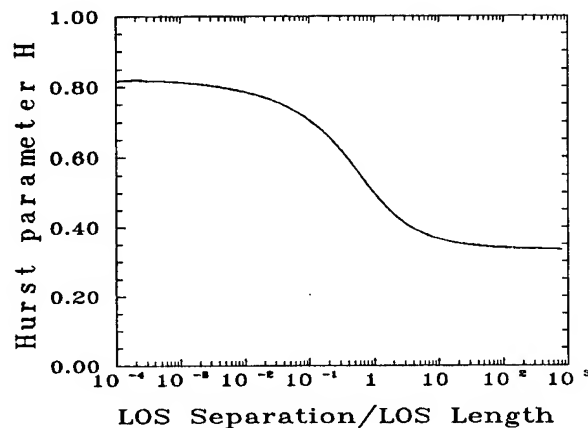


Figure 2. Hurst Parameter H for LOS Separation ρ with Each LOS of Length x .

As a wind blows obscurant across a LOS with velocity u , we can identify the turbulence-induced variations with separation ρ as spatially equivalent, through $\rho=ut$, to fluctuations in time over a single fixed LOS. This is called the "frozen-in" hypothesis for turbulence. The Hurst parameter for the CL thus determines how smoothly the CL (and thus the transmittance) fluctuates between LOS pairs or with time over a single LOS. The Hurst parameter in Fig. 2 ranges from 5/6 for very small LOS separations (or small time differences for a cloud blowing across a fixed LOS) to 1/3 for very large separations. Note that H is 1/2 and the fluctuations appear Brownian when the path separation to path length ratio is near one.

Thus, while concentration fluctuations are fractal in homogeneous turbulence, the CL path integral through an aerosol cloud of finite width does not have a constant fractal dimension. That is, the Hurst parameter, and thus the fractal dimension, changes with LOS path separations or with time separations for a single LOS. (In recent literature this changing fractal dimension might be characterized as "multi-fractal" rather than non-fractal). Since clouds are viewed through their transmitted light, this means that the cloud will appear to have relatively smooth changes at small scales (typically up to a few meters or fluctuations over seconds) and relatively large changes, including holes, at larger scales (tens of meters or tens of seconds).

3. COMPARISON WITH DATA

Much of the existing database on transmission through plumes of smoke and dust describes very obscured conditions (e.g. the SMOKE WEEK test series) or records data for aerosol sources that dissipate too rapidly to provide long time series for the statistical analysis of fluctuations through the obscurant. Therefore a small scale Atmospheric Transmission and Contrast Test (ATAC) was performed at White Sands Missile Range, NM in 1989 with smoke

and dust released at a relatively constant rate for up to 8 to 10 minutes. The concentrations released were such that a transmissometer approximately 50 m downwind of the release point would experience significant transmittance degradation, but would rarely "bottom out" at the transmissometer limit of less than 1% transmittance.

The ATAC data contain 45 minutes of transmission through white fog oil smoke in a total of 5 trials, 22 minutes through black carbon smoke in 4 trials, and 32 minutes through kaolin clay dust in 4 trials. Transmittance was measured at 4 bands in the visible through infrared and reported at a rate of one point per second, for a total of approximately 5,500 data points. Wind, temperature, relative humidity and other environmental data were taken concurrently from two towers within 500 m of the plumes. The plumes were within approximately 45 degrees of blowing perpendicular (cross wind) to the transmissometer optical path.

Figures 3 and 4 show examples of transmission during two trials. Note that the decrease in H predicted in Fig. 2 is evident in the relatively small fluctuations over small time steps and in the relatively large fluctuations over longer time scales. The clouds were 30 to 50 m wide at the LOS with wind speeds of 3 to 5 m/s. Having derived CL from the measured transmittances, Fig. 5 shows the mean squared difference in CL at constant time lags plotted against the time lag on a log-log scale. The variances for the six trials shown have been normalized to one at a time difference of one second to show the slopes more clearly. Agreement with the theory that the Hurst parameter should be about $5/6$ (0.83) at small time differences, about $3/4$ at 1 s, and about $1/3$ (0.33) at large time differences is evident. If transmittance and CL were true fractals, then each of these plots would be a straight line with constant slope equal to twice the Hurst parameter.

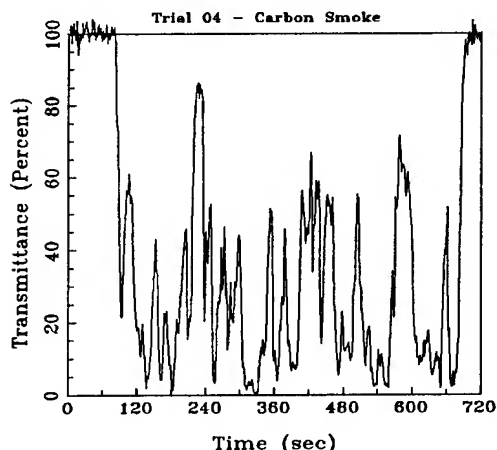


Figure 3. Visible Transmission, Trial 4.

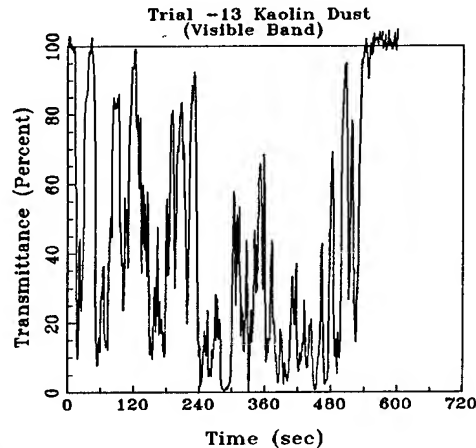


Figure 4. Visible Transmission, Trial 13.

For comparison, note the variance plotted for wind speed components in Fig. 6. The roughly straight line behavior is indicative of pure fractal behavior. The measurements generally support the Kolmogorov scaling law, with a Hurst parameter of $1/3$.

Statistically the change in Hurst parameter can be understood as follows. As two closely spaced LOS are separated they enter separate turbulent eddies of sizes smaller than the separation width. The separate very small eddies are uncorrelated and relatively numerous over the finite lengths of the LOS through the cloud, so they contribute a large change in variance to the CL as the LOS are slightly separated. At greater LOS separations, the larger

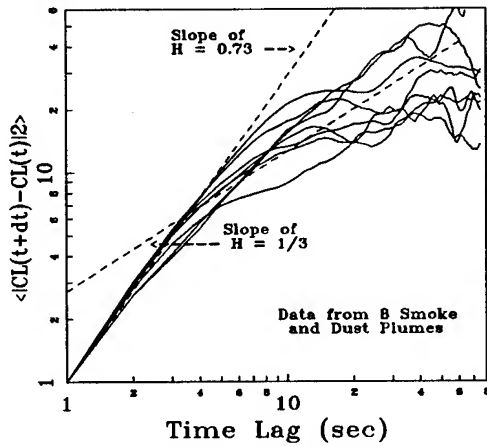


Figure 5. Measured CL Variance.

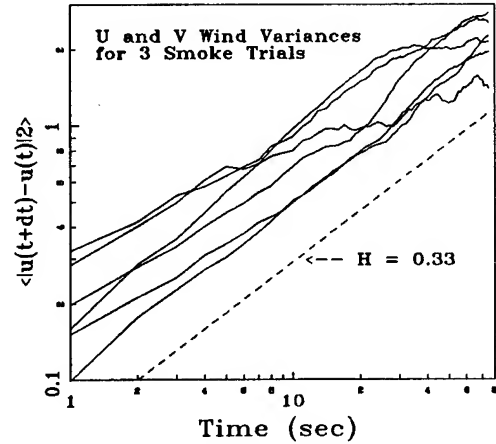


Figure 6. Measured Wind speed Variance.

eddies become less correlated between the two LOS, and they thus contribute to the variance. However, since there are fewer of the large eddies due to the finite width of the cloud, they contribute relatively less than the small eddies to an increase in variance.

It is thus the sampling property of a finite cloud width that causes the Hurst parameter for CL and transmittance to change. As the outer scale is exceeded, the turbulence becomes inhomogeneous, and the number or energy of larger eddies typically decreases. This behavior begins to appear at the larger times in Fig. 5.

4. MODELING FRACTAL CLOUDS

There are several ways to impose fractal statistics on mean distributions to allow such variations to be modeled (Barnsley, 1988). Two popular methods are successive random addition and Fourier filtering. The first method adds random displacements of the proper variance to many scales to generate fluctuations in "real" space. The second method imposes noise of the proper power spectral density and randomized phases in "frequency" or Fourier transform space. We will use a variant of the second method in this section. It uses a geometric series (as opposed to the arithmetic Fourier series) of trigonometric functions similar to the Weierstrass-Mandelbrot series (Barnsley, 1988). In an earlier paper (Hooek, 1991) this method was applied to "compressions" in concentration. Here we will use a more conventional and flexible method that allows more control over the process.

Consider a Gaussian function and its Fourier transform:

$$g(x) = \frac{1}{\sqrt{2\pi} \sigma_x} e^{-\frac{1}{2} \left(\frac{x - x_0}{\sigma_x} \right)^2}$$

$$G(k_x) = \int e^{-ik_x x} g(x) dx = e^{-ik_x x_0} e^{-\frac{1}{2} k_x^2 \sigma_x^2} \quad (10)$$

$$g(x) = \sum_j G(k_{xj}) e^{ik_{xj} x} \quad \text{where } k_{xj} = j \left(\frac{2\pi}{L_{x0}} \right)$$

where x_0 is the centroid position, and σ_x is its standard deviation. Written as a series, the

third equation shows that the original Gaussian function can be reproduced by a sum over trigonometric functions with wavenumber k_{xi} (over an outer scale L_{ox} much wider than the distribution) with coefficients given by the Fourier transform of the second equation.

One can use a similar equation to produce the fractal fluctuations in a three-dimensional concentration field, namely:

$$f_c(x, y, z) = \sum_{lmn} \frac{A_{lmn}}{F_{lmn}} e^{i[k_{xl}(x - ut) + \phi_{xl}]} e^{i[k_{ym}y + \phi_{ym}]} e^{i[k_{zn}z + \phi_{zn}]} \quad (11)$$

where u is wind speed, the phases ϕ are chosen at random on $[0, 2\pi]$, and wavenumbers increase geometrically rather than arithmetically as:

$$k_j = r^j k_o, \quad \text{where} \quad k_o = \frac{2\pi}{L_o} \quad (12)$$

where r is a magnification factor (typically chosen from 1.5 to 2.8) that controls the fractal "lacunarity", and L_o is the appropriate outer scale of turbulence. The "noise" term F is:

$$F_{lmn} = (\sqrt{k_{xl}^2 + k_{ym}^2 + k_{zn}^2})^H \quad (13)$$

which imposes a structure with Hurst parameter H . The complex coefficients A are:

$$A_j = \sum_{s_o, \sigma_o} e^{-i k_j s_o} e^{-\frac{1}{2} k_j^2 \sigma_o^2} \quad (14)$$

for each coordinate, where s_o is a randomly placed centroid coordinate of a small Gaussian "puff" of standard deviation (width) σ_o . The coefficients A are thus the Fourier coefficients of some random distribution of puff-like structures that are fixed once and for all for a simulation. Their specific number, positions and sizes are not at all critical. The coefficients A are used simply to "spread out" the effects of the noise.

One important point is that in the above geometric series in wavenumber each term represents the spectral power over a band of wavenumbers of magnitude k_{xl} , k_{ym} , k_{zn} rather than power per unit wavenumber as is the case for a Fourier series. Thus, the noise term F uses H as the exponent rather than $(2H + 3)/2$ which would be used for a Fourier series technique.

For CL and transmittance fluctuations, we integrate the y component over a region comparable to the width of the plume (say $6\sigma_y$) to give the corresponding series:

$$f_T(x, z) = \sum_{lmn} \frac{A_{ln}}{F_{lmn}} e^{i[k_{xl}(x - ut) + \phi_{xl}]} e^{i[k_{zn}z + \phi_{zn}]} \frac{\sin(3k_{ym}\sigma_y)}{k_{ym}} e^{-\frac{1}{2}k_{ym}^2\sigma_y^2} \quad (15)$$

where the y (cross wind) distances have been integrated over, and the A coefficient component for y has been replaced by the explicit Fourier transform of the mean Gaussian width σ_y .

The phases ϕ are chosen as random numbers which are allowed to shift in time as successive images of the plume are generated. The phases are correlated, however, to the mean lifetime of eddies of each size. Smaller eddies have shorter lifetimes than large eddies that

scale as time to the 2/3 power for homogeneous (Kolmogorov) turbulence. Thus, for each eddy wavenumber scale $k_j = 1/L_j$ there is a lifetime t_{oj} given by

$$t_{oj} = r^{-\frac{2}{3}j} \frac{L_o}{u} \quad (16)$$

where u is the horizontal wind speed. This applies for surface releases because the change in wind speed over the vertical scale equals the wind speed itself (i.e. it is zero at the surface). Each phase ϕ_j can be changed over time step Δt by interpolating with a new random number ϕ_{rv} distributed uniformly on the interval $[0, 2\pi]$. Independence of the new ϕ_j with its previous value occurs only between times separated by the characteristic lifetime t_{oj} , however, so a correlation function $R(\Delta t_j)$ is used:

$$\phi_j^{\text{new}} = \phi_j^{\text{old}} R(\Delta t) + \phi_{rv} [1 - R(\Delta t)], \quad \text{where} \quad R(\Delta t) = e^{-\Delta t / t_{oj}} \quad (17)$$

Variants of the basic method can include an outer-scale cut off for the noise filter F , which allows scales larger than the outer scale to be included in the sum. This reduces undesirable aliasing. The spectrum we sometimes use is (after Ishimaru, 1978):

$$F_{lmn} = (1 - e^{-\frac{1}{3} P_{lmn}^2}) \left[\frac{\sqrt{1 + P_{000}^2}}{\sqrt{1 + P_{lmn}^2}} \right]^H \quad (18)$$

The maximum scale L can exceed L_o and the magnitude $k^2 L^2$ sums over components:

$$P_{lmn}^2 = (k_{xl} L_{x0})^2 + (k_{ym} L_{y0})^2 + (k_{zn} L_{z0})^2 \quad \text{where} \quad k_j = r^j \left(\frac{L_{\min}}{2 L_{\max}} \right) \quad (19)$$

Figures 7 and 8 show a modeled Gaussian cloud of smoke with the imposed fractal structure simulated at 4 and 10 seconds using $r = 2.634$. The cloud is 250 m long and approximately 70 m high at its farthest downwind point. Outer scale dimensions are 103 m downwind, 95 m cross wind and 39 m high. Wind is 2.5 m/s at 4 m height. Contours are enhanced in these figures to better show the structure. A video tape of visualized cloud animation is shown in the paper presentation.

As the magnification r is varied or the widths of the puff-like structures in A_{ln} are varied, the quality of simulated clouds changes somewhat. Smaller values of r produce more uniform fluctuations across the cloud. The parameter r is said to control the "lacunarity" or spacing of the imposed fractal patterns. Smaller radii puffs in A_{ln} also cause more detail in to appear in the simulated clouds. However, this is not always a desirable feature since aliasing at specific regions of a simulated image can occur unless a large range of scales is summed. Typically for dimensions of those shown in Figs. 7 and 8, from 5 to 8 terms are required in the summation to span from a meter to a few hundred meters, depending on the value chosen for r .

Clouds simulated by this technique have the required Hurst parameter behavior, as shown in Fig. 9. Three values for r were used, and fluctuations at the different ratios of path separation to path length were computed. The agreement with the field data is fairly good.

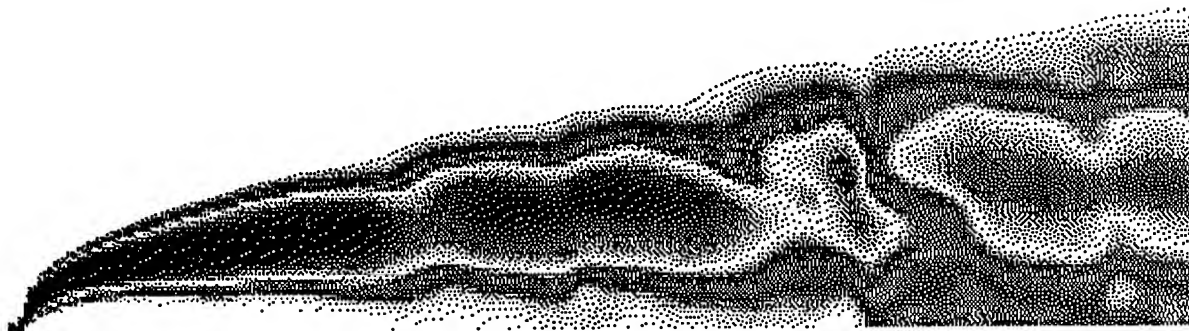


Figure 7. Simulated Fractal Smoke Cloud at $t = 4$ s and $r = 2.63$. Cloud is 250 m Long and Approximately 70 m High. Smoke Release Rate is Constant.

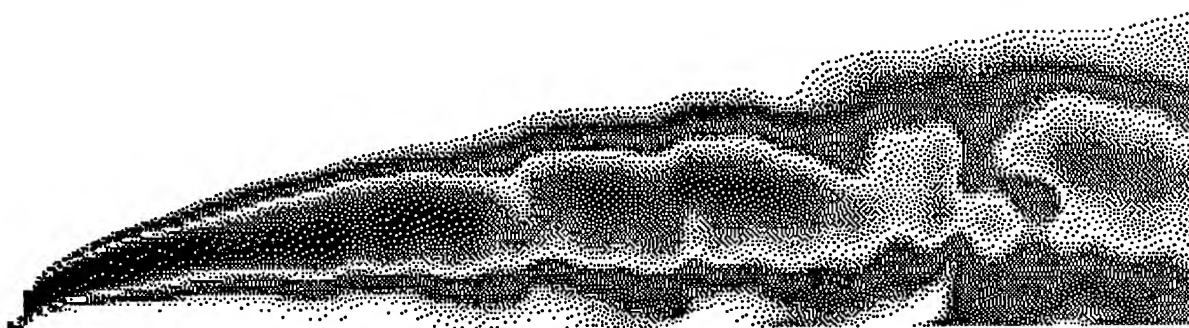


Figure 8. Simulated Fractal Cloud at $t = 10$ s and $r = 2.63$.

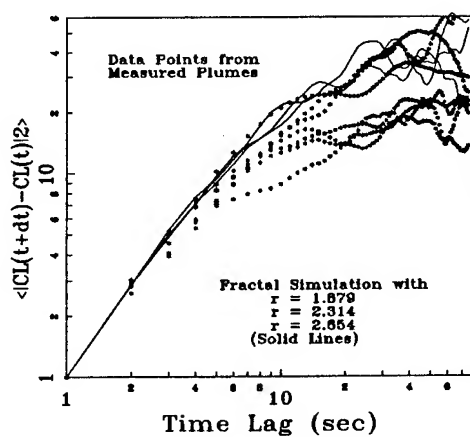


Figure 9. Comparison of Modeled and Measured Structure Function for Different r .

5. CONCLUSIONS

It has been shown that homogeneous turbulence leads to a Hurst parameter for CL through an individual plume of smoke or dust that decreases from $5/6$ to $1/3$ with increasing LOS separations or increasing time differences. The theory predicts that the important parameter is the ratio of separation to path length through the cloud, crossing through the Brownian Hurst parameter of $1/2$ when the separation distance about equals the distance through the plume (or equivalently the time difference about equals plume width divided by wind velocity). This change in Hurst parameter corresponds to CL and transmittance fluctuations with fractal dimensions that increase from $7/6$ (relatively smooth) to $5/3$ (large fluctuations) as these separations increase. The theory is supported by field measurements of transmittance through smoke and dust. A method was then demonstrated to show how these statistics can be incorporated into modeled Gaussian plumes. As part of the oral presentation, an animation of simulated cloud images was shown to illustrate the model.

REFERENCES

- Barnsley M. F. , R.L. Devaney, B. B. Mandelbrot, H. O. Peitgen, D. Saupe and R. F. Voss, 1988: The Science of Fractal Images, H.-O. Peitgen and D. Saupe, ed., Springer-Verlag, NY.
- Hoock, Donald W., 1991: Modeling Time Dependent Obscuration for Simulated Imaging of Smoke and Dust Clouds, in Proceedings of the SPIE Vol. 1486, 164-175.
- Ishimaru, Akira, 1978: Wave Propagation and Scattering in Random Media, Academic Press, NY.
- Kolmogorov, A. N., 1941: Local Structure of Turbulence in an Incompressible Fluid at Very High Reynolds Numbers, Dokl. Akad. Nauk SSSR, 30, 299-303.
- Kolmogorov, A. N., 1962, A Refinement of Previous Hypotheses Concerning the Local Structure of Turbulence in a Viscous Incompressible Fluid at High Reynolds Number, J. Fluid Mech., 13, 82-85.

VISUALIZATION OF BATTLEFIELD OBSCURANTS

Geoffrey Y. Gardner
Grumman Data Systems
Woodbury, NY 11797

G. Michael Hardaway
U.S. Army Topographic Engineering Center
Fort Belvoir, VA 22060-5546

ABSTRACT

The EOSAEL Combined Obscuration Model for Battlefield Contaminants (COMBIC) module models the transmittance of seven electro-optical wavelengths through 30 obscurant sources types. Designed as a war gaming tool, COMBIC computes the transmissivity along selected lines of sight, but does not allow realistic visualization of the obscurants. Because of their amorphous nature, obscurant clouds are particularly difficult to model with traditional computer graphics techniques, which employ flat polygons to model clearly defined features. Grumman Data Systems has developed non-traditional computer graphics techniques using fractal ellipsoids to model clouds realistically but economically. This paper describes work initiated by the U.S. Army Topographic Engineering Center to integrate Grumman graphics technology with COMBIC to provide realistic visualization of battlefield obscurants. COMBIC Phase I subroutines are used to generate an obscurant cloud envelope. This envelope is then filled with fractal ellipsoids which can be manipulated dynamically to generate animated sequences of the obscurant's development.

1. INTRODUCTION

Obscurants are such an important factor in the battlefield that smoke obscurants are generated deliberately to screen offensive operations. To provide computer models describing the physics of battlefield obscurants, the U.S. Army Atmospheric Sciences Laboratory has developed the Electro-Optical Systems Atmospheric Effects Library (EOSAEL) (Shirkey et al, 1987). The EOSAEL module, Combined Obscuration Model for Battlefield Contaminants (COMBIC) (Hoock et al, 1987) models a wide range of battlefield obscurants, predicting time histories of obscurant envelopes and transmittance from given meteorological and surface conditions. With this capability, COMBIC provides a firm basis for visualizing the effects of battlefield obscurants but does not include the graphic capability to do so. In particular, COMBIC generates smooth plumes which lack the statistical variations of real plumes. These variations are needed to simulate holes and thin regions in the plumes which are important to tactical operations as windows of opportunity.

Currently, computer simulation of battlefield scenes is limited to the representation of hard, clearly defined surfaces such as terrain and targets. Little has been accomplished in modeling obscurants because their amorphous nature does not lend itself to traditional computer graphics techniques which use flat polygons bounded by straight edges to model scene features. The U.S. Army Topographic Engineering Center's (TEC) Terrain Visualization system uses such techniques to model terrain and targets, but does not include capability to model obscurants,

Grumman Data Systems has taken a nontraditional approach using fractal ellipsoids to model cloud volumes economically (Gardner, 1985). A fractal ellipsoid is a geometric ellipsoid that has been processed by applying a 3-D fractal texture to simulate natural variations in mass distribution. By modulating the translucence and surface shading of the ellipsoid, the fractal texture simulates statistical variations in transmittance and reflectance characteristic of variations in mass.

The Topographic Engineering Center recommended integrating Grumman graphics with EOSAEL to support TEC's Terrain Visualization effort. This study was undertaken to realize this goal by applying Grumman graphics technology to COMBIC obscurant models (Gardner, 1991).

2. GRAPHICS DEVELOPMENT

2.1 INTRODUCTION

This section describes the development of graphics techniques to provide realistic visualization of COMBIC obscurants by using Grumman's fractal ellipsoids to fill the obscurant envelopes generated by COMBIC.

2.2 DESCRIPTION OF COMBIC

COMBIC was designed as a war gaming tool to predict transmittance through an obscurant as a function of sensor wavelength and optical thickness along a specified line of sight. COMBIC computes transmittance, Tr , from these factors by the following equation.

$$Tr = e^{-\alpha(\lambda) CL} \quad (1)$$

where α is the extinction coefficient dependent on the wavelength, λ , of the sensor, and CL represents the integral of the obscurant mass over the path length.

COMBIC includes geometric models for obscurant clouds which enable the computation of the *CL* term. COMBIC uses a coordinate system relative to the wind with the origin at the obscurant source, and *X*, *Y*, and *Z* representing the downwind, crosswind, and vertical directions.

COMBIC models obscurant clouds with one to five subclouds. Each subcloud is defined either by a Gaussian puff or by a continuous Gaussian plume. A Gaussian puff is modeled by an ellipsoid whose mass has a Gaussian distribution and is used to represent an instantaneous subcloud, for example, a puff of dust or a fireball from a munition detonation. Figure 1 shows the geometry of a typical Gaussian puff.

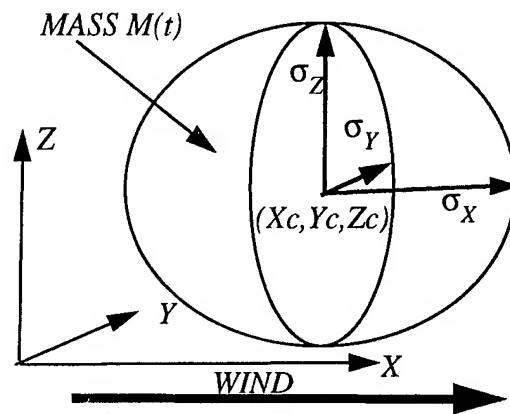


Figure 1. Gaussian puff geometry

COMBIC defines the Gaussian variation on mass concentration as

$$C(X, Y, Z) = \frac{Mass}{(2\pi)^{3/2} \sigma_X \sigma_Y \sigma_Z} e^{-\frac{1}{2} D^2} \quad (2)$$

where:

$$D^2 = \left(\frac{X - X_c}{\sigma_X} \right)^2 + \left(\frac{Y - Y_c}{\sigma_Y} \right)^2 + \left(\frac{Z - Z_c}{\sigma_Z} \right)^2 \quad (3)$$

A Gaussian plume, which looks like a bent cone, is used to represent the elongated envelope of a continuous obscurant such as smoke. Figure 2 shows a typical plume.

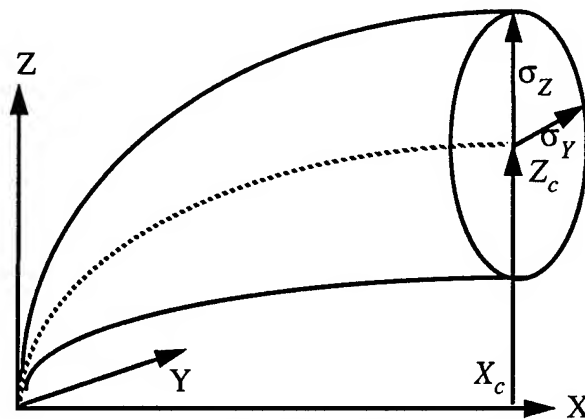


Figure 2. Gaussian plume geometry

COMBIC performs its function in two phases. Phase I uses differential equations driven by meteorological and terrain surface data to compute a time history of the obscurant trajectory. The time history represents a geometric envelope in terms of the downwind coordinate system.

For an instantaneous puff, the time history contains the X and Z positions (Y is always zero) and the X, Y and Z dimensions, computed at specific points in time. The time history for a continuous plume defines the leading (downwind) edge of the obscurant by its X and Z positions and its X, Y and Z dimensions, computed at sampled points in time. For plumes, Phase I also computes a time history of mass production from the continuous obscurant source.

In Phase II, COMBIC uses the trajectory and mass data generated in Phase I to compute transmittance through a given line of sight.

2.3 APPLICATION OF COMBIC

Development of software to allow visualization of COMBIC output was achieved in two steps:

1. The essential features of the COMBIC software for producing trajectory time histories and mass production tables were extracted from the original COMBIC code and compiled into a new program called "COMB_I." Phase II subroutines were not included.
2. Graphics techniques and software were developed to generate and display fractal ellipsoids filling the trajectory envelopes produced by COMB_I. This software comprises a second computer program called "COMBICV," standing for "COMBIC Visualization."

2.4 COMBICV DEVELOPMENT

COMBICV uses the COMBIC model to represent the geometry and transmittance of an obscurant with enough detail to allow realistic visualization. Radiance is approximated by Grumman graphics techniques which use diffuse surface reflection of ellipsoids modulated by a texturing function.

2.4.1 COMBICV Geometry Model

The strategy for developing the geometric model was to apply the Grumman ellipsoid modeling technique in the most straightforward way to fill the obscurant envelope defined by the COMBIC trajectory time history data. The key problem was to provide a realistic yet computationally economical dynamic capability to produce animation of obscurant development.

2.4.1.1 Geometric Model for Instantaneous Puffs

COMBIC models an instantaneous puff as a Gaussian ellipsoid and produces a time history of the position and size of the ellipsoid as it moves downwind. COMBICV fills the Gaussian ellipsoid with subellipsoids defined by parameters specifying the extent of the Gaussian puff, the number of subellipsoids used to fill the puff, and the X, Y and Z dimensions of the subellipsoids.

For each point in time, COMBICV accesses the trajectory data and determines by linear interpolation what the proper puff position and dimensions are. COMBICV scales these dimensions and then positions the preset number of subellipsoids to fill the puff. As the puff moves downwind in time, it expands. Because the number of subellipsoids in each direction is kept constant, their spacing is increased to fill the puff. At the same time, the dimensions of each subellipsoid are increased as a predefined fraction of the puff dimensions. Figure 3 shows the COMBICV geometric model for an instantaneous puff with random variations in subellipsoid size and position added to provide realism.

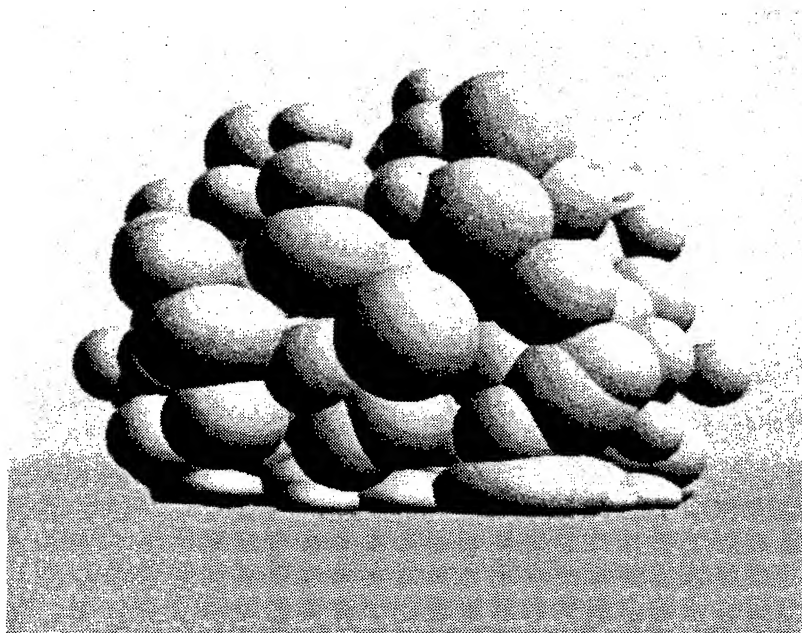


Figure 3. COMBICV geometric model for an instantaneous puff

2.4.1.2 Geometric Model for Continuous Plumes

COMBICV model uses a source footprint of circular shape with a defined radius. Within this footprint at equally spaced intervals, starting points for a specified number of ellipsoid columns are defined. The center column follows the trajectory time history center line, while the other columns fan out to fill the trajectory envelope. This is achieved by using the centerline data along with the trajectory dimension data which expands downwind. Each column is shifted from the centerline by an amount depending on its source position relative to the center of the footprint and the dimensions of the envelope.

The next step in the geometry model is to position ellipsoids along each column. An efficient approach is to space the ellipsoids to minimize overlap while maintaining realistic contiguity. This can be done in the following manner. For any given time, T_{traj} , at which we are viewing the obscurant, we position the ellipsoids starting from the plume downwind leading edge. The first (farthest downwind) ellipsoid is positioned from the trajectory time history data at time $T_1 = T_{traj}$. The downwind and vertical positions, X_{p_1} and Z_{p_1} , are computed from the trajectory data using linear interpolation. The trajectory dimensions, σ_{X_1} , σ_{Y_1} , and σ_{Z_1} at time T_1 are also determined by interpolation. These σ s are scaled by a user-specified parameter to define the dimensions, X_{s_1} , Y_{s_1} , and Z_{s_1} , of the most downwind ellipsoid in the column. The values X_{s_1} and Z_{s_1} provide data for determining the next time T_2 at which we will position the second ellipsoid slightly upwind of the first such that its center lies on the first ellipsoid to provide good overlap. Size data is computed at T_2 to determine the third ellipsoid, and the process is continued until the last ellipsoid in the column near the source is produced at time T_n . Figure 4 shows the final column produced in this manner.

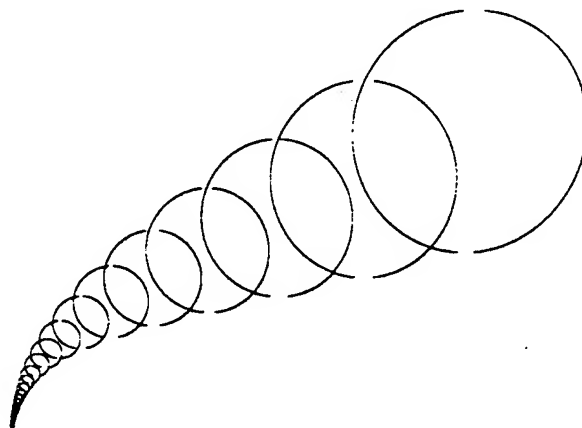


Figure 4. Subellipsoid spacing in a column

Using this approach for multiple columns which fan out fills the envelope well. Random variations in the positions and dimensions of each of the ellipsoids can be applied to add realism as shown in Fig. 5.

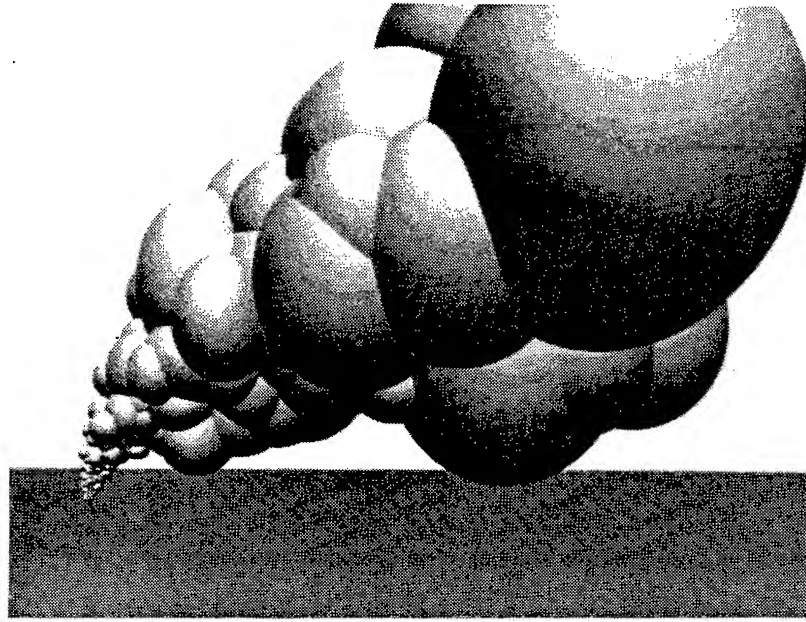


Figure 5. COMBICV geometric model for a continuous plume

2.4.2 COMBICV Transmittance Model

To provide visualization of the COMBIC obscurant model, COMBICV determines the transmittance through an obscurant for the line of sight through each image pixel in two steps. First, the transmittance through each subellipsoid covering the pixel is computed. Then the combined transmittance through all ellipsoids covering the pixel is computed. The first step is further partitioned into three substeps:

1. The transmittance through the center of the subellipsoid is computed.
2. A Gaussian variation in subellipsoid mass concentration is approximated by increasing the transmittance toward the silhouette of the subellipsoid.
3. Statistical variations in mass concentration are simulated by applying a fractal function which modulates transmittance.

2.4.2.1 Center Transmittance of Subellipsoids

The center transmittance for each subellipsoid is based on the mass contained in the subellipsoid. Mass is assigned to each subellipsoid by partitioning the total mass of the obscurant according to

the position of the subellipsoid within the obscurant envelope. COMBICV partitions mass differently for puff and plume obscurant models.

For a puff, COMBICV partitions the total puff mass among the subellipsoids by using eq. (2) to compute a weighting factor for each subellipsoid based on the coordinates of the subellipsoid center. The weighting factor is normalized to ensure that the total mass is exactly distributed among all subellipsoids. Mass assignment is independent of trajectory time, T_{traj} , of the puff, except that the total mass is adjusted for evaporation or deposition.

The plume model is treated differently to account for the time distribution of mass resulting from a continuously burning source. In this case, total airborne obscurant mass is partitioned among subellipsoids in each column using the mass production history data. For multiple columns, the mass must also be partitioned across the columns. COMBICV allows a simple averaging based on the number of columns, but also provides the option of weighting the average to approximate a Gaussian distribution across the obscurant envelope, producing a greater concentration of mass for subellipsoids in columns near the plume centerline.

Once the fraction of total mass has been determined for a subellipsoid, the distribution of mass within the subellipsoid is treated as Gaussian and the transmittance through the center is computed using digital integration of eq. (2).

2.4.2.2 Gaussian Variation of Subellipsoid Transmittance

To approximate a Gaussian variation in subellipsoid mass, a Gaussian variation in transmittance is approximated by increasing the transmittance from that at the center of the subellipsoid to a value of unity at the silhouette of the subellipsoid image. This operation is performed during image rendering using a high-order function in image coordinates based on the ellipse which represents the perspective projection of the subellipsoid silhouette.

2.4.2.3 Fractal Variation of Subellipsoid Transmittance

During image rendering, COMBICV also simulates natural variations in subellipsoid mass distribution by modulating transmittance with a three-dimensional texture function based on scene coordinates of the subellipsoid surface. The function is an abbreviated fractal function composed of short summations of cosines in each of the three scene coordinates (Gardner, 1991). At each image point on the subellipsoid, the corresponding scene coordinates of the subellipsoid are calculated and the function computed to modulate the transmittance of the subellipsoid.

2.4.2.4 Combined Transmittance for Multiple Subellipsoids

From eq. (1), for each image pixel, the total transmittance through N ellipsoids covering the pixel can be computed by taking the product of the individual transmittance values.

Figure 6 shows the result of the COMBICV geometric and transmittance models for source 30 modeled with 13 columns emanating from the footprint.

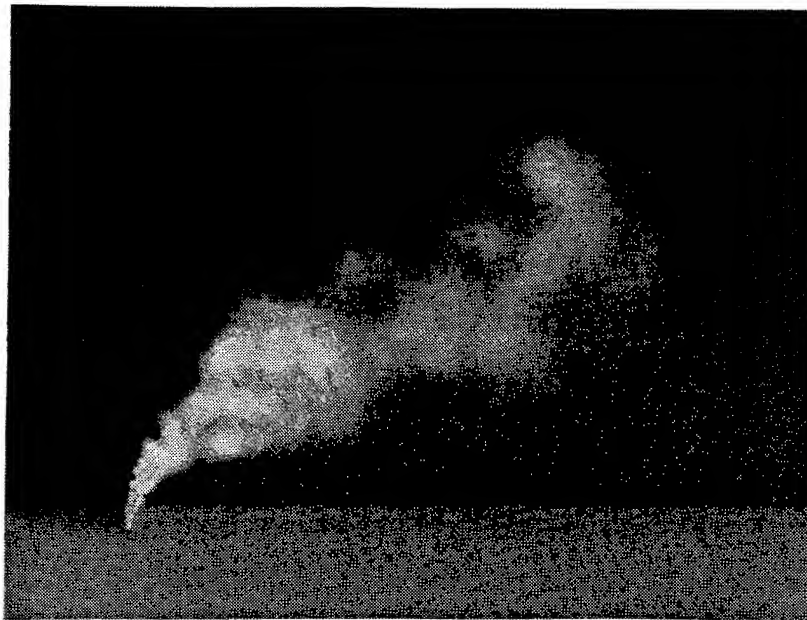


Figure 6. COMBICV model for source 30

Figure 7 shows COMBIC source 25 (fog oil) visualized in a synthetic terrain setting.

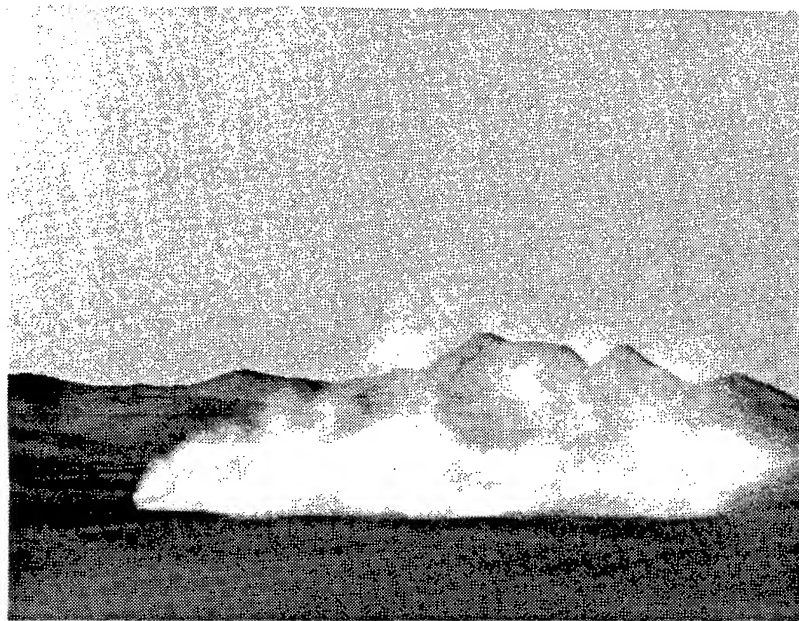


Figure 7. COMBIC source 25 (fog oil) in a synthetic terrain scene

3. VERIFICATION OF COMBICV

To provide assurance that COMBICV produces visualization representative of COMBIC, software was written to generate images of the basic COMBIC obscurant envelopes. In addition, tests were performed to provide statistical comparison with real obscurant data. Visual comparisons between COMBICV output and the approximated output of COMBIC looked reasonable, and average transmittance values agreed well for all seven COMBIC wavelengths. The comparison with real data produced similar statistical structures. The imagery generated by COMBICV should therefore provide the Army with a valid tool for visualizing battlefield obscurants with acceptable accuracy and realism.

ACKNOWLEDGMENTS

This research was supported by the U.S. Army Topographic Engineering Center under contract number DACA76-90-C-0026.

Laslo Greczy, of the Topographic Engineering Center, initiated this study by suggesting that Grumman Data Systems computer graphics techniques be applied to EOSAEL models.

The success of this research was greatly enhanced by the cooperation of Dr. Donald Hoock, the principal author of COMBIC. Dr. Hoock gave guidance in the use of COMBIC and suggested many of the approaches taken. He also suggested a means for verification and supplied data for comparing the visualization model with real obscurants. Although the original contract definition called for the modeling of a single source viewed by a single sensor, Dr. Hoock's contribution enabled the modeling of all 30 sources viewed by any of the seven sensors.

REFERENCES

Gardner, G. Y., 1985: "Visual Simulation of Clouds," Computer Graphics, Vol. 19, No. 3, pp 297-303

Gardner, G. Y., 1991: "Battlefield Obscurants", US Army Engineer Topographic Laboratories contract DACA76-90-C-0026, Final Technical report, September, 1991.

Hoock, D. W., R.A. Sutherland, and D. Clayton, 1987: Combined Obscuration Model for Battlefield Contaminants (COMBIC), ASL-TR-0221-11, US Army Atmospheric Sciences Laboratory, White Sands Missile Range, NM.

Shirkey, R. C., L. D. Duncan, and F. E. Niles, 1987: Electro-Optical Systems Atmospheric Effects Library (EOSAEL-87), ASL-TR-0221, US Army Atmospheric Sciences Laboratory, White Sands Missile Range, NM.

ACOUSTIC PROPAGATION IN THE ATMOSPHERE USING THE
SCANNING FAST FIELD PROGRAM

John M. Noble
U.S. Army Atmospheric Sciences Laboratory
White Sands Missile Range, New Mexico 88002-5501, USA

ABSTRACT

The Scanning Fast Field Program (SCAFFIP) is a full-wave solution to the acoustic-wave equation for sound propagation in a layered atmosphere over a complex impedance benign terrain. The model is based on a Hankel transformation of the Helmholtz equation in cylindrical coordinates and the integration of the resulting ordinary differential equation by analogy with an electrical transmission line. This model provides a very effective way of calculating sound pressure levels for use in predicting how sound will be propagated in the atmosphere. The SCAFFIP accomplishes this by allowing the user to enter an atmospheric profile, the geometry of the problem, the frequency of source, and the flow resistance used to calculate the ground impedance. The model provides a 0° to 360° scan of the acoustic propagation condition about a source or receiver. The accurate prediction of sound pressure levels in the atmosphere is very important for determining the effectiveness of passive acoustic sensors for detecting tanks, artillery, fixed wing aircraft, and rotary wing aircraft by the Army.

1. INTRODUCTION

The Scanning Fast Field Program (SCAFFIP) is a modification to the Fast Field Program (FFP). The FFP is a one-way solution to the acoustic-wave equation originally developed for underwater acoustics and adapted to propagation in the atmosphere by Rasp et al. (1985) and Lee et al. (1986). The FFP developed by Rasp et al. (1985) used a propagation matrix formulation. The propagation matrix views each layer in the atmosphere as an optical device, thus allowing for a transmission matrix to be constructed for each layer in the atmosphere. Multiplying each matrix together forms a new matrix representing how an acoustic signal will be affected by the atmosphere as it propagates. The next step in solving the problem is to take a Bessel function transform of the problem with respect to range. After calculating the solution in wave space, an inverse transform is performed to arrive at the final solution. This formulation of the FFP presented several numerical problems. Lee et al. (1986) resolved many of these numerical problems by using a new technique in constructing an FFP. This technique will be the focus of the discussion on the FFP.

2. ATMOSPHERIC EFFECTS ON ACOUSTICS

Before an explanation of the model can be presented, the dynamics of the atmosphere need to be addressed. The atmosphere affects how sound moves from the target to the receiver. A basic understanding of how the atmosphere breaks down and how it affects the sound waves passing through it is very important.

The meteorological variables that affect the speed of sound in air are pressure, temperature, vector windspeed, and humidity. To observe the effect of each meteorological variable, considering each independently, one can examine the equation for the speed of sound in air. The value of c , according to Laplace's adiabatic assumption for air as an ideal gas, is

$$c(T) = \sqrt{\gamma RT/M} , \quad (1)$$

where γ is the ratio of specific heats, R is the universal gas constant that is equal to 8314.16 J/(kg K), and M is the molecular weight. The dependence of the speed of sound on pressure and humidity is found in the ratio of specific heats and molecular weight of moist air. However, these dependencies are not very strong and can be ignored when confining the problem to the lower 1 to 2 km of the atmosphere.

The consideration of the windspeed to the speed of sound is a vector relation. The effective sound speed is calculated using

$$c_{eff} = c(T) + u \cdot \cos(\theta_w - \pi - \theta_R) , \quad (2)$$

where $c(T)$ is the speed of sound in the absence of wind at temperature T , u is the magnitude of the horizontal windspeed, θ_R is the bearing of the receiver from the target, θ_w is the direction from which the wind blows, and $\theta_w - \pi$ is the direction the wind is blowing to relative to north.

Since the sound speed is a function primarily of temperature and vector windspeed, the sound speed will vary with height. This will cause the acoustic wave to be refracted as it propagates through the atmosphere. The degree of refraction undergone by the acoustic wave is related to the sound speed gradient present. If the sound speed increases with height, this causes downward refraction of the acoustic wave. If the sound speed decreases with height, this causes upward refraction of the acoustic wave. In an upward refractive atmosphere, the formation of a refractive shadow zone can occur.

A refractive shadow zone is a region where no refracted direct or reflected waves can reach. The limiting ray denotes the boundary of the refractive shadow zone. The limiting ray is not a physical boundary; it denotes the region between the shadow zone and nonshadow zone areas.

3. FAST FIELD PROGRAM THEORY

The propagation of sound from a point source at the origin is given by the classical wave equation

$$\nabla^2 p - \frac{1}{c^2} \frac{\partial^2 p}{\partial t^2} = -4\pi\delta(x, y, z) , \quad (3)$$

where δ represents a delta function source of unit strength. For simple harmonic motion, eq. (3) becomes the Helmholtz equation

$$\nabla^2 p + k^2 p = -4\pi\delta(x, y, z) , \quad (4)$$

where $k = \omega/c$ is the wave number, c is the sound speed, and ω is the angular frequency. For the FFP, k and c are restricted to vary only in the z -direction.

Transforming eq. (4) into cylindrical coordinates and assuming azimuthal symmetry, the Helmholtz equation becomes

$$\frac{\partial^2 p}{\partial r^2} + \frac{1}{r} \frac{\partial p}{\partial r} + \rho \frac{\partial}{\partial z} \left(\frac{1}{\rho} \frac{\partial p}{\partial z} \right) + k^2 p = -\frac{2}{r} \delta(r) \delta(z - z_s) , \quad (5)$$

where the source is located at $r = 0$, $z = z_s$, and ρ is the density of the medium.

The FFP views the atmosphere as a series of constant sound speed layers as shown in fig. 1. Complex impedance surfaces border the top and bottom boundaries of the atmosphere. An infinite half-space with constant parameters is used to model the top boundary. At the bottom boundary, the atmospheric layer adjoins a partially absorbing surface that can be represented by the complex acoustical impedance of the ground.

To reduce the dimensionality of eq. (5), a zero-order Hankel transform is applied. To solve the resulting equation, Lee et al. (1986) used an analogy to a transmission line that results from the form of the transformed equation. The equivalent transmission line configuration to fig. 1 is shown in fig. 2.

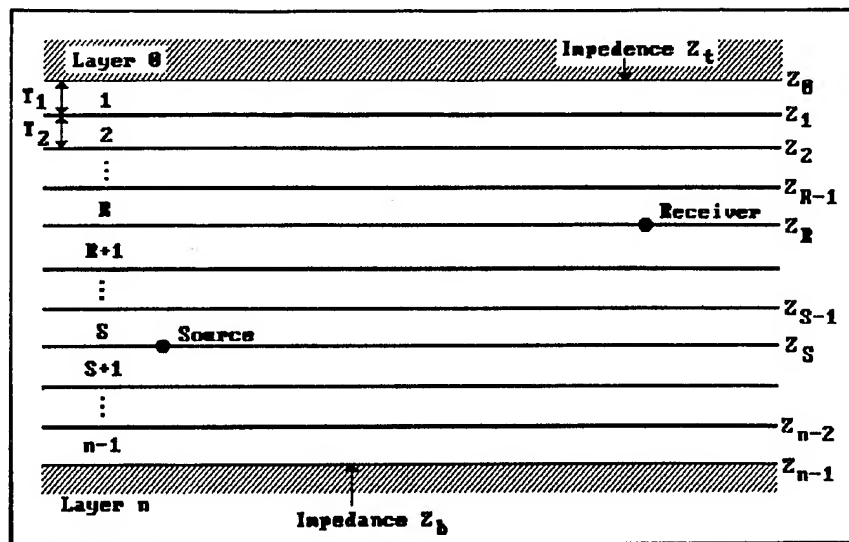


Figure 1. Layered atmosphere bounded by complex impedance surfaces.

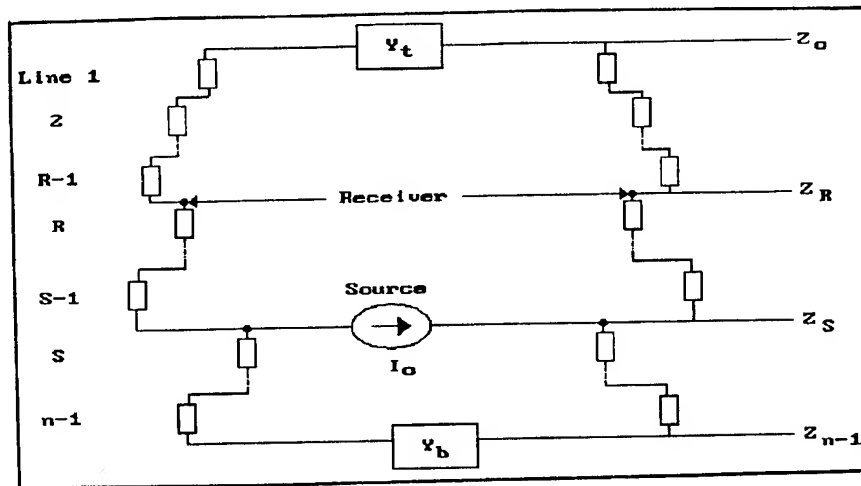


Figure 2. Equivalent transmission lines for the acoustic problem.

The analogy is made by representing each layer in the atmosphere by an element in a transmission line with a certain characteristic admittance and attenuation constant. The definition of admittance is one over the impedance or one over the sum of the resistance plus reactance of the electrical element. The admittance of the element causes the voltage running through it to be attenuated and the phase of the signal to be shifted. Viewing it from the perspective of the acoustic wave problem, the acoustic wave as it propagates through the atmosphere undergoes losses and phase shifting due to refraction and spreading of the acoustic wave. The equivalence between the transmission line and the acoustic wave problem is illustrated in table 1. This equivalence can be performed for each layer of the atmosphere, thus constructing a transmission line. The top and bottom boundaries in the atmosphere become loading admittance elements on each end of the transmission line. Now the problem changes from determining the sound pressure level at a receiver to determining the voltage in the transmission line at a point in the line. This is a well-known process in electrical engineering.

TABLE 1. RELATIONSHIPS BETWEEN TRANSMISSION LINE AND ACOUSTIC-WAVE PROBLEM

	Acoustic Wave	Transmission Line
Fields	Pressure $p(k,z)$	Voltage $V(z)$
	Velocity $\dot{w}(k,z)$	Current $I(z)$
Attenuation Constant	$\gamma = \sqrt{k^2 - (\omega/\alpha)^2}$	$\gamma = \sqrt{ZI}$
Characteristic Admittance	$Y_c = -i\gamma/\omega\rho$	$Y_c = \sqrt{Y/Z}$

The transmission line calculation process is performed in the current version of the FFP used in SCAFFIP. However, there is a problem in one of the complex numerical integrations. Due to the form of the solution, branch points and poles are present on the real axis. Because of their nature, to obtain a correct solution branch points and poles must not be included in the integration being performed. To avoid this problem, the FFP uses what is called extra loss in the calculations. The mathematical result of using this extra loss is to move the integration off the real axis, thus missing the branch points and poles present on the real axis. The effect of the extra loss is removed from the solution in an approximate manner by multiplying the computed pressure by the term $\exp(\beta r)$, where β is the extra loss attenuation constant in nepers per meters. Note that the proper choice of this "artificial attenuation" is essential if meaningful results are to be obtained from the code.

4. SCANNING FAST FIELD PROGRAM

The SCAFFIP adapts the FFP model and provides a user interface allowing for calculations of relative sound pressure levels at various azimuths. The user interface simplifies the process for incorporating the input data required for the FFP model. It also allows the user the option to enter a beginning and ending azimuth to scan. The results from SCAFFIP are passed into a polar-coordinate based objective analysis and contouring routine. This routine allows for contours of constant sound pressure level to be plotted about a receiver or target. The azimuth to be scanned can range from 0° to 360° at intervals varying from 1° to 15° .

The user interface allows the user to enter an atmospheric profile and source-receiver geometry. The user interface takes the atmospheric profile and calculates the speed of sound profile along each azimuth. The attenuation coefficient due to molecular absorption is also calculated from the atmospheric profile. The sound speed profile and the attenuation coefficient are needed by the acoustic model section of SCAFFIP.

The complex ground impedance, the complex ratio of the sound pressure to the particle velocity at the ground surface, is another input parameter needed for SCAFFIP. It determines the amount of sound reflected by the ground. The value for the ground impedance is difficult to determine either theoretically or experimentally. However, several ground impedance models allow the user to provide general characteristics of the ground. The complex ground impedance models allow the user to input a set of parameters representing the state of the ground soil conditions. Using these parameters, the model calculates the complex ground impedance for a particular acoustic frequency. The user interface for SCAFFIP is designed for entering these parameters, which can be estimated from tables.

The next generation of the user interface will be a semi-intelligent interface. The new user interface, due for completion by the end of 1992, will decide on possible modifications to the sound speed profile and estimates for extra loss values. The modifications to the sound speed profile are important because of the way SCAFFIP views the atmosphere. Each layer in the atmosphere (see fig. 1) is assumed to have the same sound speed through the entire layer. This can cause errors in the predictions if the sound speed changes too rapidly from

one layer to the next. The new user interface will examine the sound speed profile for changes in the sound speed from one layer to the next for differences that exceed critical cutoff values for valid results. If the user interface finds a large difference between two layers, it will perform a linear interpolation between the two layers and add the needed number of layers to reduce the difference down to acceptable limits.

As mentioned above, the proper choice of extra loss is essential for meaningful results to be obtained. The user interface will provide the best estimate of the extra loss based on frequency of interest and range of the problem. This will prevent the complex integration from moving too far or too close to the branch points and poles located on the real axis.

The software for SCAFFIP is currently being developed to work on the Army Command and Control System (ACCS) Common Hardware/Software (CHS) computer workstation platform. This will allow field personnel to execute the model to create acoustic decision aids for planning deployment of passive acoustic sensors. Examples of output from SCAFFIP are shown in figs. 3 and 4. Figure 3 shows a 90° scan from azimuth 270° to 360° for an atmospheric condition resulting in a sound channel near the ground. Figure 4 shows a complete 360° scan of an area with the same type of atmospheric conditions as fig. 3.

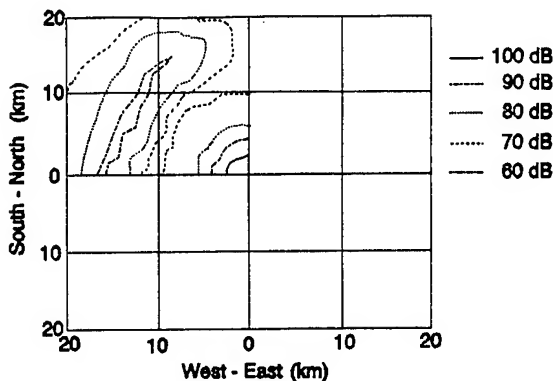


Figure 3. 90° scan of sound pressure levels about a sensor for a 140-dB source with sound channel present.

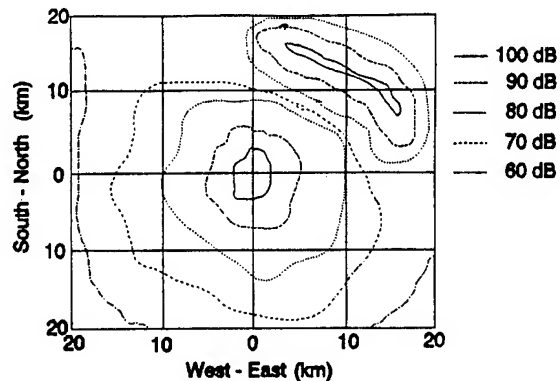


Figure 4. 360° scan of sound pressure levels around a sensor for a 140-dB source with a sound channel present.

5. SUMMARY

Battlefield acoustics is a very important means of detecting numerous types of tactical targets. Acoustics is valuable since it provides a method to detect and identify targets passively and non-line of sight. However, what must not be overlooked is the effect of the atmosphere on acoustic propagation. Computer models like the SCAFFIPs provide valuable information on how the atmosphere will alter the sound propagating from target to receiver. The use of such acoustic propagation models for determining the deployment of passive acoustic sensors in the battlefield will provide maximum detection capabilities for detecting tactical targets.

REFERENCES

- Attenborough, K., 1985: Acoustical impedance models for outdoor ground surfaces. J. Sound Vibr., 99:521-544.
- Chessell, C. I., 1977: Propagation of noise along a finite impedance boundary. J. Acoust. Soc. Am., 62:825-834.
- Delany, M. E., and E. N. Bazley, 1971: A note on the effect of ground absorption in the measurement of aircraft noise. J. Sound Vibr., 16:315-322.
- DiNapoli, F. R., 1971: A fast field program for multilayered media. Technical Report 4103, Naval Underwater Systems Center, New London, CT 06320.
- Kutschale, H. W., 1970: The integral solution of the sound field in a multilayered liquid-solid half-space with numerical computations for low-frequency propagation in the Arctic Ocean. Report No. 1 (CU1-1-70, ONR Contract N00014-67-A-0108-0016), Lamont-Doherty Geological Observatory, Columbia University, Palisades, New York.
- Lee, S. W., N. Bong, W. F. Richards, and R. Raspet, 1986: Impedance formulation of the fast field program for acoustic wave propagation in the atmosphere. J. Acoust. Soc. Am., 79:628-634.
- Pierce, Allen D., 1981: Acoustics: An Introduction to Its Physical Principles and Applications. McGraw-Hill Book Company, New York, 678 pp.
- Raspet, R., S. W. Lee, E. Kuester, D. C. Chang, W. F. Richards, R. Gilbert, and N. Bong, 1985: Fast-field program for a layered medium bounded by complex impedance surfaces. J. Acoust. Soc. Am., 77:345-352.

Session II

WEATHER DECISION AIDS

**Wednesday
4 December 1991**

**Chairperson
Mr. James Harris**

THERMAL REVERSAL TACTICAL DECISION AID EVALUATION

Stephen W. Berrick
Science and Technology Corp.
Las Cruces, NM 88001, USA

Patti S. Gillespie
U.S. Army Atmospheric Sciences Laboratory
White Sands Missile Range, NM 88002, USA

ABSTRACT

The thermal contrast model (TCM) of the thermal reversal tactical decision aid (TDA) was evaluated by comparing model-predicted results with field test measurements taken at Smoke Week XI and Smoke Week XII. The results show that the TCM is able to predict with some accuracy the likelihood of success of thermal imagers used for target acquisition. The available field test data are insufficient to validate the model rigorously, however. Specific recommendations are made for a field test that would provide the data necessary to evaluate the model more fully.

1. INTRODUCTION

Thermal reversal is a condition under which the effective temperatures of targets and scene components as viewed by a thermal imager become nearly the same. Under conditions of thermal reversal, a target becomes indiscernible or "washed out" against the background scene components. Thermal reversal often occurs at dusk and dawn due to a decrease in insolation, but also can occur under a variety of other environmental conditions. Precipitation, for instance, may cause thermal reversal conditions by bringing many scene components to nearly the same temperature.

2. THE MODEL

The TCM evaluated here is the same model used in the Air Force Infrared TDA Mark II (Higgins, 1983) and assumes no atmospheric attenuation. Attenuation increases the likelihood of thermal reversal. In order to predict the thermal contrast between a target and background components, the TCM must be able to predict the thermodynamic temperatures of the components. A first assumption is that all objects behave as black bodies or, equivalently, that their emissivities are equal to unity. A temperature derived under this assumption, which is implicit in the TCM, is called the effective temperature. In general, effective temperatures of objects do not equal their thermodynamic temperatures. The black-body assumption, however, allows the thermal imager's response to be a function of the temperature difference between the target and background. Although targets and backgrounds do not have emissivities that are equal or near unity, it is expected that the emissivity differences will not exceed 10 to 20 percent. Even this much difference may lead to significant problems, however (Lindberg and Farmer, 1989).

To model the surface temperatures of various objects, the TCM considers energy exchanges through radiation, convection, and conduction, and via moisture. The surfaces of objects interact continuously both with the environment and with their interiors. Thus, surface temperatures are affected by past and present meteorological conditions because the interior temperatures are determined by previous conditions. The effects of internal heat sources such as engine exhaust and frictional heating also are considered.

The time dependence of the TCM is governed by energy balance equations whose coefficients have been tuned empirically by measurements of specific targets and backgrounds. Therefore, thermal contrast predictions are affected by the reliability of these empirical models.

The TCM has been incorporated into a PC program that runs on any IBM-PC-compatible computer under DOS. A full description of the program, unpublished, was provided to STC by Dr. Mary Ann Seagraves (Seagraves, in press) of the U.S. Army Atmospheric Sciences Laboratory (ASL).

For a set of meteorological conditions spaced 3 hr apart and covering up to a 24-hr period, the model predicts the effective temperatures of targets and background components. These temperatures are then fit with a polynomial to determine effective temperatures at intermediate times. These inputs are required for each 3-hr interval desired.

2.1 MODEL INPUT

The model allows the user to choose from a variety of military target vehicles in off, idle, or exercised states. The available targets include an APC and several tanks. The user may also designate up to six background features from a list of 29. This list includes various trees, soils, and surfaces. A single general background must also be designated for each calculation. There are 106 choices for the general background and they fall into 10 categories: deciduous trees, coniferous trees, palmaceous trees, grasses, crops, sand, soils, roads/fields, snow, and rocks. Necessary meteorological parameters include ambient surface temperature, dewpoint temperature, visibility, wind speed, precipitation present, and amount, type and height of clouds present. The ambient temperature 3 hr prior is also needed. The necessary site parameters are the latitude, longitude, and elevation of the target site and the GMT time and date of the measurement.

2.2 MODEL OUTPUT

Two quantities related to the prediction of thermal reversal are determined by the model from the effective temperatures. The first is σ , calculated as follows:

$$\sigma = \sqrt{\frac{T_i^2}{n} - \langle T_i \rangle^2} \quad (1)$$

where T_i is the effective temperature of the i th scene component, n is the number of scene components, and $\langle \rangle$ denotes the mean. σ gives a measure of the likelihood of thermal wash-out for thermal imagers used in navigation. For target acquisition applications, the subject of this paper, a second value is used:

$$\Delta T_i = |T_i - T_t| \quad (2)$$

where T_i is the effective temperature of the i th background feature and T_t is the effective temperature of the target. ΔT_i is therefore the thermal contrast of the target with respect to the i th background component. The quantities ΔT_i were used in this study for evaluating model predictions compared to field test data.

The likelihood of thermal reversal is determined by the TCM according to the following thresholds:

$\Delta T_i < 3.0$ for all i	No go
$\Delta T_i < 3.0$ for some i	Caution
$\Delta T_i \geq 3.0$ for all i	Go

In the above definitions, "No go" means that thermal wash-out is likely, "Caution" means that it is possible, and "Go" means that thermal wash-out is unlikely. In this paper, thermal reversal is defined as in the program: the condition by which the observed temperature of the target differs by 3 °C or less from the observed temperature of some background scene component.

3. FIELD TEST DATA AND MODEL CALCULATIONS

The foundations of the TCM evaluation in this paper are thermal imager data taken at Smoke Week XI, conducted at the Defence Research Establishment Valcartier (DREV), Quebec, Canada, during 20 February to 10 March 1989, and at Smoke Week XII, conducted at Eglin Air Force Base (AFB), Florida, during 7 May to 17 May 1990 (see Kennedy et al., 1990, Locke et al., 1989, and their references). These data sets together offer the ability to test the TCM in both arctic and southern U.S. pine forest environments.

3.1 SMOKE WEEK XI -- DATA

An ASL Inframetrics 610 8- to 12- μ m imager measured target and background temperatures. The imager is calibrated using an internal black-body source. The distance between the imager and the targets was approximately 1 km. Targets at Smoke Week XI consisted of six APCs and one tank, and backgrounds were largely of snow and/or trees. Temperature measurements typically began just before a smoke trial and continued into the trial. Only smoke-free measurements were used in the analyses. The data from 41 trials were available.

The available meteorological data for Smoke Week XI trials were from 10-m towers. The 24-hr meteorological data measurements conducted by CRREL personnel were also used. Unfortunately, the 24-hr data were taken at the major instrumentation site, which was farther away from the targets than were the meteorological towers. Data for sky conditions during each trial were limited to percentage of cloud coverage and average cloud height. The presence of blowing or falling snow was noted when the temperature measurements were taken. All other meteorological parameters were available for each trial as time averages over the length of the trial.

3.1.1 Model Calculations For Smoke Week XI Data

The thermal reversal model was exercised for each of the 41 trials in which target and background temperatures were measured under conditions of clear air. For the general background, the UNDISTURBED SNOW model was used. Three target models were considered: an APC, an idle tank, and an exercised tank. The background feature model used was UNDISTURBED SNOW. Each calculation was carried out by giving the meteorological parameters for a given trial time. The time chosen was midway between the official trial start and end times. The computed temperatures for the target and background were then extracted from one of the program's output files.

3.1.2 Model Predictions For Smoke Week XI

Figure 1 shows the measured and model-predicted temperatures and contrasts. The upper plot compares the measured and modeled background temperatures using the UNDISTURBED SNOW background model. (It was found that all the snow models resulted in nearly identical predictions given the environmental conditions of this test.) The middle plot compares the measured and modeled target temperatures using the APC target model. The lower plot compares the model-predicted and measured thermal contrasts of all the targets with three target models, shown with filled diamonds. The trial numbers are referenced to the

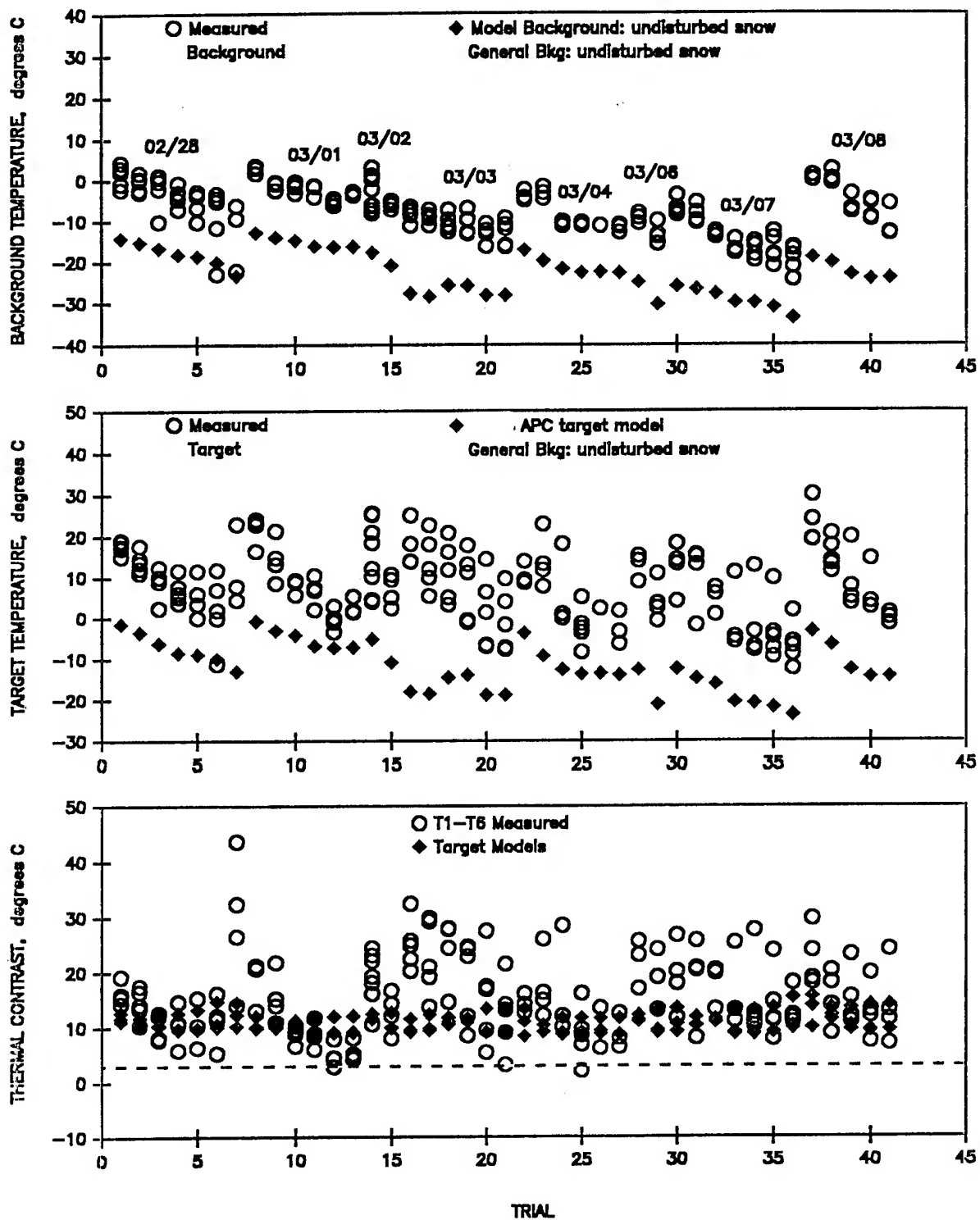


Figure 1. Comparison of measured and model-predicted background temperatures (upper plot), target temperatures (middle plot), and thermal contrasts (lower plot).

first trial conducted on February 28, 1989 (trial 11103), which is labeled trial 1 in the figure. Numbers were assigned to each of the other trials in chronological order thereafter. The horizontal dashed line in the lower plot (at a contrast of 3.0 °C) represents the thermal reversal limit as defined in Section 2.2. Thermal reversal is said to exist for thermal contrasts below this line.

3.1.3 Conclusions From Smoke Week XI

The segregation of modeled and measured data points according to day is evident from the upper two plots of fig. 1. The modeled and measured data form parallel segments, with each segment corresponding to a particular day, as indicated in the plots. The UNDISTURBED SNOW model background appears to predict the behavior of the measured background temperatures, although there is a zero-point difference of about 10 °C. A difference of 20 °C or more appears to exist between measured target temperatures and the APC model; however, the dispersion in measured target temperatures is noticeably greater than that observed for the measured background temperatures.

The discrepancies in target temperatures may be due to (1) whether or not the APC had been previously exercised and how long ago, (2) differences between the portion of the target viewed by the imager and the empirically based mean temperature behavior used by the model, (3) variability in atmospheric extinction, which is not modeled by the TCM, or (4) a breakdown in the assumption that objects behave thermodynamically as black bodies.

Regarding the ability of the TCM to predict the occurrence of thermal reversal, we note that thermal reversal is never predicted and is only observed three times. This result means that the model was incorrect less than 2% of the time. This percentage, however, may not be a valid indicator of the TCM's success because measured thermal contrasts were far from the thermal reversal limit (see Section 2.2).

The lower plot of fig. 1 reveals that the dispersion in measured target temperatures is greater than the differences between the target models. This was true for all five available target models, though only the APC and tank models are shown. Therefore, the target models cannot be validated individually with the current data. The relatively large dispersion in measured target temperatures is the major cause for the large dispersion seen in the measured thermal contrasts.

The results may be summarized as follows: Both the target and temperature behaviors are well predicted by the TCM. The TCM underpredicts the magnitude of the background temperatures by about 10 °C and the target temperatures by at least 20 °C. The scatter in the measured target temperatures is greater than the differences between the various target models (APC, idle tank and exercised tank). Therefore, no conclusions can be made about the applicability of any target model. The measured thermal contrasts apparently are well predicted by the TCM, although the scatter in the measured values is large. This scatter results primarily from the large scatter in the target temperature measurements.

3.2 SMOKE WEEK XII -- DATA

A MICOM Inframetrics 610 8- to 12- μ m imager measured target and background temperatures. The imager is calibrated using an internal black body source. The targets consisted of five tanks. Clear-air temperatures were measured for each trial. The temperature data were provided in a report (U.S Army Atmospheric Sciences Laboratory, 1990) for the five tanks.

Complete 24-hr meteorological data were taken at meteorological tower W1. The data were reported as 15-min averages. Meteorological data averaged over the length of a smoke trial were available from one of two 10-m towers.

3.2.1 Model Calculations For Smoke Week XII Data

Instead of using the thermal reversal model to predict a thermal contrast at one particular time for a set of meteorological conditions, as was done for the Smoke Week XI data, the model was used to predict temperature and thermal contrast behaviors over a 24-hr period. The necessary 24-hr meteorological data were available for three days: May 11 (JD 131), May 15 (JD 135), and May 16 (JD 136), 1990. For the model to predict thermal behavior, meteorological conditions had to be specified for eight times, spaced three hours apart, during each 24-hr period under investigation.

A tank was used as the target model in all calculations. The terrain near the tank targets at Eglin AFB was dry sandy soil interspersed with stubby foliage. This area is surrounded by a southern pine forest with some deciduous trees. In a report by Rice (1985), several background types are ascribed to the Eglin AFB terrain. These include GRASS FIELD and TREES. Various combinations of these backgrounds and other plausible backgrounds were used in the model calculations. The background feature types that appeared to describe the background terrain at Eglin AFB included LIVE GRASS; DEAD GRASS; PIGWEED, NORMAL STAND; GRASS FIELD; LIVE CROP FOLIAGE; SAND, ALL; DESERT; and PLOWED FIELD, DRY.

For the background temperatures, the imager looked at four areas surrounding the target. Background #1 was immediately above the target. This area sometimes included the more distant conifers (with some deciduous trees) in the distant forest. Backgrounds #2 and #3 were immediately to the left and right of the target, respectively. These two areas were of the terrain very near the target, but sometimes included the more distant coniferous trees. Background #4 was immediately below the target and included only the immediate terrain area next to the target. Several candidate background feature types in the thermal reversal model were tried. These included TALL GRASS, GROWING; TALL GRASS, DORMANT; MOWED GRASS, DORMANT; DECIDUOUS TREES, GROWING; CONIFEROUS TREES, GROWING; CONIFEROUS TREES, DORMANT; DIRT ROAD, DRY; PLOWED FIELD, WET; GRASS FIELD; TREES and PLOWED FIELD, DRY.

3.2.2 Model Predictions For Smoke Week XII

The program was run repeatedly, using various combinations of general background and background features from the above lists. All plausible general backgrounds resulted in similar model predictions. The general background models are most differentiated for the time when the measurements were collected. The dispersion in measured thermal contrasts, however, is too large to assign a best fit model accurately. The LIVE CROP FOLIAGE general background model was used, although other choices are valid.

The background feature model was found to have a much larger effect on the predicted temperatures than the general background model. Using the LIVE CROP FOLIAGE general background model, it was found that both the TALL GRASS, GROWING and GRASS FIELD background feature models led to predicted temperatures and contrasts that were closest to those measured.

Figure 2 shows plots of model-predicted and measured thermal contrasts versus time. The solid curves in the plots are the model predictions using LIVE CROP FOLIAGE for the general background and TALL GRASS, GROWING for the background feature model. The dashed curves in all plots are the model predictions using the GRASS FIELD background feature model. Only measurements for one tank are shown since these measurements were representative of all five tanks. The symbols represent the measurements with respect to each of the four background windows surrounding the tank. The horizontal dashed line marks the thermal reversal limit (see Section 2.2). When contrasts are below this line, thermal reversal is said to exist.

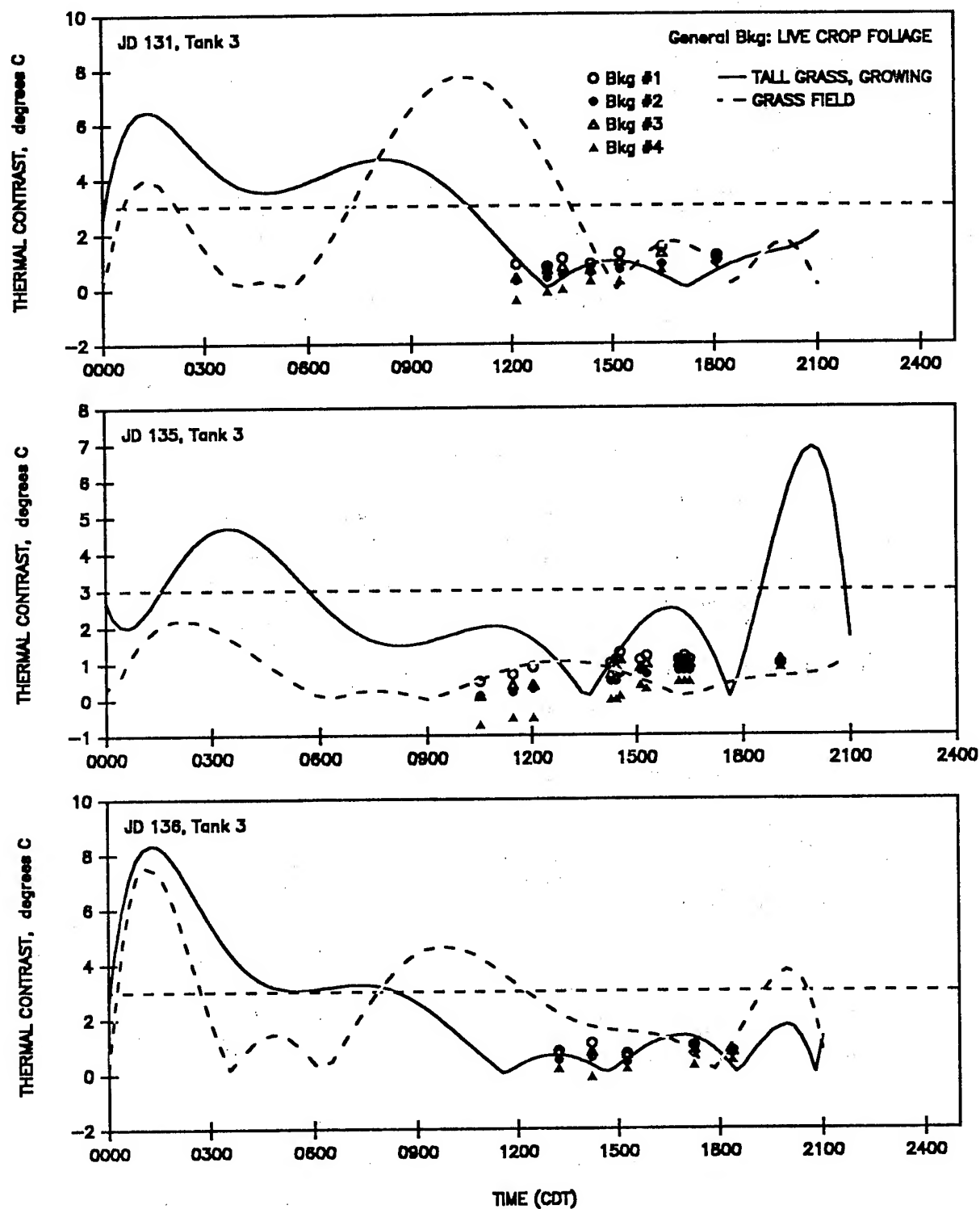


Figure 2. Comparison of measured and model-predicted thermal contrasts for JD 131 (upper plot), JD 135 (middle plot), and JD 136 (lower plot), Smoke Week XII.

Figure 2 reveals that for JD 131 and JD 136, the TALL GRASS, GROWING background model is clearly better at predicting the thermal contrasts. This result is noteworthy because the GRASS FIELD model is based on measurements carried out at Eglin Air Force Base, the location of the field test (Rice, 1989). Only for JD 135 does the GRASS FIELD model better predict the thermal contrasts. The weather was rainy on JD 135, and this fact may be connected with the better predictions of the GRASS FIELD model on that day.

3.2.3 Conclusions From Smoke Week XII

Figure 2 indicates that the model is successful if one only considers the gross ability of the TCM to predict whether thermal reversal will occur. No measurements were collected during those times when thermal reversal was not predicted, however.

The fits shown in fig. 2 are consistent with the measured data. The TALL GRASS, GROWING model fit is poorest for JD 135. The GRASS FIELD model fit is better for JD 135, however. This result may be due in part to the presence of rain during part of the period when data were collected (until 1200 CDT, see plot). Figure 2 shows that for JD 135, the measurements taken during rain are segregated from the other measurements taken when rain was not present. When determining various temperatures, the TCM does consider rain's effect on heat exchanges; however, attenuation due to rain is not considered in the model.

The conclusion to be drawn from these plots is that the magnitudes of the thermal contrast predictions are at least consistent with the measured values. Ideally, we should have measurements taken over a much greater period of time to determine whether this consistency is merely fortuitous. The results may be summarized as follows: The TCM's predictions of the occurrence of thermal reversal are consistent with the measured data. The TCM's predictions of thermal contrast behavior are consistent with the data collected on JD 131 and JD 136. Attenuation due to rain may be the proximate cause of the different results using the JD 135 data. Temperatures were measured at approximately 1 km. The TCM accounts for the effect of rain on heat exchanges, but not for its effect on atmospheric attenuation, which is thought to have been negligible on JD 131 and 136 for 1 km.

4. PROBLEMS WITH THE CURRENT DATA SET

The problems with the current data set can be summarized as follows: (1) Measurements were not collected during protracted periods; data were only collected around smoke trials that were typically scheduled only from late morning to early evening, (2) Although 24-hr meteorological data were collected, there were large gaps in the data and complete days when no data were collected, (3) Some meteorological conditions were not known at the target site. These data were only collected at meteorological towers that were some distance away from the target area, (4) There was not enough detailed information concerning the background features whose temperatures were measured, (5) There was not enough detailed information concerning the tank targets whose temperatures were measured, and (6) The data were not collected during thermal reversal crossover times when thermal reversal is predicted to go from likely to unlikely or vice versa.

5. SPECIFIC FIELD TEST RECOMMENDATIONS

The following are specific recommendations for a field test:

1. The targets should consist of modeled targets offered in the thermal reversal model. The entire target should be within the thermal imager's field of view (FOV) and all operational states of the target (off, idle, or exercised) should be tested. Notes taken during the test should include: target type, operational state of target several hours before and during test, target aspect and portion of target within imager's FOV.

2. The background features should consist of modeled background feature types offered in the thermal reversal model. Accurate descriptions of the backgrounds within the imager's FOV should be carefully recorded.
3. The terrain of the target sites should be describable by one of the general backgrounds modeled and offered in the thermal reversal model.
4. The thermal imager should be close enough to the target site so that atmospheric attenuation is negligible. The assumption of negligible extinction should be verified. Black-body calibration sources could be placed at the target site as a check on the imager's internal black-body source. No smoke should be present during the data collection.
5. The meteorological measurements should consist of wind speed, ambient air temperature, dew point temperature or relative humidity, visibility and cloud type, height and amount measured at three cloud deck levels (low, mid, and high). The presence of precipitation should be noted as well as the presence of surface moisture due to past precipitation. Meteorological data should be collected at or very near the target site at least every 3 hr during the test and over 24-hr periods.
6. Departures of targets from ideal black bodies should be monitored with, for example, thermocouples placed on the target surface facing the imager.
7. Temperature measurements should be collected over 24-hr periods, particularly during dawn and dusk.
8. Ideally, tests should be conducted under a wide range of temperature, precipitation, and wind conditions.

REFERENCES

- Higgins, G.J., 1983: Users Guide for the Operational Tactical Decision Aid (OTDA) for Infrared (8-12 μ m) Systems Mark II Computer Version, AFGL-TR-82-0274(I), Air Force Geophysics Laboratory, Hanscom AFB, MA.
- Kennedy, B.W., Walter Klimek, and Robert Laughman, 1990: Large-Area and Self-Screening and Obscurants (LASSO) (Smoke Week XII) Quick Look Report, STC Technical Report 4056, Science and Technology Corp., P.O. Box 7390, Hampton, VA.
- Lindberg, J., and W.M. Farmer, 1989: Analysis of Material Emissivity Effects on Detection/Recognition of Targets Viewed through Smokes/Obscurants with Thermal Imaging Systems, In Proceedings of the Smoke/Obscurants Symposium XIII, Office of the Project Manager Smoke/Obscurants, Aberdeen Proving Ground, MD 21005.
- Locke, B.A., 1990: Evaluation of the Target Acquisition Model in Smoke Weeks X and XI, STC Technical Report 4017, Science and Technology Corp., P.O. Box 7390, Hampton, VA.
- Rice, J.E., 1985: Validation Testing Of The Thermal Contrast Models From The Operational Tactical Decision Aid For Infrared Systems And The Development Of A Computer-Compatible Tape-Based Thermal Contrast Data Base, OptiMetrics Final Report, AFGL-TR-85-0128, AFGL/LYS, Hanscom AFB, MA.
- Seagraves, M.A., in press: A Tactical Decision Aid for Predicting Occurrence of Thermal Reversal, Atmospheric Sciences Laboratory Technical Report, Atmospheric Sciences Laboratory, White Sands Missile Range, NM.
- U.S. Army Atmospheric Sciences Laboratory, 1990: Smoke Week XII (LASSO) Target Temperature & MIDAS Cloud Dimensional Measurements, prepared by Atmospheric Sciences Laboratory, and NMSU - Physical Science Laboratory, White Sands Missile Range, NM.

TARGET ACQUISITION MODEL EVALUATION WITH SMOKE WEEK DATA

Brian A. Locke, Stephen W. Berrick, Lori Fuentes, and Ronald A. Catherson
Science and Technology Corporation
Las Cruces, NM 88001, USA

Patti Gillespie
U.S. Army Atmospheric Sciences Laboratory
White Sands Missile Range, NM 88002, USA

ABSTRACT

The Atmospheric Sciences Laboratory second-generation target acquisition tactical decision aid, called SACQ, was evaluated using data from the Smoke Week XII field test. Transmittance values from the test were used in conjunction with observer data to determine probabilities of detection under various conditions. These results were compared with SACQ predictions of probability of detection versus range. In general, SACQ predictions underestimated an observer's ability to detect a target, as indicated by the probability of detection. The reasons for this underestimation are under investigation, but may be related to the relatively low thermal contrasts that existed at Smoke Week XII. Evaluations made from Smoke Week XII will be compared with validation efforts from previous Smoke Week tests.

1. INTRODUCTION

The U.S. Army Atmospheric Sciences Laboratory (ASL) has developed a second-generation target acquisition model, called SACQ. SACQ is a later version of TACQ, a tactical decision aid developed by Mary Ann Seagraves of ASL, and is roughly equivalent to the Electro-optical Systems Atmospheric Effects Library (EOSAEL) model Targac. The SACQ model has been incorporated into a FORTRAN 77 interactive software package. Based on meteorological data and information on sensor, target, and background characteristics, the software package determines the effective ranges of target acquisition sensors.

Portions of Smoke Week X and Smoke Week XI were specifically devoted to obtaining data for the evaluation of TACQ (Locke, 1990). In this report, data from Smoke Week XII, conducted in 1990, were used to evaluate an updated version of the target acquisition model SACQ.

Smoke Week XII was conducted at Eglin Air Force Base (EAFB), FL during May 1990 (Kennedy et al., 1990). Trials began on 7 May and continued through 17 May. The test site used for Smoke Week XII was Range C-52A. The test grid was located on flat, sandy terrain surrounded by a southern pine forest. Ground cover on the test grid was burned and removed before the trials began.

2. METHODS

The SACQ model was evaluated by comparing predicted detection probabilities to measured detection responses from observers viewing the target through a thermal imager. The observer detection responses were collected with the Countermeasures and Test Division (CMTD) Personnel Response Evaluation System for Target Obscuration (PRESTO), which was operated by Science and Technology Corporation.

The PRESTO computer records the times at which observers press hand-held switches to indicate the detection or recognition of a target. Each PRESTO observer depresses the switch during the time the target is recognized or detected and

releases the switch when the target is not detected. The PRESTO computer records these times for each observer. PRESTO can accommodate up to 16 observers simultaneously. At Smoke Week XII, however, only one observer at a time was used with the thermal imager. This observer (not always the same individual) is designated observer 3 in this report. Two other observers were used for visual (naked eye) detection responses and are designated in this report as observers 4 and 5. The distance between the PRESTO observers and the target was 1.76 km throughout the data collection. Throughout the remainder of this paper, the line of sight from where the PRESTO observers were situated to the target site is referred to as the PRESTO LOS.

Software was written to take the times recorded by the PRESTO computer and convert them into a series of records for 1-s intervals spanning the length of the trial. Each record contained the proportion of that 1-s interval during which the target was detected. For each trial in which PRESTO data were taken, both the number of seconds during which the target was detected and the total number of seconds of the trial were determined. These data were used to generate probability of detection values for each 1-second interval.

Sensor performance predictions were obtained by operating the SACQ program with input parameters chosen to represent conditions at Smoke Week XII as closely as possible. SACQ presents users with a series of menus (Seagraves and Draayer, 1989; Berrick et al., 1991). The SACQ menus describe and organize user input for meteorological and other environmental conditions, and for specifications for targets and sensors.

For the thermal imaging devices considered here, the SACQ output first consists of the results of some intermediate calculations: absolute and relative humidity, solar flux, target and background temperatures, and thermal contrast and extinction coefficients for the 8- to 12- μm and 3- to 5- μm regions. When smoke is included, a pseudo-schematic is displayed illustrating the relative positions of the imager, screen, and target, and their distances from one another.

Following the schematic, information is displayed for each of the two thermal wavebands. This information consists of clear-air and smoke transmittances, the apparent target and background temperatures, and thermal contrasts versus range.

After the waveband information, the output displays the detection and recognition ranges in a table for thermal sensor systems. For each of three detection probabilities (25%, 50%, and 75%), the output table displays the detection ranges for a narrow field of view and a wide field of view corresponding to each imager. The SACQ code was modified to output detection ranges for all probabilities of detection from 0% to 100% in increments of 5%. Since the PRESTO observer-target distance was 1.76 km, detection probabilities for which the ranges were between 1.7 km and 1.8 km were then extracted from the SACQ output files and used for further analyses.

Only detection probabilities for thermal sensors 1 and 2 were extracted from SACQ output for comparison with PRESTO results from Smoke Week XII. In this report, SACQ predictions for thermal sensors 1 and 2 are referred to as sensor 1 and sensor 2.

Variations in transmittance along the PRESTO LOS during each smoke trial must be reflected in the inputs to SACQ in order to compare SACQ predictions with PRESTO results. During smoke trials, the transmittance may vary from 0% to near 100%. SACQ mimics smoke conditions by assigning constants for the mass extinction coefficient α and volume concentrations C , based on the obscurant and relative concentration chosen from the menu describing obscurants. The user must also input cloud length so SACQ can determine transmittance due to smoke by the equation $T = e^{-\alpha L}$.

Cloud lengths were chosen to mimic the transmittance levels that occurred along the PRESTO LOS. Approximately 2000 SACQ input files were constructed to represent the different transmittance levels that occurred on the PRESTO LOS during the 29 smoke trials analysed.

3. COMPARISON OF SACQ AND PRESTO

Comparisons of SACQ predictions and PRESTO measurements for trial 6702 are shown in fig. 1. The upper plot represents a comparison of SACQ sensor 1 versus PRESTO observers 3, 4, and 5. The lower plot represents a comparison of SACQ sensor 2 versus the PRESTO observers. As already indicated, observer 3 used a thermal imager, while observers 4 and 5 were naked-eye observers. Figure 1, and similar plots from the other trials, show that in general SACQ was too conservative in estimating the ability of an observer (observer 3) to detect a target through a thermal imager.

Figure 2 better quantifies the differences between the SACQ-predicted results and the PRESTO results for observer 3. The Y-axis is the transmittance at a probability of detection level of 50%. Along the X-axis are all trials in which the 50% detection level was attained by both SACQ and PRESTO. Both SACQ sensors 1 and 2 are shown. The PRESTO transmittances in the figure represent the mean transmittance level at 50% detection probability when the data are binned according to both sensor 1 and sensor 2. Figure 2 shows that SACQ generally overestimated the transmittance necessary for an observer to achieve a 50% detection probability through a thermal imager. That is, SACQ was too conservative in estimating an observer's ability to detect a target. SACQ sensor 2 seemed to give better agreement with PRESTO, but the differences are still large.

Figure 2 also shows that for trial 6702 SACQ was able to predict the transmittance for a 50% detection probability more accurately than it was for the other trials. The wind speed for this trial was lower than it was in any of the other trials examined here. This low wind speed resulted in the largest thermal contrast, both as measured by the Multispectral Imaging Data Acquisition System (MIDAS) (Atmospheric Sciences Laboratory, 1990) and as predicted by SACQ. A large thermal contrast may explain why SACQ was better able to predict the observed probabilities of detection for trial 6702.

Figures 3 and 4 illustrate the differences in the probability of detection between PRESTO and SACQ in relation to different transmittance levels. Results shown represent all model runs from each trial.

In figs. 3 and 4, transmittance is plotted against ΔPd , where

$$\Delta Pd = | Pd(PRESTO) - Pd(SACQ) | \quad (1)$$

and Pd is the probability of detection. Hence, ΔPd is an indicator of how well the SACQ-predicted results compare with the PRESTO measurements.

Figure 3 uses the SACQ sensor 1 results and fig. 4 uses the SACQ sensor 2 results. All trials are represented in both figures. In an ideal situation, where SACQ is a perfect predictor of PRESTO measurements, ΔPd would be zero at all transmittances.

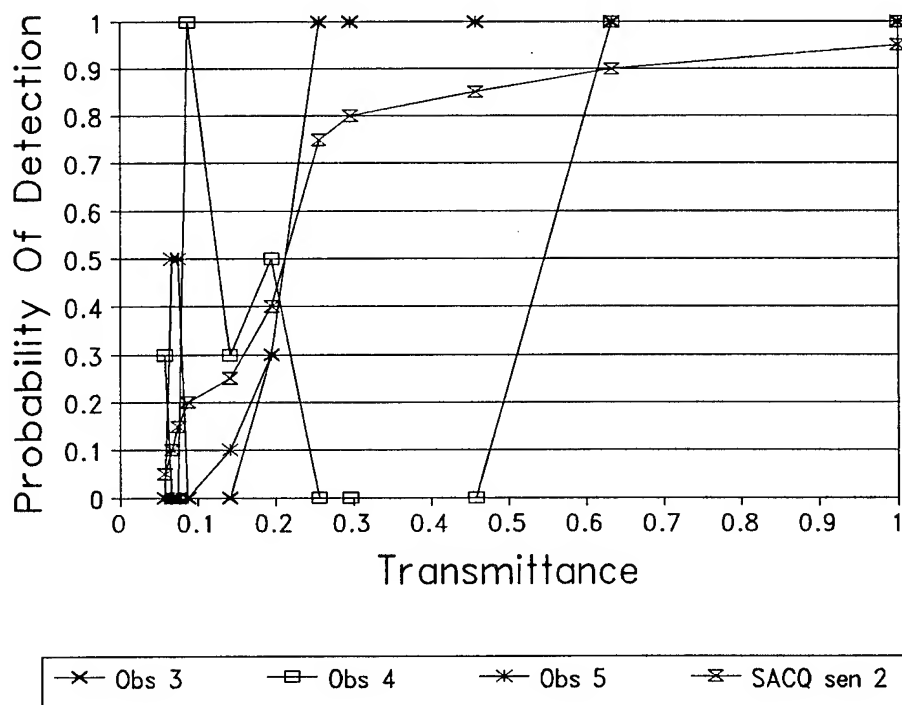
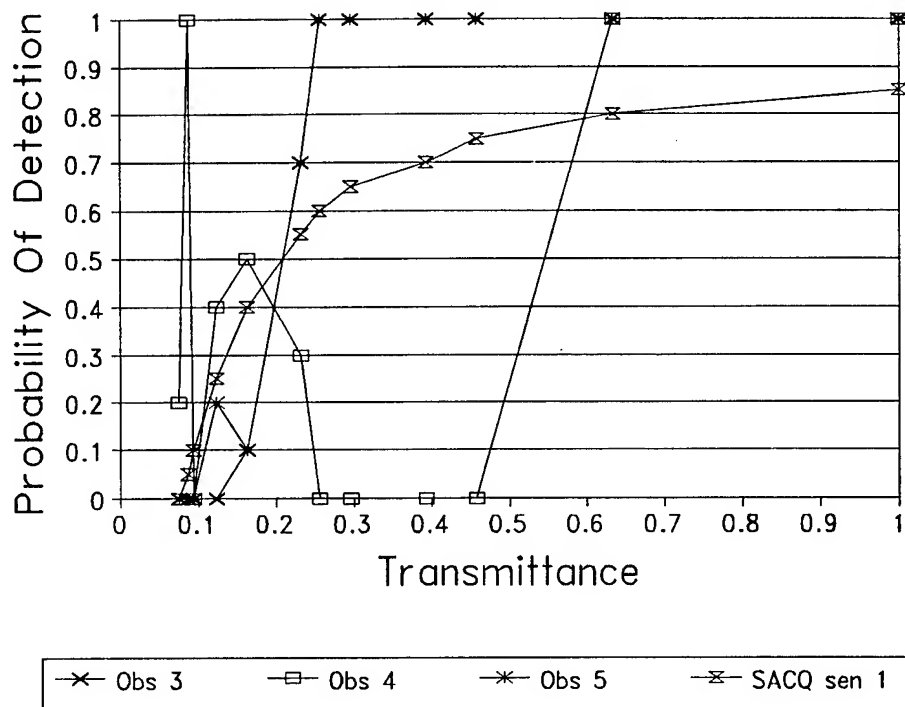


Figure 1. Probability of detection as a function of transmittance. a: sensor 1; b: sensor 2.

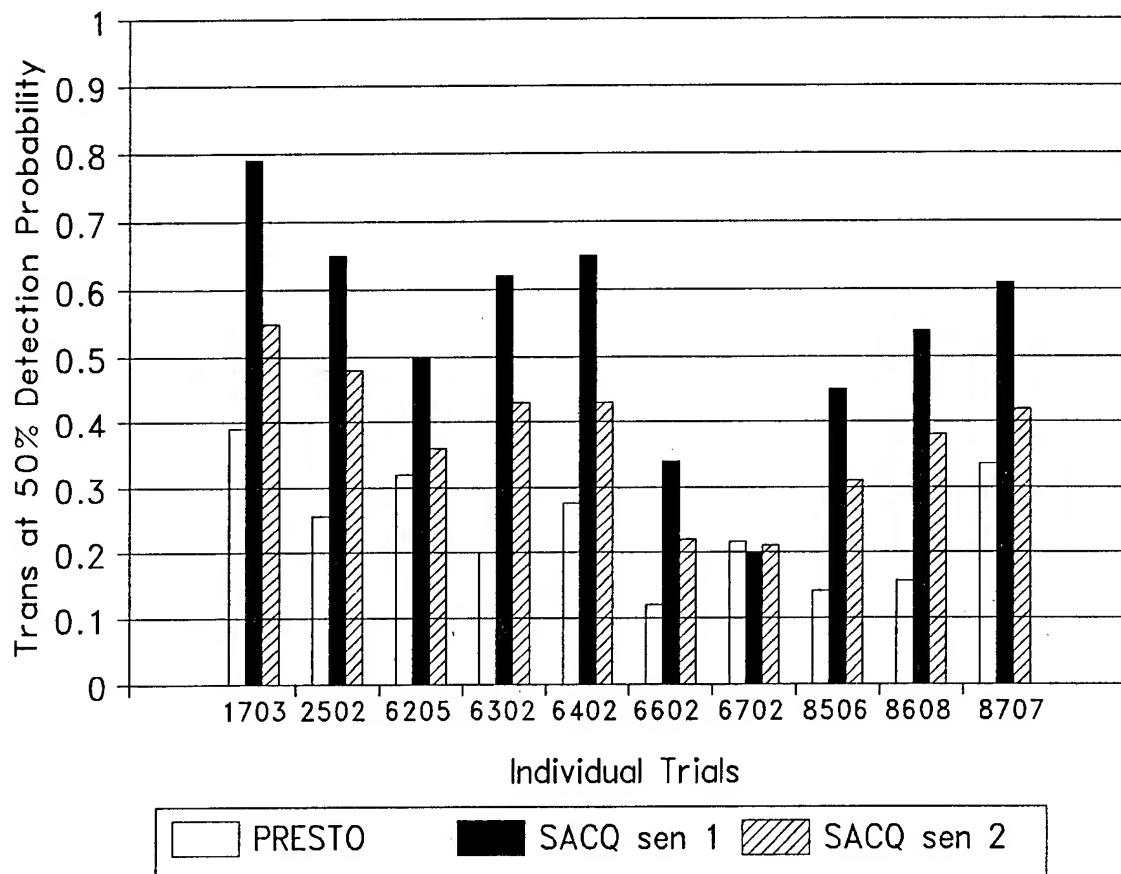


Figure 2. Comparison of SACQ sensors 1 and 2 versus PRESTO for transmittances at 50% detection probability.

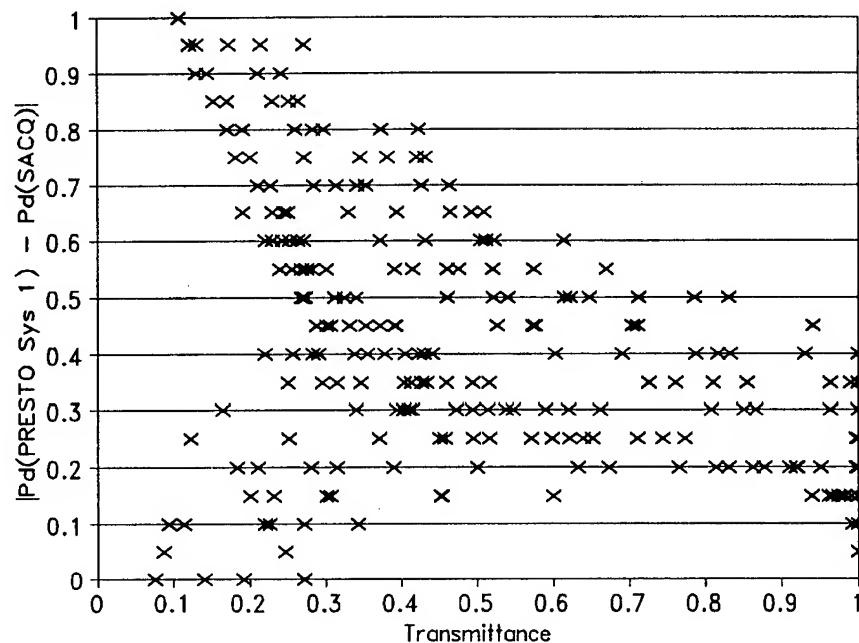


Figure 3. The performance of SACQ sensor 1 compared to PRESTO versus transmittance. The Y-axis is the absolute difference between SACQ and PRESTO.

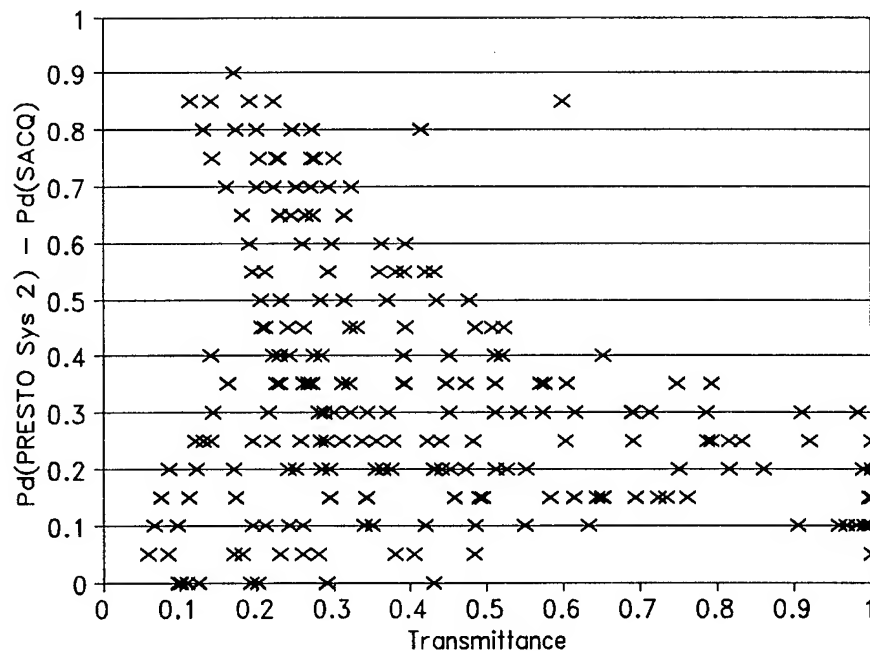


Figure 4. The performance of SACQ sensor 2 compared to PRESTO versus transmittance. The Y-axis is the absolute difference between SACQ and PRESTO.

The following conclusions can be drawn from figs. 3 and 4:

1. Most of the points in figs. 3 and 4 lie within a swath characterized by large ΔPd at low transmittances and small ΔPd at high transmittances. In addition, a significant number of points are clustered at low transmittances with small ΔPd .

This additional cluster of points may appear because the PRESTO probabilities of detection are more erratic at lower transmittances. This erratic phenomenon may be occurring at threshold transmittances where the target is barely detectable or barely undetectable. At such points, observers are likely to oscillate in their decision-making as to whether or not they see the target. This phenomenon would result in more erratic detection probabilities at low transmittances.

2. There is better agreement between SACQ and PRESTO at high transmittance levels than at low transmittance levels. At the higher transmittance levels, the differences between SACQ and PRESTO converge to some minimum value. This value is roughly 0.3 for sensor 1 and 0.2 for sensor 2. Towards lower transmittance levels, the differences between SACQ and PRESTO increase to a maximum of about 1.0 at the lowest transmittances.

4. SACQ APPARENT CONTRASTS

The question that arises is why SACQ underestimated the ability of an observer to detect a target through a thermal imager. One possibility is that SACQ underestimated the apparent thermal contrasts.

In SACQ the inherent thermal contrast is defined as follows:

$$C_o = \Delta T = T_{Targ} - T_{Bkg} \quad (2)$$

where T_{Targ} is the target temperature, T_{Bkg} is the background temperature, and C_o is the inherent thermal contrast (Seagraves and Davis, 1989). Thus the inherent thermal contrast is the temperature difference between the target and background.

The apparent contrast at some distance R is computed in SACQ by the following expression:

$$C(R) = C_o T_{Smk}(R) T_{Atm}(R) \quad (3)$$

where T_{Smk} and T_{Atm} are the transmittances through the smoke and through the clear-air atmosphere, respectively, over the range R.

In clear air, the following expression applies:

$$C(R) = C_o T_{Atm}(R) \quad (4)$$

In fig. 5 the clear-air apparent thermal contrasts computed by SACQ are compared to measured apparent thermal contrasts for selected trials. The measured values were made using a MIDAS 8- to 12- μm imager (ASL, 1990) at a distance of 1 km. The MIDAS contrasts were measured in clear air with respect to four background windows surrounding the target window. These background windows were immediately above, below, to the left, and to the right of the target window. The SACQ predicted apparent contrasts are for 1 km.

Figure 5 shows that the thermal contrasts, both measured and predicted, are small. The largest contrasts approach only 1.5 °C. Note also that although the measured contrasts for trials 2502, 6602, and 6702 were relatively large, SACQ was only able to predict the probability of detection of PRESTO observer 3 for trial 6702 (see fig. 2).

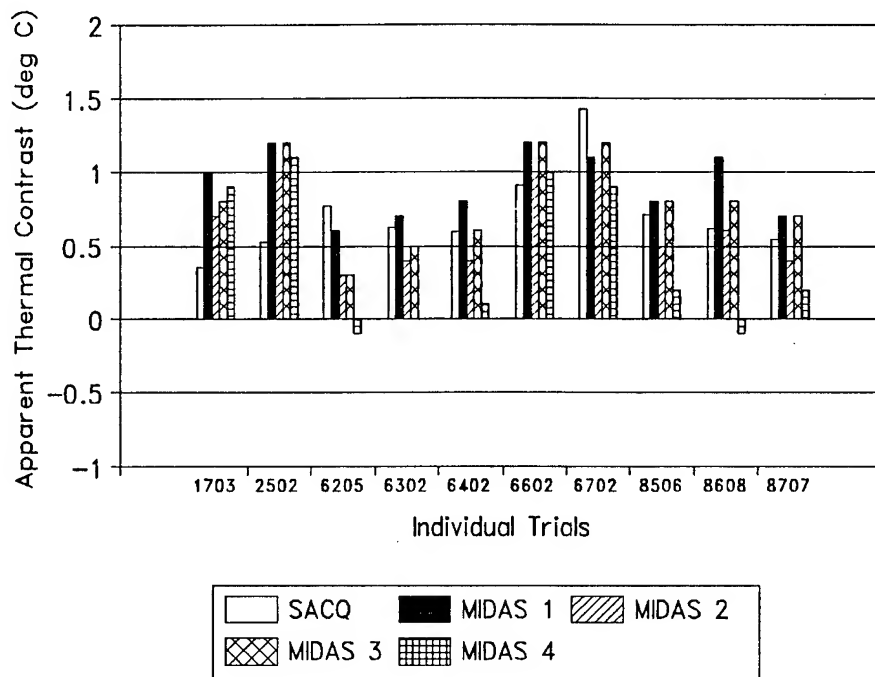


Figure 5. Comparison of SACQ apparent thermal contrasts versus MIDAS apparent thermal contrasts for the trials used in Figures 2 and 3.

Figure 5 also suggests that the SACQ-predicted apparent contrasts are uncorrelated with the apparent contrast measured by MIDAS. Indeed, a correlation analysis using data from all trials revealed that the correlation coefficient for the SACQ and MIDAS apparent contrasts was near zero, indicating no correlation. The thermal contrasts are low and noise probably dominates the measured and predicted values, however. A correlation analysis may not give a valid assessment, since the values in both data sets are of the same order as the noise. The SACQ-predicted apparent thermal contrasts are of the same order of magnitude as the MIDAS-measured apparent thermal contrasts. It may be unreasonable to expect the thermal contrast model in SACQ to perform any better than these results indicate.

5. POSSIBLE PROBLEMS IN THE SACQ EVALUATION

In comparing SACQ-predicted detection probabilities with detection probabilities measured by PRESTO, SACQ consistently underestimated the ability of an observer to detect a target using a thermal imager. The differences between SACQ and PRESTO were largest at small transmittances.

The discrepancies between SACQ and PRESTO do not seem to stem from SACQ's predictions of apparent thermal contrasts, since these predictions are of the same order of magnitude as the measured contrasts. Any discrepancies involving several factors might explain why SACQ predictions failed to match PRESTO results. These possibilities are the following:

1. Modeling human responses is an enormous undertaking. There are many physiological and psychological variables that may have complex interactions. Unknown human factors may play a larger role when the thermal contrasts are very low. When thermal contrasts are higher, these same factors may not be as important. The complexity of the human-imager interface renders it beyond the scope of this report.

2. In the region of very low thermal contrasts, almost any deviation of the model from reality is likely to be more important than in the region of larger thermal contrasts. For example, when TACQ was evaluated against data from Smoke Week X and Smoke Week XI (Locke, 1990), where the thermal contrasts were an order of magnitude larger than those at Smoke Week XII, the results were far more favorable.

6. SUMMARY

SACQ model predictions of target detection performance were compared to field test data collected at Smoke Week XII. The data consisted of times during which a target was detectable by observers viewing a scene either with the naked eye or through a classified thermal imager at a range of 1.76 km. The data were recorded by PRESTO and then converted to detection probabilities.

6.1 CONCLUSIONS

1. SACQ consistently underestimated an observer's ability to detect a target when predictions were compared with measured data from PRESTO.
2. The relatively poor performance of SACQ may be related to the very small thermal contrasts. Small apparent thermal contrasts on the order of 1 °C were both measured (Atmospheric Sciences Laboratory, 1990) and predicted by SACQ. The model may break down at low thermal contrasts.
3. Another possible problem is the observer-target range at which PRESTO data were collected. The SACQ predictions indicate that at ranges less than a few kilometers, given the low thermal contrasts, the relationship between range and detection probability is relatively flat. This observation suggests that small variations in the input parameters may result in large variations in the detection probabilities predicted.

6.2 RECOMMENDATIONS FOR FUTURE FIELD TESTS

The following recommendations can be made based upon the results of this report:

1. If possible, PRESTO data should be collected under conditions of both small and large thermal contrast. This effort might entail collecting some of the PRESTO data during smoke tests conducted at night.
2. As many observers as possible should be used to acquire detection and recognition response data to reduce the effects of observer bias.
3. When possible, several target-observer ranges should be used, including a range of at least 3 km.

REFERENCES

- Atmospheric Sciences Laboratory, 1990: Smoke Week XII (LASSO), ASL-Target Temperature and MIDAS Cloud Dimensional Measurements, Atmospheric Sciences Laboratory and NMSU - Physical Science Laboratory, White Sands Missile Range, NM.
- Berrick, S., B.A. Locke, L. Fuentes, and R. A. Catherson, 1991: Target Acquisition Model Evaluation With Smoke Week XII Data, STC Technical Report 6214, Science and Technology Corporation, P.O. Box 7390, Hampton, VA.
- Kennedy, B.W., B.A. Locke, W. Klimek, and R. Laughman, 1990: Large-Area and Self-Screening Smokes and Obscurants (LASSO), Smoke Week XII, Quick Look Report, STC Technical Report 4056, Science and Technology Corporation, P.O. Box 7390, Hampton, VA.
- Locke, B.A., 1990: Evaluation Of The Target Acquisition Model In Smoke Weeks X and XI, STC Technical Report 4017, Science and Technology Corporation, P.O. Box 7390, Hampton, VA.
- Seagraves, M.A., and J.M. Davis, 1989: Target Acquisition Tactical Decision Aid Software, Technical Documentation, Atmospheric Sciences Laboratory Internal Report, U.S. Army Atmospheric Sciences Laboratory, White Sands Missile Range, NM.
- Seagraves, Mary Ann, and Bret Draayer, 1989: Target Acquisition Tactical Decision Aids: A User's Manual, Atmospheric Sciences Laboratory Internal Report, U.S. Army Atmospheric Sciences Laboratory, White Sands Missile Range, NM.

INFLUENCE OF BATTLEFIELD-INDUCED OBSCURANTS AND ATMOSPHERIC EFFECTS ON A HIGH-RESOLUTION COMBAT SIMULATION

Martin E. Lee

**U.S. Army Atmospheric Sciences Laboratory
White Sands Missile Range, New Mexico 88002-5501, USA**

Steven J. LaMotte

**Physical Science Laboratory
New Mexico State University
Las Cruces, New Mexico 88003-0002, USA**

ABSTRACT

Path radiance effects along a sensor's line of sight reduce apparent target/background contrast. This target contrast degradation can change dramatically with typical variations in atmospheric attenuation and relative sky radiance compared to radiance from the ground; resulting contrast degradation can have a significant impact on devices that produce images by observing visible light energy. The Combined Arms and Support Task Force Evaluation Model (CASTFOREM), developed by the U.S. Army to analyze weapon system effectiveness, can be employed to study the influence of these atmospheric effects on simulated loss exchange ratio (LER) outputs. CASTFOREM also models the attenuation effects of simulated smoke introduced during a simulation. These cumulative atmospheric and smoke effects can be analyzed using CASTFOREM because it models multiple sensor, detailed search and acquisition processes. These acquisition processes are carried out via the simulation of typical observer scanning operations. These scanning operations take place over a selected battlefield through variations of static atmospheric conditions that can change imaging devices' abilities to resolve targets. The scanning operations are carried out by individual soldiers and their weapon systems. The ability of these force-structure elements to produce significant kill scores and contribute positively to CASTFOREM LER results can be shown to depend significantly upon atmospheric and battle induced obscuration conditions present during the acquisition process. This paper discusses the results of a study on CASTFOREM LER sensitivity to this simulated atmospheric and smoke obscuration effect problem over a range of typical, seasonal weather conditions and considers the significance of these results.

1. INTRODUCTION

The Combined Arms and Support Task Force Evaluation Model (CASTFOREM) is a high resolution, stochastic, simulation model of a combined arms conflict. CASTFOREM was developed at the U.S. Army TRADOC Analysis Command - WSMR (TRAC-WSMR), White Sands Missile Range, New Mexico, and models multiple sensor, detailed search and acquisition processes--down to individual weapon systems and soldiers. CASTFOREM models the attenuation effects of simulated smoke in affected acquisitions during the simulation. CASTFOREM also models static battlefield atmospheric conditions that change imaging devices' abilities to resolve targets (TRAC-WSMR-TD-4- 88, 1988). The primary CASTFOREM output of interest in this study is the loss exchange ratio (LER), which is defined as the number of RED force losses divided by the number of BLUE force losses. This study was designed to observe how much these CASTFOREM LER outputs varied by changing path radiance effects over a range of meteorological conditions for two general cases: 1) without smoke effects; and 2) with smoke effects. When selected, smoke clouds are represented in CASTFOREM using the Combined Obscuration Model for Battlefield-Induced Contaminants (COMBIC), which was developed by Hoock et al. (1987), at the U.S. Army Atmospheric Sciences Laboratory (ASL). COMBIC can model the essential physics and dynamics involved in generating hexachloroethane (HC), white phosphorus (WP), plasticized WP (PWP), red phosphorus (RP), fog oil, diesel smoke, and other user selected generator and munition produced clouds.

2. TARGET ACQUISITION PROBLEM

Visible and infrared (IR) imaging device performance is significantly affected by target scene contrast and attenuation in the intervening atmosphere (Seagraves et al., 1989). CASTFOREM explicitly models path extinction along a line of sight (LOS) to the target via wavelength dependent atmospheric attenuation coefficients (α) for all search devices (Lee and LaMotte, 1991). Path radiance effects--or sky to ground radiance (S_{gr}) effects--are also modeled in CASTFOREM (Lee and LaMotte, 1991). S_{gr} , the effect produced when sensors detect energy coming from a location other than the target scene, results in a reduction of apparent target/background contrast (Seagraves, 1989). What influence do α and S_{gr} have, via simulated target acquisition processes, on CASTFOREM LER results with and without obscurant effects (for example, artillery smoke and dust)?

3. STUDY DESIGN

CASTFOREM High Resolution Scenario 3.5 (HR 3.5) was employed in this study. HR 3.5 depicts a BLUE battalion Task Force defending against a RED tank regiment, and the engagement takes place over a 20 by 20 km complex terrain area. The primary division in the way that this scenario was played involved the inclusion and exclusion of smoke as a tactical and artillery effect. One complete study was made without smoke used by either side, and this was followed by another complete study with smoke employed as a tactical aid by both sides. Artillery was

employed in both these major studies, but simulated artillery smoke and dust effects were only introduced in the smoke study.

Each complete study set involved seven separate weather scenarios that were developed at ASL as input for CASTFOREM's simulated battlefield atmospheric environment. The specific scenario weather parameters are defined in table 1. The weather scenarios represent some typical continental, mid-latitude seasonal conditions, ranging from a clear, warm, summer day (case 1) to a subfreezing winter day with blowing snow (case 7).

TABLE 1. SEVEN ATMOSPHERIC CONDITIONS REPRESENTATIVE OF
MID-LATITUDE SUMMER (CASES 1 - 3), SPRING AND FALL
(CASES 3 - 5), AND WINTER (CASES 5 - 7).

CASE No.	PRECIPITATION mm/hr	CEILING HEIGHT m	VISIBILITY km	TEMP. c	RELATIVE HUMIDITY %	WIND SPEED m/s
1	0	∞	50	32	5	1.5
2	0	∞	12	32	5	1.5
3	0	3,660	4.5	20	20	3.0
4	0	610	3.0	5	90	8.0
5	0	305	2.0	5	95	8.0
6	3.0 moderate rain	250	1.5	5	99	8.0
7	blowing snow	183	0.7	-2	95	8.0

CASTFOREM models transmissivity degradation in six wavelength regions--visible (0.4 - 0.7 μm), near-IR (0.7 - 1.3 μm), 1.06 μm , mid-IR (3.0 - 5.0 μm), far-IR (8.0 - 12.0 μm), and 10.6 μm

--when solving for apparent target contrast during search processes. The degradation is assigned via an attenuation coefficient based on the sensor's wavelength detection region. Rural attenuation terms were tailored to the seven weather scenarios in table 1 using ASL's XSCALE transmittance module (Fiegel et al., 1989, and Duncan et al., 1987). Note that XSCALE only considers the air temperature for snow and ice fog scenarios (case 7).

Similarly, S_{gr} terms were tailored to the weather scenarios given in table 1 using the delta Ed-dington radiative transfer model in ASL's target acquisition model (Gillespie, 1989). Because S_{gr} has azimuthal variation, depending on the position of the sun, three S_{gr} terms were developed for each of the weather scenarios in table 1. These terms were developed to consider the case of looking directly away from the sun (minimum S_{gr}), looking orthogonally away from the sun (modal S_{gr}), and looking in the direction of the sun (maximum S_{gr}).

Seven cases of HR 3.5 (table 1), each having three S_{gr} variations, formed a complete study set. One study set was executed without smoke tactics, while the second study set was run with smoke tactics available to both sides. Twenty-one CASTFOREM runs were then executed for each study set. Typically, acceptable CASTFOREM studies done by TRAC-WSMR will consist of a minimum of 21 replications for each run, with a different random seed for each replication. This practice was also employed here. The no-smoke study described here required 483 replications, each taking approximately 30 min to complete on a dedicated Sun SPARCstation 1. Therefore, this part of the research took approximately 241.5 h to complete. The smoke study took significantly longer to complete. The first problem contributing to this was that each replication in the smoke study required approximately 2.5 h to complete; COMBIC is employed by CASTFOREM when obscurants are simulated, and this adds a significant calculations load to the normal execution of CASTFOREM. To compound this problem, more replications were required for the smoke study set because increased LER variance was encountered, which interfered with the statistical significance of these LER results.

Increases in LER variance apparently resulted from the introduction of obscurants into the scenario. To overcome this problem, a sample size determination test was used to identify when enough CASTFOREM replications had been run to produce statistically valid results (this test was also carried out in the no-smoke study). The smoke study eventually required a total of 591 replications, 108 more than the no-smoke study. The smoke study required approximately 1,477.5 h to complete. As a result, the total dedicated CPU time required to complete both the smoke and no-smoke runs on a Sun SPARCstation 1 was approximately 1,719 h. Figure 1 illustrates how weather effects, α , S_{gr} , and COMBIC were conceptually coupled together in the smoke study. Model coupling in the no-smoke study was essentially the same as in fig. 1 except that COMBIC was not called during no-smoke runs.

4. RESULTS

The primary CASTFOREM outputs of interest in this study were the LER summaries. Average LER values for each run, with standard deviation bars, are plotted for the no-smoke and smoke

studies in figs. 2 through 4. Minimum S_{gr} comparisons are illustrated in fig. 2, modal S_{gr} comparisons are made in fig. 3, and maximum S_{gr} comparisons are shown in fig. 4. Figures 2 through 4 show that the greatest variation of LER occurs over the cross-case results. This highly significant variation manifests itself as a skewed bell-shape pattern for cases 1 through 7 in both the smoke and no-smoke data. For example, in fig. 2 there is a 184.4 percent increase in mean LER between case 1 (2.34355) and case 5 (6.66499) in the no-smoke data. These dramatic cross-case LER variations are important to note here and were originally discovered by Duncan and Swaim (1989).

There is also some significant inner-case contrast in fig. 2; for example, there is a 43.6 percent difference between the mean smoke (3.48102) and no-smoke LER (4.99952) data for case 4. Further comparison between minimum, modal, and maximum S_{gr} within each study population also showed significant LER variations. For example, in case 4 there is a 27.9 percent difference between the mean no-smoke minimum S_{gr} (4.99952) and the no-smoke maximum S_{gr} LER (6.39596). This type of LER variation as a function of S_{gr} has been discussed by Lee and LaMotte (1991). In general, the smallest LER results were produced in case 7, and the largest LER results came from case 5 in both the no-smoke and smoke studies--which agrees well with the findings of Duncan and Swaim (1989). However, it should be noted, as a caveat, that all CASTFOREM results discussed here are very scenario dependent.

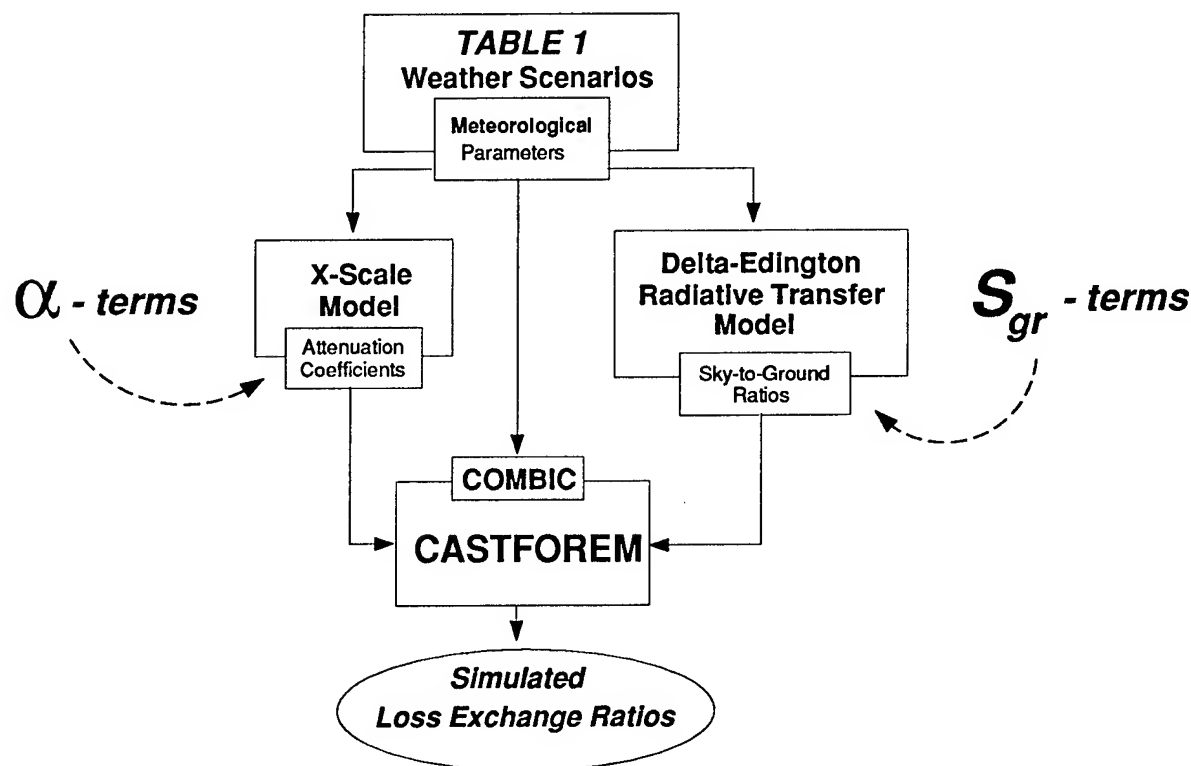


Figure 1. Conceptual model of meteorological parameter, α , S_{gr} , and COMBIC coupling to CASTFOREM for the smoke study.

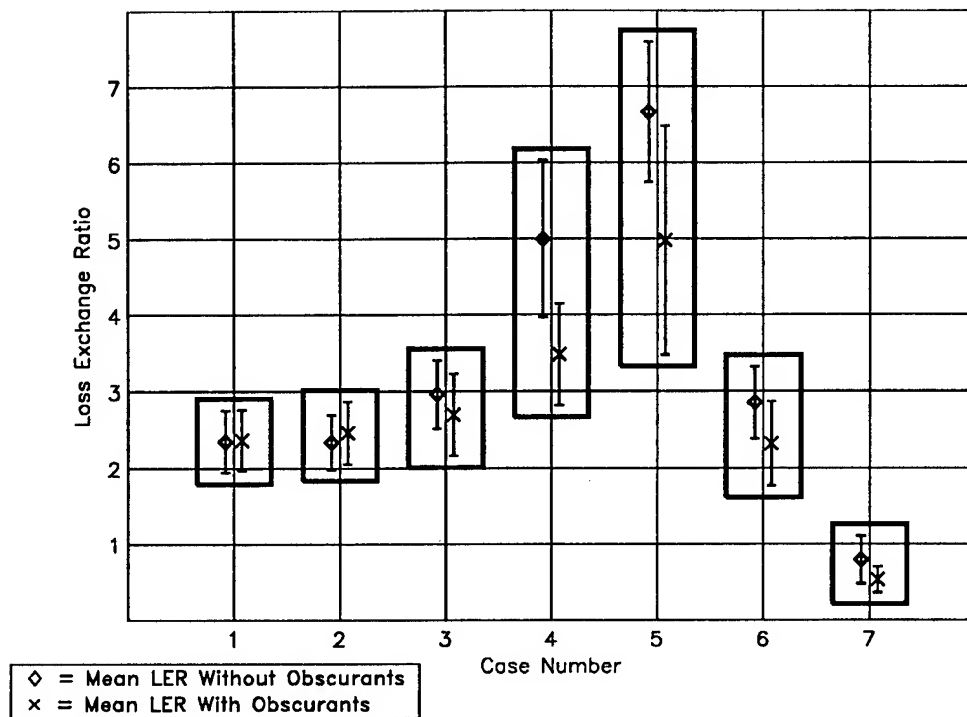


Figure 2. Comparisons of mean LER simulation results for no-smoke and smoke runs initialized with minimum S_{gr} conditions.

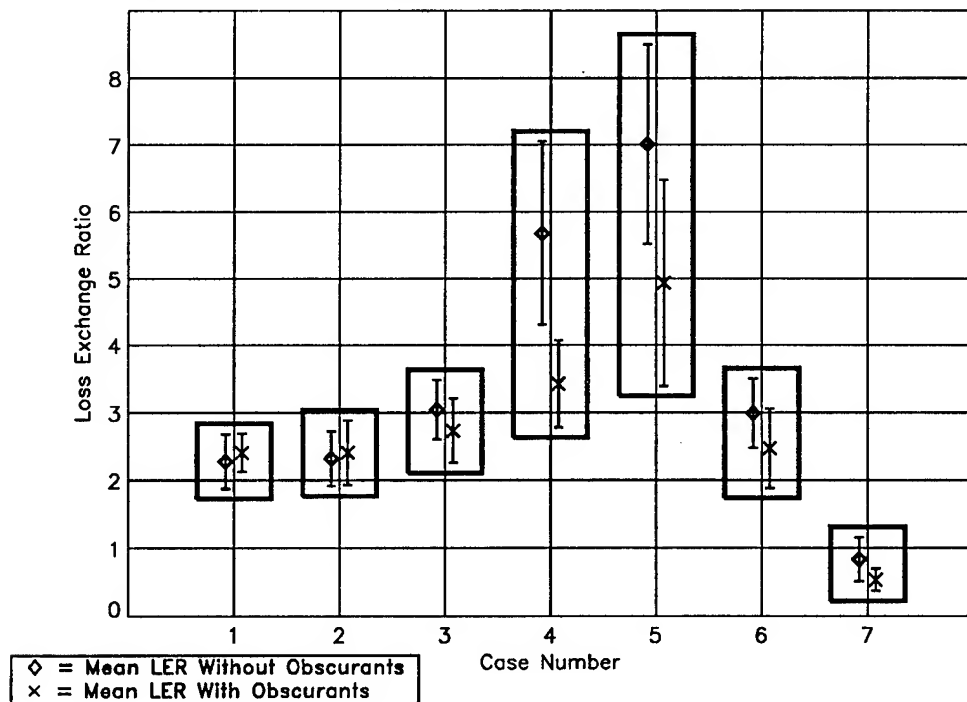


Figure 3. Comparisons of mean LER simulation results for no-smoke and smoke runs initialized with modal S_{gr} conditions.

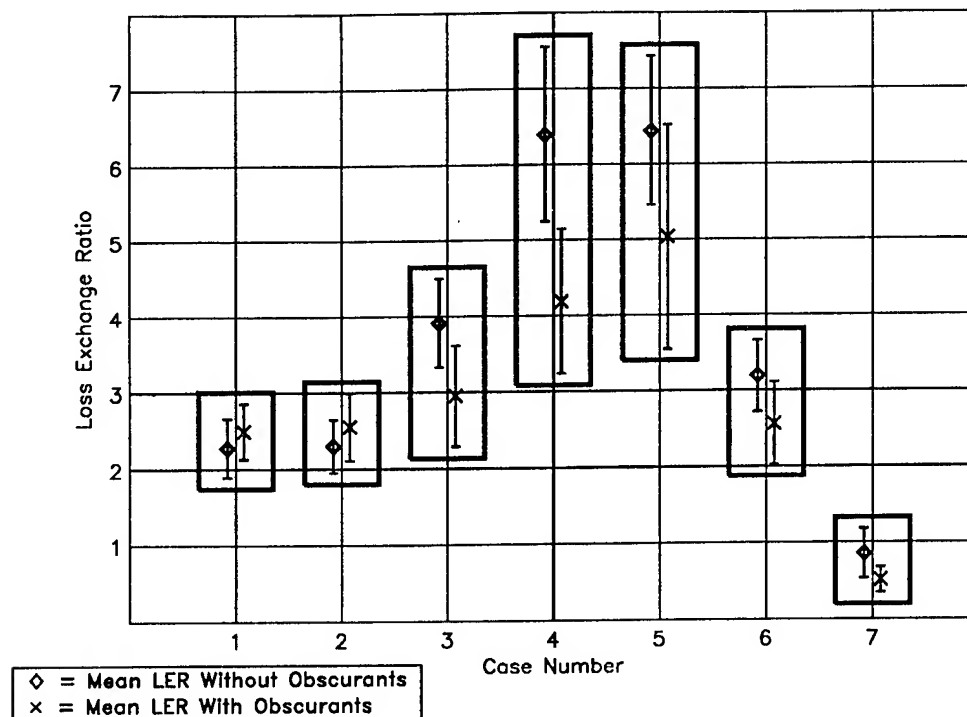


Figure 4. Comparisons of mean LER simulation results for no-smoke and smoke runs initialized with maximum S_{gr} conditions.

The Wilcoxon rank sum probability method (Lee and LaMotte, 1991) was employed to identify the significance of these results using a 95 percent confidence interval, and this analysis indicated that the increases in mean LER from the inclusion of obscurants in the maximum S_{gr} cases 1 and 2 were significant. This testing also indicated that all the mean LER decreases in cases 3 through 6 were significant. It is difficult to make any statistically valid inferences about all the relatively similar results for case 7 (minimum, modal, and maximum S_{gr} cases). The only comparisons that were not classified by the Wilcoxon method as significantly different from each other were cases 1 and 2 for the minimum and modal S_{gr} runs for cases.

5. CONCLUSION

The smallest mean LER results are found in case 7, a winter storm scenario, where there was severe atmospheric attenuation and restricted visibility from blowing snow. In this case, neither BLUE or RED forces had a significant target acquisition advantage for both the smoke and no-smoke cases. Figures 2 through 4 illustrate that mean LER values are all optimized in case 5, where visibility was reduced to 2 km. However, the greatest significant differences between smoke and no-smoke LER comparisons all occurred in case 4 (minimum S_{gr} $\Delta = 43.6\%$, modal S_{gr} $\Delta = 65.9\%$, and maximum S_{gr} $\Delta = 52.6\%$).

Figures 2 through 4 suggest that there is some benefit from inclusion of smoke in cases 1 and 2 when S_{gr} is increased (for visibilities > 4.5 km). Conversely, smoke stunted LER efficiencies in cases 3 through 6, with the greatest LER degradation (modal $S_{gr} \Delta = 65.9 \%$) in case 4. This LER degradation may be resulting in cases with visibilities at and below 4.5 km because the introduction of battlefield obscurants into the simulations, in these cases, is reducing net visibility to significantly less than 2 km.

The presence of this potentially critical, nonlinear LER damping suggests that battlefield smoke and dust effects can play an important role in determining measures of unit success attained in high-resolution combat simulation. Cross-case LER variation further suggests that obscurant effects should be coupled to some set of probable variations in atmospheric conditions, to improve predictions of what may actually elapse in a selected battlefield problem. Otherwise the validity of guidance provided by combat simulation analysts will be degraded to some degree in its ability to predict events transpiring in real battlefield environments.

ACKNOWLEDGMENTS

This work is dedicated to the late Dr. Louis D. Duncan, who originally pioneered the use of high resolution combat simulation sensitivity studies to obtain objective, stochastic measures of atmospheric impacts on battlefield processes. The authors also thank Mr. Jerry Swaim, of the U.S. Army TRADOC Analysis Command - WSMR (TRAC-WSMR), White Sands Missile Range, New Mexico, for his invaluable assistance in providing CASTFOREM support throughout this study.

REFERENCES

- Duncan, L. D., and J. Swaim, 1990: (U) Variations in Simulated Combat Outcomes with Changes in Weather Inputs, SECRET. In Proceedings of the Tenth Annual EOSAEL/TWI Conference, U.S. Army Atmospheric Sciences Laboratory, White Sands Missile Range, NM 88002-5501.
- Duncan, L. D., M. A. Seagraves, and M. G. Heaps, 1987: EOSAEL 87, Volume 7, Natural Aerosol Extinction Module XSCALE, ASL-TR-0221-7, U.S. Army Atmospheric Sciences Laboratory, White Sands Missile Range, NM 88002-5501.
- Fiegel, R. P., and M. G. Heaps, 1990: XSCALE 1989 UPDATE. In Proceedings of the Tenth Annual EOSAEL/TWI Conference, U.S. Army Atmospheric Sciences Laboratory, White Sands Missile Range, NM 88002-5501.

- Gillespie, Patti S., 1990: Preliminary Comparison of Delta Eddington Model Calculations of Contrast to Measurements, In Proceedings of the Tenth Annual EOSAEL/TWI Conference, U.S. Army Atmospheric Sciences Laboratory, White Sands Missile Range, NM 88002-5501
- Hoock, D. W., R. A. Sutherland, and D. Clayton, 1987: Combined Obscuration Model for Battlefield-Induced Contaminants (COMBIC), ASL-TR-0221-11, U.S. Army Atmospheric Sciences Laboratory, White Sands Missile Range, NM 88002-5501.
- Lee, M. E., and S. J. LaMotte, 1991: Loss Exchange Ratio Sensitivity to Variations of Sky-To-Ground Radiance in a Combat Simulation, In Proceedings of the Eleventh Annual EOSAEL/TWI Conference, U.S. Army Atmospheric Sciences Laboratory, White Sands Missile Range, NM 88002-5501.
- Seagraves, M. A., 1989: Weather and Environmental Effects on Electro-Optical Devices: A Tutorial, ASL-TR-0254, U.S. Army Atmospheric Sciences Laboratory, White Sands Missile Range, NM 88002-5501.
- Seagraves, M. A., and J. M. Davis, 1989: Target Acquisition Tactical Decision Aid Software Technical Documentation, ASL-TR-0252, U.S. Army Atmospheric Sciences Laboratory, White Sands Missile Range, NM 88002-5501.
- TRAC-WSMR-TD-4-88, 1988: Combined Arms and Support Task Force Evaluation Model (CASTFOREM) METHODOLOGIES, U.S. Army TRADOC Analysis Command-WSMR, White Sands Missile Range, NM 88002-5502.

AN APPLICATION OF AAODL METEOROLOGICAL AND NEPHELOMETER
FIELD TEST DATA: OBSCURANT PLUME CHARACTERIZATION

Roger E. Davis and John Crain
Science and Technology Corporation
Las Cruces, NM 88001, USA

Robert A. Sutherland
U.S. Army Atmospheric Sciences Laboratory
White Sands Missile Range, NM 88002, USA

ABSTRACT

Field data obtained during the preliminary fog oil trials of Smoke Week XIII are used, along with data analysis techniques developed over the years in support of the Atmospheric Aerosols and Optics Data Library (AAODL), to determine the applicability of the data to EOSAEL model validation. In particular, mass concentration data obtained from a 22-unit linear array of optical nephelometers are analyzed and compared with near-coincident transmittance measurements and modeled plume dispersion parameters. Major findings, based on the five available trials of 5- to 8-min duration, are that, overall, the EOSAEL crosswind dispersion parameters, or "Gaussian sigmas" are modeled accurately to within the range of variability allowed by the Pasquill stability category scheme. An associated incidental finding is that the field-determined Pasquill categories as reported to the AAODL are in apparent error according to both the ex posteriori plume data and determinations based upon the ambient meteorological conditions. Findings based upon comparisons of the line-integrated concentration data and measured transmittance indicate that the EOSAEL visible-band mass extinction coefficient ($7.0 \text{ m}^2 \text{ g}^{-1}$) is in reasonable agreement with the field determinations. In the mid-infrared spectral region, however, the transmittance values as calculated from the nephelometer measurements in conjunction with the EOSAEL mass extinction coefficient ($0.245 \text{ m}^2 \text{ g}^{-1}$) differ significantly from the ASL MPTR directly measured transmittance. The reason for this latter disparity could be instrumental artifacts and miscalibration, or the fact that the EOSAEL values are based upon the operation of the M3A3 pulse jet generator, whereas the newer turbine generators, which may produce a different particle size distribution, were used at the trials considered here. There is also evidence that the disparity may be due to molecular absorption bands in the 3- to 5- μm region of the fog oil spectrum that are not accounted for in the EOSAEL models. These possibilities, and other questions raised in the study, are the subject of continued research. This paper also addresses issues of plume meander in relation to ambient meteorological conditions. Suggestions are made for more detailed studies and for possible technical enhancements to EOSAEL plume models.

1. INTRODUCTION

Since the late 1970s, the U.S. Army has sponsored field demonstrations to test the effectiveness of smokes and obscurants against military electromagnetic sensor systems. The tests, referred to as "Smoke Weeks," conceived by the Office of the U.S. Army Project Manager, Smoke/Obscurants, have recently become the responsibility of the Munitions Directorate, Countermeasures and Test Division (CMTD) of the Chemical Research, Development, and Engineering Center (CRDEC).

Since the beginning, the Smoke Weeks have also served the secondary purpose of providing a database for the validation/verification of various mathematical models for predicting the behavior and effectiveness of obscurants, including those models resident in EOSAEL. Data produced as a result of these and other DoD tests are entered into a central database known as the Atmospheric Aerosols and Optics Data Library (AAODL). This data library is co-sponsored by CMTD and the U.S. Army Atmospheric Sciences Laboratory (ASL).

Data from a typical Smoke Week consist of several multi-band transmittance measurements taken over various lines of sight (LOSs) through smoke screens produced by a variety of conventional and developmental munitions. The data are normally averaged over 1-s intervals and give broadband transmittance for nominally three or four spectral regions from the visible through the far infrared. Transmittance is usually measured over (nearly) horizontal lines of sight located from 2 to 3 m above the ground surface. Some special tests have also involved elevated and vertical LOSs. In most Smoke Weeks, including Smoke Week XIII, at least one LOS has been specially instrumented with aerosol nephelometers designed to give a direct measurement of mass concentration when properly calibrated. One important aspect of the database that is of particular interest to atmospheric effects modelers is that all tests are accompanied by copious measurements from several highly instrumented meteorological towers. How these data are used with other aerosol and optics measurements is the subject of the remainder of this paper.

2. DESCRIPTION OF METHODS

Data used in this paper were collected at Smoke Week XIII, held during April-May 1991 at Eglin Air Force Base, FL. Figure 1 shows the relevant portion of the test site. For this analysis, nephelometer, meteorological, and transmittance data sets have been used. In fig. 1 the symbols labeled 1 through 22 represent the nephelometer array, which was nearly coincident with LOS 3. The 16 nephelometers were placed nominally 3 m above the ground surface and 15 m apart along a horizontal line as indicated. Nephelometers numbered 4, 6, 11, 13, 18, and 20 (not shown) were placed approximately 1 m above or below the main array line at positions 3, 12, and 19 on fig. 1 and were not used in this analysis. Nephelometer 16 was not operable during the trials considered here. Nephelometer design and operation is described by Bruce et al. (1987). Field operations have been described by Spence and Lewis (1990).

The major source of meteorological data used in this study was the W5 10-m tower located near the center of the nephelometer array in fig. 1. Supporting data were acquired from the W1 30-m tower located some distance to the southwest of the area and not shown in the figure. Major meteorological data used for this study included: wind speed and wind direction, standard deviation of wind direction, solar flux density, and cloud cover. It became evident early in the study that the Pasquill stability categories (PSCs) reported in the field were not consistent with the meteorological conditions. These stabilities were therefore discarded in favor of calculated values obtained using the graphical and analytical methods developed by Hansen (1979) and Sutherland et al. (1986). Table 1 gives a summary of meteorological data used in this study.

For the trials listed in table 1, the smoke generators were placed at location MDP-3. For the tests considered here, wind direction was generally from the south-southeast but was, of course, variable during the course of the experiments, with variations roughly as indicated by the wind vectors at MDP-3 in fig. 1. The generators were modified jet aircraft starter turbine systems operated by personnel from the U.S. Army CRDEC.

The trials studied here, identified as T00500, T00600, T00801, T00901, and T01001, were conducted during set-up week, and were primarily used for nephelometer calibration purposes. These trials are particularly well suited for the study because for each trial a single generator was used and it was held stationary during the event.

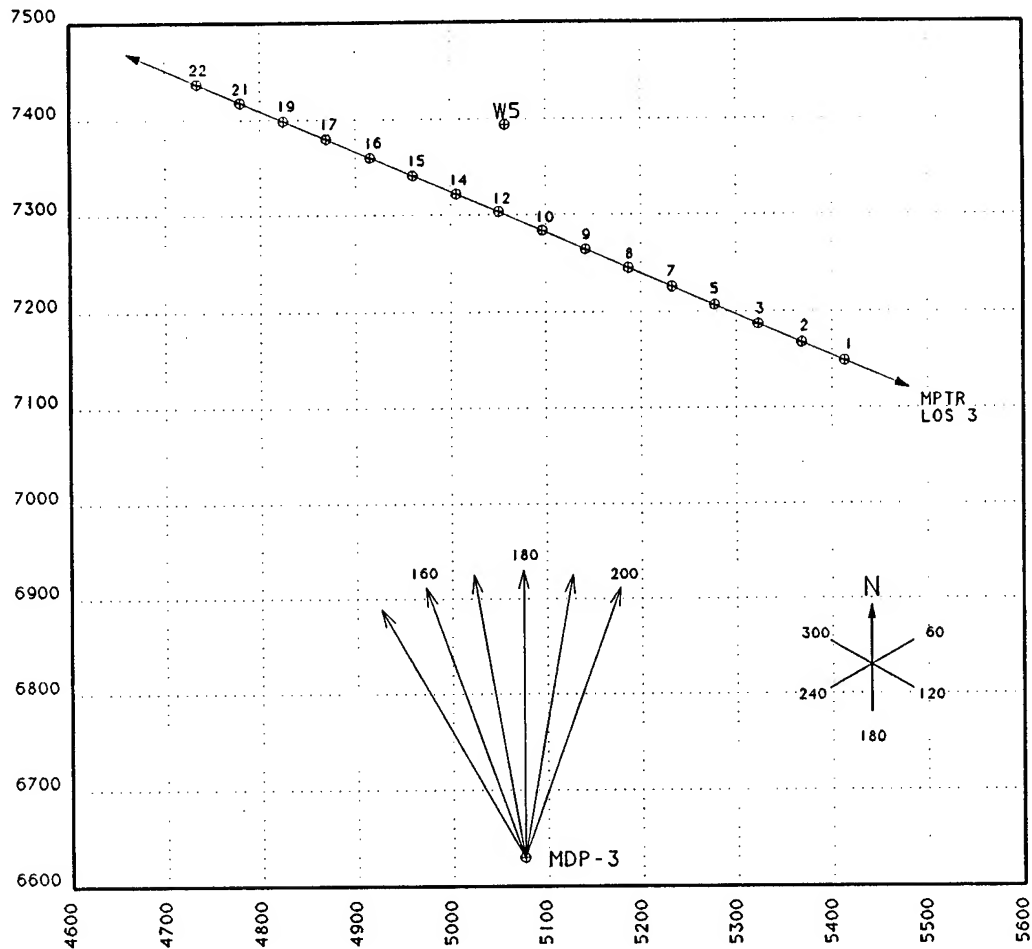


Figure 1. Sketch of the Smoke Week XIII test grid showing nephelometer line, source location (MDP-3), and meteorological tower (W5). Note that dimensions are in feet.

TABLE 1. SUMMARY METEOROLOGICAL DATA FROM TOWER W5, 10 METER LEVEL, MAY 3, 1991

Trial Number	Time (CDT)	Wind Speed (m s ⁻¹)	Wind Deviation (degrees)	Solar Flux (W m ⁻²)	Cloud Cover (%)
T00500	16:05:00	7.1	8.44	397.7	24
T00600	16:14:00	6.4	9.49	211.8	90
T00801	16:46:00	5.0	10.40	107.7	100
T00901	16:54:00	4.9	12.07	107.7	100
T01001	17:02:00	4.3	9.67	95.0	100

Transmittance data for this analysis were obtained by the ASL Multi-Path Transmissometer and Radiometer (MPTR) described by de Jong (1988) and operated by ASL. The MPTR operated with one LOS, LOS 3, designed to be coincident with the nephelometer array line. In this configuration, the measured transmittance from the MPTR can be checked against the measured concentrations from the nephelometer array by using the EOSAEL mass extinction coefficients (see Section 3).

3. RESULTS AND DISCUSSION

The remainder of this paper deals with the analysis of the transmittance, nephelometer, and meteorological data. The transmittance and the line-integrated nephelometer data are analyzed in the context of the Beer's Law approximation and compared with EOSAEL model values. The concentration data from the nephelometer array are used to estimate atmospheric dispersion parameters, which are then compared with those predicted by the Gaussian plume model used in EOSAEL. A secondary but related issue concerns the frequency and magnitude of plume meander as estimated from the nephelometer analysis.

3.1 PASQUILL STABILITY CATEGORY

The first step in the analysis involves the determination of the PSC, which serves as the basis for the calculation of the atmospheric dispersion parameters that control the lateral (crosswind) and vertical spreading of the obscurant. In the EOSAEL models, as well as other well-known atmospheric transport and diffusion models, plume dispersion is parameterized in terms of Gaussian "sigma" functions, which are strongly dependent upon the PSC. The vertical dispersion coefficient is also dependent on surface roughness. In EOSAEL, and other models, the dispersion parameters are modeled using the following empirically derived power law functions (Hansen, 1979):

$$\sigma(y) = a * x^b \quad \text{lateral dispersion} \quad (1)$$

$$\sigma(z) = c * x^d \quad \text{vertical dispersion} \quad (2)$$

where x denotes downwind travel distance from the smoke generator (source) and the coefficients a , b , c , and d , tabulated in Hansen (1979), are functions of the atmospheric stability, or PSC. Coefficients c and d are also functions of the surface roughness.

The determination of atmospheric stability category is not an exact science; numerous approaches to estimating the PSC have been offered. We have used several different algorithms for determining the PSC for the selected trials, ranging from the simple method of Hanna et al. (1982), based upon the standard deviation of wind direction, to more sophisticated procedures based on solar radiation, wind speed, and surface roughness (Hansen, 1979; Sutherland, et al., 1986). Table summarizes PSC determinations based on supporting meteorological data (see table 1) taken during the trials of interest. As noted above, the PSCs as determined in the field and originally reported to the AAODL are not consistent with the other meteorological data and were not used in this analysis.

TABLE 2. PASQUILL STABILITY CATEGORIES USED FOR THIS ANALYSIS

Trial Number	PSC Reported	PSC, Wind Deviation	PSC, Wind Speed, Solar Radiation	PSC Adapted
T00500	B	D	C	C/D
T00600	A	D	C	C/D
T00801	A	D	C	C/D
T00901	A	D	C/D	C/D
T01001	A	D	D	D

3.2 NEPHELOMETER DATA

Data from the nephelometer array provide a real-time signal at each nephelometer position that is proportional to the obscurant density at that particular location and at that point in time during cloud passage. Concentration values are reported once per second. Mass samplers or dosimeters are selectively collocated with several of the nephelometers to provide calibration information, which is then used to convert the raw signal to concentration values ($g\ m^{-3}$).

When reduced, calibrated, and plotted in three-dimensional form, the data give a good qualitative and quantitative visualization of the smoke passage in time. An example based upon trial 00500 is shown in fig. 2.

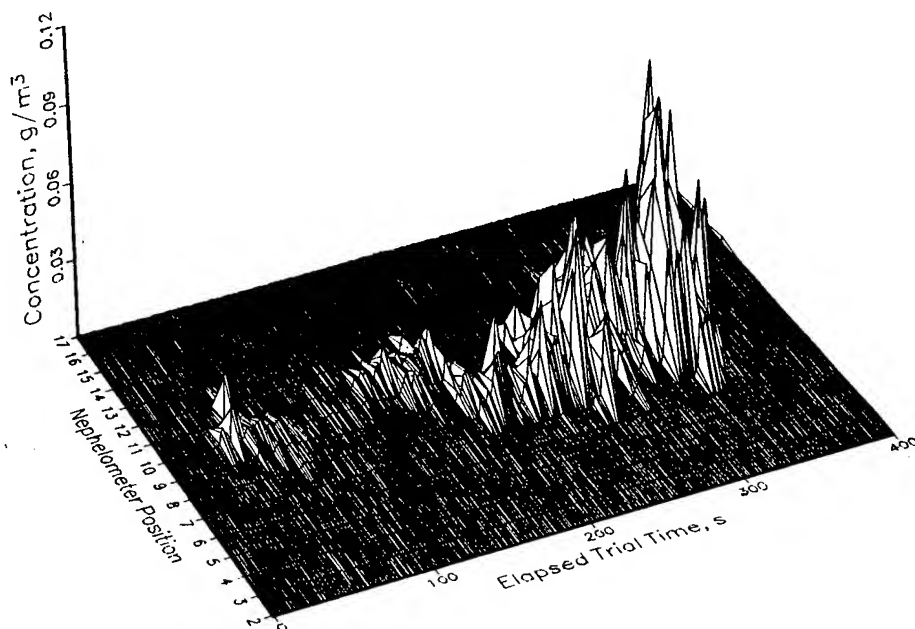


Figure 2. Three-dimensional plot of calibrated nephelometer data for trial 00500. The source for this and all other trials was a continuous turbine-driven fog oil generator.

The data in fig. 2 represent the obscurant mass concentration as sensed at each nephelometer along the line as a function of time, referenced from time of release. Note the variability in the apparent plume width, which reaches a maximum somewhat before 300 s, and the meander of the apparent centroid, or mass median. Note also that during the period near and around 100 s the plume has apparently lifted above the nephelometer line, as evidenced by the near-zero readings. The lifting of the plume contributes to the vertical dispersion parameter and is consistent with the Gaussian description in the long-averaging time limit. This random-like lifting of the overall plume is important for screening purposes, since it can give rise to apparent "holes" in smoke screens.

3.3 PLUME DISPERSION AND MEANDER

One direct application of the nephelometer data lies in the calculation of plume dispersion and meander. Meander is important in applications because it affects the time average of the mass distribution. Lateral, or crosswind, plume meander for the selected fog oil trials is studied by locating the center of mass (CM) of the obscurant at the nephelometer line height as a function of time. The CM is computed in the usual statistical sense, as the ratio of the first moment to the total mass. That is:

$$CM(t) = \frac{\sum m_i(t) r_i}{\sum m_i(t)} \quad (3)$$

where $m_i(t)$ = mass concentration, $g\ m^{-3}$, for nephelometer i at time t
 r_i = distance of nephelometer i from defined origin

Likewise, the plume mass variance along the nephelometer array is computed in terms of the second moment by:

$$\sigma^2(t) = \frac{\sum m_i(t) r_i^2}{\sum m_i(t)} \quad (4)$$

from which the instantaneous (actually 1-s average) sigma is computed as:

$$\sigma(t) = \sqrt{\sigma^2(t)} \quad (5)$$

The actual sigma value to be used in Gaussian-based models is obtained from the long time average of eq. (5). Sigma values obtained by averaging over the total event time are listed in table 3 (Section 3.4). Calculations based upon the above definitions and the nephelometer data are plotted in fig. 3, where we show the plume CM and computed dispersions as a function of time for the five trials.

Note from fig. 3 that the meander of the CM for trial T00500 was contained within a width of about 50 m on the array, while the meander for trials T00600 and T00801 was contained within a width of approximately 100 m on the array, and that the meander for T00901 and T01001 was contained in a width of approximately 150 m. With the exception of T00500, these plume meanderings are consistent with the reported deviations in wind direction for the trials. Based on the reported wind direction deviations, the meander in the T00500 plume is expected to be more like those of T00600 and T00801. It must be noted, however, that all trials were of relatively short duration (5 to 8 min) so that departures from expected values might be expected. Therefore, the smaller meander of the plume for the T00500 trial is not necessarily inconsistent with theory.

3.4 PLUME MASS DISTRIBUTIONS

As indicated previously, the dispersion parameters required in the EOSAEL plume models are time-averaged values. In table 3, we present the time-averaged results (averaged over the total trial time) as calculated from the nephelometer data, along with theoretical estimates based upon EOSAEL models. Table 3 shows theoretical results for both PSC C and D, since this spread represents the expected variability based on stability.

For the modeled values in table 3, we have accounted for the fact that, due to the mean trial wind directions and variations in the wind direction, the nephelometer line is not exactly crosswind. For this reason, each nephelometer was located at a different downwind position from the source at MDP-3.

Note from table 3 that the nephelometer-determined sigma values are either within the extremes or are otherwise very near one of the extremes of the modeling estimates. For T00500 the PSC D estimates seem to be a good match to the observed dispersion, while PSC C estimates better describe the dispersions determined for the other four trials. This result is not surprising in light of the meander data presented previously. During the trial observation periods, the

T00500 plume did not meander nearly as much as did the other four trial plumes. It is worth noting that the model predicts sigmas of approximately 65 m for PSC A, the PSC as reported in the field (see table 2).

Overall, these results support the Gaussian assumption for PSC C and D, although there may be cause for some fine tuning as additional trial observations are added to the analysis. Currently, there is no reason to doubt the validity of the Gaussian dispersion coefficients used in EOSAEL to describe the dispersion of fog oil downwind from the source.

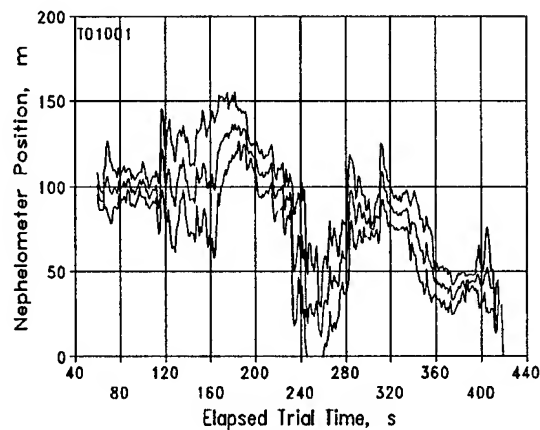
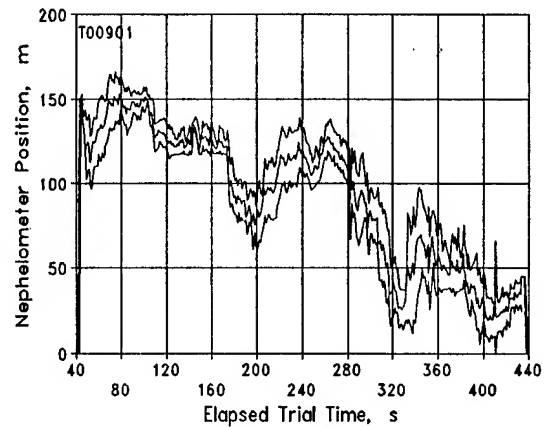
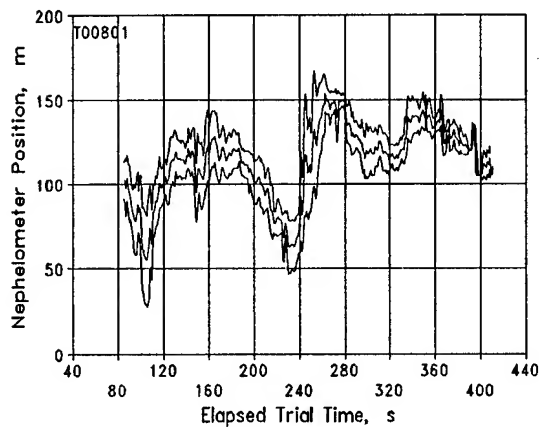
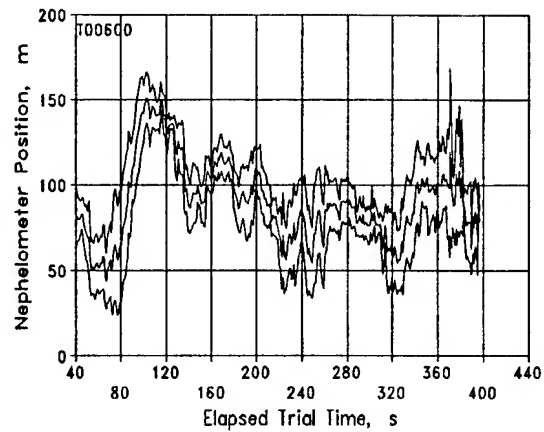
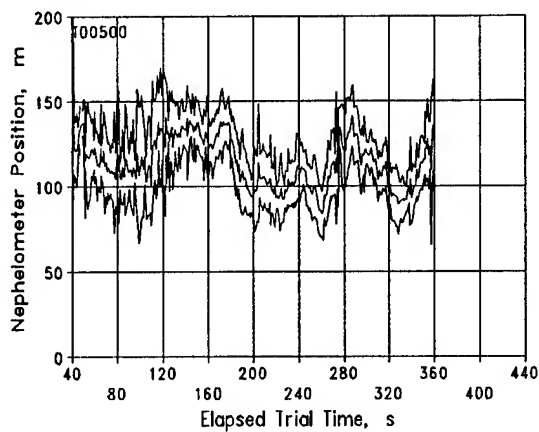


Figure 3. Plots of computed center of mass and dispersion width for the five trials as computed from the nephelometer data.

TABLE 3. TRIAL-AVERAGED PLUME DISPERSIONS IN METERS

Trial Number	Nephelometer Measurements	EOSAEL Model PSC C	EOSAEL Model PSC D
T00500	20.6	29.4	19.1
T00600	32.0	30.6	20.1
T00801	25.9	28.2	18.3
T00901	34.1	26.8	17.4
T01001	34.7	29.4	19.1

3.5 COMPARISONS OF NEPHELOMETER RESULTS WITH TRANSMITTANCE DATA

For a colinear arrangement, nephelometer-based mass concentrations and MPTR transmittance measurements are related according to Beer's law as follows:

$$T(t) = \exp[-\alpha(\Delta\lambda) \cdot CL(t)] \quad (6)$$

and

$$CL(t) = \int C(r,t) dr \quad (7)$$

where $\alpha(\Delta\lambda)$ is the obscurant mass extinction coefficient appropriate for a waveband denoted by $\Delta\lambda$, $C(r,t)$ is the obscurant mass concentration at time t and distance r along the nephelometer line, i.e., LOS 3, and L is the total length of the LOS as defined by the transmissometer source and receiver. The left-hand side of eq. (7) is termed the path-integrated concentration or concentration length, CL . The numerical equivalent of this expression is used in this section to compare transmittance and nephelometer data.

For this analysis, eq. (6) is inverted to obtain a calculated CL value from the MPTR transmittance data, which can then be directly compared with the nephelometer data. For the purpose of this study, mass extinction coefficients for the visible ($7.0 \text{ m}^2 \text{ g}^{-1}$) and the 3- to $5\text{-}\mu\text{m}$ band ($0.245 \text{ m}^2 \text{ g}^{-1}$) were taken from the EOSAEL COMBIC documentation (Hooek et al., 1987).

Nephelometer CL data are determined using eq. (7). These CL values are subject to significant error, due to the low spatial and time resolution. The nephelometers are 15 m apart, and since nephelometer 16 was down, nephelometers 15 and 17 are 30 m apart. The obscurant cloud was completely contained within the nephelometer array during these trials, however, reducing errors resulting from unsampled edges of the cloud. Figure 4 shows the comparisons of the CL data derived from the MPTR transmissometry with the results of the path-integrated CL data obtained from the nephelometer array.

Because of the large difference between the visible and mid-infrared extinction coefficients, it is usually not possible to use both bands simultaneously to compute a CL product from the transmissometry. For heavy obscuration, the visible band saturates, or "bottoms out," at the detector lower threshold, which is somewhere between 1% and 10% for the MPTR. This was the case for trials T00600, T00801, T00901, and T01001. In the case of light obscuration, such as for trial T00500, the attenuation in the mid infrared band was so low as to be in the "clear-air" noise level. In fig. 4, we have used whichever band provided the most data in the range of 10% to 90% transmittance.

Overall, the results using the visible band are surprisingly consistent. For the mid infrared band, however, the nephelometer results are consistently higher than the MPTR results. The reason for this disparity may be instrument calibration, or there may be an actual physical effect inherent in the turbine generators used in these particular trials. Also, other data indicate that there may be some molecular band absorption in the 3- to $5\text{-}\mu\text{m}$ region of the fog oil spectrum not

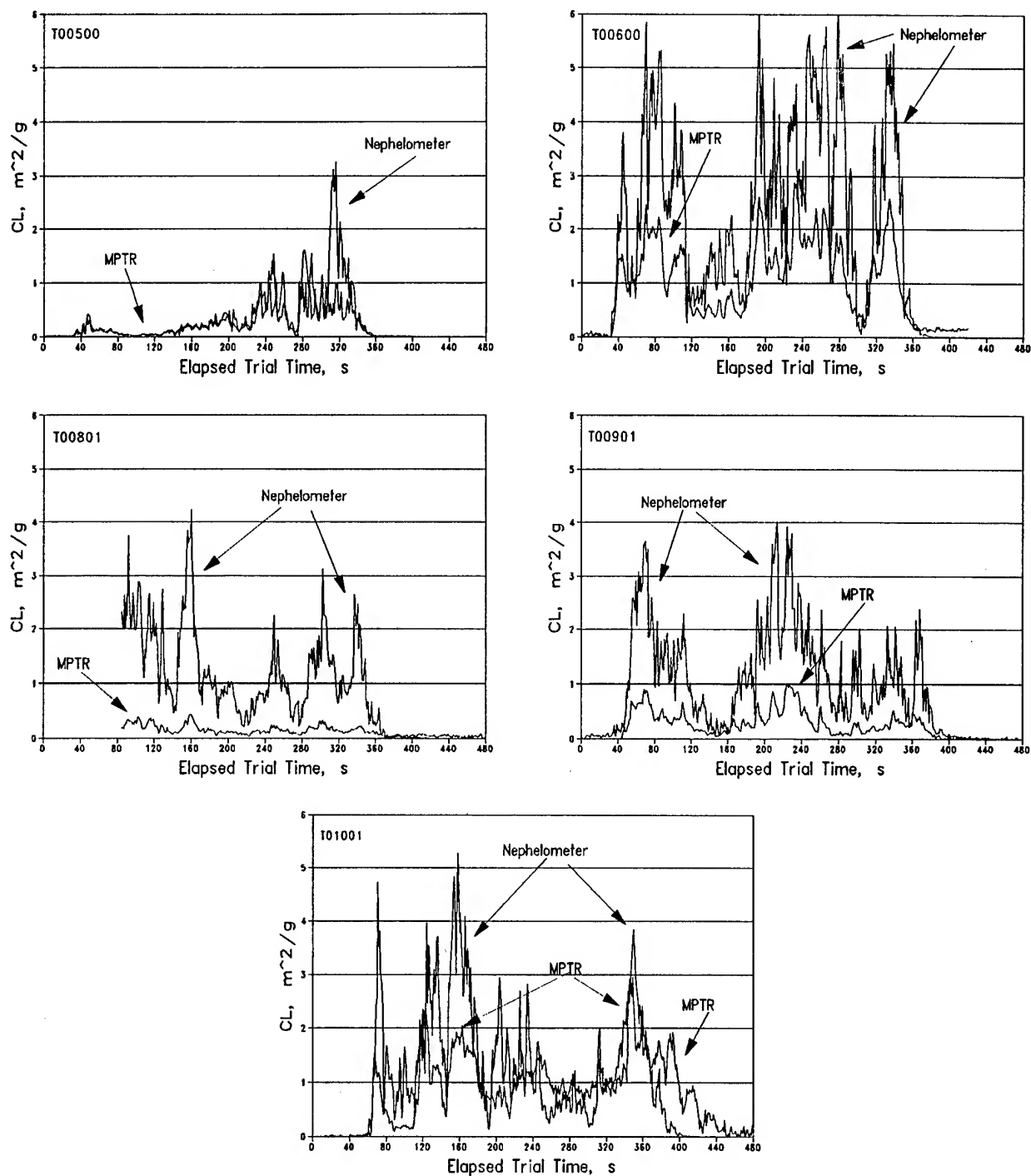


Figure 4. Plots showing comparison between nephelometer-determined CL values and CL values derived from measured MPTR transmittance data for the five trials studied. For T00500 the visible band was used. For this trial, the transmittance was occasionally below detection threshold between 240 and 330 s. No infrared data were available for this trial.

accounted for in the EOSAEL models (Yee et al., 1991). A viable solution to the problem is beyond the scope of this paper but is an object of continued research.

4. SUMMARY

Analysis of nephelometer data acquired during five fog oil trials at Smoke Week XIII shows that the atmospheric dispersion parameters used in EOSAEL models are consistent with observed data. CL values as determined from the nephelometer data agree well with directly measured visible-band CL values derived from the EOSAEL mass extinction coefficient for fog oil. Similar comparisons in the mid infrared band show disparities on the order of 2 to 3, which may be due either to instrument calibration errors or real-world variations in source characteristics. Studies are recommended to extend the analysis to a wider range of stability classes and to analyze other obscurants. Studies of generator source strengths to obtain better emission rate estimates are also recommended.

ACKNOWLEDGEMENTS

The authors wish to acknowledge Mr. Bill Gammill (PSL) for informative discussions concerning the nephelometer operations, Mr. Tony Spence (PSL) for help in obtaining the data used in the analysis, and Dr. Brian Locke (STC), and Dr. Clem Ota (STC) for helpful discussions concerning the Smoke Week XIII instrumentation, trial conditions, and field geometries. Co-authors Davis and Crain wish to acknowledge CMTD and ASL for support of this work, performed under ASL contract DAAD07-89-C-0035.

REFERENCES

- Bruce, C., L.F. Hall, J. Ku, K.E. Kunkel, L.K. Matthews, and P.R. Smith, 1987: Measuring Aerosol Density, Using Nephelometry and Dosimetry, Center for Atmospheric Sciences, New Mexico State University.
- De Jong, A.N., M.J. Roos, and P.J. Fritz, 1988: Smoke Characterization by Means of MPTR, IR1988-07, FEL-TNO, The Netherlands.
- Hanna, S.R., G.A. Briggs, and R.P. Hosker 1982: Handbook On Atmospheric Diffusion, DOE/TIC-11223, NTIS.
- Hansen, F.V., 1979: Engineering Estimates For The Calculation Of Atmospheric Dispersion Coefficients, ASL Internal Report, U.S. Army Atmospheric Science Laboratory, White Sands Missile Range, NM.
- Hook, D.W., R.A. Sutherland, and D. Clayton, 1987: Combined Obscuration Model for Battlefield-Induced Contaminants, COMBIC, ASL TR-0221-11, U.S. Army Atmospheric Sciences Laboratory, White Sands Missile Range, NM.
- Spence, T., and C. Lewis, 1990: Obscurant Concentration Measurement System (Nephelometers): Field Test Data Report for Smoke Week XII Test, PSL 90/94, Physical Sciences Laboratory, Las Cruces, NM.
- Sutherland, R.A., F.V. Hansen, and W.D. Bach 1986: A Quantitative Method For Estimating Pasquill Stability Class From Windspeed And Sensible Heat Flux Density, Boundary-Layer Meteorology, 37, 357.
- Yee, Y.P., R.A. Sutherland, J. Crain, B. McDaid 1991: PC-Based Beta Site System for AAODL Applications, Proceedings of the Battlefield Atmospheric Conference 1991, U.S. Army Atmospheric Sciences Laboratory, White Sands Missile Range, NM.

MESOSCALE WIND VARIABILITY IN GERMANY: COMPARISON OF WIND
PROFILES IN CLOSE PROXIMITY FROM FOUR PAIRS OF RADIOSONDE
LAUNCH SITES

Larry J. Levitt and Dorathy A. Stewart

U. S. Army Missile Command
Redstone Arsenal, AL 35898-5248

ABSTRACT

Wind profiles observed at the same synoptic hour were compared for four pairs of German stations. Three pairs of stations (Berlin-Lindenberg, Bergen-Hannover, Schleswig-Kiel) are in the northern lowlands and one pair (Fritzlar-Meiningen) is in the Central European highlands. The launch site separations are 42 km (2 pairs), 56 km, and 100 km. Magnitudes of vector wind differences between stations in close proximity were calculated at constant altitudes between the surface and 8 km in 500 m increments. The smallest mean differences are at the surface, and there is a relative minimum near 2.5 km. The relationship of vector wind differences to Pasquill stability will be briefly mentioned. The authors are aware of numerous reports by Electronics Command personnel and others concerning temporal and spatial variation of these winds. The influence of low-level winds during boost phase of rocket launch has been part of the error budget approach to provide delivery accuracy estimates for various systems. Much of the current interest in low-level winds is focused on predicting the wind profile in the target area.

1. INTRODUCTION

When no wind observations are available over an artillery target area, wind characteristics near the launch site are often used as an estimate. The purpose of this study is to establish data sets consisting of pairs of upper-air observations in which launch sites are a minimal distance apart and to compute spatial variability statistics at constant altitudes for long periods of record. Numerous open-literature publications and other reports exist concerning spatial wind variability (see, e.g., Danard, 1965; Lenhard, 1973; Nappo, 1977; Jaspersen, 1982; Leopold and Cionco, 1988; Orndorff and Cionco, 1988; Kitchen, 1989), but investigators often report results concentrated over a few days to a few weeks. All of these studies involved special field measurements which are not part of the routine synoptic upper-air observing network, also known as the World Meteorological Organization (WMO) operational network. Some of the launch site separations quoted were 20 m, 4.415 km, and 20.91 km (Jaspersen, 1982), 16.25 km (Lenhard, 1973), and 48 km (Danard, 1965). Kitchen (1989) utilized data from one synoptic station in conjunction with a supplemental site 52 km away. Kitchen also pointed out that the minimum separation between launch sites that are part of the synoptic upper-air network in the United Kingdom is 200 km, with an average separation of 310 km.

Since the resources were not available to conduct field trials year-round over an extended period of time, a brief search of the WMO network was

conducted to find the minimal distance between radiosonde launch sites in Europe. This distance was found to be 42 km, which is the launch site separation between Schleswig and Kiel. The Bergen and Hannover launch sites are also separated by 42 km. The authors were already cognizant of the Berlin and Lindenberg pair (56 km separation) from a previous study by Levitt and Essenwanger (1987). After Berlin/Lindenberg the best station pair is Fritzlar and Meiningen, which is separated by nearly 100 km. It should be noted that there are numerous station pairs in Europe (excluding the United Kingdom) whose separation distance is at least 150 km or more (Brown and Robinson, 1979).

Upper-air data for the four station pairs were provided on 9-track magnetic tape by the United States Air Force Environmental Technical Application Center Operating Location A (USAFETAC OL-A), which is situated in the Federal Climate Complex, Asheville, North Carolina. Both radiosondes and pibals were used.

The results that will be presented here consist of the magnitude of the mean, standard deviation, and selected percentiles of the u (i.e. zonal) and v (i.e. meridional) wind component differences for selected heights between surface and 8 km in winter and summer. Some results concerning the vector wind differences will also be presented.

These computations may be of interest to those who are evaluating the performance of mesoscale models such as SIGMET or VARYME (see Cionco, 1988), or formulae that model wind variation over space and time, which are used in weapon effectiveness studies.

2. DATA ANALYSIS

2.1 GEOGRAPHICAL CONSIDERATIONS

The footnotes to Table 1 give the locations, elevations, and WMO numbers of the stations used in this study, as well as the separation distance for each pair of stations. Note that all of these locations are in Germany and in the Central European time zone.

Schleswig and Kiel are the most northerly pair of stations. Both locations are subject to maritime influences as Kiel lies at the head of a deep inlet of the Baltic Sea (at the eastern end of the Kiel Canal) and Schleswig is also near the Baltic Sea. Sea breezes occur about 20 percent of the time in summer along the shores of the Baltic Sea (Defant, 1951).

The station pairs of Bergen and Hannover and Berlin (Tempelhof) and Lindenberg are in the north German plain (lowlands) and are characterized by a more continental climate than the more northerly stations.

Fritzlar and Meiningen are situated in the central European highlands where the terrain is more complex. Fritzlar is close to the transition from highlands to lowlands at an elevation of 222 m, whereas Meiningen is at an elevation of 448 m. Channeling may influence the low-level winds at Meiningen.

Table 1. Means, Standard Deviations (σ), and Percentiles of Magnitudes of Vector Wind Differences (m/s)

Height (m)		Winter				Summer			
		F-M ¹	S-K ²	B-H ³	B-L ⁴	F-M ¹	S-K ²	B-H ³	B-L ⁴
500	Mean	3.77	3.28	3.47	3.52	3.07	2.79	2.70	2.70
	σ	2.41	2.24	2.26	2.25	1.95	1.97	1.59	1.72
	90 %	7.1	6.0	6.8	6.5	5.8	4.9	4.8	4.8
	99 %	11.8	10.9	9.7	10.1	9.7	9.4	7.2	8.3
1500	Mean	4.78	3.01	3.17	3.51	3.50	2.51	2.51	2.81
	σ	3.51	2.87	2.39	2.61	2.23	1.92	1.64	2.07
	90 %	9.3	5.8	5.7	6.4	6.5	4.7	4.6	5.1
	99 %	18.7	14.2	9.9	12.1	11.4	9.7	7.8	9.5
2500	Mean	4.44	2.74	2.82	3.22	3.32	2.23	2.22	2.67
	σ	2.82	2.74	2.46	2.24	2.11	1.95	1.46	2.06
	90 %	8.3	5.0	4.7	5.8	6.1	3.9	4.1	5.0
	99 %	13.9	15.6	9.4	10.0	10.7	10.3	5.9	9.6
3500	Mean	4.97	2.90	2.78	3.28	3.45	2.29	2.17	2.63
	σ	3.22	2.95	2.59	2.51	2.53	2.09	1.47	1.96
	90 %	10.0	5.5	5.2	5.9	6.2	4.1	4.0	4.7
	99 %	15.8	15.9	10.9	10.0	12.6	11.0	7.6	9.1
5000	Mean	5.57	3.88	3.71	3.70	4.31	2.69	2.60	2.76
	σ	3.64	4.65	3.51	3.17	2.96	2.76	1.90	2.03
	90 %	9.9	7.4	7.0	6.8	8.0	5.0	4.4	5.1
	99 %	17.9	27.0	18.6	14.5	15.0	15.9	9.6	9.4
6000	Mean	6.34	4.50	4.13	3.95	4.63	3.20	3.12	3.02
	σ	4.24	5.98	3.79	3.43	3.33	3.49	2.75	2.09
	90 %	11.2	8.5	8.5	7.4	8.8	5.8	6.0	5.6
	99 %	18.8	31.4	20.5	15.7	19.1	19.7	10.0	10.7

¹Fritzlar (WMO # 10437), 51°08'N, 09°17'E, 222 m -> 100 km apart
Meiningen (WMO # 10548), 50°34'N, 10°23'E, 448 m

²Schleswig (WMO # 10035), 54°32'N, 09°33'E, 48 m -> 42 km apart
Kiel (WMO # 10046), 54°23'N, 10°09'E, 32 m

³Bergen (WMO # 10238), 52°49'N, 09°56'E, 68 m -> 42 km apart
Hannover (WMO # 10338), 52°28'N, 09°42'E, 52 m

⁴Berlin (WMO # 10384), 52°29'N, 13°25'E, 52 m -> 56 km apart
Lindenberg (WMO # 09393), 52°13'N, 14°07'E, 110 m

2.2 INTERPOLATING WINDS TO CONSTANT ALTITUDES

For various applications in missile design, winds are required at constant altitude levels. The radiosonde, however, measures pressure directly but not altitude. Weather services routinely assign altitudes to wind measurements by the hypsometric equation which requires the mean virtual temperature of the layer between the two pressure levels. The virtual temperature for each level may be calculated using the radiosonde measurements of temperature and humidity.

For this report, an interpolation procedure was developed to yield winds at the following heights: 200 m, 500 m, 1000 m, 1500 m, 2000 m, 2500 m, 3000 m, 3500 m, 4000 m, 4500 m, 5000 m, 6000 m, 7000 m, and 8000 m. This procedure was terminated at 8000 m in order to remain in the troposphere.

A linear interpolation between the scalar wind speeds nearest the desired height (one above and one below) was performed. To determine the wind direction at the desired altitude, the nearest winds were split into the rectangular components: $u_1 = -V_1 \sin \theta_1$, $v_1 = -V_1 \cos \theta_1$, $u_2 = -V_2 \sin \theta_2$, and $v_2 = V_2 \cos \theta_2$, where the scalar wind speed is denoted by V . The subscripts 1 and 2 refer to the nearest levels above and below the desired altitude, respectively. A linear interpolation for each component was then made separately (denoted by u and v) and the wind direction was computed by the equation $\theta = \tan^{-1}(u/v)$. Additional processing was performed to insure that the wind direction was recovered in the proper quadrant.

Note that in determining acceptable wind ascents from the data tapes, a criteria that at least 7 data points be available between the surface and an altitude at or slightly above 8 km was imposed. In addition, wind ascents that did not start at the surface were also rejected, as these wind ascents usually contained numerous deficiencies.

3. DATA LIMITATIONS

In addition to local micrometeorological effects (e.g. the urban heat island), wind measurements at nearby locations may also be different because of turbulent fluctuations and instrumental errors. Questions exist concerning the ability of radiosondes to measure high-frequency wind fluctuations (e.g., Susko, 1987 or Parlange and Brutsaert, 1990). Because radiosondes partially damp turbulent fluctuations, the true mean magnitude of the wind differences may be larger than the measured mean difference determined by the radiosonde. This damping may be an advantage if the measured wind profile is being used to approximate winds far enough away so that the turbulent fluctuations are uncorrelated.

An important consideration in evaluating the wind difference between two locations at various altitudes is that the wind soundings are not exactly simultaneous. One can anticipate that launch time separation may be at least 15 minutes. In some cases it may be as large as one hour, which is permissible according to WMO regulation.

Radiosonde observations are always assigned to the launch site location, but the balloon becomes displaced horizontally from the launch site after it is released. By the time it has reached the upper troposphere, this displacement may be several tens of kilometers (Kitchen, 1989). The xyz coordinates for each balloon would be required to compute the true separation distance between the balloons (if one ignores the launch-time separation), but these data are not routinely available.

4. RESULTS

Table 1 summarizes the seasonal variation (winter and summer only) of the magnitude of the vector wind differences at selected heights above sea level for four pairs of stations. Winter is December, January, and February, and summer is June, July, and August. Figures 1 through 4 show the mean, 70, 90, 95, and 99 percentile values of the u and v wind component differences in summer and winter for each of the station pairs.

The period of record is 1973-74 for Bergen-Hannover, 1975-1983 for Berlin-Lindenberg, 1973-82 for Schleswig-Kiel, and 1977-82 for Fritzlar-Meiningen.

Analysis of these data produced the following results:

1. Means of the magnitudes of the vector wind differences are generally greater than 1.0 m/s and less than 3.0 m/s at the surface where wind differences are a minimum.
2. There is a relative minimum near 2.5 km. The magnitude of differences here is usually within the range of 2 to 4 m/s. This relative minimum difference near 2.5 km is noteworthy because mean speeds increase from 1.0 km to 2.5 km throughout the year.
3. Vertical changes of mean differences are typically rather small between one and five kilometers.
4. Largest mean differences between nearby wind profiles occur above 5 km. Magnitudes of mean vector differences may be more than 7 m/s.
5. Wind differences between stations near each other are usually largest in winter and smallest in summer.

An attempt was made to stratify the vector wind difference according to Pasquill stability category for the Berlin-Lindenberg pair. This was somewhat inconclusive because the full range of vector wind differences was observed for the Pasquill category D, which is the category which contained most (71%) of the surface observations at Berlin.

5. SUMMARY

Wind profiles at a nearby location are often used to characterize a site where no wind measurements are available. The minimal distance between launch sites in Europe was determined so that spatial wind variability statistics at constant altitudes for sufficiently long periods of record could be derived. Four pairs of stations in Germany were selected, Bergen/Hannover, Schleswig/Kiel, Berlin/Lindenberg, and Fritzlar/Meiningen, whose separation distances are 42, 42, 56, and 100 km, respectively. Results include selected percentiles of the absolute values of u and v wind component differences and vector wind differences for winter and summer. Mesoscale modelers or those

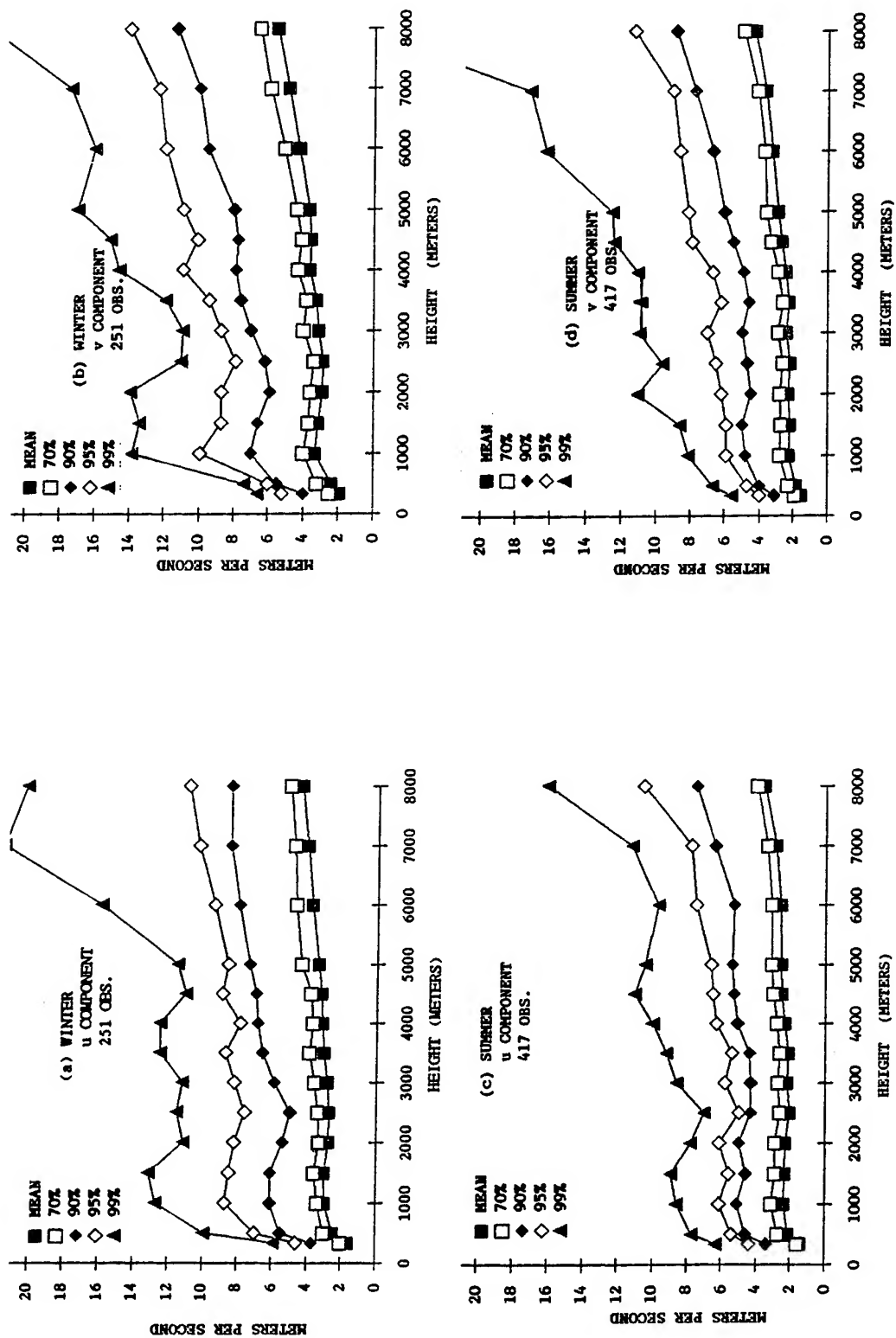


Figure 1. Differences between Fritzlar and Meiningen. Absolute values of differences for u and v components in winter and summer.

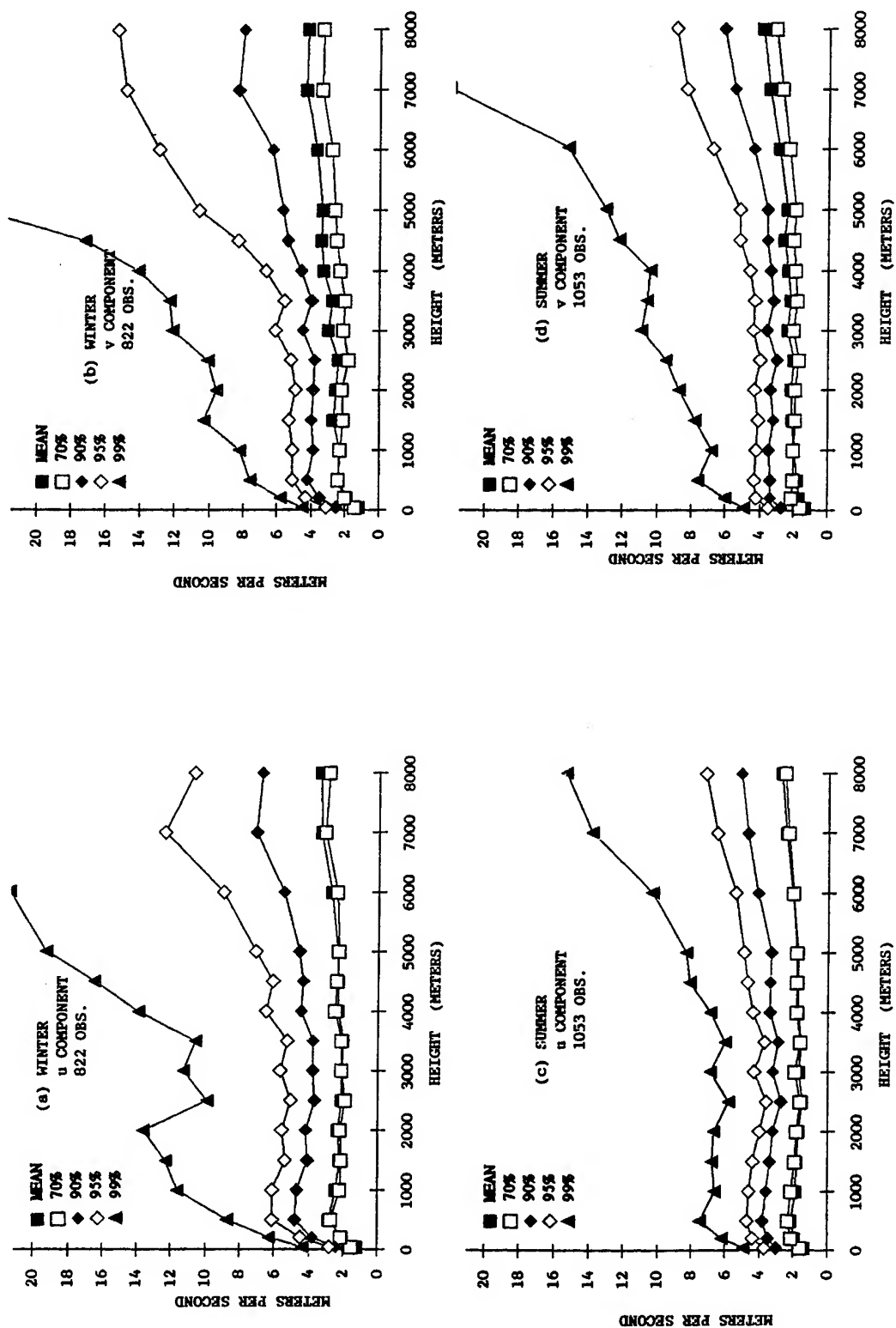


Figure 2. Differences between Schleswig and Kiel. Absolute values of differences for u and v components in winter and summer.

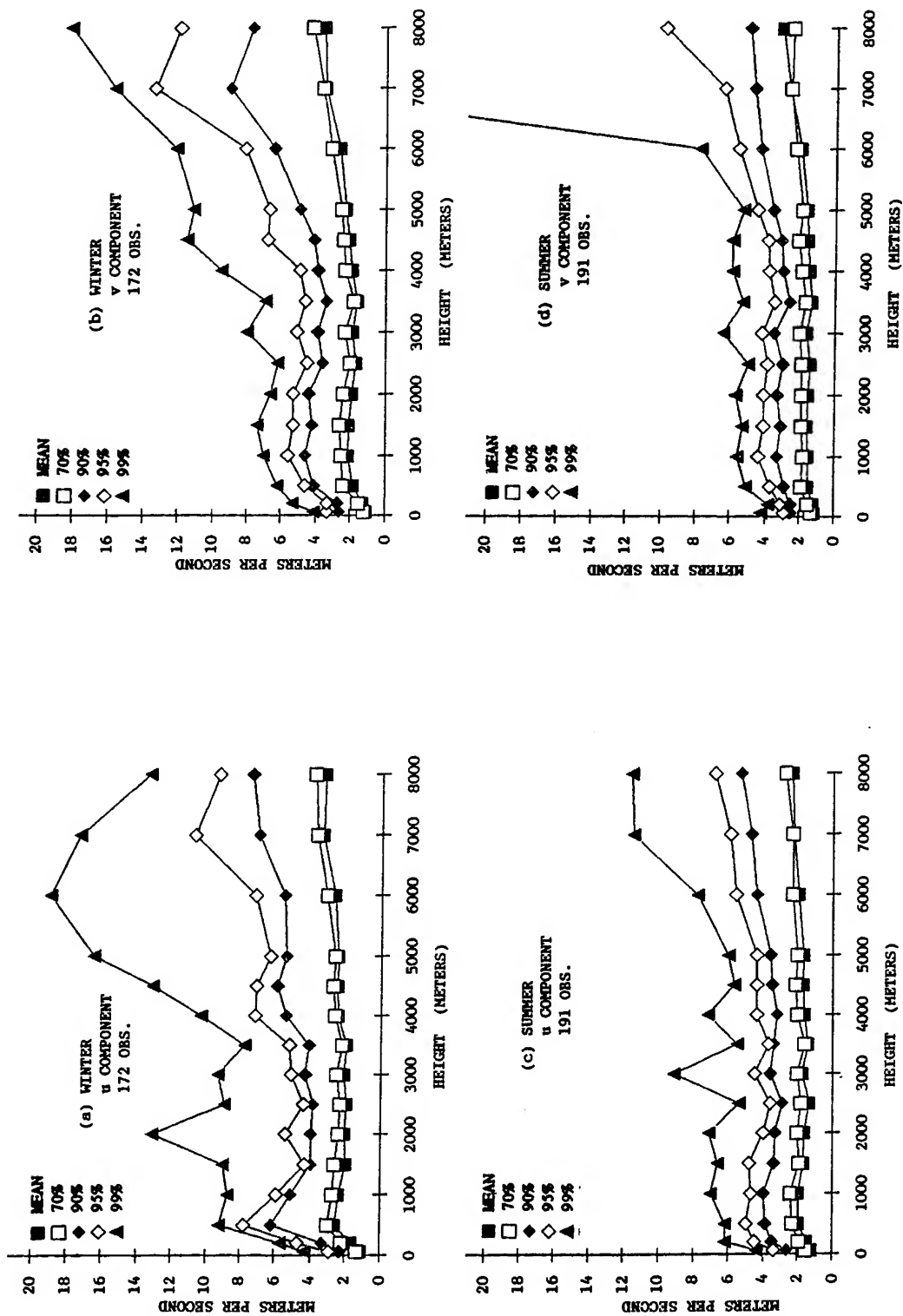


Figure 3. Differences between Bergen and Hannover. Absolute values of differences for u and v components in winter and summer.

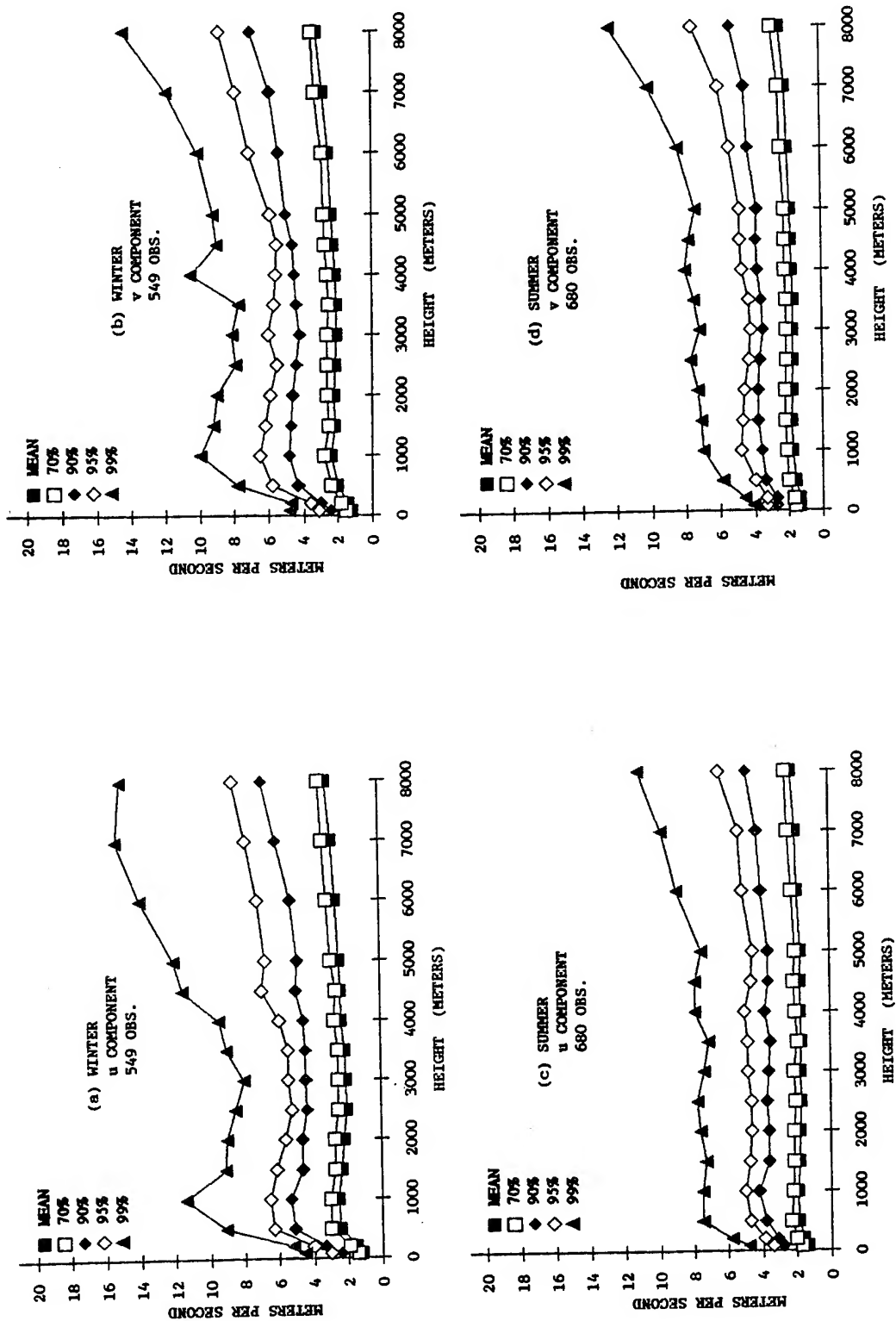


Figure 4. Differences between Berlin and Lindenberg. Absolute values of differences for u and v components in winter and summer.

involved in formulating mathematical models to predict spatial and temporal wind variability for various Army applications may benefit.

6. REFERENCES

- Brown, P. S., and G. D. Robinson, 1979: The Variance Spectrum of Tropospheric Winds Over Eastern Europe. J. Atmos. Sci., 36:270-286.
- Cionco, R. M., 1988: On Simulating Meteorological Fields Over Complex Terrain at Project Wind (Phase I). In Proceedings of the Ninth Annual EOSAEL/TWI Conference, Physical Sciences Laboratory, Las Cruces, NM 88002-5501.
- Danard, M. B., 1965: On the Dependence of Wind Variability on Surface Wind Speed, Richardson Number, and Height Above Terrain. J. Appl. Meteor., 4:394-399.
- Defant, F., 1951: Local Winds. In Compendium of Meteorology, T. F. Malone (Editor), American Meteorological Society, Boston, MA 02108.
- Jasperson, W. H., 1982: Mesoscale Time and Space Wind Variability. J. Appl. Meteor., 21:831-839.
- Kitchen, M., 1989: Representativeness Errors for Radiosonde Observations. Quart. J. Roy. Meteor. Soc., 115:673-700.
- Lenhard, R. W., 1973: Variability of Wind Over 16.25 km. J. Appl. Meteor., 12:1075-1078.
- Leopold, S. A., and R. M. Cionco, 1988: Analysis of Horizontal Meteorological Fields Over the Complex Terrain of Project Wind (Phase I). In Proceedings of the Ninth Annual EOSAEL/TWI Conference, Physical Sciences Laboratory, Las Cruces, NM 88002-5501.
- Levitt, L. J., and O. M. Essenwanger, 1987: Mesoscale Wind Variability in the Vicinity of Berlin, Germany. U. S. Army Missile Command Technical Report RD-RE-86-7, Redstone Arsenal, AL 35898-5248.
- Nappo, C. J., 1977: Mesoscale Flow Over Complex Terrain During the Eastern Tennessee Trajectory Experiment (ETTEX). J. Appl. Meteor., 16:1186-1196.
- Orndorff, B. L., and R. M. Cionco, 1988: Analysis of Vertical Structure of Meteorological Fields Over Complex Terrain at Project Wind (Phase I). In Proceedings of the Ninth Annual EOSAEL/TWI Conference, Physical Sciences Laboratory, Las Cruces, NM 88002-5501.
- Parlange, M. B., and W. Brutsaert, 1990: Are Radiosonde Time Scales Appropriate to Characterize Boundary Layer Wind Profiles? J. Appl. Meteor., 29:249-255.
- Susko, M., 1987: Analysis of the Bivariate Parameter Wind Differences Between Jimsphere and Windsonde, NASA Technical Memorandum 4014, George C. Marshall Space Flight Center, AL 35812.

THE AIRLAND BATTLEFIELD ENVIRONMENT PROGRAM AT ASL

David Sauter
U.S. Army Atmospheric Sciences Laboratory
White Sands Missile Range, New Mexico 88002-5501, USA

ABSTRACT

The Airland Battlefield Environment (ALBE) program is an advanced technology demonstration program initiated by the U.S. Army Corps of Engineers to provide the Army with the capability to assess and exploit battlefield environmental effects for tactical advantage. Some of the key characteristics of the program are the following:

- the integration of terrain and weather in the prediction of battlefield environmental effects,
- the acquisition and integration of near real-time environmental data,
- the planned distribution of the ALBE software to over 400 Military Intelligence Echelons for user feedback and incorporation of this feedback in subsequent ALBE software releases, and after releases,
- the transfer of software to and enhancement of targeted, soon to be fielded, Army systems.

As a participating laboratory, the U.S. Army Atmospheric Sciences Laboratory (ASL) is primarily responsible for the weather related effects on systems and operations. This includes tactical decision aid categories of weapon system performance; nuclear, biological, and chemical; and army aviation. In addition, ASL is involved in weather data collection and dissemination and processing of these data into atmospheric utilities. This paper discusses in some detail the topics mentioned above as well as the current hardware configuration and programming efforts in the Ada language.

1. INTRODUCTION

The Airland Battlefield Environment (ALBE) program includes participation by several Corps of Engineer Laboratories, one Army Materiel Command Laboratory, and associated contractors. Each of these entities is focusing primarily on software that will provide the Army with the capability to assess and exploit battlefield environmental effects for tactical advantage. For example, the Corps of Engineer laboratory Waterways Experiment Station (WES) in Vicksburg, Mississippi, has a terrain mobility program to predict the mobility of various military vehicles over various types of terrain. Cooperation and exchange of

data are required between the laboratories. As an example, WES will obtain the necessary precipitation estimate inputs for their mobility model from ASL. For the most part, however, this paper will concentrate on ASL's efforts associated with ALBE.

2. ALBE KEY CHARACTERISTICS

2.1 INTEGRATION OF WEATHER AND TERRAIN

One of the primary goals of ALBE is to insure that both weather and terrain effects on military systems and applications are considered. ASL is primarily responsible for the weather related effects (discussed in more detail in section 3), while the Corps of Engineer laboratories for the most part address terrain related products. Also of importance is the cooperation of the laboratories in producing integrated weather and terrain software products. These products represent the combined effects of weather and terrain on systems and operations. ASL's weapon system performance tactical decision aid (TDA) is a prime example of this integrated product. Weather can degrade the performance of target acquisition devices, which is predicted by the TDA. However, unless the line of sight to the target is unobstructed, the weather effects do not matter. As a result, this TDA also determines whether or not there are any intervening terrain features between the sensor and target. Thus it is a totally integrated (with respect to weather and terrain) package.

A planned weather-terrain integrated package for FY92 will involve an ASL-WES joint effort. A foot soldier mobility TDA from WES will use any nuclear, biological, and chemical (NBC) hazard zones (which are determined as a function of several weather variables) along the planned route in determining the degraded mobility. The degraded mobility will be the result of soldiers being in mission oriented protective posture (MOPP). Other integrated TDAs also exist or will exist in future ALBE releases.

2.2 NEAR REAL-TIME ENVIRONMENTAL DATA

As a technology demonstration program there will be no fielding of ALBE hardware; however, meteorological sensors will be utilized as part of a near real-time environmental data ingest capability. These sensors will be a part of any ALBE field demonstration and will collect weather data such as wind velocity, temperature, and atmospheric pressure. In addition, ASL is developing the capability of using the Air Force's Automated Weather Distribution System (AWDS) weather products received over a link with Air Force Global Weather Central. These weather products will then be distributed to ALBE participating laboratories and demonstration sites over a military network in an automated manner to drive the ALBE TDAs requiring near real-time weather at the remote locations.

2.3 DISTRIBUTION OF ALBE SOFTWARE TO USERS FOR CRITIQUE

The latest release of ALBE software will be capable of running on a 386 or 486 personal computer (see section 3), which will make the products accessible to many more organizations than with prior releases of the software running on a micro-VAX. Along with field demonstrations of ALBE this will allow for the

collection of data to facilitate the transition of ALBE software to targeted field systems.

2.4 TRANSFER OF ALBE SOFTWARE TO TARGETED ARMY SYSTEMS

Current ALBE software is being developed on a 486 personal computer under the Unix operating system. Graphical displays are being handled via XWindows calls. A significant portion of our software is being rewritten from the Pascal programming language to Ada. All of this is being done to make the ALBE software portable to a number of planned fielded systems such as the Maneuver Control System (MCS), the Integrated Meteorological System (IMETS), and the Digital Topographic Support System (DTSS). The current ALBE development effort under Unix/XWindows will allow for an easier and smoother transition of code to the fielded system. Due to the critique of ALBE software as described in section 2.3 above, this should also result in a more mature version of code for the initial releases of software on the fielded systems.

3. ALBE HARDWARE/SOFTWARE

In 1990 the ALBE community decided to switch from the VMS operating system on a micro-VAX to Unix on a 486 personal computer. The rationale behind this decision was discussed in sections 2.3 and 2.4. Specifically, the ALBE hardware and software that are common among the ALBE laboratories include:

- AST 486 personal computer with super VGA and 32 MB RAM
- SCSI 1.3 GB DAT backup
- Sony CD-ROM (used for Defense Mapping Agency data ingest)
- SCO Unix operating system
- WES geographic information system (GIS)
- FORTRAN and C compilers

In addition to the above, ASL has been using Ada in the rewrite of some of its TDA software. The vast majority of ASL's software has been rewritten to run under SCO Unix from VMS during 1991. It is now being integrated into WES's GIS and should be completed by the end of December 1991.

As was previously mentioned, ASL is primarily responsible for weather related effects on systems and operations as well as weather data collection and processing. These specific products will now be discussed in greater detail.

3.1 TACTICAL DECISION AIDS

Terrain and weather affect combat more significantly than do any other physical factors. With this in mind, ASL has incorporated into ALBE a number of TDAs to assist the commander in the field with the capability to assess and exploit battlefield environmental effects for tactical advantage. As stated in the ALBE Demonstration and Evaluation Program Draft of 1987, ALBE TDAs "enable the commander to evaluate weapon system effectiveness, determine the advantages of

one system over another, and anticipate how operations will be degraded or improved during engagements. TDAs are not intended to make decisions by themselves, but rather to supplement the tactician's knowledge base and help guide him during the decision-making process by providing information useful in the formulation and execution of operations. The TDAs are based on a priori digital terrain data, both feature and elevation data; historical climatological data; and near real-time environmental sensor data. The TDAs enhance the ability to plan operations in a dynamic tactical situation, and let commanders use weather and terrain as force multipliers." (U.S. Army Engineer Topographic Laboratory, 1987)

ASL has three TDA categories: Weapon system performance, NBC, and Army aviation. Each of these three will be addressed in further detail at this point.

3.1.1 Weapon System Performance

This TDA provides information on the effectiveness of electro-optical and seismic/acoustic sensors and systems, as well as top attack and other advanced munitions. Environmental effects considered are terrain, weather, and battlefield-induced conditions such as smoke and fire products. Weapon systems effective ranges and windows of opportunity (temporal and spatial) and threat vehicle locations will be provided in tables and in graphical displays such as video map overlays. The information is based on environmental data obtained from in situ measurements, forecasts, and terrain data bases. These capabilities will enable the battlefield commander to plan more effective tactical operations and to more effectively utilize his resources.

3.1.2 Nuclear, Biological, and Chemical

These TDAs provide information on the location, extent, and persistence of NBC hazards and smoke and the side effects of chemical protective clothing. The ability to overlay nuclear fallout plots and chemical hazard areas on digital terrain map backgrounds is also provided. Software to design and analyze smoke screens generated by smoke munitions or mechanical generators is provided.

3.1.3 Army Aviation

These products provide information on and analyze conditions that affect aircraft performance, routes, and altitudes. The aircraft icing TDA estimates the severity of icing for either rotary-wing or fixed-wing aircraft. The user can specify whether to input cloud data manually or to use RTNEPH data (automated cloud analysis product). The user can then specify a flight path of up to five different locations, with icing conditions displayed graphically.

The night vision goggles (NVG) TDA provides the capability for determining the effects of the environment on the performance of the NVGs. This product assists the aviator and interested staff officers in determining optimal times for NVG use. Nocturnal illumination levels are predicted as a function of lunar position and phase as well as cloud type and amount.

3.2 WEATHER DATA COLLECTION AND PROCESSING

As previously discussed in section 2.2, weather data will be ingested from AWDS and local meteorological sensors to drive the ALBE TDAs requiring this information. In addition to the weather data collection, ASL has a number of utilities and products (weather decision aids) to process this information. These aids are discussed below.

a. The weather effects matrix aid is a briefing tool that graphically depicts how present and forecast weather conditions will affect 13 types of battlefield military operations. The matrix is a table of colored blocks representing unfavorable (red), marginal (yellow), favorable (green), or unknown (black) conditions for the various operations.

b. The tactical weather effects messages (TWEM) aid is a tool for assessing environmental effects on combat resources. TWEM selects and displays messages that are dependent on critical values of weather parameters and/or current available weather data. At present there are four data bases: Blue Division/Brigade, Blue Artillery, Blue Armored Cavalry Regiment, and Red Forces. An example of a message would be a warning for Blue Artillery that if winds are greater than 16.0 kn then smoke operations will not be effective.

c. The consolidated weather effects decision aid is a product designed to estimate overall weapon system performance for a given environment, operation, and threat. These weapon systems are considered as a collection of subsystems that may be sensitive to the weather, terrain, and battlefield environment. A series of rules is used to determine favorable, marginal, and unfavorable subsystem status. The subsystem performance measures are then combined into an overall weapon system performance measure. Five weapon systems are currently available:

- AH-1F Cobra helicopter
- AH-64 Apache helicopter
- M1 Abrams Main Battle Tank
- M60A3 Main Battle Tank
- M2 and M3 Bradley Fighting Vehicle

d. The contouring aid allows for the contouring of various weather parameters (for example, air temperature) at user-specified intervals. The results are displayed over the digital map background.

e. The streamline analysis aid is an automated graphical analysis of wind vectors over an area of interest. The results are displayed over the digital map background.

f. The upper air analysis aid allows for easily visualized state of the atmosphere in the vertical (temperature, dew points, and wind vectors).

g. The historical climatology aid displays a number of climatological variables for a number of worldwide locations. The display can be either alphanumeric or graphical.

h. The target area weather aid visually depicts the weather over a user-designated target area.

4. SUMMARY

In summary, ALBE

- is an advanced technology demonstration program,
- will demonstrate the integration of weather and terrain, and
- will provide for a smoother transition of software to fielded systems in the future.

REFERENCE

U.S. Army Engineer Topographic Laboratory, 1987: AirLand Battlefield Environment Demonstration and Evaluation Program Master Plan FY 1987-1991, U.S. Army Engineer Topographic Laboratory, Fort Belvoir, VA 22060-5546.

Session III

BATTLE SCALE WEATHER

**Wednesday
4 December 1991**

**Chairperson
Col. Grant Aufderhaar**

RESEARCH AT THE U.S. ARMY CENTER FOR GEOSCIENCES

RELATED TO TACTICAL WEATHER INTELLIGENCE

T. H. Vonder Haar and J. L. Behunek
Colorado State University
Fort Collins, CO 80523 USA

ABSTRACT

The U.S. Army Center for Geosciences at Colorado State University conducts basic research as a Center of Excellence funded under the University Research Initiative. Results from several of the research projects funded under this Center are related to the Army's need for Tactical Weather Intelligence. Summaries of the Atmospheric Modeling, Hydrologic Modeling, Information Extraction and Visualization, High Spectral Resolution Lidar, and Satellite Remote Sensing projects are presented.

1. INTRODUCTION

The U.S. Army Center for Geosciences was established at Colorado State University in 1986 under the congressionally mandated University Research Initiative. The Center performs interdisciplinary basic research on a number of topics in the geosciences. These topics include atmospheric and hydrologic modeling, satellite, radar and lidar remote sensing, boundary layer studies, climatic geomorphology, and information extraction and visualization. The results of several of these projects may have an impact on the analysis and prediction of the effects of weather on battlefield operations. We will summarize the results of five of the projects. The projects to be summarized are Atmospheric Modeling, Hydrologic Modeling, Information Extraction and Visualization, High Spectral Resolution Lidar (HSRL) Measurements, and Satellite Remote Sensing.

2. ATMOSPHERIC MODELING

The atmospheric modeling effort under the Center for Geosciences has concentrated on the simulation of atmospheric conditions at the mesoscale (horizontal scales near 300 km) and at convective storm scales (of order 10 km). The primary tool of this investigation is the Regional Atmospheric Modeling System (RAMS), which was developed at CSU by the merger and integration of a mesoscale and a cloud scale model. RAMS employs a telescoping, two-way nested grid, and it typically is used to generate 2-dimensional and 3-dimensional simulations. The primary foci of RAMS research under the Center for Geosciences have been on Quantitative

Precipitation Forecasting (QPF), and Large Eddy Simulation (LES). In addition, we have a joint 4-Dimensional Data Assimilation (4DDA) project in cooperation with our Information Extraction and Visualization research.

2.1 QUANTITATIVE PRECIPITATION FORECASTING

Quantitative precipitation forecasting research has been accomplished primarily for wintertime cases with snowfall. Simulations have been created for cases occurring over the High Plains and Front Range of Colorado and for the Sierra Nevada of California. Both sets of studies made extensive use of observations for initialization and verification of model results. Investigations of the 9-10 February and 30-31 March 1988 Colorado storms indicated the importance of cold air mass interactions with topography to produce convergence zones by blocking. The strength and location of those zones explained much of the mesoscale snowfall variability. An example is displayed in Figure 1. 2-D and 3-D simulations for California orographic storms demonstrated the profound influence of the rawinsonde profile used for initialization on the resulting simulated snowfall distribution. Variations in the simulation of cloud microphysical processes also were found to influence the precipitation distribution. Efforts are being made to improve the microphysical simulation of primary ice nucleation by RAMS.

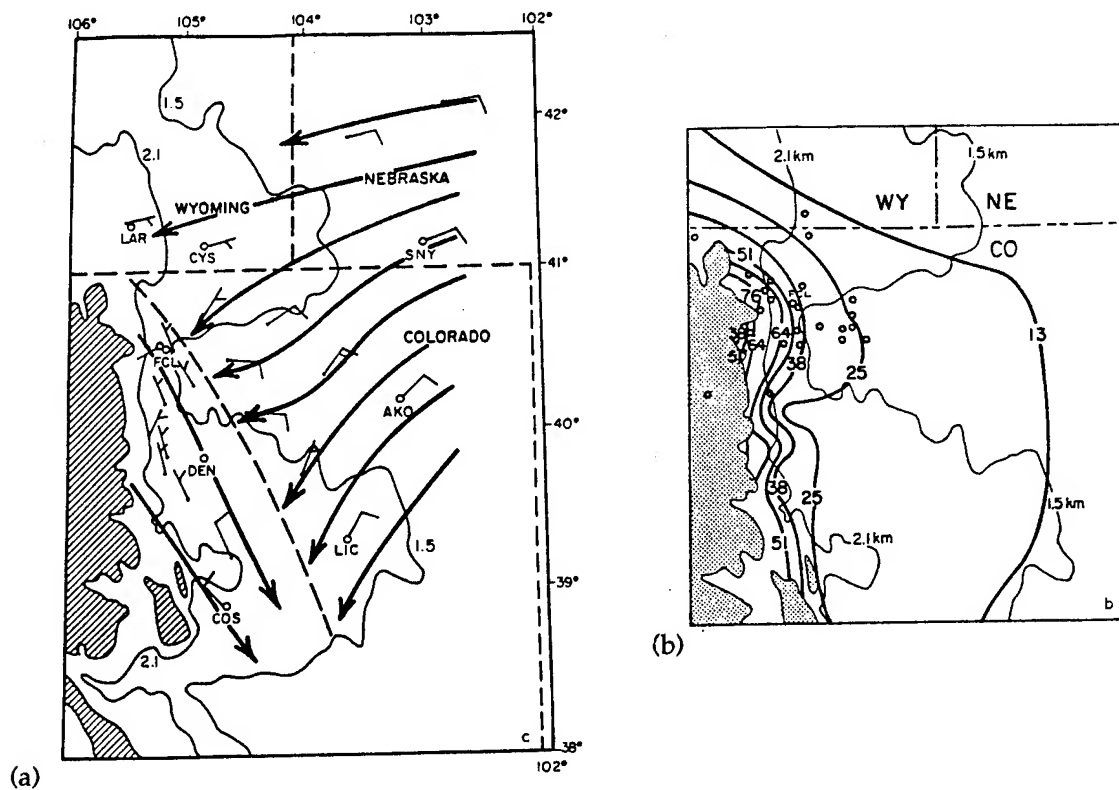


Figure 1. (a) Surface streamline analysis over northeastern Colorado for 0100 UTC on 31 March 1988; (b) Thick lines are snowfall contours (cm) for the 30-31 March 1988 storm, thin lines and shading show topography.

2.2 LARGE EDDY SIMULATION

The Large Eddy Simulation studies utilized RAMS to investigate the evolution of the atmospheric boundary layer under the influence of surface forcing. Grid resolutions for these studies were quite fine, ranging down to 125 meters. Passive tracers were dispersed by a Lagrangian particle model to study boundary layer transport, and a sub-grid scale turbulence scheme was used to parameterize diffusion. Snapshots of the boundary layer circulation were used to show the influence of terrain features on its evolution. Ensemble statistics were calculated to show the regional effect of small scale terrain on boundary layer processes. It was found that the horizontal dimensions of the eddies tend to be the same as those of the terrain. Horizontal averages showed that variations in terrain have little or no effect on the net fluxes, however. 2-D simulations have been run for comparison with field observations from the Phoenix II experiment in eastern Colorado. These runs were successful in simulating boundary layer circulation and thermal features, and they revealed the development of separate plains and mountain boundary layers. The mountain boundary layer was found to advect eastward over the plains boundary layer.

2.3 4-DIMENSIONAL DATA ASSIMILATION

The 4-Dimensional Data Assimilation effort is an ongoing investigation of new methods for assimilating a variety of different data types into mesoscale models. These same methods often also serve as the basis for 4-D data set preparation for visualization algorithms. The requirements for these 4DDA methods can differ significantly from the requirements of larger scale or hydrostatic models. Likewise, mesoscale models rely more heavily on remotely sensed and other unconventional data because of the lack of conventional mesoscale atmospheric observations. We have investigated assimilation methods known as nudging (Stauffer and Seaman, 1989) and the variational adjoint method (Talagrand and Courtier, 1987). We have chosen to concentrate on the adjoint method because of its greater ability to assimilate data in a way that is compatible with the dynamics of the model. The process of deriving the adjoint equations for the RAMS model is by no means trivial, and is still in progress. The adjoint technique also is well-suited to sensitivity studies, which reveal the impact of model initialization parameters on intermediate or final solutions. These studies also are underway.

3. HYDROLOGIC MODELING

Hydrologic modeling at the Center for Geosciences has focused on 1-D and 2-D simulation of surface runoff in small watersheds. Experiments have been performed using both finite element and finite difference models. Finite element modeling began with a simple 1-D model of runoff on a plane of constant width, slope, and roughness and a constant, uniform rain rate. The ability to model runoff from spatially and temporally varying rainfall on a plane of variable width, slope, and roughness then was added. This version of the model was used to study the effect

of moving rainstorms on runoff. We found that the requirements for dynamical formulation of the model are different for storms moving up a watershed versus those moving down the watershed. Storms moving up the terrain can be simulated using the kinematic wave approximation and a simplified form of the momentum equation. Storms moving down terrain at dimensionless velocities between 0 and 2 require that the local and convective acceleration and pressure gradient terms be retained in the momentum equation. The 1-D model also was used to determine the minimum grid resolution needed to accurately predict runoff under conditions of spatially and temporally varied precipitation.

A 2-D finite element model composed of converging planes was created. The runoff hydrographs generated by this model were significantly different from those of the 1-D model, especially in terms of longer time to equilibrium because of runoff convergence. The 2-D finite difference model also was completed and put into use. Much of the testing of these models was accomplished with a watershed at Mack's Creek, Idaho, which was equipped for ground truth verification studies. We were able to achieve close agreement between modeled and observed runoffs in Mack's Creek. The 2-D models also were applied to the study of temporal and spatial rainfall sampling variations on the accuracy of the resulting simulation. Finally, the study of moving rainstorms effects performed previously was done again in two dimensions.

Several supporting studies were accomplished in addition to purely modeling-oriented work, including:

- an investigation of radar rainfall estimates as input to the models and the effects of radar spatial resolution,
- radar - raingage intercomparisons,
- investigation of automated hydrologic data acquisition systems and Watershed Information Systems for model data input,
- an ongoing study of Army training maneuver impacts on the environment and on trafficability using hydrologic models.

4. INFORMATION EXTRACTION AND VISUALIZATION

The Information Extraction and Visualization project has examined various visualization techniques and has studied the influence of human factors on the ability to gain access to and interpret the information displayed using those techniques. The investigation of visualization methods began five years ago with 3-D polygon approximation techniques, which are now widely used within the computer graphics and other scientific communities. One of our visualization requirements was for fused depictions of data products from multiple sensor types. For example, we wished to display a radar precipitation echo along with a satellite-derived represen-

tation of the cloud generating that precipitation. We discovered that theoretical difficulties exist with the algorithms utilized for polygonal representations when the data fusion issue is considered. We abandoned research on the polygon visualization method for this reason.

Another information extraction and visualization technique that was investigated is called octree encoding. We concentrated on this method after concluding that the polygon technique did not meet our needs. Octree encoding involves subdividing a Cartesian representation of a 3-dimensional data field until each cube within this volumetric depiction represents a uniform characteristic or data value. An example is shown in Figure 2, in which a cubic data volume is subdivided until each cube is uniform. Octree encoding essentially results in a transformation of the original data field into a (frequently) more compact form. Certain spatial structure relationships within the field also may be more readily observed in the octree encoded version. Thus, octree encoding can aid the process of obtaining information from the data. This technique also allows the data volume to be graphically rendered in 3 dimensions. We have applied octree encoding to the 3-D depiction of cloud boundaries derived from satellite data and to radar observations of precipitation volumes. We also have fused the radar and satellite octrees into a unified depiction of precipitation within the cloud. The data fusion task is much more tractable via the octree method than by polygon techniques. The most significant difficulties that we have encountered with the data fusion task concern the spatial and temporal alignment of the data fields being fused. The octree visualization method has been enhanced by the addition of graphical clipping capabilities in all three of the dimensions displayed, allowing the inside of the data volume to be viewed, and by the creation of a unique rotation algorithm for changing the spatial orientation of the volume.

Human factors effects on information extraction and interpretation were studied with the help of a prototype weather analysis computer workstation developed by NOAA's Forecast Systems Laboratory (formerly PROFS). This study examined the influence of user interface format on the accessibility of the system and the ability to interpret output from the system as a function of the number of output fields displayed and the use of color. The single, full-screen window user interface employed by that system was found to be quite effective for providing access to the system with minimal training. The ability of users to interpret the information displayed as output sometimes was degraded by the sheer volume of information that could be displayed on the workstation terminal. Appropriate use of color tended to mitigate that problem.

The most recent activity of the Information Extraction and Visualization project is the generation of atmospheric simulations using a 2-D version of RAMS. The purpose of these simulations is to create model output fields such as cloud liquid water and vertical motion which can be fused with observational data and visualized using the octree technique.

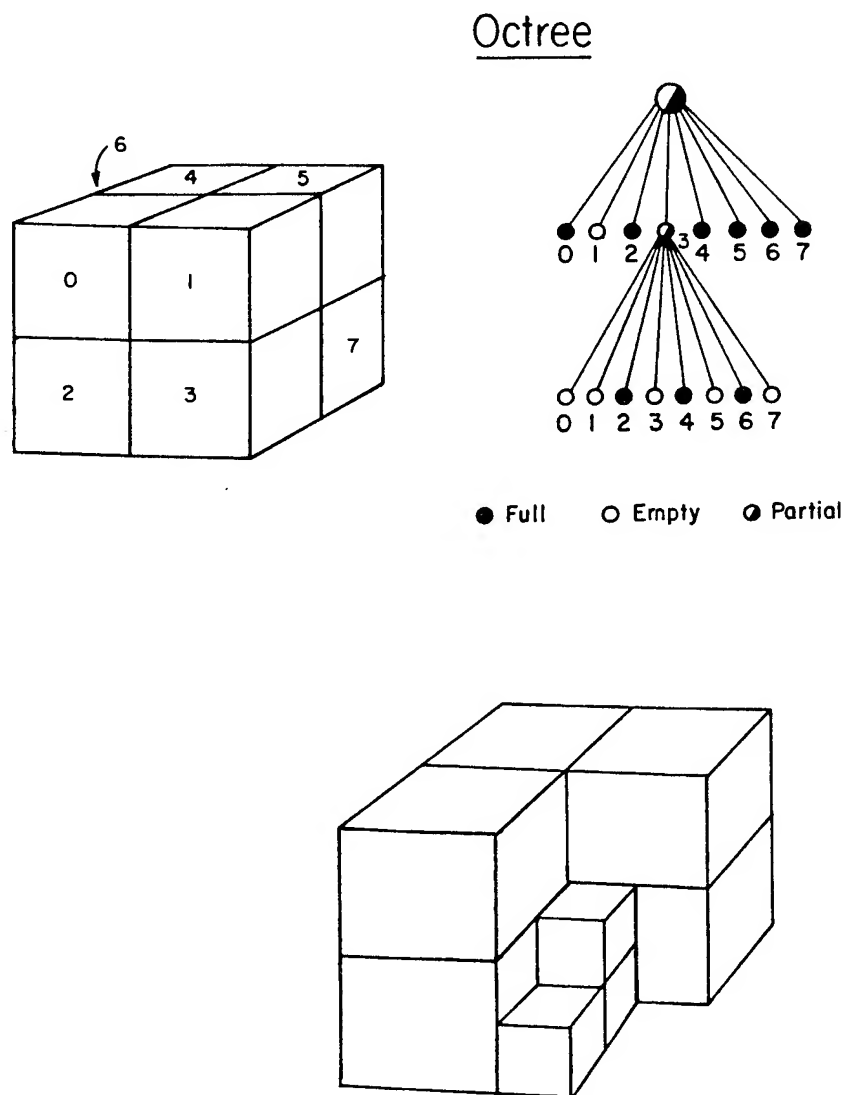


Figure 2. An example of OCTREE encoding. The lower right hand panel shows the full volume of Block 1 removed and three subelements of Block 3.

5. HIGH SPECTRAL RESOLUTION LIDAR

The objective of this project was to develop and test a lidar system for measuring atmospheric backscatter ratio and temperature profiles using a high spectral resolution technique. This technique requires comparison of Rayleigh and Mie scattering calculations for molecular and aerosol scattering, respectively, with measurements of actual scattering of the lidar beam. The returned signal is filtered to eliminate on-resonance interference. Backscatter ratio, r , and atmospheric temperature, T , are determined from

$$r = (N_1/N_2)f_m \quad (1)$$

$$N_2/N_2' = f_m/f_m' \quad (2)$$

$$f_m = R(v,P,T)F(v) dv \quad (3)$$

where N_1/N_2 and N_2/N_2' are the measured ratios of the total scattering signal to the filtered signal and the molecular scattering signal passed through two different filters, respectively. The factors f_m and f_m' are normalized molecular scattering signals after filtration, and $F(v)$ and $F'(v)$ are their measured spectral transmission functions. The function R is the theoretical normalized molecular scattering spectrum, which partly depends on atmospheric temperature.

The hardware which makes up the HSRL includes an argon-ion laser, a tunable pulsed dye laser, a dye amplifier pumped by a doubled Yag laser, barium atomic vapor filters, and a photon counting detection system, which extends the range of the HSRL to approximately 10 km. This system was designed and assembled by scientists at the Center for Geosciences. The system was tested both in the laboratory and the field. Numerous changes and repairs were made to the system during the course of these tests.

Figure 3 shows field test results for aerosol attenuation coefficient and vertical temperature profile. A simultaneous radiosonde temperature profile also is plotted on Figure 3b for comparison. An uncertainty in temperatures estimated by the HSRL of approximately 10°K has been noted and can be seen in Figure 3b. Both laboratory and field tests also have indicated a warm bias of up to 30°K in the HSRL measurements. The search for the cause of this persistent bias has led to the discovery that the lidar system receives light scattered by a rotation Raman process, in addition to Rayleigh and Mie scattering processes. Inclusion of the Raman process in the scattering calculation eliminates the temperature bias.

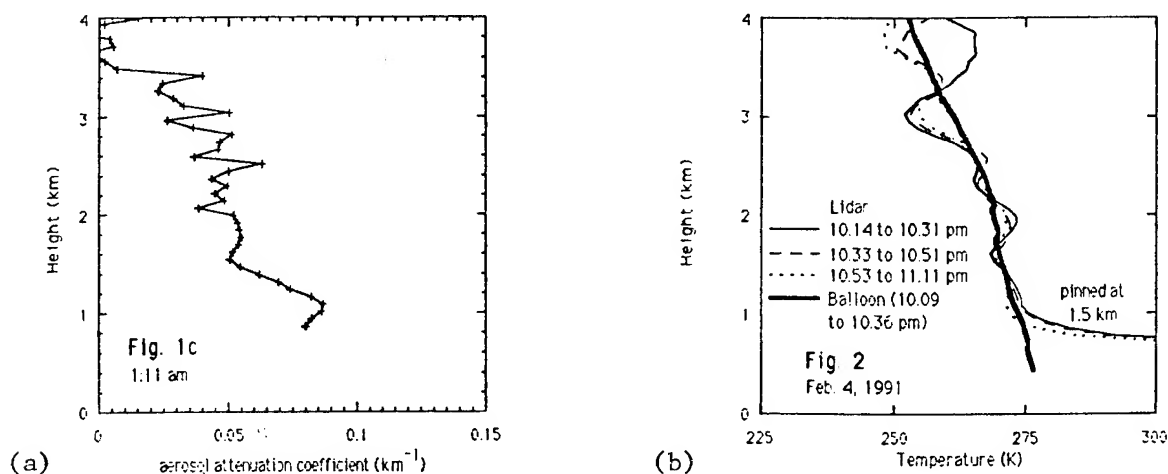


Figure 3. (a) Aerosol extinction coefficient vs. height from the HSRL at 0811 UTC on 15 August 1990; (b) Temperature vs. height from HSRL (thin line) and radiosonde (thick line) taken near 1730 UTC on 4 February 1991.

6. SATELLITE REMOTE SENSING

The Satellite Remote Sensing project investigated a variety of topics. The first study that we will summarize involved the use of satellite observations to diagnose atmospheric and surface conditions, providing input to a 2-D version of the RAMS mesoscale atmospheric model (Lipton and Vonder Haar, 1990a, b). This study utilized a coupled approach to combining satellite-derived estimates of surface temperature and vertical profiles of water vapor with model forecasts of those quantities. These analyses incorporated the spatial and temporal structure of the satellite estimates of those fields while maintaining the gradients of the model-generated fields. We discovered that water vapor gradients were more realistically determined by the coupled analysis method than from either the satellite data or the model analysis alone. The inclusion of surface temperature estimates from satellite data also had a positive impact on model forecasts of the horizontal and vertical wind.

Another study examined the analysis of cloud liquid water and surface wetness from Defense Meteorological Satellite Program (DMSP) Special Sensor Microwave/Imager (SSM/I) 85 GHz data and Geostationary Operational Environmental Satellite (GOES) infrared data (Jones and Vonder Haar, 1990). The 85 GHz SSM/I radiances were influenced by the temperature and wetness of the earth's surface, the integrated liquid water contained in clouds, and the intensity and phase of precipitation within the sensor field-of-view. The surface contribution was estimated using GOES IR measurements of surface temperature and SSM/I data under clear-sky conditions. The surface emittance values obtained in this way were related to surface wetness. Precipitating clouds were eliminated from the analysis through the use of a microwave radiance threshold. The remaining signal was due to emission by cloud liquid water. This method was applied to cloud liquid water analysis for both summer and winter cases. Cloud liquid water uncertainty decreased as the temperature contrast between cloud top and ground increased.

Satellite precipitation estimation was studied via the Area-Time Integral (ATI) technique. The ATI estimates the total precipitation volume over a mesoscale area given measurements which have sensitivity to precipitation, such as those from radar or satellite. ATI is defined as

$$P(x,y,t) = \int_t \int_A F_N R(N) dA dt \quad (4)$$

where F_N is the frequency of occurrence of rain events of rainrate $R(N)$. The precipitating area (A) is defined in a way that is compatible with the type of measurement that is taken. It is delimited by an echo intensity contour when radar data are used, and by a cloud top temperature threshold for satellite data. The ATI precipitation volume estimate increases as the areal coverage above the specified threshold and its duration increase. The satellite cloud top temperature threshold initially was selected to create the closest possible match with the area of precipitation determined from radar data. Further studies revealed a strong relationship between the

coldest IR cloud top temperature of a cloud mass and the temperature threshold required to define the precipitating area. The satellite ATI has been tested using satellite and radar data from the Cooperative Convective Precipitation Experiment, the Convection Initiation and Downburst Experiment, and the Cooperative Huntsville Meteorological Experiment.

Cloud detection and cloud climatology work also was accomplished within the Center for Geosciences. These studies began with a survey and quantitative comparison of automated cloud edge detection methods. Three different edge detection techniques were applied to digital satellite data, and they were verified by a method called Imagery Randomized Block Analysis (IRBA) (Kelly and Vonder Haar, 1989). Edge detection then was applied to the study of climatological convection frequencies and locations. Inferences were drawn from these cloud climatologies to very short range forecasting of convection.

An investigation of fog detection, prediction, and microphysical characterization was begun recently. These studies have been reported in the past at the EOSAEL/TWI Conference (Behunek and Vonder Haar, 1989) and at the current Battlefield Atmospherics Conference (Behunek and Vonder Haar, 1991).

7. CONCLUSION

The ultimate goal of basic research support for the Center for Geosciences is to discover new knowledge that will enhance the ability of the Army to do its job. Some of the research results obtained by the Center have applications that could affect battlefield operations. The development of mesoscale atmospheric modeling QPF and LES capabilities certainly will impact the prediction of battlefield trafficability and target acquisition conditions.

Advances in model data assimilation capabilities will have a less direct effect on the battlefield, but they will provide more realistic simulations. The hydrologic modeling effort at the Center has developed a unique modeling tool that can accurately simulate runoff from small watersheds with relatively modest computing resources. This tool also could affect battlefield trafficability estimates. The ability of the HSRL and satellite remote sensing methods to remotely measure battlefield atmospheric parameters may provide data where no *in situ* measurements are available. The efforts on information extraction and visualization will supply the methods to present information derived from various sources to battlefield commanders in a way that provides a distinct tactical advantage. The investment in research at the Center for Geosciences will have been worthwhile even if these are the only resulting battlefield applications, but there likely will be more.

ACKNOWLEDGEMENTS

This research was supported by the U.S. Army Research Office under Grant DAAL03-86-K-0175. The authors wish to thank Dr. Roger Pielke, Dr. William Cotton, Dr. Pierre Julien, Dr. Thomas Brubaker, Dr. C.-Y. She and the other members of their respective research projects who accomplished the research summarized in this paper. Thanks also go to Ms. Loretta Wilson, who helped prepare the manuscript.

REFERENCES

- Behunek, J.L., and T.H. Vonder Haar, 1989: Nighttime fog detection from satellite data. In Proceedings, Tenth Annual EOSAEL/TWI Conference, Las Cruces, NM, U.S. Army Atmospheric Sciences Lab, White Sands Missile Range.
- Behunek, J.L., and T.H. Vonder Haar, 1991: Fog microphysics from multi-spectral reflectance data. In Proceedings, Battlefield Atmospheric Conference, El Paso, TX, U.S. Army Atmospheric Sciences Lab, White Sands Missile Range.
- Jones, A.S., and T.H. Vonder Haar, 1990: Passive microwave remote sensing of cloud liquid water over land regions. J. Geophys. Res., 95(D10), 16673-16683.
- Kelly, F.P., and T.H. Vonder Haar, 1989: Imagery Randomized Block Analysis (IRBA) applied to the verification of cloud edge detectors. J. Atmos. Oceanic Tech., 6(4), 672-679.
- Lipton, A.E., and T.H. Vonder Haar, 1990a: Mesoscale analysis by numerical modeling coupled with sounding retrieval from satellites. Mon. Wea. Rev., 118(6), 1308-1329.
- Lipton, A.E., and T.H. Vonder Haar, 1990b: Preconvective mesoscale analysis over irregular terrain with a satellite-model coupled system. Mon. Wea. Rev., 118(6), 1330-1358.
- Stauffer, D.R., and N.L. Seaman, 1989: Use of four-dimensional data assimilation in a limited-area mesoscale model. Part I: Experiments with synoptic-scale data. Mon. Wea. Rev., 118, 1250-1277.
- Talagrand, O., and P. Courtier, 1987: Variational assimilation of meteorological observations with the adjoint vorticity equation. Part 1: Theory. Quart. J. Royal Meteor. Soc., 113, 1311-1328.

**DIRECTORY OF ATMOSPHERIC TRANSPORT AND
DIFFUSION MODELS, EQUIPMENT, AND PROJECTS**

by

Colonel Floyd F. Hauth, USAF
Office of the Federal Coordinator for Meteorological
Services and Supporting Research
Rockville, MD 20852

The Office of the Federal Coordinator for Meteorological Services and Supporting Research (OFCM) Working Group for Atmospheric Transport and Diffusion (WG/ATD) developed a directory of models, equipment, and projects for use by Government agencies that have responsibilities related to meteorological support for releases of hazardous substances into the atmosphere. Many individuals or groups are involved in direct or indirect support of the emergency response system to accidental or planned releases of hazardous materials into the atmosphere. The OFCM directory provides a means to cross feed key ATD information among Federal agencies and other interested/involved organizations. It also serves to minimize duplication of model development, focuses Federal efforts toward more effective sharing of resources, and helps to harmonize ATD support where it is possible or appropriate. The paper will be presented by the secretary of the WG/ATD, Colonel Floyd F. Hauth.

(The full text of this paper was unavailable at press time.)

AIR WEATHER SERVICE BATTLEFIELD WEATHER PROGRAMS

J. D. Fink and P.B. Roohr
Headquarters Air Weather Service
Scott Air Force Base, Illinois 62225-5008, USA

ABSTRACT

Headquarters Air Weather Service (HQ AWS) has a number of programs to improve battlefield weather support over the next few years. The upgrades start with the activation of Detachment 4, HQ AWS at Hurlburt Field FL and continue with upgrades to observing, communication, forecasting, and modeling capabilities. Detachment 4, HQ AWS will provide weather organizations with improved applications and standard methods to enhance both fixed-base and tactical weather support. The Tactical Weather Observing Systems Statement of Operational Need (SON) (1990) documents requirements for automated observing systems for atmospheric profiles, tactical ground observations, expendable tactical observations, lightning detection, and manual ceiling and visibility systems. The Tactical Forecast System SON (1990) documents the requirement to integrate communications, analysis, and forecasting capabilities into a modular tactical system. Models will be acquired through an operational weather support technology transition program to exploit laboratory research and development efforts.

1. INTRODUCTION

The original Tactical Concept of Operations Plan (TCOP) for battlefield weather support was approved for implementation on December 6, 1985. It was updated and approved on March 7, 1989 as the AWS Tactical Concept of Operations Plan 1990-2005 (1989). The purpose of the 1989 TCOP was to update the 1985 TCOP and to blend in changes based on the Air Force Mission Area Analysis, Weather 2000 (1984). The tactical concepts were developed using lessons learned, based on the doctrine of the supported unit and requirements of the operational customer. The future of programs to implement these long-range plans fits well with the newly reorganized AWS responsibilities to provide centralized weather support, technical advice and assistance, standardization and interoperability; access quality and technical goodness; and field standard weather systems.

2. DETACHMENT 4, HQ AWS

2.1 One of the newest units dedicated to enhancing battlefield weather support is Detachment 4, HQ Air Weather Service (Det 4, HQ AWS). When fully operational in 1993, Det 4 will be the Air Force focal point for evaluating transition of technology to tactical and base weather station environments. Additionally, it will serve as the primary center for testing and training on tactical weather equipment and communications.

As a training unit, Det 4 will concentrate on tactical readiness with added focus on continually improving and expanding tactical and fixed weather support concepts. The unit will also have a worldwide mobility commitment supporting mobile upper atmospheric observations and Air Force Forces (AFFOR) Headquarters forecast requirements.

2.2 With the restructure of AWS and the introduction of new technology, such as the Automated Weather Distribution System (AWDS) into the base weather station (BWS), there is a need for a centralized facility that will develop, demonstrate, and market new techniques. Additionally, the AWS experience in Operation DESERT STORM reemphasized the positive value of a proven, aggressive tactical readiness program. An effective readiness program is needed to provide unique weather equipment training and to develop tactical forecasting techniques that will be transitioned into operational use.

2.3 Det 4 will provide weather organizations with improved methods for enhancing both tactical and fixed-base weather support. This involves the proper transition of BWS and tactical weather technology to operations as well as the administration, management, and execution of tactical readiness training. Det 4 will establish methods to exploit interoperability of Air Force and Army tactical observing and forecasting systems, as well as Navy capabilities, to maximize wartime weather support quality. Det 4 will develop techniques, methods, and procedures based on existing and new technologies that can be readily incorporated into the standard BWS, tactical forecast unit, and weather units supporting AF and Army combat operations. After validation, Det 4 people will market these techniques and applications to Air Force and Army support agencies for tactical and fixed-base use. The marketing process includes continuous coordination and communication with the Army's Research and Systems Laboratories. An integral part of the Det 4 mission is to maintain the capability to deploy and tactically operate ground communications and meteorological equipment supporting Department of Defense (DOD) contingency operations. Det 4 will also test and evaluate prototype and newly acquired operational systems, forecast models, and observational sensors in realistic tactical and fixed-base settings.

2.4 The requirements for tactical and fixed-base weather support are continuous and wide ranging. Most, if not all, DOD combat weapon systems are highly dependent on accurate and effective weather support for successful execution. Over the past decade, actual combat operations such as URGENT FURY, JUST CAUSE, and DESERT STORM have proven accurate conventional and specialized weather forecasts significantly enhanced the operational success of Air Force tactical and strategic, as well as Army weapon systems. The future outlook is that as new and more technologically complex weapon systems are fielded, their dependence upon highly accurate weather support will significantly increase. As an integral part of AWS, Det 4 must continually train, test, evaluate, and field new and improved capabilities to satisfy future combat force requirements. As the focal point for tactical readiness and technology transition, Det 4 will develop the methods and means to satisfy the requirements to improve fixed weather station operational effectiveness, tactical observing and forecasting capabilities, expanded tactical

equipment operator training, and upper air measurement capabilities.

2.5 Det 4 has numerous mission objectives which will provide training and recommend improvements in the operation of tactical meteorological and communications equipment. They will develop new applications and procedures to forecast weather conditions for tactical operations using newly deployed technology and research. They assist BWSs in creating customer or mission specific applications, rules of thumb, or forecast studies to solve unique support problems. Det 4 will do a number of things to assist AWS in identifying technical shortfalls such as the testing of models, equipment, or applications supporting tactical or fixed base operations. Development of training goals based on field experience and evaluation of tactical and fixed-base training materials will be accomplished. Det 4 will also maintain an immediate mobile capability to provide upper atmosphere (RAWIN) and Tactical Weather Analysis Center (TWAC) weather support. For mobility, Det 4 will integrate RAWIN and TWAC teams into joint/combined field training exercises.

3. TACTICAL WEATHER OBSERVING SYSTEMS

3.1 The Tactical Weather Observing System (TWOS) program is designed to provide the next generation of tactical weather observing equipment starting in 1995. It will enable AWS weather teams (WETMs) to provide the frequency, density, and specification of weather elements required to provide tactical weather support to battlefield commanders and weapon systems past the year 2000. TWOS will provide several sets of simple rugged tactical weather sensor suites that will be modular in design, autonomous, reliable, mobile, and built to maximize survivability. These sensor suites will meet the theater observation requirements required to support the meteorological models and microscale forecast techniques in the Tactical Forecast System (TFS).

3.2 The Tactical Ground Observing System (TGOS) is an automated sensor suite with a modular sensor capability to provide different sensor configurations depending on the needs of the mission being supported. These sensor suites will automatically sense, collect, format, and transmit observations with location information. Observation elements are currently being evaluated and will include an optimized subset of (in prioritized order): cloud coverage and bases; visual transmissivity; infrared transmissivity; surface pressure; surface wind speed and direction; surface temperature; surface dewpoint; precipitation rate and phase; aerosol character and concentration; illumination; soil moisture and temperature; vertical profiles (surface to 5,000 ft) of wind, temperature, pressure, and dewpoint; atmospheric scintillation; cloud type; lightning detection; and inversion height and mixing depth.

3.3 The Mobile Profiler is an automated, transportable system to provide sensing of the upper atmosphere from surface to 30,000 ft. Observed and inferred elements are currently being evaluated and will include a subset of (in prioritized order): cloud bases; vertical profiles of wind speed and direction; temperature; pressure; dew point; icing; turbulence; cloud thickness; aerosol concentration; liquid water content; inversion height;

and mixing depth. This sensor suite will automatically sense, collect, format, and transmit the observation with location information.

3.4 The expendable Tactical Observations (TACOBS) is a low cost, self contained, automated sensor package for manual or air drop emplacement. These expendable sensor packages will automatically sense, collect, format, and transmit the observation with location information. The sensor package is planned to observe surface temperature, dewpoint, pressure, wind speed and direction, cloud bases, soil moisture and temperature.

3.5 The Lightning Detection System is a transportable sensor system that will automatically sense, collect, and transmit observations of lightning location and strength.

3.6 Two manual sensors, such as a hand-held sensing device, that specify visual transmissivity, infrared transmissivity, and height of cloud bases and a man-portable profiler to provide observations of vertical winds from surface to 3,000 ft, are required for use by soldiers in the battlefield and special operations forces.

3.7 The automated sensor suites will have a tactical communications package integrally developed with the suite. Manual sensors will have no embedded communications package. Transmissions from the sensors will be designed so they do not reveal the type of information being transmitted. The tactical communications package will consist of a communications processor to automatically provide secure high speed transmissions to tactical battlefield receivers and a receiver to automatically receive, store, and display theater weather observations received from sensor suites.

4. TACTICAL FORECAST SYSTEM

4.1 The Tactical Forecast System (TFS) program will consist of a range of integrated computer and communications equipment to provide everything from a first in weather support to the long duration tactical weather forecast capability. The primary goal of the TFS is to field computer and communications equipment that is rapidly deployable and field maintainable, providing an automated link to command and control and mission planning systems. Another goal of the TFS is to reduce dependency on Air Force Global Weather Central (AFGWC) by producing a theater size mesoscale forecast at the force level. Complete TFSs will then distribute the forecast to all units in the theater. The TFS will have different configurations to provide tailored weather products at each level. Complete TFS units will be deployed at component command headquarters and strategic command centers. Partial TFS units will be deployed at Wing Operations Centers (WOC) and Airlift Control Elements (ALCEs). Basic TFS elements will be deployed at Forward Operating Bases (FOBs) and with special operations. The TFS will be a convergent outgrowth of the AWDS, Transportable AWDS (TAWDS), its PrePlanned Product Improvement (P3I), DMSP Small Tactical Terminal (STT), and the Army's Integrated Meteorological System (IMETS). These systems will provide for a single Air Force/Army weather forecast system and man-machine

interface. It will enable weather teams to provide timely, critical weather support to tactical forces on the battlefield in much the same manner as support is provided in garrison. The TFS will specifically provide an autonomous, survivable, mobile/tactical forecast capability in theater to receive, ingest, process, and disseminate environmental information to the tactical user.

4.2 Any TFS functional capability will be interoperable with other TFS capabilities to provide a modular building block system. This will provide the flexibility required to adapt the TFS to Complete, Partial, or Basic TFS configurations to support the battlefield user. Complete TFS functional capabilities include communications, data ingestion/fusion and analysis, operator displays/system management, climatology, mesoscale models, applications software, and forecast techniques. These functional capabilities will be linked together and controlled at the TFS workstation. The key capabilities are the receiving and processing of weather information in a tactical environment. The TFS processor will be a standard Air Force (AF) high power computer workstation combined with as many AF standard externals as possible, this will allow for the interchange of components allowing for growth. Communications will be organized to provide a first-in capability that can be built up and connected to standard AF communication systems as they are installed.

4.3 Complete TFS units will be highly automated, tactically deployable systems, that will incorporate all available forecast-relevant weather data; prepare, quality control, and analyze the data; run theater analysis and forecast models which incorporate standard digital terrain; translate models output to customer tailored forecasts, displays, and data sets upon forecaster demand; compact and transmit to AFGWC analyses or syntheses of theater observations from the TWOS, unmanned aerial vehicles (UAVs), profilers, symbiotic sources, etc.; communicate with tactically deployed systems at other TFS nodes, AWDS, IMETS, and C3I systems; and have access to a current climatological data base. The system will have redundant communications capability so during the contingency various types of communications can be used, at various times outages can be expected due to circuit interruptions or damage. The redundant communications include receipt of SATCOM broadcasts originating from AFGWC, data directly from meteorological satellites (METSAT), data from the High Frequency Regional Broadcast (HFRB) system, Tri-Service Tactical Communications (TRI-TAC) compatibility, dial-up telephone modems that are internationally compatible, and FM/UHF Pilot-To Metro (PMSV) radio.

4.4 Partial TFS units will have most of the capability of the Complete TFS primarily without a mesoscale model. It will receive products from Complete TFS nodes; SATCOM broadcasts of data originating from AFGWC; data directly from meteorological satellites; information from the HFRB system; TRI-TAC; dial-up telephone modems that are internationally compatible; have access to combat climatology; possess display and analysis hardware and software; and communicate with intratheater TFS units.

5. BATTLEFIELD WEATHER MODELS PROGRAM

5.1 The Battlefield Weather Models Program is designed for acquisition of software models. Hardware will be acquired via a separate program such as TFS. Planned software includes mesoscale models, Artificial Intelligence/Expert Systems (AI/ES), and Artificial Intelligence/Neural Networks (AI/NN) for the tactical and aerodrome applications.

5.2 The Battlefield Weather Models Program includes analysis, initialization, and forecast models designed to specify and forecast tactical theater-scale (mesoscale) meteorological phenomena. Models will use observations from present and planned sensor systems including the Weather Surveillance Radar 1988-Doppler (WSR-88D or NEXRAD), Mark IV-B Meteorological Data Station, Defense Meteorological Satellite Program (DMSP), the TWOS, and sensor systems being developed and acquired by the Army (principally the Atmospheric Sciences Laboratory (ASL)). Models will also use Uniformed Gridded Data Fields (UGDF) provided by AFGWC. The following are descriptions of four models currently being examined for transition to BWS:

5.2.1 A DOD Regional Battlefield Forecast Model for a theater-scale (mesoscale) battlefield analysis and forecast model to be run as a prototype on an advanced weather workstation. Data sources are planned to include TAWDS (AWDS), Mark IV-B Direct Read-Out Satellite/Small Tactical Terminal, Automated Weather Network/NODS, HFRBs, customer command and control systems, and classified in-theater data. The model is being jointly developed by Naval Research Laboratory (NRL), Army Scientific Laboratory (ASL), and Phillips Laboratory/Geophysics Directorate (PL/GD).

5.2.2 A Single Station Forecast Model, being developed by PL/GD, is a PC-based expert system used to make a short-range site-specific terminal weather forecast using only single station data. Data sources include local observation (asynoptic data), climatological data, and geographical data (including terrain, and surface type).

5.2.3 A Regional Forecast Model, being developed by PL/GD, is a PC-based expert system (using neural networks) used to make a short-range weather forecast from limited input. Data sources include local observations (asynoptic data), climatological data, and geographical data (including terrain, and surface type). The system will allow for graceful degradation as the amount of real-time data is denied.

5.2.4 A Local-area Battlefield Weather Model, being developed by the University of Lowell for PL/GD, is a super-micro computer local area (mesoscale) model which will provide forecast guidance in the 3 to 24 hour time frame. The model output includes pressure, temperature, winds, and moisture that can be extrapolated to mandatory levels. This model can be used to forecast non-convective winds, advection and radiation fog, ceiling/visibility, precipitation, and stratus.

5.2.5 Software models will be modularized so that individual components can be run on micro-, "laptop," or multi-user computers, AWDS and TAWDS

host processors, TFS computers, AFGWC mainframes (if desired), or such other computer systems as may be acquired for use to support distributed processing at tactical/theater forecast centers as recommended by Weather 2000.

6. SUMMARY

Air Weather Service has battlefield weather support programs as one of its top priorities. AWS has organized for the successful implementation of battlefield programs by putting in place the organizational structure, organizing acquisition of observing and forecasting hardware into viable programs, and working with developers of models to support the requirements of battlefield weather.

REFERENCES

- HQ AWS/XT, 1989: Air Weather Service (AWS) Tactical Concept of Operations. HQ AWS, Scott AFB, IL 62225-5008.
- HQ Electronic Systems Division/XR, 1984: WX 2000 Technical Report. HQ ESD/XR, Hanscom AFB, MA 01731-5000.
- HQ USAF/XOW, 1990: USAF 211-89 Statement of Operational Need (SON), Tactical Weather Observing Systems (TWOS). Department of the Air Force, Washington DC 20330-5050.
- HQ USAF/XOW, 1990: USAF 212-89, Statement of Operational Need (SON) Tactical Forecast System (TFS). Department of the Air Force, Washington DC 20330-5050.

SOURCE STRENGTH TERMS FOR WINTER DISPERSION MODELS

A. Hogan and D. Leggett
USA Cold Regions Research and Engineering Laboratory
Hanover, N. H. 03755 U.S.A.

ABSTRACT

It is now frequently necessary to prepare an estimate of atmospheric dispersion of aerosols, vapors, and gases before beginning Engineer operations. Several dispersion models prepared by the DOD/DOE/NOAA community have been examined for application in data-sparse winter settings. The combustion rate terms, or thermodynamic properties of gases, used to estimate the contaminant input to the atmosphere from uncontrolled sources acquire an additional degree of complexity over snow-covered ground. Multiple inversions may limit the applicability of even nearby soundings of atmospheric structure to wind field analysis. We present some analyses of organic vapor permeation in snow cover, coincident with nearby atmospheric structure observations, as a preliminary approach to over-snow dispersion modelling.

1. INTRODUCTION

Atmospheric transport and diffusion models are commonly used to analyze or forecast the potential dispersion of materials made airborne by Army operations and the transport of airborne material released elsewhere to a selected site, or to map the path of airborne material released in the vicinity of the site. There are several models available within DOD/DOE/NOAA and the public domain (Anonymous, 1991) that predict local and long-distance dispersion of gaseous, vapor, and particulate plumes. These models vary considerably with respect to the local, mesoscale, and synoptic-scale meteorological data required as inputs, the method of internal computation of the properties of the aero-dispersed material, and the computing capacity required to provide concentration vs time and space outputs.

Additional degrees of complication are added when winter Engineer operations are considered. These include sparse meteorological data in pioneering locales, the frequent necessity to provide dispersion analysis on a smaller scale than the limited fine mesh (LFM) model used in NWS meteorological analysis, and the prolonged stagnation that may occur over snow-covered terrain. This paper combines experimental results of measurement of organic vapor permeation through snow with nearby measurements of atmospheric structure as a preliminary step toward defining some winter atmospheric dispersion problems.

2. WINTER TEMPERATURE STRUCTURE IN COMPLEX TERRAIN

The diminution in mean mixing depth during the winter season, relative to the summer season, is well established (Slade, 1968) and is considered in all dispersion models. Several models, includ-

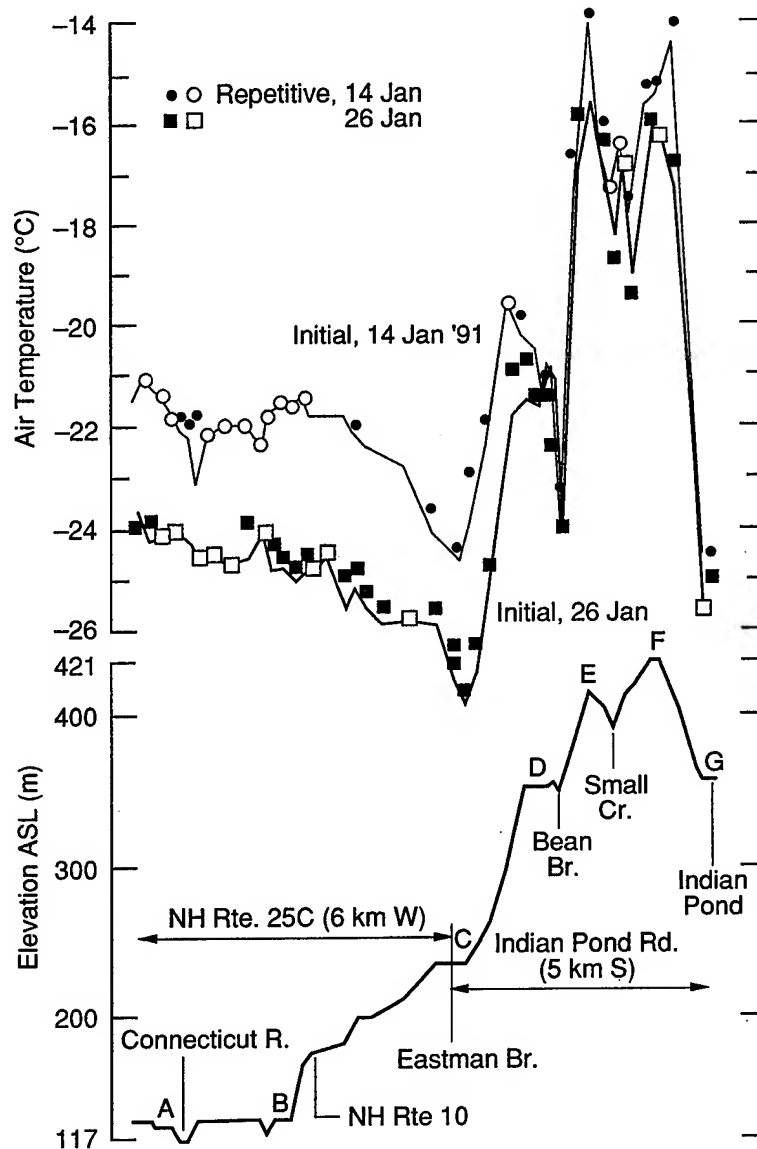


Figure 1. Horizontal cross section of early morning surface air temperatures in a snow-covered valley.

ing AFTOX (Kunkel, 1988), consider in the model calculations the influence of snow on the ground on atmospheric stability and the influence of subfreezing temperature on the vapor pressure of the material to be dispersed. The vertical structure of temperature used as input is usually derived from nearby NWS or other soundings or, at major installations, from dedicated meteorological towers. Snow-covered, hilly terrain is often overlain by multiple inversions that may persist for 12 or more hours and that do not appear in the nearest radiosonde temperature report. A cross-section analysis of early winter morning temperature structure is given in fig. 1, from Hogan and Ferrick (1991), to illustrate this.

Figure 1 shows horizontal cross sections of near-surface air temperature measured about 1.2 m above the mean snow surface along an approximately east-west transect of the Connecticut River valley on two winter days. Temperatures measured during the period 0630–0700 LCL on each

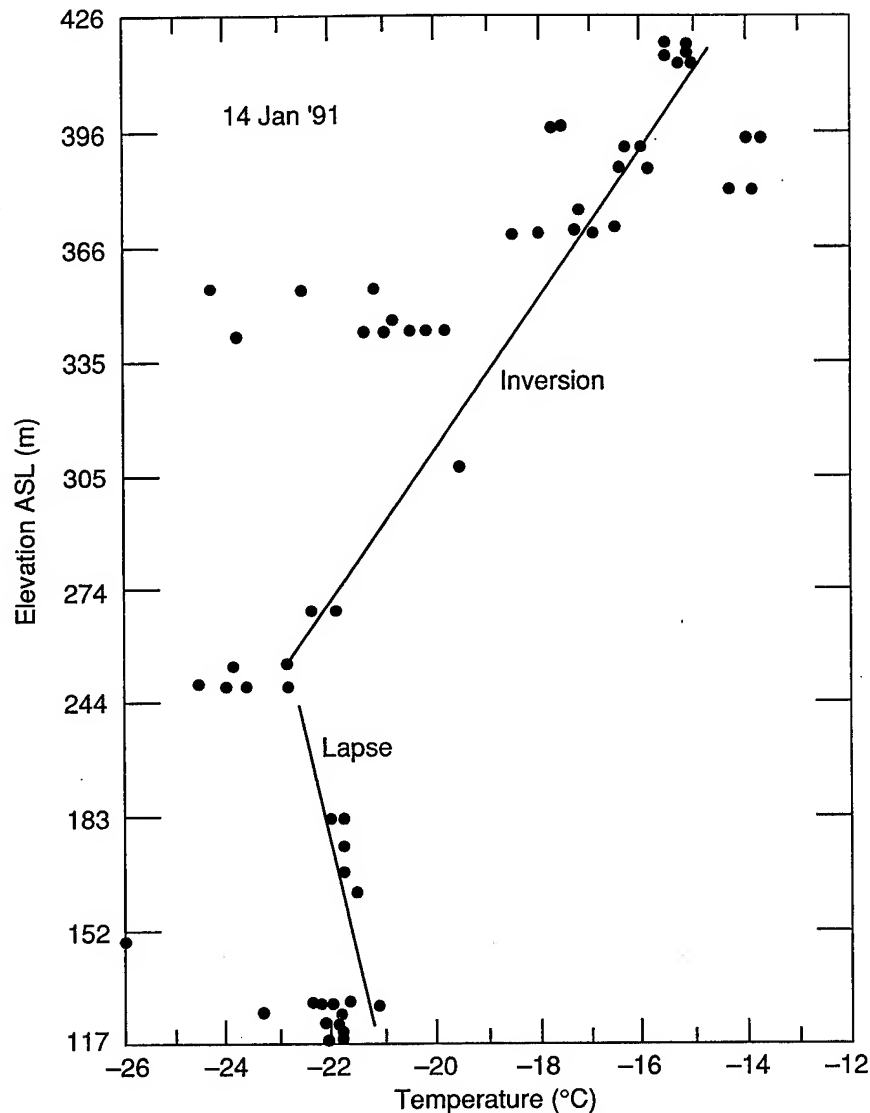


Figure 2. A vertical temperature profile synthesized from the data of Figure 1. Note that the air in the inner basin is neutrally stable, although capped by a strong inversion in the outer basin.

day are connected by the plotted lines; temperatures measured at the same points during the period 0700–0730 are overlain on the line with open symbols if within $\pm 0.1^\circ\text{C}$ of the original measurement. Temperatures that deviate by more than $\pm 0.1^\circ\text{C}$ are indicated by solid symbols. The temperatures are plotted above an elevation cross section of the transect route.

These two cross sections were obtained during periods of warm advection. Southwesterly winds were observed at the highest elevations, corresponding to the warmest air temperatures measured on both days. Although the magnitudes of the plotted values differ, the characteristic shape of the temperature cross section is quite similar on both days. The data of 14 Jan 1991 is replotted as a vertical air temperature sounding in fig. 2. Comparing fig. 1 with fig. 2 facilitates identification of terrain-induced temperature variations and their relation to local inversions. The minimum air

temperature along this transect is generally observed on the small flat at C, although other small flats and basins may be within a degree of that temperature. The warmest air, on days with warm advection, is found at the maximum elevations and on southwest-facing slopes just below the apex of each ridge. A line is plotted on fig. 2 connecting the maximum temperature measured along the flat at C with the maximum temperature measured at the ridge crests E and F; a second line connects C with the maximum temperature observed on the lower river plane along AB. The slope of the line above C is an inversion of $40^{\circ}\text{C}/\text{km}$; the slope of the line below C approximates an adiabatic lapse of $-10^{\circ}\text{C}/\text{km}$. The surface air temperatures along the slope BC lay near the adiabat; those along the slopes CD, DE, and FG lay near the inversion. Several points along the lower river plain AB, the small flats C and D, the lake basin G, and in the small creek valley between E and F lay to the left (cold side) of the plotted lines.

This interpretation of the elevation cross section in fig. 1 is offered: there is an inversion at about 230 m that isolates the lower river basin from the warm advection that is occurring above, and this warm advection is strongly influencing the apex of the ridges and the southwesterly slopes and less strongly influencing slopes of other aspect. There are additional strong inversions isolating the surfaces above small flats, stream basins, and the lower river plain.

The presence of an inversion between the river level and the apex of the adjacent ridges would certainly be forecast by conventional analysis. It would be extremely difficult to predict the level of the major inversion, the presence of the neutral layer beneath it, and the vigorous but sporadic exchange occurring above. An organic material of some vapor pressure $P(T)$ released along the river plain would be confined to a layer about 100 m thick, even though the nearest soundings might show vigorous exchange and surface warming.

However, a relatively dense array of surface temperature measurements, as used to provide the data input for figs. 1 and 2, might provide sufficient input for successful application of a winter dispersion model on small space and time scales.

The snow surface and the thin layer of air immediately adjacent to it have the minimum temperatures observed in these conditions. This cold surface may present an additional complicating factor that influences the rate of release of organic vapor. Preliminary experiments have been conducted to investigate permeation of organic vapor in snow.

3. PERMEATION OF ORGANIC VAPOR THROUGH SNOW

Preliminary experiments indicate that organic compounds, such as the ordnance components DNT, TNT, and RDX, will permeate porous materials if driven by a temperature gradient or other outside energy source. A field experiment was conducted at a point about 300 m from C in fig. 1 to estimate the permeation rate of these materials in snow.

The experiment site was prepared before winter, and thermistors were placed to measure ground temperature about 3 cm below the sod/air interface. A stake array was laid out to facilitate emplacement and later recovery of the organic vapor sources. The sources were prepared by placing a few grains of DNT, TNT, and RDX in glass petri dishes and offsetting the petri lids with small wires to allow vapor to escape. Thermistor beads were attached to the top and bottom surfaces of two petris. The sources were emplaced on 2 Jan 1991, on 1–2 cm of snow cover. Several minor

snowfalls occurred during the next few days, covering the petris but not obscuring their presence. A thermistor was inserted at the sod/snow interface 1 m from the petri array as a significant snowfall began on 9 Jan 1991, and the experiment was begun. A second fall began at 1745, 10 Jan, which produced 30 cm of snow depth by 0800, 11 Jan. This snow cover was rained upon on 16 Jan, and then remained, with no detectable melting, through 28 Jan 1991.

Snow specimens were collected from above the vapor sources on 15 Jan, about 100 hr after the snowpack accumulated. A trench 40 cm wide was then opened above the specimens, and the snow was removed. Uncontaminated snow was obtained about 50 m from the site, and the test area was "reconstituted." Surface air temperature approached 0°C on 28 Jan, and a second set of specimens was extracted. Several freeze-thaw cycles and a period of light drizzle occurred between 28 Jan and 5 Feb; a final series of specimens was obtained from 20 cm of warm ripe snow on 5 Feb.

Profiles of DNT concentration relative to snow depth are given for 15 and 28 Jan, 1991, in fig. 3; the origin corresponds to the sod/snow interface level where the sources were placed. The snow specimens were collected in glass bottles as a function of depth and strata; the nature of shallow snow limits the precision of the location of sample collection to ± 1 cm or more, unless a well-defined crust is present. The lower half of the pack suffered some metamorphosis, although no real depth hoar formed. The snow samples were weighed to determine density, the organic residue was extracted with benzene, and the concentration was measured with electron capture gas chromatography.

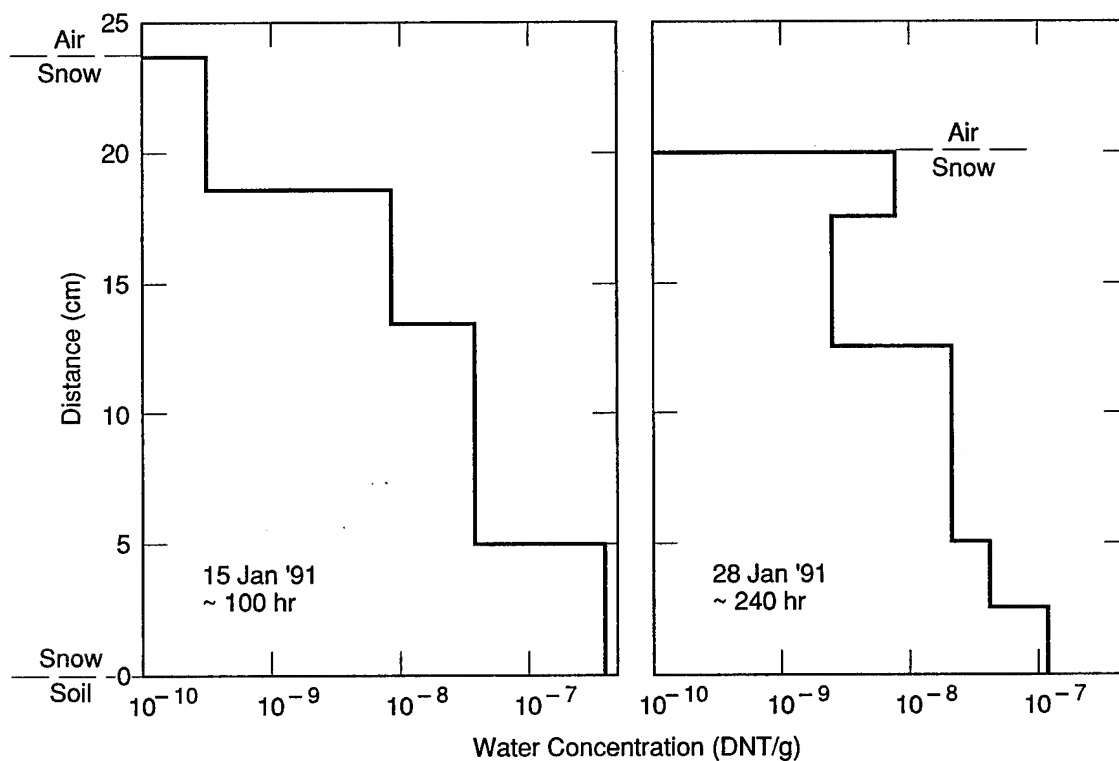


Figure 3. Concentration of DNT in snow above a solid source placed at the snow/soil interface.

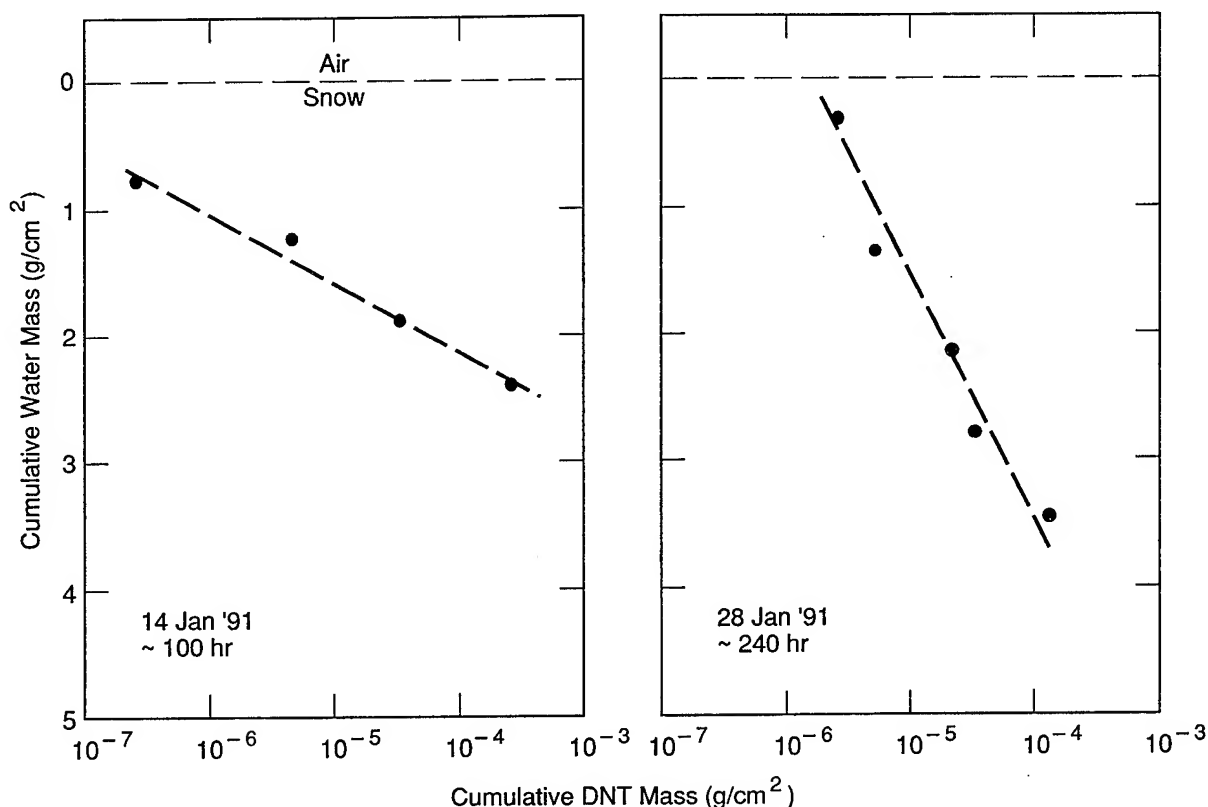


Figure 4. Continuum plot of DNT mass vs water mass in snowpack.

Air, snow, and sample temperatures were measured at 0600, 1800, and 2100 hr local time each day. The temperature at the sod/snow interface remained in the range $-2^{\circ}\text{C} < T < 0^{\circ}\text{C}$ throughout the experiment, and the temperature at the air/snow interface varied through $-25^{\circ}\text{C} < T < +2^{\circ}\text{C}$; the temperature of the base and top of the source petris was frequently less than that of the snow/sod interface. The temperatures measured produce temperature gradients of $1^{\circ}\text{C}/\text{cm}$ in the cold dry snow of 11–15 Jan, represented in the left panel of fig. 3. The reconstituted snow approached temperature uniformity during the rain on 16 Jan and experienced a wide range of temperature gradients, including $1^{\circ}\text{C}/\text{cm}$ on 26 Jan, prior to collection of the specimens in the right panel of fig. 3. The collection from ripe snow (i.e., liquid water present throughout the pack) on 5 Feb showed little gradient of temperature or DNT concentration with depth, and it contained one tenth the concentration of DNT in the vicinity of the source as the samples shown in fig. 3.

Figure 4 shows the amount of DNT relative to water in the same snow samples given in fig. 3, but in this case as a function of mass rather than geometric location. The y-axis is in units of total water column mass overlaying the sample, and the x-axis is the total DNT column mass above the plotted point. The plotted points approximate a straight line indicative of a continuity of flux away from the source petris. The profiles of concentration and mass vs depth in figs. 3 and 4 cannot be uniquely interpreted. The lesser DNT mass and concentration measured near the top of the snowpack can be attributed to flux of vapor from snow to air, or it can be attributed to insufficient elapsed time for the vapor to achieve equilibrium through the snowpack. The increase in slope of the mass and concentration with respect to height as elapsed time increases supports the interpretation that a long period (10^6 s or more) may be required for material of this vapor pressure to equilibrate through 30 cm of snowpack.

4. DISCUSSION

This work has defined several interesting problems relative to atmospheric dispersion over snow-covered ground. We have shown that multiple inversions can be present over snow-covered ground on a space scale much smaller than compatible with most analytical and forecast methods. The surface measurement techniques we have used to define these horizontal and vertical temperature structures may be capable of providing meteorological input to dispersion models on the scales considered.

The surface air temperatures measured differ sufficiently from the snow/soil interface temperatures at the base of the snowpack to provide large gradients to drive thermal redistribution of condensed vapor within the pack. Simultaneously, the minimum temperatures are near the snow/air interface and slow the thermal migration there, while providing a condensation trap for the vapor. RDX, TNT, and DNT were used as vapor sources in the experiment, but only DNT, the material with the greatest vapor pressure, was consistently detected in the snowpack. The DNT was confined to a 20-cm circle directly above the 10-cm-diameter source petris, indicating vapor permeation was occurring along the temperature gradient. Control measurements made in cold dry snow between the sources have undetectable DNT concentrations.

Although the permeation of these low-vapor-pressure materials is relatively slow in snowpack, the atmospheric dispersion above the snow is correspondingly weak. A similar experiment using materials of greater vapor pressure might provide valuable inputs to empirical diffusion models applicable in complex but data-sparse settings.

BIBLIOGRAPHY

- Anonymous, 1991: Directory of Atmospheric Transport and Diffusion Models, Equipment, and Projects. Office of the Federal Coordinator for Meteorological Services and Supporting Research, FCM I3 1991, Washington, DC, March 1991
- Slade, D.H., 1968: Meteorology and Atomic Energy. USAEC 1968
- Kunkel, B.A., 1988: User's Guide to the Air Force Toxic Chemical Dispersion Model (AFTOX). AFGL TR 88 0009, Hanscom AFB, MA.
- Hogan, A., and Ferrick, M., 1991: Investigation of Temperature Variation over Snow Covered Ground. In Proceedings of the 48th Eastern Snow Conference, in press.

AN ASSESSMENT OF THE POTENTIAL OF THE UK MET OFFICE
MESOSCALE MODEL FOR PREDICTING ANOMALOUS
RADIOWAVE PROPAGATION CONDITIONS

Keith S. Groves, Ian D. Todd and Jonathan D. Turton
Meteorological Office
Bracknell, U.K.

ABSTRACT

Under certain atmospheric conditions the anomalous propagation of radiowaves can affect the performance of radars and radio communications. This paper examines the potential of the UK Meteorological Office Mesoscale Model for predicting anomalous propagation conditions. From March to July 1991 radiosonde and model data were collected and from this the skill of the model predictions, made using a variety of different methods, was assessed. The results of this evaluation are presented and discussed.

1. INTRODUCTION

Anomalous propagation (anaprop) of radio waves has been recognised as a problem since the development of radar many years ago. The phenomenon known as "ducting" is an extreme form of anaprop and describes those occasions when radio waves can be trapped in a shallow quasi-horizontal layer. Under such conditions significantly extended detection ranges can occur when both the radar and the target are in the duct, whilst reduced detection ranges can be experienced adjacent to the duct. Turton, Bennetts and Farmer (1988) (hereafter referred to as TBF) have described radar ducting and discussed the meteorological conditions that lead to it.

One of the major reasons for the formation of elevated ducts is the subsidence associated with anticyclones, particularly where a temperature inversion is formed at the interface between the subsiding air and the turbulent boundary layer. Depending upon the strength of the hydrolapse, elevated ducts may form in association with the inversion; such ducts tend to be extensive and persistent. Other conditions which can lead to elevated ducts are subsidence at frontal surfaces, nighttime radiative cooling over land and advection. However, ducts formed by these processes tend to be less pronounced and shorter lived. Also, ducting can occur locally as a result of sea breezes and thunderstorm outflows.

This paper briefly discusses the methods currently used to predict ducting and examines the potential of the Meteorological Office Mesoscale Model for predicting the propagation conditions (e.g. ducting). Only those ducts caused by elevated trapping layers are considered here. A more comprehensive description of the work is given by Todd, Turton and Groves (1991). Such predictions could prove useful as a Tactical Decision Aid in planning the disposition of sensors to exploit, or mitigate, the effects of anaprop.

2. DIAGNOSING RADAR DUCTS

As described by TBF the propagation conditions can be diagnosed from conventional radiosonde or minisonde measurements. The refractivity N (or modified refractivity M) can be calculated from the temperature and humidity. Thus the temperature and dew point profiles obtained from sonde ascents can readily be converted into a refractivity profile, from which the propagation conditions can be determined. There are 4 different propagation categories which can be defined in terms of the refractivity gradient dN/dz (in N -units km^{-1}), or modified refractivity gradient dM/dz , as shown in table 1.

TABLE 1. RADIO PROPAGATION CATEGORIES

Propagation category	dN/dz	dM/dz
Ducting	$dN/dz < -157$	$dM/dz < 0$
Super-refraction	$-157 \leq dN/dz < -79$	$0 \leq dM/dz < 78$
Standard refraction	$-79 \leq dN/dz < 0$	$78 \leq dM/dz < 157$
Sub-refraction	$0 \leq dN/dz$	$157 \leq dM/dz$

3. CURRENT FORECASTING PRACTICE

At present forecasts of radar ducting conditions are being issued by the met office at Headquarters Strike Command (HQSTC) on a trial basis. These forecasts are prepared by identifying regions of (elevated) ducting from radiosonde ascents (made routinely at 00Z and 12Z), and mapping these areas onto the surface and 850 hPa fields. Numerical model predictions are then used to assist the forecaster in determining the likelihood and extent of areas of ducting for 12 and 24 hours ahead. The predictions, although using numerical products for guidance, are rather subjective and are presented in terms of a probability forecast. Areas with "high-medium", "medium-low" and "nil" likelihood of ducting are delineated.

The accuracy of the forecasts was examined by assessing each forecast against the actual conditions (for the forecast time). Comparisons were made for Hemsby (eastern England) and Valentia (southern Ireland), locations where radiosonde ascents are made, for data from mid May to August 1991. For the forecasts, several different measures of performance were calculated, the hit rate, false-alarm rate and skill score as defined in Todd, Turton and Groves (1991). For the 12 hour forecasts, the hit rate for predicting ducting conditions (based on both the "high-medium" and "medium-low" probabilities) was 59%, with a false-alarm rate of 58% and a skill score of 17%. The results were similar for the 24 hour forecasts, where the predictions of ducting had a hit rate of 53%, false alarm rate 58% and a skill score of 16%.

Although the levels of skill are rather low, it should be noted that the HQSTC forecasters have had no previous experience in making such predictions, and some improvement in skill with experience would be expected. However, the preparation of these forecasts is labour intensive and so it would be desirable if an automated method could be developed. The remainder of this paper examines the potential of using numerical model output for making ducting/anaprop predictions.

4. PREVIOUS WORK

TBF noted that, whilst numerical models can help identify the airmass and provide guidance on the general synoptic development, they could not give vertical profiles to the accuracy required to predict ducting. The work to investigate the potential of numerical model output for making predictions of elevated ducts was started in 1987, and originally assessed products from the Met Office Fine-Mesh Model. The approach taken was to use a method based on Model Output Statistics, where a linear regression equation was derived between the strength of the duct or super-refracting layer and a number of various model parameters which described the state of the atmosphere. However, the accuracy of the derived equations was poor due to the inability of the Fine-Mesh Model to forecast strong temperature inversions and steep hydrolapses in anticyclonic conditions (Farmer, 1990, personal communication).

Thus further work was undertaken using output from the 16-level Met Office Mesoscale Model (MM), Golding (1990) (described briefly in the following section), in the hope of exploiting the improved vertical resolution and better humidity forecasting of the MM compared to the Fine-Mesh. This work was started by one of the present authors (IT) who showed that, with the improved vertical resolution, it was now possible to use the model refractivity profiles directly and get results comparable to those using a MOS technique with MM data. However, the accuracy of the predictions still appeared to be relatively poor, although no specific assessments of the skill of the predictions were made.

5. THE MET OFFICE MESOSCALE MODEL

The Mesoscale Model (MM) has been described elsewhere, most recently by Golding (1990), so only a brief description will be given here. The MM is a short period weather forecasting model which covers the British Isles and most of the North Sea. The MM area and horizontal resolution (15 km) is shown in fig. 1(a), this resolution allows a reasonably realistic representation of the topography to be included in the model. The number of vertical grid levels in the model has recently been doubled to 32, and the enhanced version of the model has been run routinely since March 1991. The 32 levels are all at fixed heights above the surface, and of these 13 levels are between 100 m and 3 km, i.e. in the height range relevant to predicting ducts due to elevated trapping layers. Fig. 1(b) shows the vertical levels of the enhanced MM used in this study. Sub-grid scale parametrizations of boundary layer processes (radiation, turbulence, heat conduction into the ground), layer and convective cloud are all included in the MM. The initialization procedure used for the MM is described by Wright and Golding (1990).

The vertical structure of the enhanced 32 level MM is sufficiently detailed that it might be expected to be capable of making forecasts of ducting conditions, since it should be much better at resolving the temperature and humidity profiles. Indeed, an experimental study of MM forecasts of the haar off north east Scotland (Ballard et al, 1990) shows that the higher resolution model is capable of representing the profiles much more realistically.

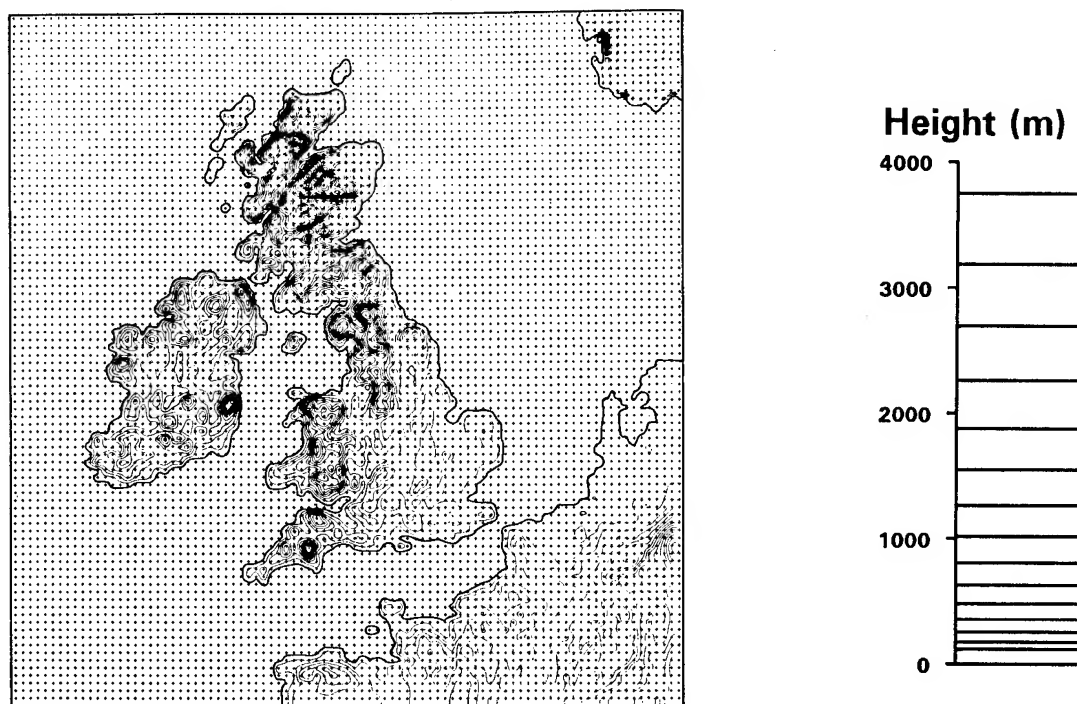


Figure 1. (Left) Mesoscale Model domain and horizontal resolution and (right) vertical grid levels used.

6. PROPAGATION CONDITIONS FORECASTING FROM THE MM

The approach adopted in this work was rather different to that of the earlier studies (as described in section 4). It was decided to concentrate on the more direct approach and to quantify the results in terms of the measures of forecast performance used above, thus the results are presented in a form which demonstrates the ability of the model to make useful forecasts. From March to August 1991 (nearly all of) the MM profiles for the land grid points nearest to the Hemsby and Valentia radiosonde stations were archived for the T+0 (analysis) and T+12 (forecast) times of the 00 and 12 MM forecast runs. The corresponding radiosonde ascents were also archived. Thus each actual radiosonde ascent could be compared against a model analysis and a 12 hour model forecast (from the previous integration).

6.1 DIRECT FORECASTING

The simplest approach to forecasting the propagation conditions is to use the MM output directly to calculate a refractivity profile from the MM profiles of temperature and dew-point, and the corresponding propagation category (as given in table 1) can then be identified. Table 2 shows a matrix of the propagation classes diagnosed from the actual (radiosonde) and MM (12 hour forecast) refractivity profiles for the Hemsby and Valentia data, the individual results for these locations were similar so they were combined. In these analyses ducts are counted in preference to any coexisting super-refracting or sub-refracting conditions. Table 2 shows that there were 165 examples of ducting diagnosed from the radiosonde ascents, but of these

only 10 were correctly predicted from the MM forecast (i.e. a hit rate of only 6%, with a false alarm rate of 63% and a skill score of just 2%).

TABLE 2. PROPAGATION CONDITIONS MATRIX FOR MM FORECAST

MM f/c	Radiosonde				Total
	Ducting	Super	Standard	Sub	
Ducting	10	6	3	8	27
Super	81	60	35	32	208
Standard	71	113	123	70	377
Sub	3	3	0	0	6
Total	165	182	161	110	618

The results suggest that the direct predictions of propagation conditions from the MM show only a very limited amount of skill, and cannot be considered sufficiently reliable to be useful. Although there are a few occasions where the model profiles show close agreement with those from the radiosonde and give a good prediction of ducting, as illustrated in Fig. 2 for example, this is not generally the case as shown by the results above. The main reason why the model predictions have rather little skill is due to the tendency of the model to underpredict the temperature and humidity (and consequently the refractivity) gradients, such that most ducting situations are not adequately modelled. This is also limited by the decrease in model resolution further away from the surface, so higher level ducts are often not represented. Fig. 3 shows a more typical example where a duct was diagnosed from the radiosonde ascent, but the underprediction of the gradients in the model means that the model does not represent the duct. However, although the model profile is too bland, it still shows some deviation from the mean standard refractivity lapse (-40 N units km^{-1}). Therefore, if some allowance is made for the models inability to develop gradients as large as those that actually occur, it should be possible to improve on the skill of the predictions from the MM.

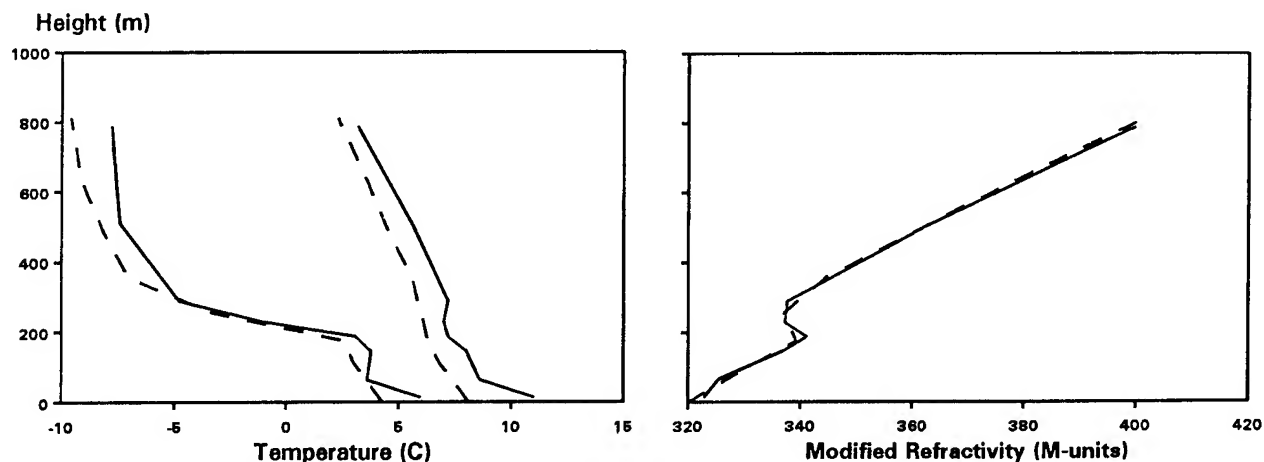


Figure 2. Radiosonde (—) and Mesoscale Model forecast (----) profiles of (left) temperature and dewpoint, and (right) modified refractivity for Hemsby at 12Z on 8 May 1991.

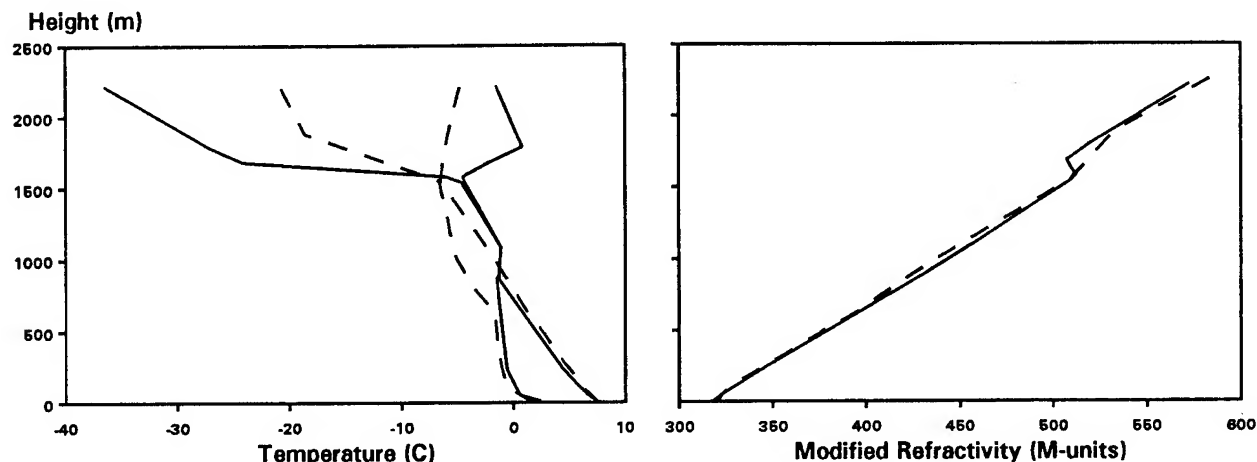


Figure 3. Radiosonde (—) and Mesoscale Model forecast (----) profiles of (left) temperature and dewpoint, and (right) modified refractivity for Hemsby at 12Z on 16 April 1991.

6.2 RELAXING THE CRITERIA

One way of improving skill is to relax the criteria for the diagnosis of ducts and super-refracting conditions from the model profiles. This compensates for the model gradients being less than those actually occurring, which gave rise to an under-prediction of ducting cases. The relaxed criteria then applied to the model N profiles were $-80 \text{ N-units km}^{-1}$ to predict ducting and $-50 \text{ N-units km}^{-1}$ for super-refraction, no change was made to the criterion for predicting sub-refraction. Using these modified criteria the following results (table 3) were obtained.

TABLE 3. PROPAGATION CONDITIONS MATRIX FOR MM FORECAST USING RELAXED CRITERIA

MM f/c	Radiosonde				Total
	Ducting	Super	Standard	Sub	
Ducting	83	62	38	40	223
Super	65	87	64	48	264
Standard	14	30	59	22	125
Sub	3	3	0	0	6
Total	165	182	161	110	618

This modification led to many more ducts being predicted and a marked improvement in the hit rate to 50%, with a false-alarm rate of 63%. The skill score improved to 19%. Note that the results are now comparable to the manual forecasts prepared by HQSTC met office. Also, when the results from the MM forecasts are compared to those from the analyses they are seen to be somewhat better with an analysis skill score of 14%. This is an interesting result which will be discussed later.

6.3 DUCTING PROBABILITY FORECASTS FROM THE MM

Since the previous results gave rather limited levels of skill for the deterministic predictions of ducting conditions from the MM it was considered that a probabilistic approach might be more suitable. The results shown in table 3 (i.e. the forecasts based on the relaxed criteria) can be expressed in terms of probabilities and these are shown below in table 4.

TABLE 4. DUCTING PROBABILITIES BASED ON RESULTS GIVEN IN TABLE 3

MM f/c	P _{Ducting}	P _{Super}	P _{Stand/Sub}
Ducting	0.37	0.28	0.35
Super	0.25	0.33	0.42
Stand/Sub	0.13	0.25	0.62

The table shows that when the (relaxed) criteria for ducting is satisfied by the model the probability of ducting is only 0.37. The most definite prediction is for when the model gives standard/subrefracting conditions, and the probability of this being correct is 0.62. Overall, the probabilities tend to be rather too similar for this approach to be considered useful.

6.4 PROBABILITY PREDICTIONS USING AN ANAPROP INDEX

One of the limitations of the techniques assessed so far is the fact that the predictions are based solely on the refractivity gradient and no consideration is made of the depth of the layer. It would be expected that shallow supers/ducts would be much more difficult for the model to predict than deeper features. Also, a deep super-refracting layer might actually have more impact on a radar than a shallow duct. Therefore, it was considered that some other method, which takes into account both the gradients and the depth of the layer, should be examined. The way in which this was done was to define an index of super/ducting, which was a function of both the gradient and the layer depth, such that higher values of the index refer to super/ducting conditions that deviate most from standard.

For the earlier work an index I_1 was defined by Farmer (1986). However this index, whilst well behaved, is somewhat empirical and difficult to justify theoretically. Therefore a second index I_2 , based on theoretical ideas, was also developed and this is given by Todd, Turton and Groves (1991). In general, ducting conditions give higher values of the indices than do super-refracting conditions, but not necessarily so since the depth of the layer is also taken into account. It was expected that the higher the value of the index, the more likely ducting conditions would be to arise, so that the probability of ducting conditions could be related to the model predicted index. The results for I_1 and I_2 are given in figs. 4(a) and 4(b) and show that for predicted values of I_1 up to 2.5 and I_2 to 20 the probability of ducting increases, reaching a maximum value of 0.59 ± 0.10 for $2.0 \geq I_1 > 2.5$, and 0.67 ± 0.13 for $15 \geq I_2 > 20$. For larger values of I_1 and I_2 the probabilities rather surprisingly decrease, but these estimates are subject to large errors since there are fewer data. Nonetheless, the results suggest that, using this approach, it is possible to make probability forecasts with a reasonable degree of discrimination and that the method shows some promise.

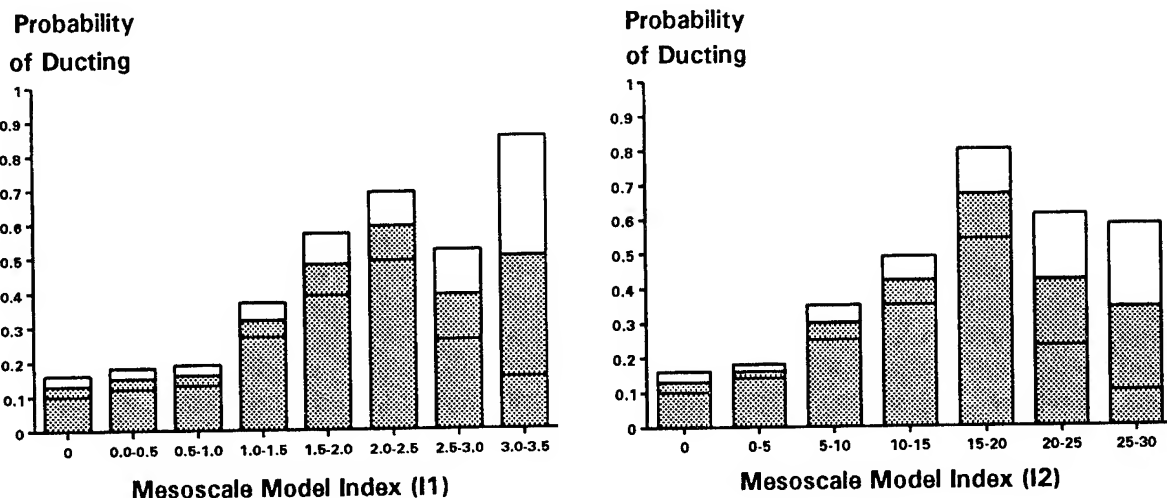


Figure 4. Probability of ducting conditions for the values of the anaprop indices I_1 (right) and I_2 (left) predicted by the Mesoscale Model. The upper and lower bars indicate the error in the probability.

7. DISCUSSION AND CONCLUSIONS

Although none of the methods investigated in this study have been particularly successful in predicting ducting conditions, some improvement has been made over that found in the earlier work, and a number of important factors have come to light.

The direct predictions of ducting conditions from the MM profiles showed only a very limited level of skill, only 2%. However, better results (19% skill) were obtained using the relaxed criteria for the diagnosis of ducting and super-refracting conditions, which partly compensates for the underestimation of the vertical gradients in the model profiles. These results were comparable in accuracy to those produced manually (on a trial basis) by the HQSTC met office. However, the accuracy of these forecasts was still considered to be relatively low.

The results from this approach can also be interpreted in terms of probabilities, but the probability predictions were rather too bland to be considered useful. Some further improvement in probabilistic forecasts were achieved by using an index to define the level of anaprop, which gives little significance to weak and shallow ducts and better accounts for deeper features. When the values of the indices I_1 and I_2 are used to give a probability forecast then it is possible to produce predictions that show some degree of discrimination with probabilities in the range 13% to 67%, which was an improvement on those determined more directly.

For the MM the better performance of the forecast compared to the analysis was unexpected. All other things being equal, the analysis would normally be better than the forecast since errors would be expected to grow over the forecast period. The reason that this was not so is due to the way in which the MM is initialized. Upper air data are passed to the MM from the Limited Area Model (LAM) and these are interpolated onto the MM grid. Therefore the

profiles are highly smoothed (since the LAM vertical resolution at low levels is much coarser), so the better vertical resolution of the MM is not being exploited in the analysis. This initialization procedure was adopted because the (spatial) resolution of the upper-air (radiosonde) observations was considered to be too low to justify the effort of incorporating them directly onto the 15 km MM grid. However, this clearly degrades the ability of the MM to predict the structure of inversions/hydrolapses and so the resulting forecasts of the propagation conditions are not as good as they could be.

When the forecast profiles are compared to the initial profiles it can be seen that the model is capable of sharpening up the gradients of temperature and humidity. An example of this is shown in Fig. 5 where an event during a static synoptic situation is examined. It can be seen that the forecast has steeper gradients compared to the analysis for the same time and location (taken from the next model integration). This sharpening up of the vertical detail explains why the MM forecasts performed better at predicting ducting conditions than the analysis.

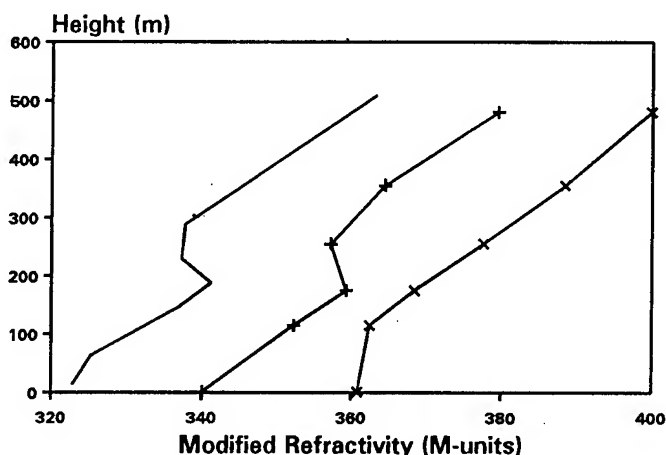


Figure 5. Comparison of radiosonde (—), Mesoscale Model forecast (---) and analysis (-x-) modified refractivity profiles for Hemsby at 12Z on 8 May 1991. The model profiles have been offset by 20 M-units for legibility.

Levy and Craig (1991) have discussed the possibility of using MM data directly in a Tactical Decision Aid model to predict sensor performance and illustrated the potential of this approach. However this application will demand improvements in the capability of the MM to reliably predict the atmospheric refractivity structure in three dimensions.

At present, the main factor which limits the ability of the MM to predict ducting or anaprop conditions reliably is the way in which the model is initialized. The profiles of temperature and humidity (derived from the LAM) specified at the start of the model integration are much too smooth, and the improved vertical resolution of the MM is not being fully exploited. Although some success was achieved, it is considered that no method at present is sufficiently good to justify implementing operationally.

Improving the way in which the MM is initialized should lead to significantly better predictions of ducting/anaprop conditions from the model. It is highly desirable that more detailed information from the upper air observations reaches the model, and that the initial conditions are specified with more vertical detail. This could be achieved by using the Interactive Mesoscale Initialization facility (Wright and Golding, 1990) whereby the operator can add this detail to the vertical profiles. However, one of the problems with this approach is (as noted by Ballard et al, 1990) that the temperature (and humidity) field needs to be carefully balanced with the wind field to avoid generating spurious winds. Alternatively, actual upper air data could be used directly in the initialization procedure and incorporated automatically, which should avoid problems in balancing the wind field.

There are plans to incorporate the MM into the Met Office operational Unified Model (Global and LAM) suite. This will lead to the MM having a better initialization procedure which should increase the vertical detail specified in the analysis, and so improve the ability of the model to predict ducting/anaprop conditions. When these changes have been implemented, reliable predictions of anaprop conditions from the MM ought to become possible.

REFERENCES

Ballard, S.P., Golding, B.W., and Smith, R.N.B., 1990: Mesoscale Model Experimental Forecasts of the Haar of North East Scotland. Met Office, Short-Range Forecasting Research Division, Sci. Note No. 20.

Ballard, S.P., 1991: Assessment of the Performance of the 32 Level Version of the Mesoscale Model. Met Office, Short-Range Forecasting Research Division, Tech. Note No. 62.

Farmer, S.F.G., 1986: Forecasting Radio Ducts. Met Office, Special Investigations, Unpublished Note.

Golding, B., 1990: The Meteorological Office Mesoscale Model. Meteorol. Mag., 119, 81-96.

Levy, M.F., and Craig, K.H., 1991: Use of Mesoscale Models for Refractivity Forecasting. NATO AGARD CP502.

Todd, I.D., Turton, J.D., and Groves, K.S., 1991: Forecasting Elevated Radio Ducts using Mesoscale Model Data. Met Office, Defence Services Division, Tech. Note.

Turton, J.D., Bennetts, D.A., and Farmer, S.F.G., 1988: An Introduction to Radar Ducting. Meteorol. Mag., 117, 245-254.

Wright, B.J., and Golding, B.W., 1990: The Interactive Mesoscale Initialization, Meteorol. Mag., 119, 234-244.

Variation of Cloud Base by Season and Climate Zone

Dr. Oskar Essenwanger
University of Alabama in Huntsville
c/o Department of Mathematical Sciences
Huntsville, AL 35899

ABSTRACT

Operation in the battlefield may be affected by low clouds. Ordinarily a global survey of the variation of the cloudbase and fraction of skycover by clouds in different climatic zones would require the processing of a multitude of stations determining the frequency of occurrence. A tentative study was performed by selecting "typical" stations in 9 climatic regimes delineating these variations from September through April. As expected e.g. the frequency of total skycover with clouds below 300 m is highest for the winter months, December and January, but not in all climatic zones. For skycover by a "ceiling" the result is similar, however, the ranking of climatic zones by frequency of occurrence changes. Finally the changes in the altitude for which total skycover and ceiling are below 2.5, 5.0, and 10% of the hours is shown.

1. INTRODUCTION

In many cases clear line of sight statistics may suffice. However, for some systems it may be of interest to know a probability of finding a cloudlayer below a certain altitude. Then information about the vertical distribution of clouds (such as Gringorten, 1982) may not be sufficient. In addition, it is difficult to find climatological information of seasonal variation of the cloudbase and their differences in individual climate types. Although the cloudbase can be predicted for short time periods such as one or two days it may still be of interest to know the long term average frequency of occurrence in individual climatic regimes.

Ordinarily such a study requires the processing of numerous stations on a global basis. This may be a very laborious and costly task. A different approach is being used here. "Typical" stations in 9 different climatic regimes were selected to delineate the variation of the cloudbase by season and climatic zone. The author is aware that this

technique can produce only tentative results, and should be considered as a pilot study. However, significant differences between individual climatic regimes have become visible. These differences are in line with climatic expectations but this study produced some numerical estimates for them.

Since the cloudbase is usually higher in summer the summer months were not processed in this study. Thus the seasonal variations are reflected for the months of September through April. Due to space limitations for this manuscript only two altitude levels, 300m, and 1km, were chosen. Although the results for other altitude levels are not included, these two levels permit us to evaluate whether tabulations for other altitude levels must be processed on an individual basis or whether a general evaluation is sufficient.

A second part in this manuscript discloses the changes of the altitude of the cloudbase for a specified frequency of occurrence.

2. CLOUDBASE AND ALTITUDE BOUNDARY

2.1 CLIMATIC ZONES.

Classification of climatic regimes are not based on cloud parameters. Since clouds are functions of moisture and temperature, however, they are implicitly included. Thus any reasonable climate classification system could be used. The author found that the widely known system developed by Koeppen as modified by Trewartha (1954) serves our purpose. The 13 major types by Trewartha are reduced to 9 by combining all tropical regimes into one type, and eliminating the icecaps and highlands. Then typical stations were selected for these remaining 9 types, whereby the (Central) European climate comprises an average of 6 stations, and two stations each are presented for the Mediterranean type and one of the continental types. This results in the following different climatic zones and their station representation whose symbols have been used in Tables 1 and 4.

CLIMATE ZONES

ZONE	STATION	SYMBOL
Tropical	Honolulu, HI	HON
Arid:		
Steppe	Denver, CO	DENV
Desert	Cairo, Egypt	CAIR
Moderate:		
Subtropical	New Orleans, LA	NORL
Maritime	Central Europe	EUR
Mediterranean	Rome, Italy	ROME
	San Francisco, CA	SFRIS
Continental:		
Snow-Forest	Chicago, IL	CHIC
	Seoul, Korea	SEOUL
Taiga	Fairbanks, AK	ALAS
	(supplemented by Fort Greely)	
Polar:		
Tundra	Thule, Greenland	THUL

2.2. DATA PROCESSING

Most of these stations comprise the time period 1973 - 1988, or 1989, collected by the National Weather Service in DATSAV format. This data were received on magnetic tapes but processed on floppy disks for use on a PC. The data was run through a quality assurance program. Cloud information was supplemented from special observations whenever the cloudgroups in the synoptic code were missing. For this reason US stations were selected if typical for a climatic zone because they had the better observation records. Although the World Meteorological Organization (WMO) has aimed to agree on a uniform synoptic code every individual station had to be checked for "peculiarities", and processed into a uniform code on floppy disks.

TABLE 1. FREQUENCY (IN %) OF TOTAL SKYCOVER

A) BELOW 300m

	HON	DENV	CAIR	NORL	EUR	ROME	SFRIS	CHIC	SEOUL	ALAS	THUL
Sep	0.05	1.7	0.10	1.2	3.7	0.34	6.1	4.7	0.28	0.3	3.3%
Oct	0.28	2.1	0.01	2.1	9.5	0.66	3.9	6.9	0.22	0.5	1.4
Nov	0.41	2.9	0.03	7.3	15.0	1.00	4.2	9.1	0.01	3.1	0.3
Dec	0.22	2.5	0.03	8.5	17.4	1.13	7.1	10.8	0.21	1.0	1.2
Jan	1.20	1.9	0.01	11.5	19.9	1.51	6.1	8.4	0.34	1.0	0.9
Feb	0.70	2.7	0.01	10.3	18.9	1.25	3.3	9.2	0.15	0.4	1.2
Mar	0.15	3.7	0.03	8.3	10.3	0.99	3.2	9.3	0.21	1.1	0.3
Apr	0.67	3.8	0.06	5.1	5.8	0.93	2.2	9.1	0.66	0.5	0.8

B) BELOW 1km

	HON	DENV	CAIR	NORL	EUR	ROME	SFRIS	CHIC	SEOUL	ALAS	THUL
Sep	0.3	4.3	0.2	3.3	10.2	0.9	9.8	10.0	2.9	11.0	9.5%
Oct	0.9	4.5	0.3	4.8	19.4	2.0	7.4	14.8	2.4	10.6	9.4
Nov	5.0	5.5	0.1	13.3	27.3	2.8	8.1	27.5	2.9	7.8	5.8
Dec	2.8	4.7	0.2	14.8	33.5	3.6	13.5	30.4	5.5	6.4	3.6
Jan	3.1	4.8	0.2	21.2	32.6	5.0	12.0	26.9	6.3	4.9	2.9
Feb	3.0	4.7	0.2	17.3	30.5	3.8	8.0	27.7	5.1	4.3	3.0
Mar	1.5	7.9	0.4	16.7	20.6	2.1	10.5	27.6	3.8	5.9	1.8
Apr	2.8	6.8	0.3	10.0	12.0	2.0	7.1	22.7	6.7	2.6	2.5

TABLE 2 FREQUENCY (IN %) OF CEILING

A) BELOW 300M

	HON	DENV	CAIR	NORL	EUR	ROME	SFRIS	CHIC	SEOUL	ALAS	THUL
Sep	0.1	1.9	0.4	2.3	7.1	1.6	10.9	5.8	1.1	6.1	5.4%
Oct	0.4	2.4	0.3	2.9	14.9	2.9	6.9	7.6	1.5	5.3	2.5
Nov	0.9	3.8	0.3	8.9	21.2	3.8	7.9	9.4	1.0	4.5	0.8
Dec	0.4	2.8	0.2	10.8	27.1	4.7	11.0	11.1	1.2	1.3	1.5
Jan	1.8	2.3	0.3	13.3	25.2	5.2	9.8	8.6	1.5	1.2	1.4
Feb	1.0	3.1	0.1	12.1	23.1	5.4	5.8	9.4	0.5	1.0	1.4
Mar	0.3	4.6	0.3	11.3	14.7	5.0	5.5	9.5	0.6	1.8	0.6
Apr	0.8	5.3	0.1	6.9	12.9	5.1	4.5	9.6	2.1	1.3	1.6

B) BELOW 1km

	HON	DENV	CAIR	NORL	EUR	ROME	SFRIS	CHIC	SEOUL	ALAS	THUL
Sep	17.8	5.1	8.5	12.2	32.5	9.1	20.2	17.6	18.0	23.1	21.5%
Oct	24.5	5.2	6.5	11.6	40.6	14.8	17.6	18.6	14.9	20.2	18.9
Nov	27.7	7.2	10.6	22.4	51.5	18.4	19.0	31.8	19.8	12.6	10.2
Dec	25.2	5.5	8.3	23.6	58.7	19.9	25.2	35.0	24.8	10.7	5.6
Jan	27.5	6.4	12.5	29.4	57.4	21.2	24.3	32.6	22.4	8.7	5.3
Feb	25.5	5.9	11.0	26.1	50.1	21.3	21.6	31.8	19.8	8.2	4.2
Mar	25.4	10.3	10.1	29.3	44.2	19.1	27.5	34.7	16.3	9.0	3.2
Apr	10.0	9.8	6.7	21.7	39.5	17.3	20.6	29.3	22.0	6.9	5.6

2.3. FREQUENCY OF CLOUDBASE BELOW 300 m AND 1 km.

Tables 1 and 2 show the frequency of occurrence for total skycover and ceiling (> 50% skycover) for the specified altitudes. The frequency represents an average over all hours of the day. Thus the diurnal trend is not included.

Four climate zones display significant frequencies of total skycover below 300 m with the highest frequency in the winter months (Table 1). Europe shows about 19% in January and February. New Orleans and Chicago reach only about 11% . While the highest frequency at New Orleans also occurs in January and February, Chicago has a peak in November and December. It should be noticed that Chicago has the highest frequency of all stations of April.

At an altitude of 1km again the (Central) European zone emerges with the highest frequency from December through February with about 30 to 33%. At Chicago the total sky is covered below 1km from November through March between 27 to 30% of the hours. Again, Chicago's frequency is the highest of all used stations in April. The seasonal trend in Alaska is worth to call to the attention because the frequency of total skycover below 1 km decreases from September through February. This trend is apparently an effect of the sun's cycle, and can also be found at Thule. We learn that the ranking of stations by their frequency of total skycover below 300 m and 1 km differs in individual months. In January the ranking is: Europe, New Orleans, Chicago, San Francisco. In April we find: Chicago, Europe, New Orleans, and San Francisco. The latter has the lowest frequency of the four stations except for September and October.

For a ceiling (Table 2) the frequency of occurrence is almost twice as high in Central Europe as for the other stations in the winter months. Again, Chicago is next, with a ceiling below 1 km in 30% of the hours from November through April. The same trend for the ceiling is visible in Alaska and Thule as found for the total skycover. The increase of the frequency for a ceiling below 1 km at Honolulu is called to the reader's attention. It is not unexpected due to the tropical passat inversion.

2.4 ALTITUDE OF CEILING AND SKYCOVER FOR SPECIFIED FREQUENCY.

The difference in the frequency of occurrence for total skycover and ceiling in these 9 climatic zones are illustrated in Tables 1 and 2. It may be of interest to study the variation of the cloudbase by altitude in these 9 zones for a specific frequency. Although it was originally intended to choose 10 and 25% as the thresholds it can be deduced from Tables 1

TABLE 3. ALTITUDE BOUNDARY FOR TOTAL SKYCOVER (in meters)

A) 97.5% OF HOURS

	HON	DENV	CAIR	NORL	EUR	ROME	SFRIS	CHIC	SEOUL	ALAS	THUL
Sep	2500	300	2500	500	180	2500	170	215	2500	180	270m
Oct	2500	270	2500	360	105	2500	190	150	2500	250	420
Nov	950	170	2500	150	90	580	215	135	2500	270	650
Dec	910	230	2500	100	70	420	150	120	2500	450	675
Jan	865	300	2500	90	70	450	145	125	2500	500	820
Feb	850	230	2500	100	75	450	240	110	2500	510	800
Mar	1000	150	2500	130	120	2500	270	130	2500	550	1050
Apr	1000	150	2500	175	150	2500	330	125	2500	1000	1060

B) 95% OF HOURS

	HON	DENV	CAIR	NORL	EUR	ROME	SFRIS	CHIC	SEOUL	ALAS	THUL
Sep	2500	700	2500	2500	490	2500	260	330	2500	300	520m
Oct	2500	650	2500	2400	175	2500	340	230	2500	380	700
Nov	2500	450	2500	230	130	2500	375	190	2500	500	1020
Dec	2500	550	2500	170	110	2500	225	160	2500	1100	1040
Jan	2500	600	2500	130	105	2500	250	180	2500	1300	1430
Feb	2500	600	2500	170	105	2500	350	190	2550	1300	1470
Mar	2500	300	2500	200	155	2500	410	190	2500	950	1620
Apr	2160	340	2500	300	220	2500	540	165	2500	1500	1620

*) 2500 means Total Skycover occurs above or no total skycover

TABLE 4. ALTITUDE BOUNDARY FOR CEILING ABOVE (IN METERS)

A) 95% OF HOURS

	HON	DENV	CAIR	NORL	EUR	ROME	SFRIS	CHIC	SEOUL	ALAS	THUL
Sep	805	1000	590	450	230	455	210	290	1000	150	290m
Oct	775	1000	760	440	120	360	230	225	860	220	420
Nov	720	750	680	190	110	330	230	190	850	300	610
Dec	505	750	680	150	90	305	195	175	675	600	980
Jan	485	740	590	120	95	290	190	180	740	580	990
Feb	660	740	635	145	95	280	280	180	760	600	1050
Mar	735	340	635	160	145	300	290	185	780	640	1140
Apr	815	300	735	230	200	300	320	165	810	750	890

B) 90% OF HOURS

	HON	DENV	CAIR	NORL	EUR	ROME	SFRIS	CHIC	SEOUL	ALAS	THUL
Sep	880	2120	2500	760	365	2500	290	590	2500	250	545m
Oct	835	2125	2500	660	215	495	340	440	2500	350	740
Nov	800	1670	1860	340	185	445	385	300	2500	600	1110
Dec	800	1690	1660	280	155	425	290	280	1225	970	1260
Jan	775	1610	940	215	145	405	290	305	1250	1325	1575
Feb	800	1000	1450	250	155	400	400	315	2000	1550	1845
Mar	805	530	1770	275	230	420	400	310	2500	1600	1775
Apr	1000	650	2500	415	295	435	460	315	2500	1675	1585

*) 2500m means ceiling above or no ceiling

and 2 that for most stations the altitude, for which the cloudbase for total skycover or ceiling is below that altitude boundary, is quite high for all the stations except Europe. Therefore, different frequency thresholds were selected.

For total skycover it may be of interest how often the cloudbase is higher than the altitude boundary in 95 or 97.5% of the hours. For a ceiling these thresholds were chosen at 90 and 95%. It must be stressed that this study dealt with low clouds only although cumulus and cumulonimbus clouds may have a considerable vertical extent. However, here the investigation was limited to low clouds as reported in the synoptic code of low clouds. Thus an altitude of 2500 m does not always mean the precise altitude of 2500 m but should be interpreted as 2500 m or above.

As expected, the Central European region has the lowest altitude boundary for the specified frequency threshold (Table 3 and 4). We learn from these tables that for total skycover in 2.5% of the hours the cloudbase is below 150 m from October through March. For San Francisco it is December and January, for New Orleans from November through March. At the 5% threshold October drops out for Europe but only January remains for New Orleans. By a comparison between Table 1 and Table 3 we notice that for an altitude boundary Denver shows 150 m for the 2.5% threshold but in March and April. Again, the rise in the altitude boundary for Alaska and Thule is in agreement with the first two tables. Although the altitude boundary is low for Rome when 2.5% are considered, the drastic increase of the altitude boundary to 2500 m is called to the reader's attention. The significant difference between Rome and San Francisco is one reason why two stations have been included for this climate zone. A similar difference can be seen for Chicago and Seoul. These differences indicate that the present study should be considered as a pilot investigation.

Table 4 provides the altitude boundary for a ceiling but in this case the altitude for which a ceiling is below in 5 and 10% of the hours has been chosen. As we can deduce only for the Central European area the boundary remains below 150 m for the 5% threshold and the months of October through March. At New Orleans November and March drop out, at Chicago and San Francisco that altitude is higher than 150 m for all months. Now we find that only at Seoul the fall months, September through November, and March and April have a ceiling in 90% of the hours which is 2500 m or higher, or Cairo in September or April.

3. CONCLUSIONS

The frequency of hours for which the total skycover or the ceiling is below 300 m or 1 km was studied for 9 different climatic regimes. It may be a surprise that the Central European zone showed the highest frequency of the hours, with about 20% in January and February below 300 m, and about 33% below 1 km. For a ceiling, Central Europe appears

again as the zone with the highest frequency for the selected altitudes. In this case, the number of hours is almost twice as high as for the next highest stations.

The same pattern is found when the altitude boundary is calculated for which a specified percentage of the hours of total skycover or ceiling occurs below that altitude. In this case, in 2.5% of the hours the continental zone (Chicago) parallels the European zone. The boundary is below 150 m from October through April in both zones. Other details can be deduced from Tables 1 to 4.

The variation of the cumulative distribution for skycover by clouds from total skycover to $\frac{1}{8}$ can be found in a separate manuscript by the author (1991).

ACKNOWLEDGMENTS

The author thanks Messrs. Jim Puckett and David Watson for processing the data information from magnetic tapes to floppy disks. The author is also acknowledging that the data were furnished in DATSAV format by ETAC for the use in earlier studies. Thus the data base for this study was available to the author. Finally, Mrs. Tami Lang must be thanked for her zealous effort to prepare the stencil of this manuscript in the shortest time in order to meet the deadline.

REFERENCES

Essenwanger, O.M., 1991: Cumulative Frequency of Skycover by Clouds Below Selected Levels.

Manuscript in print: Proceeding of CIDOS-91, 0-12 July, pp 6, Geophysics Directorate,

Phillips Laboratory, Air Force Systems Command, Hanscom AFB, MA, 01731.

Gringorton, I.I., 1982: Climatic Probabilities of the Vertical Distribution of Cloudcover, pp 48,

AFGL-TR-82-0078, Env. Research Papers, No 773, Air Force Geophysics Laboratory,

Hanscom AFB, MA 01731

Trewartha, G.T., 1954: An Introduction to Climate, McGraw-Hill, New York, pp. 442.

FORECASTING CONVECTIVE PRECIPITATION AND SEVERE WEATHER BY
APPLYING ARTIFICIAL INTELLIGENCE APPROACHES

Robert E. Dumais, Jr., and Jeffrey E. Passner
U.S. Army Atmospheric Sciences Laboratory
White Sands Missile Range, New Mexico 88002-5501, USA

ABSTRACT

The U.S. Army Atmospheric Sciences Laboratory will evaluate the skill (against climatologies) involved in forecasting spring season (April-May-June) convective precipitation events over Oklahoma by applying two different types of artificial intelligence techniques. The Thunderstorm Intelligence Prediction System is an in-house U.S. Army development and is an expert system driven by a human-derived set of rules and designed to issue a subjective probability of thunderstorm and severe weather forecast for both the day and the region of interest. The other system, which is called Goal-Oriented Pattern Detection (GOPAD), is an adaptive-learning expert system in which the rule set is machine-derived. GOPAD is designed to issue a point-probability of measurable precipitation forecast for some specified valid period using preselected predictor variables. The authors discuss the results of these tests and analyze the two systems and their performances, using data from the 1990 spring thunderstorm season.

1. INTRODUCTION

The Thunderstorm Intelligence Prediction System (TIPS) and the Goal-Oriented Pattern Detection (GOPAD) are both examples of weather-based expert systems. TIPS is a rule-based expert system that is designed to advise the staff weather officer (SWO) on the possibility of thunderstorm/severe weather activity across the forecast domain. The TIPS is run within a PC environment, and its rule base is programmed in the "C" Language Production System (CLIPS) developed at the Lyndon B. Johnson Space Center.

Within CLIPS, the facts are the data that induce execution, while the rule set resides inside of the knowledge base (Giarratano, 1989). The rules in the TIPS are based on the past experience of a human expert and the current comparison between meteorological parameters and the atmosphere. The necessary meteorological parameters are provided by a single-station nowcast analysis program (SSNAP) that was developed in-house at the U.S. Army Atmospheric Sciences Laboratory (ASL), White Sands Missile Range, New Mexico, to examine individual atmospheric soundings (Scheinartz et al., 1990).

Additionally, the TIPS is run in a forward chaining mode; that is, questions are asked internally and the answers returned are then annexed into the program's memory. Passner, Lee, and Raihl (1991) and Passner et al. (1990) provide a complete description of the TIPS overall design and internal decision making process.

GOPAD is essentially a machine-derived expert system, created by Dr. Kenneth Young of the University of Arizona's Atmospheric Sciences Department. By machine-derived, the authors mean that human input is not necessary in creating the rule base. The knowledge base consists of a large source of historical meteorological data (such as rawinsonde, surface mesomet, and numerical model output) and associated ground truth (the outcomes of the parameter that the model is attempting to forecast).

Actually, GOPAD exists in two versions, which for simplicity will be labeled GOPAD I and GOPAD II throughout the remainder of the text.

The more recent version, GOPAD II, operates in a VAX environment and is generally superior to GOPAD I. GOPAD II extends the multidiscriminant analysis (MDA) variable selection process of Miller (1962) and the analogue forecasting method of Kruizinga and Murphy (1983). Essentially, GOPAD II finds the optimal combination of variables and linear indices of correlated variables that contain the majority of the predictive information within a given historical data set. Having done so, GOPAD II optimizes the n-space scaling and the neighborhood size to maximize a measure of forecast performance such as the Brier-based skill score (Murphy and Daan, 1985). This approach is similar to the k-nearest neighbor search of Leon Cooper's Reduced Coulomb Energy (RCE) algorithm; and it has the advantage of direct access to all the other forecast parameters that were not used in training the model. Hence, a GOPAD II forecast model can display a wide spectrum of forecast parameters desired from the data variables (Young and Lampru, 1989).

GOPAD II has been run with a high degree of success at SHOOTOUT-89 (Moninger, 1991) and over West Germany (Young and Dumais, 1991a and 1991b). The papers of Young and Lampru (1989), Young and Dumais (1991a and 1991b), and Young and Gall (1991) all discuss the GOPAD II software in much greater detail.

The earlier version of the software, GOPAD I, is essentially a hybrid neural net approach based on the back propagating learning algorithm. This algorithm is a network of discriminants (perceptrons) with vectors of weights corresponding to the variables of the input data vector. The algorithm is trained rather than programmed, by providing a large number of input data examples with the associated ground truth. As each new set of historical data is fed into the learning model, each discriminant is evaluated by multiplying the discriminant vector by the input data vector. Positive values are interpreted as true and negative values as false. If the discriminant is incorrect, it is adjusted to correct the classification; otherwise, it is left alone (Lampru, 1989).

Unlike the original treatise of MDA, GOPAD I permits (1) an unlimited number of linear discriminants to be placed between groups and (2) the data field to be partitioned into regions defined by the probability of occurrence of the

given event. Probability classes are defined by a set of linear discriminants called a binary prediction unit (BPU). Young (1987) discusses the GOPAD I software in complete detail.

Due to the in-house availability of the GOPAD I software and the desire to test a strictly neural net, the GOPAD I software was selected for this experiment, even though the GOPAD II software would probably provide a more skillful probability of precipitation (PoP) forecast model for Oklahoma.

There have been two previous tests using GOPAD I. The first was conducted in 1987 at Tucson, Arizona, where five separate models were developed to forecast warm season PoP for the weather service office in Tucson. This forecast was designed as a 19- to 31-h PoP forecast using 12 yr of Tucson rawinsonde data as potential predictor variables (PPV). Results showed that model Brier-based skill scores (fractional improvement over climatology) ranged from +10.2 to +20.6 percent compared to +1.3 percent at the weather service office (Young, 1987). Murphy (1985) gives average skill scores for warm season PoP forecasts for 85 stations in the United States during 1980. He notes an average skill score of +26.5 percent for the 12- to 24-h forecast period and +21.8 percent for the 24- to 36-h period.

The second test was done at Atlanta's Hartsfield International Airport in 1987. This PoP model(s) used 1200 Universal time coordinated (UTC) rawinsonde data for three stations near Atlanta as PPV and was designed to forecast summer PoP. The test valid period was 1200 to 0000 UTC. Results indicate that GOPAD-Atlanta possessed a Brier-based skill score of +23.6 percent compared to +20.9 percent for the Atlanta National Weather Service (NWS) and +16.3 percent for the Limited Finite Mesh (LFM)/Model Output Statistics (MOS) (Lampru, 1989).

2. RESEARCH STRATEGY

Both the TIPS and GOPAD I utilized data from 1 April through 30 (29 for GOPAD I) June 1990 for model verification. The TIPS thunderstorm and severe weather tests run on a PC microcomputer, and the GOPAD I PoP model runs on an IBM-compatible PC.

2.1 THE TIPS EXPERIMENTAL DESIGN

The TIPS was used daily to produce a subjective probability forecast of thunderstorm and severe weather for the 12-h period 1500 to 0300 UTC (the next day). The possible subjective probabilities issued by a TIPS forecast were for thunderstorms: 0, 30, 60, 80, and 100 percent; and for severe weather: 0, 25, 35, 45, and 70 percent. Each forecast was generated after analyzing the 1200 UTC morning sounding (for Norman) received from the SSNAP program. If convection was occurring at Norman at 1200 UTC, then no forecast was made for that day (Passner et al., 1990).

The test was for an area within 100 km of the Norman sounding site. Brier-based skill scores versus the 1990 sample and monthly climatologies were calculated for this region and computed separately for thunderstorm and severe weather probability forecasts. Verification criteria for severe weather follow that of the NWS discussed in Passner et al. (1990).

For this experiment, the TIPS rule set developed was site specific. Rules were developed for the prediction of convective activity in Oklahoma using the 1989-1990 skew T - Log p data from Norman, Oklahoma. These rules were derived by subjectively finding the most "consequential" meteorological variables in the prediction of thunderstorms and severe weather. Since the rule set was trained on data from April and May only, a decision was made not to include June as part of the TIPS forecast domain, although GOPAD I did make forecasts for that month.

2.2 GOPAD I EXPERIMENTAL DESIGN

GOPAD I was used to produce daily PoP forecasts for a circular region of 100 km radius enclosing Norman. This region is identical to that used by the TIPS model and has been discussed previously. The GOPAD I Oklahoma model was designed to issue one of five possible PoP forecasts for the period 1200 to 1200 UTC, those being 0, 20, 40, 60, and 80 percent. Each probability level was defined by a BPU consisting of a set of 11 linear discriminants.

The daily forecasts were generated from the 1200 UTC upper-air sounding data of several sites in the Southern Plains and the Southeast. These data comprised the original set of historical PPV. Similar to TIPS, Brier-based skill scores were calculated against both the sample and monthly climatologies of the training set (1985 to 1989) to get a measure of the model's forecast ability.

The following nine U.S. rawinsonde sites used 1200 UTC sounding data as PPV: Amarillo, Brownsville, Midland, and Stephenville, Texas; Dodge City and Topeka, Kansas; Little Rock, Arkansas; North Platte, Nebraska; and Monett, Missouri. Precipitation totals (1200 to 1200 UTC) were available from 30 sites within the 100-km radial GOPAD I forecast region, representing the ground truth data (table 1). Note that since the TIPS only needed 1990 ground truth data, it was verified using actual radar summary data that was available. Data was obtained from the U.S. Air Force Environmental Technical Applications Center in Asheville, North Carolina, and the Oklahoma Climate Survey (OCS). These data covered the months of April, May, and June of the years 1985 to 1990, with 1990 being left as the independent verification year.

TABLE 1. GOPAD I OKLAHOMA GROUND TRUTH

Ada	El Reno	Pauls Valley
Amber	Guthrie	Piedmont
Anadarko	Kingfisher	Prague
Blanchard	Konawa	Purcell
Chandler	Lindsay	Seminole
Chickashaw NRA	Lookeba	Shawnee
Chickasha Station	Marlow	Stella
Cox City	Meeker	Tecumseh
Crescent	Norman	Union City
Duncan	Oklahoma City	Wewoka

From each sounding, data from 18 levels were retained as PPV for the GOPAD I model. Temperature and u,v wind components were analyzed between 850 and 100 mbar at increments of 50 mbar (except for 25 mbar increments above 200 mbar). Dew-point temperatures were taken every 50 mbar between 850 and 400 mbar. All missing data were interpolated for using a method identical to that discussed by Young (1991) and Dumaïs et al. (1991). Interpolation skills (compared to using climatological mean values) proved to be substantially high, typically greater than +40 percent. The exceptions were dew-point temperature interpolations in the summer, which tended to possess skills only slightly better (less than +10 percent) than the long-term averages.

Once the data set was complete, additional PPV were added by creating simple single-station linear indices (really just differences), including vertical lapse rates, dew-point spreads, and wind shears. This is similar to but substantially less complex than the approach taken by the GOPAD II model to create linear indices of correlated variables. Due to computer considerations, not all possible differences were incorporated as PPV; however, we felt that enough were included that the essential predictive information inherent in these indices could be captured--1170 PPV were used.

MDA's variable selection process was used to reduce the original 1170 PPV into a small subset of model predictor variables (PV) that best discriminated between the rain and no rain days. MDA was run utilizing all of the data from 1985 to 1990, and was done separately by month. Hence, the best set of predictors for April, May, and June was merged into a final PV set for the GOPAD I Oklahoma model. Only 29 PV were selected to train the model. Before training, all PV were normalized (zero mean, unit variance) since the GOPAD I heuristics behave better on variables of nearly the same size.

3. MODEL RESULTS

The verification (1990) skill scores of both the TIPS and GOPAD I models are presented in table 2 and table 3, respectively. The training results of the GOPAD I model showed an overall skill of +41.3 percent over the sample climatology and +39.4 percent over the individual monthly climatologies.

The GOPAD I model showed training skill scores for April (+54.8 percent) substantially higher than for either May or June. This may largely be because the atmospheric PV used by the model are derived from a synoptic network of rawinsonde data. These types of predictors are probably most important in the early spring, when synoptic scale forcing still dominates. However, as meso-scale and smaller scale forcing mechanisms become more dominant later in the summer, a model derived on synoptic scale predictors can be expected to degrade. Additionally, verification becomes more difficult as the size of individual convective elements decreases.

Since radar data was available for the region in 1990 (to verify the TIPS forecasts), we compared the number of 1990 days with rain occurrence with the number of "hits" the GOPAD I ground truth network of point sites had indicated, to see how many occurrences the GOPAD I network had missed. The results showed that not a single "hit" was missed. However, due to a small gap in coverage located in the south-central sector of the GOPAD I ground truth verification region, it is quite possible that a number of "hits" were missed over the

training period. Nonetheless, the comparison of the 1990 GOPAD I network data to that of the 1990 radar summary data lend confidence that the model is at least a quasi-low-resolution single region model as defined by Young and Lampru (1989).

TABLE 2. TIPS MODEL SKILL SCORES OF 1990

TIPS Results for Thunderstorms			
Months	Skill Scores		Bias
	Sample (%)	Monthly (%)	
April	+38.8	+36.4	+0.9
May	+59.8	+59.4	+0.4
TIPS Results for Severe Weather			
Months	Skill Scores		Bias
	Sample (%)	Monthly (%)	
April	+32.8	+32.1	-0.2
May	+7.5	+2.6	+1.0

TABLE 3. GOPAD I SKILL SCORES OF 1990

Months	Skill Scores		Bias
	Sample (%)	Monthly (%)	
April	+22.5	+33.4	-4.4
May	+10.9	+13.6	+0.6
June	+30.3	+31.8	-1.2
Overall	+21.6	+26.1	-5.0

Neither the GOPAD I nor the TIPS model skill scores were substantially different using the monthly climatologies rather than the sample climatology.

Following Young (1987), the overall bias of the models was computed for the verification year. It was discovered that the GOPAD I model possessed a substantial bias that reduced the overall skill of the forecast performance.

The GOPAD I model tended to "underforecast" rain events, as is evidenced by the high bias score of -5.0. However, this bias is largely a result of the April forecasts (bias of -4.4) rather than the May (+0.6) or June (-1.2) forecasts. We expect that the skill of the April GOPAD I forecasts can be improved further by "adjusting" the probability forecasts for this bias.

The validity of the GOPAD I model was checked using a Monte-Carlo approach discussed by Young (1987). The p-value returned was less than 0.01, indicating that the skill scores were much higher than should be expected given the GOPAD I distribution of 1990 PoP forecasts.

Overall, both models performed extremely well when compared side by side in April and May. Skill scores were significantly high for both models, and when used together, they provided very informative forecasts. Table 4 lists all verified severe weather days for April and May 1990. Note that on all 12 days, at least one model gave a high probability of either rain, thunderstorms, or severe weather. TIPS only missed 2 days, but on each of those days GOPAD issued a PoP of 80 percent.

TABLE 4. SEVERE WEATHER DAYS OF 1990

APRIL AND MAY

Day	GOPAD I PoP	TIPS PoP Thunder	TIPS PoP Severe
<u>April</u>			
13	80	100	45
16	80	100	70
21	80	100	25
22	80	0	0
25	80	100	45
<u>May</u>			
5	80	0	0
11	80	100	45
15	80	100	70
18	80	100	70
19	80	100	45
26	40	80	70
29	80	100	25

TIPS forecast a PoP for thunderstorms of at least 60 percent on 30 occasions during April and May. During that time, there were 28 forecast days when thunder was observed. On only three of those days did TIPS forecast a thunderstorm probability of less than 60 percent. However, on each of those three days, the GOPAD I model issued a PoP of 80 percent. Additionally, out of a total of 62 possible rain days in 1990, GOPAD I issued a PoP of less than 40 percent on those days only three times. On 13 days during the period, the GOPAD I model issued a PoP of at least 60 percent when no measurable rain occurred.

4. CONCLUSION

Both the TIPS and GOPAD I Oklahoma forecast models proved to be very skillful at forecasting spring season convection over Oklahoma. If a substantial bias to "underforecast" April events is removed from the GOPAD I model, that model's performance would improve substantially. Used together, the models correctly forecast every one of the 30 thunderstorm days reported in region 1 during April and May of 1990. Over this same period, TIPS correctly forecast 10 of the 12 days when severe weather was reported in a 100-km region around Norman. On the 2 days that it missed, GOPAD I issued a PoP of 80 percent for the same region.

Although the models cannot be compared directly, the results show that when used together both expert systems have shown the ability to handle spring season convection quite well. Also, both human-derived and machine-derived knowledge bases can be used to successfully drive these systems. At the very least, these types of systems can be used to give sound guidance to the experienced forecaster, or particularly, to the SWO in a battlefield environment.

ACKNOWLEDGMENTS

The authors thank all personnel at the Oklahoma Climate Survey and the U.S. Air Force Environmental Technical Applications Center who provided the data necessary for us to develop our models.

REFERENCES

- Dumais, R. E., Jr., R. Flanigan, and K. Young, 1991: Applying Goal-Oriented Pattern Detection to the Problem of Precipitation Forecasting in West Germany. In Proceedings of the Eleventh Annual EOSAEL/TWI Conference, U.S. Army Atmospheric Sciences Laboratory, White Sands Missile Range, NM 88002-5501, 238-246.
- Giarratano, J. C., 1989: CLIPS User's Guide. Artificial Intelligence Section, Lyndon B. Johnson Space Center, Houston, TX.
- Kruizinga, S., and A. H. Murphy, 1983: Use of an Analogue Procedure to Formulate Temperature Forecasts in the Netherlands, Mon. Wea. Rev., 111:2244-2254.
- Lampru, P. D. Jr., 1989: Artificial Neural Nets for Weather Forecasting. In Proceedings of the Ninth Annual EOSAEL/TWI Conference, Vol II, U.S. Army Atmospheric Sciences Laboratory, White Sands Missile Range, NM 88002-5501, 172-179.
- Miller, R. G., 1962: Statistical Prediction by Discriminant Analysis. Meteorol. Monogr., 4:54.
- Moninger, W. R., 1991: Shootout-89, A Comparative Evaluation of Knowledge-based Systems That Forecast Severe Weather. Bull. Amer. Meteorol. Soc., 72:1339-1354.

- Murphy, A. H., 1985: Probabilistic weather forecasting. Probability, Statistics, and Decision Making in the Atmospheric Sciences. Westview Press, 337-377.
- Murphy, A. H., and H. Daan, 1985: A forecast evaluation. Probability, Statistics, and Decision Making in the Atmospheric Sciences. Westview Press, 379-438.
- Passner, J., R. Scheinhartz, R. Lee, and K. Larkin, 1990: Forecast Applications for the Staff Weather Officer. In Proceedings of the Tenth Annual EOSAEL/TWI Conference, U.S. Army Atmospheric Sciences Laboratory, White Sands Missile Range, NM 88002-5501, 310-316.
- Passner, J., R. Lee, and P. Raihl, 1991: An Evaluation of the U.S. Army Atmospheric Sciences Laboratory's Thunderstorm Expert System During the 1990 Thunderstorm Season. In Proceedings of the Eleventh Annual EOSAEL/TWI Conference, U.S. Army Atmospheric Sciences Laboratory, White Sands Missile Range, NM 88002-5501, 391-400.
- Scheinhartz, R. L., R. Lee, and K. Larkin, 1990: Development of a Single Station Analysis Package Phase I: Focus on Sounding Analysis and Severe Thunderstorm Forecasting. Interim Technical Report, U.S. Army Atmospheric Sciences Laboratory, White Sands Missile Range, NM 88002-5501.
- Young, K. C., 1987: An Adaptive Learning System Applied to the Problem of Forecasting Convective Precipitation. Technical Report, Department of Atmospheric Sciences, University of Arizona, Tucson, AZ 85721.
- Young, K. C., and R. E. Dumais, Jr., 1991a: The Role of the Westerlies South of Australia in Triggering Strong El Nino Episodes. (Submitted to Mon. Wea. Rev. for publication.)
- Young, K. C., and R. E. Dumais, Jr., 1991b: Using Artificial Intelligence for Single-Station Quantitative Precipitation Forecasting in West Germany. (To be submitted to Wea. Forecasting for future publication.)
- Young, K. C., and R. L. Gall, 1991: A Streamflow Forecast Model for Central Arizona. (Submitted to Mon. Wea. Rev. for publication.)
- Young, K. C., and P. D. Lampru, 1989: Goal-Oriented Pattern Detection (GOPAD) for Tactical Mesoscale Weather Forecasting. In Proceedings of the Tenth Annual EOSAEL/TWI Conference, U.S. Army Atmospheric Sciences Laboratory, White Sands Missile Range, NM 88002-5501, 72-81.

RESULTS OF MAN-MADE FOG EXPERIMENTS

Robert A. Sutherland
Young P. Yee
Frank D. Eaton
William A. Peterson
U.S. Army Atmospheric Sciences Laboratory
White Sands Missile Range, NM 88002-5501

Miklos Z. Kiss and Craig E. Foster
New Mexico State University
Las Cruces, NM 88003

ABSTRACT

An update on the results of an experimental program designed to explore the possibility of producing man-made fogs for use in cloud physics research, materiel testing, and possibly large area screening applications is presented. Previous research, published in the 1990 EOSAEL/TWI Proceedings, has shown that it is possible with existing state-of-the-art commercial systems to produce very dense, optically thick, artificial fogs over length scales on the order of 100 meters or so under moderate to favorable meteorological conditions. Experiments to date have been performed in the field with a high pressure 240 nozzle direct impaction spray atomization system manufactured by Mee Industries, Inc. Screening effectiveness is sensitive to both the ambient temperature and the relative humidity as borne out by both theoretical models of droplet evaporation and direct observation. Previous measurements of droplet size spectra indicate a broad droplet size distribution with a mass median diameter on the order of 10-20 μm . Results are comparable to values reported for natural fogs although the man-made fogs contain additional submicron droplets not reported for natural fogs. New results, based upon spectral transmission measurements, support the conclusion that the artificial fogs are indeed multiband obscurants out to the far infrared. In fact the extinction spectrum from the visible through the mid infrared spectral regions is remarkably flat even in the 3 - 5 μm region where we would expect some line absorption due to water droplets and water vapor. In the far infrared region, the transmittance spectrum exhibits a marked peak at about 12 μm although extinction is still relatively strong.

1. INTRODUCTION

In a previous paper (Sutherland, et al., 1991) we reported on preliminary results derived from our initial efforts to explore the concept of using modern, high throughput, liquid spray atomization systems to generate large area water fogs as a tool for cloud physics research studies and possibly large area screening applications. In this earlier work we were able to demonstrate that a dense "artificial fog" on the order of a few hundred meters or so in length could be produced with a commercially available system manufactured by Mee Industries (Mee, 1976, 1977). The success of the Mee system is attributed to the high pressure direct impaction spray atomization method which allows for a significantly higher throughput than other methods based upon the more common evaporation-condensation technique used in previous studies to produce fogs (Carlson, 1989; Carlson and Shaffer, 1980).

A photograph of the Mee system as configured during the 1990 experiments is shown in Fig. 1 along with a photograph of the resultant "artificial" fog plume.

The heart of the Mee systems is the specially manufactured high pressure direct impaction spray atomization nozzles that actually convert the water stream into small droplets. The particular system used here is comprised of several manifolds each consisting of a 5 by 8 array of 40 nozzles total spaced from 8 to 10 centimeters apart. Experiments here were conducted using either one, two, or three manifolds operating simultaneously. When operated at the recommended

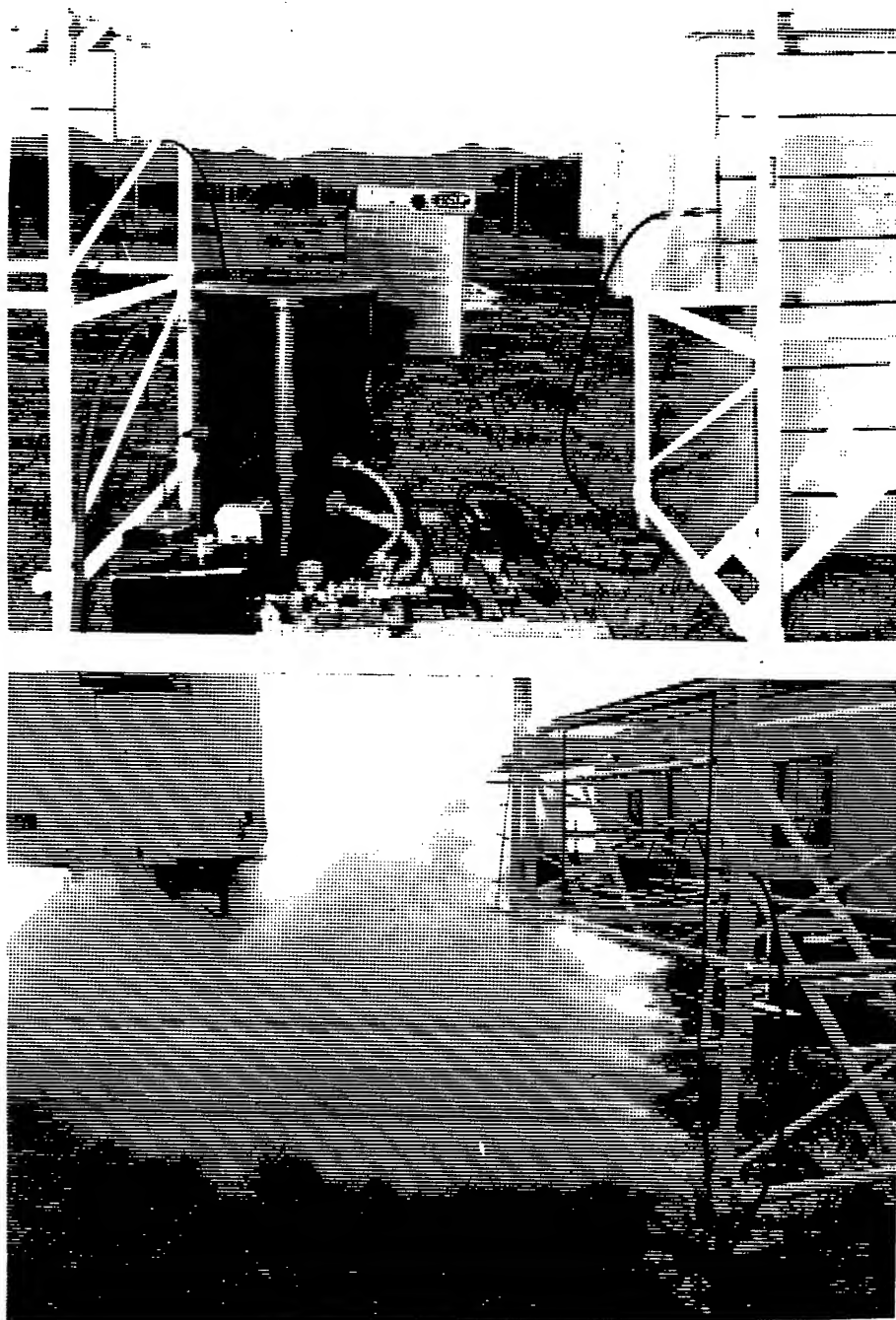


Figure 1. Photograph of the Mee Industries artificial fog system. The 55 gallon holding drum and gasoline powered high pressure pump is shown in the foreground. The system is connected to one of the 40 nozzle manifolds to the right in the photograph and shown producing fog in the lower photograph. The instrument in the center is a Knollenberg drop size spectrometer.

pressure of 1000 pounds per square inch the flow rate is 1.2 gallons per 40 nozzle array per minute in the form of a dense white spray very similar in appearance to a natural fog.

Earlier measurements were focused on overall system performance, plume size, and the droplet size spectra. In this paper we continue the study on artificial fogs and report on new measurements obtained in the field with the Mee system and the ASL Mobile Atmospheric Spectrometer (MAS, Peterson, et al. , 1991) system. In particular, we report on results of spectral transmittance measurements from the visible through far infrared spectral regions.

2. EXPERIMENTAL METHODS

Two series of experiments were conducted; one was concentrated on the visible and near infrared spectral region and the other was concentrated on the mid and far infrared spectral region. The experimental set up is shown in the sketch of Fig. 2 which shows the three basic elements involved, that is; (a) a high intensity broadband radiation source, (b) a visible-through-infrared high resolution receiver, and (c) the Mee water fog generator system.

As configured here, the total source-receiver line of sight was 200 meters in length along a horizontal line 2 meters above the surface. The fog was released at a point approximately one quarter the distance between the source and receiver and from 3 to 5 meters up wind. During the course of the experiments the wind conditions were such that transmissometer optical path was nearly crosswind. During the first set of experiments the fog arrays were arranged vertically so

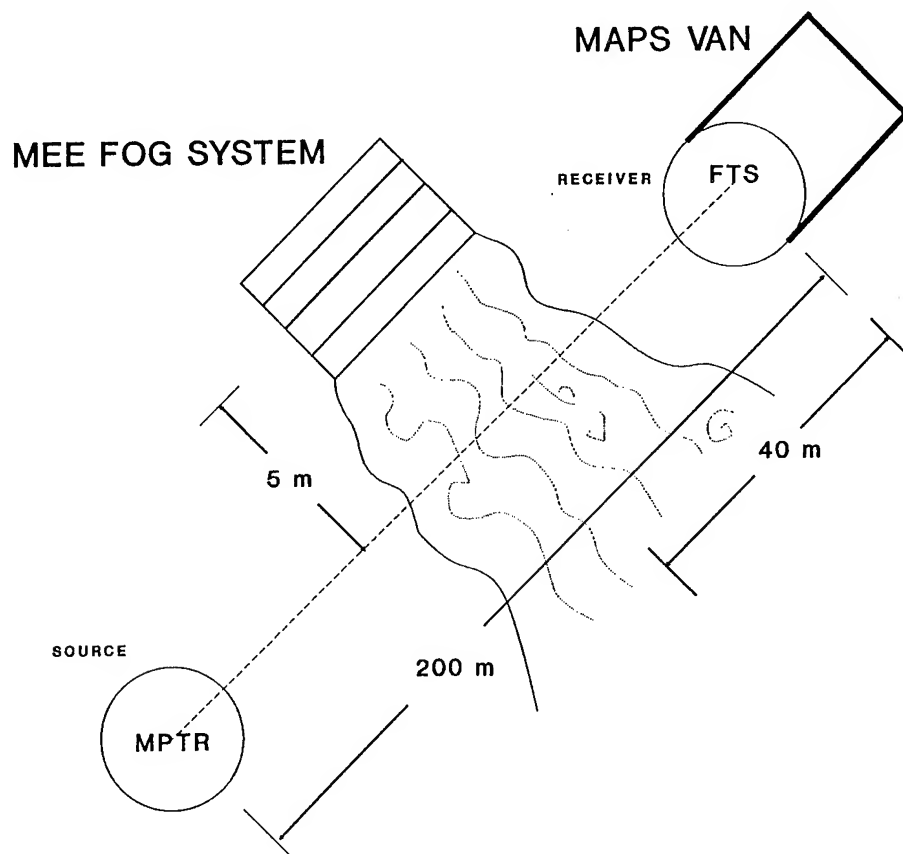


Figure 2. Sketch of the experimental arrangement showing general locations of the spectrometer source (A), receiver/detector (B), and artificial fog generator (C).

that the fog exited the system in an initial horizontal direction. In the latter experiments we found it to be more convenient to arrange the arrays horizontally so that the fog exited the system in an initial upward direction. In any case the resultant plume would tend to be lower to the ground because of the negative buoyancy caused by evaporative cooling.

The radiation source is a two part visible/infrared composite made up of two tungsten-halogen-quartz (visible band) lamps and five infrared "glow bars" arranged in a hexagonal array. This source is essentially uncollimated and provides a broad spectral emission range from the visible through infrared in a single unit. The system has been field tested as a part of the U.S. Army version of the Multi-Path Transmissometer Radiometer (MPTR) system described by De Jong, et al. (1988). For our experiments the source was operated in the steady, unchopped, mode.

The heart of the receiver system is a Fourier transform spectrometer (FTS) described in more detail by Peterson, et al. (1991). The collector is an 0.80 meter Coude type Cassegrainian telescope aligned horizontally on a three meter long optical bench housed inside a 4 meter diameter astronomical dome. The dome is supported on an independent chassis directly to the earth and as such is isolated from unwanted external vibrations. In order to cover the entire visible to far-infrared spectral region two interchangeable receiver systems were used; one consisting of a quartz beam splitter and silicon photodetector for the shorter wavelengths (8,500 to 15,000 cm^{-1}) and the other consisting of a potassium bromide beamsplitter and cryogenically cooled mercury-cadmium-telluride photodetector system for the longer wavelengths (750 to 7000 cm^{-1}). Configured as such the system resolution is 8 cm^{-1} for the lower wavelength region and 4 cm^{-1} for the higher wavelength region. At this resolution, the system is limited to a maximum spectral scan rate of approximately one scan per second. This is a limitation of the system which can cause problems in co-adding, or averaging, spectra in the presence of rapidly varying signals due, for example, to fluctuations in obscurant concentrations. Our experiments were all performed early in the morning when conditions were relatively stable, however, it was clear from observation that even under these conditions the plume concentrations were highly fluctuating, thus all single scan data were considered in the analysis. During the experiments a video camera, aligned along the optical axis, was operated continually to record the actual behavior of the fog spray as it crossed the line of sight.

In field applications, the obscurant line of sight transmittance is computed from two measurements, one usually taken either before or after the event to serve as a (unobscured) clear air baseline, and the other taken after the obscurant release. It is usually assumed that the plume width is small compared to the total source-receiver distance so that any modification of the intervening clear air due to the obscurant is negligible. Under this assumption the fog transmittance, also termed the "relative" transmittance is obtained from the following ratio:

$$T_{\text{fog}}(\nu) = \frac{I_{\text{tot}}(\nu)}{I_{\text{clr}}(\nu)} \quad (1)$$

where $I_{\text{tot}}(\nu)$ is proportional to the total direct radiance received in the presence of the obscurant and $I_{\text{clr}}(\nu)$ is proportional to the clear air direct radiance.

The signal at the spectrometer receiver is comprised of two parts; one being the directly transmitted radiance from the source that is needed in Eq. (1), and the other being an error, or background, signal due to scattering of radiation into the line of sight from the surroundings and thermal emission and reflections from the system internal optics. Under these circumstances the signals in Eq. (1) must be corrected to remove the effects of the background component, thus Eq. (1)

is more completely expressed as:

$$T_{fog}(\nu) = \frac{S_{tot}(\nu) - B_{tot}(\nu)}{S_{clr}(\nu) - B_{clr}(\nu)} \quad (2)$$

where B represents the background, or error signal. The four radiational quantities in Eq. (2) are all measured independently and are more completely defined as follows:

$S_{tot}(\nu)$ = the raw spectrometer signal obtained along the direction of the (transmissometer) source with the fog present,

$B_{tot}(\nu)$ = the raw spectrometer signal obtained along the direction of the (black) background with the fog present,

$S_{clr}(\nu)$ = the raw spectrometer signal obtained along the direction of the source without the fog present,

$B_{clr}(\nu)$ = the raw spectrometer signal obtained along the direction of the background without the fog present.

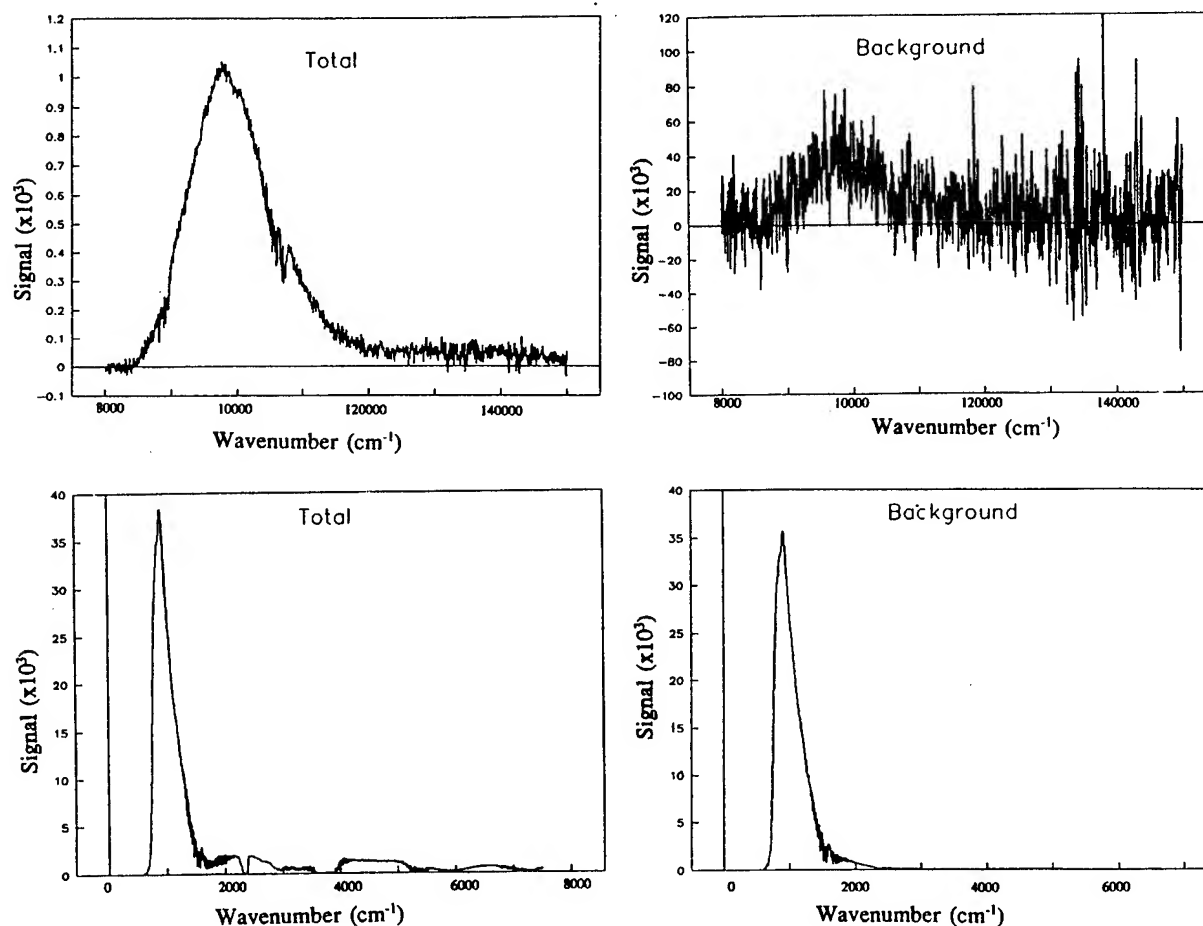


Figure 3. Typical plots of total raw spectrometer signals obtained with the fog present; (a) total signal for short wavelength region, (b) background signal for short wavelength region, (c) total signal for long wavelength region, and (d) background signal for long wavelength region.

In operation the procedure is to measure the four quantities in as short a time interval as possible in order to avoid complications due to the changing conditions. In practice the clear air spectrum is usually obtained both prior to and after the event in order to detect changes and then one or the other is used in Eq. (2). The background terms are obtained by simply taking a reading with the source blocked or with the collecting telescope aligned slightly off the source. The former method is preferred in conventional "chopped" source transmissometers, however, the latter method is preferred here because it can be fully implemented at the receiver end of the path. Some typical plots of the raw spectrometer signals collected during the experiments are shown in Figs. 3 and 4.

In Figs. 3 and 4 the vertical axis is proportional to the raw spectrometer signal and as such is represented by arbitrary units. Also some caution is advised in interpreting the actual spectral shape because the signals have not been corrected for the system response function which is strongly wavelength dependent. The units are rigorous in the relative sense, however, so that intercomparisons can be made. It is clear, for example, for the shorter wavelengths (3a and 3b) that the total signal is much larger than the background signal (note difference in vertical scale) so that errors in differencing in

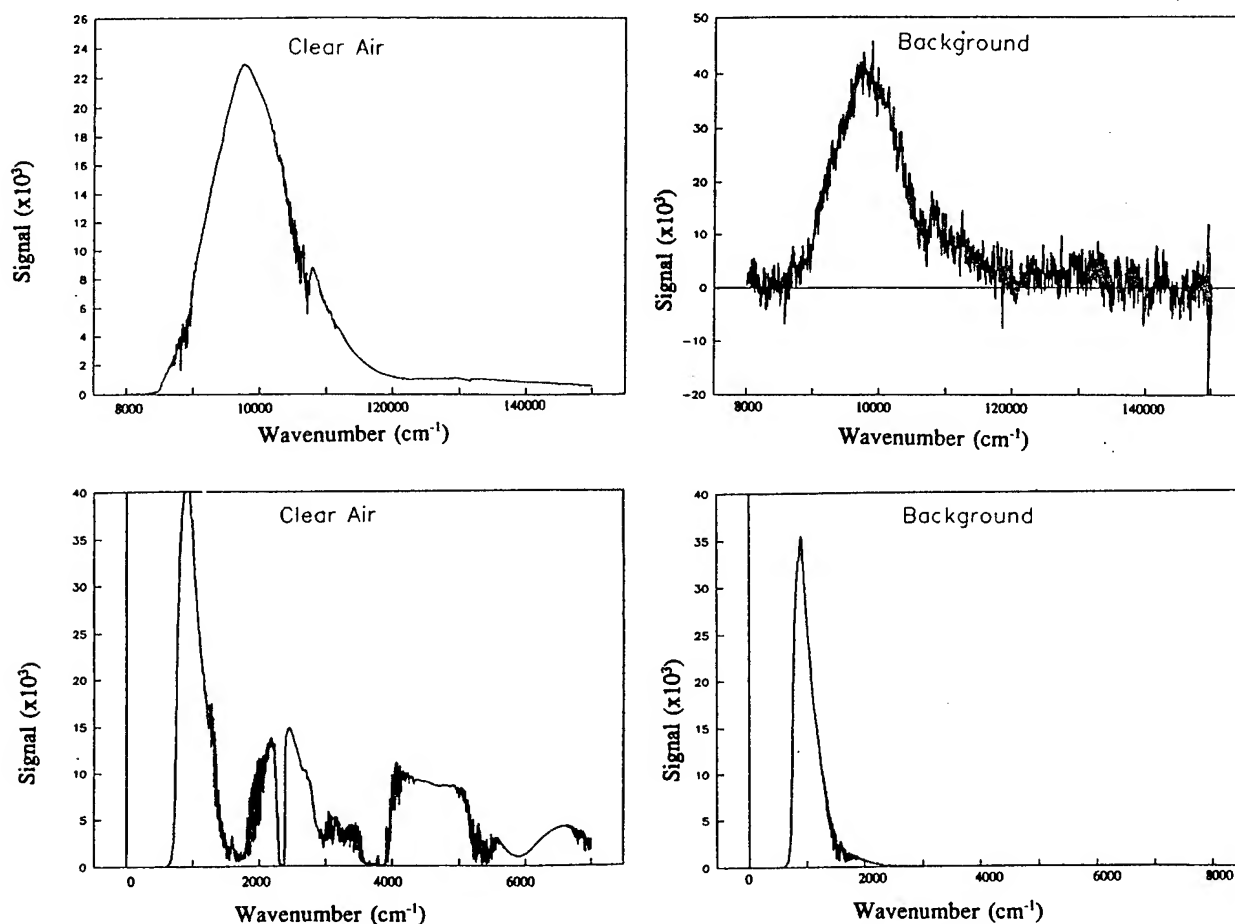


Figure 4. Typical plots of clear air raw spectrometer signals obtained without the fog present; (a) total signal for short wavelength region, (b) background signal for short wavelength region, (c) total signal for long wavelength region, and (d) background signal for long wavelength region.

Eq. (2) are minimal. For the longer wavelengths, however, the differences are not as large and this is due to the fact that most of the error signal is due to thermal emissions from internal optical components rather than path radiance.

This also explains why the background signal for both the total and clear air spectra are nearly identical as evidenced from comparison with the plots of Fig. 3d and 4e.

With the four basic spectra so determined, Eq. (2) is then applied on a wavelength by wavelength basis to determine the fog transmittance as reported in the next section.

3. RESULTS AND DISCUSSION

Fog transmittance plots as obtained from the two sets of experiments are shown in the four plots of Fig. 5, where, for convenience we have broken the spectrum up into the four commonly treated atmospheric spectral window regions. The first set of experiments were performed during the early morning of 25 July 1991 and

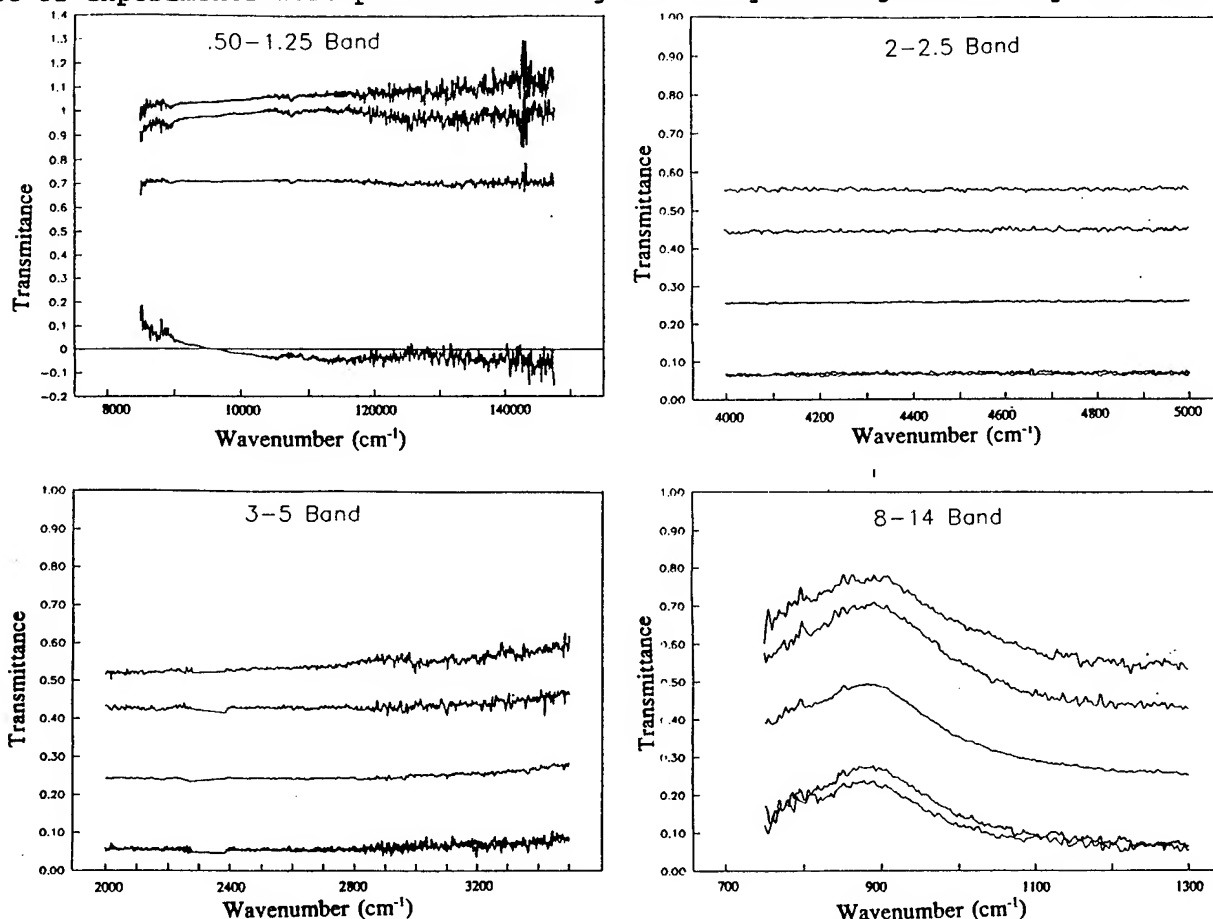


Figure 5. Transmittance spectra of artificial water fogs as generated with the Mee system; (a) 0.50 - 1.50 μm , (b) 2.0 - 2.5 μm , (c) 3.0 - 5.0 μm , and (d) 8.0 - 14.0 μm .

covered the lower wavelength spectral region. Meteorological conditions during this period were overcast with 93% relative humidity and 20°C air temperature. The second set of experiments were performed during the early morning of 26 September 1991 and covered the long wavelength spectral region. Meteorological conditions during this period were clear with 65% relative humidity and 18°C air temperature.

In Fig. 5 we show the results from several individual scans obtained at different times plus the ensemble average (plotted in bold) obtained from several individual spectra. The individual spectra shown in Fig. 5 were taken at widely

separated times during the experiments and this is the reason for the different overall transmission levels. That is, in conducting the experiments the overall obscuration level was periodically raised and/or lowered by either turning on or off one or more of the three fog arrays. This was done so that we could observe any differences in the individual spectra that might occur as a function of obscurant concentration level, which, according to the results did not occur, as evidenced by the reproducibility in the overall spectral shape.

The fine structure in the plots, which tends to diminish in the average, is, in part, due to noise in the system, being somewhat enhanced at the shorter wavelengths as expected for this system. However, even though the experiments were, by design, all conducted early in the morning during stable conditions the plume was generally observed to be non-homogeneous even over length scales on the order of the collecting aperture and this may also be an origin of some of the fine structure in the data. The fact that the noise tends to be suppressed in the average tends to rule out the influence of any unidentified absorptions due to impurities. One possible exception may be the enhancement peaks in the 700 to 800 cm^{-1} region which seem to persist even in the average. It is worth noting that the source of water used here was ordinary tap water characteristic of the White Sands Missile Range area which our chemical analysis showed to have significant amounts of salts and minerals, as expected. The origin of these peaks are not certain but may be due to emission lines from certain as yet unidentified impurities.

A most noteworthy aspect of the spectra is the near featureless nature of the (averaged) plots and the fact that, for the lower three bands, the overall transmittance is independent of wavelength as evidenced by the remarkably flat spectrum. The next most marked feature is the increase in transmittance in the far infrared band, beginning very near 700 cm^{-1} and resulting in a peak at approximately 900 cm^{-1} followed by a decrease back to the original level beyond the peak. This general behavior is at least in part consistent with measurements of droplet size in our 1990 paper (Sutherland, et al., 1990) which indicated a very broad droplet size spectrum up to at least 10 - 20 microns in diameter. It is known from the well established Mie scattering theory that under these circumstances one may expect a nearly flat transmission spectrum. On the other hand the apparent peak at around 900 cm^{-1} is explained from consideration of the bulk refractive index spectra of water which shows a marked increase beginning near 900 cm^{-1} (Hale and Querry, 1973).

The most surprising result in the data is the near featureless form of the transmittance spectra in the mid infrared band. This band is known to contain a strong absorption peak due to both water droplets and water vapor (Klett and Sutherland, 1988) which has been found to be manifest in the extinction spectra of water bearing, or hygroscopic, chemical smokes (Peterson, et al., 1991). The major difference here is, of course, the droplet size spectrum which indicates much smaller droplets for the chemical smokes than for our artificial fogs.

4. SUMMARY

Results of our experiments show that artificial water fogs generated using the high pressure direct impaction technique can be produced that are effective as obscurants over the entire visible to far infrared spectral region. Actual measurements of spectral transmittance indicate a remarkably constant extinction coefficient from the visible through mid infrared spectral regions with surprisingly little structure in the 3 - 5 μm water band absorption region. In the far infrared the fog transmittance spectrum shows a broad peak beginning at about 750 cm^{-1} and reaching a maximum at about 900 cm^{-1} . Results here are in qualitative agreement with our earlier experiments which showed a broad droplet size spectrum with droplets ranging from as small as 0.10 μm to as large as 20 μm in diameter which is similar to natural fogs.

Further experiments are planned involving an upcoming LIDAR and optical scintillations field test and possible materiel testing. Further analysis of the data is under way to compare results with expectations based upon both theory and

measurements in natural fogs. Other experiments using a laboratory scale system are underway to test the effects of trace impurities on the optical and physical properties of the artificial fog plumes.

ACKNOWLEDGEMENTS

The authors acknowledge the assistance of Mr. William M. Gutman of the New Mexico State University Physical Sciences Laboratory in setting up the MAPS van and in assisting with the collection of the FTS data. Portions of the research were supported through the LABCOM In-house Laboratory Independent Research (ILIR) Program. Ms. Irene Pittsenbarger of the Atmospheric Sciences Laboratory typed the final manuscript.

REFERENCES

Carlson, H.R., 1989: Anomalous Absorption by Atmospheric Water Vapor and Stabilized Water Fogs in the Infrared and cm-Wave Regions, Chemical Research, Development and Engineering Center Technical Report CRDEC-TR-111, Aberdeen Proving Ground, MD.

Carlson, H.R. and R.E. Shaffer, 1980: Optical Properties (0.63-13 μm) of Water Fogs Stabilized Against Evaporation by Long-Chain Alcohol Coatings, Journal of Colloid and Interface Science, 82(1), 203-207.

De Jong, A.N., M.J. Roos, and P.J. Fritz, 1988: Smoke Characterization by Means of MPTR, IR1988-07, FEL-TNO, The Netherlands.

Hale, G.M. and M.R. Querry, 1973: Optical Constants of Water in the 200 nm to 200 μm Wavelength Region, Applied Optics, 12, 555-563.

Klett, J.D., and R.A. Sutherland, 1988: Effects of Atmospheric Moisture in Determining Obscurant Optical Properties from Field Data, Proceedings of the 9th Annual EOSAEL/TWI Conference, Physical Sciences Laboratory, New Mexico State University, Las Cruces, NM, 29-30 November 1988.

Mee, T.R., 1977: Man-made Fog for Freeze Protection & Microclimate Control, Proceedings of the International Society of Citriculture, 1, 203-208.

Mee, T.R., 1976: Research and Development of an Airborne Hygroscopic Spray System, Final Report Contract Number 14-060D-7634, Bureau of Reclamation, U.S. Department of Interior, Denver Colorado.

Peterson, W.A., D.M. Garvey, and W.M. Gutman, 1991: Spectrally Resolved Transmittance Measurements at Smoke Week XIII, Proceedings of the 1991 Battlefield Atmospherics Conference, Hinman Hall, Fort Bliss, Texas, December 1991.

Sutherland, R.A., F.D. Eaton, S.M. Squires, and M.Z. Kiss, 1990: Properties of Mechanically Generated Water Fogs, Proceedings of the 11th Annual EOSAEL/TWI Conference, Physical Sciences Laboratory, New Mexico State University, Las Cruces, NM, 27-30 November 1990.

Session IV

REMOTE SENSING

**Thursday
5 December 1991**

**Chairperson
Dr. Thomas Vonder Haar**

FOG MICROPHYSICS INFORMATION
FROM MULTISPECTRAL REFLECTANCE DATA

J. L. Behunek and T. H. Vonder Haar
Colorado State University
Fort Collins, CO 80523 USA

ABSTRACT

The diagnosis of fog microphysical characteristics such as drop size distribution and liquid water content have been investigated using near and middle infrared radiometric data from aircraft and satellite-borne sensors. Drop size information was estimated from 0.85 μm and 1.6 μm reflectance values. The 0.85 μm reflectances were related to the optical depth of the fog layer by application of the Mie scattering theory. Similar scattering calculations using the 1.6 μm data yielded information on drop size distribution, given the fog layer optical depth. Observations at 3.7 μm were added in order to estimate an index of liquid water content. The latter observations were interpreted with the help of LOWTRAN radiative transfer calculations and the previously derived estimate of drop size distribution. These techniques for estimating the microphysical properties of fog were applied to aircraft and satellite radiometer data collected near San Diego, California. The resulting estimates of drop size distribution and liquid water content were compared with microphysical measurements taken with in the fog layer by the instrumented aircraft. Future work will relate the estimated microphysical parameters to bulk properties such as the physical depth of the fog layer and horizontal variability.

1. INTRODUCTION

The diagnosis of fog microphysical characteristics such as drop size distribution and liquid water content have been investigated using radiometric data from aircraft and satellite-borne sensors. Detection of these quantities is important for a number reasons, including their impact on aircraft icing, visibility and multispectral extinction coefficient within the fog layer, and their potential as input for prognostic modeling of fog evolution. *In situ* microphysical measurements within fog layers rarely are available. Therefore, reliable remote sensing estimates of those quantities would be quite valuable. This fog microphysics investigation builds upon previous studies of the remote detection of nighttime fog by satellite (Behunek and Vonder Haar, 1990; Ellrod, 1989).

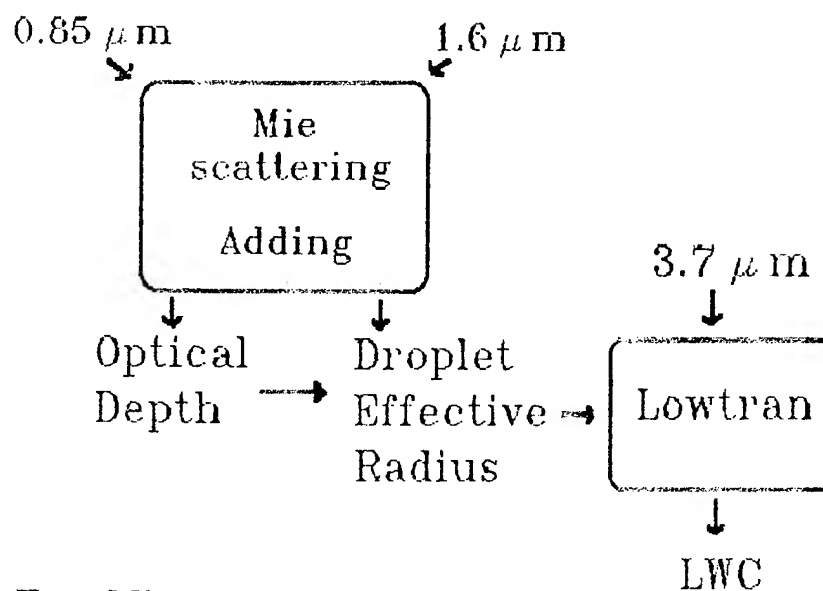
2. METHODOLOGY

Papers such as those by Twomey (1987), Wetzell and Vonder Haar (1986, 1990, 1991), and Stephens (1978a, b, c) have indicated the feasibility of diagnosing cloud optical depth, droplet effective radius, and liquid water content of water clouds from radiometric observations in the near infrared. It may be possible to apply similar techniques to fog, although this has not been demonstrated previously.

Whether fog layers typically have sufficient optical depth to allow reliable microphysical characterization is a question which needs to be addressed. This issue is examined using reflected radiance measurements in the $0.85\text{ }\mu\text{m}$ spectral band. $0.85\text{ }\mu\text{m}$ is a water vapor window band, in which negligible amounts of incident radiation are absorbed by water vapor. In addition, $0.85\text{ }\mu\text{m}$ radiation is not absorbed by water droplets to any significant degree, and backscattered radiation at this wavelength is virtually independent of droplet sizes within the cloud. $0.85\text{ }\mu\text{m}$ spectral reflectances depend primarily on the scaled optical depth of the scattering cloud layer. The scaled optical depth of fog layers is estimated in this study by comparing observations to theoretical radiative transfer calculations for cloud layers of varying optical depths in this band. These calculations are based on Mie scattering theory for the simulation of a single scattering event. The Adding method (Grant and Hunt, 1968) is utilized to represent multiple scattering given the single scattering characteristics.

Radiation in the $1.6\text{ }\mu\text{m}$ band differs from that at $0.85\text{ }\mu\text{m}$ in that it is absorbed significantly by water droplets. The amount of absorption, and thus the reflectance, is influenced by droplet size distribution. Wetzell and Vonder Haar (1990) have shown that droplet effective radius can be categorized from the cloud bidirectional reflectance at $1.6\text{ }\mu\text{m}$ given the optical depth estimate from $0.85\text{ }\mu\text{m}$. The current study estimates fog droplet effective radius by comparison of theoretical and observed $1.6\text{ }\mu\text{m}$ reflectance values, where the droplet size distribution specified in the theoretical calculation is varied in order to match the observed reflectance. The scaled optical depth must be at least four in order for the technique to attain the required precision for effective radius.

Observations at $3.7\text{ }\mu\text{m}$ are added in order to estimate an index of liquid water content within the fog. Ackerman and Stephens (1987) show the dependence of near-IR reflectance on liquid water content given an estimate of droplet size. The daytime $3.7\text{ }\mu\text{m}$ measurements include both reflected and emitted radiation from the fog layer. The dependence of these effects on liquid water content are interpreted using the LOWTRAN radiative transfer code. Figure 1 depicts the scheme for deriving the desired microphysical quantities from available radiometric observations.



Fog Microphysics Schematic

Figure 1. Summary schematic of the methodology for analyzing fog microphysics from radiometric data.

3. DATA

Data were collected by satellite and aircraft platforms during a field experiment conducted near San Diego, California in June, 1986. Aircraft data consisted of cloud microphysics and radiometer data. Upward and downward-looking Eppley Precision Spectral Pyranometers provided solar flux measurements in the near-IR (0.7 to 2.8 μm) and total shortwave (0.3 to 2.8 μm) bands. Narrowband upwelling radiances were obtained from a spectral radiometer equipped with a rotating filter wheel. Cloud particle size distributions were measured by a variety of optical probes. These aircraft data provide the necessary experimental radiometric and *in situ* microphysical truth data for the evaluation of the fog microphysics analysis method described above. Digital satellite data were collected from the Geostationary Operational Environmental Satellite - VISSR Atmospheric Sounder and the NOAA Advanced Very High Resolution Radiometer (AVHRR). These data are useful mainly for fog/stratus field surveillance because of their relatively coarse spatial resolution and incomplete coverage in the required spectral bands.

4. CONCLUSION

The analysis of fog microphysics from remotely sensed radiometer data is ongoing at the time that this is written. In addition to analyses of fog optical depth, droplet size distribution, and liquid water content, we plan to derive diagnoses of the physical depth of fog layers, horizontal visibility, and predicted extinction coefficients at other wavelengths. Opportunities to analyze these quantities from satellite measurements will increase in the near future with the launch of the next generation AVHRR, which will take operational measurements in the 1.6 μm spectral band. When that band is added to the currently available observations near 0.85 μm and at 3.7 μm , all required data will be obtainable from satellite.

ACKNOWLEDGEMENTS

This research is supported by the U.S. Army Research Office through the Army Center for Geosciences under Grant DAAL03-86-K-0175. The authors wish to thank Dr. Melanie Wetzel for her advice and discussions, and Ms. Loretta Wilson, who helped prepare the manuscript.

REFERENCES

- Ackerman, S.A., and G.L. Stephens, 1987: The absorption of solar radiation by cloud droplets: An application of anomalous diffraction theory. J. Atmos. Sci., **44**, 1574-1588.
- Behunek, J.L., and T.H. Vonder Haar, 1990: Nighttime fog detection from satellite data. In Proceedings of the Tenth Annual EOSAEL/TWI Conference, 28-30 November 1989, Las Cruces, NM, U.S. Army Atmospheric Sciences Lab.
- Ellrod, G., 1989: GOES I-M image products. In Program of the GOES I-M Operational Satellite Conference, April 3-6, 1989, NOAA, 105-109.
- Grant, I.P., and G.E. Hunt, 1968: Solution of radiative transfer problems in planetary atmospheres. Icarus, **9**, 526-534.
- Stephens, G.L., 1978a: Radiation profiles in extended water clouds. I: Theory. J. Atmos. Sci., **35**, 2111-2122.
- Stephens, G.L., 1978b: Radiation profiles in extended water clouds. II: Parameterization schemes. J. Atmos. Sci., **35**, 2123-2132.
- Stephens, 1978c: Radiation profiles in extended water clouds. III: Observations. J. Atmos. Sci., **35**, 2133-2141.

Twomey, S., 1987: Influence of internal scattering on the optical properties of particles and drops in the near infrared. (P.N. Cheremisinoff, ed.) Appl. Optics, 26, 1342-1347.

Wetzel, M.A., and T.H. Vonder Haar, 1986: The impact of stratocumulus microphysical variations on near-infrared radiance. In Extended Abstracts, Sixth Conference on Atmospheric Radiation, May 12-16, Williamsburg, VA, 153-156. Amer. Meteor. Soc.

Wetzel, M.A., and T.H. Vonder Haar, 1990: Remote sensing of cloud droplet effective radius. In Preprints of the Seventh Conference on Satellite Meteorology and Oceanography, July 23-27, San Francisco, CA, 277-283. Amer. Meteor. Soc.

Wetzel, M.A., and T.H. Vonder Haar, 1991: Theoretical development and sensitivity tests of a stratus cloud droplet size retrieval method for AVHRR-K/L/M. Remote Sens. of Environ., 36, 105-119.

RAPID DEPLOYMENT IMAGERY TERMINAL (RDIT) USING DMSP SPECIAL SENSOR DATA

Thomas L. Harris and Jimmy A. Jensen
Harris Corporation
Government Information Systems Division (GISD)
Omaha Operations
Bellevue, NE 68005

ABSTRACT

Recently, Harris Corporation developed a Rapid Deployment Imagery Terminal (RDIT) which the Government deployed in support of Desert Shield/Desert Storm operations. This small, lightweight, and rapidly deployed terminal can ingest, process, and display the Defense Meteorological Satellite Program (DMSP) visual and infrared imagery. DMSP imagery is used to identify clouds, bodies of water, fires, and pollution. However, DMSP special sensors also have the ability to remotely sense additional information. This ability can help identify cloud type and height, land and water surface temperatures, water currents, ocean features, ice and snow, and vertical temperature and moisture profiles of the atmosphere. Harris IR&D efforts have now made it possible, using only DMSP data, to create in real-time most of the meteorological analyses needed to support deployed combat forces. This presentation will provide an overview of the RDIT system and applications of DMSP special sensor data as an approach to providing these technologies to deployed IMETS.

INTRODUCTION

Harris engineers fully understand that American battlefield commanders require accurate environmental information to aid them in their tactical and strategic decisions. Their needs include more accurate and detailed weather information and decision aid products that are tailored to their individual situations. The value of weather information can deteriorate in a matter of hours and timeliness is essential. Harris understands the need to acquire, process, and display environmental products not only in real-time but using small, lightweight, highly

mobile terminals. Since the earliest of time, the idea that bigger and faster was better has permeated most meteorologist's thinking. As a result, many weather centers have a super computer and other large mainframe computers that are used for modeling and creating forecaster support products. Since these large systems are not mobile, combat weather products have been manually generated by forecasters and observers located in the combat theater.

Since the late 1970's, Harris has been part of the Government's team established to develop an integrated computing system to deliver timely weather information to sites around the world. We helped design, build, install and integrate upgrades to the AFGWC Data Reconstruction Site (Site III) and the Satellite Data Handling System to help AFGWC meet newly emerging and vital combat weather support requirements. For example, Harris has been involved with blending data from conventional sources with data ingested from military and civilian meteorological satellites, including the DMSP and TIROS polar-orbiting satellites and the GOES, METEOSAT, and GMS geosynchronous orbital satellites. Harris has also worked extensively in applying this conventional and satellite data to support military requirements.

RAPID DEPLOYMENT IMAGERY TERMINAL (RDIT)

Following a very short notice competitive procurement, Harris delivered seven (7) Harris Model 3000 terminals, otherwise known as the DMSP Rapid Deployment Imagery Terminal (RDIT), to support Desert Storm combat operations.

The RDIT receives and processes both DMSP smooth and fine data for both short range forecasting and now casting. The whole system is designed to be deployed and operated by personnel wearing full chemical protection equipment. It contains its own antenna, data acquisition, processing and display systems, and operates totally independent from any meteorological data bases. This DMSP receiving terminal comes stored in 12 transit cases weighing less than 1300 pounds total. The heaviest case weighs approximately 150 pounds. The entire system can be transported on a HMMWV and then deployed by two personnel, wearing full chemical protection equipment, in less than one hour.

The Antenna Subsystem tracks the DMSP satellite as it passes overhead and receives the Real Time Data (RTD) being transmitted to earth. The subsystem consists of a pedestal-mounted positioner, a 1.4 meter circularly polarized parabolic antenna, a high gain down converter, a hermetically sealed Low Noise Amplifier (LNA), and stabilizing outriggers. The Antenna Subsystem weighs approximately 175 pounds and is designed with special quick release fasteners for ease in assembly and disassembly. This design also prevents difficulties

resulting from lost fasteners. The antenna subsystem can be deployed 100 feet from the Data Acquisition Subsystem. The pedestal positioner is outfitted with stabilizing outriggers and can withstand 55 mph winds when deployed for operations or 90 mph winds when stowed. The Antenna subsystem can withstand temperatures as low as -25°C or as high as 80°C. The subsystem has sufficient gain and noise temperature characteristics to provide a positive 10db signal-to-noise margin at satellite elevation angles of 10 degrees and higher, and an RF bandwidth sufficient to cover worst-case Doppler shift and temperature variation.

The Data Acquisition Subsystem (DAS) is responsible for predicting the satellites orbit with assistance from the operator and then directing the Antenna Subsystem so that it can track the satellite. The DAS consists of an antenna control computer with peripherals, an antenna positioner, a receiver, and a bit synchronizer. The antenna control computer is an industrial ruggedized PC-AT designed to withstand shock, vibration, and a wide operating temperature range. The 80286 CPU contains a 10MHz clock, 1 megabyte of RAM, keyboard and monitor which has a 640 x 480 pixel display resolution. The system provides the user with a real-time satellite display of the path and area covered by each satellite. The system is capable of calculating and maintaining orbit information for up to 16 different satellites. In addition, the system accurately predicts and displays information regarding the relationship between the site, the satellite, and the sun or moon. The user can select the satellite, the pass length, and the start time. After the signal is acquired, the subsystem is responsible for demodulation and bit synchronization. The bit synchronizer provides Non-Return-to-Zero (NRZ) data and a 0 degree clock output. All this equipment is stored in two cases that weigh a total of 208 pounds. The first case consists of the receiver, bit synchronizer, antenna controller, and the antenna control computer. The second case contains the monitors, keyboard, and peripherals. The output of the DAS is fed into the Processing Subsystem.

The Processing Subsystem consists of a ruggedized 80486 CPU, a GPS clock, and Communications Security equipment. The 80486 contains a 25MHz clock, 16MB of RAM, 1024 x 768 pixel color monitor, one 3.5 inch floppy disk drive, and two 380MB hard disk drives. The subsystem comes packed in two cases that weigh a total of 246 pounds. The first case has the GPS clock, Communications Security equipment, and the imagery computer. The second case contains the monitor, keyboard, and peripherals.

The Processing Subsystem allows the user to manipulate, color enhance, and annotate satellite image data. During data ingest, one fine image and one smooth image are received. If the visual image is at fine resolution, the infrared image will be at smooth resolution. If the visual image is at smooth resolution, the infrared image will be at fine resolution. This system decimates the fine data to the same resolution as DMSP smooth data for display but also

maintains a copy of the fine image. When a user finds that the DMSP smooth data does not have the resolution desired, a portion of the high resolution data can be retrieved in a zoom box without exiting the DMSP smooth data display. By activating the Quicklook feature, the user can display the image even as the system is ingesting the data. The selected image may be zoomed, rotated, or inverted. Infrared images are normally displayed as inverted images. Histograms of the images may be created to analyze particular areas. All images have the necessary land/sea boundaries and geopolitical boundaries applied. Ten degree latitude and longitude lines are also applied to assist the user in determining locations over large ocean areas. Images may also be saved and referenced later.

The user may apply a color enhancement table to the image using a very friendly interface. This is especially useful with infrared images as the color can denote temperatures of the features displayed. By moving sliders with a mouse, users may change the color ramps as they desire. Features that the user wishes to communicate to others may be annotated. The Processing Subsystem also allows the user to input and manipulate station reports. Both surface and upper air station reports are entered into the system by the keyboard. Station plots may be added, deleted, or modified. The stations are automatically displayed as they are updated. Images may be interrogated to display surface plot data.

Direct Mode Data Messages (DMDM) messages are textual messages that are embedded in the RTD data stream. The DMDM message may be extracted and displayed by the Processing Subsystem. The subsystem can be modified to automatically extract the ephemeris data from Special Message 8 (when implemented in the DMDM message). The ephemeris data is required to allow the system to accurately locate satellites to be tracked.

Also included in the system is a work surface, chair, portable generator, GPS antenna, cables, shipping cases, and an operation and maintenance manual. A 32 gray scale, 200 lines/inch, 300 pixels/inch-horizontal thermal printer is also included.

Battlefield commanders require more environmental information than just visual and thermal imagery to aid them in their tactical decisions. While the following capabilities do not currently exist in the Rapid Deployment Imagery Terminal, they could be easily added to the system to augment the existing capabilities.

DMSP SPECIAL SENSOR DATA

Weather systems are driven by temperature, moisture, and pressure. To support mission needs, forecasters require more accurate and detailed data describing these parameters

upon which to base their forecast. The requirements are accentuated in data sparse or data denied areas of the world. Because the value of weather information can deteriorate in a matter of hours, timeliness is essential to provide critical support to battlefield locations on a world-wide basis. Providing the environmental information required through communications circuits is less than desirable due to the low priority assigned to them. The DMSP 5D-2 satellite currently supports Mission Sensors that can be used to provide the data required. Of particular interest are the Special Sensor Microwave/Imager (SSM/I), Special Sensor Microwave/Temperature Sounder (SSM/T) and in the near future the Special Sensor Microwave/Moisture Sounder (SSM/T-2). These sensors will provide the tactical user in a remote or data denied area access to the parameters necessary for accurate forecasting and nowcasting.

SSM/I SENSOR DATA

The microwave imager (SSM/I) is a passive microwave radiometer that measures the thermal energy emitted and reflected by the earth's atmosphere in the microwave portion of the electromagnetic spectrum. This sensor measures microwave energy in four frequencies, 19.35GHz, 22.235GHz, 37.0GHz, and 85.5GHz. In three of these, both the vertical and horizontal polarizations are measured which results in seven channels of data. The long wavelengths of microwave radiation compared to the visual part of the spectrum cause strong interactions with particles on the molecular level, especially molecules of water and oxygen. This is caused by rotations induced in these dipole molecules by the electromagnetic field of the radiation.

The sensor collects upwelling microwave radiation through a parabolic reflector fed by a corrugated, broad-band, seven-port horn antenna. The antenna samples, in addition to the earth samples, calibration information from a mirror that reflects cold sky radiation and from a hot reference. The instrument collects data over an angular sector of 102.4 degrees about the sub-satellite track. The scan covers a swath width of 1300km. The scan direction is from left to right when looking in the direction opposite to the direction of the spacecrafts travel. Each scan contains 128 discrete uniformly spaced radiometric samples from the two 85.5GHz channels and, on alternate scans, 64 discrete samples are taken at the remaining five lower frequency channels. This results in a resolution of approximately 12.5km for the 85GHz samples and 25.0km for each of the other channels.

The seven channels of data are then combined using well developed algorithms into Environmental Data Records (EDRs). Currently, there are eleven approved algorithms. Included are algorithms for Water Vapor over the Ocean, Cloud Water over the Ocean, Surface

Wind Speed over the Ocean, Total Ice Concentration, Ice Age, Rain Rate over the Ocean, Rain Rate over Land, Land Surface Type, Land Surface Temperature, Land Surface Moisture, and Snow Depth. These parameters can be combined with available conventional data to develop forecasts to support the military in Arctic operations, Army and Marine Corps. ground operations, aircraft operations, ship navigation information, ocean wave forecasting, ocean surface ambient noise, submarine surfacing, and tropical cyclone warning to name only a few.

SSM/T SENSOR DATA

The SSM/T sensor measures microwave radiation emitted by the Earth's surface and atmosphere. Passive microwave remote sensing offers the advantage of providing global coverage under both clear and cloudy conditions, thus overcoming the infrared sensors' inability to see through clouds. SSM/T data can provide a three dimensional view of atmospheric temperatures. In the eleven years that the SSM/T has been operational, numerous studies have been conducted on the quality of the data produced. The Air Force Geophysical Laboratory has shown that the SSM/T can offer a considerable improvement over estimates based on climatology. NOAA/NESDIS has shown that data collected by the SSM/T compares favorably with radiosonde data collected in the same area even without calibration updating. At Air Force Global Weather Central, comparisons of SSM/T data and TOVS data have shown that at almost all pressure levels, regardless of cloud cover, temperature retrievals are more accurate from the SSM/T sensor than from the TOVS sensor.

Certain radiometric characteristics of the atmosphere can be determined by the absorption and emission characteristics of the oxygen molecule in the 50-60GHz and 118GHz region of the electromagnetic spectrum. The SSM/T sensor collects microwave energy in seven channels; 50.5GHz, 53.2GHz, 54.35GHz, 54.9GHz, 58.4GHz, 58.825GHz, and 59.4GHz. This data has a spatial resolution of 208km at nadir and a thermal resolution of 0.3 to 0.5 Kelvin. Each scan requires 32 seconds and covers a field of view of ± 36 degrees from nadir. The amount of energy received by the sensor depends upon the wavelength and the optical length through the atmosphere. Emissions from the different channels indicate statistically the emission from a particular level in the atmosphere. It is possible to determine the temperature of 15 different levels through the atmosphere. The sensor can therefore be used to create a temperature profile of the atmosphere. If the output of the sensor is combined with a 1000mb height field a barometric profile through the atmosphere can be determined as well. Through well- known algorithms, the characteristics about the location of the tropopause may be determined.

From the SSM/T sensor the temperature, atmospheric pressure and the speed and direction of geostrophic winds can be calculated at mandatory isobaric levels and plotted. These can also be displayed to examine the atmosphere through cross sectional analysis.

The data received from the SSM/T sensor, along with a 1000mb height, can be used to plot environmental data on the Skew-T-Log-P chart. The Skew-T-Log-P chart is a very valuable tool for diagnosing atmospheric stability and thermal structure. These charts are created by plotting vertical profiles of temperature, dewpoint, and the speed and direction of the wind in the atmosphere. The chart is logarithmic and contains a fixed background with pressure lines that indicate pressures from 1050mbs to 100mbs and then an overlaid area that contains pressure lines from 100mbs to 25mbs. It also contains lines that depict the dry and moist adiabatic lapse rate. The final set of background lines is a set of mixing ratio lines in grams of water per kilogram of air. The 1000mb height can be calculated using a barometric pressure, a 6 hour mean temperature, and the elevation at which these two parameters were taken. The chart is constructed by placing a dot at the locations where the SSM/T sensed environmental temperatures intersect with the particular pressure level. From a single sample 15 combinations of temperature and level are determined. The 15 dots are then connected to produce a temperature profile of the atmosphere from the surface to a level of 10mbs.

Most weather phenomenon depends upon the stability of the atmosphere. Stability is the state of equilibrium in which a parcel of air has a tendency to resist displacement from its current level, or if displaced, to return to its original position. Instability is the tendency to move farther away from its original position. Using the Skew-T diagram, the forecaster can determine a parcel's temperature if it was lifted dry adiabatically. If that temperature is higher than the environmental temperature as plotted on the Skew-T, the parcel would have a tendency to continue to rise, seeking air of its own density. This type of instability indicates weather changes. If the temperature of the parcel is equal to or lower than the surrounding air, the parcel will tend to remain at that level or return to its original level.

An inversion is a naturally occurring cap that prevents the normal movement of the atmosphere. It may result in fog in low laying areas that will affect E/O weapons. The instability can prevent the natural tendency of smoke to rise resulting in smog obscuring a battlefield. It can also prevent moist air from rising until the inversion cap is broken. The breaking of this cap can result in the formation of thunderstorms. If the slope from the base of the inversion to the top of the inversion is nearly horizontal, it is known as a deep inversion and may be an area of dangerous wind shear.

At a high altitude, a rise in temperature shown on the Skew-T from left to right that does not terminate but continues upward to the extent of the graph indicates the transition from the troposphere to the stratosphere. This is known as the tropopause. If violent thunderstorms form and extend up through the tropopause, a fact that can be determined from the DMSP IR channel, the thunderstorm will collapse. This collapse often results, if additional conditions are met, in the formation of tornadoes.

The SSM/T data can be used to determine upper air temperatures and stability. These can be used to forecast precipitation, snow, vertical wind shear, icing, turbulence and thunderstorms. This data can also be used to predict the types of clouds that will form which is especially useful in forecasting thunderstorm development, intensity and coverage. The data also is used to enhance existing cloud analysis models. The forecasts generated from this data are used to support DoD operations in the following ways:

1. Providing tactical decision information on the best routes of flight, areas of concern, target area conditions, arrival conditions and alternate stations.
2. Providing forecast information on flight hazards to include thunderstorms, icing, and vertical wind shear.
3. Providing severe weather warning for theaters of operation, bases, and installations to include snow, flooding, thunderstorms, instability, and vertical wind shear.
4. Providing tactical decision information on the use of E/O weapons, support to intelligence collection systems, and reentry forecasts for ICBM forces.

With the arrival of the SSM/T-2 sensor, which will be flown on F11, it will also be possible to create a moisture profile through the atmosphere.

SSM/T-2 SENSOR DATA

The SSM/T-2 sensor will be a linear scanning passive microwave sensor that will measure the upwelling radiance from the earth in five channels, $183.310 \pm 3.000\text{GHz}$, $183.310 \pm 1.000\text{GHz}$, $183.310 \pm 7.000\text{GHz}$, $91.655 \pm 1.250\text{GHz}$, and $150.0 \pm 1.250\text{GHz}$. The spatial resolution is 46 km at nadir and the sensor has a thermal resolution of 1.0K. The sensor's field of view is ± 40.5 degrees from nadir in the cross track position. With algorithms which are currently under development, water vapor mass, relative humidity, and specific humidity will be determinable for specified levels up to 300mb.

With the addition of the SSM/T-2, a moisture profile could be determined that would allow the determination of various thermodynamic parameters. The Lifted Condensation Level (LCL) is one such parameter. The LCL is calculated by extrapolating the dewpoint parallel to the mixing ratio line and the temperature parallel to the dry adiabatic line until they intersect (saturation). This point is then extrapolated parallel to the moist adiabatic line until it intersects with the mixing ratio line. This is the level at which cloud bases form and is very valuable in determining the type of E/O weapon to select for aircraft. If the LCL is below the top of an inversion, severe thunderstorms are likely. Another parameter, the Lifted Index (LI), is a severe weather index that can determine the possibility of severe weather. This index is determined by taking the parcel in the lowest 100mbs and lifting it dry adiabatically to the LCL. It is then lifted moist adiabatically to the 500mb level. The LI is then calculated by subtracting the derived parcel temperature from the environmental temperature at 500mbs. If the LI is less than zero, the atmosphere is unstable. If it is from -2 to -4, thunderstorms are predicted, possibly severe. If it is -4 to -6, there is an increased chance of severe thunderstorms. If it is less than -6, there is a good chance of severe thunderstorms if a strong inversion exists.

Through the analysis of the SSM/T-2 data, forecasters will be able to determine the where and with what intensity cyclones and fronts will form, the location of easterly waves, intertropical convergence zones, clouds, precipitation, fog, and haze.

SSMIS SENSOR DATA

The Special Sensor Microwave Imager/Sounder (SSMIS) is planned for flight with OLS 17 sometime around the mid-1990's. This sensor system will be a combination of the SSM/I, SSM/T-1, SSM/T-2, and an Upper Air Sounder (UAS). The SSMIS sensor will be a passive conical scanning microwave radiometer that will retrieve microwave emissions to 73km. Without the UAS the system would only be able to retrieve data to 30km above the earth. One difficulty encountered in attempting to use the SSM/I and the SSM/T data is the difference in spatial resolutions of the different sensors. The SSMIS simplifies this procedure as the sensors will have coincident footprints with a spatial resolution of 14km. This resolution is a marked improvement over that of the SSM/T and SSM/T-2 sensors. Also since the sensor is conical scanning, anomalies that result at the ends of the cross track scans of the SSM/T and the SSM/T-2 are eliminated due to differences in the length of the optical path from nadir to the extreme cross track position.

With the SSMIS sensor, all the applications that have been previously mentioned for the SSM/I, SSM/T-1, and SSM/T-2 will be achievable as well as those additional capabilities that

the UAS will provide. Because of the coincident positioning, additional EDR's that are dependent upon combinations of sensors will be achievable.

SUMMARY

RDIT has been proven to be an effective tactical meteorological display system in providing environmental support to deployed combat systems. Experience gained from Desert Storm operations confirmed the need to deploy small, lightweight, and highly mobile meteorological terminals to support combat operation. Additionally, the results of recent Harris IR&D efforts have shown the value of DMSP Special Sensor data in supporting the production of forecaster aids required to support combat operations.

PC-BASED RAINFALL ESTIMATION FROM INFRARED GEOSTATIONARY SATELLITE IMAGERY

D. L. Reinke, C. L. Combs, and T. H. Vonder Haar
METSAT, Inc.
Fort Collins, Colorado 80521, U.S.A.

ABSTRACT

The Area-Time-Integral (ATI) technique is implemented on a PC. The PC host serves as both the ingest and processing system for producing a rain rate estimate over a user selectable grid. The UNIX operating system and X-windows are used to provide an image processing and display platform. A specially designed user interface allows the operator to interrogate and display satellite images and extract cloud-top temperature and areal coverage values which form the basic input to the rain estimation algorithm. A description of the system and results of several field cases comparing model estimates and actual field measurements is presented.

1. INTRODUCTION

The detection of precipitation, and more importantly the ability to estimate the duration and intensity, is a vital input to many decision matrices that are used to predict system performance. Accurate precipitation estimates affect systems as diverse as those which operate in the visible and infrared portion of the electromagnetic spectrum, to the workhorse combat vehicles that don't function very well in mud and snow. Just knowing that adverse conditions exist, or will exist, in the battle area can give the commander a decisive edge in the selection of weapons and tactics.

The detection and forecasting of areas of precipitation has made great strides in the past decades, but much research is still under way to improve on quantitative rainfall rate and volume measurements from satellite. This poses a challenge for the meteorologist, the systems designers, and ultimately for the field commander. Historically the detection of precipitation in the battlefield environment has been accomplished with ground, and later airborne observers. The limitation, of course, was that the observers had to be within line-of-sight of the area of interest. By the latter part of WWII, radar was being used to locate areas of thunderstorms. In the succeeding years we have developed techniques for adding more quantitative information about rain rates and volumes which can be used by the hydrologists to predict stream flow and surface trafficability. Radars, however, have limitations too. They are not well suited for the forward battle area because of their size and their requirement to transmit electromagnetic pulses which can be detected and neutralized. These limitations are overcome for the most part, by the fact

that the current radars have a range of hundreds of miles. This advantage, however, is growing weaker as the modern weapons outstrip that range. It is

also very difficult to put radars within range of your adversary's backyard to see if he too is playing in the mud.

Recognizing the tremendous potential for an "Eye in the sky", some of the earliest experiments to fly on satellite platforms were meteorological picture taking instruments. Since 1959, when we began with photos showing crude outlines of cloud features hundreds of miles below, we have engineered highly accurate digital imaging systems which give us a "window" into the atmosphere in the visible, infrared, and microwave spectra. One of the limitations of satellite observations has been that they are limited to viewing only the tops of clouds and didn't have the important information about the vertical structure and consequently the precipitation characteristics of the cloud. Some important work has been done to allow us to make inferences about the characteristics of the clouds viewed from satellite, but we are just now making inroads into making quantitative estimates of precipitation rate and volume.

Although no single comprehensive technique has been developed to date, rain rate, rain volume, and areal extent of precipitation can be estimated from infrared satellite imagery. The techniques vary greatly, but have a common requirement for the capability to perform temperature thresholding and in most cases determining the location and/or areal coverage of a given cloud-top temperature value from the infrared data. Each technique requires the ability to interrogate digital infrared satellite data to determine a radiance (or brightness count) which can be converted to a temperature. This temperature is then used to apply a threshold or compute a gradient. The purpose of this project is to provide the capability to analyze digital satellite imagery to make such a determination, and to display gridded precipitation probability estimates derived from infrared temperature measurements.

This effort, titled "PC-based Rainfall Estimation from Infrared Geostationary Satellite Imagery" is designed to provide the microcomputer-based interactive processing and display capability to perform ATI rainfall estimates.

2. AREA-TIME-INTEGRAL TECHNIQUE

An EOSAEL paper presented by Reinke, et al., (1989) gives a thorough description of the ATI technique and is briefly reviewed here.

The use of geostationary satellite imagery to estimate rain rate has some limitations. The most notable is the fact that the existent visible and infrared (multi-spectral imager) data allows only a view of the cloud tops associated with the precipitation. Inferences must be made from the cloud characteristics as to the nature and intensity of the precipitation beneath the cloud shield.

The Area-Time-Integral technique, as originally defined for radar, was modified for application to areas identified by infrared images from a

geostationary satellite. The technique was used to produce a rain volume estimation for the life of convective cells.

To compute the ATI from satellite, the infrared imagery was used to determine the temperature threshold which produced an area which most closely matched the area of the 25dBz reflectivity area on the radar echo. This was done for each time step during the lifetime of the storm. The temperatures used for the thresholding of the satellite image were then optimized for a set of 17 cells to produce a single optimized temperature threshold which would produce a rain volume estimate from the satellite which matched the estimate from radar. Coefficients from radar-satellite comparisons are used to estimate rain volume from each cell or area. This rain volume is then distributed over the grid and the time interval is used to estimate a rain rate at each grid point.

3. PC SYSTEM DESCRIPTION

The components chosen for this system are:

a 25 Mhz 486 PC configured with:

- . 128K Cache RAM
- . 8 MB RAM
- . 1.2 MB 5.25" Drive
- . 1.44 MB 3.5" Drive
- . (2) 210 MB 15MS IDE Drives
- . 14" 1024 Z 768 Color Monitor
- . 1 Parallel/2 Serial ports
- . DMA DMV-11 Interface card
- . Super VGA (16 bit, 1MB)
- . Mouse

4. SOFTWARE SUMMARY

Software requirements include: UNIX OS/environment, C/C++ compiler, and X-Windows environment.

Applications software has been written to perform the basic functions required for producing a rainfall estimate using the Area-Time Integral (ATI) technique. These functions will also allow for the test and evaluation of other similar techniques which rely on the capability to process digital satellite images.

The software package called CREST (C-based Rainfall Estimation Testbed) allows the user to work with a series of satellite images to determine rainfall estimates over a user-defined grid. These estimates can then be displayed graphically, or used as input to hydrologic analysis and/or prediction models.

The primary functions of the CREST program are to provide the user with the capability to:

- A. Generate a histogram of infrared brightness counts/temperatures. The brightness count is the digital value assigned to each picture element on the satellite image and represents a measure of the amount of radiation reaching the satellite from that point on the scene. This brightness count value can be converted directly to a radiating temperature. A histogram is generated to show the distribution of brightness counts (temperatures) for the entire image.
- B. Identify regions of the image which exceed a threshold temperature. This function is useful for determining the coldest cloud tops which are most often associated with the heaviest precipitation. This is an interactive routine which allows the user to specify a threshold temperature and mask portions of the image which exceed (are below) that threshold.
- C. Define and select a grid and grid sampling method. This routine allows the user to define the grid spacing and location for the extraction of temperature and area information from an image. It is designed to be multi-functional, allowing the user to do point or area sampling. All grid definition parameters are stored for later retrieval, and the actual data that is extracted from an image is stored as both a special database file, and a text file that can be reviewed by the user.
- D. Store historical information about rain cells and areas. The ATI technique (as well as others) rely on historical information that identifies the growth/decay and max/min values for a rain cell or area. The user is given the capability to retrieve historical data and compare/merge it with the most recent analysis. Each cell or area is uniquely defined and labeled for future retrieval.
- E. Produce a rainfall estimate using the ATI technique. Gridded temperature and areal coverage measurements from satellite images area used to produce a rain rate over each grid point. Coefficients from radar-satellite comparisons are used to estimate rain volume from each cell or area. This rain volume is then spread over the grid and the time interval used to estimate a rain rate at each point.
- F. Graphic display of results. The rainrate (or any of the gridded data for each cell) can be used to create a graphic overlay for the image.

5. FUTURE CAPABILITIES

The CREST system will be modified to perform the following functions:

- A. Perform GOES data ingest via a frame synchronizer board.

- B. Perform navigation (geo-location) from raw image header.
- C. Produce rainfall estimates from real-time satellite ingest.

To date, the system has only been run on archived data sets that have been collected and preprocessed (navigation/calibration). The PC-based CREST system will be upgraded to allow for the processing of real-time data on the PC. The system will initially be limited to GOES infrared imagery.

Support for the development of CREST was provided by the U.S. Army Corps of Engineers, Hydrologic Engineering Center in Davis, CA.

6. REFERENCES

Reinke, D.L., 1989: Satellite Area-Time Integral Technique for Estimation of Convective Rain Volumes. In Proceedings of the Tenth EOSAEL/TWI Conference, Las Cruces, NM, 28-30 Nov 1989, pps. 483-491.

A COMPARISON OF MEASURED AND DIFFERENTIAL CORRECTED

GLOBAL POSITIONING SYSTEMS DATA

Thelma Chenault and John Fox
U.S. Army Atmospheric Sciences Laboratory
White Sands Missile Range, New Mexico 88002-5501, USA

Don Foiani
Physical Science Laboratory
New Mexico State University
Las Cruces, New Mexico 88003

ABSTRACT

During the Joint Acoustics Propagation Experiment in July 1991 Global Positioning System (GPS) receivers were used to acquire velocity and position data for target vehicles. Measured and differential corrected GPS data were compared. Overall, the GPS gives good results for tank and helicopter position data acquisition.

1. INTRODUCTION

The cost of radar coverage and mission timing is becoming a larger and larger percentage of the total mission cost. Agencies such as the U.S. Army Atmospheric Sciences Laboratory (ASL) are looking for ways to cut these costs and still obtain position data in the required accuracy range. If specified projects can accept position data acquisition rates of less than one per second and mean value accuracy of 25 m (200 m uncorrected), then the use of the Global Positioning System (GPS) should be considered as an option for acquiring position data.

During the Joint Acoustics Propagation Experiment, ASL's GPS receiver and two Waterways Experimental Station GPS receivers were used. These GPS receivers can autonomously record position and velocity data at a maximum rate of one record per second with mean value accuracy of 25 m, assuming selective availability is not active. Mean value accuracy of 25 m means that half of the points are inside a circle of 25 m in radius from the point where position data is being recorded. With selective availability in effect, the mean accuracy can be degraded to a mean accuracy of as great as several hundred meters. Figure 1 shows our mean accuracy degraded between 200 and 235 m.

Selective availability is the purposeful degrading of GPS accuracy by the controllers of the satellite network. The Department of Defense controls this network. The use of two GPS recording systems, one based at a known location and the other on the vehicle for which position data is being recorded, allows differential postprocessing corrections to be applied to the vehicle position data, thus increasing horizontal position accuracy even when selective availability is active.

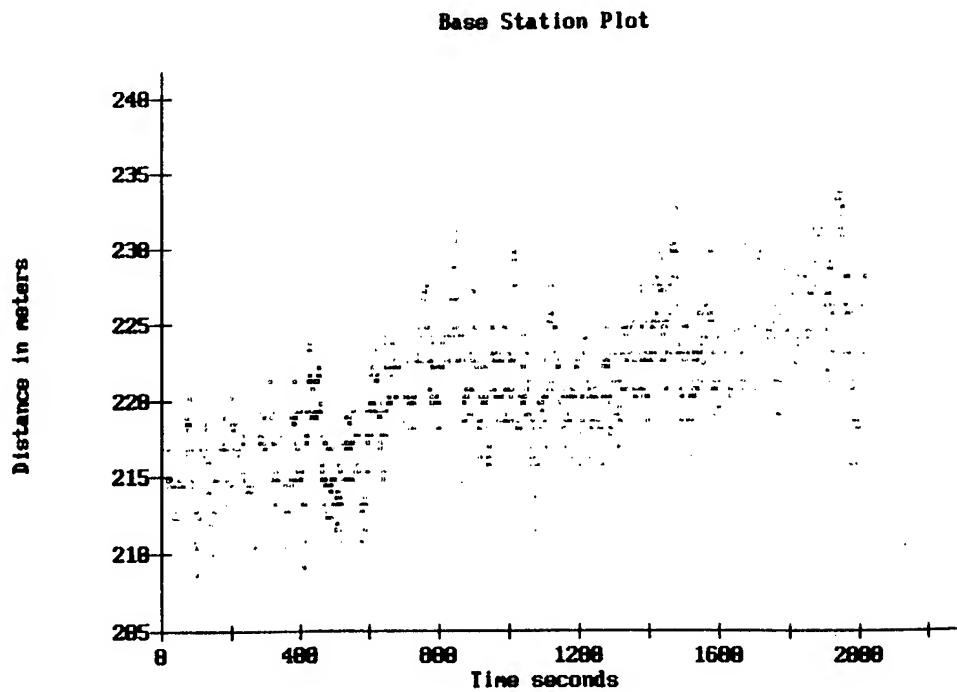


Figure 1. Degraded mean accuracy in meters from survey point.

2. DATA ACQUISITION EQUIPMENT

Base station and target location data were acquired by using Trimble Navigation (GPS Pathfinder, 1989) GPS equipment. All receivers were identical in design. These GPS receivers work in conjunction with the GPS satellite network to provide portable and durable navigation and position recording. Figure 2 shows the equipment layout and interfacing.

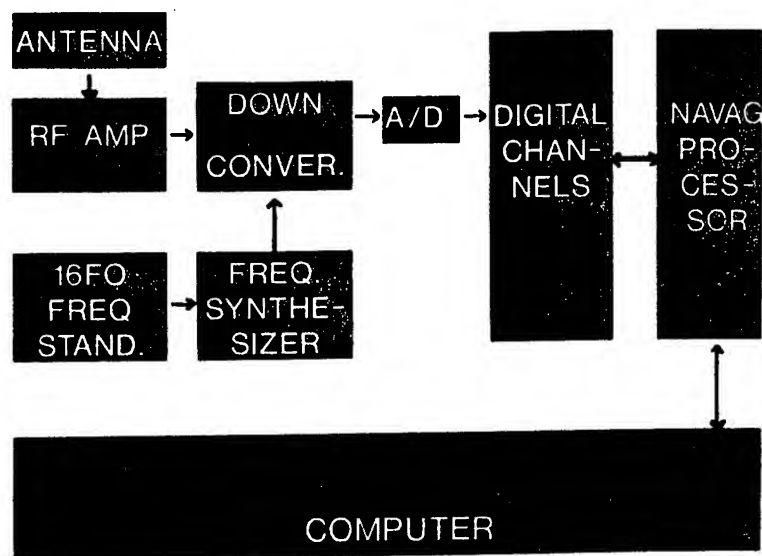


Figure 2. GPS equipment layout.

Our base station consisted of a GPS antenna located on the top of the equipment van, a GPS receiver, and a 12-MHz 286 clone desktop computer system. Our remote system consisted of a GPS antenna, GPS receiver, and a Zenith laptop with hard drive. The remote GPS receiver and the data acquisition and display computer were battery operated in the ground vehicle and terrain masking experiments. For the helicopter long-range detection tests, aircraft power was used to power the remote GPS receiver and data acquisition computer. Our remote system had the GPS antenna either mechanically or magnetically mounted to the vehicle that the position data was being obtained from.

3. GPS SETUP AND CALIBRATION METHODS

The GPS receivers input/output modes were set to result in output data in the following format:

- latitude and longitude (degrees, minutes) World Geodetic System (WGS)-84 survey,
- altitude in meters above WGS-84 geoid (above ground level),
- velocities in meters per second, and
- time in UTC (universal time coordinated - Greenwich mean).

Calibration points were set up to calibrate the vehicle GPS at the beginning of a series of trials. Figure 3 shows the calibration points as stars on the plot. The vehicle GPS collected data at each of these surveyed calibration points for several minutes during calibration trials. The data the GPS receiver recorded was checked against these survey data points. Data from the base station could be similarly compared to the base station survey point (see fig. 1). Any large biases between the base station GPS and the vehicle GPS could be detected and corrected.

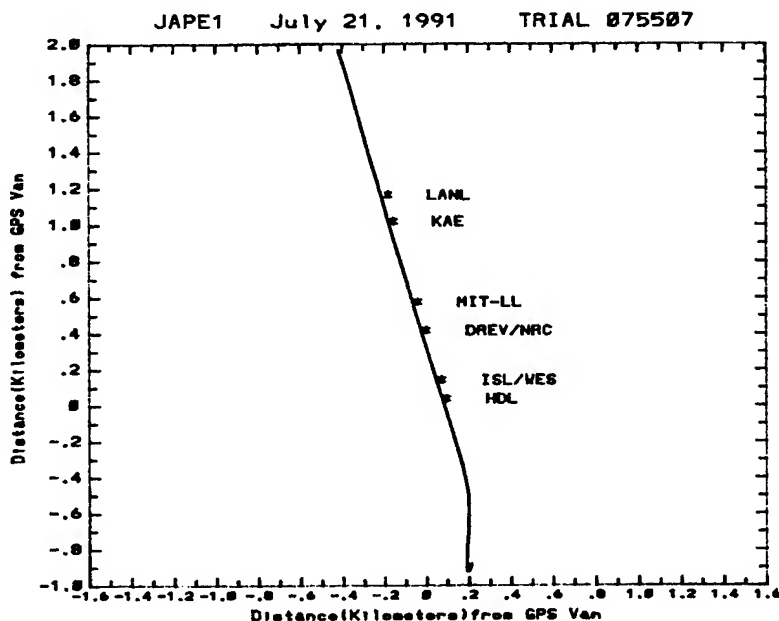


Figure 3. GPS survey points.

This plot is data obtained by running a base station for a little over an hour (see fig. 1). Note that most of the points were in the same general area. The data show that over 99 percent of the recorded points are at a radial distance of over 200 m from the base station surveyed point. This large radial distance indicates that selective availability was being used. Differential post-processing must be done to obtain acceptable data.

Our final data was plotted against calibration points to verify data accuracy. Also other surveyed points such as meteorological towers and instrument hill were used to provide better data visualization (fig. 4).

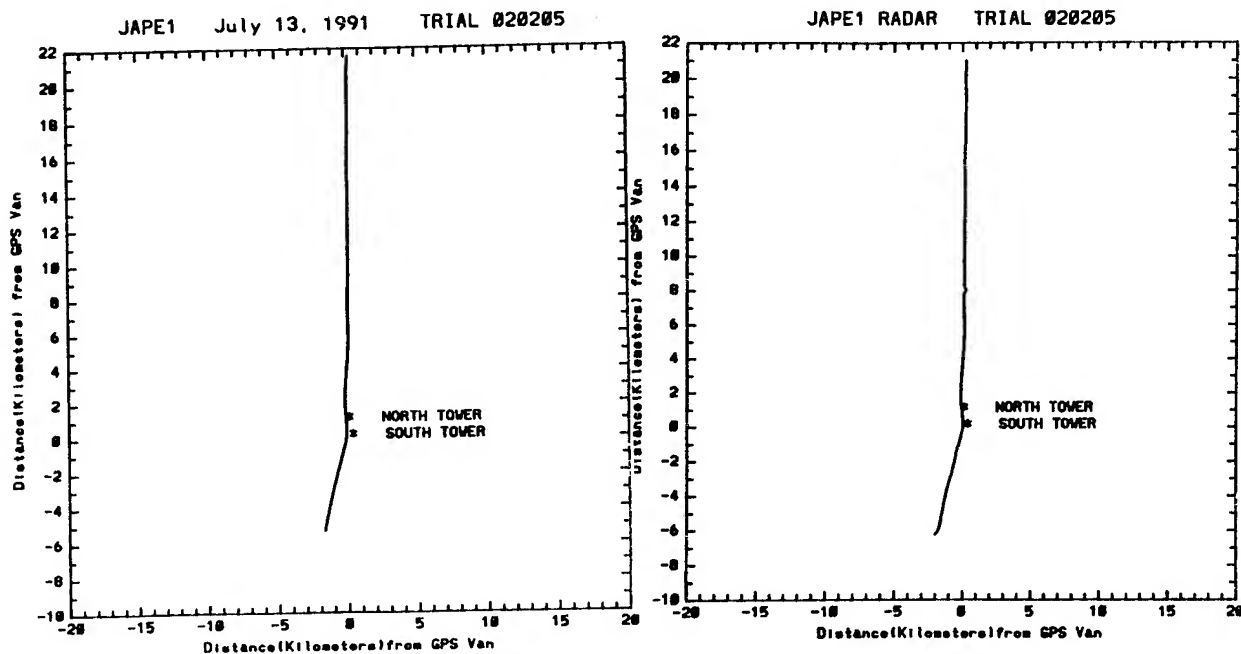


Figure 4. Comparison of GPS and radar for trial 1.

4. COMPUTER SOFTWARE

Two Trimble software programs were used: GPSREC and GPSLST. The GPSREC program was used to obtain data from the receiver, display the data, and store the data in a compressed data format. GPSLST was used to convert data from the compressed data format back to ASCII file format for further postmission data processing. Postmission data processing software programs were developed by ASL to perform the following:

- merge the time sequenced vehicle and base station data,
- convert data from latitude/longitude to universal transverse Mercator coordinates,
- make differential postprocessing corrections, and
- smooth data.

5. RESULTS

For the following data analyses a mean radial distance will be calculated with a standard deviation. For GPS-radar comparison a mean was calculated of the distances between all time matched GPS-radar data points.

The following data analysis summary gives data acquisition rates, trial start and stop times, and the percentage of time GPS was in the three-dimensional (3D) mode for the six GPS trials for which detailed data will be discussed. Table 1 shows the GPS analysis summary.

TABLE 1. GPS ANALYSIS SUMMARY

Trial No.	Trial Start	GPS Start	Trial End	GPS End	Acq /min	% 3D	Diff Corr
1	05:18:00	05:18:00	05:26:00	05:25:59	37	95	0
2	10:35:10	10:35:10	10:44:46	10:44:46	53	0	95
3	05:32:00	05:32:00	06:01:20	06:01:20	48	100	100
4	06:41:00	06:41:00	06:47:51	06:47:51	47	100	100
5	07:03:00	07:03:00	07:08:47	07:08:47	41	100	100
6	07:22:00	07:22:00	07:28:15	07:28:15	43	100	0

Trial 1 was a trial in which radar and GPS data were available (fig. 4). No base station was available to use for differential corrections of the data. We compared these data to the radar data for the same trial and obtained a mean radial distance of 215.15 ± 31.20 m.

Trial 2 was tracked by radar and by GPS (fig. 5). This trial had GPS differential correction 100 percent of the time and a high data acquisition rate. The tracking was in 2D mode because of inadequate satellite availability. The mean radial distance between the radar and GPS track was 48.75 ± 20.75 m.

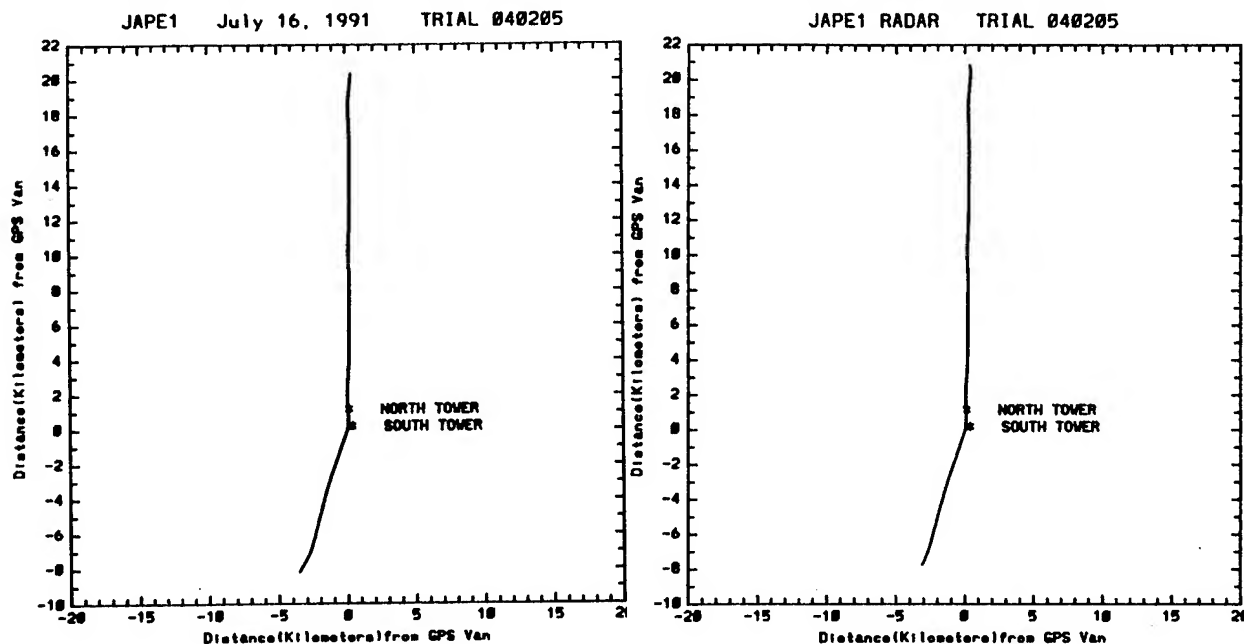


Figure 5. Comparison of GPS and radar for trial 2.

Trials 3 through 6 are trials in which a tank is traveling down the same road in a south to north direction (fig. 6). These trials are made over a 2½-h period. Plots of the raw data and the differential corrected data are presented. Trial 6 was corrected by using base station data from the previous trial. The left side of the figure is raw data, and the right side is processed data. Note how differential correction and smoothing improve results.

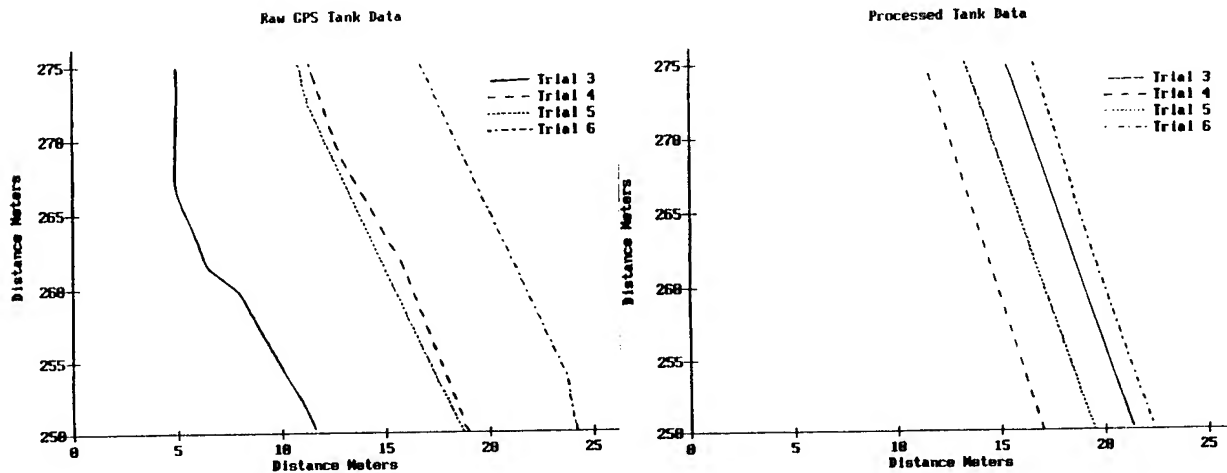


Figure 6. Comparison of GPS for trials 3 through 6.

Our best and worst trackings were done on July 25 against the Black Hawk. For one trial the mean radial distance between radar and GPS data was 17.15 ± 8.32 m. The GPS was unable to obtain any data from several of the other trials.

Position data collected from this test is well in the accuracy range required for acoustics testing. The GPS gives good results for tank and helicopter position data acquisition and should be considered as a method of obtaining position data in future testing.

REFERENCE

GPS Pathfinder User's Manual, November 1989, Trimble Navigation Limited, Sunnyvale, CA.

TESTING A MICROWAVE RADIOMETER IN ARCTIC, TEMPERATE,
AND TROPICAL CLIMATES

Edward M. Measure and Teddy L. Barber
U.S. Army Atmospheric Sciences Laboratory
White Sands Missile Range, New Mexico 88002, USA

Randall J. Hulsey and Dick R. Larson
Physical Science Laboratory
New Mexico State University
Las Cruces, New Mexico 88003, USA

ABSTRACT

Vertical profiles of atmospheric temperature and moisture are required for artillery accuracy, aviation operations planning, and calculation of smoke, chemical, nuclear, and biological agent transport and diffusion. Ground-based microwave radiometers offer a promising technology for remote, automated, covert, and real-time battlefield sensing of these profiles. These remote sensors make a direct measurement of atmospheric microwave radiance from which an indirect measurement of the desired profiles can be inferred. These profiles are computed by means of retrieval algorithms that use the direct measurements in conjunction with other information about the behavior of the atmosphere. Development of such systems for military use requires retrieval software suitable for use in the varied climates in which the army is likely to operate. This paper describes some of our results from recent tests made in arctic, tropical, and temperate climates.

1. INTRODUCTION

The U.S. Army Atmospheric Sciences Laboratory (ASL) is interested in developing mobile and portable instruments for real-time remote sensing of vertical profiles of atmospheric temperature, moisture, and wind. Radiometric temperature profilers operating in the 50 to 60 GHz spectral region are promising systems for measuring the temperature portions of these profiles. ASL's research profiler is shown in fig. 1. Among the advantages of radiometric profiler systems are their capabilities for passive, remote, automated, and near real-time operation in a compact, portable system.

For such systems to be useful to the tactical army, they must be able to perform their functions in a very wide variety of environmental conditions. To investigate this performance, we are testing a microwave radiometric temperature profiler. Our radiometer is a four-channel elevation-scanning instrument operating in the 50 to 60 GHz region. The tests are designed to evaluate both the instrument itself and the performance of the temperature retrieval algorithms.

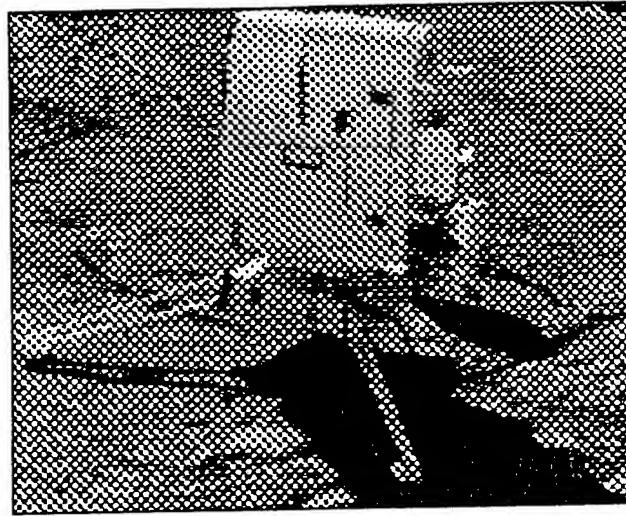


Figure 1. The ASL passive microwave temperature profiler.

During the past 2 yr we have undertaken a series of comparisons of radiometer measurements with simultaneous radiosonde measurements in a variety of climates. Measurement sites included White Sands Missile Range, New Mexico; Redstone Arsenal, Alabama; Plattville, Colorado; Fort Greeley, Alaska; and Hilo, Hawaii.

2. THEORY OF OPERATION

Like any other matter at a temperature above absolute zero, the atmosphere emits natural thermal radiation. The microwave radiometric temperature profiler measures a portion of this radiation and uses it to infer temperature profiles of the atmosphere. In the microwave region, scattering from aerosols is usually a small effect, so the atmosphere satisfies local thermodynamic equilibrium to a good approximation. Consequently, the source function is purely emissive, and each measurement is, in effect, an altitude weighted average of the atmospheric temperature profile. Because the opacity of the atmosphere varies dramatically with frequency, measurements of downwelling microwave radiation at different frequencies provide differently weighted averages of the atmospheric temperature profile.

More quantitatively, in the 20 to 60 GHz region, the measured brightness temperatures satisfy (to a good approximation) the following equation:

$$T_{bv} = \int_0^{\infty} T(s) \alpha_v(s) \exp \left[-\int_0^s \alpha_v(s') ds' \right] ds + T_{bv}^{\infty} \exp \left[-\int_0^{\infty} \alpha_v(s) ds \right] \quad (1)$$

where

$T_{b\nu}$ = brightness temperature at frequency ν

$T(s)$ = temperature at height s

$\alpha_\nu(s)$ = absorption coefficient

$T_{b\nu}^\infty$ = downwelling cosmic background brightness temperature at the top of the atmosphere

Inferring atmospheric temperature structure from microwave brightness temperature measurements thus becomes the problem of inverting eq. (1) for $T(s)$. The retrieval algorithm used to retrieve temperatures from the microwave radiance measurements was based on a least squares fit of the brightness temperatures measured to such brightness temperatures computed from historical radiosonde data measured at Fairbanks, Alaska (about 100 miles distant). (See, for example, Westwater and Sweezy, 1983, for a discussion of retrieval techniques applied to surface based radiometric temperature profiling.)

3. EXPERIMENTAL PLAN

Because the retrieval algorithms are based on climatological data, performance of the retrieval algorithms is potentially sensitive to the climate in which the radiometer is being operated. We have performed simulation studies to test this dependence, and we are developing retrieval algorithms intended to be suitable for a wide variety of climatological circumstances. One of our primary goals in conducting comparison measurements in highly varied climates was to obtain actual radiometer data with which to compare our simulations and to test our retrieval algorithms.

In addition, the radiometer system hardware, which was designed to operate in a wide range of environmental conditions, also needs to be tested in a variety of environments.

Our simulations indicated that the most important influences on the performance of the radiometers would be altitude, moisture, and surface temperature. Our plan therefore was designed to test the instrument in places where the weather approximated climate extremes, as well as in locations representing common climates; for example, Huntsville, Alabama, has a warm, moist, temperate climate of modest elevation; White Sands Missile Range is warm, dry, and high; Fort Greeley, Alaska, is cold, and arctic; and Hilo, Hawaii, is tropical.

4. PRELIMINARY RESULTS

Figures 2, 3, and 4 show example comparisons between radiometric retrievals (triangles and solid lines) and the radiosonde observations (boxes). Note that the agreement is generally good.

Figure 2 is a comparison of radiosonde and passive microwave temperature profiler data at White Sands Missile Range, New Mexico. Figure 3 shows similar data from Redstone Arsenal, near Huntsville, Alabama; and figure 4 shows data from Fort Greeley, Alaska.

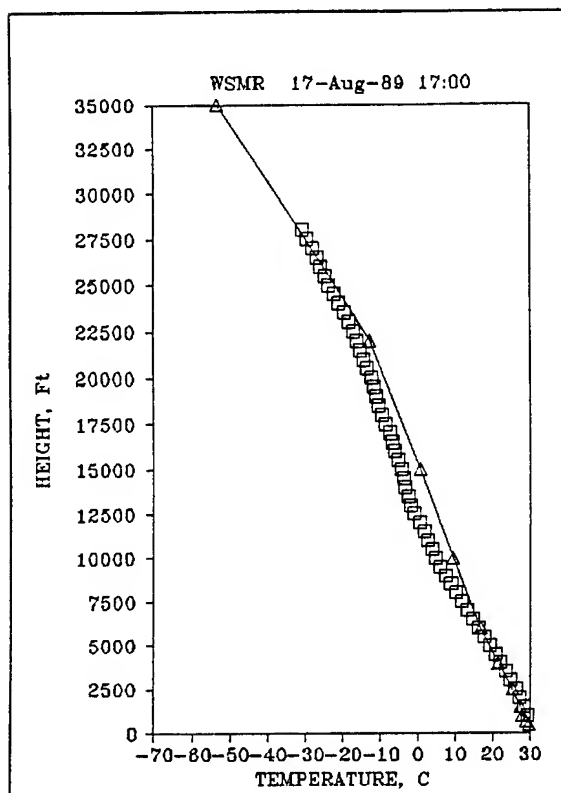


Figure 2. Radiosonde (boxes) versus radiometer (triangles) at White Sands Missile Range, New Mexico.

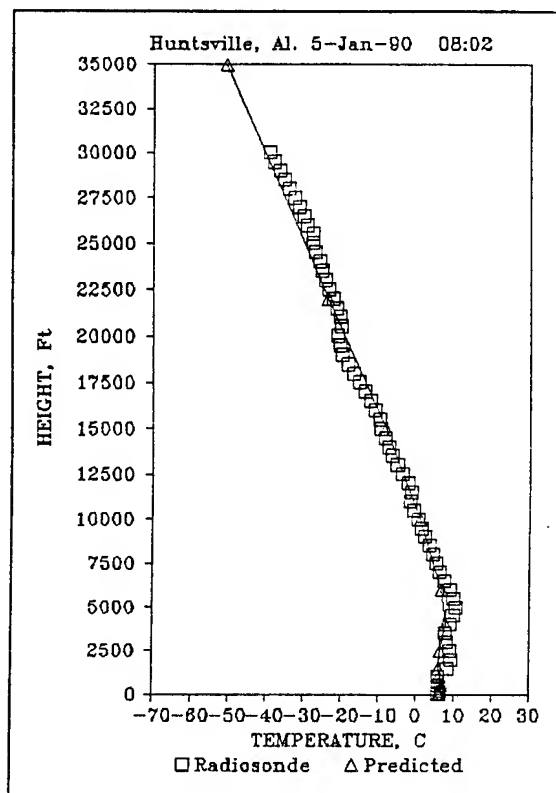


Figure 3. Radiosonde (boxes) versus radiometer (triangles) at Huntsville, Alabama.

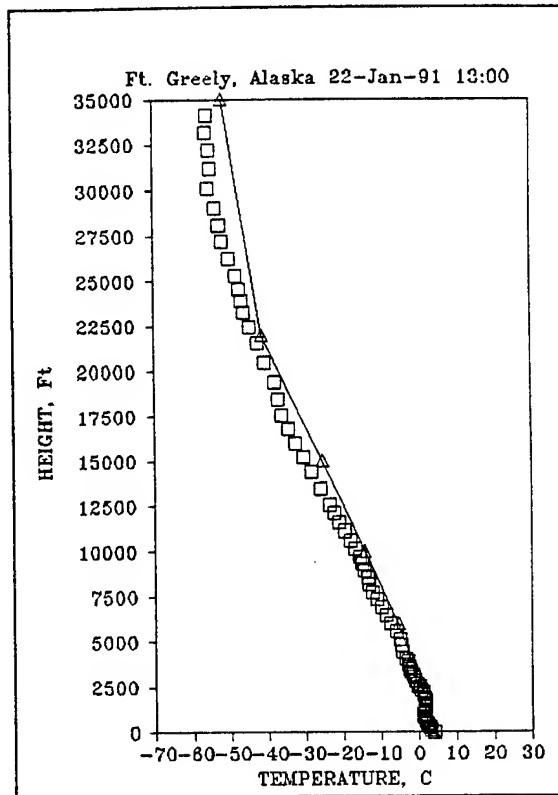


Figure 4. Radiosonde (boxes) versus radiometer (triangles) at Fort Greely, Alaska.

REFERENCE

Westwater, E. R., and W. B. Sweezy, 1983: Profile retrieval algorithms used in thermal sounding of the atmosphere. Reprint SPIE, vol. 412, Inverse Optics, Society of Photo-Optical Instrumentation Engineers, Bellingham, WA, pp. 143-147.

IMPROVING ATMOSPHERIC CHARACTERIZATIONS AT HELSTF: WINDS AND HUMIDITY

**Gail Tirrell Vaucher
Science and Technology Corporation
White Sands Missile Range, NM 88002 USA**

**Robert W. Endlich
U.S. Army Atmospheric Sciences Laboratory
White Sands Missile Range, NM 88002-5501 USA**

ABSTRACT

The need to improve the atmospheric characterizations at the High-Energy Laser Systems Test Facility (HELSTF) was demonstrated, in part, by two observations. First, when increasing the averaging time periods for winds simultaneously measured along a 1-km range and at a uniform height, the resultant winds diverged. Second, a variety of dew point values (spanning 5 to 7 °C) were simultaneously measured along a 1-km range during normal data acquisition periods. These two critical meteorological elements were isolated for analysis. The focus of this presentation is on the instruments, including sensor limitations, calibration, and other influences on the data collection. Part I describes the investigation of the Gill anemometers (polypropylene and polystyrene propellers) employed at HELSTF. Part II describes research on the calibration techniques and implementation utilized on the HELSTF General Eastern hygrometers.

1. INTRODUCTION

To improve meteorological characterization at the High-Energy Laser Systems Test Facility (HELSTF), White Sands Missile Range (WSMR), New Mexico, three critical atmospheric elements (wind, humidity, and optical turbulence) were isolated for analysis. This investigation was subdivided into three phases:

- Phase I: Analyzing the main instrument(s) used to acquire each element;
- Phase II: Conducting an intercomparison of calibrated instruments; and
- Phase III: Implementing phase I and II results into the HELSTF operation.

This article presents the Phase I summary and conclusions from the wind and humidity analyses (Vaucher and Endlich, 1991a; 1991b). Information regarding the events leading up to this research can be found in another paper presented at this conference (Freeman and Endlich, 1991).

2. PART I: WIND ANALYSIS

2.1 WIND ANALYSIS BACKGROUND

Winds are critical to HELSTF laser propagation. An insufficient crosswind can lead to thermal blooming, vertical wind shear coupled with a vertical temperature gradient produces optical turbulence, and high winds flowing across the WSMR desert floor can generate blowing dust. All of these conditions are detrimental to laser propagation. For this reason, the characterization of winds at the HELSTF site is an essential part of facility operations.

The primary HELSTF wind sensor is the 27106 R.M. Young Gill UVW Anemometer. This instrument is composed of three helicoid propeller sensors (each an anemometer) mounted orthogonally on a common mast. The individual anemometers consist of two

main components, the generator and the propeller. The two types of propellers used in this research were the 18-cm x 30-cm (diameter x pitch) polypropylene propeller currently employed at HELSTF, and a 19-cm x 30-cm polystyrene propeller under consideration for possible use at HELSTF. Generators with polypropylene propellers are referred to here as polypropylene anemometers. A generator/polystyrene propeller combination is called a polystyrene anemometer.

The operational calibration for these instruments is a three-point check of the generator output. The output is checked at known generator speeds of +1800 rpm, 0 rpm, and -1800 rpm; the sign indicates direction of propeller rotation.

A HELSTF wind variability study along a 1-km range showed that wind speeds averaged over increasing time periods tended to diverge. Four cases, representing a variety of conditions, were reviewed. Figure 1 displays data from 14 August 1990, representing one of these four cases. On this occasion, when the HELSTF winds were averaged along the 1-km path at a uniform height of 8 m, the resultant wind direction converged after 64 min. The wind speed, however, diverged by 20% to 25%.

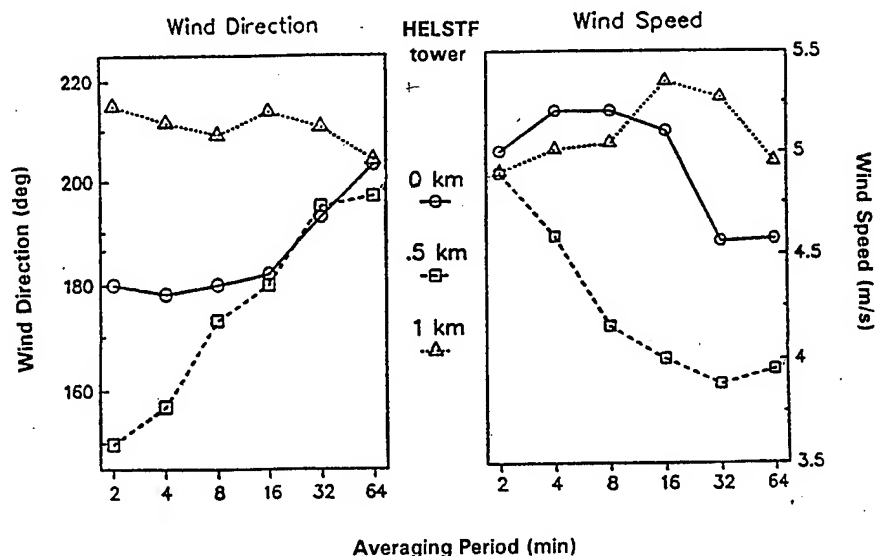


Figure 1. Average Wind Speed and Direction for 8-m height, 14 August 1990.

The three-phase experiment described in Section 1 was developed in an attempt to explain these observations. Specifically, for the anemometer analysis, these phases were

1. Calibration and analysis of current HELSTF anemometers,
2. Intercomparison of calibrated anemometers, and
3. Rerun of the wind variability case study/statistics.

The following paragraphs describe the initial phase. Reports on the other two phases will be published after they have been completed.

2.2 ANEMOMETER EXPERIMENT METHODS

The anemometer experiment utilized 13 generators and 14 propellers (7 polypropylene and 7 polystyrene). Each anemometer was inspected by a HELSTF technician and labelled; generators were numbered and propellers were labelled with a letter. Using a pre-determined pairing of generators and propellers, calibration measurements were acquired at the WSMR wind tunnel. The wind tunnel configuration placed a standard anemometer, a 10-hole chopper model 27106D generator (WT02) using HELSTF polystyrene propeller "B," and the HELSTF anemometer being calibrated along the air flow of the wind tunnel. Two types of

wind tunnel procedures were performed: starting/stopping threshold runs, and incremental wind speed runs.

Using modified wind tunnel software, the procedure for acquiring data during the starting/stopping threshold runs was as follows: All systems began at rest; the wind tunnel generator, which drove the fan regulating the wind tunnel air flow, was incrementally increased by 10 V. This increase continued until the standard chopper anemometer measured an air flow of 1 m s^{-1} ; at 1 m s^{-1} , the wind tunnel generator voltage was incrementally decreased by 10 V, until all systems were again at rest. A sample value from both the wind tunnel standard chopper anemometer and the HELSTF anemometer was acquired at every 10-V increment of the wind tunnel generator. The calibrated standard chopper anemometer system provided a known wind speed (m s^{-1}), which was correlated to the mV generator output of the HELSTF anemometer being calibrated. Each anemometer was subjected to five independent threshold runs. The threshold data were stored as ASCII files on 5.25-in floppy disks.

The incremental wind speed runs measured generator voltages at the following wind speeds: 0.8, 0.5, 1.2, 1.6, 2.0, 2.4, 2.5, 8.8, and 15.0 m s^{-1} . Unlike the continual increase/decrease of wind tunnel air flow employed in the threshold runs, the incremental wind speed runs required the wind tunnel to stabilize at a given wind speed, using a 1% tolerance. At each stabilized wind speed, 100 sequential mV output values from the HELSTF anemometer were collected and averaged. The order of wind speed sampling (0.8, 0.5, 1.2, m s^{-1}) was selected so that instrument hysteresis would be minimized. Each anemometer was run through the incremental wind speed sequence three times. The results were tabulated in hard copy. These data were hand-entered into the threshold files.

2.3 WIND TUNNEL RESULTS

Wind tunnel results consist of two parts. Thirteen averaged starting and stopping thresholds were generated from the five runs performed on each anemometer. In addition, a calibration curve was generated for each of the 13 anemometers. The appendix presents the calibration curve coefficients. To assist in evaluating the quality of the calibration curves, the appendix also presents some pertinent anemometer calibration curve statistics.

2.3.1 Starting/Stopping Thresholds

The five individual starting and stopping thresholds per anemometer were extracted from each starting (0 to 1 m s^{-1}) and stopping (1 to 0 m s^{-1}) threshold run and then averaged. The results are shown in Table 1. The averaged polypropylene starting thresholds ranged from 0.4 to 0.6 m s^{-1} , and the averaged stopping threshold range was 0.1 to 0.2 m s^{-1} . Due to the wind tunnel limitations at low speeds, spurious polystyrene starting threshold values were recorded; these values were deleted. The averaged polystyrene stopping thresholds were generally between 0.1 and 0.3 m s^{-1} .

2.3.2 Anemometer Calibration Curves

The 13 anemometer calibration curves were determined by first designing three data arrays: the STARTING data, which consisted of data from the incremental wind speed runs and the starting runs; the STOPPING data, which consisted of data from the incremental wind speed and the stopping runs; and ALL data, which consisted of data from the incremental wind speed, starting, and stopping runs. Linear, quadratic, and cubic regressions were then applied to each array. The "best fit" curve selected was the linear one,

$$Y = (m * X) + b \quad , \quad (1)$$

where X is the anemometer generator voltage measured in mV and Y is wind speed measured in m s^{-1} .

TABLE 1. Averaged Starting and Stopping Threshold Data

Anemometer ^a	Average Starting Threshold (m s ⁻¹)	Average Stopping Threshold (m s ⁻¹)
1T-P	0.47	0.13
2A-P	0.44	0.16
3C-P	0.38	0.10
4D-S	0.29	0.18
5E-P	0.49	0.11
6F-S	0.30	0.27
7G-P	0.55	0.15
8H-S	*	0.16
9I-P	0.57	0.14
10J-S	*	0.15
11K-P	0.47	0.10
12L-S	*	0.16
13M-S	*	0.16

^aNumber = generator; letter = propeller; -S, -P = polystyrene, polypropylene respectively; * = Deleted data

The polypropylene STARTING and STOPPING linear fits displayed distinct slopes; therefore, two separate polypropylene calibration curves were generated (fig. 2 and the appendix). The two calibration curves generated for the polypropylene anemometer represent the following data runs:

- Case 1. Starting threshold runs for values greater than 30 mV, stopping threshold runs, and incremental wind speed runs;
- Case 2. Starting threshold runs from 0 to 30 mV.

The application of the polypropylene calibration curves is as follows: For voltages above, or initiating above, 30 mV, use the Case 1 calibration curve. For generator voltages initiating at 0 mV up to 30 mV, use the Case 2 calibration curve. A scenario for using Case 1 would be when a still environment is suddenly interrupted by a wind gust producing an initial anemometer voltage greater than 30 mV. An example of Case 2 would be when winds gradually increase from rest or from a low speed.

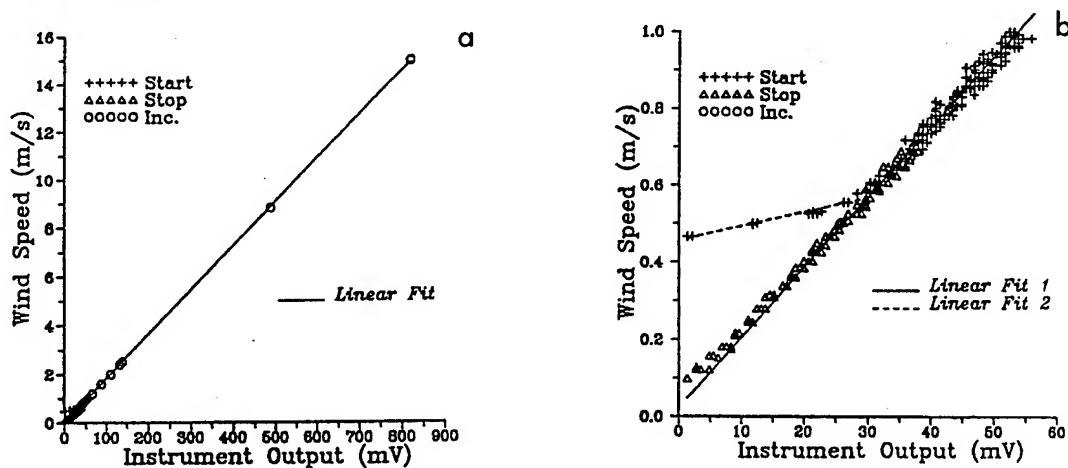


Figure 2. Polypropylene anemometer (1T) wind tunnel data and calibration curve. a: 0-900 mV (0-15 m s⁻¹) range; b: 0-60 mV (0-1 m s⁻¹) range. For clarity, b does not include stopping threshold data above 30 mV.

The slopes of the polystyrene STARTING and STOPPING linear fits were effectively the same. Thus, only one "best fit" curve was required per polystyrene anemometer (fig. 3 and the appendix). The single set of coefficients given in the appendix for the polystyrene anemometers was based on the ALL data array, which is nearly equivalent to the Case 1 data for the polypropylene anemometers. Polystyrene starting threshold data below 23 mV were found to be unreliable; therefore, these values were not included in the linear regression calculation.

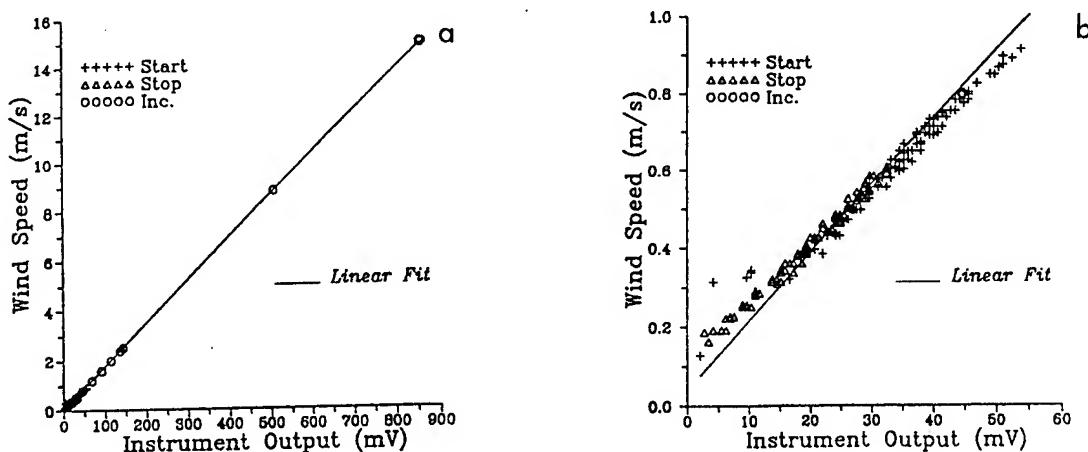


Figure 3. Polystyrene anemometer (2A) wind tunnel data and calibration curve. a: 0-900 mV ($0-15 \text{ m s}^{-1}$) range; b: 0-60 mV ($0-1 \text{ m s}^{-1}$) range. For simplicity, b does not include stopping threshold data above 30 mV.

An intercomparison of the calibration curves was performed by inserting a given set of generator voltages into each of the 13 calibration curves. Based on the maximum and minimum wind speeds calculated at a given voltage, the largest maximum/minimum difference (0.82 m s^{-1}) was found at high voltages/high wind speeds (Table 2). Using the midpoint between the maximum and minimum, the percent error was calculated. The greatest percent error (7.6%) was at low wind speeds. This result means that if a generator voltage of 25 mV (approximately 0.5 m/s) is inserted into any of the 13 calibration curves, the resulting wind speed will be no greater than 7.6% away from the midpoint. As the generator voltages were increased from 25 to 120 mV, the percent error decreased. Between 120 mV and 800 mV, the percent error was 2.9%.

TABLE 2. Calibration Curve Intercomparison Statistics

Generator Voltage (mV)	Wind Speed generated from the 13 calib. curves			
	Maximum (m s^{-1})	Minimum (m s^{-1})	Midpoint (m s^{-1})	Percent Error based on midpt(%)
25	0.53	0.45	0.49	7.6
40	0.79	0.71	0.75	5.5
60	1.15	1.05	1.10	4.2
80	1.50	1.40	1.45	3.6
20	2.21	2.08	2.14	2.9
140	2.57	2.42	2.50	2.9
500	9.11	8.60	8.85	2.9
800	14.56	13.74	14.15	2.9

A linear regression was calculated using all 2705 starting threshold run, stopping threshold run, and incremental wind speed run data generated by the 13 HELSTF anemometers at the wind tunnel. The result was

$$Y = (0.017450 \pm 0.000075) * X + (0.0367 \pm 0.0048) .$$

A second equation was formulated by averaging the 13 intercepts and 13 slopes from the Case 1 anemometer calibration curves. Since the averaged slope and intercept fell within the standard error of the initial curve, the above equation was accepted as a generic curve representing all 13 anemometers calibrated at the wind tunnel. Additional analysis and implementation of these results will be incorporated into future publications.

3. PART II: HUMIDITY ANALYSIS

3.1 HUMIDITY ANALYSIS BACKGROUND

Water vapor is responsible for 95% of laser beam absorption, and therefore for potential thermal blooming. The primary tool used to evaluate water vapor along the HELSTF range is the 1200 Series General Eastern Hygrometer (GEH). The GEH is an extremely accurate, though sometimes maintenance intensive, fundamental dew point measuring device (Beal, 1991). Figure 4 diagrams the operation principle of this thermal-electrically cooled, optically detected, automatically controlled condensation hygrometer used by HELSTF to measure dew point temperature. The acquisition of dew point data is the focus of the humidity analysis.

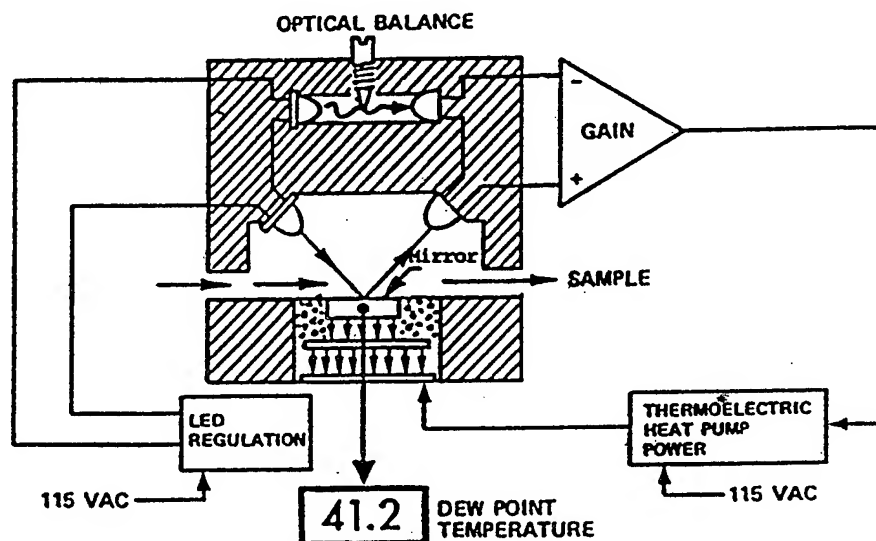


Figure 4. Basic Hygrometer Control Loop (General Eastern Corp., 1976).

In 1988 and 1990, three 1200MP GEH units were calibrated at the National Bureau of Standards, later renamed the National Institute of Standards and Technology (NIST). The result was a calibration curve such that resistance was a non-unique function of dew point temperature (fig. 5). In 1991, the NIST was sent two 1200AP GEH units. Each system consisted of a sensor head, control unit, and a short transportable cable like those normally used during laboratory work with the instruments. Three HELSTF investigators with various pertinent backgrounds went to NIST to participate in the calibration effort.

3.2 RESULTS OF THE 1991 NIST HELSTF HYGROMETER CALIBRATION

Figure 6 displays the individual linear calibration curves produced by the 1991 NIST measurements. During the NIST calibration, the Standard Calibration

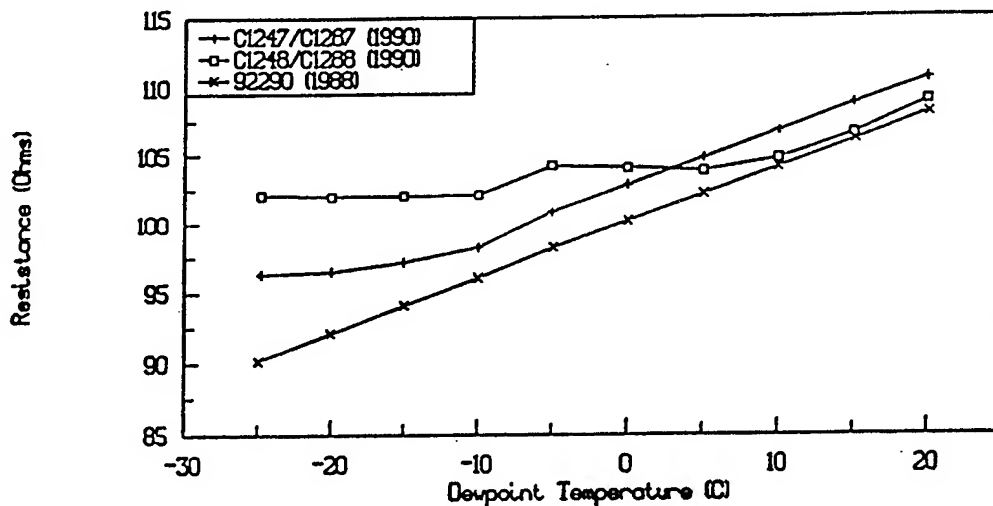


Figure 5. NIST hygrometer calibration curves, 1988 (92290), 1990 (C1247/C1287 and C1248/C1288). Note that C1248/C1288 displays resistance as a non-unique function of dewpoint temperature.

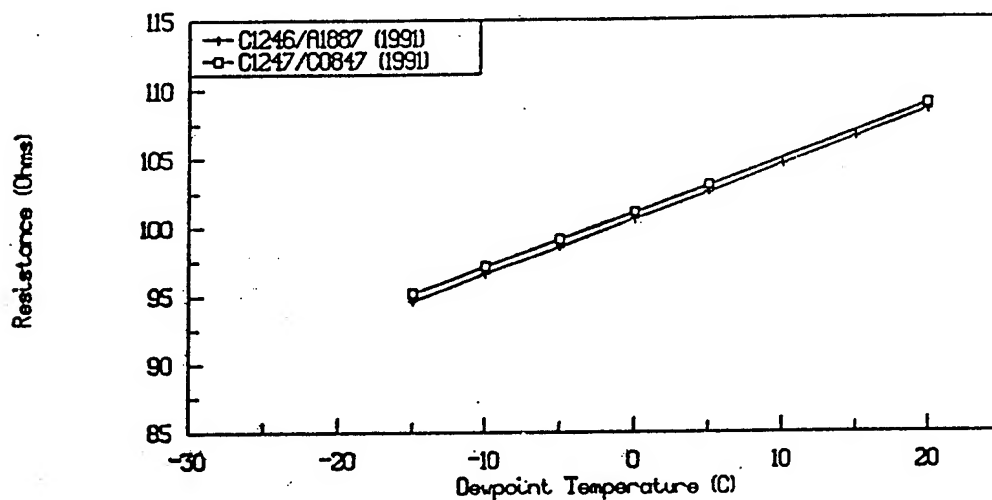


Figure 6. NIST hygrometer calibration curves, 1991. Legend numbers are unit/sensor head bar code references. Both curves are linear.

Procedure (SCP) used to calibrate the control unit electronics with the sensor head was found to be ineffective during periods of high dew point. Through a systematic analysis, a new SCP was developed. The revised SCP included potentiometer (pot) settings that allowed the GEH control unit to accommodate the abundance of moisture present at high dew points. This revised SCP was used during the NIST calibrations. It was also used for the post-NIST calibration implementation that was carried out during July-September 1991, coincident with the relatively high humidity of the New Mexico monsoon season.

3.3 POST-NIST CALIBRATION IMPLEMENTATION

Upon returning to HELSTF from NIST, the two GEH units were reassembled and recalibrated using the latest "absolute" NIST measurements and the revised SCP pot settings. Subsequent dew point temperature differences between the two units averaged approximately 1 °C. A comparison against a calibrated sling psychrometer confirmed that the GEH measurements were reasonable.

Using the revised SCP and a third short laboratory cable, a third sensor (1200MP) was field calibrated at HELSTF. All three units were brought to a HELSTF field site (the Gas Aerosol Sampling System van), where the longer tower cables were attached. The "zero" calibration was adjusted for the increased resistance of the tower cables, and six weeks of field experimentation commenced. The two 1200AP (NIST-calibrated) sensors maintained a separation of approximately 1 °C; the 1200MP sensor (not calibrated at NIST) displayed a separation of approximately 2 to 3 °C from the 1200AP units. A zero pot offset of +0.5 °C and -0.5 °C was imposed on the two 1200AP units. The nearly identical dew point temperatures measured following this offset persisted throughout the remaining test period. An unnatural variability in the 1200MP time series prohibited defining an offset for the 1200MP. The shape of the 1200MP time series curve, however, followed the other two 1200AP time series curves.

3.4 OBSERVED SPECIFICATIONS FOR THE CALIBRATED HELSTF HYGROMETERS

Observations showed that the 1200AP units track each other to within ± 0.2 °C. Without an absolute definition of "truth", the standard of accuracy was defined as the average of the two 1200AP NIST-calibrated GEH units measured at their respective "zero" points. Specifications for the 1200MP unit will be ascertained once new tower cables are installed on the instrument.

4. CONCLUSIONS FROM THE WIND AND HUMIDITY ANALYSES

The practical understanding of the anemometer and hygrometer gained during this effort has already enhanced the assessment and improvement of the HELSTF data acquired by the R.M. Young Gill UVW Anemometers and the GEH instruments. One of the anemometer experiment objectives was to compare the suitability of the polypropylene and polystyrene anemometers for the HELSTF mission. While the extremely low wind speed data (0 to 0.4 m s⁻¹) generated inconclusive results, the fact that the averaged polypropylene starting thresholds were well below the critical wind speed required for crosswind ventilation at HELSTF indicates that the polypropylene anemometers currently in use are the appropriate instruments for this requirement.

A differential of approximately 0.4 m s⁻¹ separated the averaged starting and stopping polypropylene anemometer thresholds. Since the HELSTF mission does not actively utilize wind speed data in the starting/stopping threshold region, the three-point operational calibration of the generator and the pre-mission relative wind speed check by tower is acceptable.

A second anemometer experiment objective was to ascertain the validity of utilizing a generic calibration curve in the operational software. While more research is recommended, the greatest uncertainty, based on the combined six polystyrene and seven polypropylene anemometer calibration curves compared in this study, was approximately 8%.

The two main improvements generated by the humidity analysis were (1) two linear, NIST-measured calibration curves for two HELSTF hygrometer sensor heads and (2) a revised SCP (calibrating the control unit interaction with the sensor head) that accommodates both "low" and "high" humidity conditions

Future work will involve incorporating the above improvements into the meteorological predictive/post-analysis database at HELSTF. Since critical decisions are based, in part, upon the dew point and wind measurements, the increased accuracy of the operational database should ultimately lead to more reliable mission judgements.

ACKNOWLEDGMENTS

The authors would like to acknowledge the WSMR wind tunnel personnel, as well as the HELSTF technical staff, for their support during the anemometer calibrations. Likewise, Dr. Peter Huang, Jimmy Yarbrough, and Alan Rishel are acknowledged for their participation in the hygrometer calibrations.

REFERENCES

- Beal, D., 1991: Evaluating Humidity Sensors: Practical Considerations, Sensors, The Journal of Machine Perception, 8:76-85.
- Freeman, K.P., and R.W. Endlich, 1991: Improving Atmospheric Characterizations at the High-energy Laser Systems Test Facility, *These Proceedings*.
- General Eastern Corporation, 1976: Instruction Manual System 1200M Meteorological/Environmental Dew Point and Temperature Monitoring System, General Eastern Corporation, Watertown, MA.
- Vaucher, G.T., and R.W. Endlich, 1991a: Improving Atmospheric Characterizations at HELSTF: Wind Analysis. STC Technical Report 6217, Science and Technology Corp., P.O. Box 7390, Hampton, VA.
- Vaucher, G.T., and R.W. Endlich, 1991b: Improving Atmospheric Characterizations at HELSTF: Humidity Analysis. STC Technical Report 6216, Science and Technology Corp., P.O. Box 7390, Hampton, VA.

APPENDIX

ANEMOMETER CALIBRATION CURVE COEFFICIENTS AND STATISTICS

TABLE A-1. POLYPROPYLENE AND POLYSTYRENE ANEMOMETER CALIBRATION CURVE COEFFICIENTS*

Anemometer	Case 1: 900-0 mV		Case 2: 0-30 mV Starting Only	
	b(intercept)	m(slope)	b(intercept)	m(slope)
1T-P	0.0234	0.018172	0.457	0.003647
2A-P	0.0469	0.017257	0.276	0.009443
3C-P	0.0230	0.017285	0.361	0.006311
4D-S	0.0413	0.017397		
5E-P	0.0417	0.017731	0.469	0.003389
6F-S	0.0853	0.017678		
7G-P	0.0324	0.017272	0.530	0.002057
8H-S	0.0255	0.017523		
9I-P	0.0239	0.017325	0.545	0.001964
10J-S	0.0208	0.017484		
11K-P	0.0241	0.017156	0.443	0.00339
12L-S	0.0405	0.017322		
13M-S	0.0286	0.017390		

*Based on the anemometer calibration data collected in July 1991 at the WSMR wind tunnel. Table A-1 incorporates the same anemometer labelling convention employed in Table 1.

TABLE A-2. ANEMOMETER CALIBRATION CURVE STATISTICS*

Anemometer	Standard Error(+/-)		Correlation Coefficient	r ²
	b(intercept)	m(slope)		
1T-P	0.0017	0.000015	0.9999	99.99
2A-P	0.0019	0.000016	0.9999	99.98
3C-P	0.0021	0.000016	0.9999	99.98
4D-S	0.0028	0.000023	0.9998	99.96
5E-P	0.0019	0.000014	1.0000	99.99
6F-S	0.0034	0.000030	0.9997	99.93
7G-P	0.0018	0.000013	1.0000	99.99
8H-S	0.0022	0.000017	0.9999	99.98
9I-P	0.0017	0.000013	0.9999	99.99
10J-S	0.0025	0.000021	0.9998	99.97
11K-P	0.0019	0.000014	0.9999	99.99
12L-S	0.0022	0.000018	0.9999	99.98
13M-S	0.0021	0.000018	0.9999	99.98

*based on the Case 1: 900- to 0-mV linear regression "best fit" calibration curves.

Session V

PBL ENERGY BUDGET

**Thursday
5 December 1991**

**Chairperson
Dr. Austin Hogan**

ESTIMATING EFFECTS OF TEMPERATURE AND MOISTURE ON C_n^2 IN THE DAMP UNSTABLE
BOUNDARY LAYER FOR VISIBLE, INFRARED, RADIO, AND MILLIMETER WAVELENGTHS

Arnold Tunick and Henry Rachele
U.S. Army Atmospheric Sciences Laboratory
White Sands Missile Range, New Mexico 88002-5501, USA

ABSTRACT

Data collected over barren and vegetated ground surfaces were used to obtain estimates of C_n^2 for the damp unstable boundary layer. These data consisted of latent and sensible heat fluxes. Results from this study show that moisture effects on C_n^2 can be larger than generally reported in the literature. Results presented emphasize the relative contributions of temperature and moisture to C_n^2 for visible, infrared, radio, and millimeter wavelengths.

1. INTRODUCTION

The battlefield environment affects the degree to which high-resolution advanced sensors and systems operate, including lasers and imaging systems (Miller and Ricklin, 1990). A parameter of primary interest in assessing atmospheric effects on imaging is the optical turbulence structure parameter C_n^2 , which is strongly a function of temperature and moisture gradients. The purpose of this paper is to present formulations and results of the effects of temperature and moisture on C_n^2 in the visible, infrared (IR), radio, and millimeter (mm) wavelengths under clear skies and for unstable atmospheric conditions over moist grass and barren surfaces.

2. DATA

One set of data came from a field experiment conducted at Davis, California, during the summer of 1966 (Stenmark and Drury, 1970; Brooks, 1968; and Morgan et al., 1970). The data were taken during periods when the surrounding fields were covered with fescue grass and well irrigated, giving, in effect, homogeneous surface conditions with respect to temperature and moisture. Basic data consisted of net, latent, and sensible heat fluxes. Raw data were processed to give 1/2-h average values.

A second set of data, three cases, was measured by Fritschen and Nixon (1965) in Arizona during late April and early May 1961. Basic data consisted of net, latent, and sensible heat fluxes. Energy balance components were measured over open water, then over wet and dry bare soil for 3 different days. Both sets of data were used to determine the values of θ^* and q^* , required to evaluate C_n^2 (see eqs. (26) through (32)).

3. EQUATIONS

The parameter of interest, C_n^2 , that we use evolved from a number of researchers, including Tatarski (1961), Panofsky (1968), Wyngaard (1973), Hill (1989), Hill and Clifford (1978), and Andreas (1988), giving

$$C_n^2(z) = b K_H \epsilon^{-1/3} \left[\frac{\partial n}{\partial z} \right]^2, \quad (1)$$

where

b = Obukhov-Corrsin constant = 3.2 (Hill, 1989; Wyngaard, 1973; Andreas, 1988).

$$\epsilon = \text{energy dissipation rate} = u^{*3} (\phi_m - \zeta) / kz \text{ (Panofsky, 1968)} \quad (2)$$

z = height above ground

K_H = turbulent exchange coefficients for heat = $u^* kz / \phi_H(\zeta)$

u^* = friction velocity

$\phi_H(\zeta)$ = dimensionless lapse rate = $(1 - 15\zeta)^{-1/2}$ (Dyer, 1974; Hicks, 1976; Hansen, 1980)

k = von Karman's constant = 0.4

$\phi_m(\zeta)$ = dimensionless wind shear = $(1 - 15\zeta)^{-1/4}$

ζ = scaling ratio = z/L

L = Monin-Obukhov length = $u^* \theta / kg \theta_v^*$, (Lumley and Panofsky, 1964)

θ = potential temperature

θ_v^* = virtual potential temperature scaling parameter (see eq. (29))

g = acceleration due to gravity

$\partial n / \partial z$ = the gradient of the mean refractive index

The expressions we use for determining $\partial n / \partial z$ are based on expressions given by Andreas (1988) for various wavelengths of interest. However, note that we modified Andreas' formulations, which are expressed in terms of temperature and absolute humidity gradients, to expressions in terms of potential temperature and specific humidity gradients as required by Tatarski (1961). Expressions for n and $\partial n / \partial z$ for visible, IR, radio, and mm regions are given below.

a. Visible region (wavelengths from 0.36 to 3 μm). Andreas (1988) writes

$$n_v = 1 + \left\{ M_1(\lambda) \frac{P}{T} + 4.6150(M_2(\lambda) - M_1(\lambda))Q \right\} 10^{-6}, \quad (3)$$

where

$$M_1(\lambda) = 23.7134 + \frac{6839.397}{130 - \sigma^2} + \frac{45.473}{38.9 - \sigma^2}, \quad (4)$$

$$M_2(\lambda) = 64.8731 + 0.58058\sigma^2 - 0.0071150\sigma^4 + 0.0008851\sigma^6, \quad (5)$$

σ is λ^{-1} for λ in micrometers, Q is absolute humidity (kilograms per cubic meter), P is pressure in millibars, and T is temperature in degrees kelvin.

Transforming eq. (3) in terms of potential temperature (θ) and specific humidity (q) gives

$$n_v = 1 + \left\{ M_1(\lambda) \frac{P}{\theta - \gamma_d(z - z_r)} + 1.60948 [M_2(\lambda) - M_1(\lambda)] \frac{Pq}{\theta - \gamma_d(z - z_r)} \right\} 10^{-6} \quad (6)$$

For steady state, homogeneous conditions, eq. (6) yields

$$\begin{aligned} \frac{\partial n_v}{\partial z} = & \left\{ -M_1(\lambda) \frac{P}{T^2} - 1.61 (M_2(\lambda) - M_1(\lambda)) \frac{Pq}{T^2} \right\} \times 10^{-6} \frac{\partial \theta}{\partial z} \\ & + 1.61 (M_2(\lambda) - M_1(\lambda)) \frac{P}{T} \times 10^{-6} \frac{\partial q}{\partial z} . \end{aligned} \quad (7)$$

b. IR window (wavelengths from 7.8 to 19 μm). Andreas (1988), who credits Hill and Lawrence (1986), writes

$$n_i = 1 + \{ n_{vd} + n_{iw} \} \times 10^{-6} , \quad (8)$$

where for $-40 \leq T \leq 40$ $^{\circ}\text{C}$

$$n_{iw} = Q \left[\frac{957 - 928 \alpha^{0.4}(X - 1)}{1.03\alpha^{0.17} - 19.8X^2 + 8.2X^4 - 1.7X^8} + \frac{3.747 \times 10^6}{12499 - X^2} \right] , \quad (9)$$

and

$$n_{vd} = M_1(\lambda) \frac{P}{T} - 4.6150 M_1(\lambda) Q , \quad (10)$$

where $\alpha = T/273.16$, and T is in degrees kelvin.

$X = 10 \mu\text{m}/\lambda$, where λ is wavelength in micrometers.

Substituting $Q(\text{kg}^{-3}) = 3.4875 \times 10^{-1} Pq/T$ into eqs. (9) and (10), and taking the derivative of eq. (8) in terms of θ and q gives

$$\begin{aligned} \frac{\partial n_i}{\partial z} = & (-M_1(\lambda) \frac{P}{T^2} + 1.6095 M_1(\lambda) \frac{Pq}{T^2} \\ & + 0.34875 \frac{Pq}{T} \left[\left[- \frac{1.359\alpha^{-0.6}(X - 1)}{1.03\alpha^{0.17} - 19.8X^2 + 8.2X^4 - 1.7X^8} \right. \right. \\ & \left. \left. + \frac{0.5949\alpha^{-0.43}(X - 1)}{(1.03\alpha^{0.17} - 19.8X^2 + 8.2X^4 - 1.7X^8)^2} \right] \right] \\ & - 3.4875 \times 10^{-1} \left[\frac{Pq}{T^2} \right] \times 10^{-6} \frac{\partial \theta}{\partial z} \\ & + \left(3.4875 \times 10^{-1} \left[\frac{Pq}{T} \right] - 1.6095 M_1(\lambda) \right) \frac{P}{T} \times 10^{-6} \frac{\partial q}{\partial z} . \end{aligned} \quad (11)$$

where [] is the coefficient in eq. (9).

c. Radio region (wavelengths greater than 3 mm)

For this wavelength region Andreas writes

$$n_r = 1 + (n_{rd} + n_{rw}) \times 10^{-6} \quad (12)$$

where, from Hill et al. (1982) and Boudouris (1963),

$$n_{rd} = 77.6 \frac{(P - e)}{T}, \quad (13)$$

$$n_{rw} = 72.0 \frac{e}{T} + 0.375 \times 10^6 \frac{e}{T^2}, \quad (14)$$

and

$$e \text{ (vapor pressure)} = 4.6150 QT. \quad (15)$$

Since $Q \text{ kg}^{-3} = 0.34875 \frac{Pq}{T}$, for P in millibars,

(16)

eq. (15) becomes

$$e = 1.6096Pq. \quad (17)$$

Substituting eq. (17) into eqs. (13) and (14) results in

$$n_{rd} = 77.6 \frac{P}{T} - 1.249 \times 10^2 \frac{Pq}{T}, \quad (18)$$

and

$$n_{rw} = 1.159 \times 10^2 \frac{Pq}{T} + 6.0356 \times 10^5 \frac{Pq}{T^2}. \quad (19)$$

From eqs. (18), (12), and (19) we obtain

$$\begin{aligned} \frac{\partial n_r}{\partial z} = & \left\{ -77.6 \frac{P}{T^2} + 9 \frac{Pq}{T^2} - 1.2071 \times 10^6 \frac{Pq}{T^3} \right\} \times 10^{-6} \frac{\partial \theta}{\partial z} \\ & + \left\{ -9 \frac{P}{T} + 6.0356 \times 10^5 \frac{P}{T^2} \right\} \times 10^{-6} \frac{\partial q}{\partial z}. \end{aligned} \quad (20)$$

d. Near-millimeter region (wavelengths from 0.3 to 3 mm). From Andreas

$$n_m = 1 + (n_{rd} + n_{rw} + n_{mw1} + n_{mw2}) \times 10^{-6}, \quad (21)$$

where n_{rd} and n_{rw} are given in section c., and n_{mw1} is due to vapor resonances at wavelengths < 0.3 mm, and n_{mw2} for water-vapor resonances at wavelengths of > 0.3 mm. According to Andreas, Hill (1991) evaluated the n_{mw1} and n_{mw2} terms, and although the n_{mw2} term requires a line-by-line summation of the resonances and consequently does not have a single analytical form, he did produce an approximation for n_{mw1}

$$n_{mw1} = Q \sum_{j=1}^4 \alpha_j (296/T)^{a_j} [1 - B_j (296/T)] (0.303/\lambda)^{2j}, \quad (22)$$

where α_j , a_j , and B_j are given in table 1 below.

TABLE 1. THE COEFFICIENTS IN EQ. (20)

j	α_j	a_j	B_j
1	1.388221×10^3	1.650000	0.1993324
2	-0.2135129×10^3	0.1619430	3.353494
3	-0.1485997×10^3	0.1782352	3.100942
4	-0.1088790×10^3	0.1918662	3.004944

For the sake of an analytic solution, Andreas does not consider the effect of n_{mw2} . We follow his lead in this study. As such the approximation should be accurate to ± 10 percent in the window regions 0.31 - 0.34 mm (880 - 970 GHz), 0.42 - 0.44 mm (680 - 720 GHz), and 0.83 - 3 mm (100 - 360 GHz).

Rewriting eq. (22) in terms of q gives

$$n_{mw1} = 0.34875 \frac{Pq}{T} \sum (). \quad (23)$$

The contribution of eq. (23) to $\frac{\partial n_m}{\partial z}$ is

$$\frac{\partial n_m}{\partial z} = -0.34875 \frac{Pq}{T^2} \sum () \times 10^{-6} \frac{\partial \theta}{\partial z} + 0.34875 \frac{P}{T} \sum () \times 10^{-6} \frac{\partial q}{\partial z}. \quad (24)$$

Combining eqs. (21) and (24) gives

$$\begin{aligned} \frac{\partial n_m}{\partial z} = & \left\{ -77.6 \frac{P}{T^2} + \frac{9Pq}{T^2} - 1.2071 \times 10^6 \frac{Pq}{T^3} - 0.34875 \frac{Pq}{T^2} \sum () \right\} \times 10^{-6} \frac{\partial \theta}{\partial z} \\ & + \left\{ -9 \frac{P}{T} + 6.0356 \times 10^5 \frac{P}{T^2} + 0.34875 \frac{P}{T} \sum () \right\} \times 10^{-6} \frac{\partial q}{\partial z}. \end{aligned} \quad (25)$$

Values of $d\theta/dz$ and dq/dz required to evaluate the dn/dz equations are based on Obukhov similarity forms, where we assumed that the environment is in steady state and homogeneous. For the unstable case we write $\partial\theta/\partial z$ and $\partial q/\partial z$ in accordance with Dyer (1974), Hicks (1976), and Hansen (1980).

To obtain θ^* and q^* , however, we augment eqs. (26) and (27) with similarity forms for the windspeed V and Monin-Obukhov length L :

$$\frac{\partial \theta}{\partial z} = \frac{\theta^*}{kz} \left[1 - 15 \frac{z}{L} \right]^{-1/2}; \quad \frac{\partial q}{\partial z} = \frac{q^*}{kz} \left[1 - 15 \frac{z}{L} \right]^{-1/2}; \quad (26), (27)$$

$$\frac{\partial v}{\partial z} = \frac{u^*}{kz} \left[1 - 15 \frac{z}{L} \right]^{-1/4} \quad (28)$$

where

$$L = \frac{u^{*2} \theta_{vr}}{kg \theta_v^*}, \text{ or } L = - \frac{u^{*3} C_p \rho \theta_{vr}}{kg H_v}, \quad (29a), (29b)$$

where from Busch (1973), Businger (1973), and Van Boxel et al. (1989)

$$\theta_v^* = \theta^* + 0.61 \theta q^*. \quad (30)$$

Since in this study we used data that was primarily in buoyant and latent heat flux form, we approximated θ^* , q^* , and u^* from the flux equations given in eqs. (31) and (32) together with eq. (29b) and the integrated form of eq. (28),

$$H_v = - C_p \rho u^* \theta^* - C_p \rho u^* (.61 \theta_r q^*) \quad (31)$$

$$L'E = - L \rho u^* q^*. \quad (32)$$

4. RESULTS

Figures 1 through 8 provide estimates of the total reference level (2 m) C_n^2 , as well as the portion of C_n^2 due to sensible heat and moisture for 2 days, clear sky periods at Davis, California, for the visible, IR, radio, and millimeter wavelengths. Values of C_n^2 were computed for every 30 min period for each case. Figures 9 and 10 illustrate the windspeed and relative humidity values for the two cases considered above.

Table 2 gives the total and portioned values of reference level C_n^2 for the water cover, wet and dry soils of the Salt River Valley, Arizona, site for the four wavelengths of interest. Note that for the results presented, we require that any term that contains q or $\partial q / \partial z$ as a factor is a contributor to the moisture effect.

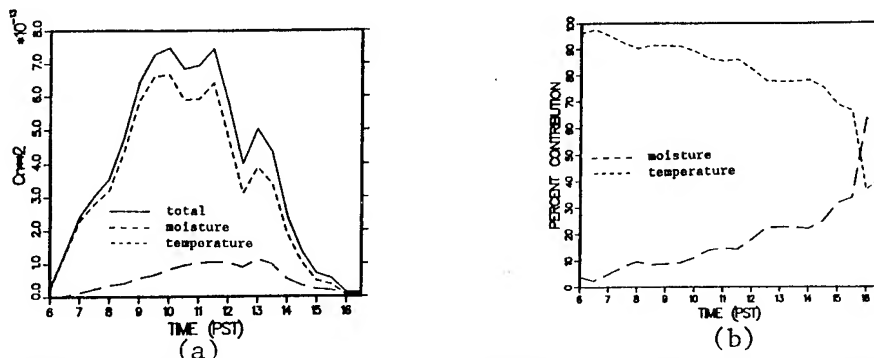


Figure 1. CASE 1--Total and portioned reference level C_n^2 - visible.

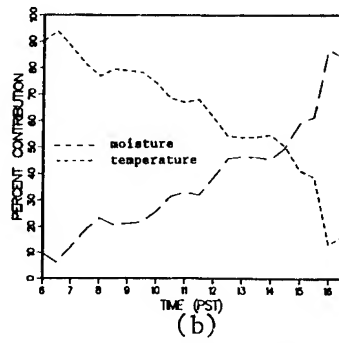
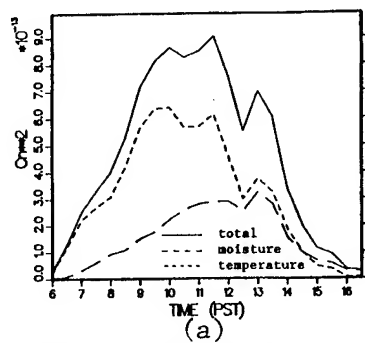


Figure 2. CASE 1--Total and portioned reference level C_n^2 - IR.

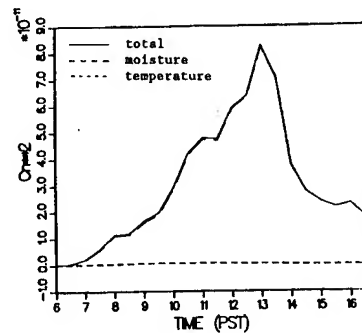
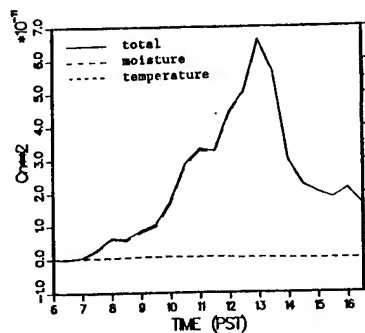


Figure 3. CASE 1--Total and portioned reference level C_n^2 - radio.

Figure 4. CASE 1--Total and portioned reference level C_n^2 - mm.

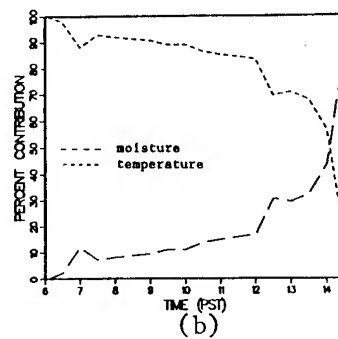
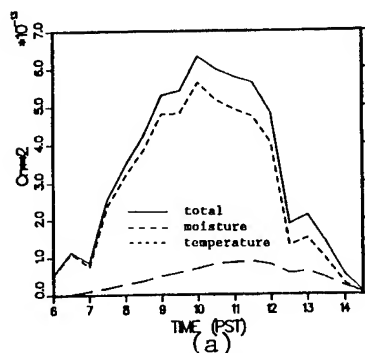


Figure 5. CASE 2--Total and portioned reference level C_n^2 - visible.

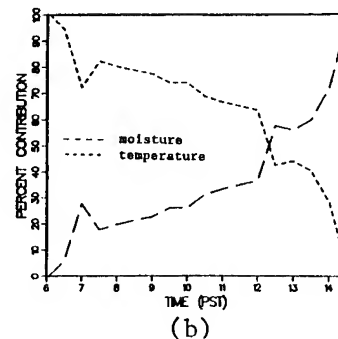
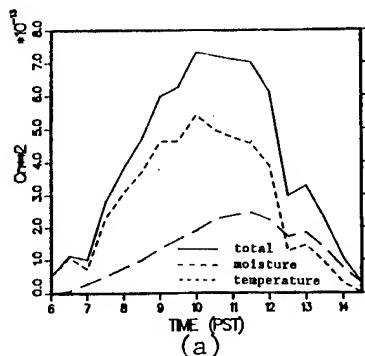


Figure 6. CASE 2--Total and portioned reference level C_n^2 - IR.

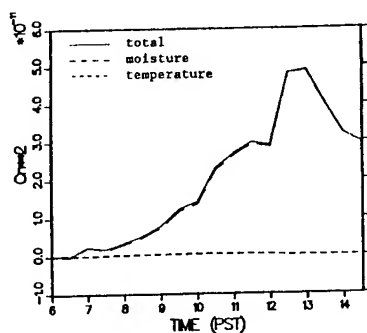


Figure 7. CASE 2--Total and portioned reference level C_n^2 - radio.

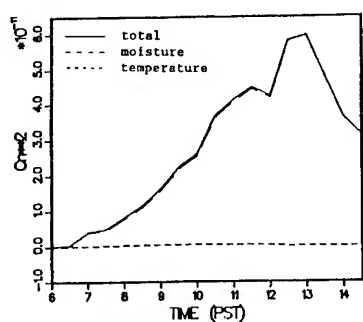


Figure 8. CASE 2--Total and portioned reference level C_n^2 - mm.

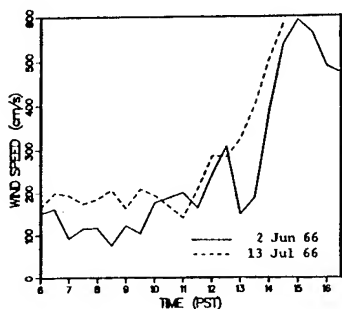


Figure 9. Windspeed vs time, Davis, CA, data.

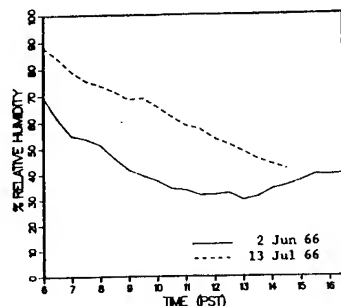


Figure 10. Relative humidity vs time, Davis, CA, data.

TABLE 2. TOTAL AND PORTIONED VALUES OF REFERENCE LEVEL C_n^2 FOR THE SALT RIVER VALLEY, ARIZONA

		Total C_n^2	% Temperature Effect	% Moisture Effect
A. Water Covered Soil				
T = 17.1 °C	visible	3.12×10^{-13}	77.0	23.0
V(m/s) = 2.1	IR	4.37×10^{-13}	53.0	47.0
RH = 18.0%	radio	4.53×10^{-11}	0.5	99.5
	mm	5.50×10^{-11}	0.4	99.6
B. Wet Soil				
T = 23.9 °C	visible	4.48×10^{-14}	2.0	98.0
V(m/s) = 1.8	IR	2.58×10^{-13}	0.3	99.7
RH = 15.5%	radio	3.49×10^{-10}	~0	~100
	mm	3.63×10^{-10}	~0	~100
C. Dry Soil				
T = 25.9 °C	visible	2.43×10^{-13}	80.0	20.0
V(m/s) = 2.3	IR	3.26×10^{-13}	57.0	43.0
RH = 15.8%	radio	2.45×10^{-11}	0.8	99.2
	mm	3.11×10^{-11}	0.6	99.4

5. ANALYSES AND CONCLUSIONS

Figures 1 through 8 show that C_n^2 increases with wavelengths for the cases considered in this paper. We expect that this is true in general. The effect of moisture on C_n^2 also increased with wavelength.

However, in contrast with other authors, Antonia et al. (1978), Friehe et al. (1975), Hill et al. (1988), McBean and Elliot (1981), we found that the moisture effects in the visible cannot only be greater than reported in the literature, but can actually exceed the temperature effect (see figs. 1 and 5). This is due to the fact that as windspeed increases (fig. 9) the sensible heat flux decreases and the latent heat flux increases. This could occur any time of the day. Similarly, for a given soil type the sensible heat flux decreases as soil wetness increases (Angus-Leppan and Brunner, 1980). Also, as indicated by Angus-Leppan, the sensible heat flux decreases when the ground is covered by plants and when the windspeed is considered. Since the wetness, plant cover, and wind have an effect on the estimates of sensible and latent heat fluxes, then they also have an effect on the moisture contributions to C_n^2 at all wavelengths.

Finally, we emphasize that the primary effects of temperature and moisture on C_n^2 is through their gradients, not their magnitudes. For instance, in fig. 10, we note that early in the morning the relative humidity is high, but the moisture contributions to C_n^2 is small; whereas, in the afternoon the relative humidity is small, but the moisture contribution is large.

REFERENCES

- Angus-Leppan, P. V., and F. K. Brunner, 1980: Atmospheric Temperature Models for Short Range EDM. The Canadian Surveyor, 34(2):153-165.
- Antonia, R. A., A. J. Chambers, C. A. Friehe, 1978: Statistical Properties of Optical Refractive Index Fluctuations in the Marine Boundary Layer. Boundary Layer Meteorol.
- Andreas, E. L., 1988: Estimating C_n^2 Over Snow and Sea Ice from Meteorological Data. J. Opt. Soc. Am., 5(4).
- Boudouris, G., 1963: On the Index of Refraction of Air, the Absorption and Dispersion of Centimeter Waves by Gases. J. Res. NBS, Sec. D, 67:631-684.
- Brooks, F. A., et al., 1968: Analysis in Transfers of Energy, Momentum and Moisture Near the Ground. Final Report, ECOM 66-G26-F, U.S. Army Electronics Command, Atmospheric Sciences Laboratory, Fort Huachuca, AZ.
- Busch, N. E., 1973: On the Mechanics of Atmospheric Turbulence, Chapter 1. In Workshop on Micrometeorology, D. A. Haugen (ed), American Meteorological Society, Boston, MA, pp 1-66.
- Businger, J. A., 1973: Turbulent Transfer in the Atmospheric Surface Layer, Chapter 2. In Workshop on Micrometeorology, D. A. Haugen (ed), American Meteorological Society, Boston, MA.
- Dyer, A. J., 1974: A Review of Flux-Profile Relations. Boundary Layer Meteorology, 1:363-372.
- Friehe, C. A., J. C. LaRue, F. H. Champagne, C. H. Gibson, G. F. Dreyer, 1975: Effects of Temperature and Humidity Fluctuations on the Optical Refractive Index on the Marine Boundary Layer. J. Opt. Soc. Am.

- Fritschen, L. J., and P. R. Nixon, 1965: Microclimate Before and After Irrigation, Presented at the Section on Applications for Ground-Level Climatology, Annual Meeting of American Association for Advancement of Science, Berkley, California, 27-30 December 1965, Contribution from the Soil and Water Conservation Research Division, Agricultural Research Service, U.S. Department of Agriculture, Phoenix, AZ.
- Hansen, Frank V., 1980: Flux-Profile Relationships for Development of Standard of Comparison. Internal Report, U.S. Army Atmospheric Sciences Laboratory, White Sands Missile Range, NM 88002-5501.
- Hicks, B. B., 1976: Wind Profile Relationships from the Wangara Experiment, Quart. J. Roy. Meteorol. Soc., 102:535-551.
- Hill, R. J., 1991: Dispersion by Atmospheric Water Vapor at Frequencies Less Than 1 THz. IEEE Trans. Antennas Propag. (to be published).
- Hill, R. J., 1989: Implications of Monin-Obukhov Similarity Theory For Scalar Quantities. J. Atmos. Sci., 46:2236-2244.
- Hill, R. J., R. A. Bohlander, S. F. Clifford, R. W. McMillian, J. T. Priestly, and W. P. Schoenfeld, 1988: Turbulence - Induced Millimeter-wave Scintillation Compared with Micrometeorological Measurements. IEE Transactions on GeoScience and Remote Sensing.
- Hill, R. J., and S. F. Clifford, 1978: Modified Spectrum of Atmospheric Temperature Fluctuations and its Application to Optical Propagation. J. Opt. Soc. Am., 68:892-899.
- Hill, R. J., and R. S. Lawrence, 1986: Refractive Index of Water Vapor in Infrared Windows. Infrared Physics, 26:371-376.
- Hill, R. J., R. S. Lawrence, and J. T. Priestley, 1982: Theoretical and Calculational Aspects of the Radio Refractive Index of Water Vapor. Radio Sci. 17:1251-1257.
- Lumley, J. L., and H. A. Panofsky, 1964: The Structure of Atmospheric Turbulence. John Wiley and Sons, Inc. New York - London - Sydney.
- McBean, G. A., and J. A. Elliot, 1981: Pressure and Humidity Effects on Optical Refractive Index Fluctuations. Boundary Layer Meteorology.
- Miller, W. B., and J. C. Ricklin, 1990: A Module for Imaging Through Optical Turbulence: IMTURB. ASL-TR-0221-27, U.S. Army Atmospheric Sciences Laboratory, White Sands Missile Range, NM 88002-5501.
- Morgan, D. L., et al., 1970: Evaporation From an Irrigated Turf Under Advection of Dry Air at Davis, California. ECOM-68-G10-1, U.S. Army Electronics Command, Atmospheric Sciences Laboratory, Fort Huachuca, AZ.
- Panofsky, H. A., 1968: The Structure Constant for the Index of Refraction in Relation to the Gradient of Index of Refraction in the Surface Layer. J. Geophys. Res. 73:6047-6049.
- Sternmark, E. B., and L. D. Drury, 1970: Micrometeorological Field Data From Davis, California: 1966-67 Runs Under Non-advective Conditions. ECOM-6051, U.S. Army Electronics Command, Atmospheric Sciences Laboratory, Fort Huachuca, AZ.
- Tatarski, V. I., 1961: Wave Propagation in a Turbulent Medium. McGraw-Hill Book Company, Inc., New York - Toronto - London.
- Van Boxel, J. H., H. F. Vugts, and F. Cannemeijer, 1989: Effect of the Water Vapour Gradient on the Obukhov Length and the Profile-Derived Fluxes. Zeitschrift fur Meteorologie, Band 39, Heft 6.
- Wyngaard, J. C., 1973: On Surface-layer Turbulence. In Workshop on Micrometeorology, D.A. Haugen, (ed), American Meteorological Society, Boston, MA, pp 101-149.

ENERGY BALANCE MODEL FOR IMAGERY AND ELECTROMAGNETIC PROPAGATION

Henry Rachele and Arnold Tunick
U.S. Army Atmospheric Sciences Laboratory
White Sands Missile Range, New Mexico 88002-5501, USA

ABSTRACT

The optical turbulence structure parameter C_n^2 typically appears in formulations used to estimate the effects of temperature and moisture (gradients) on imagery and electromagnetic propagation. Temperature and moisture gradients can be approximated from sensible and latent heat flux estimates; these fluxes can be obtained from radiation/energy balance equations. Numerous energy balance models exist requiring different kinds and numbers of inputs. The semiempirical model developed and presented in this paper was constrained to require a minimum number of conventional measurements at a reference level (2 m). These measurements include temperature, pressure, relative humidity, and windspeed. The model also requires a judgment of soil type and moisture (dry, moist, or saturated), cloud characteristics (tenths of cloud cover and density), the day of the year, time of day, and longitude and latitude of the site of interest. Model estimates of net radiation and sensible and latent heat fluxes are compared with measured values.

1. INTRODUCTION

Numerous radiation/energy balance models appear in the literature (Angus-Leppan and Brunner (1980), Webb (1984), Campbell (1985), Pielke (1984), Danard et al. (1984), Yamada (1981), and Carson (1987) to name a few) varying from comparatively simple to academically complex, requiring different amounts and numbers of inputs and computer capabilities. In this paper we present a model (hereafter known as the RT model) that was developed for imaging and electromagnetic propagation applications when a minimum of atmospheric information is available. The primary outputs of the RT model are estimates of sensible and latent heat fluxes, which, in turn, are used for estimating gradients of potential temperature and specific humidity, making use of similarity relations. These gradients are then used to estimate the optical turbulence parameter C_n^2 needed in the imaging and propagation equations.

Because of the many formulations in the RT radiation/energy balance model and the page limitation of the paper, the remaining sections of this paper are limited to brief discussions of model concept, computational procedure, model results, summary and conclusions, and references. A detailed development of the model is in preparation as a U.S. Army Atmospheric Sciences Laboratory technical report.

2. MODEL CONCEPT

The model concept is a fallout from the following operational scenario. One is interested in estimating the optical turbulence parameter C_n^2 at a temporary site for different times of 1 day. The day of interest is known and the longitude and latitude of the site is known. From geologic maps one knows the soil composition; and from meteorological reports one has an estimate of soil wetness, that is, dry, moist, or saturated. However, if the geologic and meteorological reports are not available, one judges on-the-spot by examining samples of soil from the surface to 10 cm below the surface. In addition to the soil judgment, one also judges sky conditions--in particular, the amount of cloud cover (in tenths from 0 to 1) and the density of the clouds (0 to 3). From the above information, one proceeds to estimate the sensible and latent heat fluxes by using numerous equations consistent with convention and formulations of radiation and energy balance by Carson (1987), briefly stated below.

2.1 RADIATION BALANCE CONCEPTS

Net radiation flux, R_N , at the soil surface is equal to the sum of the net shortwave radiative flux, R_{SN} , and the net longwave radiative flux, R_{LN} ,

$$R_N = R_{SN} + R_{LN} , \quad (1)$$

where, in turn,

$$R_{SN} = R_{S\downarrow} - \alpha R_{S\downarrow} . \quad (2)$$

$R_{S\downarrow}$ is the downward shortwave radiative flux (including both the direct solar flux and diffuse radiation from the sky) and $\alpha R_{S\downarrow}$ is the shortwave radiation reflected at the earth's surface, where α is the surface shortwave reflectivity commonly called albedo.

The net longwave radiative flux R_{LN} is

$$R_{LN} = a R_{L\downarrow} - \epsilon \sigma T_g^4 , \quad (3)$$

where $R_{L\downarrow}$ is the downward longwave radiation and a is the surface absorptivity to longwave radiation. The upward flux (Stefan's law) due to thermal emission at the earth's surface is $\epsilon \sigma T_g^4$, where T_g is the surface temperature, ϵ is the longwave emissivity at the surface, and σ is the Stefan-Boltzman constant.

2.2 SURFACE ENERGY FLUX BALANCE CONCEPTS

The energy flux balance at the soil surface is

$$R_N = H + L/E + G_g , \quad (4)$$

where R_N is the net radiative flux, H is the turbulent sensible heat flux, L/E is the latent heat flux, and G_g is the flux of heat into the soil.

3. COMPUTATIONAL PROCEDURE

The following parameters are assumed to be known at a geographical site where one wishes to compute estimates of sensible and latent heat fluxes: (1) longitude and latitude of the site; (2) day of year and time of day; (3) reference level (2 m) values of temperature (T_r), pressure (P_r), relative humidity (f_r), and windspeed (V_r); (4) a measure or judgment of cloud cover in tenths and cloud density on a scale of 0 to 3 (3 being most dense); (5) the albedo of the soil, including vegetative cover; and (6) composition and wetness of the soil (dry, moist, saturated).

Step 1: Compute the elevation angle $\theta = 90^\circ - Z$ of the sun at the times of interest using Woolf's (1968) formulations. See eqs. (15) through (27) in steps 7 and 8.

Step 2: Compute a first approximation of the sensible heat flux H for dry ground and cloudless skies using Angus-Leppan and Brunner (1980), that is,

$$H = 450C W \sin \theta \text{ for } C = W = 1 \text{ (in fig. 1) .} \quad (5)$$

Step 3: Compute the friction velocity u^* and the Monin-Obukhov length L

$$u^* = V_r k \left\{ \ln \left[\frac{x-1}{x+1} \right] + 2 \tan^{-1} x \right\} \Big|_{z_0}^{z-d} \quad (6)$$

$$X = \left[1 - 15 \frac{Z}{L} \right]^{1/4} \quad (7)$$

$$L = - u^{*3} C_p \rho T_r / kgH , \quad (8)$$

where V_r is the reference level windspeed, k is von Karman's constant (0.4), C_p is the specific heat of air, ρ is the air density, T is the temperature at reference height, g is acceleration due to gravity, and z_0 is the roughness length for momentum, where from Liu et al. (1976)

$$\ln(z_0) = -2.85 + 1.19 \ln z_e , \quad (9)$$

where z_e is the height of the roughness element.

Step 4: Compute the potential temperature scaling constant θ^* using

$$\theta^* = u^{*2} T_r / kgL . \quad (10)$$

Step 5: Knowing T_r , θ^* , and L compute the effective temperature T_g at height z_h (RT modification of Verma (1989)) using

$$T_g = T_r + \frac{\theta^*}{k} \ln \left[\frac{y-1}{y+1} \right] \Big|_{z_h}^{z_r-d} , \quad (11)$$

where

$$y = \left[1 - 15 \frac{Z}{L} \right]^{1/2} \text{ for unstable conditions}$$

d = displacement height = $0.7H^*$

$$z_h = \frac{L}{15} \left\{ 1 - \left(\frac{1 + B^*}{1 - B^*} \right)^2 \right\} \quad (12)$$

$$B^* = \left(\frac{y(z - d) + 1}{y(z - d) - 1} \right) e^{(kB^{-1} + A)} \quad (13)$$

$$A = \left\{ \ln \left(\frac{x - 1}{x + 1} \right) + 2 \tan^{-1} x \right\} \Big|_{z_0}^{z-d} \quad (14)$$

z_0 = roughness length for momentum over vegetated surface = $0.14H^*$

H^* = average height of roughness elements.

kB^{-1} = Stanton number (Verma, 1989).

Step 6: Compute $R_{Li} = -17.09 + 1.195 \sigma T_r^4$, where R_{Li} is in milliwatts square centimeters and T_r is in degrees kelvin (Swinbank, 1963).

Step 7: Meyers and Dale (1983) compute R_{si} for cloudless skies as

$$R_{si} = I = I_o T_r T_g T_w T_a \cos Z, \quad (15)$$

where I_o is the extraterrestrial flux density at the top of the atmosphere on a surface normal to the incident radiation; Z the solar zenith angle and T_i are the transmission coefficients for Rayleigh scattering (R), absorption by permanent gases (g), water vapor (w), and absorption and scattering by aerosols (a).

$$I_o = 1353 \text{ (Wm}^{-2}\text{)} \left\{ 1 + 0.034 \cos \left[2 \pi (n' - 1) / 365 \right] \right\}, \quad (16)$$

where n' is the Julian day, and

$$Z = \cos^{-1} (\sin \phi \sin D + \cos \phi \cos D \cos H'), \quad (17)$$

where ϕ is the latitude, D the declination angle, and H' the solar hour angle (see step 8).

$$\sin D = \sin (23.4438) \sin B \quad (18)$$

$$B(^{\circ}) = \delta + 0.4087 \sin \delta + 1.8724 \cos \delta - 0.0182 \sin 2 \delta + 0.0083 \cos 2 \delta \quad (19)$$

$$\delta = 279.9348 + d, \quad (20)$$

where

$$\begin{aligned} d & \text{ is the angular fraction of a year, that is,} \\ d & = (\text{Julian day} - 1) (360/365.242) \end{aligned} \quad (21)$$

$$T_r T_g = 1.021 - 0.084 [m (949 P \times 10^{-5} + 0.051)]^{1/2}, \quad (22)$$

where P is the surface pressure (kPa), and m is the optical air mass at a pressure of 101.3kPa

$$m = 35 (1224 \cos^2 Z + 1)^{-1/2} \quad (23)$$

$$T_w = 1 - 0.077 (um)^{0.3}, \quad (24)$$

where u is the precipitable water vapor (Smith, 1966), and

$$u = P_o W_o / g (\lambda + 1), \quad (25)$$

where P_o is the pressure at the earth's surface, and W_o is the mixing ratio. Values of λ are tabulated in Smith (1966).

$$T_a = x^m, \text{ where } x = 0.935. \quad (26)$$

Step 8: Compute sunrise, local noon, and sunset time using Woolf's formulations. From Woolf (1968) the solar hour angle H' that relates to sunrise and sunset is

$$H' = \arccos \left\{ \frac{\sin A - \sin \phi \sin D}{\cos \phi \cos D} \right\}, \quad (27)$$

where ϕ is the latitude, D the solar declination angle, and A is the sunrise/sunset solar elevation angle. At ground level Woolf sets $A = -0.9^\circ$. H' is in degrees but is transformed to time in hours by dividing by 15. The solar day extends from $M - H'$ to $M + H'$.

Step 9: Compute $(1 - \alpha) R_{s\downarrow}$ using α from Paltridge and Platt (1976)

$$\alpha = \alpha' + (1 - \alpha') \exp [-k(90^\circ - Z)], \quad (28)$$

where $k = 0.1$, Z = zenith angle, and α' is albedo at high solar elevations.

Step 10: Compute $R_{L\uparrow}$ using Yamada (1981)

$$R_{L\uparrow} = \epsilon_g \sigma T_g^4 + (1 - \epsilon_g) R_{L\downarrow}. \quad (29)$$

Step 11: Compute net radiation (steps 1 through 15)

$$R_N = (1 - \alpha) R_{s\downarrow} - (R_{L\uparrow} - R_{L\downarrow}). \quad (30)$$

Step 12: Compute $T_g - T_{gn}$ using $T_{gn} = T_{rn} + \gamma_d (z_r - (z_h + d))$, where T_{gn} is the temperature in degrees kelvin at z_h , and γ_d is the dry adiabatic lapse rate and T_{rn} is the reference height temperature at the time t_n (relative to midnight) of neutral conditions (see step 13).

Step 13: Compute dry value of G , that is, G_d using a formulation by Rachele and Tunick

$$G = -G^* + (T_g - T_{gn})K_o \sin \left\{ \frac{\pi}{12} (t - t_n) \right\} \quad (31)$$

where

$$G^* = (T_g(t_n + 2) - T_{gn})K_o \sin \left\{ \frac{\pi}{12} ((t_n + 2) - t_n) \right\} \quad (32)$$

$K_o = k_s / 2\sqrt{K}$ from Angus-Leppan (1971), where k_s is thermal diffusivity and K is thermal conductivity.

Since for dry neutral conditions,

$$H = L'E = 0, \text{ then } R_N = H + L'E + G_d = G_d, \text{ and } G_d \text{ reduces to } G_d = -G^*. \quad (33)$$

Also, since

$$R_N = R_{S\downarrow} - (R_{L\uparrow} - R_{L\downarrow}), \quad (34)$$

then

$$R_{S\downarrow} = (R_{L\uparrow} - R_{L\downarrow}) - G^*. \quad (35)$$

Hence, t_n must be selected so that the above eq. (35) is satisfied.

Step 14: For $t > t_n$ we compute a second approximation of H_d , that is,

$$H_d = R_N - G_d. \quad (36)$$

Step 15: Repeat steps 2 through 14 until convergence is attained giving dry values of H , R_N , and G .

$$\text{Step 16: Redefine } H \text{ as } H = H_d CW. \quad (37)$$

Step 17: Determine C and W from Angus-Leppan and Brunner (1980) as a function of cloud cover and soil wetness (fig. 1).

Step 18: Compute H using Rachele/Tunick function, that is,

$$H = H_d CW(v_r), \quad (38)$$

where $W(v_r)$ is shown on fig. 2 (RT modified Angus-Leppan and Brunner plot).

Step 19: Compute u^* , θ^* , L , and T_g for $H = H_d CW(v_r)$.

Step 20: Compute $R_{S\downarrow}$ for cloudy skies using Haurwitz (1945).

Step 21: Compute $(1 - \alpha) R_{S\downarrow}$.

$$\text{Step 22: Compute } R_{L\downarrow} = 5.31 \times 10^{-14} T_r^6 + (1 - 0.7) \epsilon_c \sigma T_c^4 (cc), \quad (39)$$

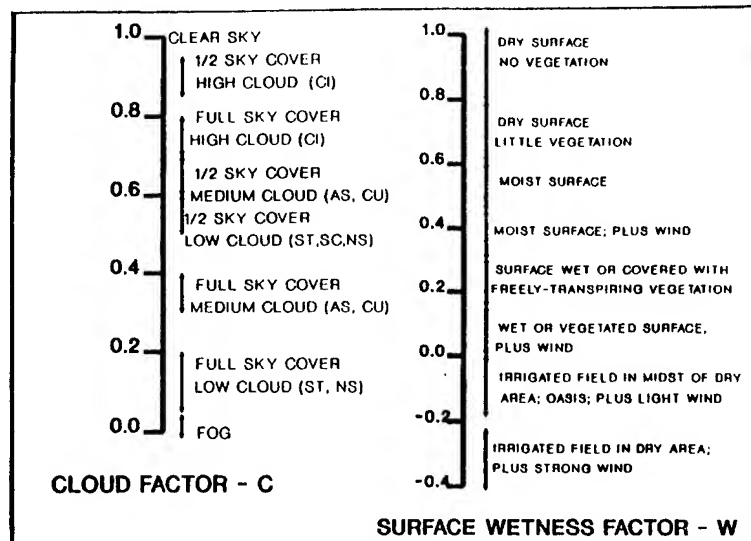
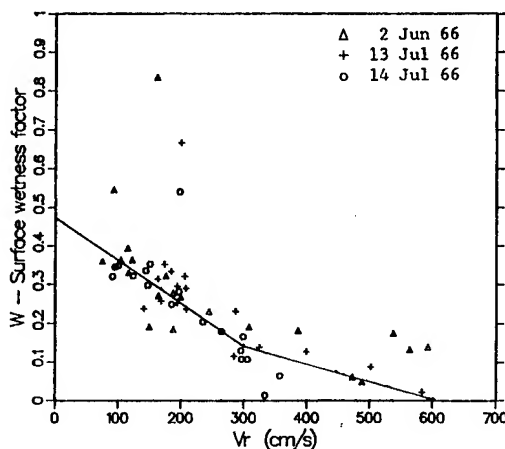


Figure 1. Estimation of parameters C and W.



$$\begin{aligned} \text{For } V_r < 3.0 \text{ m/s } W &= -1.0714 \times 10^{-3} V_r + 0.47143 \\ \text{For } V_r > 3.0 \text{ m/s } W &= -4.74346 \times 10^{-4} V_r + 0.292857 \end{aligned}$$

Figure 2. The Rachele/Tunick function $W(V_r)$ (a modified Angus-Leppan and Brunner plot) for Davis, CA.

where $R_{L\downarrow}$ is in milliwatts per square centimeters, ϵ_c is cloud emissivity, T_c is temperature at cloud base, and cc is tenths of cloud cover.

Step 23: Compute $R_{L\uparrow}$ using the wet value of T_g , that is,

$$R_{L\uparrow} = \epsilon_g \sigma T_g^4 + (1 - \epsilon_g) R_{L\downarrow} . \quad (40)$$

$$\text{Step 24: Compute } R_N = (1 - \alpha) R_{S\downarrow} - (R_{L\uparrow} - R_{L\downarrow}) . \quad (41)$$

Step 25: Compute $T_g - T_{gn}$.

Step 26: Compute moist value of G using expression in step 13, when K_0 is the moist value in Angus-Leppan (1971).

$$\text{Step 27: Compute } L'E \text{ from } L'E = R_N - G - H . \quad (42)$$

4. MODEL RESULTS

The results of this study are based on two sets of measured data (1/2 h averages) from Davis, California, including reference level values of temperature, pressure, relative humidity, and windspeed. In addition, 1/2 h values of net radiation and sensible latent and soil heat fluxes were available. The terrain at Davis was relatively smooth and was covered with fescue grass (average height 10 cm). The soil was assumed to be peat and was moist. Both sets of data were collected during cloudless sky conditions.

Figure 3 shows the 1/2-h average values of reference level temperature, relative humidity, and windspeed for the 2 days at Davis, California. Figures 4, 5, and 6 show the measured and model values of sensible, latent, and ground heat fluxes for both days. Figure 7 shows the measured and model net radiation for both days.

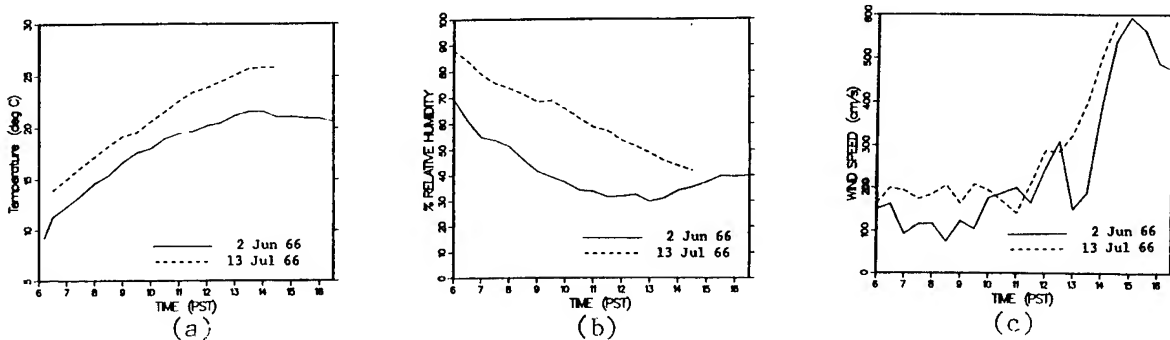


Figure 3. 1/2 h average values of reference level (2 m) temperature, relative humidity, and windspeed for Davis, CA.

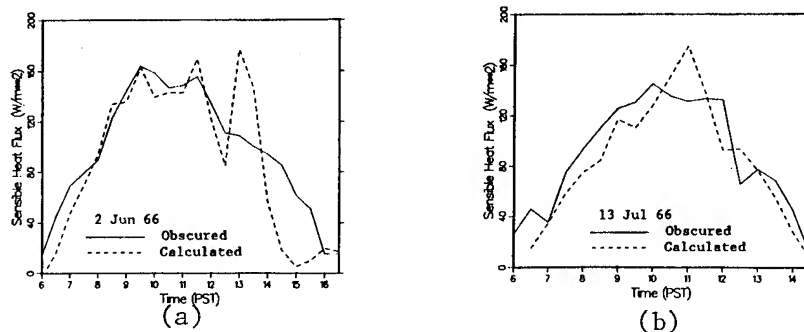


Figure 4. Measured (solid line) and modeled (dashed line) values of sensible heat for Davis, CA.

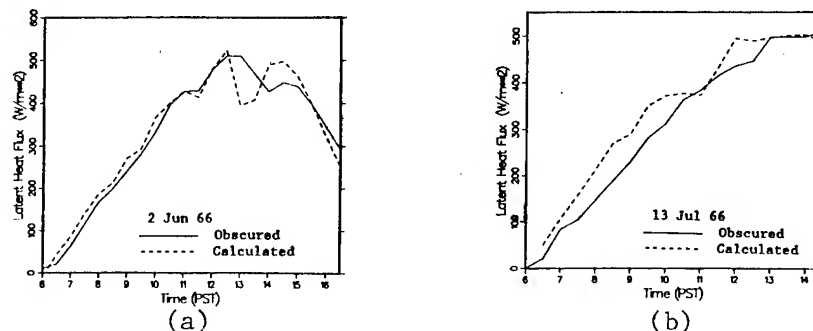


Figure 5. Measured (solid line) and modeled (dashed line) values of latent heat for Davis, CA.

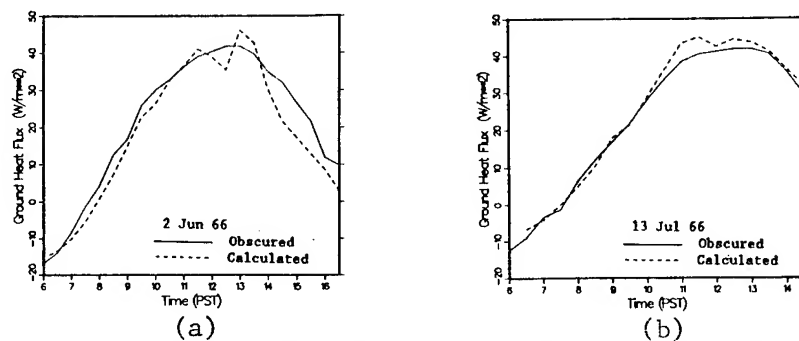


Figure 6. Measured (solid line) and modeled (dashed line) values of ground heat flux for Davis, CA.

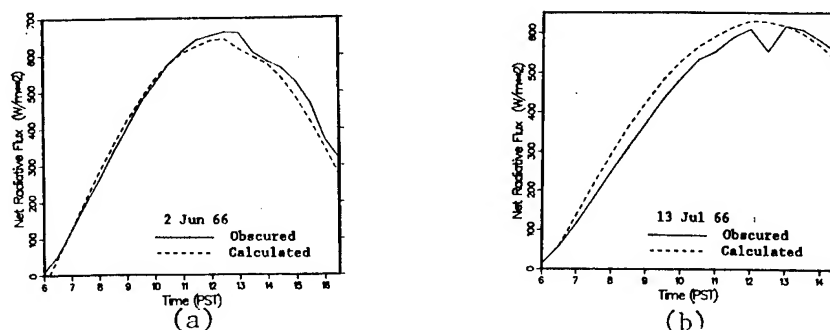


Figure 7. Measured (solid line) and modeled (dashed line) values of net radiative flux for Davis, CA.

5. SUMMARY AND CONCLUSIONS

The purpose of this study was to determine the feasibility of structuring a radiation/energy balance model that would yield estimates of sensible and latent heat fluxes (suitable for imagery and electromagnetic propagation assessments, research, and applications) when constrained to require atmospheric measurement of temperature, pressure, relative humidity, and wind at a reference height (say 2 m) only. The model presented satisfies the above constraints; however, one must also know the day of the year, time of day, longitude and latitude of the site of interest, a judgment of soil type and moisture (dry, moist, saturated), and cloud characteristics (tenths of cloud cover and density). The model is a composite of formulations, some purely physical and well founded, others semiempirical, and a few that are strictly empirical. Our major contributions include formulations for estimating the effect of wind on the sensible heat flux, an expression for estimating ground heat flux, a modification of Verma's (1989) expression for the computation of the roughness length of temperature, and most critically a tying together of all the formulations and establishing a calculation procedure. The two cases presented in this paper were restricted to daytime cloudless conditions using data from Davis, California. Results are most encouraging for determining qualitative estimates of C_n^2 throughout the day over fescue grass. Finally, we believe that the model should be used and refined for barren surfaces and other vegetative cover. A joint effort with the U.S. Department of Agriculture is currently planned.

ACKNOWLEDGMENT

We wish to thank Frank V. Hansen of the U.S. Army Atmospheric Sciences Laboratory for his willing and enthusiastic support and encouragement during the development of the model. He not only searched out many pertinent documents but also gave his time for discussion.

REFERENCES

- Angus-Leppan, P. V., and F. K. Brunner, 1980: Atmospheric Temperature Models for Short-Range EDM. The Canadian Surveyor, 34:(2)153-165.
- Angus-Leppan, P. V., 1971: Meteorological Physics Applied to the Calculation of Refraction Corrections. In Proceedings of the Conference of Commonwealth Survey Officers, Cambridge, England, pp 107-111.
- Campbell, G. S., 1985: Soil Physics with Basic Transport Models for Soil-Plant Systems. Elsevier Publishing Co, Amsterdam, Oxford, New York, Tokyo.
- Carson, D. J., 1987: An Introduction to the Parameterization of Land-Surface Processes: Part 1. Radiation and Turbulence. Meteorological Magazine #1381, 116:229-242.
- Danard, M., G. Lyv, and G. MacGillivray, 1984: A Mesoscale Bulk Model of the Atmospheric Boundary Layer. Atmospheric Dynamics Corp. Report, Victoria, B.C.
- Haurwitz, B., 1945: Insolation in relation to cloudiness and cloud density. J. Meteorol., 2(3):154-166.
- Liu, M. et al., 1976: The Chemistry Dispersion and Transport of Air Pollutants Emitted From Fossil Fuel Plants in California: Data Analysis and Emission Impact Model. National Technical Information Center, Springfield, VA, PB-264-822, pp 136-140.
- Meyers, T. P., and R. F. Dale, 1983: Predicting Daily Insolation with Hourly Cloud Height and Coverage. J. Climate and Appl. Meteorol., 22:537-545.
- Paltridge, G. W., and C. M. R. Platt, 1976: Radiative Processes in Meteorology and Climatology. Elsevier Scientific Publishing Co., Amsterdam, Oxford, New York.
- Pielke, R. A., 1984: Mesoscale Meteorological Modeling. Academic Press, Orlando, San Diego, San Francisco, New York, London, Tokyo, Toronto, Montreal, Sydney.
- Smith, W. L., 1966: Note on the Relationship Between Total Precipitable Water and Surface Dew Point. J. Appl. Meteorol. 5:726-727.
- Swinbank, W. C., 1963: Longwave Radiation from Clear Skies. Quart. J. Roy. Meteorol. Soc., 89:339-348.
- Verma, S. B., 1989: Aerodynamic Resistances to Transfers of Heat, Mass, and Momentum. Estimation of Areal Evapotranspiration (Proceedings of a Workshop held in Vancouver, BC Canada, Aug 1987) IAHS Publication #177.
- Webb, E. K., 1984: Temperature and Humidity Structure in the Lower Atmosphere. In Geodetic Refraction - Effects of Electromagnetic Wave Propagation Through the Atmosphere, (ed. F. K. Brunner), Springer Publishing, Berlin, Heidelberg, New York, Tokyo, pp 85-141.
- Woolf, H. M., 1968: On the Computation of Solar Elevation Angles on the Determination of Sunrise and Sunset Times. National Meteorological Center, Environmental Sciences Services Administration, Hillcrest Heights, MD.
- Yamada, T., 1981: A Numerical Study of Turbulent Air Flow in and above Forest Canopy. J. Meteorol. Soc. of Japan, 60:(1)439-454.

**BOUNDARY LAYER ILLUMINATION RADIATION
BALANCE MODEL: BLIRB**

**Andrew Zardecki
Science and Technology Corporation
White Sands Missile Range, NM 88002, USA**

**Alan E. Wetmore
U.S. Army Atmospheric Sciences Laboratory
White Sands Missile Range, NM 88002, USA**

ABSTRACT

BLIRB, a computer model integrating clouds, background aerosols, and gaseous absorption, provides both direct and diffuse insolation at the earth's surface in the spectral range between 0.4 and 40 μm . The model is an extension of LOWTRAN 7 to the three-dimensional cloud and aerosol formations in the lower atmosphere, up to 5 km above the surface. Using rectangular geometry, four cloud options are available. These options are: (i) cloud-free, aerosol-loaded atmosphere; (ii) horizontally homogeneous clouds specified in terms of their cloudiness and patchiness; (iii) rectangular clouds described in terms of their composition; and (iv) Cloud Scene Simulation prototype model developed by the Analytical Science Corp.

1. INTRODUCTION

One of the primary objectives of the Balanced Technology Initiative (BTI) Smart Weapons Operability Enhancement (SWOE) program is the simulation of complex thermal infrared background images to support the designers and users of smart weapons systems. The boundary layer illumination radiation (BLIRB) computer code, conceived as an extension of LOWTRAN 7 (Kneizys et al., 1988), calculates direct and diffuse illumination at the earth's surface in the spectral range between 0.4 and 40 μm . In the visible, clouds scatter and absorb incident solar and sky-light radiation; in the infrared, clouds act as scatterers and emitters of radiation, interacting with the radiation emitted from the earth.

The radiative transfer process is implemented through the two-stream approximation (Meador and Weaver, 1980), combined with the adding method (Van de Hulst, 1980). Section 2 is devoted to a summary of the underlying concepts. The section includes a brief section on the stochastic ray tracing algorithm that permits emulation of the penumbra effect. Section 3 discusses the radiation model. In the visible, incident solar radiation is supplemented by sky irradiance. Section 4 discusses the atmospheric and surface model used by BLIRB. This model includes the aerosol database, borrowed from Air Force Geophysics Laboratory (AFGL) compilation. In addition, the actual cloud model and surface albedo implementation are described. In Sec. 5, an example of BLIRB's output, in which the effect of boundary conditions plays a role, is discussed.

2. RADIATIVE TRANSFER THROUGH THREE-DIMENSIONAL CLOUDS

Typically, the clouds encountered in nature have their optical depth in the range of 100--500. This fact precludes the application of the single-scattering approximation to the equation of radiative transfer. As in LOWTRAN 7, the approach in BLIRB is based on the two-stream approximation (Meador and Weaver, 1980), which provides rapid approximate answers to problems of radiative transfer in particulate materials. For a spatially inhomogeneous cloud distribution, the

two-stream approximation is combined with the adding method, and supplemented by a ray-tracing algorithm to yield the penumbra effect.

Of the different methods of implementing the two-stream approximation reviewed by Meador and Weaver (1980), the hemispheric constant method of Coakley and Chylek (1975) was chosen for this work. The Coakley and Chylek two-stream model is usually employed in water cloud parameterization because it is the simplest.

To provide the necessary information, the model must compute separately the direct and diffuse components of radiation. The direct component is attenuated exponentially, with the attenuation specified by the volume extinction coefficient. The diffuse component undergoes transmission and reflection, in addition to absorption, when traversing a layer of optical depth τ . If μ denotes the direction cosine of the incident radiation, which is considered to be isotropic over the downward hemisphere, the reflection and transmission functions for the total radiation are

$$R(\mu) = \frac{(Q+1)(Q-1)[\exp(\alpha\tau/\mu) - \exp(-\alpha\tau/\mu)]}{(Q+1)^2\exp(\alpha\tau/\mu) - (Q-1)^2\exp(-\alpha\tau/\mu)} \quad (1)$$

$$T(\mu) = \frac{4Q}{(Q+1)^2\exp(\alpha\tau/\mu) - (Q-1)^2\exp(-\alpha\tau/\mu)} \quad (2)$$

where

$$Q = \frac{[1 - \omega_0 + 2\omega_0\beta(\mu)]^{1/2}}{[1 - \omega_0]^{1/2}} \quad (3)$$

$$\alpha = [1 - \omega_0 + 2\omega_0\beta(\mu)]^{1/2} [1 - \omega_0]^{1/2} \quad (4)$$

In eqs. 3 and 4, ω_0 refers to the single-scattering albedo, whereas $\beta(\mu)$, the backscatter fraction, is given as an integral over the phase function P :

$$\beta(\mu) = \frac{1}{2} \int_0^1 P(\mu, -\mu') d\mu' \quad (5)$$

assuming phase function normalization to 4π over the entire solid angle.

For the diffuse component of radiation, the reflection function is still given by eq. 1. The transmission function is obtained by subtracting the direct component $\exp(-\tau/\mu)$ from eq. 2.

To compute the reflection functions of a system composed of layers, the adding method is applied successively. This method requires the evaluation of complicated integrals over angles, a procedure that slows down the numerical implementation of the algorithm. For these reasons, Coakley and Chylek (1975) introduced an average two-stream model, in which the reflection and transmission functions with an average cosine of the incident radiation are employed. After Liou (1980), let R_i and T_i , where $i = 1$ or 2 , refer to reflection and diffuse transmission functions of the two layers. Similarly, τ_1 and τ_2 denote optical depths of layers 1 and 2, respectively. Define S as follows:

$$S = \frac{R_1 R_2}{1 - R_1 R_2} \quad (6)$$

With this definition, the equations governing the diffuse reflection and transmission are obtained by first constructing D and U , the combined diffuse transmission and reflection functions between the layers. These functions are

$$D = T_1 + ST_1 + Se^{-\tau_1/\mu} \quad (7)$$

$$U = R_2D + R_2e^{-\tau_1/\mu} \quad (8)$$

In terms of D and U , the diffuse reflection and transmission functions of the combined system become

$$R_{12} = R_1 + e^{-\tau_1/\mu}U + T_1U \quad (9)$$

$$T_{12} = e^{-\tau_2/\mu}D + T_2e^{\tau_1/\mu} + T_2D \quad (10)$$

Note that the direct transmission function is simply $\exp[-(\tau_1 + \tau_2)/\mu]$.

To validate the algorithm, a standard discrete-ordinates transport code of Stamnes et al. (1988) is used. Table 1 gives the results of the comparison for a highly scattering medium. For ω_0 of 0.4 and lower, the algorithm becomes inadequate for large zenith angles; this situation requires a parametric change.

Table 1. Transmittance for the Henyey-Greenstein Phase Function. Asymmetry parameter of 0.75, $\omega_0 = 0.99$.

τ	μ	Exact	BLIRB
2	0.1	0.346	0.344
	0.5	0.598	0.468
	1.0	0.816	0.763
4	0.1	0.241	0.323
	0.5	0.439	0.387
	1.0	0.646	0.605
8	0.1	0.152	0.143
	0.5	0.276	0.318
	1.0	0.416	0.402

In surface illumination, stochastic ray tracing---when applied to a rectangular cloud---produces the penumbra region by virtue of the difference in optical paths of individual rays. The method relies on choosing a number of random ray directions around the direction normal to the surface. For each random ray, the illumination is calculated; the surface illumination is obtained as an arithmetic mean of the illuminations corresponding to the individual rays. This computation method is similar to the Monte Carlo approach to radiative transfer.

3. RADIATION MODEL

In a clear atmosphere, scattering of long-wave radiation is neglected relative to the absorption and emission of electromagnetic energy. When clouds are

present, their water content strongly influences the optical path length for infrared radiation. Under the conditions of local thermodynamic equilibrium, the average atmospheric irradiance is computed as

$$F\downarrow(\nu) = \int_{t_f}^1 B(\nu, T) dt_f \quad (11)$$

where $B(\nu, T)$ is the average Planck function corresponding to the wavenumber ν and temperature T of an atmospheric layer, and where t_f is the angle-averaged flux transmissivity. To account for scattering, the integrand in eq. 11 is multiplied by the flux scattering transmissivity term.

Surface illumination in the visible spectral range is composed of the directly incident solar radiation and the sky radiance. Incident solar radiance at the top of the region under consideration (usually 5 km in BLIRB) can be obtained from LOWTRAN 7 or by computing solar radiance at the top of the atmosphere.

When dividing the radiation into direct and diffuse parts, it is usually assumed that no diffuse radiation enters at the top of the atmosphere. With the top of the physical region located at 5 km, the sky radiance contribution to surface illumination cannot be neglected. Sky radiance is the dominant factor for large zenith angles. In BLIRB, sky radiance is viewed as an additional source of direct radiation. This approach is valid because sky radiance contributes to illumination even in the absence of aerosols in the physical region; on the other hand, the contribution from the diffuse radiation vanishes in a vacuum.

4. ATMOSPHERIC AND SURFACE MODEL

The distribution of radiation in the atmosphere is a complex function of molecular and aerosol characteristics. For a wide range of the solar spectrum, between 0.2 and 40 μm , in addition to the model of attenuation based on the U.S. standard atmosphere, detailed models describing different environments with varying humidity conditions were developed by the AFGL (Shettle and Fenn, 1979).

Within the boundary layer (up to 2 km), rural, urban, maritime, or tropospheric aerosol models are used, each with five meteorological ranges between 2 and 50 km. When relative humidity is included in the boundary layer models, the 46 models that form the AFGL database result.

When cloud cover is absent, an essentially one-dimensional model applies. If aerosols are also suppressed from the model, the solar radiation propagates in a vacuum. Apart from this trivial case, three different cloud models have been incorporated into BLIRB. In the simplest case, the clouds are described in terms of the cloudiness and patchiness parameters (Schneider and Dickinson, 1976), defined for each of the five 1-km layers between 0 and 5 km. The rectangular cloud model allows the construction of clouds of various extent and composition. The Cloud Scene Simulation model includes both sawtooth and fractal clouds.

The starting point of the model is a collection of rectangular regions, numbered by their identification numbers. The materials filling the regions can be

composed of up to three different aerosols, by weighting their extinction (σ_t) and scattering (σ_s) coefficients according to

$$\sigma_t = \sum_{i=1}^3 w_i \sigma_t^{(i)} \quad (12)$$

$$\sigma_s = \sum_{i=1}^3 w_i \sigma_s^{(i)} \quad (13)$$

where the weighting factors w_i are not necessarily normalized to unity. Here the superscript (i) refers to the components forming the mixture. The mixture phase function $P(\Omega, \Omega')$ then satisfies

$$\sigma_s P(\Omega, \Omega') = \sum_{i=1}^3 w_i \sigma_s^{(i)} P^{(i)}(\Omega, \Omega') \quad (14)$$

The cloud data rely on EOSAEL (Shirkey et al., 1987) and LOWTRAN 7 databases. In the actual model implementation, the appropriate database is selected at an early stage of the algorithm.

The Cloud Scene Simulation (CSS) prototype model software package (Cianciolo, 1990) was developed at the Analytical Science Corp. (TASC) to generate three-dimensional cloud scenes based on user-specified input parameters. In this model, water clouds are described in terms of the water content specified on a grid with a maximum resolution of 40x40x20 grid points. The user has a choice between fractal clouds and clouds generated by the Boehm sawtooth-wave algorithm. For details of the model, see Cianciolo, 1990.

The user also specifies rectangular areas at ground level to which surface albedos are assigned. There are three ways to define the surface albedo. First, an array of wavelength-independent albedos can be read from the input file. Second, surface albedo remains wavelength-independent, but its identification number determines its value. Third, as a way of exercising the model until realistic data are available, six models of spectral albedos were implemented, defined in terms of arrays whose entries are given for 16 wavelengths, identical to wavelengths used in Shirkey et al. (1987).

5. AN EXAMPLE OF USE

This section illustrates the effect of boundary conditions on surface irradiance. In battlefield applications, large solar zenith angles are important. They mimic the conditions prevailing at sunset and sunrise. For a given physical region, two types of boundary condition are available: vacuum and periodic boundary. In the former case, there are no clouds outside the physical region; the aerosol cover, though, remains uniform in any horizontal plane. In the latter case, the cloud arrangement is repeated periodically in the X and Y directions, with the period given by the extent of the physical box.

Consider a volume 5x4x5 km in directions X, Y, and Z, respectively, with a fine grid structure given by the grid points 0.5 km apart, creating a grid of 10x8x10 cells. The boundary layer is filled with rural aerosol, having 0% relative humidity and a meteorological range of 23 km. The two cloud regions are given by the bounding coordinate pairs (1,2), (1,2), (0,5) and (3,4), (2,4), (0,5) km. The AFGL database is used, with cumulus and altostratus clouds selected as materials; these materials, with weighting factors of 2 and 3, fill regions 1 and 2, respectively.

Figures 1 and 2 show the results of BLIRB computation for direct radiation corresponding to a solar zenith angle of 60 deg. For vacuum boundary conditions, the surface in the vicinity of the origin is in shadow. When the boundary conditions are periodic, the clouds outside the physical region cast shadow on the surface away from the origin.

6. CONCLUSIONS

The BLIRB model computes surface irradiance by extending the results of LOWTRAN 7 to three dimensions. A combination of the two-stream approach, adding method, and stochastic ray tracing facilitates the computation of the direct and diffuse components of radiation for a variety of atmospheric and cloud scenarios. In the future, the model will provide an input to SWOE imaging models. It should also be useful in energy budget and temperature computations.

REFERENCES

- Cianciolo, M.E., 1990: Cloud Scene Simulation Model Version 1.0 User's Guide, Memorandum 6042-2, TASC, Boston, MA.
- Coakley, J.A. Jr., and P. Chylek, 1975: The Two-stream Approximation in Radiative Transfer: Including the Angle of Incident Radiation, J. Atm. Sci. Vol. 32, pp. 409-418.
- Kneizys, F.X., E.P. Shettle, L.W. Abreu, J.H. Chetwynd, G.P. Anderson, W.O. Gallery, J.E.A. Selby, and S.A. Clough, 1988: User's Guide to LOWTRAN 7, AFGL-TR-88-0177, Air Force Geophysics Laboratory, Hanscom AFB, MA.
- Liou, K-N., 1980: An Introduction to Atmospheric Radiation, Academic Press, New York.
- Meador, W.E. and W.R. Weaver, 1980: Two-stream Approximations to Radiative Transfer in Planetary Atmospheres: a Unified Description of Existing Methods and a New Improvement, J. Atmos. Sci. Vol. 37, pp. 630-643.
- Schneider, S.H. and R.E. Dickinson, 1976: Parameterization of Fractional Cloud Amounts in Climatic Models: the Importance of Modeling of Multiple Reflections, J. Appl. Meteor. Vol. 15, pp. 1050-1056.
- Shettle, E.P. and R.W. Fenn, 1979: Models of the aerosols of the lower atmosphere and the effects of humidity variations on the optical properties, report AFGL-TR-79-0214, Air Force Geophysics Laboratory, Hanscom AFB, MA.
- Shirkey, R.C., R.A. Sutherland, and M.A. Seagraves, 1987: Aerosol phase function database PNFDAT, TR-0221-26, U.S. Army Atmospheric Sciences Laboratory, White Sands Missile Range, NM.
- Stamnes, K., S-C. Tsay, W. Wiscombe, and K. Jayaweera, 1988: Numerically Stable Algorithm for Discrete-ordinate-method Radiative Transfer in Multiple Scattering and Emitting Layered Media, Appl. Opt. Vol. 27, pp. 2502-2509.
- Van de Hulst, H.C., 1980: Multiple Light Scattering: Tables, Formulas, and Applications, Academic Press, New York.

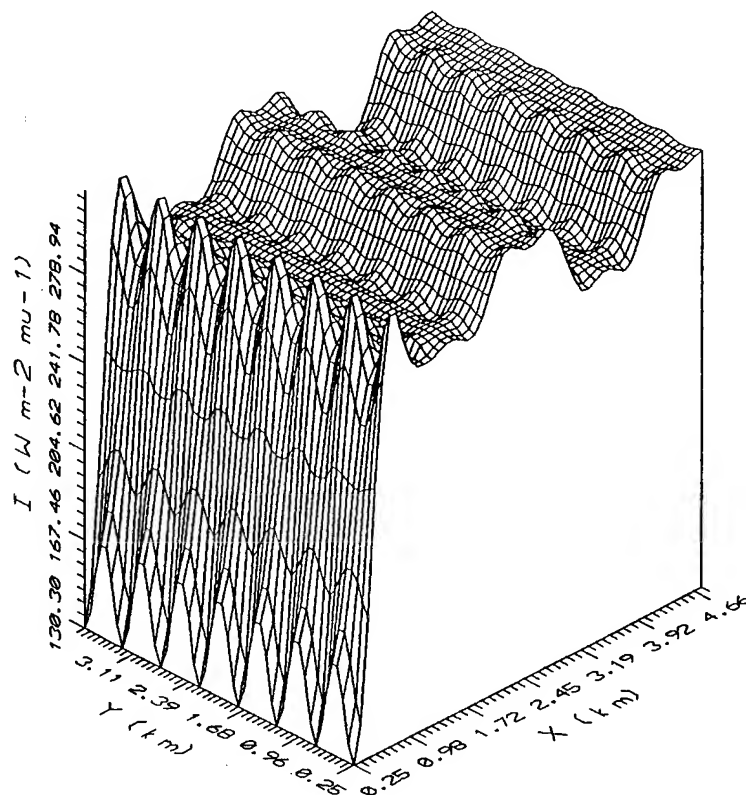


Figure 1. Direct illumination for the solar zenith angle of 60 deg. Vacuum boundary conditions.

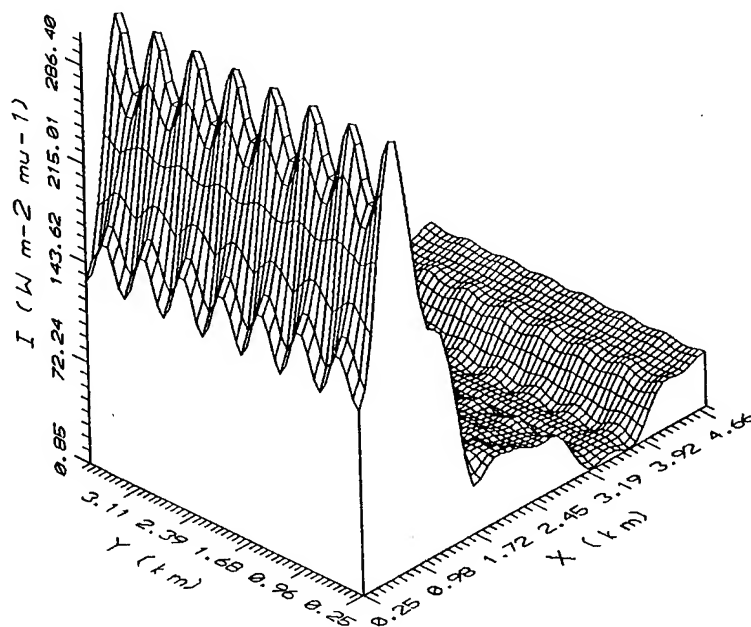


Figure 2. Direct illumination for the solar zenith angle of 60 deg. Periodic boundary conditions.

TACTICAL CORRECTION OF NEAR SURFACE ATMOSPHERIC REFRACTION

David H. Tofsted and James B. Gillespie
U.S. Army Atmospheric Sciences Laboratory
White Sands Missile Range, New Mexico 88002-5501, USA

ABSTRACT

The need for tactical correction of near surface atmospheric refraction effects in deserts has recently been emphasized by the Desert Storm operation. Optical refraction causes objects to vary in apparent elevation as a function of time of day. These variations can result in errors in tank lay position under certain conditions. A simplified method of correcting for refraction is presented. Test results are discussed which validate this technique. Meteorological and terrain conditions which affect the application of this method are described. These conditions can often be considered during intelligence preparation of the battlefield. Alternative hardware based correction methods are also considered.

1. INTRODUCTION

The U.S. Army Atmospheric Sciences Laboratory (ASL) has investigated the nature of atmospheric refraction and has developed techniques to compensate for refractive lay errors in tank gunnery in deserts. This paper discusses the rationale for these techniques and presents supporting data.

Refraction can be remotely sensed as a function of time through point-to-point measurements of the elevations of a distant object relative to its elevation at the atmospheric neutral events which occur approximately one-half hour before sunset and one-half hour after sunrise. The vertical position change of a distant object can be measured either by using a fixed reference point in the field of view (another object close enough to the observer that refraction effects will be minimal) or by using a theodolite which has its own internal reference through the leveling bubble. We have made extensive measurements of diurnal variations in elevation of distant objects at White Sands Missile Range (WSMR), NM; Aberdeen Proving Ground, MD; Fort Stanton, NM; and other locations which all exhibit similar vertical shifting characteristics. However, in tactical situations direct measurements are currently not feasible and therefore predictive means of compensating for mean refractive error have been developed. These predictions have been compared against measured data and compensate for mean refractive effects under standard conditions. Other techniques are available to provide varying compensation, but depend on notional implementation methods. These methods are discussed.

When viewing a target with an electro-optical (EO) sensor, one can think of the atmosphere as an optical system component. The atmosphere is not as homogeneous an optical system as it appears to the human eye. Phenomena such as scattering and extinction by aerosols and scintillation by optical turbulence both affect how clearly a target can be seen. These subjects have been dealt with extensively in the literature.

A third phenomenon, optical path bending (or atmospheric refraction), has largely been ignored for EO sensors which look horizontally along paths near the earth's surface. Because in the past most tank EO sensor targeting has been limited to path lengths of less than two kilometers, vertical aiming errors caused by refraction have been much smaller than other aim errors inherent

in these systems. As the maximum effective ranges of systems increase, though, refractive effects play an ever greater role in the tank error budget. Figure 1 illustrates the effect of refraction for a tank on the left viewing a target on the right. The light from the target does not propagate in a straight line to the receiver. Instead, light propagates along an optical path which takes a minimum propagation time. The incoming ray thus arrives at an angle different from the geometric line connecting target and observer. The viewing angle will be raised at night and lowered during the day when refraction is present. Since the sensor looks tangent along the incoming ray, the vertical aiming angle will be in error—sometimes by as much as a milliradian or more for long paths in desert type situations.

2. THEORY

The vertical bending of the optical path of a beam of light propagating horizontally is caused by a vertical refractive index gradient. This gradient is produced by the temperature gradient resulting from diurnal solar heating of the earth's surface. Refraction in a nonhomogeneous medium such as the earth's atmosphere can be quite adequately described by classical geometrical optics (which uses the assumption that the wavelength of the light is negligibly small). Refraction can be described by either Huygen's wave front construction method, Fermat's principle

$$\delta \int n ds = 0; \quad (1)$$

Snell's Law

$$n_1 \sin \theta_1 = n_2 \sin \theta_2; \quad (2)$$

or the Eikonal equation

$$(\text{grad } L)^2 = n^2; \quad (3)$$

where L is the optical path length, ds is the incremental change in path of the ray, n is the refractive index, and θ_i is the angle of propagation in the i th layer.

Using equation (3), we can derive the following expression for atmospheric ray tracing for horizontal, near-surface propagation:

$$d\phi = \frac{ds}{n} \frac{\partial n}{\partial z}, \quad (4)$$

where $d\phi$ is the incremental angular change of the optical path with respect to some fixed axis, z is the vertical dimension, and propagation is nearly horizontal.

For propagation paths near the surface, the atmosphere does not follow a spherical symmetry; instead the optical path is more strongly dependent on distance from the local surface. The surface fluxes of latent and sensible heat dominate the structure of temperature and humidity. The temperature gradient has a much stronger influence on density gradient than does the pressure gradient. This temperature gradient is largely a function of the degree of heating or cooling occurring at the surface. During the day sensible heat flows upward as the surface transfers heat to the near surface air by convection. During the night, as the surface cools, the atmosphere closest to the surface also cools, setting up an inversion condition (Oke, 1970). The effect of daytime atmospheric heating is to couple the structure of the temperature lapse rate to the immediately surrounding terrain. An adequate model of this would be to calculate the structure of the air temperature with height for an average case and then apply that profile to the terrain along the line of sight over which we wish to propagate. By determining the height of the line of sight above this terrain at any particular point along the line of propagation we could calculate the temperature gradient at that point. The approach for nocturnal conditions is handled similarly.

The refraction of the atmosphere is conveniently described in terms of a parameter, N , called the refractivity. It is defined as

$$N = (n - 1) \times 10^6. \quad (5)$$

For most atmospheric conditions N has a value near 250. It varies with wavelength, temperature, pressure, and absolute humidity (Hill *et al.*, 1980). The refractivity can be written as the sum of two contributions, a dry air part and a water vapor part:

$$N = N_{dry} + N_w; \quad (6)$$

$$N_{dry} = \{1 + (5.337 - .0157 T)P \times 10^{-6}\} \frac{0.3789 N_o P}{T}; \quad (7)$$

$$N_w = -0.0059 \{1 - 0.0109 \lambda^{-2}\} A; \quad (8)$$

where P is the pressure in millibars, T is the temperature in kelvin, A is the absolute humidity in grams per cubic meter, λ is the wavelength in microns, and N_o is a wavelength dependent refractivity term.

Using the hydrostatic equation,

$$dP = -\frac{mg}{kT} P dz \quad (9)$$

along with equations (6) through (9), we can derive an expression for the gradient of n :

$$\frac{\partial n}{\partial z} = -78.2 \times 10^{-6} P T^{-2} \left(\frac{\partial T}{\partial z} + .0344 \right). \quad (10)$$

We model the terrain profile by using a local terrain profile, $H(x)$, and the distance between the ray and the local surface, z' . The local height can be described by

$$z' = z - H(x). \quad (11)$$

Disregarding any y dependence for H , we can write the gradient of the refractive index as

$$\text{grad}(n) = \frac{\partial n}{\partial z'} \left\{ \frac{\partial z'}{\partial x} \hat{i} + \frac{\partial z'}{\partial z} \hat{k} \right\}. \quad (12)$$

Using equation (11), equation (12) can be rewritten as

$$\text{grad}(n) = -78.2 \times 10^{-6} P T^{-2} \left\{ \frac{\partial T}{\partial z'} + 0.0344 \right\} \left\{ -\frac{\partial H}{\partial x} \hat{i} + \hat{k} \right\}. \quad (13)$$

We utilize two methods to obtain a terrain profile — assume a flat earth or survey the terrain and interpolate between the surveyed points. Our refraction ray tracing model, REFRAC (Tofsted, 1987), uses a Fourier series to fit to the terrain.

Temperature gradients for our model are obtained through application of Similarity Theory (Obukhov, 1971; Kunkel and Walters, 1983). In general, the temperature gradient goes as z^{-1} for neutral conditions, as $z^{-4/3}$ for day conditions, and as $z^{-2/3}$ for night conditions. However refraction in nocturnal conditions can be highly terrain dependent: Pockets of cool air can accumulate in depressions and flow downhill. Targets may exhibit dramatic vertical motion (greater than half a milliradian) within a few minutes.

In addition to an atmospheric ray tracing model, we have developed surface energy budget (SEB) models to infer the vertical temperature gradient from standard meteorological data (Tofsted

and Gillespie, 1986). A basic model called SURFA is a near copy of a model described by Deardorff (1978); TGRAD is an upgrade of SURFA that incorporates new methods for determining sensible heat flux, solar radiation, and foliage temperature; and TGGEN is a modification of TGRAD that includes algorithms that account for water phase change during freeze or thaw. These models take air temperature, pressure, relative humidity, windspeed, precipitation amount, percent cloud cover, percent surface foliage cover, surface roughness length, soil moisture content, soil type, Julian date, longitude, latitude, and time of day as inputs. The model will then estimate the balance of energy fluxes passing through the earth-atmospheric interface. Mathematically the energy balance is described by the equation

$$S_{\downarrow} - S_{\uparrow} + R_{\downarrow} - R_{\uparrow} - H - LE - G = 0. \quad (14)$$

The arrows describe the direction of the flux of radiation, downward to the surface or upward from the surface. S represents the solar energy incident from the sun or reflected from the surface. R represents the thermal radiation flowing from the heat sink of the atmosphere and from the ground. H is the sensible heat, where H is positive if the air is being heated. LE is the latent heat flux due to evaporation (positive) or dew formation (negative). G is the sensible heat flux into the soil.

That the SEB model can be used to predict refractive effects was verified from optical refraction and meteorological data taken at WSMR, NM, in June 1983 over a relatively flat desert terrain. The verification is shown in fig. 2. However, subsequent measurements indicated much larger temperature gradients were possible at night that were not accurately predicted by the SEB models (Tofsted, 1989).

To be useful in a tactical situation the ability to predict refractive effects based on knowledge of the terrain and temperature gradient must be translated into statistics of temperature gradients as a function of time of day and synoptic weather parameters as well as typical tactical terrain profiles. Surface energy budget models have been useful predictors of temperature structure (Tofsted and Gillespie, 1989); but at night, because the assumptions that form the basis for these models can become invalid, the results obtained often merely indicate that refractive events are expected, but not their magnitude. Since nocturnal effects are often more significant than daytime effects, statistical averages of nocturnal synoptic weather conditions and measured effects under those conditions must be relied on rather than model predictions. In relation to terrains, long-range gunnery typically occurs from overwatch positions. These positions are often on significant terrain features where the height of the lines of sight will be elevated. Because of the rapid decrease in gradient with height it is essential that an operator only apply a daytime correction when the line of sight is less than 5 m above the terrain.

The SEB models predict that the greatest temperature gradients occur when winds are low, skies are clear, and the soil is dry. These conditions occur most often in deserts. Relative to these findings an analysis of the probability of occurrence of nocturnal refractive events was performed by E. P. Avara of ASL. Several Middle Eastern sites of interest were selected and the available weather data sets from these sites were processed to determine the frequency of occurrence of the conditions: 1) cloud cover less than or equal to 25 percent, 2) windspeed less than or equal to two meters per second, 3) data averaged over seasons, and 4) reporting times between 2 AM and 8 AM local time. The results of this study (seen in table 1) indicate that the conditions most likely to result in nocturnal refractive events occur 10 to 50 percent of the time at these sites. Note that the Dhahran site is on the Persian Gulf where higher average winds are present due to sea/land breeze effects. This proximity limits the probability of observing refraction. Similar results were obtained for daytime studies.

These statistics do not account for humidity effects. The exact degree of influence of humidity on the overall probability of occurrence is currently an unanswered question. High humidity conditions should limit the degree of refractive path bending present because radiative energy

TABLE 1. FREQUENCY OF OCCURRENCE STATISTICS

Site Name	Winter %	Spring %	Summer %	Autumn %	Annual %
Dhahran, SD	13	16	19	27	19
Kuwait City	20	19	25	31	24
Basrah, IQ	29	24	22	36	27
Baghdad, IQ	30	23	23	35	28
Riyadh, SD	33	24	33	53	35

loss at the surface can be effectively replaced by energy gained in dew formation instead of cooling of the nocturnal atmosphere. Without cooling, the nocturnal inversion condition never becomes strong. During testing at White Sands the atmosphere has been below its saturation level on all but one occasion. Data collected at Aberdeen Proving Ground was inconclusive because nocturnal data was not available, yet strong nocturnal effects were observed. For the Dhahran and Kuwait City sites (both on the Gulf) when saturated humidity cases are removed the probability of occurrence values drop significantly. The difficulty in assessing this impact on overall probabilities of occurrence in the Middle East devolves to the sparcity of the database: 1) The database in the Middle East depends on surface observations made at airports, but 2) most major airports are located near water sources such as the Euphrates river or the Persian Gulf. 3) Locations where battles occur may not be near these water sources. For locations further from water sources the statistics given in the table should be accurate. Results about 10 percent lower are valid near bodies of water at night if humidity does play a decisive role.

3. MEASUREMENTS AVAILABLE

Recently we discussed the techniques of sensing refractive shifting of images using theodolites or photographic techniques (Gillespie and Tofsted, 1991). These optical measurements provide a means of verifying the accuracy of model predictions of refractive effects. From the propagation model discussed we know that refraction will occur when the vertical temperature gradient is large, and gradients will be large when skies are clear and winds are low. Measurements were made at various sites under these conditions. Table 2 lists a compendium of tests where refractive effects were observed.

The data listed in table 2 includes the test name: WSFT refers to White Sands Firing Tests conducted on 3 consecutive days. The weather on the first two days was similar, as evidenced by the similar Avg D/N Shifts (average day to night refractive shift observed in the centers of impact of groups of rounds fired each afternoon and night). WSOT refers to a series of four optical tests conducted at White Sands over a period of several years. The D/N Shifts referred to here and in the other test results are the observed average elevation shifts of a distant target relative to a nearby reference marker. APGOT, FtSOT, and NTCOT were refractive optical tests conducted at Aberdeen Proving Ground, MD; Fort Stanton, NM; and the National Training Center, CA, respectively. The range listed is that used to define the average height of the line of sight above the surface (Hgt ASL) and the range at which refractive effects are judged. Meteorological parameters listed include the range of windspeeds, cloud covers, and day to night maximum temperature difference present during the 24-hour measurement period.

TABLE 2. COMPENDIUM OF TESTS

Test Name	Date	Range (m)	Ht AGL (m)	Winds (knots)	Cld Cvr (8ths)	D/N ΔT (deg F)	Avg D/N Shift (mils)
WSFT 1	Dec 81	2000	2.0-2.5	1-2	0-2	22	0.67
WSFT 2	Dec 81	2000	2.0-2.5	0-4	0-2	31	0.53
WSFT 3	Dec 81	2000	2.0-2.5	2-8	2-8	21	0.20
WSOT 1	Oct 82	2000	1.5-2.5	0-2	1-3	33	0.50
WSOT 2	Jun 83	1750	2-4	2-4	0-3	24	0.35
APGOT	Jun 85	2650	1-2	?	?	?	0.50
FtSOT	Mar 86	2000	1-2	1-4	0-8	25	0.70
WSOT 3	Sep 87	2000	7-9	0	0	24	0.20
WSOT 4	Sep 87	3000	10-15	0-2	0-1	29	0.20
NTCOT	Apr 90	2000	10-20	Calm	CLR	17	0.10

The data indicate that there is a strong correlation between the observed refractive effects and the ΔT parameter. Significant effects were always observed if $\Delta T > 30^\circ$ F. ΔT depends on the weather conditions. In particular, relatively uniform weather patterns of clear skies and low winds over a few hours are required to obtain significant nocturnal refractive effects. For example, WSFT3 began with clear skies at midnight, but as a front moved in (2-4 m/s winds with increasing cloud cover) beginning around 0200 the refraction effects observed quickly eroded, becoming nonexistent during the firing periods between 0300 and 0600.

Also apparent in the data is the effect of elevated lines of sight. The weather conditions during WSOT2 and WSOT3 were very similar, yet the observed effects during WSOT3 were significantly less than those observed during WSOT2 because the height of the line of sight is significantly higher during OT3. The daytime effects seen in WSOT3 were significantly reduced below those observed in WSOT1 and WSOT2.

Some typical results are seen in figs. 2 through 4. Data were collected more often than once every hour, but the data presented are representative. In particular, the high variance readings obtained at night maintain their character down to time periods on the order of a few seconds. The day-to-night shift information listed in table 2 was calculated by determining average image positions during the day and at night and taking the difference.

We discovered during these investigations that the point measurement of the vertical temperature structure made by tower measurements could only model the refractive structure of the air during the day. At night the tower data set was usually an inappropriate measure of the atmospheric state over the entire path because the temperature gradient would vary from point to point along the path due to irregular flow of pockets of air mentioned previously. The Fort Stanton site was somewhat of an anomaly in this regard, simply because our observation site was located at the upper end of a shallow draw. At night the katabatic flow off Sierra Blanca mountain carried the same air mass past the met tower and over the entire optical path. In the WSMR measurements we were observing lines of sight where the wind was moving air masses transverse to the line of

sight. Thus a met tower set up at any point along the path would only sense a fraction of the overall air mass characteristics at night. A sample data plot showing this problem is given in fig. 6.

4. RULE OF THUMB AND INTELLIGENCE PREPARATION OF THE BATTLEFIELD

To correct for the effects of refraction in direct fire weapons systems in a desert environment, we initially developed a simple algorithm to correct for refraction bias based on model calculations from our TGRAD SEB model and measured data. Ten years of weather data from Beersheba, Israel, collected at three hour intervals were used for the calculations. A height of 2.3 meters was used for the observation height, and a range of two kilometers selected for the target distance. The predicted diurnal temperature gradients were converted into refraction correction angles in milliradians assuming flat terrain. The shape of the diurnal effect was nearly a cosine with maxima of about 0.4 mrad occurring in the afternoon and in the middle of the night. Neutral (no refraction correction) points occurred near sunrise and sunset. Different curves were developed for each month. With little or no loss in prediction accuracy, the nine-term Fourier series fit to the model predictions was replaced with a simpler series of four straight lines as shown in fig. 7. This algorithm was applied to experimental observations and produced good results when applied to situations that met the circumstances for which the model was derived, but produced errors if applied to cases where there was cloud cover, wet soil, high winds, or nonflat terrain.

The difficulty with this approach was in translating its results into a product useable by the Armor community. In an operational setting the use of a numerical correction is not currently feasible because the tank gunner has no way of correcting by fractions of milliradians. Similarly, there are problems posed by requiring the gunner to decide when to apply a correction. To resolve these problems a two-step approach has been developed. The first step is a rule of thumb based on typical overwatch terrain, typical ranges of engagement, and desert conditions. The second step is to provide commanders with information during the intelligence preparation of the battlefield (IPB) regarding the likelihood of encountering refraction problems during a given operation day.

Figure 8 shows the rule of thumb method proposed to correct for refraction. The justification for the rule of thumb is that at 1500 m or greater, aiming at the base of the target typically provides the correct aimpoint for a fully exposed target. The daytime correction is only used on very level terrain because daytime refraction decreases rapidly with height of the line of sight above the surface. The IPB portion is designed to alert a tank commander of those conditions when refractive effects can be expected. When this warning is included in the IPB and the crew encounters difficulty in hitting targets, they will have a direction to adjust to hit the target.

5. NOTIONAL REFRACTION COMPENSATION TECHNIQUES

As an alternative to the rule of thumb/IPB approach several alternatives exist to automatically correct for refraction or to remove the problem from the gunner's perspective.

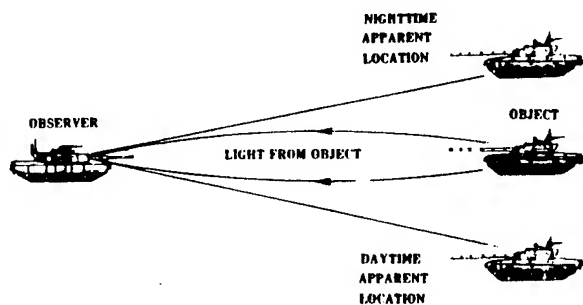
- First, the fire control computer could be made to act as an image processor to detect refraction via analysis of optical distortion visible in the gunner's primary sight image field. This system could also be used to remove optical turbulence effects from the image, allowing the gunner to observe targets at longer ranges. Such a technique is admittedly years from practical implementation.
- A second technique, somewhat more practical, would introduce a clock to the fire control computer and utilize latitude and longitude information obtained from the GPS to compute sun position. In a future tank the fire control computer will likely be in direct contact with computers at higher command elements and thus wind, cloud, and terrain information should be available as passive inputs to the computer. From these inputs the computer could predict

the refraction. A variant of this technique would entail a remote calculation of refraction effects, based on the current tank position and orientation, as reported by the tank through a future communications network. The refractive correction would then be transmitted passively to the tank via the communications network. This latter technique would entail less information traffic between tank and higher headquarters, but the information processing load would be heavier at a central processing node.

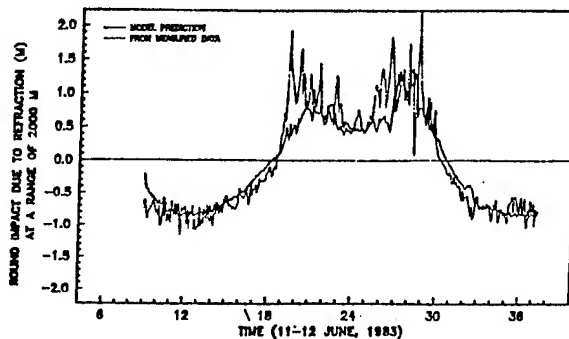
- A third technique would entail the development of a refraction measurement sensor. This device would operate with either a dual laser system, or passively sense a visible target, limiting its usage to conditions where visible sources were available at the target range (sunlight or artificial illumination). The device would sense the apparent difference in elevation of an object at two wavelengths.

REFERENCES

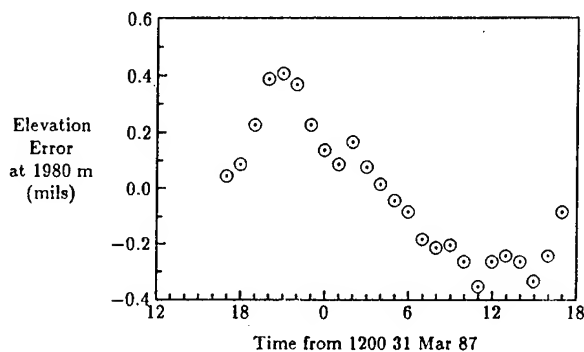
- Deardorff, J. W., 1978: Efficient Prediction of Ground Surface Temperature and Moisture, With Inclusion of a Layer of Vegetation. *J Geophys Res*, 83:C4:1889-1903.
- Gillespie, J. B., and D. H. Tofsted, 1991: "Optical Refraction in the Atmospheric Surface Layer. In *Proceedings of the 1991 AGARD Conference*, Istanbul, Turkey.
- Hill, R. J., S. F. Clifford, and R. S. Lawrence, 1980: Refractive Index and Absorption Fluctuations in the Infrared Caused by Temperature, Humidity, and Pressure Fluctuations. *J Opt Soc Am*, 70:1182-1205.
- Kunkel, K. E., and D. L. Walters, 1983: Modeling Diurnal Dependence of the Optical Refractive Index Structure Parameter. *J Geophys Res*, 88:C15:10,999-11,004.
- Obukhov, A. M., 1971: Turbulence in an Atmosphere with a Non-Uniform Temperature. English translation in *Boundary Layer Meteorology*, 2:7-29.
- Oke, T. R., 1970: Turbulent Transport Near Ground in Stable Conditions. *J Appl Meteorol*, 9:771-786.
- Tofsted, D. H., and J. B. Gillespie, 1986: Comparing Results From Three Surface Energy Budget Models. In *Proceedings of the Sixth Annual EOSAEL/TWI Conference*, R. C. Shirkey, ed., 401-412.
- Tofsted, D. H., 1987: *Optical Path Bending Code Module REFRAC, EOSAEL 87, Volume 25*. ASL-TR-0221-25, US Army Atmospheric Sciences Laboratory, WSMR, NM 88002-5501.
- Tofsted, D. H., 1989: *Evaluation of the REFRAC Refractive Raytracing Algorithm*. ASL-TR-0242, US Army Atmospheric Sciences Laboratory, WSMR, NM 88002-5501.



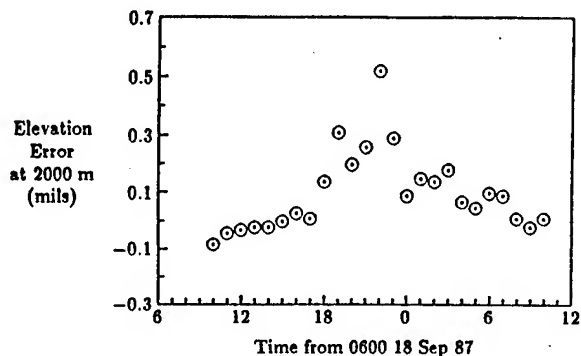
1. Sighting scenario illustrating diurnal variations in apparent target location.



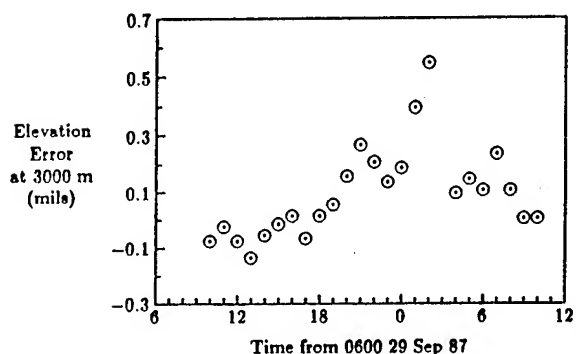
2. Comparison of SEB model prediction of refractive elevation change and observed motion for WSOT2.



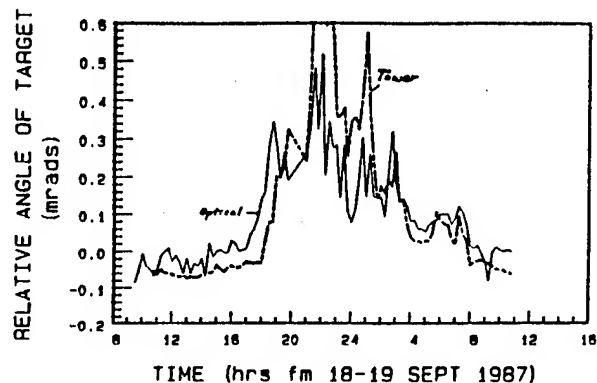
3. FSOT results: observed elevation changes of the 1980 m target.



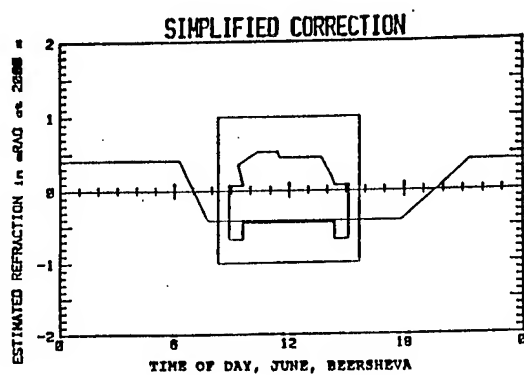
4. WSOT3 results: observed elevation changes of the 2000 m target.



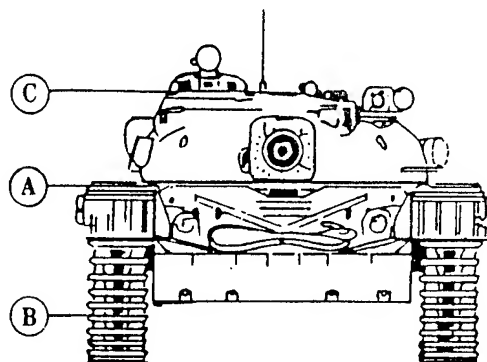
5. WSOT4 results: observed elevation changes of the 3000 m target.



6. Time plot of optical elevation changes for WSOT3 compared to elevation changes inferred by tower temperature measurements.



7. Simple refraction prediction model for June in Beersheba, Israel.



8. Rule of thumb for refraction corrections:
A - Normal aimpoint. B - Nighttime aimpoint, when winds low, skies clear, and soil dry. C - Daytime aimpoint, when skies clear, soil dry, and terrain flat.

Session VI

BEST TWO

**Thursday and Friday
5 - 6 December 1991**

**Chairperson
Ir. J. Rogge**

BEST TWO : AN OVERVIEW OF THE TEST, THE SIMULATION OF ARTILLERY-

PRODUCED DUST, AND THE TARGET VEHICLES TRACKING

Jacques VESQUE
Test Director

Etablissement Technique Central de l'Armement
16bis, avenue Prieur de la Côte d'Or
94114 ARCUEIL CEDEX
FRANCE

ABSTRACT

The Battlefield Emissive Sources Test under European Theater Weather and Obscurants (BEST TWO) of NATO AC243/PO4.RSG15 was conducted 23 July - 17 August 1990 at Camp de Mourmelon - France with the participation of six countries : Denmark, France, Germany, the Netherlands, the United Kingdom and the United States.

The test objectives were to determine the effectiveness of electro-optical systems in European battlefield environment, to obtain data on the acquisition of static and moving ground vehicles at ranges out to 4 km, to evaluate target acquisition models and models to characterize battlefield events and their effectiveness, and to establish a data base for the evaluation of aided target recognition and smart weapons.

Different scenarios were performed with single vehicles or groups of vehicles - single static vehicle, single vehicle approaching, column of vehicles, attack formation - using target vehicles from the French Army (AMX30, AMX10, trucks, jeep) and from the Dutch Army (LEOPARD 2, PRAT, PRI).

In addition to natural clutter conditions and vehicular dust, the scenarios included simulated battlefield effects : simulation of artillery-produced WP smoke by using LUST (Limited Use Smoke Test) devices from CRDEC - Aberdeen Proving Ground; simulation of artillery-produced dust by using explosive dustbags.

The following experiments were performed : detection - recognition - identification experiments with real-time observers and recording, CCD and thermal imaging with standard or experimental cameras ground located or airborne, thermal signatures including top signatures from elevated platforms, characterization of fires, dust and WP smoke, laser experiments, radar experiments, camouflage experiments, atmospheric MTF measurements, acoustic and seismic measurements.

This paper gives an overview of the BEST TWO Test with a description of the general set-up and the measurements that were carried out. It also describes the simulation of artillery-produced dust by using explosive dustbags, and the results obtained, and the target vehicles tracking by a radar RASIT coupled with a geographic data base.

(The full text of this paper was unavailable at press time.)

**METEOROLOGICAL CONDITIONS AND DATA
FOR THE BEST TWO FIELD TRIAL**

**ROBERT W. SMITH
TED CORBIN**

**TECOM FT BELVOIR METEOROLOGICAL TEAM
FT BELVOIR, VA 22060-5677**

ABSTRACT

The BEST TWO field trial was conducted at Camp Mourmelon, France in July and August 1990. The Ft Belvoir Meteorological Team was pleased to participate in the collection of ground truth meteorological data for the test as well as providing forecasting support with the able assistance of the French Air Force. The trials were conducted under very hot and dry conditions. But to perhaps lay a foundation for the other papers on BEST TWO this paper will discuss the general weather conditions, the data collection and processing and give examples of a typical days data and expand that to a typical test period. Finally, since data from four countries will be included in the final report, a comparison of some key parameters will be presented.

1. INTRODUCTION

Extensive meteorological measurements were planned for BEST TWO. We had planned to provide measurements of atmospheric transmission, optical turbulence, light levels, sky-to-ground ratio, average aerosol concentration, and four remote sites with the more standard parameters of temperature, humidity, solar radiation, soil temperature and moisture, wind, pressure, and visibility. We also planned a 50 foot tower with data at the 50 ft level plus a temperature differential. But, alas, this was not to be. Shipping difficulties prevented the U.S. meteorological trailer from arriving. Knowing that we were in trouble, we hand carried enough equipment for basic measurements at two remote sites and believed that this would get us by until our trailer arrived. It turned out to be our only instrumentation. Now for some good news. The German delegation brought their met station as did France and the Netherlands. Also, weather conditions were such as to make some of the specialized measurements of less importance. So while the available data is not as extensive as we had planned, it is still quite complete and much larger than we had for BEST ONE. In this paper, we discuss the availability of data, compare data from the various sources, and present and discuss some calculated values.

2. METEOROLOGICAL CONDITIONS

The conditions we experienced during BEST TWO do not require much explanation. It was clear to partly cloudy and very hot. Figure 1 depicts the daily maximum and minimum temperatures as recorded by the German met system. During this period we had weak frontal passages on July 29 and August 7. The only recorded

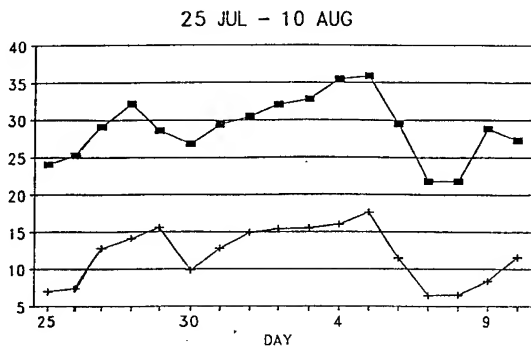


Figure 1. MAX/MIN TEMPERATURES
DEGREES C

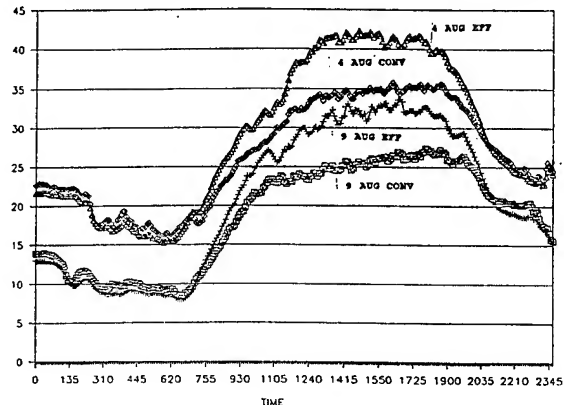


Figure 2. AMBIENT VS EFFECTIVE
TEMPERATURES DEGREES C

rain fell on July 28 for about 50 minutes. But being a Saturday, we were not in the field. Figure 2 gives another indication of how hot it felt. Here we show the ambient temperature plotted with the temperature of a black body for two days - one cool and one hot. Note that on August 4, the effective temperature rose to about 42C or 108F while the ambient temperature was only 36C or 97F. As far as the other weather conditions are concerned, visibility never went below five kilometers and that was in smoke from the burning of fields, the winds were in general light from the north or north east which was directly opposite of the climatological data, and the cloud cover ranged from clear to broken fair weather cumulus with some occasional scattered mid level clouds and thin cirrus. The ground was very dry causing much dust in the vicinity of moving vehicles.

3. METEOROLOGICAL MEASUREMENTS

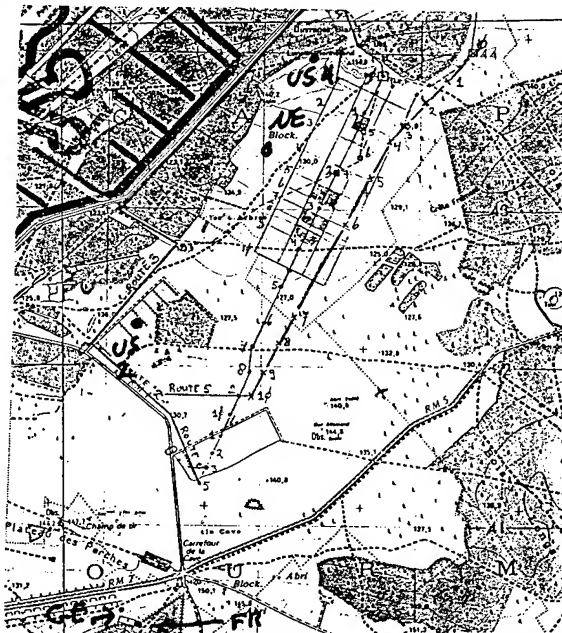
3.1 DATA LOCATION

Meteorological data as mentioned is available from four nations. Figure 3 shows the location of each data collection site. The German site was slightly in front of the sensor line and on the left hand side looking down range. It was placed just below the height of the sensors. Exposure was very good. The French site was just behind the sensor line with the instruments placed on the top of a van so that they were above the sensor the sensor height by about 2 meters. The site was just right of center. Down range we had the Netherlands site on the left hand side at about 3 kilometers. The U.S. sites were both on the left hand side, one at 2 KM and one at 4 KM. The 2 KM site was placed

to be in a clearing in a wooded area and site 4 was the highest data being at the top of the sloping terrain and in the open.

Figure 3.

SITE MAP SHOWING MET SITE LOCATIONS



3.2 DATA AVAILABILITY

Good data is available for all scenerios. The German data is available for all except scenerios of 10 August. French data is available for all scenerios as are the U.S. cloud and visibility observations. The Netherlands data is mostly available from July 30 to August 9. Figure 4 provides a table indication data availability for each trial. A more detailed discussion of each data set will follow.

TRIAL	GE	FR	NE	US	US2	US4	TRIAL	GE	FR	NE	US	US2	US4
26.2	X	X		X			3.2	X	X	X	X	X	
26.3	X	X		X			3.3	X	X	X	X	X	
27.2	X	X		X			3.4	X	X		X	X	
27.3	X	X		X			6.2	X	X	X	X	X	X
30.2	X	X	X	X			6.3	X	X	X	X	X	X
30.3	X	X	X	X			6.4	X	X		X		
31.2	X	X	X	X			7.2	X	X	X	X	X	
31.3	X	X	X	X			7.3	X	X	X	X	X	
31.4	X	X	X	X			8.1	X	X	X	X	X	
1.2	X	X	X	X			8.2	X	X	X	X	X	X
1.3	X	X	X	X	X	X	8.3	X	X		X	X	
2.1	X	X	X	X			9.2	X	X	X	X	X	
2.2	X	X	X	X			9.3	X	X	X	X	X	X
2.3	X	X	X	X	X		10.2		X		X	X	X
							10.3		X		X	X	

Figure 4. AVAILABILITY OF METEOROLOGICAL DATA

3.2.1 French Meteorological Data

The French data included wind, temperature, rain, and solar radiation in watts/cm². Figure 5a shows the format provided to us. We adjusted the date/time for consistency and placed in columns as shown in figure 5b and is the format found in our

data base. This data is at 30 minute intervals.

```

Date: 10 / 8 / 1990      1 h 0 - 1 h 30

Numéro demi-heure       :      3.0

Température minimale    :      18.2 °C
Température maximale    :      18.8 °C
Température instantanée :      18.2 °C
Hauteur de Pluie       :      0.0 mm
Direction moyenne du Vent : 200.0 degrés
Vitesse moyenne du Vent :      1.0 m/s
Direction a vitesse maxi : 200.0 degrés
Vitesse maxi du Vent    :      1.0 m/s
Humidité minimale       : Capteur absent ou valeur hors norme
Humidité maximale       : Capteur absent ou valeur hors norme
Humidité instantanée    : Capteur absent ou valeur hors norme
Rayonnement Global      :      0.0 J/cm²
  
```

Figure 5a. EXAMPLE OF FRENCH DATA PRINTOUT

DATE/TIME YYMMDDTIME	TEMPERATURE			RAIN RATE	WINDS		PEAK WIND		SOLAR RAD
	MIN	MAX	INST		DIR	SPD	DIR	SPD	
9007231830	24.4	24.6	24.4	0.0	360.0	4.0	360.0	7.0	16.0
9007231900	23.4	24.6	23.6	0.0	20.0	5.0	20.0	7.0	67.0
9007231930	22.8	23.8	22.9	0.0	20.0	5.0	360.0	7.0	43.0
9007232000	21.8	22.9	21.8	0.0	20.0	4.0	40.0	7.0	71.0

Figure 5b. FRENCH DATA AFTER REFORMATING

3.2.2 German Meteorological Data

The data from the German delegation came to us in two files; one with wind, temperatures, humidity, and pressure, and the other with solar radiation and rain rate. An example is in figure 6a. We combined both into a single file and again standardized the time tag. This is shown in fig 6b. Note that under temperature, "conv" is the ambient temperature and "eff" is the temperature of a blackbody. Ignore "surf" temperature because that column was used in their program for another purpose. The German data is at 5 minute intervals.

WindDir	WindVel	T conv.	T eff.	T @surf	T @10cm	rel. Hum	Pressur	Net. Rad	Solar	Gauge	Drops	
degrees	m/sec	°C	°C	°C	°C	%	hPa	W/m²	W/m²	mm/h	mm/h	
2 24-7 13:10	6	3.9	18.8	23.1	32.2	15.3	26	862	406	847	0.0	0.000
3 24-7 13:15	13	4.4	21.6	26.7	36.2	17.9	30	1005	477	987	0.0	0.000
4 24-7 13:20	345	2.8	21.5	26.8	33.2	18.0	30	1005	487	992	0.0	0.000
5 24-7 13:25	45	3.4	21.7	27.0	36.8	18.0	28	1006	571	1001	0.0	0.000
6 24-7 13:30	38	3.1	21.6	26.8	35.5	18.1	29	1006	397	636	0.0	0.000
7 24-7 13:35	32	3.9	20.9	25.6	34.1	18.1	29	1006	347	576	0.0	0.000

Figure 6a. EXAMPLE OF GERMAN DATA

DATE/TIME YYMMDDTIME	WIND		TEMPERATURE			10CM	RH	PRES	RADIATION	GAUGE	DROPS	
	DIR	SPD	CONV	EFF	SURF							
9007241310	6	3.9	18.8	23.1	32.2	15.3	26	862	406	847	0.0	0.0
9007241315	13	4.4	21.6	26.7	36.2	17.9	30	1005	477	987	0.0	0.0
9007241320	345	2.8	21.5	26.8	33.2	18.0	30	1005	487	992	0.0	0.0
9007241325	45	3.4	21.7	27.0	36.8	18.0	28	1006	571	1001	0.0	0.0

Figure 6b. GERMAN DATA AFTER REFORMATTING

3.2.3 The Netherlands Meteorological Data

The Netherlands data provides a variety of information. Besides wind, temperature, humidity and solar radiation, much other data are provided such as visual radiation on 5 sides of a cube and

visual irradiation at various angles. This data is available at 15 minute intervals, which we have included, and at 10 seconds which is available through the AAODL. In our data base, we have only standardized the time tag. We will recommend to reader the very fine technical report prepared by TNO Physics and Electronics Laboratory (FEL-90-A368) for additional details. Figure 7 provides an example of their data.

YYMMDDTIME	"bvnknt"	nord	1"	oost2"	zuid3"	west4"	rad2Tb"	rad2T"	rad3Tb"	rad3T"	Tamb"	vocht"	zonR"	wind"	plaat1"	plaat2"	plaat3"
9008011030	162.	225.	51.	50.	90.	29.4	33.5	28.7	48.1	25.6	46.	594.	2.0	442.	495.	460.	
9008011045	169.	229.	52.	51.	78.	30.7	33.7	30.1	49.3	26.0	44.	629.	2.2	451.	512.	477.	
9008011100	178.	231.	54.	53.	67.	31.9	34.0	31.4	50.3	26.7	41.	667.	2.1	458.	528.	494.	
9008011115	184.	230.	55.	54.	58.	32.6	34.4	32.3	51.0	27.1	40.	694.	2.3	457.	535.	504.	

Figure 7

3.2.4 The United States Data

Figure 8 gives an example of our data. Cloud and visibility observations were made through-out the test with down range measurements taken as dictated by the scenerio being run. In the interest of some real time data, our observers down range radioed the data readings to our tent where we copied them down. When we discovered that our data retrieval from the data loggers did not work, we were left with this hand written copy of more or less instantaneous readings. This situation was just a continuation of the luck which we enjoyed the entire test.

SITE 2									
DATE/TIME	PRES	TEMP	RH	WND	WND	VIS	WX	SKY	CONDITION
YYMMDDTIME	mb	C	%	DIR	SPD	KM			
9007312130	1008.5	23.3	62	CALM		15.0	K OVR MIA	2CI250	
9007312200	1008.4	22.8	66	CALM		15.0	K OVR MIA	2CI250	
9007312230	1008.8	22.1	69	CALM		15.0	K OVR MIA	1CI250	
9007312300	1009.0	21.9	75	CALM		15.0		1CI250	
9007312330	1009.2	20.7	82	CALM		15.0		1CI250	
9007312400	1009.3	19.7	89	CALM		15.0		CLR	

Figure 8. EXAMPLE OF U.S. DATA AT 2 KM

3.3 DATA COMPARISONS

In making comparisons of the various data from BEST TWO one must be mindful of difference in location and averaging times. In the interest of space, we will look only at a few key parameters.

3.3.1 Temperature

Figure 9a shows a complete 24 hr plot of temperature from the German system which shows a well behaved cycle. Note that the maximum occurs later in the afternoon than might have been expected but that was consistent for the test. Figures 9b and 9c provide a comparison of the various data sets. August 6 was one of our cloudiest days (but never overcast) and we see some small differences probably due to cloud cover. August 9 had uniform scattered high clouds and the differences are very small.

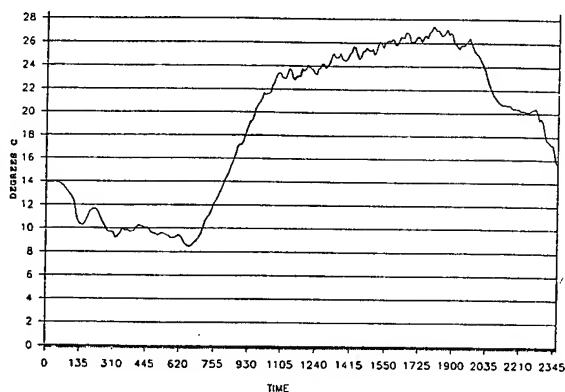


figure 9a TEMP 9 AUG 91(GE)

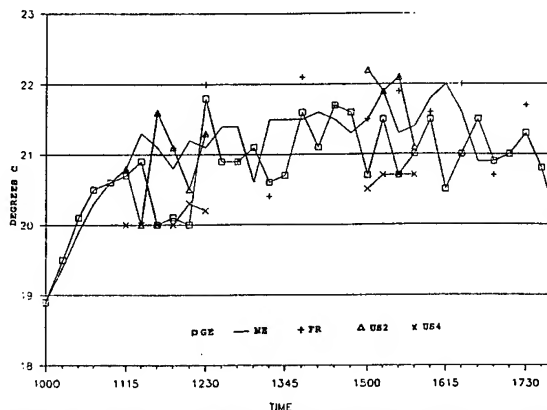


Figure 9b TEMP COMPARISON 6 AUG

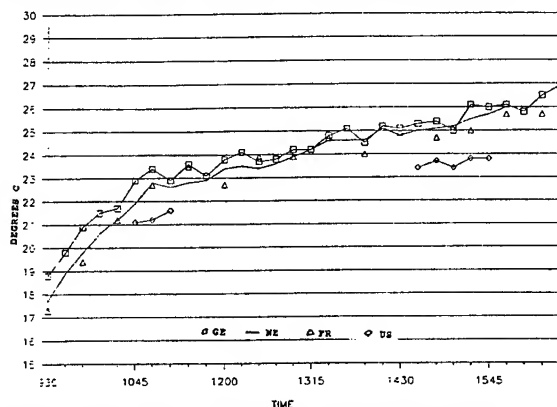


Figure 9c. TEMP COMPARISON 9 AUG

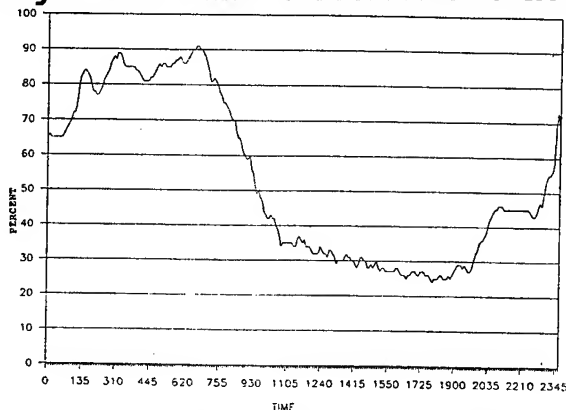


Figure 10a. RH 9 AUG (GE)

3.3.2 Relative Humidity

The same dates of comparison are made for this important parameter. Figure 10a shows a nice diurnal curve. The comparison on August 6 jumps around during the morning when clouds were most variable and smooths out in the afternoon. The August 9 comparison again good agreement with the U.S. site 2 data being a little higher, probably due to being lower and in foliage.

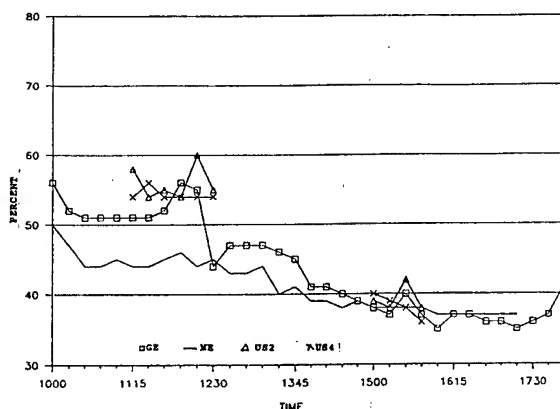


Figure 10b. RH COMPARISON 6 AUG

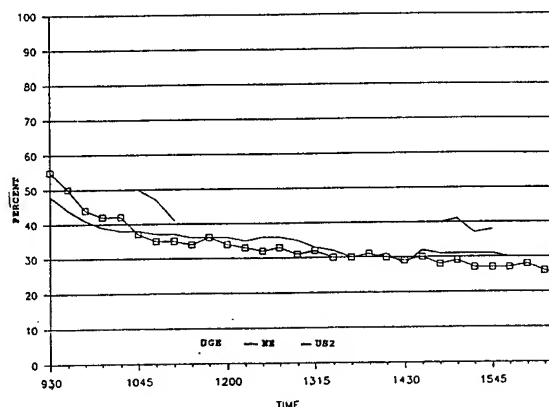


Figure 10c. RH COMPARISON 9 AUG

3.3.3 Solar Radiation

The 24 hour plot for 9 August looks good as Figure 11a shows. The comparison in figure 11b also looks good and needs no further comment.

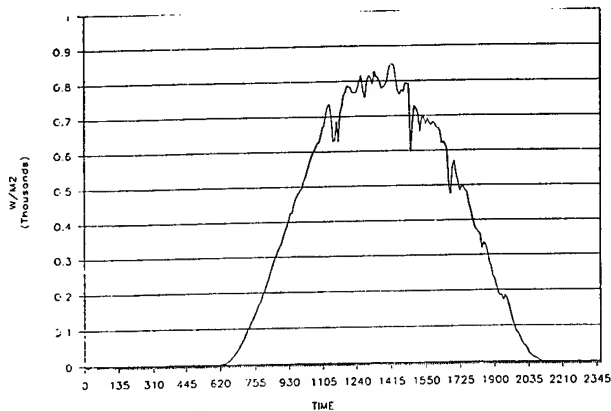


Figure 11a. SOLAR RAD. 9 AUG

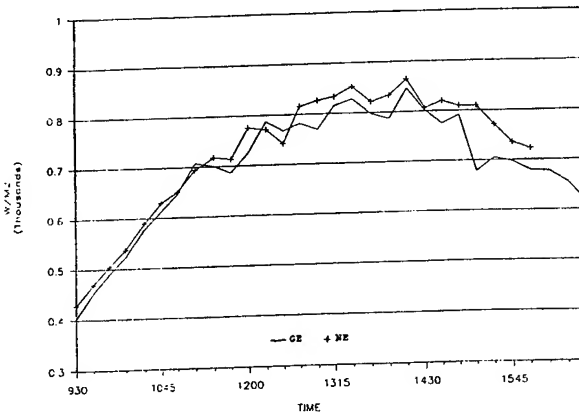


Figure 11b. SOLAR RAD
COMPARISON

3.3.4 Wind Comparison

Figures 12 and 13 compare wind speed and direction. Considering the light winds and differing locations, comparison is good.

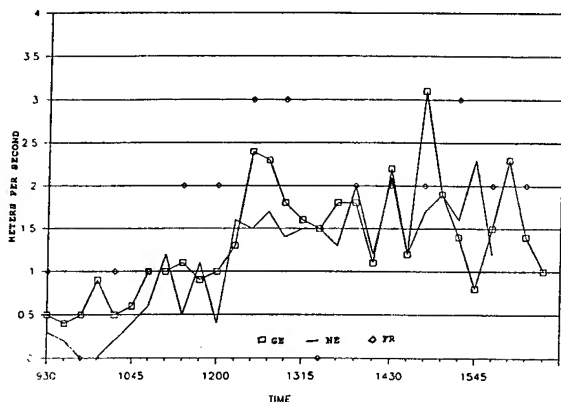


Figure 12. WIND SPEED COMPARISON

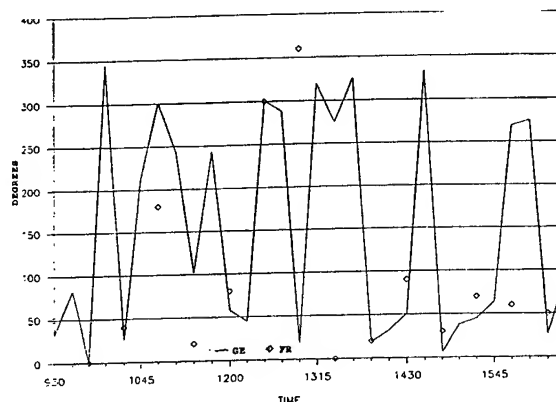


Figure 13. WIND DIRECTION

4. DISCUSSION OF CALCULATED DATA

Using the data from section 3 and known solar and lunar positions, one can estimate parameters such as light level, turbulence, stability, and transmission. This has been done.

4.1 LIGHT LEVELS

Using the Atmospheric Sciences Laboratory model called ILLUM (Duncan 1987) three days were calculated. On July 26 the moon was only 26% illuminated. On August 2, we had 90% illumination

but the moon set about 2am. On the 9th we had 83% illumination but the moon was up until mid morning. Values are in LUX. This model normally does very well. A paper by Smith (1989) compares the model to actual data.

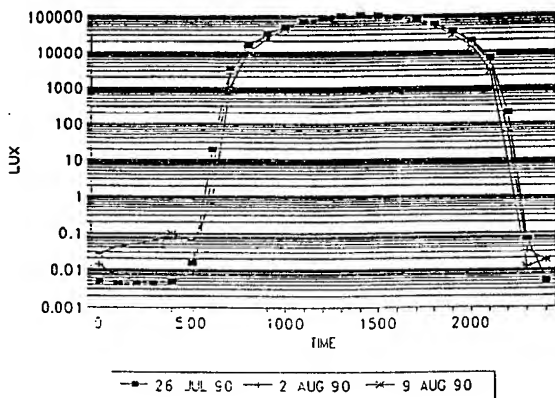


Figure 14. LIGHT LEVELS

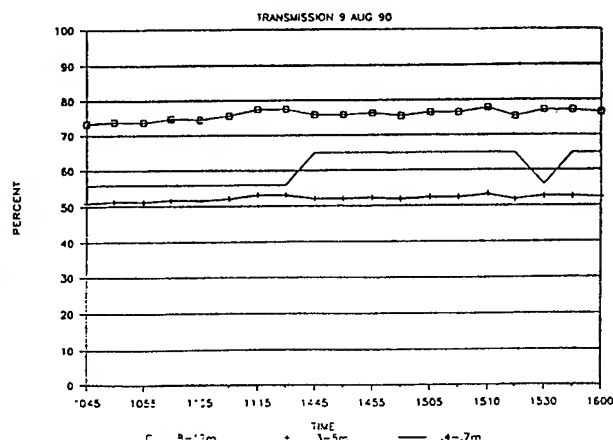


Figure 15. TRANSMISSION

4.2 TRANSMISSION

Figure 15 shows calculated values of 2 km transmission in the visible, 3-5 micron, and 8-12 micron bands using LOWTRAN 7 (Kneizys, 1988). This day is typical of the entire test. A warning here is the estimated visibility, which is so important to the calculation, may not represent the actual line of sight considering the dust around moving vehicles. Smith (1991) discusses this type of problem when using LOWTRAN.

4.3 STABILITY AND TURBULENCE

We were asked to provide estimates of these parameters as part of the final report. Let's first dispense with turbulence. We attempted to use the ASL program IMTURB (Miller, 1990) to make these calculations. We found that it would not provide reasonable results. We will address this in an upcoming paper comparing the model to collected data. We then turned to a manual method suggested by Kopeika (1988) to estimate the turbulence. Usually the turbulence was in the light category but did reach moderate on occasion. Figure 16 contains this data for each trial.

Now considering stability, we wanted an estimate of the pasquill stability category. To do this we used the traditional methods and derived categories for each trial. We then used the ASL model FSCAT (Pena, 1990) to calculate the categories and the fractional stability category. Figure 16 also provides these. We feel that the agreement is good and differences are produced mainly in the traditional method. The ability to have a fractional representation is very desirable. Figure 17 provides a sample output of FSCAT. Figure 18 is a plot of 24 hours using

FSCAT, Hourly data was used except at the cross over time when 5 minute data was used. We feel that using the BEST TWO met data and the FSCAT code, one can get a realistic characterization of stability.

TRIAL	DATE	LCL TIME	EST PASQUILL	FSCAT PSC FSC	EST CN2	TRIAL	DATE	LCL TIME	EST PASQUILL	FSCAT PSC FSC	EST CN2
26.2D	26 JUL	0900	A-B	B -2.17	1.7E-14	3.2	3 AUG	1100	A-B	B -2.42	1.7E-14
26.2E		1300	B	B -2.05	1.1E-14	3.3D		1400	B	B -2.38	1.7E-14
26.3D		1400	B	A -2.72	1.1E-14	3.3E		1800	A	B -2.45	1.7E-14
26.3E		1800	D-C	D -1.58	4.4E-15	3.4B		2200	G	G 2.70	1.1E-14
27.2D	27 JUL	0900	B	D -1.00	1.1E-14	3.4E	4 AUG	0200	G	G 2.75	1.1E-14
27.2E		1300	B	D -2.22	1.1E-14	6.2	6 AUG	1200	B-C	C -1.02	4.4E-15
27.3D		1400	B	A -2.75	4.4E-15	6.3D		1500	C	C -0.70	9.7E-16
27.3E		1800	C	B -1.98	4.4E-15	6.3E		1700	D	D -0.55	1.7E-16
30.2	30 JUL	1000	A	A -2.67	1.7E-14	6.4B		2200	E	F 1.55	2.8E-15
30.3B		1400	A	B -2.53	1.7E-14	6.4E	7 AUG	0200	F	F 1.95	8.6E-15
30.3E		1600	A	B -2.67	1.7E-14	7.2		1100	A-B	B -2.20	1.1E-14
31.2D	31 JUL	0900	B	D -2.20	1.1E-14	7.3B		1400	B-C	C -1.08	4.4E-15
31.2E		1300	B	B -2.45	1.1E-14	7.3E		1600	B	C -1.40	1.1E-14
31.3D		1400	B	B -2.40	1.1E-14	8.1B	8 AUG	0400	G	G 2.85	1.1E-14
31.3E		1800	C	B -1.88	4.4E-15	8.1E		0700	B	G 2.42	1.1E-14
31.4B		2200	C	F 2.35	8.6E-15	8.2B		0900	B	B -1.92	1.1E-14
31.4E	1 AUG	0200	G	G 2.65	8.6E-15	8.2E		1200	A-B	C -1.42	1.7E-14
1.2		1100	A	B -2.53	1.7E-14	8.3B		1300	A	B -1.65	2.2E-14
1.3B		1400	B	B -1.92	1.1E-14	8.3E		1500	A-B	A -2.63	1.7E-14
1.3E		1700	B	B -2.10	4.4E-15	9.2		1100	A	A -2.75	2.5E-14
2.1B	2 AUG	0200	G	G 2.55	8.6E-15	9.3		1500	B	B -2.22	4.4E-15
2.1E		0600	B	G 2.80	1.1E-14	10.2B		0900	A	B -2.25	1.7E-14
2.2B		0800	A-B	B -2.33	1.7E-14	10.2E		1200	A-B	A -2.60	1.1E-14
2.2E		1100	B	B -2.17	1.1E-14	10.3		1500	B	B -2.55	1.1E-14
2.3		1300	B	B -2.00	1.1E-14						

Figure 16. STABILITY AND TURBULENCE CALCULATIONS

F S C A T				STABILITY CATEGORY INPUTS			
STATION ID				= 26.2B			
1. LATITUDE	- DEGREES	=	49.12	NORTH			
2. LONGITUDE	- DEGREES	=	4.40	EAST			
3. STATION ELEVATION	- METERS	=	100.00				
4. GREENWICH MEAN TIME	- HOUR	=	7.00				
LOCAL TIME	- HOUR	=	.00				
5. JULIAN DATE	- DAY	=	207.				
6. WINDSPEED	- M/SEC	=	1.30				
7. CLOUD COVER	- PERCENT	=	.0				
8. CEILING HEIGHT	- METERS	=	7000.0				
9. RELATIVE HUMIDITY	- PERCENT	=	.00				
10. TEMPERATURE	- DEGREE C	=	.00				
11. GROUND CONDITION		=	1.				
12. ROUGHNESS LENGTH	- METERS	=	.0300				
SCALING LENGTH (L)		=	-12.17	METERS			
SCALING RATIO (z/L)		=	-.82				
NET RADIATION INDEX (NRI)		=	2.0				
FRACTIONAL STABILITY CATEGORY (P)		=	-2.17				
PASQUILL STABILITY CATEGORY (PSC)		=	B				

Figure 17. FSCAT OUTPUT

STABILITY VS TIME
2 AUG 90

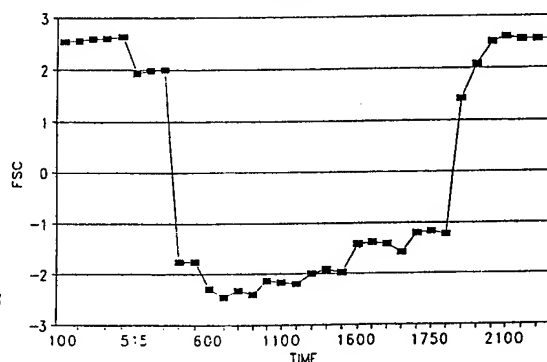


Figure 18. FSCAT STABILITY VS TIME

SUMMARY

Knowledge of the meteorological conditions existing during the BEST TWO trials is essential to the proper analysis and interpretation of the data collected by the various systems present. We have presented a brief outline of the availability of meteorological data and some comparisons. We have a good data set which can be used with confidence. The final report will expand on this paper and we hope to further address the important area of optical turbulence.

ACKNOWLEDGEMENTS

We wish to express out thanks to the other members of our met team, Karl Hammerdorfer and Richard Savage. We also thank our French hosts who provided so much help to us especially Jacques and Francis and most especially Tilly Gaillard who was our interpreter and who became our friend. Special thanks must also go to Uwe Muller of Germany, Thierry Blanchet, Muriel Monjanes, and Dominique Lenfort of France, and W.van Bommel of the Netherlands for their data collection efforts. We must also express our appreciation to J.L. Combs, Le Chef du CDM de REIMS, Centre Departmental de la Meteorologie Reims and his staff for their excellant forecasting support and for supplying maps and charts for background.

REFERENCES

- Duncan, L.D. and D.P. Sauter, 1987: Natural Illumination Under Realistic Weather Conditions, ASL TR-0212, U.S. Army Atmospheric Sciences Laboratory, White Sands Missile Range, N.M. 88002-5504.
- Kneizys, F.X. et al., Users Guide to LOWTRAN 7, AFGL-TR-88-0177, Air Force Geophysics Laboratory, Hanscom A.F.B., Ma 01731.
- Kopeika, N.S. 1988: IMAGING THROUGH THE ATMOSPHERE, Science and Technology Institute Tutorial 416, Hampton, Va 23666.
- Miller, W.B. and J.C. Ricklin, 1990: A Module for Imaging Through Optical Turbulence - IMTURB, ASL TR-02221-27, U.S. Army Atmospheric Sciences Laboratory, White Sands Missile Range, N.M. 88002-5504.
- Pena, R and D. DeSutter. 1990: FSCAT: A Fractional Stability Category Computer Code, ASL TMR-0004, U.S. ARMY Atmospheric Sciences Laboratory, White Sands Missile Range, N.M. 88002-5504.
- Smith, R.W., 1989: Light Level Measurments in Support of Electro Optical Systems Development, in Proceedings of the Tenth Annual EOSAEL/TWI Conference, U.S. Amry Atmospheric Sciences Laboratory, White Sands Missile Range, N.M. 88002-5501.
- Smith, et al, 1991: LOWTRAN 7 Comparisons with Field Measurements, DoD Transmission Review 1991, Geophysics Laboratory, Hanscom A.F.B., Ma 01731

OBSCURANT MEASUREMENTS DURING BEST-TWO BY MEANS OF MPTR

A.N. de Jong
TNO-Physics and Electronics Laboratory
The Hague, 2509 JG, The Netherlands

ABSTRACT

During the BEST-TWO trials, organized by AC/243 (P4/RSG.15) in August 1990 in Mourmelon (France) a number of measurements has been carried out on obscurants with the Multi Path Transmission Radiometer (MPTR), developed at FEL-TNO (Netherlands). These obscurants were: dust from simulated artillery barrage, smoke from oil fires, and dust from single and multiple vehicles. In this paper results are presented on transmission properties of these obscurants as obtained in a direction perpendicular to the line of sight from the Main Instrumentation Area to the target area.

1. INTRODUCTION

As indicated in the BEST-TWO testplan, RSG.15 (1990) the Multi Path Transmission Radiometer was scheduled to perform measurements on different battle-effects, occurring during the different scenarios. This time the major battle effect concerned the production of obscurants as may be expected in real scenarios:

- dust from explosions,
- dust from vehicle motion (single and multiple) and
- smoke from oil fires.

Unfortunately it was not possible to co-locate the transmissometry with the main instrumentation lines of sight. The transmissometry was carried out cross range at about 2,5 km from the main instrumentation area. An advantage of this location was the wide field of view (180°) and the shorter distance to the obscurant.

The transmission measurements were combined with a number of other experiments at the same location:

- contrast loss measurements by means of CCD camera's and the IR 18 thermal camera.
- contrast measurements for model validation of simple targets.
- measurement of turbulence effects by means of MPTR.
- IR-target signature measurements.

The major goal of the MPTR measurements was to study quantitatively the optical properties of the abovementioned obscurants, which lead to contrast losses in the battle field:

- size of the clouds, horizontally and vertically
- time evolution of the clouds
- spectral transmittance

This paper contains measured data on these phenomena.

2. DESCRIPTION OF THE SETUP

For a description of the MPTR system, reference is made to De Jong (1987). Here both the prototype MPTR1 and the extended system MPTR4 are described. The specifications are briefly summarized:

- MPTR1** - Spectral bands 0,4 - 0,7 μm ; 0,7 - 1,0 μm and 1,0 - 1,8 μm .
 - Field of view 120°
 - Instantaneous FOV 2 mrad
 - Scans per second: 20 sec^{-1}
 - Source: Tungsten + Reflector 15 cm
 - Integration time: 1 sec.
- MPTR4** - Spectral bands: 0,4 - 0,7 μm ; 0,7 - 1,0 μm ; 1,0 - 1,4 μm ; 2,0 - 2,2 μm ; 3,5 - 4,8 μm ; 7,9 - 12,3 μm .
 - Field of View 60°
 - Instantaneous FOV 1,3 mrad
 - Scans per second: 60 sec^{-1}
 - Source: 5 x IR 1200 °C + 2 x Tungsten + Reflectors 15 cm
 - Integration time: 1 sec.

The receiver system block diagram is given in fig. 1. System setup and data processing is done by means of a PC; quick look data are presented directly on a screen or on a printer. The reason for using two MPTR systems is the possibility to measure at two different heights through the obscurant.

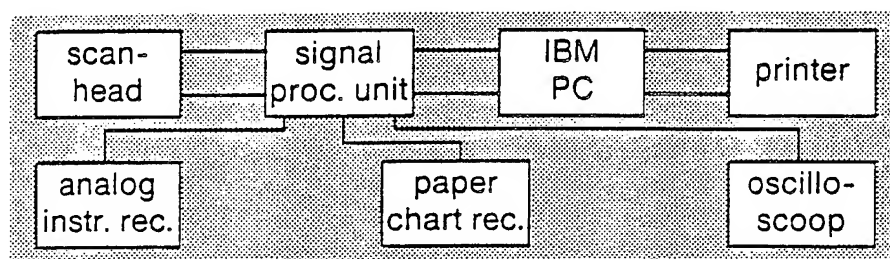


Figure 1. MPTR system block diagram (receiver side).

In fig. 2 the setup (top view) of the MPTR systems in the forward instrumentation area is indicated. In total 12 lines of sight (LOS) are used for the MPTR4, covering an angle of about 47,5°. The width of the scene, over which dust transmittance can be measured is approximately 500 m. The range between sources and receiver varies from 850 m (LOS4) to 1050 m (LOS12).

The LOS 2, 5, 8 and 11 were made double: the MPTR1 receiver and sources were both installed 2 m higher than the 12 MPTR4 sources and receiver. The alignment of the sources was facilitated by the fact, that they could be positioned on a nearly straight line.

The terrain was reasonably flat. In the centre area the depth of the terrain was about 5 m below the MPTR4 plane. This depth went up to about 3 m closer to the LOS 3-10 sources and 2 m closer to LOS 1, 2, 11 and 12. This meant that vehicles could cross these "MPTR4" LOS's, giving effects on the transmission values. The MPTR1 LOS's were never blocked by "hard" obscurers, because of the 2 m higher altitude.

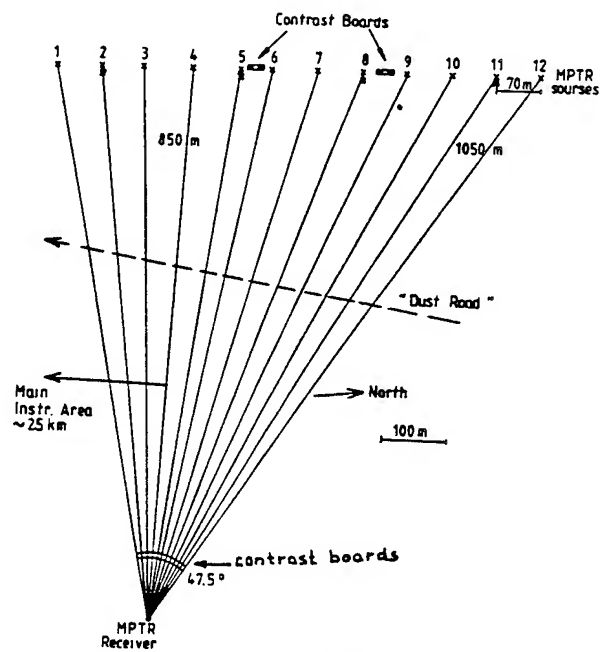


Figure 2. Overview of MPTR setup at BEST-TWO.

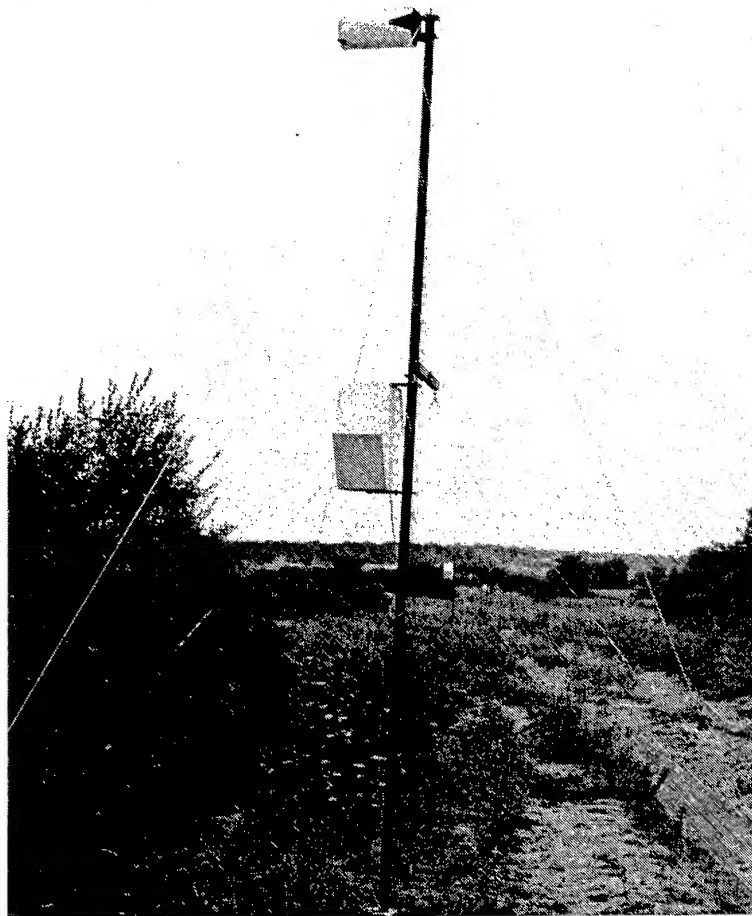


Figure 3. Two MPTR sources on one pole; (LOS5), 2m height difference.

In fig. 3 the mounting of a double source is illustrated on a 4,5 m long pole with fixation cables to 4 sides.

In fig. 4 both MPTR scanners are shown, one on an elongated tripod. The tripods were put on wooden blocks, giving sufficient stability in order to provide adequate alignment. The installation of the auxiliary equipment was done in a measurement van.

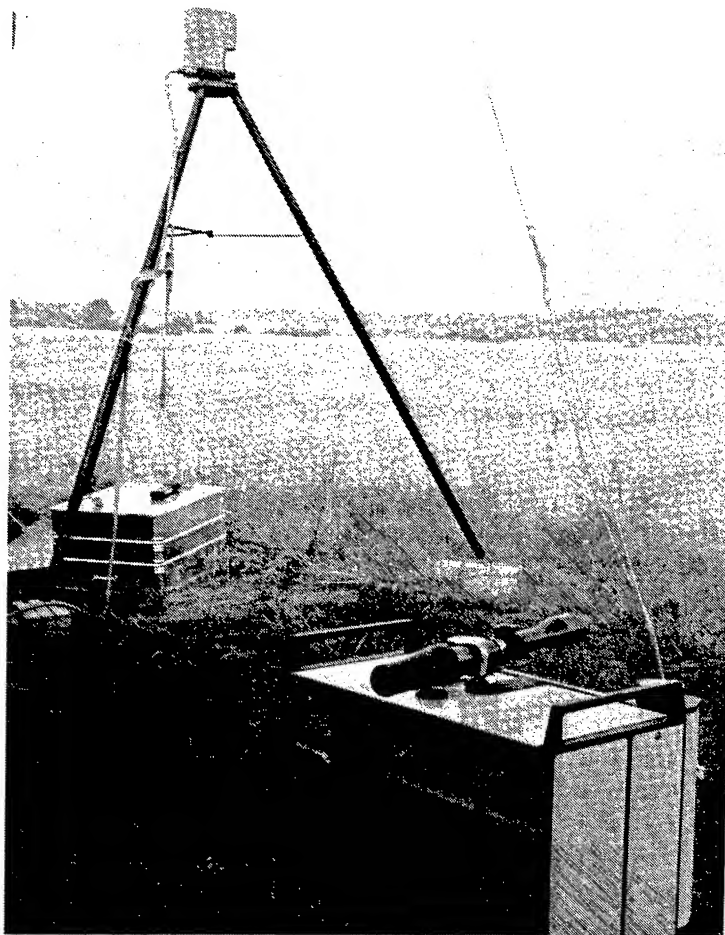


Figure 4. MPTR1 (top) and MPTR4 (bottom) receivers; 2m height difference.

During installation an experimental 6-channel detector set was used in stead of the standard 4-channel. Due to this some adaption of the amplification of the channels in this particular setup had to be realized. Not reported in this paper are the results of turbulence measurements, carried out with the MPTR system during some night/early morning sessions.

Reference is made to de Jong (1988) in order to demonstrate the capabilities of the MPTR system.

3. REVIEW OF TRIALS

In order to avoid too much redundancy it was decided to carry out measurements on a limited number of trials and to obtain a set with representative data on each of the types of obscurant. As the setup was not completed before the 27th of July and as a storm on the 28th caused some damage on the contrast boards, testing and measurements with MPTR started on the 1st of August.

A review of the MPTR transmission measurements is given in fig. 5.

FIGURE 5. REVIEW OF MPTR MEASUREMENTS

Date	Time	Trial no	Obscurant
2-8	14.01 -14.17	2824	Dust of 1 High Speed Driving Leopard II
3-8	11.55 -12.01	3802	Same; Dust hiding YPR
3-8	11.05 -11.08	3832	Dust of Attack Formation; Scen. 4E
6-8	12.20 -12.22	6862	Dust of Exploding Sandbags during Scen. 4B
6-8	15.02 -15.12 15.21 -15.24 15.46 -15.47 16.20 -16.25 16.54 -16.57	6863	Column Vehicles & Oil Fire; Scen. 3B Same Same Same Same
7-8	11.03 -11.07	7872	Dust of Attack Formation; Scen. 4C
7-8	14.00 -14.05 14.34 -14.38 15.14 -15.18 15.51 -15.54	7873	Column of Vehicles; Scen 3A; run 1 Same; run 2 Same; run 3 Same; run 4
8-8	09.18 -09.23 10.03 -10.07 10.51 -10.54 11.34 -11.38	8882	Column of Vehicles; Scen 3A; run 1 Same; run 2 Same; run 3 Same; run 4
9-8	11.02 -11.06	9892	Dust of Attack Formation; Scen. 4D

During trials 6863, 7873 and 8882 the column of vehicles made several passings, where some variation in the distance between the vehicles was applied. These runs provide possibilities to carry out statistical analysis on the data. In the scenario 3B a mixture is obtained of vehicle dust and smoke of oil fire. For some LOS's the oil smoke is dominant, where for other LOS the dust is dominant. In this short duration trials the sample frequency of the MPTR sensor was increased from 1 to 2 samples/sec, in order to get more data.

4. RESULTS

The results will be discussed separately according to the different obscurants produced. In this paper only limited results can be reproduced. A more comprehensive package of data is presented in De Jong (1990).

4.1 Dust of 1 high speed driving vehicle

Results are given for MPTR1 and MPTR4 respectively in fig. 6. The higher positioned MPTR1 apparently and expectably gives higher transmission values. Transmission is during the 3 passes (right-left; left-right and back again) never below 1% for MPTR1. For MPTR4 the transmission comes below 1% for the short wave bands, but not for the 4 μ m and 10 μ m. Although this dust is a reasonably multispectral screener, the obscuration is less in the thermal bands. This can also be observed in the optical depth plots of fig. 7. The histograms of fig. 7 show the time, the transmission is below a certain value for the whole trial.

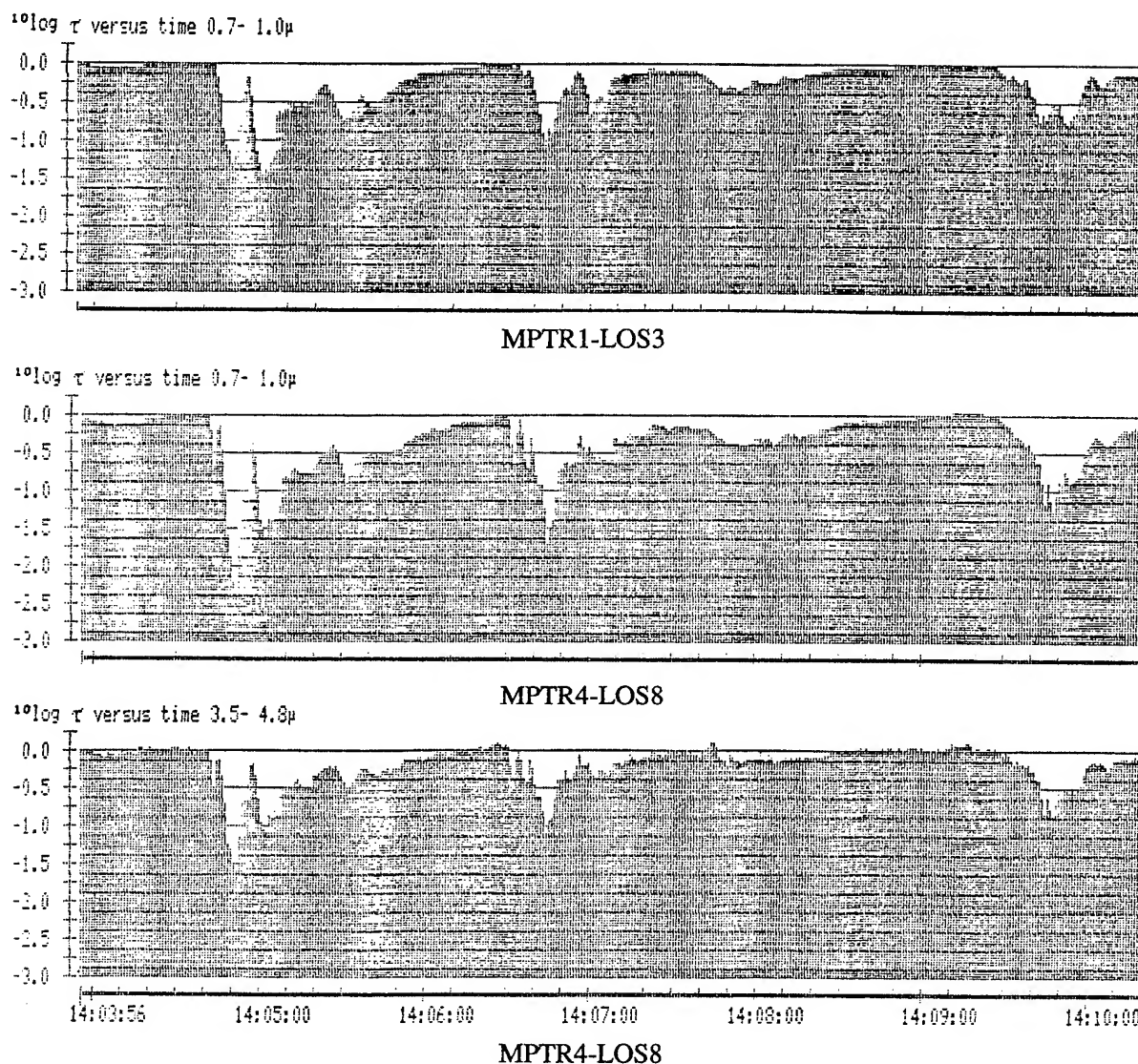


Figure 6. Transmission versus time for trial 2824; high speed driving vehicle; MPTR1-LOS3 and MPTR4-LOS8 for 2 spectral bands.

4.2 Dust from exploding sandbags

The overall result of trial 6862 is presented in fig. 9 with a review over all LOS and 3 of the 6 spectral bands. The ratio of the time that the transmission is below 3% or 10% with respect to the observation time is presented. The dust apparently is present for LOS 5-12 only (and for MPTR1 for LOS3 and 4). The dust is again a multispectral obscurer, blocking the LOS for about 50 seconds. The fall-out at the end is less effective in the thermal bands. In fig. 8 one may find data on the absorption index : $(1 - \text{transmission}) * \text{time}$ integrated over the whole trial.

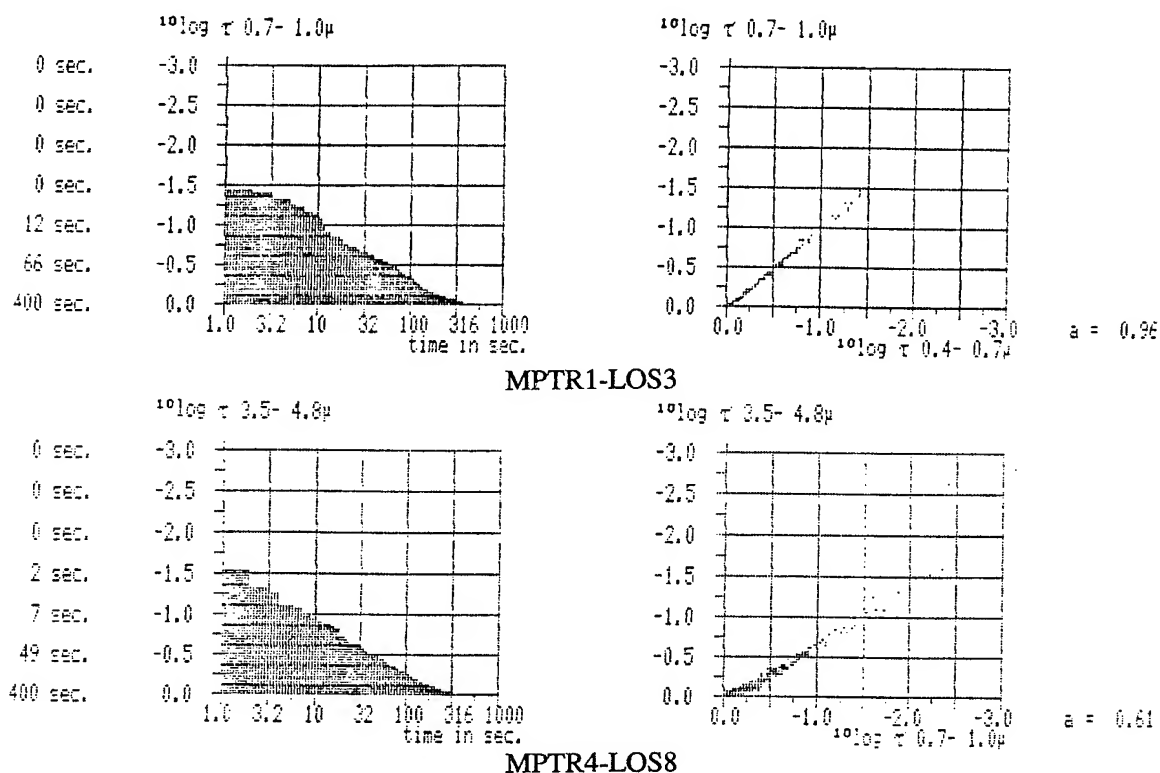


Figure 7. Histograms and optical depth plot for trial 2824 (see fig. 6).

LOS	0.7- 1.0 μ	1.0-1.4 μ	3.5- 4.8 μ	7.9-12.3 μ	0.4- 0.7 μ	2.0- 2.2
1	10.5sec.	8.0sec.	0.0sec.	36.1sec.	16.5sec.	14.0sec
2	2.6sec.	2.0sec.	0.0sec.	0.0sec.	7.5sec.	8.5sec
3	10.7sec.	10.5sec.	0.0sec.	38.0sec.	14.6sec.	23.9sec
4	13.9sec.	13.2sec.	20.2sec.	45.0sec.	17.2sec.	16.3sec
5	22.5sec.	23.1sec.	13.1sec.	47.8sec.	25.0sec.	0.0sec
6	56.1sec.	57.1sec.	53.6sec.	70.3sec.	59.2sec.	37.7sec
7	83.6sec.	83.7sec.	83.1sec.	99.4sec.	85.1sec.	66.2sec
8	79.6sec.	78.5sec.	48.6sec.	84.4sec.	81.8sec.	63.8sec
9	78.0sec.	78.3sec.	67.0sec.	86.7sec.	79.9sec.	64.0sec
10	73.3sec.	72.5sec.	66.8sec.	83.7sec.	75.3sec.	59.8sec
11	71.2sec.	72.6sec.	70.8sec.	80.8sec.	73.9sec.	59.8sec
12	70.9sec.	71.8sec.	33.6sec.	72.4sec.	74.0sec.	58.8sec

Figure 8. Transmission overview; absorption index, defined by the product: (1-transmission) * (time); trial 6862; MPTR4.

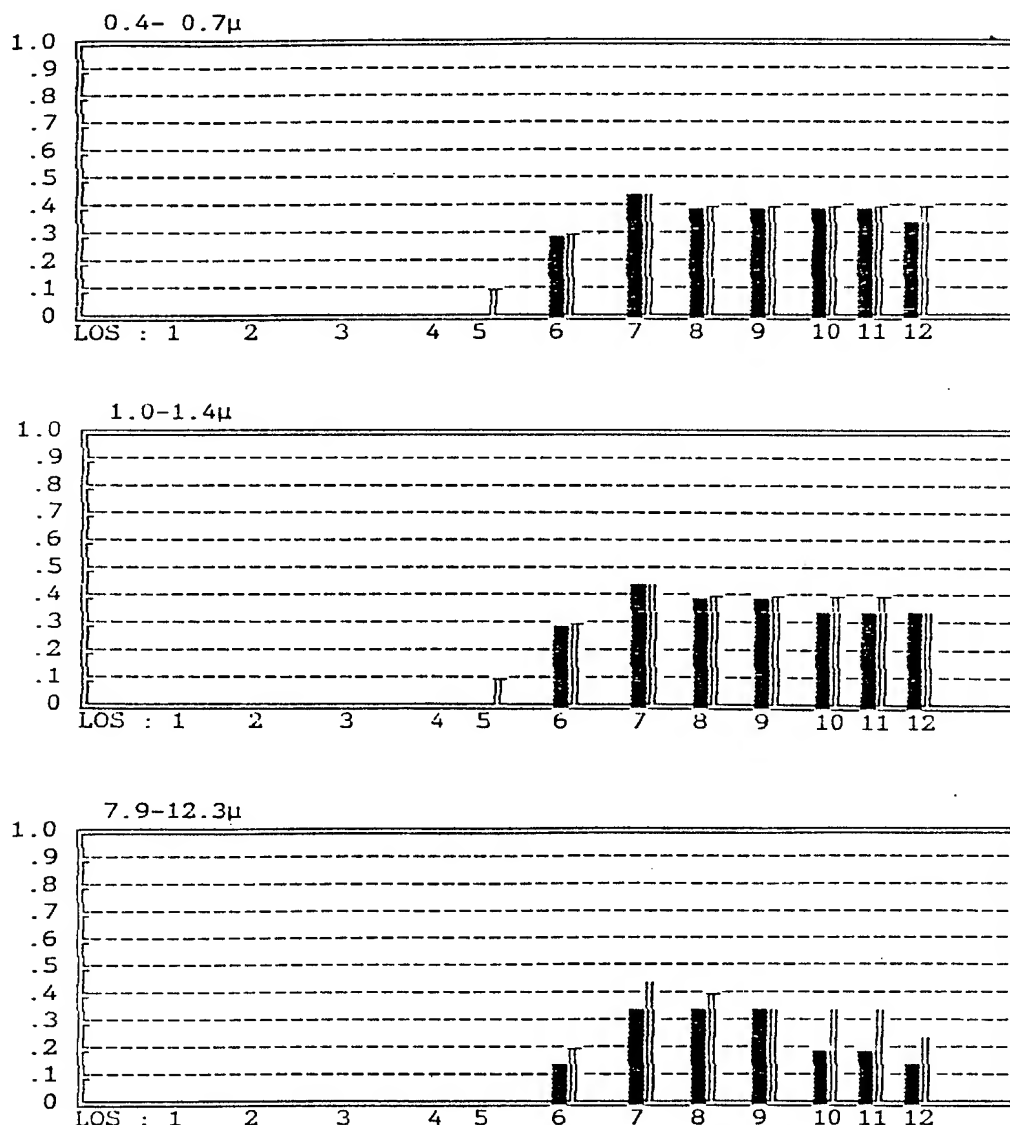


Figure 9. Absorption efficiency α for dust from explosion, trial 6862; MPTR4. α is defined by the ratio of time, the transmission is below 3% (■) or 10% (□), to the total trials time, here 163 sec.

4.3 Dust from attack formation

Typical for attack "formation dust" is that the formation travels from right to left in the field of view, first passing LOS12 and finally LOS1. As the vehicles crossed normal, vegetated terrain, the amount of dust produced was limited, furthermore caused by the "low" speed of the vehicles. Transmission values normally stayed above 30%. In fig. 10 the 0.7 - 1.0 μ m band transmission plots are given for LOS 12 and 1 for trial 3832. The dust gave less obscuration in the thermal bands. The attack formation passed in about 1 min.

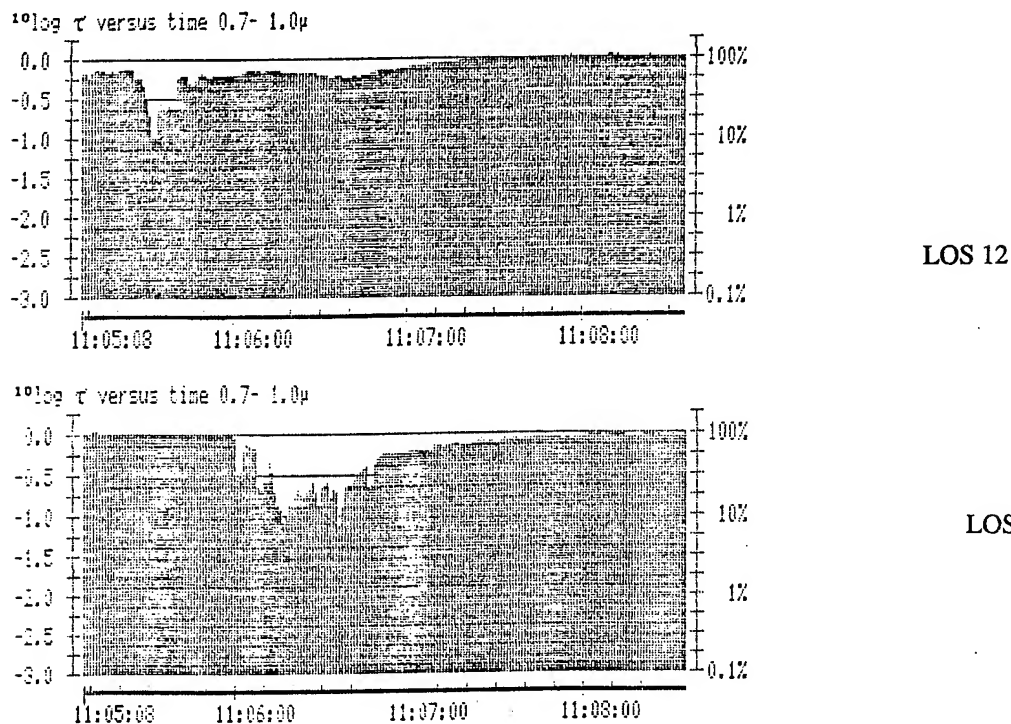


Figure 10. Dust from attack formations; trial 3832, transmission plots for LOS 12 and 1.

4.4 "Dust" from oil-fire-smoke

The oil-fire was built close to LOS7 but did not produce smoke during the whole 2 hours period of the trial. Most of the smoke was present during the first 15 minutes, only in front of LOS7. the other LOS's did not receive significant amounts of smoke. From the transmission plots a strong increase in absorption for the shorter wavebands was found as may be expected. The same conclusion can be drawn from the histograms and optical depth plots (trial 6863).

4.5 Dust from column of vehicles

Similar to the case of attack formations, dust transmission data for columns of vehicles are different for each session. The reasons for the variations are evident:

- different compositions of the columns,
- different distances between the vehicles; different tracks, different speeds,
- differences in compositions of ground material, height variations,
- differences in weather (wind, temperature, turbulence).

The dustclouds are generally of limited height. the transmittance values increase considerably with height.

Study of the transmission plots learns that different LOS penetrate the dust column in different directions, causing differnt plots. Comparison of transmission values in different spectral bands learns that the dust is a good multispectral screener, somewhat better in the bands below 3 μm. The first vehicles of a column may not produce a dust screen which is fully opaque, but the next vehicles built up the screen with transmission values sometimes around 1%.

5. DISCUSSION

The MPTR sensor has given appropriate data to learn about the propagation properties of dust from explosions and driving vehicles and of smoke from oil fires. It has to be investigated how this transmissometry relates with the obscuration effects for the imagers at the main instrumentation area. The dust is a multispectral screener. The dustcloud density depends upon the terrain- and vehicle features. the cloud duration generally is less than 1 minute. the cloud height is of the order of several meters and generally does not exceed 10 m, at least for the Mourmelon situation. Oil smoke screens only the visible. Explosion dust covers a larger area with extended height (up to 30 m) hanging for about 1 min and screening in all spectral bands.

ACKNOWLEDGEMENTS

The MPTR setup was realized by J.J. van der Ende, A. Offerman and P.J. Fritz during the setup week. The operation of the sensor was carried out by J.J. van der Ende. All participants are greatly acknowledged for their contributions.

REFERENCES

- RSG15; 1990, BEST-TWO TESTPLAN;*
Battlefield effects on long range (4 km) target acquisition; Camp Mourmelon (France), 23 July - 17 August 1990; NATO AC/243 (Panel 4/RSG.15), January 1990
- De Jong A.N. and M.J.J. Roos; 1987
Description of the MPTR system; Multi Path Transmission Radiometer; Report FEL-1987-14.
- De Jong A.N., M.J.J. Roos and P.J. Fritz; 1988
Smoke characterization by means of MPTR; Report IR 1988-07
- De Jong A.N.; 1990
Obscurant measurements during Best Two by means of MPTR; Report FEL-90-A290

**MULTISPECTRAL TRANSMISSION THROUGH DUST, (INFRARED)
SIGNATURES OF TARGET VEHICLES AND TARGET BOARDS**

by

**J. Rogge
Royal Military Academy**

No abstract was available at press time.

This paper is Confidential and restricted to Representatives of RSG.15 Member Nations Only.



MISL MEASUREMENTS AT THE NATO BEST TWO*

Wendell R. Watkins, Samuel B. Crow,
Daniel R. Billingsley, and Fernando R. Palacios
U.S. Army Atmospheric Sciences Laboratory
White Sands Missile Range, New Mexico 88002-5501, USA

Richard W. Dutro
New Mexico State University
Las Cruces, New Mexico 88003, USA

ABSTRACT

Modelers beware! There are important issues that must be considered in modeling of infrared systems--issues that are not being appropriately extrapolated for applications of today's more complex and sophisticated sensors to ever increasing ranges. What is measured vertically may not be directly applicable to horizontal paths. The Mobile Imaging Spectroscopy Laboratory (MISL) results from the NATO BEST TWO indicate that several areas need improvement in understanding the degradation of horizontal path imaging performance. The degradation of the atmosphere is not merely an absorption coefficient derived from LOWTRN calculations, nor can the spatial degradation due to propagation be considered as an atmospheric modulation transfer function (AMTF) of unity, especially for hot desert regions of current interest. The same is true for the nonuniformity of aerosol obscuration whose spatial degradation is not fully characterized by a single extinction coefficient. A large area thermal target board was designed for use with the MISL at BEST TWO and produced excellent characterization measurements of the AMTF as well as contrast transmission measurements that compared well with LOWTRN calculations. Additionally, the combined effects of solar loading and windspeed changes were found to produce tremendous changes in target contrast.

1. INTRODUCTION

With the ever increasing sophistication of today's weapon systems, characterization of the propagation environment has increased in its importance. This is especially true for the horizontal lines of sight (LOSs) near the ground (Watkins et al., 1989a). With increasing spatial resolution of second- and third-generation forward-looking infrared (FLIR) systems, target acquisition is being degraded by more than just an extinction coefficient as longer range

*Originally presented at the NATO 49th AGARD-EPP Remote Sensing Symposium held in Cesme, Turkey, October 1991, with the title, "Far-Infrared Characterization of Horizontal Path Image Degradation."

detection is sought. Optical turbulence has been shown to degrade infrared imagery as well (Miller et al., 1989). This distortion has been characterized as a complex point spread function or atmospheric modulation transfer function (AMTF) (Watkins and Jordan, 1991). In addition to the thermally induced degradation, there is also nonuniformity in extinction coefficients along the LOSs to the individual scene areas comprising the pixels of the target and background, which alters the AMTF and contrast transmission, as well as solar loading changes that also influence the contrast transmission (Crow et al., 1991).

The North Atlantic Treaty Organization (NATO) Battlefield Emissive Sources Trial under European Theater Weather and Obscurants (BEST TWO) was held at Camp Mourmelon, France, from 26 Jul-11 Aug 1990. The U.S. Army Atmospheric Sciences Laboratory (ASL) participated, in part, by fielding the Mobile Imaging Spectroscopy Laboratory (MISL) for characterizing the propagation environment, assessing the effectiveness of state-of-the-art camouflage, and determining the degradation of emissive sources and their associated smoke and dust clouds. This paper highlights the most significant findings of the MISL data acquisition and analyses from the BEST TWO.

2. BACKGROUND

For several years the ASL has been developing a unique research tool--the MISL (Watkins, Crow, and Kantrowitz, 1991). The MISL is comprised of a Fourier transform spectrometer (FTS) and an imaging component termed the target contrast characterizer (TCC). It is the use of the TCC that is stressed here. The TCC has two far-infrared 8- to 14- μ m imagers that are used to characterize the AMTF. The complex means to accomplish this is described in detail elsewhere (Watkins and Jordan, 1991); but, in essence, the target and background of interest are viewed with two optically matched imagers along a common LOS. One imager is placed at close range or in the near field (NF), and the other is placed at a distant location or in the far field (FF) and is equipped with a compensating telescope. The resulting images are registered pixel for pixel using an image processing system and remote control and data transfer via fiber optics. Paramount to the success of this alignment process is the use of single detector scanning imagers, even though their spatial resolution and sensitivity are less than most FLIRs. Also the development of a large area (1.78 by 1.78 m) blackbody with uniform surface temperature was essential. The unique design of tilting the oven surface of this blackbody back, coupled with an offset see-through front bar pattern for near perfect hot-to-cold bar transition, has made the measurement of the AMTF and contrast transmission with the TCC possible.

In theory, characterization of the AMTF is straightforward with the TCC (Watkins and Jordan, 1991). If the imagers have identical impulse functions, $h_i(x,y)$, and the degradation is a deterministic point spread function, $h_d(x,y)$, then the zero-range or "truth" image, $f(x,y)$, as observed by the close-up imager, is $f_{NF}(x,y) = f(x,y) * h_i(x,y)$, where $*$ denotes a two-dimensional spatial convolution. The image, $f(x,y)$, as observed by the distant imager, is $f_{FF}(x,y) = f(x,y) * h_i(x,y) * h_d(x,y)$. The AMTF (the Fourier or Laplace transform of the degradation point spread function) is simply the ratio of the Fourier (or Laplace) transforms of the long- and short-range images.

$$AMTF = H_d(x, y) = \frac{F_{FF}(x, y)}{F_{NF}(x, y)} = \frac{F(x, y) \cdot H_i(x, y) \cdot H_d(x, y)}{F(x, y) \cdot H_i(x, y)} \quad (1)$$

In practice, however, several difficulties arise. The imagers are not identical and each has an associated noise process that must be characterized. Each imager exhibits a different line-to-line scan anomaly, and the imagers are neither line-to-line nor frame synchronized. Finally, the AMTF is not a deterministic point spread function but, rather, a complicated nonstationary random process.

Spatial degradation along horizontal paths is only one issue that must be considered in assessing imaging system performance. Another is the loss in contrast due to propagation and weather related conditions. Many assessments of FLIR system performance are based on an absorption coefficient derived from LOWTRN or, better yet, an extinction coefficient that includes scattering losses. But the quantity that is really needed for assessment is contrast transmittance, $\tau_c(R)$, which is the ratio of the distant range, R , to inherent range (zero) contrasts or $C(R)/C(0)$. Again detailed derivations are given elsewhere (Watkins et al., 1989b) that allow a simplified expression for $\tau_c(R)$.

$$\tau_c(R) = \frac{C(R)}{C(0)} = \frac{1}{1 + \frac{\int_{\nu_1}^{\nu_2} L_p(R, \nu) F(\nu) d\nu}{\int_{\nu_1}^{\nu_2} L_b(0, \nu) F(\nu) \tau(R, \nu) d\nu}} \quad (2)$$

where ν is the spectral frequency; $F(\nu)$ is the system response function that spans frequencies ν_1 to ν_2 ; $L_p(R, \nu)$ is the path spectral radiance over the distance, R ; $L_b(0, \nu)$ is the background spectral radiance at zero range; and $\tau(R, \nu)$ is the spectral atmospheric transmission over the distance, R . Note that optimization of $\tau_c(R)$ for humid conditions requires proper selection of the system response function, F . The TCC imagers have cold finger optimizing filters based on FTS measurements (Kantrowitz et al., 1990).

Now, for the condition where the path spectral radiance does not have an appreciable component from external sources such as cold sky or solar reflections or pyrotechnic smokes (not in general a good battlefield environment assumption), the expression for contrast transmission reduces to

$$\tau_c(R) \cong \frac{1}{1 - \frac{1 - \bar{\tau}(R)}{\bar{\tau}(R)}} = \bar{\tau}(R) \quad (3)$$

where $\bar{\tau}(R)$ is the system weighted atmospheric transmission given by

$$\bar{\tau}(R) = \frac{\int_{\nu_1}^{\nu_2} \tau(R, \nu) F(\nu) d\nu}{\int_{\nu_1}^{\nu_2} F(\nu) d\nu} \quad (4)$$

The TCC is ideally suited to measure directly contrast transmission because the NF imagery can be used to obtain an excellent approximation of the zero-range contrast $C(0)$, and the FF imagery the distant contrast $C(R)$. The computational

procedures for arriving at the value of τ_c from measured target and background apparent temperatures described elsewhere (Watkins et al., 1989b) can be approximated within a couple percent for target and background temperatures near 300 K by simply taking the ratio of the FF and NF difference temperatures, ΔT_s , or

$$\tau_c(R) \cong \frac{T_t(FF) - T_b(FF)}{T_t(NF) - T_b(NF)} . \quad (5)$$

Measurements of $\tau_c(R)$ using the TCC can be compared with LOWTRAN 7 (Kneizys et al., 1988) calculations by using eqs. (4) and (5); however, to avoid the problems experienced previously (Watkins et al., 1989b) some spatial resolution issues must be addressed. To overcome these problems the large area blackbody was used without any front bar pattern to produce a resolvable uniform hot surface for NF to FF comparisons.

The issue of image resolution brings up an interesting question of how best to describe image degradation. If the NF and FF images are compared pixel by pixel to obtain values of contrast transmission, the values obtained will vary greatly because of the spatial resolution differences. The optical turbulence degradation, AMTF, will increase these differences. The issue of how best to use TCC comparison of NF to FF images for overall image degradation quantification is being investigated. One metric, the "complexity measure," is currently being used (Carlson et al., 1988). The complexity measure is a quantity from 0 (disjoint distributions) to 1 (indistinguishable distributions) based on the overlap of the distributions of gray scale values in equal pixel areas of target and background.

3. MEASUREMENT AND ANALYSES

The MISL was set up at the BEST TWO site to the west of the main search sector to avoid interference. A target area was situated at a range of 1,637 m from the MISL instrumentation van as shown in fig. 1. The scene shows a large area blackbody target board that was used for characterization of the atmospheric degradation of scene content between the NF and FF TCC imagery. To the left of the target board was an exposed tank that, at times, was covered with natural vegetation for signature suppression. To the left of the exposed tank was an identical tank with state-of-the-art camouflage netting over it. The TCC measurements at the BEST TWO include contrast transmission, the AMTF, the degradation of simulated artillery explosions, and solar loading changes of camouflage netting.

The analysis of the TCC measurements of atmospheric degradation at the BEST TWO will begin with the conceptually simpler contrast transmission instead of the AMTF. The TCC 8- to 14- μ m imagers were positioned at NF = 96 m and FF = 1,637 m from the large area (1.78 by 1.78 m) target board and a large evergreen tree for the background. The FF was matched to the NF with a 17X lens whose transmission properties were determined by initially positioning it at the NF location and comparing target and background temperatures measured by the NF and FF imagers. To obtain the apparent target and background temperatures for the contrast transmission value, the average target temperature was calculated for a square region in the center of the target board with 1/4 the length and height of the target board as in fig. 2a. A comparable square region in the

background was used to obtain the average background temperature. This was done for both the NF (fig. 2a) and FF (fig. 2b), and the resulting $\tau_c = 0.80$ was obtained using eq. (5). The meteorological parameters used in LOWTRAN 7 calculations at this time were temperature of 21 °C, pressure of 1006 mbar, relative humidity of 53 percent, typical minor constituent concentrations, and rural aerosols with 20 km visibility. The resulting LOWTRAN 7 calculations for the path difference between the NF and FF resulted in a $\tau_c = 0.82$, which considering the uncertainty in the LOS aerosol extinction is quite good compared to previous measurements with a small area target board (Watkins et al., 1989b).



Figure 1. Visible picture of the target area used for the MISL measurements at BEST TWO showing the large area blackbody target board.

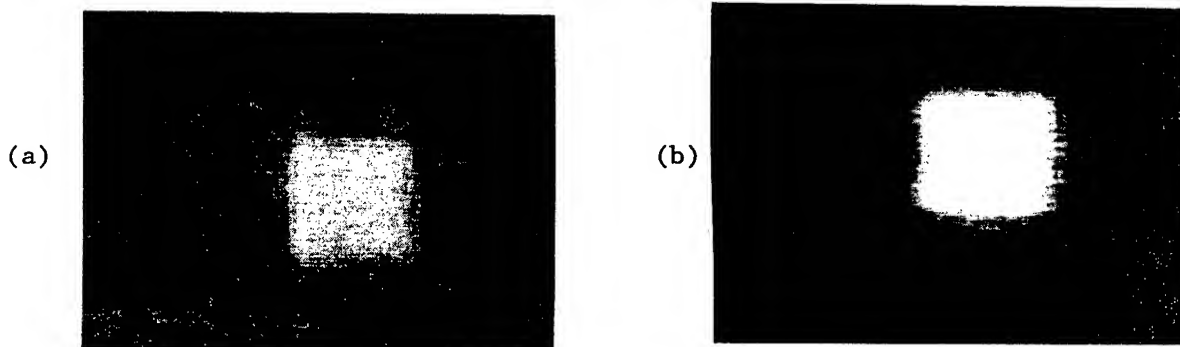


Figure 2. (a) Close-up or NF (96 m range) 8- to 14- μ m image with 65 by 87 mrad field of view showing the exposed 1.78 by 1.78 m blackbody (right) and evergreen tree background (left) on a 50 °C full-scale setting. (b) Distant or FF (1,637 m range) 8- to 14- μ m image with 4 by 5 mrad field of view showing the exposed 1.78 by 1.78 m blackbody (right) and evergreen tree background (left) using a 20 °C full-scale setting.

Now, the question is what happens when the bar pattern target board required to measure the AMTF is used as in figs. 3a and 3b. The same square averaging region cannot be used. If a vertical strip is taken as the new averaging region to obtain average temperature for the hot and cold bar centers as well as the background, a couple of options are possible. The target to background contrast temperatures can be between hot and cold bars or hot bar and cold vegetative background. The resulting values for τ_c are for bar to bar $_{BB}\tau_c = 0.13$ and for hot bar to vegetation $_{BV}\tau_c = 0.65$. The discrepancies between the τ_c values obtained with these contrast sources and the exposed whole target board to uniform background are related to spatial resolution and the AMTF.

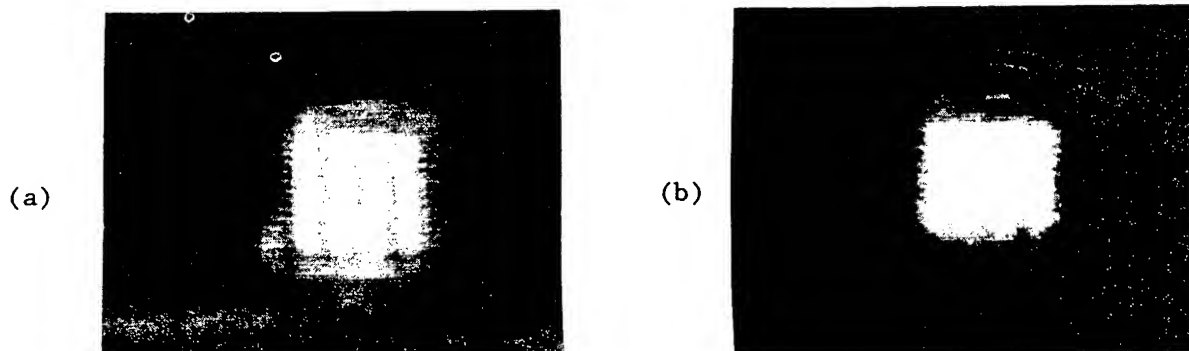


Figure 3. (a) Same NF scene as fig. 2a except the target board has the 3.5-cycle bar pattern in place using a 20 °C full-scale setting. (b) Same FF scene as fig. 2b except the target board has the 3.5-cycle bar pattern in place using a 10 °C full-scale setting.

The manufacturer specified instantaneous field of view (IFOV) for the single detector scanning imager is 2 mrad for the 1X lens that is positioned 96 m from the target board, with 25 cm separation between the vertical bars. Figure 3a shows the resulting infrared image with a 4X electronic blowup and an implied 19 by 19 cm IFOV; the imager slit response function (SRF) should be around 0.7. This was verified by measuring the uniform blackbody surface with the bar pattern removed to show that only 40 percent of the inherent bar pattern ΔT was detected in good agreement with an SRF of 0.7. When the recorder MTF was considered, the resulting area in the image (which was averaged to obtain a single scene pixel value) was 21 pixels high and 26 pixels wide, the bars being 15.5 pixels wide. The results in the FF using a 17X lens at 1,637 m were essentially the same under quiescent atmospheric conditions. During most of the day, optical turbulence was present (fig. 3b), resulting in marked distortion of the target board bar pattern. This spatial distortion produces significant errors in the contrast transmission values derived from the narrow hot bars of the target board that are not present when the central portion of the whole 1.78 by 1.78 m blackbody source is used. The large errors in the bar pattern measured τ_c values would be less if an FLIR with better resolution were used, but they would not disappear. To see this better the magnitude of the optical turbulence distortions must be quantified as an AMTF.

Again all the details of deriving the AMTF from images such as figs. 4a and 4b using eq. (1) are given elsewhere (Watkins and Jordan, 1991) and will only be summarized here. To begin an approach utilizing one-dimensional discrete Fourier transforms (DFTs) of horizontal scans through the target board pattern instead of two dimensional fast Fourier transforms was used because the noise reduction and field-to-field phase correction algorithms needed for the latter process are still under development for the recently acquired database presented here. Line scans horizontally through the center of the target board bars in figs. 4a and 4b are shown in fig. 5 for 256 by 256 pixel portions of the scenes. With a 15.5-pixel spacing between bars or a 31-pixel cycle the DFT of these line scans will have a peak at index 8 associated with the 3.5-cycle bar target. This is shown in fig. 6 where the whole target board has a significant peak at index 1 and harmonics at indices 3 and 5. The energy content of indices 12 and above are basically noise, because these frequencies cannot be resolved with the imager. Note that there is about a 70 percent loss

of energy content for the index 8 between the NF and FF because of optical turbulence. This translates into a significant loss in the resolving capability of 0.1 mrad features that the bars represent at 1.6 km over a horizontal path when the temperature is only 25 °C. This measure of AMTF was consistent over frames spaced 10 s apart in fig. 7, and the average of these three images yields an AMTF whose shape, based on the high-energy indices 1, 3, 5, and 8, shows a consistent falloff and represents an average or slow AMTF in fig. 8. The bottom line is that the increased spatial resolution of today's FLIRs is going to be degraded by optical turbulence over horizontal paths near the ground in warm climates such as those of current interest.

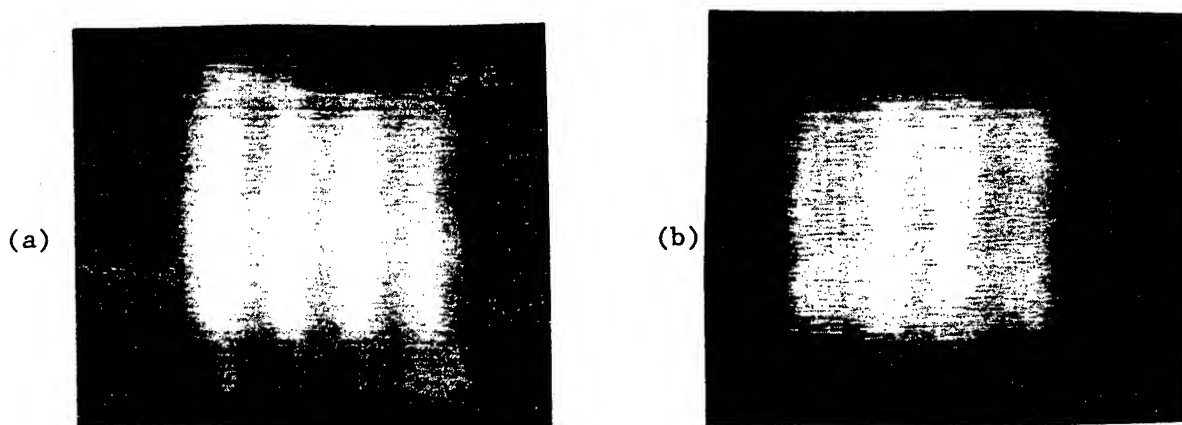


Figure 4. (a) Near-field blowup image of the target board with bar pattern in the afternoon with 25 °C ambient temperature. (b) Far-field blowup image of the target board with bar pattern in the afternoon with 25 °C ambient temperature showing optical turbulent distortion of the bars.

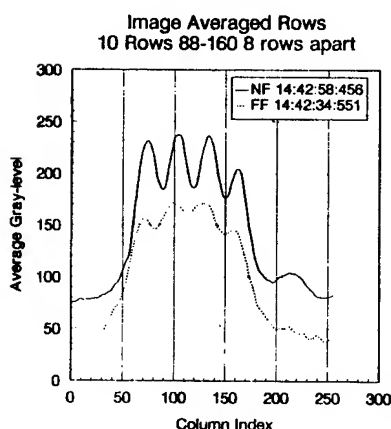


Figure 5. Average gray scale plots of 10 horizontal line scans through NF and FF scenes illustrated in figs. 4a and 4b.

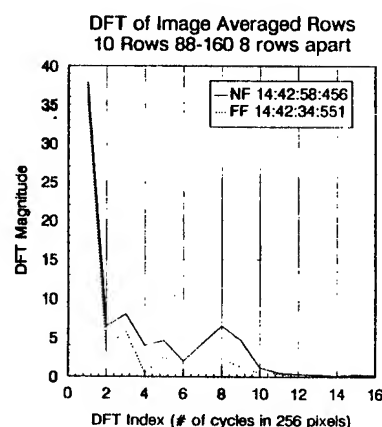


Figure 6. DFTs of plots shown in fig. 5 with the peak at index 8 corresponding to the bar pattern spacing frequency.

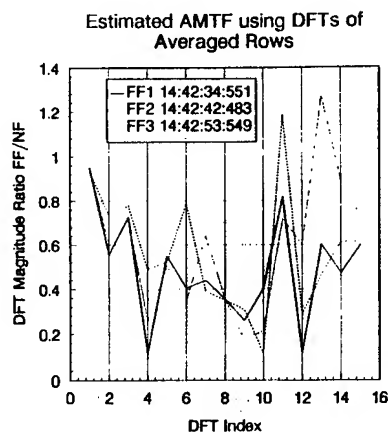


Figure 7. Set of three ratios of FF/NF DFTs like fig. 6 yielding estimates of the AMTF for image pairs spaced approximately 10 s apart.

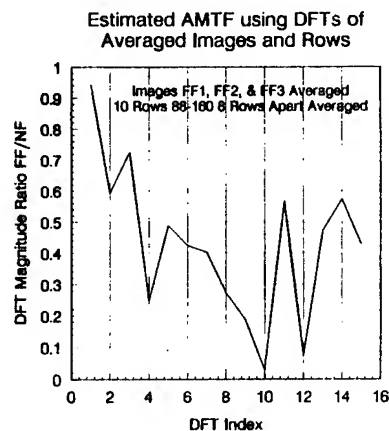


Figure 8. Smoothed estimate of the AMTF using the average images from fig. 7 showing a 70 percent drop in energy content for the bar pattern frequency at index 8.

The issue of dust cloud obscuration will now be addressed. Often the attenuation produced by large clouds of vehicular dust is uniform. By observing a vehicular dust cloud that passed between the NF and FF during a time of minimal optical turbulence distortion, the effect of the obscurant attenuation was observed as a dust modulation transfer function (MTF) of essentially unity. Unfortunately, battlefield obscurants are not uniform and can have significant emissive or reflective components that can influence the overall AMTF by adding clutter to the target scenes. Another measure of changes in target contrast is the "complexity measure" (Carlson et al., 1988), which essentially is the overlap of equal area target and background intensity distributions. Like the AMTF the complexity measure is essentially independent of attenuation or gain change. When the complexity measure was applied to TCC imagery of an exposed tank against a vegetative background at midday, the low NF and FF complexity measure values are shown in fig. 9. Three separate simulated artillery smoke events occurred during this 7.5 min time interval. During the heavy dust event the attenuation was so severe that the target scene became blank; and, hence, the target and background areas were identical or had a complexity measure of 1.0. During the other two events the dust cloud attenuation was not uniform and was mixed with hot explosion by-products. The result was that the complexity measure, which like the AMTF is insensitive to uniform attenuation, increased significantly because of the nonuniform attenuation and path radiance characteristics of simulated battlefield conditions. Finally, even though the baselines of the NF and FF complexity measures track each other quite well, they are not constant. In fact, the NF complexity changes from 0.2 to 0.1 in less than 7 min due to solar loading changes.

The dramatic influence that solar loading changes have on target contrast is not fully appreciated when remote sensing is applied to characterizing the vertical structure for extrapolation to the ground level propagation environment. What goes on under the clouds is remarkable. As it turns out the windspeed is the driving parameter to contrast changes of camouflage netting

and vegetative backgrounds. For 2 days with nearly the same relative humidity, temperature, and variability of solar loading, a change of from 2 to 3 m/s windspeed to 5 to 6 m/s windspeed can have tremendous impact on target contrast. During the higher wind conditions, the camouflage net has a high complexity value or blends well with the background over an 8-min time interval (fig. 10). The exposed tank complexity starts out near 0.2 for sunny conditions and then drops sharply to 0.05 when the target area is shaded. During the low windspeed conditions a remarkable change occurs. The camouflage net cannot follow the cooling cycle of the vegetative background as illustrated in fig. 11. Only during shady conditions does the camouflage blend into the background (high complexity). When the sun comes out, the low thermal mass camouflage net actually becomes easier to see than the exposed vehicle (lower complexity). In fact, the camouflage net almost flickers as the solar loading changes. What a difference windspeed can make!

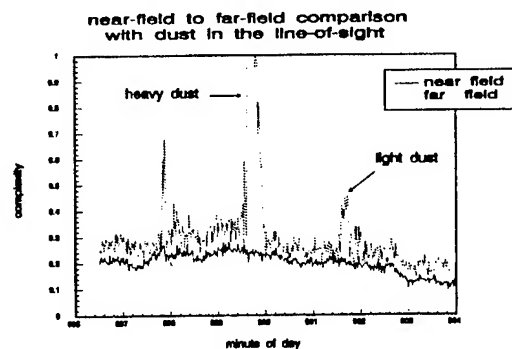


Figure 9. NF versus FF tank-to-background complexity for dust clouds in the line of sight.

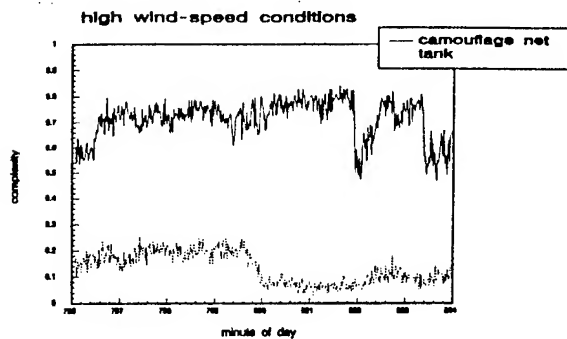


Figure 10. Complexity during high windspeed conditions for a target of high thermal mass (tank) compared to a target of low thermal mass (camouflage net).

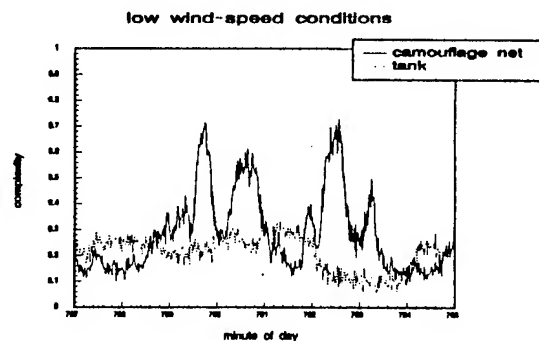


Figure 11. Complexity during low windspeed conditions for a target of high thermal mass (tank) compared to a target of low thermal mass (camouflage net).

4. SUMMARY

We hope that this material will prove useful to researchers tasked with modeling of far-infrared imaging system performance for horizontal path applications. Because of the increased spatial resolution for longer range

applications, FLIRs are now susceptible to degradation from optical turbulence. The magnitude of this AMTF degradation is not easily estimated from remotely sensed vertical profiles nor is the nonuniformity of aerosol obscuration that can include cold sky reflection as well as emissive path radiant clutter. Besides the spatial distortions that must be included in system performance modeling, target contrast reduction due to natural attenuation cannot be fully characterized with a single absorption coefficient. The more accurate measure of the degradation due to atmospheric propagation, the contrast transmission, which includes path radiance contributions and inherent contrast changes, can be correlated to LOWTRN calculations; but extreme care is important for this measurement comparison. Of interest are target metrics that are least sensitive to the propagation environment. One metric, the complexity measure, was used to illustrate uniform attenuation insensitivity, but solar loading changes coupled with low levels of windspeed can cause dramatic fluctuations in this metric. Research continues for better methods of longer range target detection, and proper characterization of cloud cover induced contrast changes may be useful in these pursuits.

ACKNOWLEDGMENTS

The author would like to thank Jay Jordan of New Mexico State University for data reduction and figures and Young Yee of the U.S. Army Atmospheric Sciences Laboratory for assistance in collecting of the AMTF and contrast transmission related imagery data.

REFERENCES

- Carlson, J. J., J. B. Jordan, and G. M. Flachs, 1988: Task Specific Complexity Metrics for Electronic Vision. In SPIE Conference Proceedings, 901, Los Angeles, CA.
- Crow, S. B., W. R. Watkins, F. R. Palacios, and D. R. Billingsley, 1991: Technique for Measuring Atmospheric Effects on Image Metrics. In SPIE Conference Proceedings, 1486, Orlando, FL.
- Kantrowitz, F. T., W. R. Watkins, D. R. Billingsley, and F. R. Palacios, 1990: Characterization and Optimization of Infrared Imager Detector Response for Long Path Research. In SPIE Conference Proceedings, 1311, Orlando, FL.
- Kneizys, F. X., E. P. Shettle, L. W. Abreu, G. P. Anderson, J. H. Chetwynd, W. O. Gallery, J. E. A. Selby, and S. A. Clough, 1988: Users Guide to LOWTRAN 7. AFGL-TR-88-0177, Air Force Geophysics Laboratory, Hanscom AFB, MA. (NTIS; AD A206773).
- Miller, W. B., J. C. Ricklin, and D. H. Marlin, 1989: Effect of Atmospheric Turbulence on Electro-Optical Systems. AGARD-CP-454, pp. 45-1, 45-10.
- Watkins, W. R., F. T. Kantrowitz, and S. B. Crow, 1989b: Transmission Measurements with the Target Contrast Characterizer. In SPIE Conference Proceedings, 1115, Orlando, FL.
- Watkins, W. R., F. T. Kantrowitz, and S. B. Crow, 1989a: (Nato Restricted) Dynamic Changes in Images and Scenes Due to Environmental Factors (U). AGARD-CP-454 (Sup), pp. 44-1, 44-12.
- Watkins, W. R., and J. B. Jordan, 1991: Characterization of Turbulence Effects on Infrared Imagery. ICO Topical Meeting Proceedings on Atmospheric, Volume, and Surface Scattering and Propagation, Florence, Italy.
- Watkins, W. R., S. B. Crow, and F. T. Kantrowitz, 1991: Characterizing Atmospheric Effects on Target Contrast. Optical Engineering, 30(10):1563-1575.

Operational efficiency of different lasers
through battlefield effects*

BEST II - july / august 90
FRANCE

Author : Alain Le Dortz
Organism : DGA/DAT/SEPT

Introduction

Using laser as rangefinders is nowadays strongly widespread in different armies in the world.

Choosing the good wavelength still remains difficult as regards of diversity of environmental conditions fit for battlefield : visibility, dust, humidity...

If free propagation of a laser wavelength in the atmosphere is quite good understood, it's quite different in operational conditions (Dust, explosions, fire..).

So, it becomes important to have a better knowledge of this behaviour, in order to determine, if it's feasible, the optimum wavelength for rangefinding in all conditions.

Methods and means

During the BEST II experiment, the mains lasers used have been the following:

- a rangefinder emitting at 1.06µm
- a rangefinder emitting at 1.54µm
- a rangefinder emitting at 10.6µm
- data processing for real time acquisition of signals
- several referenced targets

In order to separate the effects due to battlefield events from atmospheric conditions, the trigger action of rangefinders were precisely synchronised. Every measure was made at the same time and in the same place.

Results

The results that have been obtained allow a classification between the different tested wavelengths.

It appears that 10.6µm is always better than 1.06µm and 1.54µm.

Results between 1.06µm and 1.54µm clearly point out a better behaviour of 1.54µm.

All these results have been obtained in atmospheric conditions that are not representative of the global transmission during a year. To assess the real advantages of a wavelength, you have to introduce the mean value of atmospheric transmission at the same wavelength.

This paper is Confidential and restricted to Representatives of RSG.15 Member Nations Only.

RELIABILITY OF OBSERVER RESPONSES USING INVENTORY THERMAL
IMAGERS

by

J. Rogge
Royal Military Academy
Breda, the Netherlands

LCol D.M. Vonhof
Infantry School
Harderwijk, the Netherlands

In order to eliminate an enemy target, it is first of all necessary to acquire this target. Since the selection of the weapon system to be employed can also depend on the target type, the reliability of the first acquisition of the target plays an important role. The percentage of correct first-given acquisition responses depends on the quality of the thermal imager, the atmospheric conditions (including battlefield effects), the time of the day, the target type, behaviour and distance etc. During the BEST TWO experiments the detailed oral acquisition responses of military observers (using several inventory thermal imagers) have been registered in a number of single target vehicle scenarios. These acquisition responses are currently being analysed. It is expected that some relations can be found between the reliability of the acquisition responses and the distance to the target vehicles under different conditions. Results of the study will be presented; some military implications will be indicated.

This paper is Confidential and restricted to Representatives of RSG.15 Member Nations Only.

CCD-CAMERA MEASUREMENTS DURING BEST TWO

by

J. A. Boden and R. J. L. Lerou

No abstract was available at press time.

This paper is restricted to Representatives of RSG.15 Member Nations Only. For further

A SIMPLE TRANSMISSION MODEL OF INFRARED LASER BEAM IN LOW TROPOSPHERE : TRANSMIR

Philippe BATAILLE

Laboratoire Radiocommunication
Département Antennes
UNIVERSITÉ DE RENNES I
Campus de Beaulieu
35042 RENNES
FRANCE

The lasers applications are various and their use has been generalized to systems such as :

- point to point atmospheric optical communications
- detection
- designation
- telemetry

As all optical systems, these materials are very sensitive to the medium in which the radiation is propagating.

After a succinct description of physical mechanisms, a simplified propagation model for few optical laser lines in the low troposphere is presented. This model do not include artificial perturbations such as smoke and dust (clear atmosphere).

It is important during the conception, the valuation and the use of optical systems to be able to know with precision the propagation loss along the path between the transmitter and the receiver. The knowledge of the laser transmission in free space through the atmospheric channel is fundamental to supply these systems the appropriate specifications.

A simple model, TRANSMIR, calculating the transmission for few infrared laser lines in clear atmosphere has been developped. It is based on the fact that the total transmission, at a given wavelength, can be decomposed into its elementary components : the molecular and aerosolar transmissions.

The molecular contribution is calculated by using the model with high spectral resolution FASCODE2 ("line by line" calculation), which contains the large spectroscopic database, HITRAN. This code takes account of molecular line and continuum absorption due to water vapor and carbon dioxide for example.

The transmission through aerosols is deduced from the low resolution model LOWTRAN6. Several size distributions of aerosols are included in this model to describe three types of particles according to the environment: maritime, urban and rural.

Numerous results from FASCODE2 and LOWTRAN6 codes have been synthesized by simple polynomial expressions, providing attenuation coefficients as a function of meteorological parameters (humidity, temperature and visibility) for an horizontal path and few infrared wavelengths. The polynomial coefficients are determined by a linear regression on the multiple results of attenuation. The range of variability of the meteorological parameters are fixed at the beginning of the procedure. So, polynomial expressions are available only in this range.

A comparison between our model and FASCODE2 shows that the relative precision is about 0.1 % for the molecular case and about 5 % for the aerosolar case. Results of calcul obtained from TRANSMIR model are in good agreement with LZTRAN model . A good accordance exists between predictions and measurements for several infrared optical wavelengths.

The full text of this paper is limited to RSG.15 Representatives of Member Nations Only.

BEST TWO

THE INFLUENCE OF CUES ON THE OBSERVER PERFORMANCE

**Hogens Caspersen
Danish Defense Research Establishment
DK-2100 Copenhagen, Denmark**

ABSTRACT

Scenarios 1 and 2 are typical target acquisition scenarios. Scenario 1 was acquisition in a static scenario, for example, as defined in the TARGAC models. Scenario 2 was acquisition when the target was moving in the presence of battle effects. Both scenarios deal with the head on engagement of the target.

The variety of targets in the trial was limited. This paper discusses the acquisition of the targets based on the cues in the targets. The cues are discovered based on discussions with the observers. The paper shows the performances of the observers and relates the performances to the cues. This paper briefly discusses which of the tasks, recognition or identification, are best modelled by the TARGAC model for the specific targets.

The full text of this paper is limited to **Representatives of NATO and RSG.15 Member Nations Only.**

**MEASUREMENTS DURING BEST TWO WITH A
CO₂ LASER SYSTEM**

by

R. J. L. Lerou

The full text of this paper is limited to **RSG.15 Representatives of Member Nations Only.**

**British Aerospace Acoustic Experiments
During the BEST 2 Field Trial 1990.**

A.R. Tooth.
British Aerospace PLC.,
Sowerby Research Centre,
Filton,
Bristol. UK.

Abstract.

Two experimental acoustic / seismic sensing systems were jointly taken for evaluation and data collection to the BEST 2 Trial (Camp Mourmelon 1990) by the Sowerby Research Centre, the research organisation for British Aerospace and British Aerospace Electronic Systems and Equipment Division. The first system was for the collection of vehicle and background signature data and consisted of a triangular microphone array, a signature microphone at the centre of the array, and a geophone. The other system was a combined acoustic / seismic and IR detector which detects the presence of a potential target and locates its current position.

The signatures from the vehicles that were taking part in the trial and background signatures were recorded on analogue tape and later digitised. It was anticipated that the collected signatures would be processed such that after the evaluation of the experimental equipment they could be collated to form a data base which could be used in the analysis of future equipment. For many reasons not connected with the trial or the quality of the data that was collected at BEST 2 the task of analysis has not been completed, although it is hoped that in the future the data base of signatures will be completed.

This paper describes the the rationale behind our attendance at the trial, our experimental design and the 'lessons' that were learnt.

1. Introduction.

When developing any new equipment the transitional phase between research equipment and production is often hindered by the lack of suitable evaluation data. The collecting of suitable field trial data is a time consuming processes and often only results in a limited sample of pertinent data being collected.

The BEST 2 trial (Camp Mourmelon 1990) presented itself as a unique opportunity to gather, at a single trial, a sufficiently wide range of ground truth and vehicle signature data such that a data base of typical battlefield signatures could be developed for the evaluation of existing and future systems. The trial was also an opportunity to evaluate an experimental acoustic / seismic / IR sensor system.

2. Acoustic / Seismic Experimental Site Location.

The majority of the equipment that was taken by the various nations to the BEST 2 trial was operating in the infrared region of the electro magnetic spectrum and consequently relied on a direct line of sight between the equipment, such as a thermal imager etc, and the target vehicles. Extraneous signatures in other spectrums, acoustic and seismic, from

ancillary equipment such as generators were not of undue concern. However the equipment that we were taking to the trial was by its very nature susceptible to these unmonitored signatures and would confound any results.

Ideally we wanted our equipment to be sited where extraneous vibrations were minimal but close enough to the trial vehicles for realistic signatures to be collected. A suitable site was located in a circular clearing alongside the 'return' road that was used by trial vehicles when they had finished the main trial run and were returning to the IR signature measurement area. This road was also used by the trial vehicles during their 'warm up' phase prior to their calibration. The location and schematic of the acoustic site clearing is shown in Figures 1 & 2.

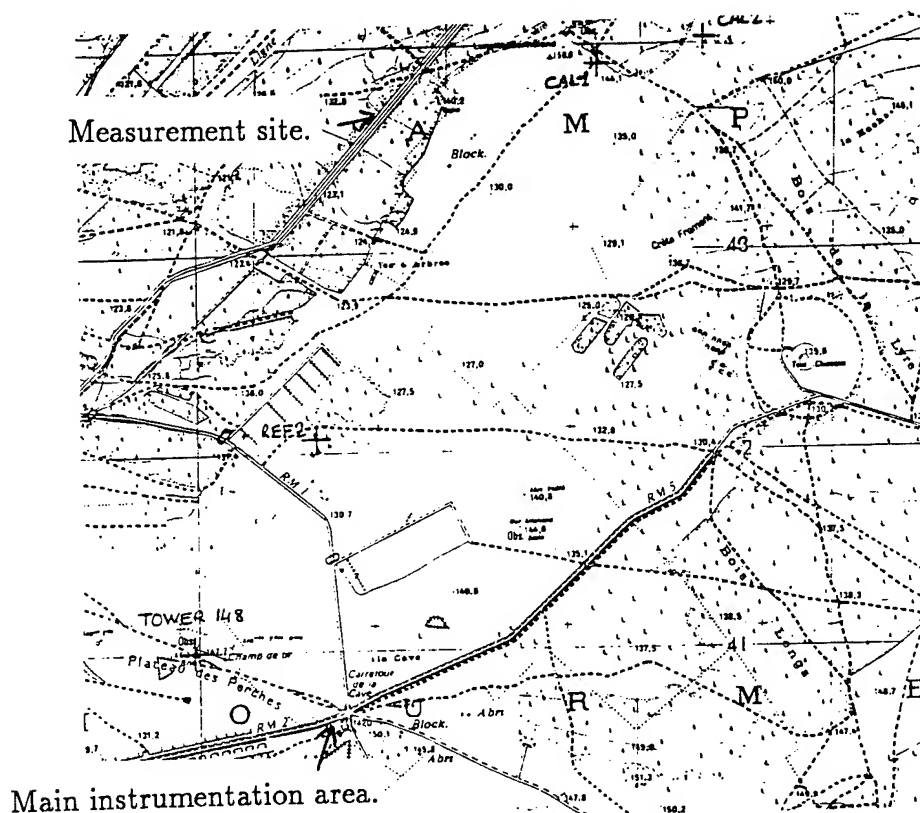


Fig. 1. Map of Trial Site.

The circular clearing was of a nominal radius of 200m. and was surrounded by trees. The return road, with separate tracks for wheeled and tracked vehicles, divided the clearing into two parts. The experiments were sited in two locations, 50m. and 100m from the road, and from these positions a clear line of site was available in both directions along the road. The generator which was required to provide electricity for the equipment was sited 100m. from the experiments and was successfully shielded by straw bales and the trees at the edge of the clearing in order to minimise vibrations. Although the site was ideal for many reasons it lacked facilities such as detailed target range and micro meteorological information for the clearing. Target range data therefore had to be measured locally and assessments were made of the meteorological conditions.

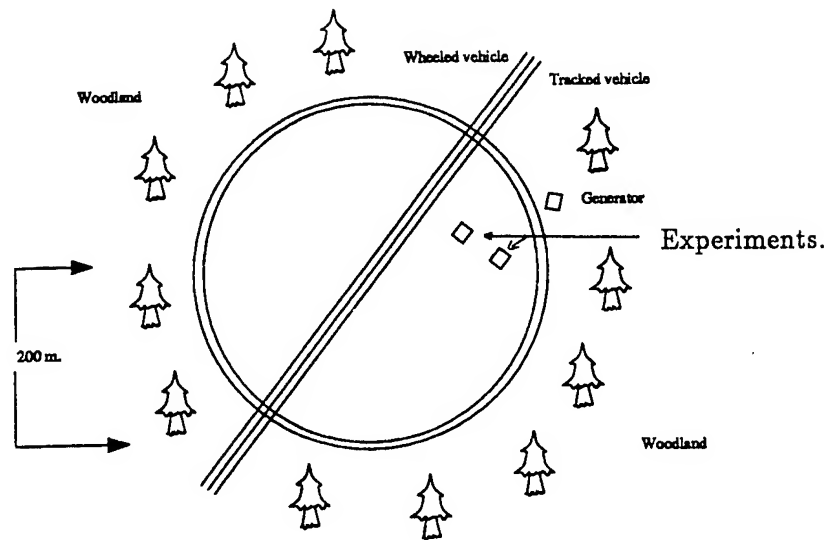


Fig. 2. Schematic of Experimental Area.

2.1 Target Range Measurements.

A set of marker posts were accurately positioned along the side of the road. The first post was directly opposite the experimental equipment, other posts were positioned, in both directions, at 50, 100, and 200m. intervals. This technique enabled crude estimates of target range to be found. Although the lack of accuracy was not desirable the range markers were only used to enable 'spikes' to be put on the audio channel of the data recordings, i.e. when the vehicle entered the clearing the recording equipment was manually switched on and when, visually, a vehicle passed each range marker a button was pressed that put the spike on to the data channel. Apart from the lack of accuracy of the range measurement due to parallax the major problems with the ranging system was the inability to see the marker posts, during the night time scenarios, through the dust clouds that were generated by the vehicles and the problem of vehicles running over the posts.

2.2 Meteorology.

Due to the lack of meteorological equipment in the clearing we had to rely on meteorological records, in the analysis phase, from the main trial site. Knowledge of wind speed and direction are considered to be important factors for the propagation of acoustic signatures and these parameters could easily be influenced by the microclimate of the clearing. Estimates of local wind direction, and to a lesser extent wind speed, were made using 'ribbons' tied to each range post. These estimates were correlated with the results from the main trial site. The wind as observed in the clearing tended to 'swirl' without any specific direction but fortunately the wind speeds during the trial were low so problems with the lack of specific meteorological data were minimal.

2.3 Benefits.

The main benefits from the use of the clearing for our experimental site were as follows:

- Recordings of the natural environment were able to be recorded without any contaminating vibrations from other trial participants.
- Recordings of vehicles other than those taking part in the trial were able to be collected i.e. signatures of vehicles, cars and trucks etc, visiting the vehicle calibration area.
- The speed and formation of vehicles in the main trial's area was strictly maintained but on the return road, where our experimental site was located the rules for speed and formation were not applied. This gave rise to signatures of vehicles at multiple speeds and in random groupings.

Despite the fact that our experimental site was remote from the main trials area we were successfully able to make vibrational recordings of the trial battlefield effects and were able to record signatures of the aircraft that were taking part in the trial. Although there were disadvantages in using our location these were secondary to the many advantages.

3. Experimental Equipment.

3.1 Experiment 1.

Experiment 1 consisted of a triangular microphone array, a signature microphone at the centre of the array, and a geophone which was on the ground under the central signature microphone. In order to minimise any unwanted resonances which could be picked up by the microphones they were all mounted on anti vibration pads. The geophone was mounted on an aluminium spike that had been 'driven' approximately 10 cms. into the surface of ground. The prime purpose of taking this experiment to the trial was to simultaneously collect acoustic and seismic vehicle signatures and where possible record ambient background signatures. As the trial site had a chalk substratum excellent seismic propagation was anticipated.

Signals from all sensors were recorded on analogue tape and these were later digitised at a sampling rate of 2kHz. The arms of the microphone array were adjustable such that two different microphone separations could be evaluated. The microphone separations were 100 and 30 cm. The 100 cm. separation was considered to be 'acceptable' for the recording of phase differences whilst the 30 cm separation was considered to be acceptable for the design of practical systems. It was hoped that the results from the two different microphone separations could be compared so that we could assess what the implications were when changing from one to another.

The central microphone was recording integrated power signature, i.e. the time averaged amplitude. The three array microphones were used to record amplitude information but phase difference information could also be gathered and from this the direction of the vehicle could be inferred. The geophone was used to directly record seismic vibrations.

3.2 Microphone Specification.

The pass band specifications for the three array microphones were identical, 100Hz. - 1kHz. and for the central signature microphone the pass band specification was 10Hz. - 1kHz. All the microphones had a dynamic range of 40dbs and had a uniform frequency response across the band. Although the microphones were not exactly matched their responses were within 5 percent in amplitude and 1 percent in phase. A weighted spring type geophone was bonded to the top of the aluminium ground spike to monitor the seismic signatures, it had a pass band of 15Hz. - 100Hz.

3.1 Experiment 2.

The second experiment, essentially a sensor fusion experiment, that was taken to BEST 2 was designed to evaluate a sensing system that was currently being developed within the laboratory. The experimental system was of a twofold nature combining both acoustic / seismic and infra red sensor technology. The operation of the system was such that the acoustic presence of the target vehicle switched on the IR sensors and alerted the system.

The IR sensor contains separate, far infrared, detectors each having a narrow field of view. When a target is detected by the first detector the signal processing begins i.e. the timing starts, and when the target is detected by the next detector the timing stops. Using knowledge of the detector field of view and the predefined range to target the velocity and position of the vehicle can be calculated. When the position of the vehicle has been calculated a 'triggering pulse' is generated and during our experiment was used to electronically trigger a camera which took a photograph of the passing vehicle. From the photography we were able to assess the accuracy of the sensing system using marker posts which had been accurately positioned directly opposite the experimental site. The photographs also showed approximate wind direction as monitored by the ribbons on the range markers.

4. Data Recording.

All the outputs from the triangular microphone array were recorded on multi-channel analogue tape and were later digitised at a rate of 2kHz. Prior to recording the outputs from the four microphones and geophone all signals were pass band filtered, using a Butterworth filter. The data recorded from the acoustic / seismic / IR system were directly stored digitally on floppy discs.

4.1 Data Collected.

During the course of the trial the following data was recorded:

- Acoustic signatures from the three array microphones and the central signature microphone.
- Seismic signatures from the geophone.
- Photographic records from the sensor system
- Timing pulses from the manual range observations.

All of the trial scenarios were monitored where it was possible. In addition many vehicles other than those which took part in the trial were also monitored as they passed by our measurement site. Signatures from aircraft that were used to take measurements during the trial were also recorded. Several night trials had to be aborted for safety reasons.

5. Data Analysis.

The first task that had to be performed for data analysis was the digitisation of the analogue field data tapes. Although the task of digitisation was quite straightforward using an in-house software package the number and length of the recordings gave rise to massive amounts of data which presented a significant data storage problem. Typically each of the digitised recordings occupied 4 mbytes and several records were in excess of 8mbytes. The digitised data was analysed on a Compac 286 using a package called DADiSP (Data Acquisition Digital Signal Program). This package enabled a statistical analysis of the data to be performed and plots of signature as a function of time to be generated. Although this should also have been another straightforward task the size of each of the data arrays was such that the performance of the package was impaired. Whilst the limited storage of the package could be overcome by analysing the data in sections the process was very time consuming. Figures 3 - 6 show typical analysed results from the trial.

5.1 Results.

All the figures show scaled acoustic amplitude signatures as a function of time, at the present time seismic signatures have not been analysed. Figure 3 shows the signature of three explosions, each separated by a one minute time delay, with a background signal from a light aircraft.

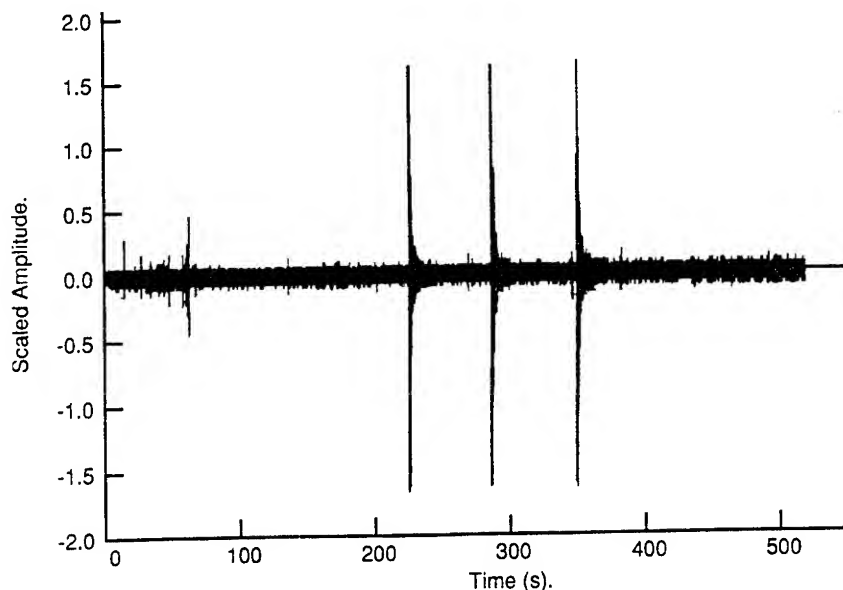


Fig. 3. Signature of Explosions and Light Aircraft Background.

Figure 4 shows the signature of a large battle tank. It is interesting to see that the vehicle is quieter in approach than in retreat. The tank signature has two basic components; the tracks, and from the engine. As the engine is in the rear of the vehicle the engine noise is shielded by the vehicle in approach but no shielding is present in retreat.

If the tank signature, Figure 4, is compared with that of Figure 5, signature from a personnel carrier, we can see that the front engined vehicle has a stronger signature in approach than when in retreat. The magnitude of the signature is also, not unexpectedly, smaller than that of the tank.

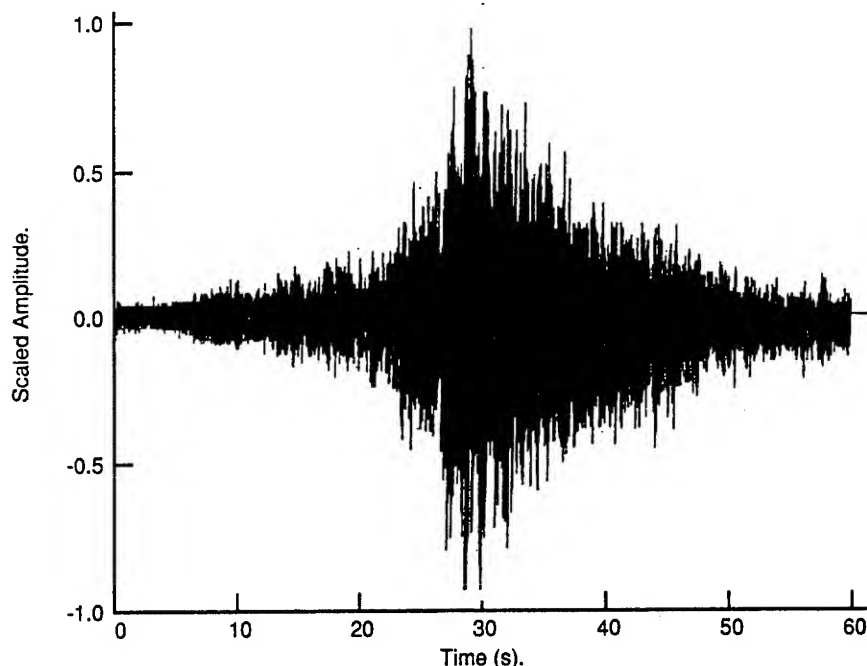


Fig. 4. Signature of Tank.

Figure 6 represents the signature from two aircraft. The aircraft were flying on parallel tracks one aircraft slightly behind the other. When they were overhead one of them turned and became obscured by the woodland at the edge of the clearing, it is thought that this manoeuvre is the cause of the slightly different signatures between the aircraft. The small signature after the main body of the two aircraft signatures is considered to be the reflected signal from the woodland at the edges of the clearing.

The acoustic / seismic / IR sensor system worked better than anticipated. Although the three signals were monitored for later analysis the final indication that the system is viable and the sensor fusion algorithms are working correctly is demonstrated by the fact that the fused signals are used to generate an electronic pulse which automatically triggers a camera. If the camera is triggered at the correct time then the signature source will be photographed. If the camera is triggered at the wrong time then the photograph will be empty.

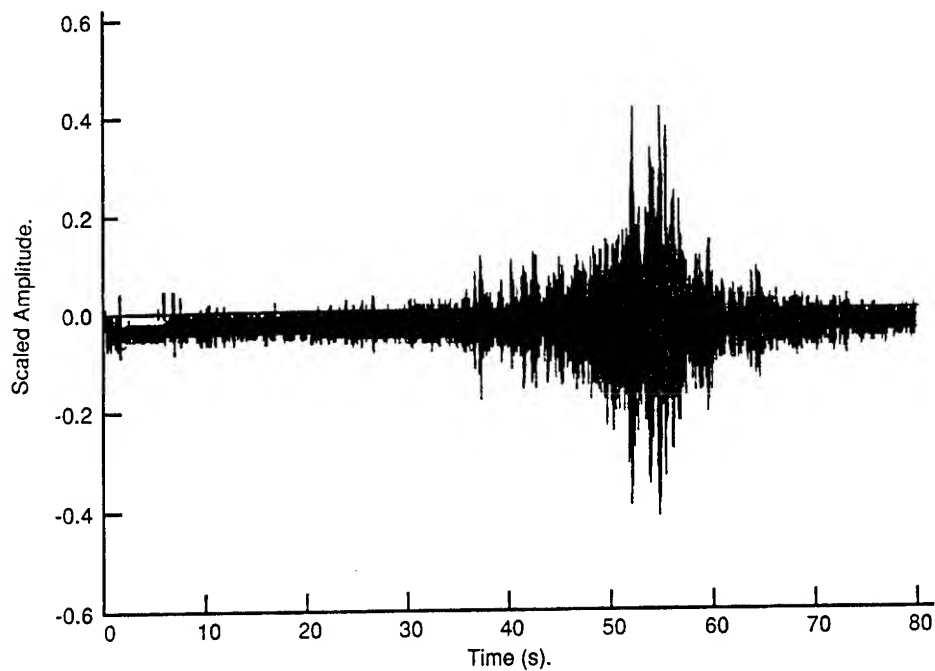


Fig. 5. Signature of Personnel Carrier.

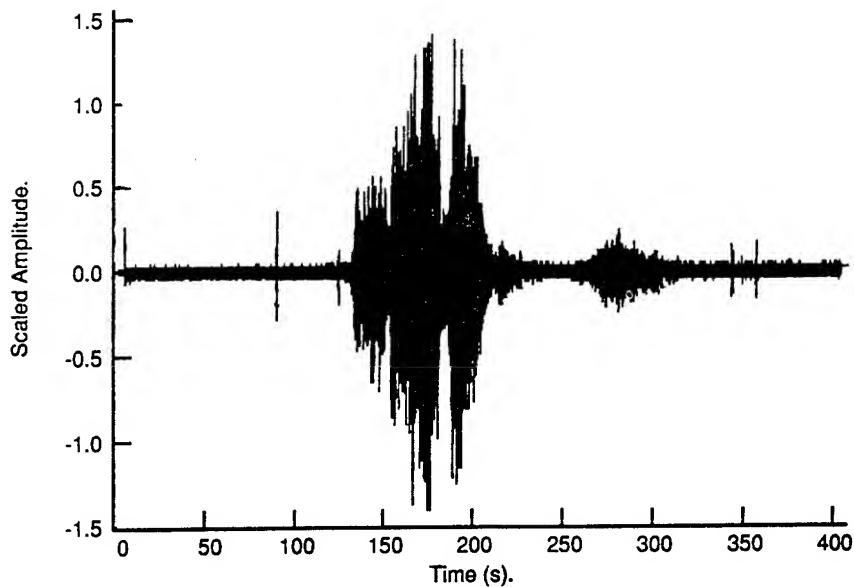


Fig. 6. Signature of Two Jet Aircraft.

The photographic records that were automatically taken, by the multi-sensor, of the predicted vehicle position contained on greater than 95% of the time a signature source, i.e. the predicted vehicle position was the true vehicle position. On many occasions when convoys of vehicle were passing large clouds of dust and exhaust gases were created. Although vehicles could not be visually detected through these clouds the IR system was still able to detect and then subsequently locate the source of the signature.

6. Lessons Learnt.

The majority of the problems that were encountered during the course of the trial were overcome without undue difficulty. The anticipated problems such as those from excessive heating of the equipment and the ingress of dirt and dust from the surrounding terrain were solved by the use of shielding and dust proof containers. All the equipment worked without fail during the trial period. The lack of local micro meteorological data for the clearing was not critical due to low wind speeds, however future trials should have this facility.

In retrospect data was recorded over too great a time range and when the analogue data was digitised for analysis an excessive amount of data resulted causing many computer manipulation problems. This problem was the only real one that occurred that was not anticipated prior to the start of the trial.

7. Future Work.

Due to other commitments insufficient time has been spent on the analysis of the recorded data. However it is anticipated that time will be made available in the not to distant future to enable further analysis, such as Fourier transforms, length of series, integrations and regressions etc, to be made using the DADiSP package. The collected data will also be collated into a unique and valuable data base for the analysis of future systems.

OBSERVER PERFORMANCE EXPERIMENTS WITH BEST TWO THERMAL IMAGES

J.M. Valeton and P. Bijl

TNO Institute for Perception
PO Box 23 3769 ZG Soesterberg The Netherlands

Tapes recorded from the Philips UA9092 Thermal Imager during the BEST TWO trials contain of large number of events, an event being a stationary or moving target at a certain distance. Short video sequences (e.g. 30 - 120 frames) of all scenario 1 and 2 events were transferred from video tape to an analogue video disc system. The advantage of using a video disc is that the events can be presented to observers in random order at fast pace, and that the dynamic character of the imagery is retained, even for stationary targets. Computer controlled experiments are carried out with four observers in parallel. Tandy model 100 notebook computers are used as 'intelligent' response boxes. Observers indicate which target they think they see, along with a confidence score on scale of 1-5. The notebook display is used to pass messages to the observers and to give feedback during training. The experimental setup, organization of the image database and the method of analysis will be described.

BEST TWO imagery was recorded under a wide variety of conditions (e.g. approach route, time of day). A first experiment was carried out to determine whether there are differences in observer performance between conditions. Next, observer scores over all comparable conditions are combined to yield accurate recognition and identification probabilities and distances.

This paper is Confidential and restricted to Representatives of RSG.15 Member Nations Only.

Session I

ELECTROMAGNETIC AND ACOUSTIC TRANSMISSION POSTERS AND DEMONSTRATIONS

**Chairperson
Mr. Bob Rubio**

DIFFERENCES IN THE LOWTRAN-7 AND XSCALE CALCULATIONS OF INFRARED AEROSOL EXTINCTION

James Williams, Robert Fiegel, and Alan Wetmore
U.S. Army Atmospheric Sciences Laboratory
White Sands Missile Range, NM 88002-5501, USA

ABSTRACT

We have examined the different methods used by natural aerosol extinction (XSCALE) and LOWTRAN-7 for calculating infrared extinction as a function of relative humidity. Both models use tabulated (function of relative humidity) values of extinction coefficients relative to $0.55\ \mu\text{m}$ and interpolate between them. The set of relative humidities used by XSCALE is a proper superset of the values used by LOWTRAN-7.

Because of the nonlinear nature of the extinction versus relative humidity dependence and different interpolation algorithms, there are significant differences in calculated extinction coefficients. For rural aerosols, $10.6\ \mu\text{m}$ wavelength, and 95 percent relative humidity the LOWTRAN-7 value is 27 percent higher than the XSCALE value.

Several proposals for modifying the aerosol extinction calculations in LOWTRAN have been made. These proposals improve the accuracy of infrared extinction with a minimal change to LOWTRAN.

1. INTRODUCTION

Both the LOWTRAN-7 [Kneizys *et al.*, 1989] and XSCALE [Duncan *et al.*, 1987] computer codes trace their handling of aerosol extinction to the work of Shettle and Fenn [1979] in the 1970's. Also, both computer codes have evolved over the years [Duncan, 1981; Duncan *et al.*, 1982; Richardson *et al.*, 1984; Selby *et al.*, 1978; Kneizys *et al.*, 1980; Kneizys *et al.*, 1983], XSCALE growing more detailed in its treatment of aerosols and LOWTRAN simplifying some aspects of aerosol effects. Early versions of XSCALE did not follow directly from the physical description of the chemical and geometric properties of natural aerosols. Rather, several "representative" models were used. The later versions of XSCALE followed directly from the physical description of the optical properties (as a function of aerosol type, wavelength, and humidity) described by Shettle and Fenn. XSCALE interpolates between the eight values of the relative humidity used by Shettle and Fenn: 0, 50, 70, 80, 90, 95, 98, and 99 percent.

The interpolation scheme in recent versions of LOWTRAN [Kneizys *et al.*, 1980; Kneizys *et al.*, 1983; Kneizys *et al.*, 1989] uses only four values of the relative humidity: 0, 70, 80, and 99

percent. Both LOWTRAN-7 and XSCALE use the same wavelengths to tabulate the aerosol extinction properties. Figures 1 and 2 show the extinction calculated by LOWTRAN-7 and XSCALE for rural aerosols in the infrared band.

It is the choice of relative humidities used in the interpolation scheme of LOWTRAN-7 that we suspect should be reevaluated for infrared wavelengths. Errors of more than 25 percent have been found in the infrared extinction coefficients calculated by this model for rural aerosols. These errors are illustrated in figs. 3 and 4.

2. EXTINCTION COEFFICIENTS 8-12 μm

Extinction coefficients (per kilometer) were determined for LOWTRAN-7 and XSCALE using the current EOSAEL versions of both models. The focus of the investigation was the 8- to 12.5- μm wavelength band for rural aerosols because this combination results in the greatest differences in the infrared aerosol extinction.

Both models were run under the following conditions: rural aerosols (constant visibility of 5 km), 1 km altitude, and a horizontal path with range of 3 km. Default parameters were used in both models for the temperature, pressure, and concentration of atmospheric gases. The rural aerosol represents continental-type atmospheric conditions in areas not affected by industrial aerosols; this aerosol is composed of 70 percent water soluble substances and 30 percent dust-like aerosols.

Computer runs for both models were made at 0.1- μm increments between 8.0 and 12.5 μm for each of the eight relative humidity values of Shettle and Fenn {0, 50, 70, 80, 90, 95, 98, 99}. XSCALE automatically produced extinction coefficients at 1 km. LOWTRAN-7 was run in transmittance mode and the results were converted to extinction at 1 km. Coefficients for both LOWTRAN-7 and XSCALE have been normalized to the extinction at 0.55 μm . An examination of figs. 1 through 4 shows that a substantial difference in extinction exists between the models at approximately 95 percent relative humidity. Figure 5 depicts the contribution of aerosols to total transmittance for LOWTRAN-7 as a function of infrared wavelength and relative humidity. From this it may be generally observed that at humidities in excess of 90 percent rural aerosols play a significant role in total transmittance in the infrared.

3. CALCULATING AND INTERPOLATING EXTINCTION

Shettle and Fenn [1979] tabulate the extinction, absorption, and scattering coefficients at 40 wavelengths and 8 relative humidities for rural, maritime, and urban air masses. Figure 6 shows the Shettle and Fenn calculations of extinction for three infrared wavelengths with respect to humidity. XSCALE contains a table of extinction and absorption coefficients normalized to the 0.55 μm extinction at the first 31 wavelengths (those above 12.5 μm were dropped) and the same 8 humidities as Shettle and Fenn. XSCALE determines the extinction at any wavelength and humidity by interpolation. First the bounding wavelengths and humidities are determined. Then a linear interpolation on the wavelength is performed to find the extinction at the wavelength of interest and the two bounding humidities. The last step is a logarithmic interpolation to the humidity of interest. At the tabulated values XSCALE reproduces the Shettle-Fenn tables if the appropriate visibility is input to XSCALE (that is, $3.912/E(0.55 \mu\text{m})$ where E is the Shettle-Fenn extinction). LOWTRAN-7 employs only four humidities {0, 70, 80, 99} for interpolation end points; the four relative humidities 50, 90, 95,

and 98 percent are not used. As a result, where the Shettle and Fenn model and XSCALE show a dip near 95 percent, LOWTRAN-7 interpolates across the structure. The dip is filled in and the extinction is overestimated as indicated in fig. 7.

Shettle and Fenn point out that a functional relationship between humidity and visibility is not possible for the free atmosphere. For a closed system they suggest the expression:

$$\frac{V(f_1)}{V(f_2)} \approx \left(\frac{1-f_1}{1-f_2} \right)^\nu, \quad (1)$$

where V is the meteorological range, f_i is the fractional relative humidity, and ν is model dependent.

LOWTRAN-7 uses a form of eq. (1) to interpolate between relative humidity end point values. First the equation is rewritten for extinction as a function of humidity:

$$E = \frac{k}{3.912} (1-f)^{-\nu}, \quad (2)$$

where k is a constant of proportionality. The natural logarithm is taken of both sides to obtain

$$\ln(E) = \ln\left(\frac{k}{3.912}\right) - \nu \ln(1-f). \quad (3)$$

The ν is the slope of a log-log plot of E vs $1-f$. The leading term on the right-hand side is just the intercept which can be reset to one of the bounding points. LOWTRAN-7 performs an interpolation by finding this slope through the two bounding end points and then scaling to the humidity of interest:

$$E(f) = \ln(E_1) + \frac{\ln(E_2) - \ln(E_1)}{\ln(1-f_2) - \ln(1-f_1)} [\ln(1-f) - \ln(1-f_1)] \quad (4)$$

Figure 7 shows two proposed solutions to improve the accuracy. Both involve a better choice of humidity values for the interpolation boundaries. One set of relative humidity values is {0, 70, 95, 99}, another possible set is {0, 80, 95, 99}. Both of these re-create the original valley reported by Shettle and Fenn. The use of the extinction coefficient for 95 percent relative humidity is the essential point in the accurate interpolation for these infrared wavelengths.

4. CONCLUSIONS

The interpolation scheme used in LOWTRAN-7 could be improved by including an alternative relative humidity (95 percent) for use in the interpolation. This would be a minor change to the program and require no additional storage. A more accurate LOWTRAN could be created almost as easily by using the complete set of relative humidity values 0, 50, 70, 80, 90, 95, 98, 99 in the interpolation scheme. This would be consistent with the physical models discussed by Shettle and Fenn and used in XSCALE.

ACKNOWLEDGMENT

This study was suggested by Dr. Louis Duncan who had been concerned about the LOWTRAN interpolation for many years.

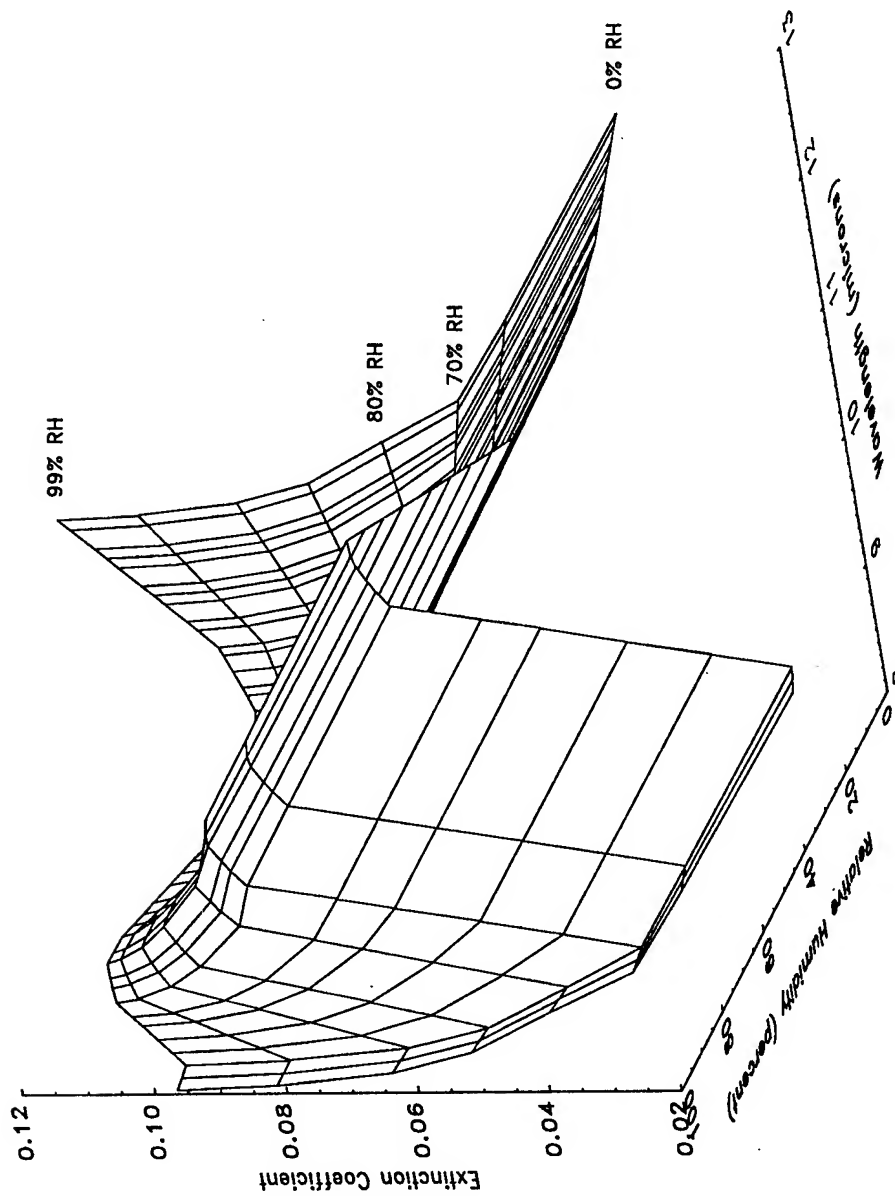


Figure 1. Extinction as a function of Humidity and Wavelength for LOWTRAN-7

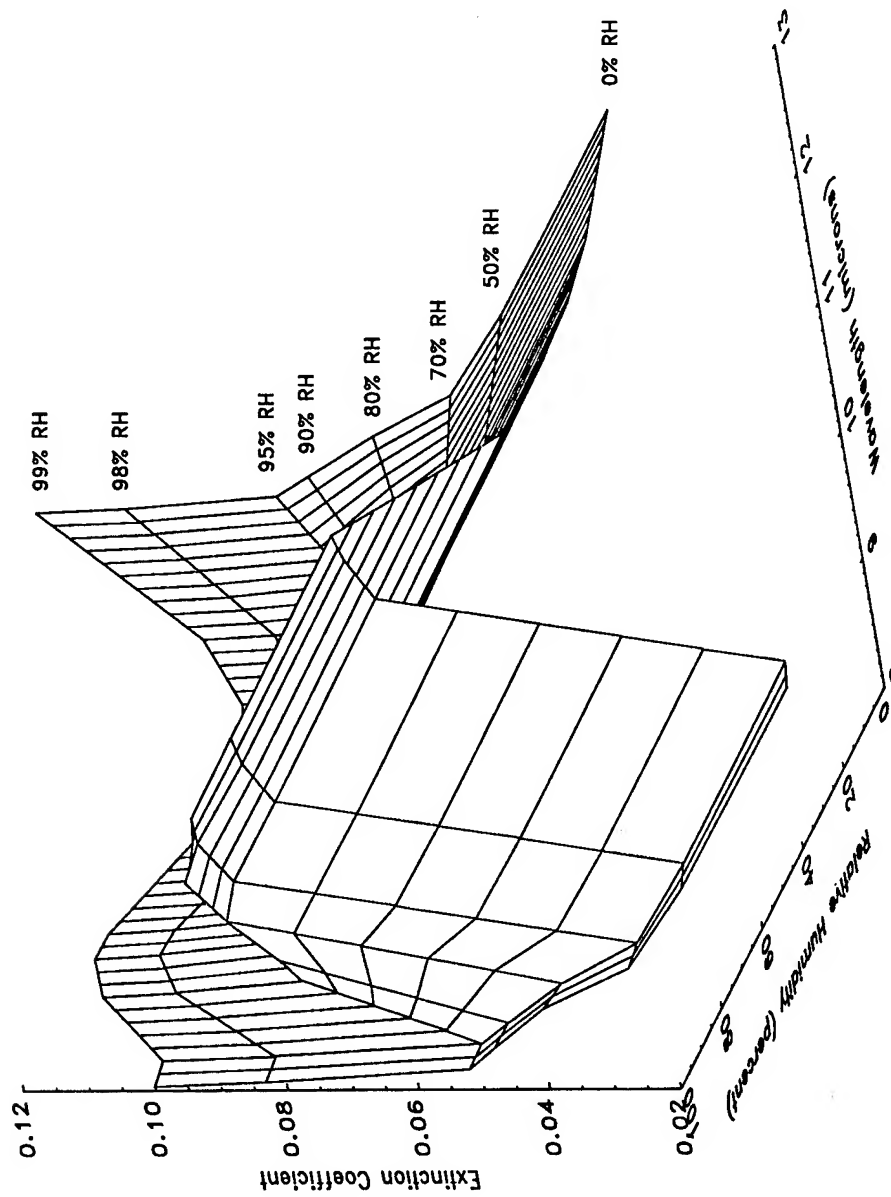


Figure 2. Extinction as a function of Humidity and Wavelength for XSCALE

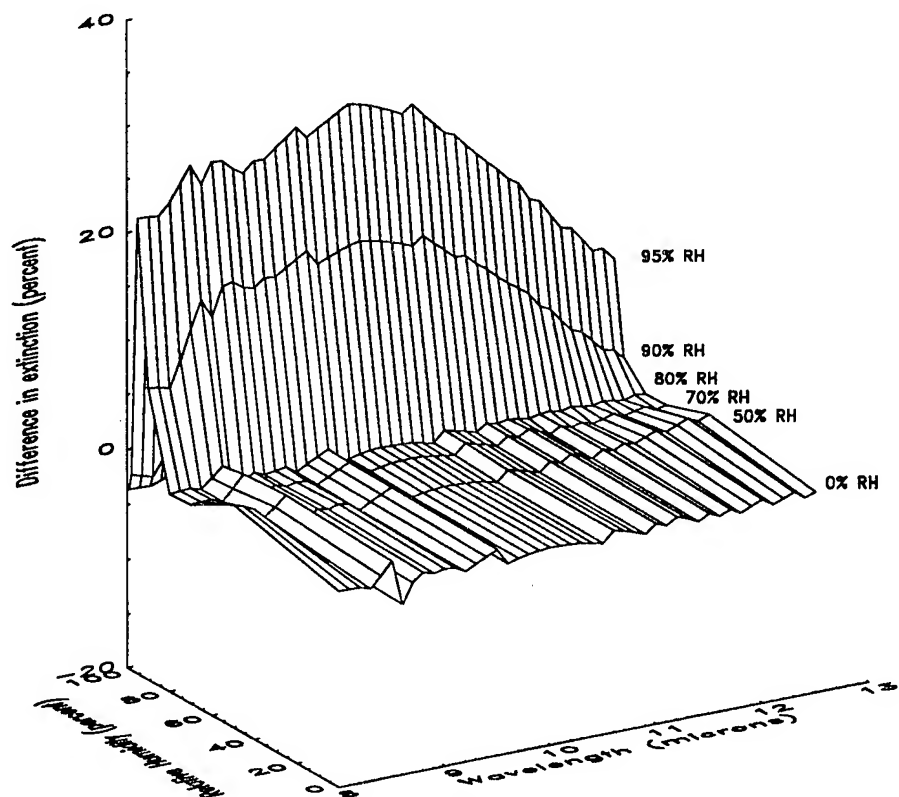


Figure 3. Surface plot of percent differences in extinction of LOWTRAN-7 and XSCALE as a function of Humidity and Wavelength (relative to XSCALE)

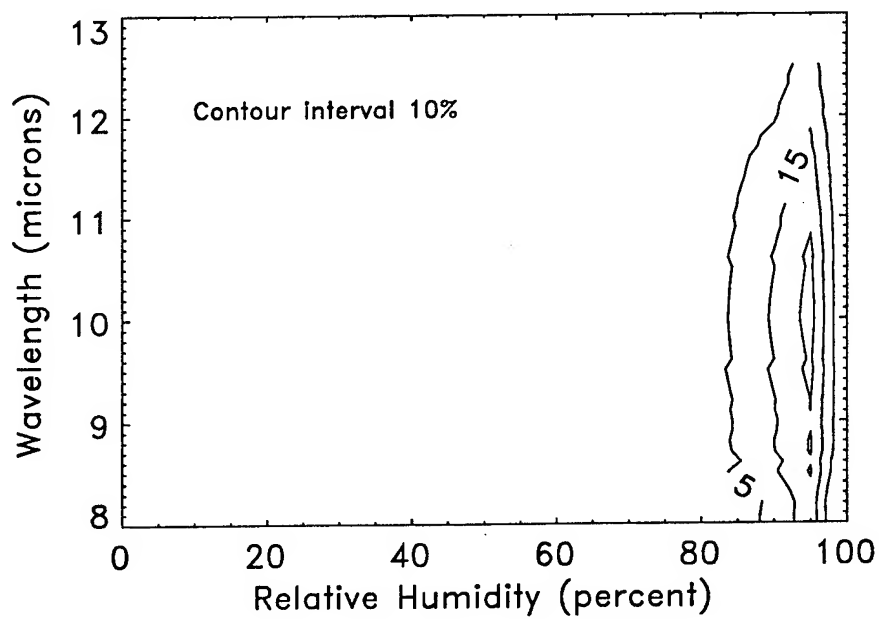


Figure 4. Contour plot of percent differences in extinction of LOWTRAN-7 and XSCALE as a function of Humidity and Wavelength (relative to XSCALE)

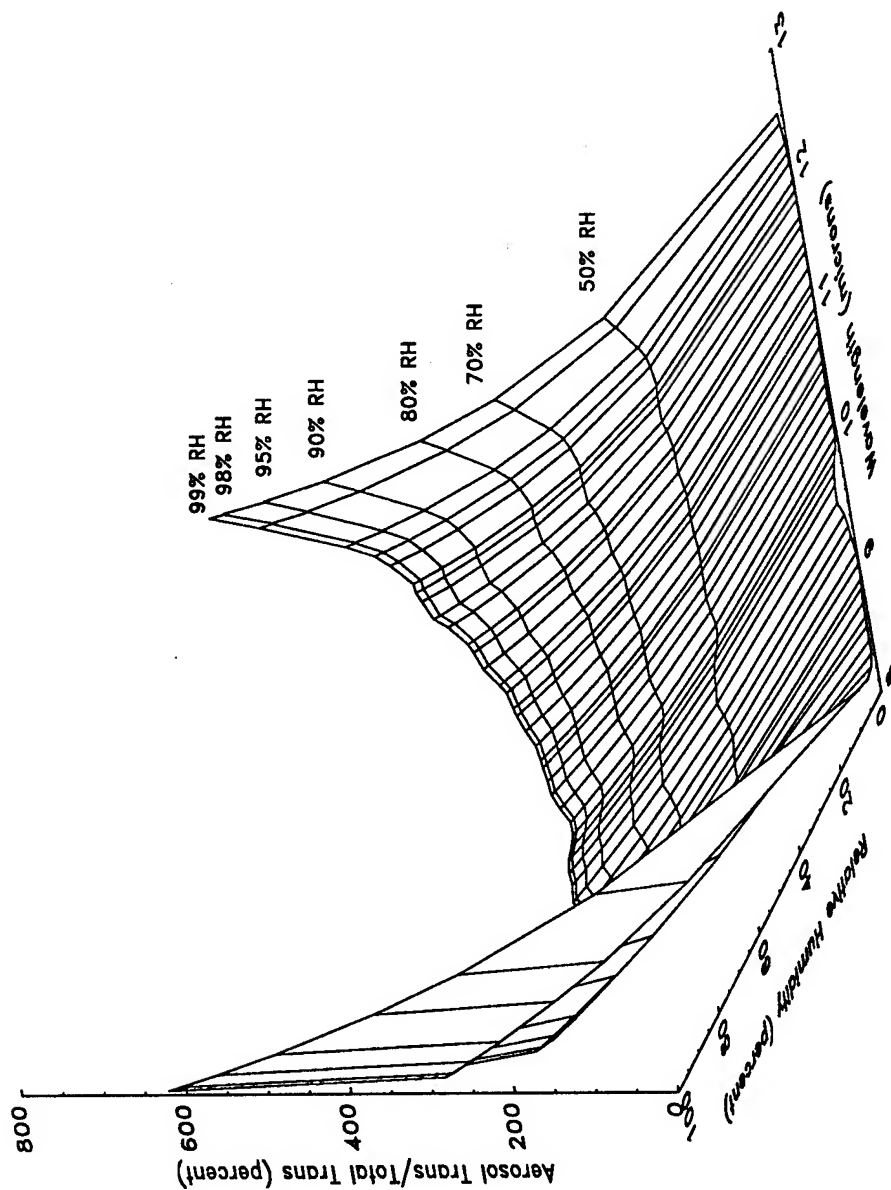


Figure 5. LOWTRAN-7 aerosol transmittance relative to total transmittance as a function of Humidity and Wavelength

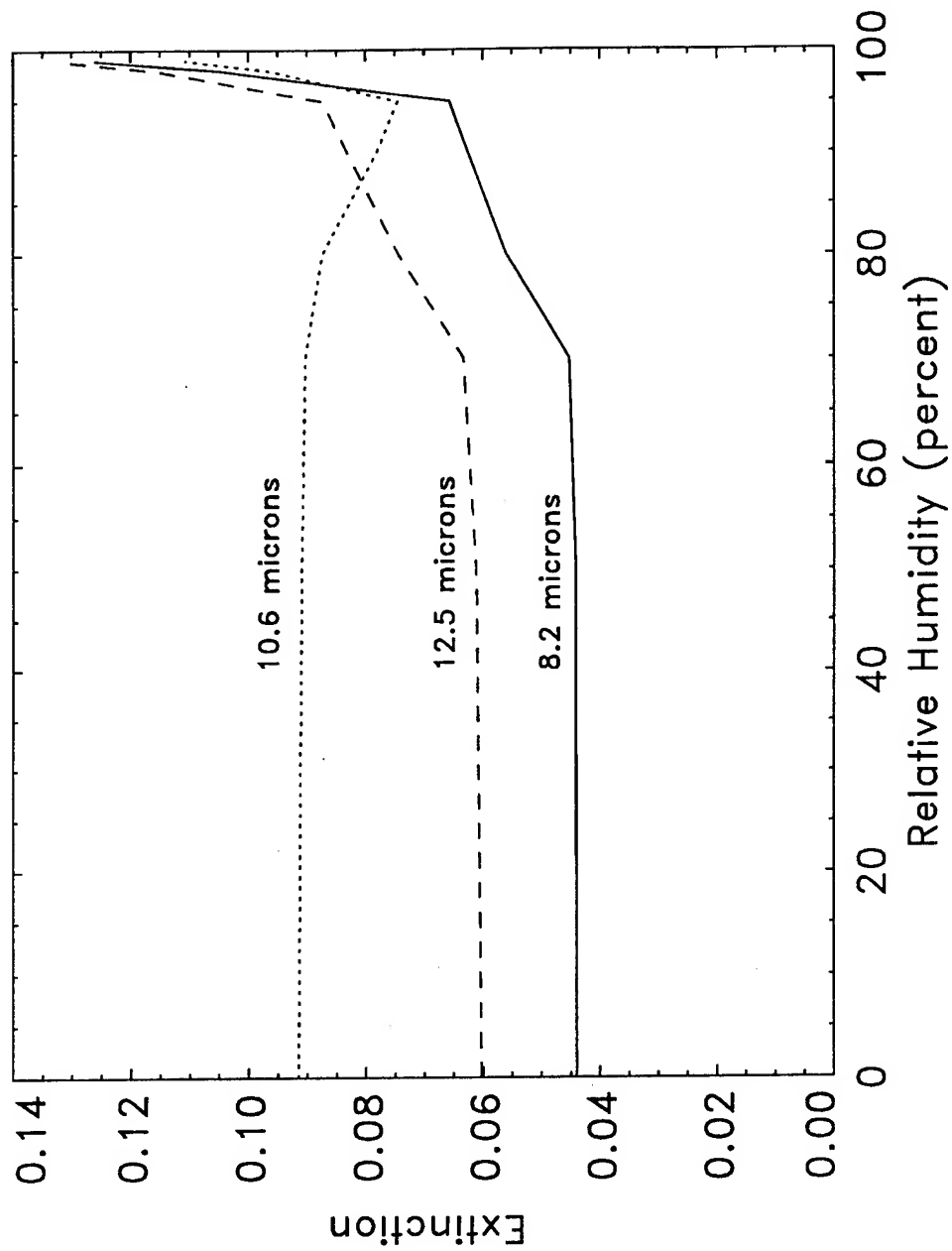


Figure 6. Shettle and Fenn calculations of infrared extinction as a function of Relative Humidity (normalized to 0.55 microns)

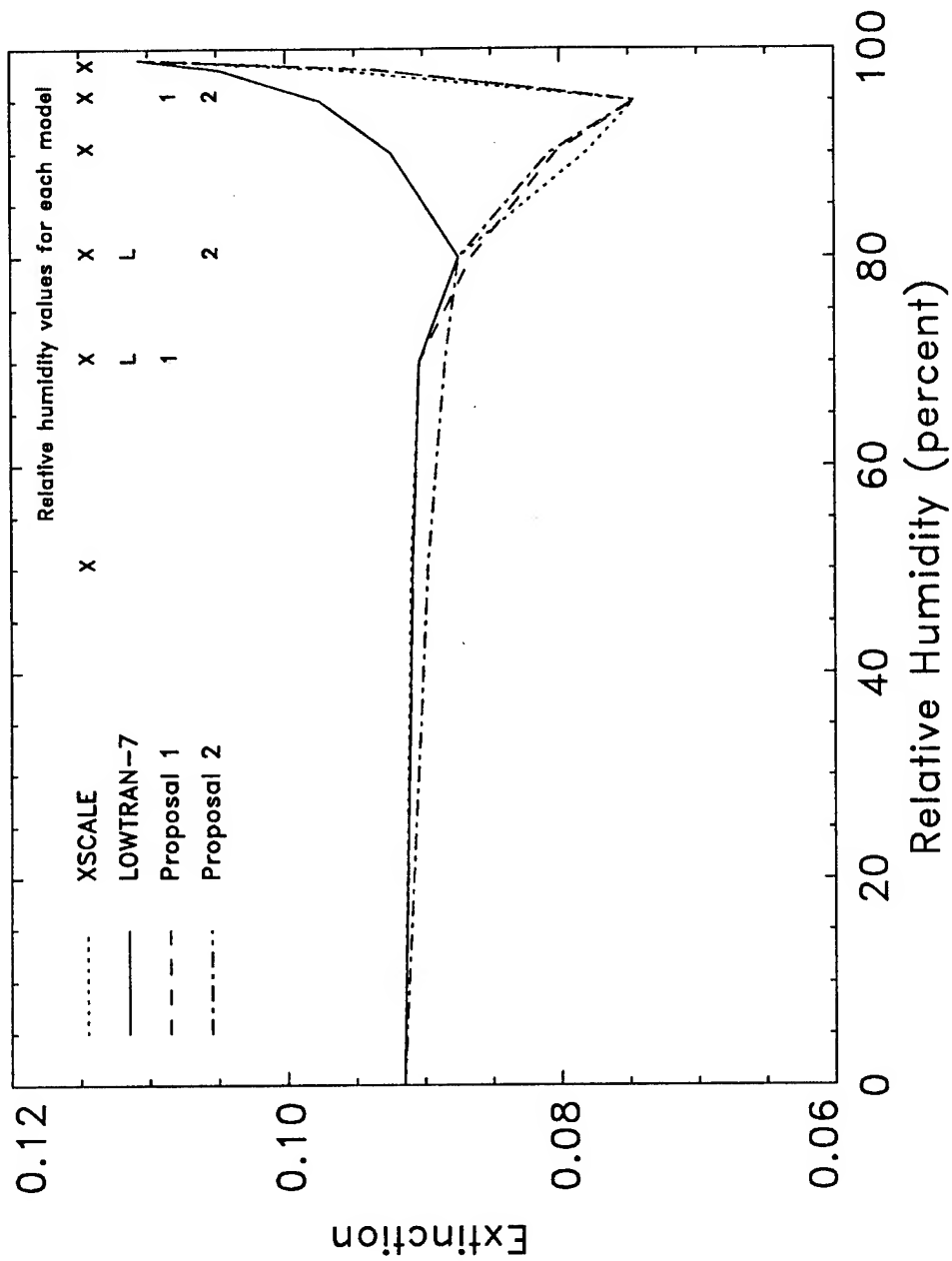


Figure 7. Extinction as a function of Humidity for LOWTRAN-7 and XSCALE with the proposed changes to the Humidity values used by LOWTRAN-7

REFERENCES

- Duncan, Louis D., R. C. Shirkey, and M. B. Richardson, 1982: *EOSAEL 82, Volume II, Transmission Through Gases and Natural Aerosols*. ASL-TR-0122, U.S. Army Atmospheric Sciences Laboratory, White Sands Missile Range, NM 88002-5501.
- Duncan, Louis D., Mary Ann Seagraves, and Melvin G. Heaps, 1987: *EOSAEL 87, Volume 7, Natural Aerosol Extinction Module XSCALE*. ASL-TR-0221-7, U.S. Army Atmospheric Sciences Laboratory, White Sands Missile Range, NM 88002-5501.
- Duncan, Louis D., 1981: *EOSAEL 80, Volume I, Technical Documentation*. ASL-TR-0072, U.S. Army Atmospheric Sciences Laboratory, White Sands Missile Range, NM 88002-5501.
- Kneizys, F. X., E. P. Shettle, W. O. Gallery, J. H. Chetwynd, L. W. Abreu, J. E. A. Selby, R. W. Fenn, and R. A. McClatchey, 1980: *Atmospheric Transmittance/Radiance: Computer Code LOWTRAN 5*. AFGL-TR-80-0067, Air Force Geophysics Laboratory, Hanscom Air Force Base, MA 01731.
- Kneizys, F. X., E. P. Shettle, W. O. Gallery, J. H. Chetwynd, L. W. Abreu, J. E. A. Selby, S. A. Clough, and R. W. Fenn, 1983: *Atmospheric Transmittance/Radiance: Computer Code LOWTRAN 6*. AFGL-TR-83-0187, Air Force Geophysics Laboratory, Hanscom Air Force Base, MA 01731.
- Kneizys, F. X., E. P. Shettle, L. W. Abreu, G. P. Anderson, J. H. Chetwynd, W. O. Gallery, J. E. A. Selby, and S. A. Clough, 1989: *Users Guide to LOWTRAN 7*. AFGL-TR-88-0177, Air Force Geophysics Laboratory, Hanscom Air Force Base, MA 01731.
- Richardson, M. B., L. D. Duncan, M. A. Seagraves, and M. G. Heaps, 1984: *EOSAEL 84, Volume 7, Natural Aerosol Extinction Module XSCALE*. ASL-TR-0160-7, U.S. Army Atmospheric Sciences Laboratory, White Sands Missile Range, NM 88002-5501.
- Selby, J. E. A., F. X. Kneizys, J. H. Chetwynd, and R. A. McClatchey, 1978: *Atmospheric Transmittance/Radiance: Computer Code LOWTRAN 4*. AFGL-TR-78-0053, Air Force Geophysics Laboratory, Hanscom Air Force Base, MA 01731.
- Shettle, Eric P., and R. W. Fenn, 1979: *Models for the Aerosols of the Lower Atmosphere and the Effects of Humidity Variations on Their Optical Properties*. AFGL-TR-79-0214, Air Force Geophysics Laboratory, Hanscom Air Force Base, MA 01731.

NEAR INFRARED TRANSMITTANCE VARIABILITY

Edward D. Creegan

U.S. Army Atmospheric Sciences Laboratory
White Sands Missile Range, NM 88002-5501, USA

ABSTRACT

Transmittance variability in the 1.8- to 3.0- μm wave band (near IR) for a fixed 7-km visual range was calculated using the EOSAEL87 modules LOWTRN and XSCALE. Variations caused by changes in the air mass type, relative humidity, and standard atmosphere are examined.

1. INTRODUCTION

The atmosphere is studied and modeled by examining small parts of it individually. These results are then combined by using superposition to yield an overall transmittance. Studying the smaller portions of the larger atmospheric propagation problem not only makes the problem manageable, but also gives greater detail and flexibility to the final solution. This flexibility, however, complicates the calculation of transmittance by adding to the number of variables involved. The infrared (IR) region of the electromagnetic spectrum is of particular interest. An earlier examination of the effect of this complexity for the 3.0- to 5.0- μm (mid IR) and 8.0- to 12.0- μm (far IR) regions [Creegan *et al.*, 1990] indicated that a wide range of variations in total transmittance is possible for certain IR wave bands. This study in the 1.8- to 3.0- μm was done in an attempt to evaluate the sensitivity of these variations for regions closer to the visible wave band where the variability is minimal.

Specification of a 7-km visual range as the parameter for calculating transmittance in the 1.8- to 3.0- μm wave band (near IR) will allow for considerable variation in the results. This variation arises from the choices available for calculating the individual portions of the total transmittance. Many combinations of aerosol type, standard atmosphere, and relative humidity are possible in a 7-km visual range scenario and, depending on the sets of parameters chosen, will cause variations in the total transmittance in the near IR.

To address this variability, a study of the effects of different aerosol types, relative humidities, and standard atmospheres on the calculation of transmittances in the 1.8- to 3.0- μm region was undertaken. Calculations were made over 1 km, 5 km, and 10 km horizontal constant pressure paths at 0.5 km altitude mean sea level using, the EOSAEL modules atmospheric transmittance and radiance (LOWTRN), for the effects of gases [Pierluissi and Maragoudakis, 1987], and natural aerosol extinction (XSCALE), for the effects of aerosols [Duncan *et al.*, 1987].

Transmittances were calculated for 30, 50, and 80 percent relative humidity, using the mid-latitude summer, US standard (1976), and tropical standard atmospheres in LOWTRN as well as the rural, urban, and maritime aerosol types in XSCALE. The humidity profiles of the standard atmospheres were modified to match the desired surface conditions of 30, 50, and 80 percent relative humidity. The effects caused by changing between one parameter while holding the other two parameters fixed were examined. Combinations of various parameters that produced a worst case were also studied.

The total transmission is the product (superposition) of the transmission degraded by gaseous absorption and scattering, T_g , calculated using LOWTRN and the transmission degraded by the scattering and absorption of energy by particles suspended in the atmosphere, T_a , calculated using XSCALE.

$$T = T_g T_a. \quad (1)$$

The visible wave band region, 0.4 to 0.7 μm , is very well behaved, and different underlying parameters such as relative humidity, aerosol type, and standard atmosphere have a small effect on the total transmittance. This lack of variability naturally gave rise to "rules of thumb" that for years have worked as fair approximations for atmospheric transmittance in many areas. The use of visual range as a parameter by itself to determine transmittance in the infrared wave bands, however, is insufficient. As research provides an increasingly more detailed description of the atmosphere, an awareness of what parameters will contribute to transmittance variability, in which wave bands, becomes critical.

2. RESULTS

An overall view of the many possible variations in transmittance for the 1.8- to 3.0 μm region is shown in fig. 1. These transmittances all occur for a 7-km visual range over a 5-km horizontal constant pressure path.

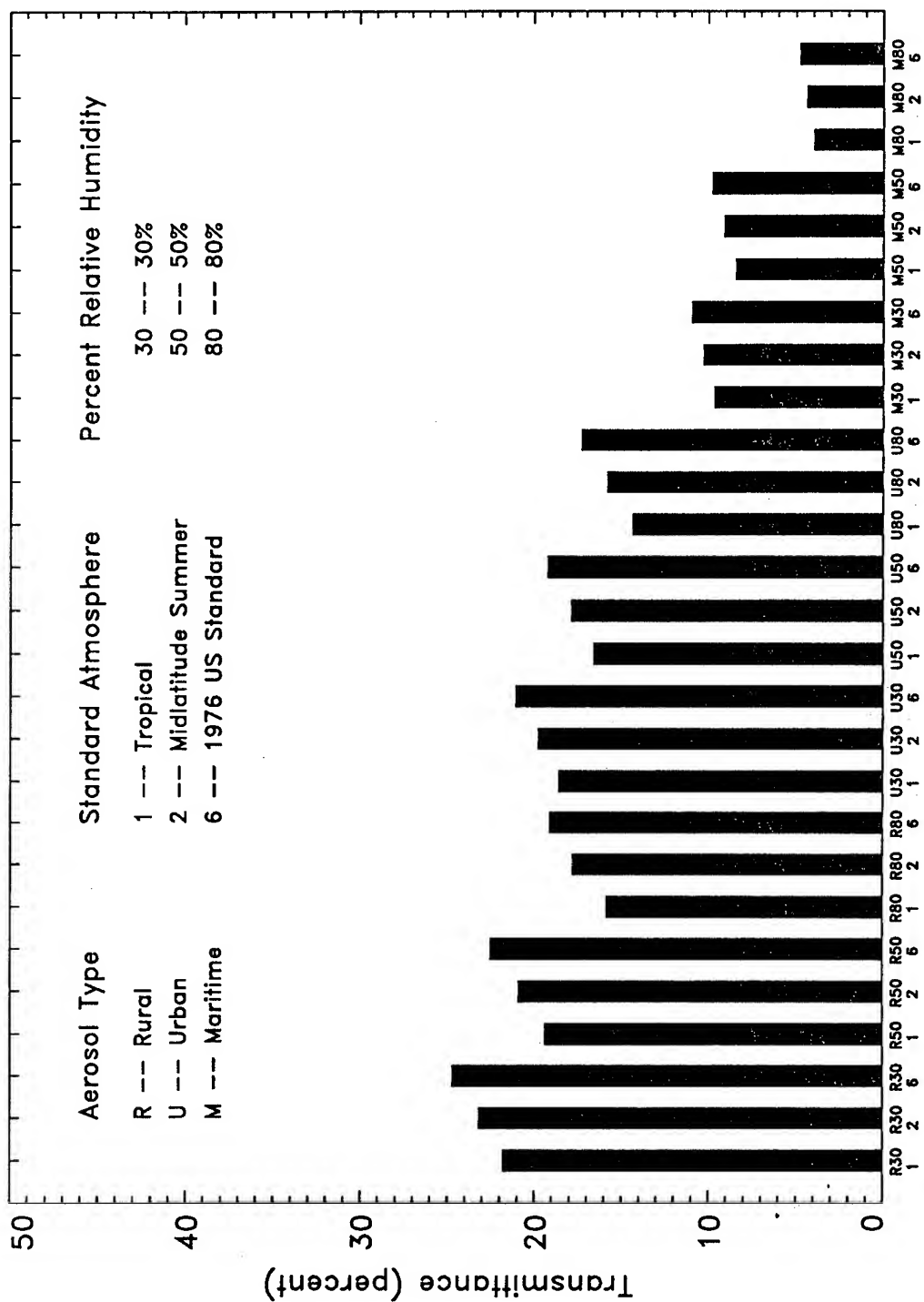
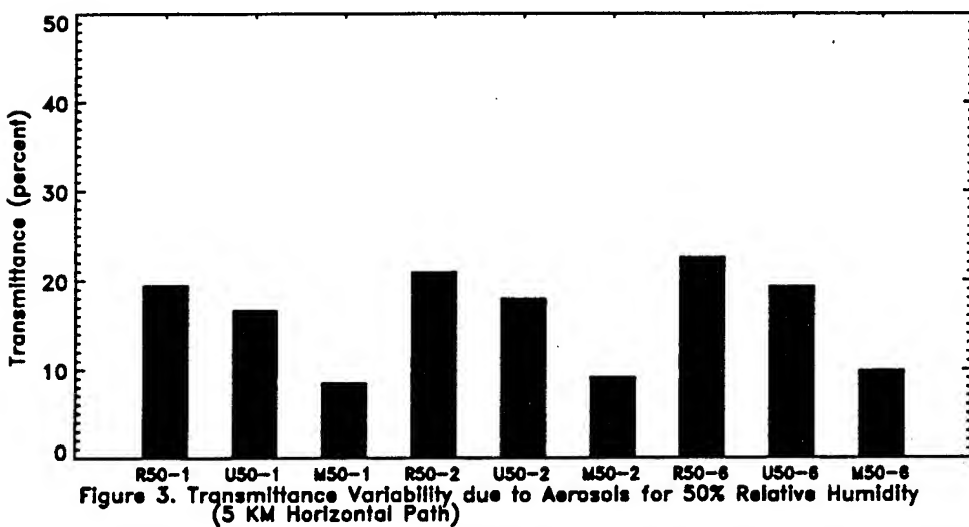
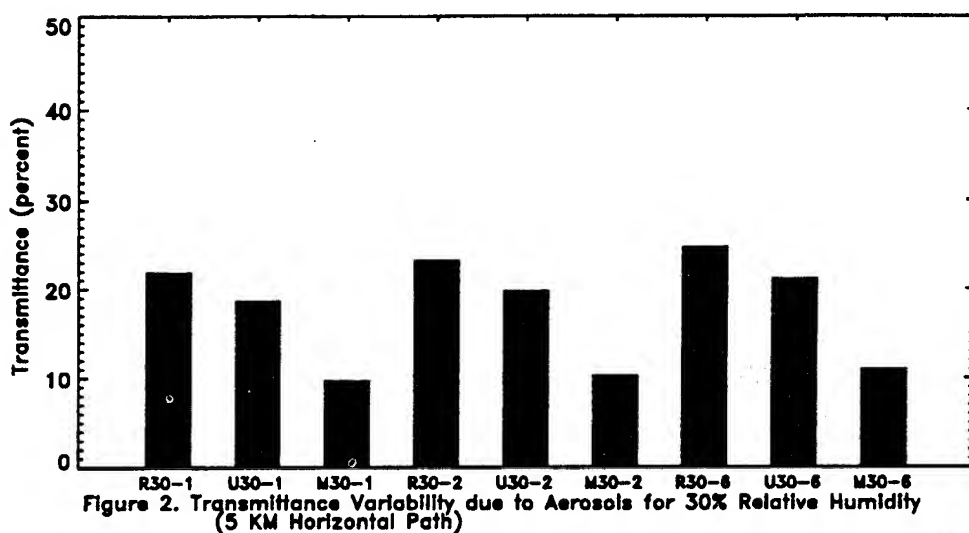


Figure 1. Transmittance as a function of Aerosol Type, Standard Atmosphere, and Relative Humidity.

The variation in transmittance for changes between like parameters is significant. As shown in figs. 2 through 4, the variations in transmittance that occur between the different aerosol types alone will vary $2\% \leq \delta T \leq 14\%$. The variations caused by changing the standard atmosphere (figs. 5 through 7) vary $1\% \leq \delta T \leq 3\%$, and the variations from increasing or decreasing the relative humidity (figs. 8 through 10) can change the total transmittance by $2\% \leq \delta T \leq 6\%$.



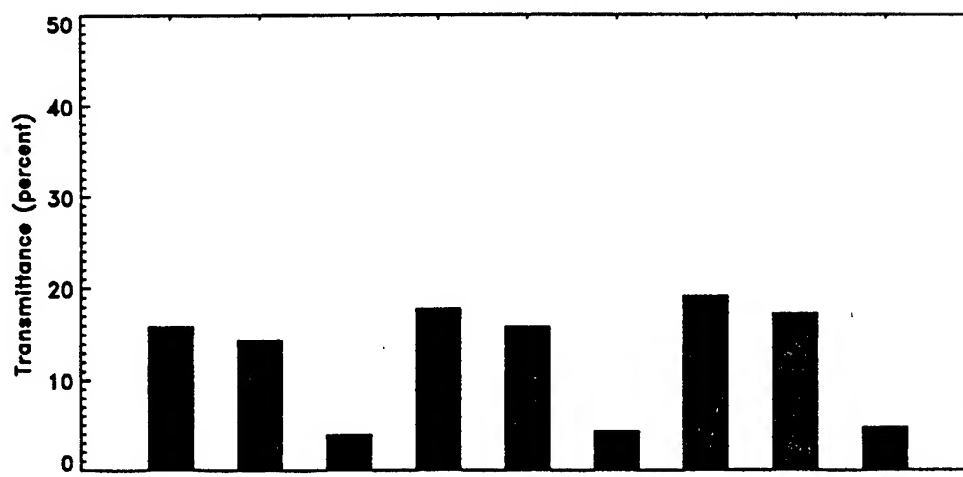


Figure 4. Transmittance Variability due to Aerosols for 80% Relative Humidity (5 KM Horizontal Path)

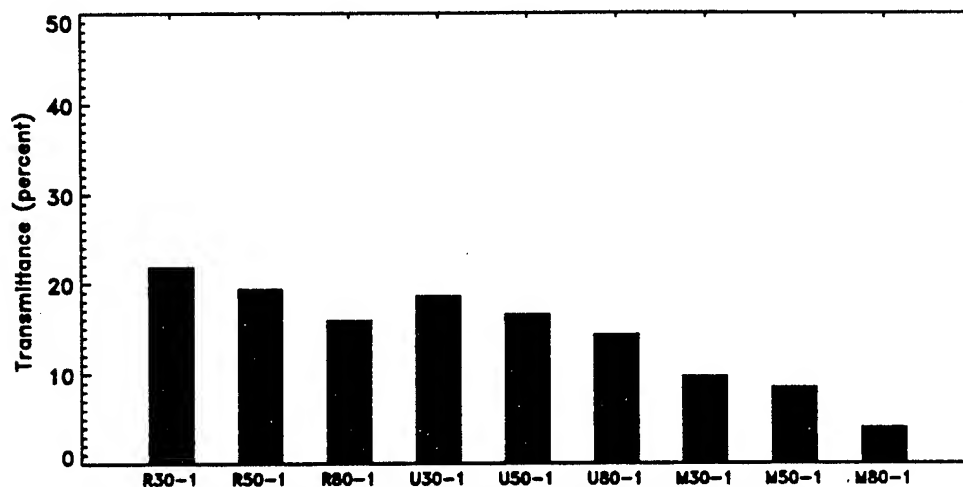


Figure 5. Transmittance Variability due to Relative Humidity for the Tropical Standard atmosphere (5 KM Horizontal Path)

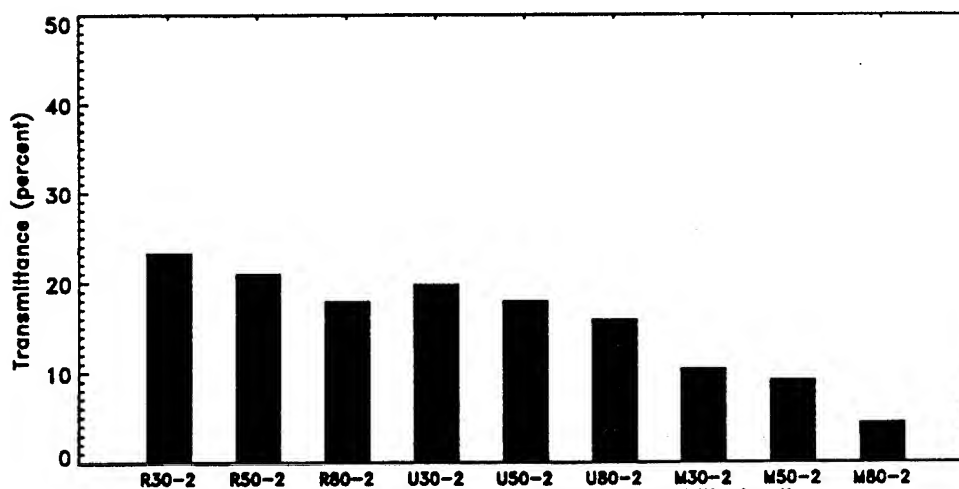


Figure 6. Transmittance Variability due to Relative Humidity for the Midlatitude Summer atmosphere (5 KM Horizontal Path)

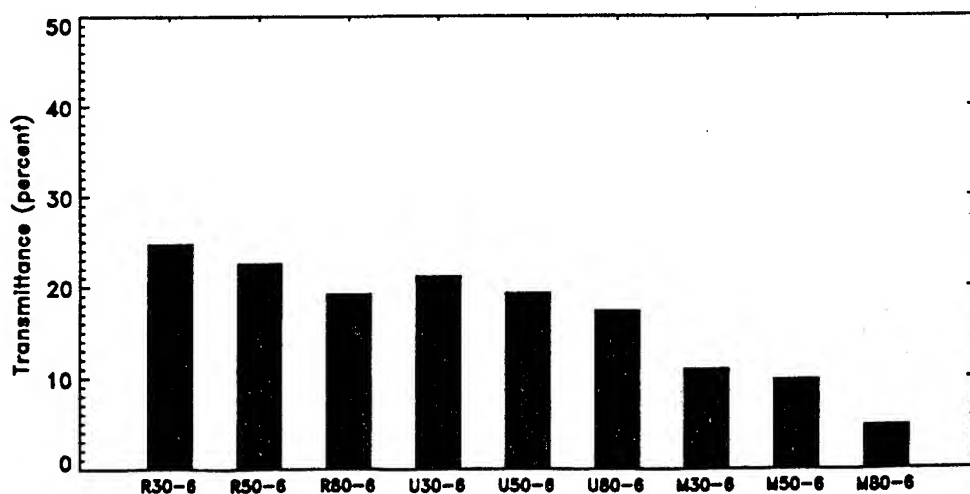


Figure 7. Transmittance Variability due to Relative Humidity for the 1976 US Standard atmosphere (5 KM Horizontal Path)

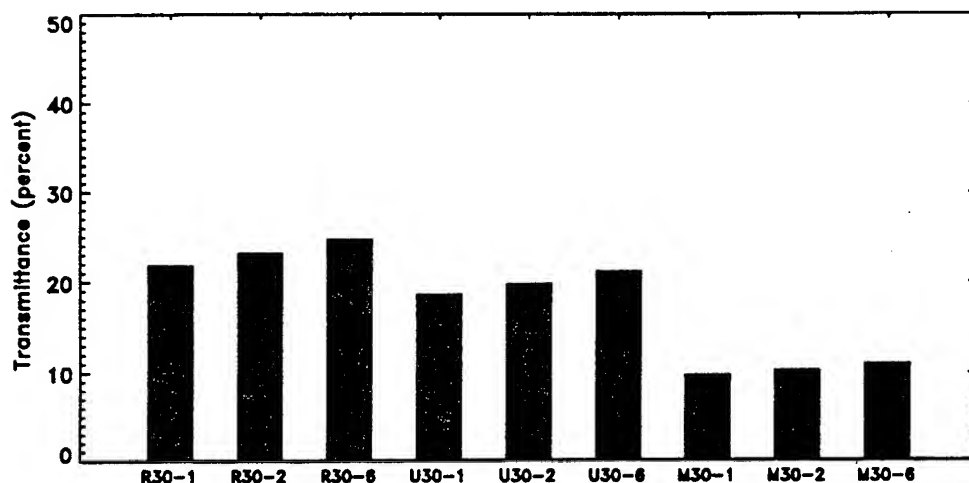


Figure 8. Transmittance Variability due to standard atmosphere for 30% Relative Humidity (5 KM Horizontal Path)

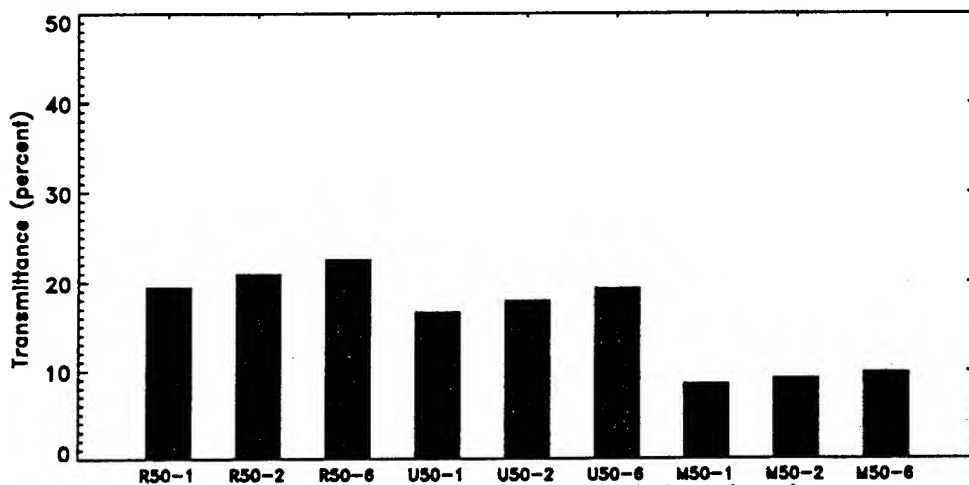
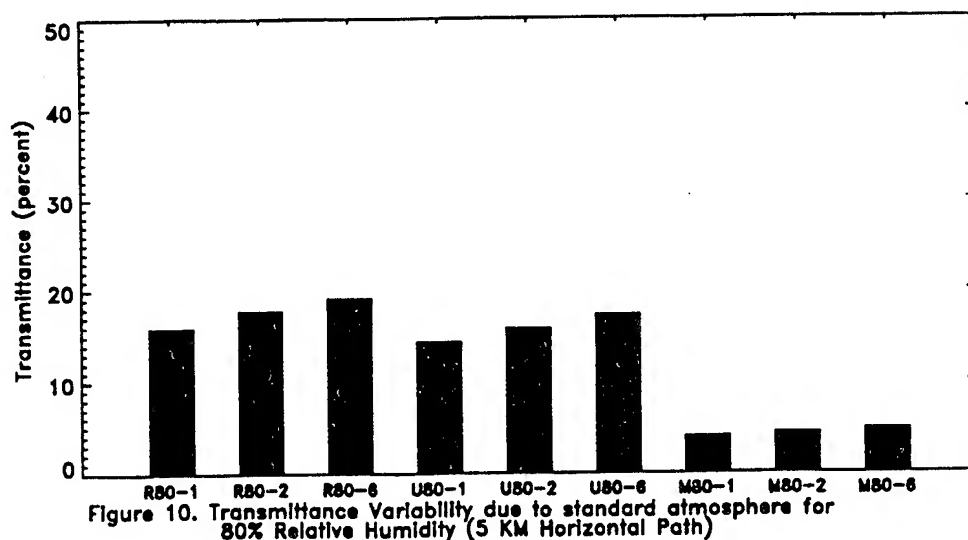


Figure 9. Transmittance Variability due to standard atmosphere for 50% Relative Humidity (5 KM Horizontal Path)



Changing more than one parameter, such as aerosol type and relative humidity, can alter the total transmittance by up to 20 percent. This can be seen by comparing the magnitudes of the transmittances in fig. 1.

3. CONCLUSION

The various parameters used in defining the subset solutions make the overall transmittance calculation complex as a result of the work done to define the atmosphere. This complexity has become necessary to accurately describe the atmosphere. The parameters that determine T_g and T_a will exhibit a surprisingly large degree of variability in the total transmittance and still have a visual range of 7-km. Of the three parameters studied, the choice of aerosol type demonstrates the most variability. The other two do not provide a significant change in total transmittance by themselves, but when coupled with the aerosol type will increase the variability even farther.

This complexity indicates the increase in understanding of the atmosphere and will provide the detail demanded and flexibility required to successfully incorporate the atmosphere into calculations regarding the propagation of electromagnetic energy.

REFERENCES

- [Creegan *et al.*, 1990] Creegan, Edward D., A. E. Wetmore, and J. J. Martin, 1990: "Problems Relating to the Calculation of Infrared Transmittances with Data Derived from Visibility Observations". In *Proceedings of the Eleventh Annual EOSAEL/TWI Conference*, pages 693-701, wsmr. U.S. Army Atmospheric Sciences Laboratory.

[Duncan *et al.*, 1987] Duncan, Louis D., Mary Ann Seagraves, and Melvin G. Heaps, 1987: *EOSAEL 87 Volume 7 Natural Aerosol Extinction Module XSCALE*. ASL-TR-0221-7, U.S. Army Atmospheric Sciences Laboratory, White Sands Missile Range, NM 88002-5501.

[Pierluissi and Maragoudakis, 1987] Pierluissi, Joeseeph H., and Christos E. Maragoudakis, 1987: *EOSAEL 87 Volume 4 Atmospheric Transmittance/Radiance Module LOWTRN*. ASL-TR-0221-4, U.S. Army Atmospheric Sciences Laboratory, White Sands Missile Range, NM 88002-5501.

ILLUSTRATION OF FITTE/FGLOW 4-D MODEL OUTPUT

by

**Dorothy Bruce
U.S. Army Atmospheric Sciences Laboratory
White Sands Missile Range, NM 88002-5501**

The Fire Induced Transmission and Turbulence Effects (FITTE) model has been modified to simulate effects of a temporally and spatially varying fire plume. Illustrations of information output from the model for time-series calculations will be shown for both single line of sight and imaging (FGLOW) effects.

(The full text of this paper was unavailable at press time.)

A NOVEL APPROACH TO REDUCING ATMOSPHERIC OBSCURATION EFFECTS ON NEURAL NETWORK PATTERN RECOGNITION

Donald W. Hoock
U. S. Army Atmospheric Sciences Laboratory
White Sands Missile Range, NM 88002-5501, USA

John C. Giever
Physical Science Laboratory, New Mexico State University
Las Cruces, NM 88003-0002, USA

ABSTRACT

Future electro-optical systems will need to be adaptive and robust to different environments. At the 1990 EOSAEL/TWI conference we showed that atmospheric path radiance and transmittance have significant but predictable effects on the performance of neural network pattern recognition algorithms. We also demonstrated on synthetic images that more robust performance can be obtained by training a neural network on additive effects, such as atmospheric path radiance, as a separate class. The method has now been successfully tested on actual field measurements of targets partially obscured by smoke. The neural networks considered are single-layer and multi-layer backpropagation networks. A novel method is given to train networks to ignore the atmospheric degradation effects of path radiance on the target classes. Performance improvement is shown for several classification examples of pixel-based recognition.

1. INTRODUCTION

Neural network pattern recognition is an established method for identifying signals with given patterns and for separating images into predefined classes. A neural network can be trained to use raw images or signals (e.g., a string of pixel intensities), transformed images or signals (e.g., spatial or spectral Fourier coefficients), derived features (e.g., object width to length ratio, geometric moments, intensity histogram moments, spectral line widths,...) or any mixture of these types of input data. Once trained, the pattern classifier can be used as part of an automated process for machine aided target recognition (ATR).

In most battlefield ATR applications, target classifiers will be required to operate in less than ideal environments. In addition to a reduced signal and increased noise from imperfect segmentation, an ATR classifier will face target and background signatures that change with illumination, range-dependent atmospheric contrast and resolution losses, partial obscuration, camouflage and other variations in characteristics. Classification performance will be degraded by these modifications to the extent that actual input data do not match those used for classifier training.

In earlier papers we simulated the impacts that multiplicative atmospheric transmission losses and additive atmospheric path radiance have on image-based linear classifiers (Hoock and Giever, 1989; 1990) and on single- and multi-layer backpropagation neural networks (Giever and Hoock, 1991a). We showed that the outputs can be directly corrected in the linear classifier if the local mean transmittance and mean path radiance are known or can be measured (Hoock and Giever, 1989; 1990). However, a more promising method was also

found to mitigate sensitivity to atmospheric path radiance in both linear and neural net classifiers. This method modifies the classifier design to include examples of atmospheric path radiance (i.e., images with no target) in the training set on an equal footing with target images. In addition, the classifier is taught not just to "recognize" that certain additive atmospheric effects are present but also to "ignore" their impact in the target class channels. This is accomplished by a special training strategy that shunts energy into the atmospheric channel or output neuron while minimizing its effects on the target channel outputs (Giever and Hoock, 1991a; 1991b). Output from the atmospheric channel is later ignored when comparing outputs from target channels to determine the class to which the object belongs.

This paper tests this technique on measured images of a target partially obscured first by white fog oil smoke and then by black graphite smoke. Earlier results (Giever and Hoock, 1991b) are extended to compare performance between extreme cases of unsegmented targets and perfectly segmented targets using both single- and multi-layer neural nets. The nets were also trained on different targets to examine sensitivity. The next section reviews the approach and extends the ideas to non-image based classification. Section 3 describes data sets, section 4 presents the performance results, and section 5 presents conclusions.

2. NEURAL NET PATTERN RECOGNITION

Figure 1 is a multi-layer perceptron network. A string of N numbers X_i^0 are input to N neurons in layer $p=0$. These inputs could be: the intensities of N pixels from an image; coefficients of a spatial or spectral image transform; or derived quantities describing features of the image. A weight matrix $A_{ij}^{(p)}$ and additive factor $\Theta_j^{(p)}$ linearly combine neuron outputs from the previous ($p-1$) layer into a vector $Y_j^{(p)}$ as shown in eq. 1. $Y_j^{(p)}$ is then further transformed by a non-linear sigmoidal function $X_j^{(p)} = S[Y_j^{(p)}]$ given in eq. 2. The final neuron layer outputs M decision values, one for each of the classes to which the image might belong. It is known that three layers (i.e., two internal or hidden layers) are sufficient for arbitrary mappings (Lapedes and Farber, 1988; Lippman, 1987). Performance on input pixels typically improves if the number of neurons in each hidden layer decreases by a factor of three or more.

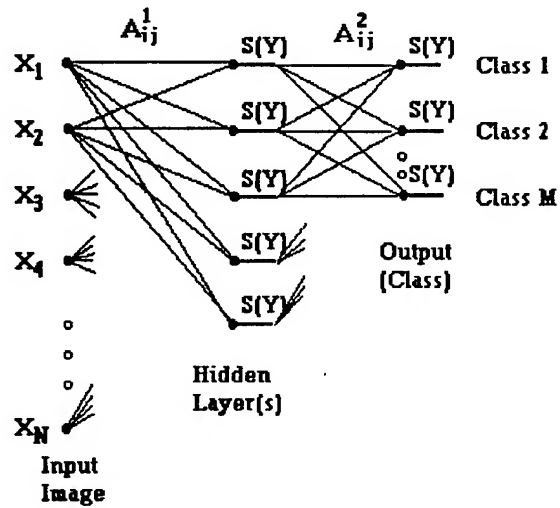


Figure 1. Multi-layer Perceptron Net.

$$Y_j^{(p)} = \sum_{i=1}^{N^{(p-1)}} X_i^{(p-1)} A_{ij}^{(p)} + \Theta_j^{(p)} \quad (1)$$

$$X_j^{(p)} = S[Y_j^{(p)}] = \frac{1}{1 + e^{-Y_j^{(p)}}} \quad (2)$$

Backpropagation network training consists of iteratively adjusting the weights $A_{ij}^{(p)}$ and $\Theta_j^{(p)}$ in each layer p , proceeding backward from the output layer to the input layer as input "training" data or images are presented at random to the network. The weights are then corrected by amounts $\Delta A_{ij}^{(p)}$ and $\Delta \Theta_j^{(p)}$ to reduce the squared error between the output

vector α_j and the desired or "target" classification vector t_j . A step size or multiplicative "learning rate" η is arbitrarily chosen such that adjustments proceed smoothly to find the minimum error. A "momentum" term λ is also sometimes used to speed convergence:

$$\overline{\Delta_i} A_{ij}^{(p)} = \beta \Delta_i A_{ij}^{(p)} + \lambda \Delta_{(i-1)} A_{ij}^{(p)} \quad (3)$$

where β is usually chosen as either one or $(1-\lambda)$. Typically $\eta \approx 0.1$ to 0.3 and $\lambda \approx 0.9$. Iteration continues until $(t_j - \alpha_j)$ is sufficiently small in absolute value, say 0.01 , for all classes j . Details of the procedure have been provided elsewhere (Giever and Hooch, 1991b).

Suppose that "clear air" inputs X_i^k represent individual image pixels "i" (or perhaps members "i" of a feature data set) for targets in training class "k". When viewed through a realistic atmosphere, the X_i^k data or images will be altered by a multiplicative effect f_i and an additive effect $g_i \times h_i$. For example, if X_i^k are actual image pixels, then f_i would be atmospheric transmittance T , h_i would be a path radiance limit L_s , and g_i would be $(1-T)$, so that transmittance T interpolates between the clear image X_i^k and totally obscured image L_s :

$$X_i'^k = f_i X_i^k + g_i h_i = T X_i^k + (1-T) L_s \quad (4)$$

(Or if X_i^k are Fourier coefficients of a target from class k with increasing wavenumber i , then f_i could be the optical transfer function of the atmosphere, and $g_i \times h_i$ could be the Fourier transform of additive noise, atmospheric radiance and obscuration fluctuations.)

Note that the second term in Eq. 4 containing $(1-T) L_s$ (or $g_i \times h_i$) is independent of any particular target class k and thus will be the same for all targets viewed under similar atmospheric conditions. It is this separation of the atmospheric response into a sum of a target class-dependent term and a class-independent term that leads to an atmospheric mitigation training strategy. Consider the separation of the sigmoidal response S' in output neuron j to an image (or feature data set) from class k that has been degraded by a multiplicative atmospheric factor f_i and an additive atmospheric factor $g_i \times h_i$:

$$S_j'^k = S(Y_j'^k) = \frac{1}{1 + e^{-\sum_i f_i (A_{ij} X_i^k + \theta_j / N) - \sum_i g_i (A_{ij} h_i + \theta_j / N) - \theta_j [1 - \frac{1}{N} \sum_i (f_i + g_i)]}} \quad (5)$$

$$\approx \frac{1}{1 + \left[\frac{1}{S_j^k} - 1 \right]^f \left[\frac{1}{S_j^{(M+1)}} - 1 \right]^g}$$

The second equality in eq. 5 shows how $S_j'^k$ for a target in the atmosphere varies with the pristine (no atmosphere) target training output S_j^k and an atmospheric (no target) training output $S_j^{(M+1)}$. This second equality is exact only if $f+g$ equals one and if f and g are independent of i . It is approximate if f and g represent weighted averages over i . Based on eq. 5, the output $S_j'^k$ will be least affected by the additive atmospheric effects if one adds to the training set an atmospheric class of output $S_j^{(M+1)}$ and trains to the target values:

$$\text{Require } t_j^k = S(Y_j^k) = \begin{cases} 1 & \text{if } j = k \\ 0 & \text{if } j \neq k, k \neq (M+1) \\ 0.5 & \text{if } j \neq k, k = (M+1) \end{cases} \quad (6)$$

This neural net training strategy to mitigate additive atmospheric effects is summed up in fig. 2. In traditional training the atmospheric class would not be present.

3. DATA SETS

Visible images were used to test the performance of backpropagation networks on targets from the classes: pickup truck (side view), tank (front view), tank (side view), and airplane (side view). Single- and multi-layer neural networks were trained on various combinations or subgroups of three of the four targets and also on the complete group of all four target classes. This was done to test that no single target class dominated the results.

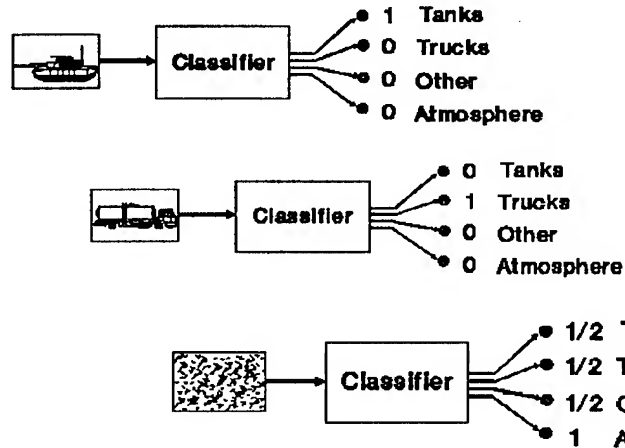


Figure 2. Atmospheric mitigation training strategy

The multi-layer neural networks used consisted of 200 or 800 input neurons (pixel intensities), 80 neurons in the first hidden layer, 20 neurons in the second, and 3 to 5 neurons in the final classification (output) layer. Single-layer networks contained no hidden layers.

Training was done on a tight rectangle of pixels around the vehicle: 40 wide by 20 high for single-layer backpropagation; and 20 wide by 10 high for multi-layer backpropagation. Smaller images were derived from the larger by averaging pixels. Targets were segmented out manually to remove backgrounds from training images. Training images representing additive atmospheric effects (no target) were synthetically produced as a modulated grey image of the same size and average brightness as other training images. Smoke images from the field test were used in testing but were not used in training the networks.

Segmented training images were rescaled to an average brightness of 100 on a scale of zero to 255 so that no target would be recognized based solely on its brightness. A constant intensity of 100 was then added to all pixels. This maintains average brightness between training images and was required to prevent large weights from being produced at the zero intensity training pixels. If not so corrected, the latter situation would cause black training pixels to dominate, with classification sensitive to even small amounts of noise entering in these pixels in actual test images. An alternative, which gives similar results to adding a uniform grey level, was to initialize neural net weights to zero at all black training pixels.

During backpropagation training, images were presented to the network in random order within each epoch (i.e., one presentation of the entire set of training images.) The network was trained until its outputs matched target values within a specified error (typically 0.01). For traditional training the target outputs were a one in the correct class and zero in all other classes. For the atmospheric mitigation strategy, target outputs were those of fig. 2.

Training worked best with a small learning coefficient η between 0.1 and 0.25 and with a momentum coefficient λ of 0.9. For multi-layer backpropagation it was best to start with η at about 0.19 and then change to 0.1 after a few steps. Fixing η at either value for the entire training process often caused the neural net not to train to the desired tolerance.

Initial random weights were then changed, and the network was retrained in random order to assure that both minimum error and training within tolerance were being achieved.

Test images consisted of rectangular regions from 512 by 512 pixel images of a pickup truck obscured by white fog-oil smoke and black graphite smoke. Sixteen test images were taken in both types of smoke. Average transmittance ranged from 0.25 to 0.75. The smoke plumes, which were approximately 20 to 30 meters thick and about 5 meters above ground level, had significant fluctuations in obscuration over the truck images. Test images were taken within a few minutes of the clear-air training images to insure that performance changes were due primarily to obscuration and not to illumination changes. Test images were processed to match the size and to register as closely as possible with the training images. Both segmented and unsegmented truck images were tested. Segmentation was done using the segmented training image mask. Test images were never rescaled in brightness.

4. PERFORMANCE RESULTS

Classifier results are now presented to compare the traditional backpropagation method to the atmospheric mitigation training method. The same training and test images were used in both methods, including two sets of sixteen test images of a pickup truck obscured by white and by black smoke. Results for the traditional method are shown with X's, and results for our method are shown with O's. Outputs from the truck class neuron are plotted on the horizontal axis. The largest of the outputs in the other target classes are plotted along the vertical axis. A dotted line shows where the truck class output equals the maximum of the other target classes. For points above this line the neural network misclassifies the truck. For points near this line the target is unclassifiable. Perfect classification performance for the truck would produce points at the lower right corner.

Figure 3 compares effects of white fog-oil smoke (fig. 3a) and black graphite smoke (fig. 3b) on a single-layer backpropagation network trained on three target classes: pickup truck, tank (side), and plane. The 16 test images are unsegmented, containing some background around the wheels and over the truck bed. In fig. 3a, traditional backpropagation produces values in the truck class of 0.3 to 0.8, but relatively large values in the other classes of 0.2 to 0.5. The atmospheric mitigation method classifies very well, producing values greater than 0.8 in the correct class and less than 0.1 in the largest of the other classes. In fig. 3b the improvement over the traditional backpropagation technique is even more evident.

Figure 4 shows corresponding results for the multi-layer backpropagation network using the same test and training images as in fig. 3. Figure 4a, the fog-oil test set, and fig. 4b, the graphite test set, produce relatively small outputs in all classes using traditional training, but excellent classification when the atmospheric mitigation training strategy is used.

Figures 5 and 6 show the effects on a slightly different three-class training set: truck, plane, and tank (front). Figure 5a corresponds to fig. 3a, fig. 6a corresponds to fig. 4a, etc. with the change in tank training images from side to front views producing only small changes in classifier output. (Similar results were produced when the plane image was dropped and both tank aspects were kept in a three target-class training set.)

Figures 7 and 8 show performance when all four of the target types are used as classes. Test images are the same unsegmented, obscured truck images used in previous examples. Performance is somewhat worse overall than for the three-class cases. This is to be expected, since the network must recognize an extra class. The pattern of improvement by using atmospheric mitigation training is consistent with earlier figures, however, although outputs of up to 0.3 in incorrect classes somewhat reduce classifier performance.

Figures 9 and 10 show results using perfectly segmented test images in place of completely unsegmented test images for the three-class case of truck, tank (side), and plane, as in figs. 3 and 4. Traditional backpropagation, as used in figs. 9a and 10a, often produces very good performance if the target has been well segmented. (Compare with the unsegmented test image performance of figs 3a and 4a.) Perhaps this is because the traces of background present in unsegmented images confuse the traditional neural net, while background variations are not much different than atmospheric variations as far as the atmospheric mitigation technique is concerned. As seen in fig. 9b for absorbing black smoke, perfect segmentation does not guarantee that the traditional approach will work. Figures 9 and 10 also demonstrate that the atmospheric mitigation training strategy improves classification of even perfectly segmented targets when they are partly obscured across their surface.

5. CONCLUSIONS

Methods to include the atmosphere as a training class and to train neural nets to "ignore" additive atmospheric effects have successfully been tested for target recognition in obscuring white and black smoke of average transmittances between 0.25 and 0.75. (No pattern recognition method should be expected to work at much lower transmittance.) Multi-layer neural networks showed improved performance over single-layer networks as expected. The atmospheric mitigation training strategy produced the greatest improvement when classifying unsegmented targets containing some background. The method also improved performance somewhat for perfectly segmented target images. Most segmentation algorithm performance lies somewhere between the two extremes of no segmentation and perfect segmentation tested here. The method should also apply to feature-based and transformed data inputs to neural net pattern recognition when additive atmospheric effects (independent of specific targets present) are present in the test data. However, this assertion has not yet been demonstrated.

REFERENCES

- Hoock, D. W. and J. C. Giever, 1989: Accounting for the Atmosphere in Extrapolating System performance to Different Environments. In Proceedings of the SPIE Technical Symposium on Aerospace Sensing, Propagation Engineering, SPIE Vol. 1115, 308-319.
- Hoock, D. W. and J. C. Giever, 1990: Propagation Effects on Image Moments, Edges and Linear Classifiers. In Proceedings of the Tenth Annual EOSAEL/TWI Conference, U.S. Army Atmospheric Sciences Laboratory, White Sands Missile Range, NM 88002-5501.
- Giever, J. C. and D. W. Hoock, 1991a: Analyzing Atmospheric Propagation Effects on Neural Network Pattern Recognition. In Proceedings of the Eleventh Annual EOSAEL/TWI Conference, U. S. Army Atmospheric Sciences Laboratory, White Sands Missile Range, NM 88002-5501.
- Giever, J. C. and D. W. Hoock, 1991b: Atmospheric Propagation Effects on Pattern Recognition by Neural Networks. In Proceedings of the SPIE Technical Symposium on Characterization, Propagation and Simulation of Sources and Backgrounds, SPIE Vol. 1486, 302-313.
- Lapedes A. and R. Farber, 1988: How Neural Networks Work. In Neural Information Processing Systems, D. Anderson, ed., American Institute of Physics, NY.
- Lippman R., 1987: An Introduction to Computing with Neural Nets, IEEE Acoustics, Speech and Signal Processing, April, 4-22.

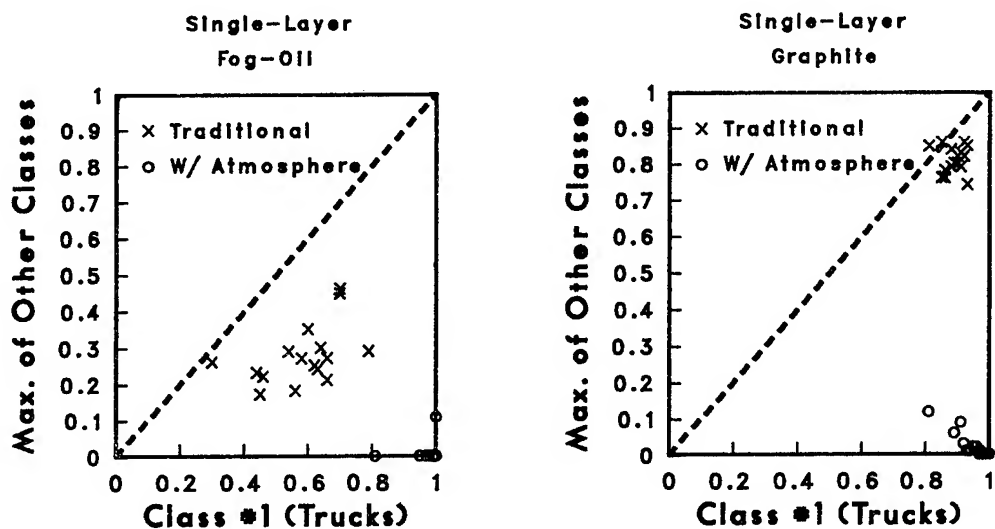


Figure 3. Single-layer backpropagation performance for an 800 pixel, unsegmented (a) fog-oil and (b) graphite smoke-obscured truck image based on 3 target classes [truck, tank (side), and plane].

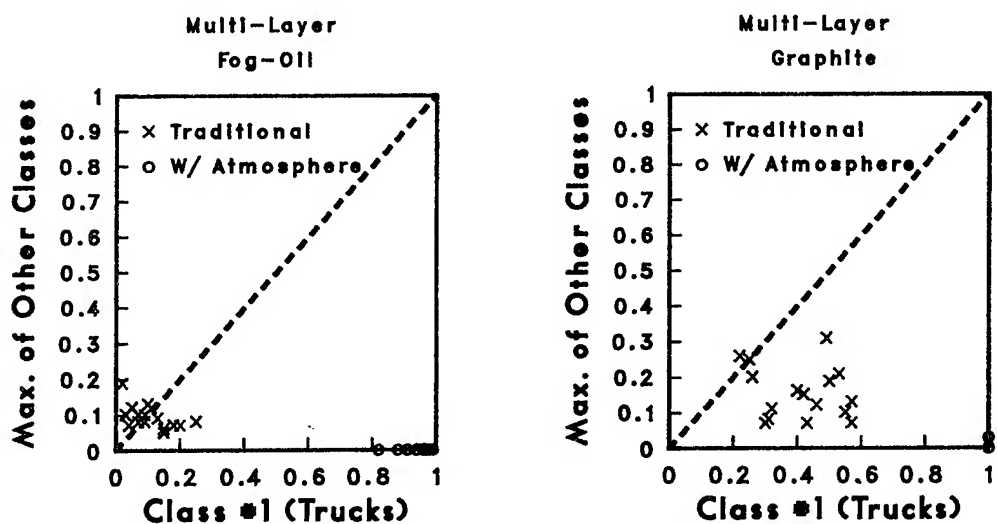


Figure 4. Multi-layer backpropagation performance for a 200 pixel, unsegmented (a) fog-oil and (b) graphite smoke-obscured truck image based on 3 target classes [truck, tank (side), and plane].

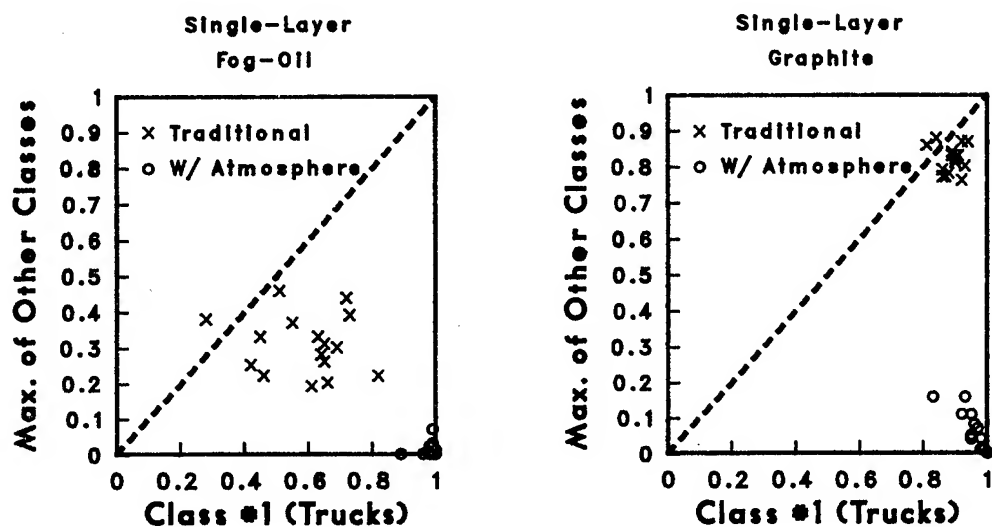


Figure 5. Single-layer backpropagation performance for an 800 pixel, unsegmented (a) fog-oil and (b) graphite smoke-obscured truck image based on 3 target classes [truck, tank (front), and plane].

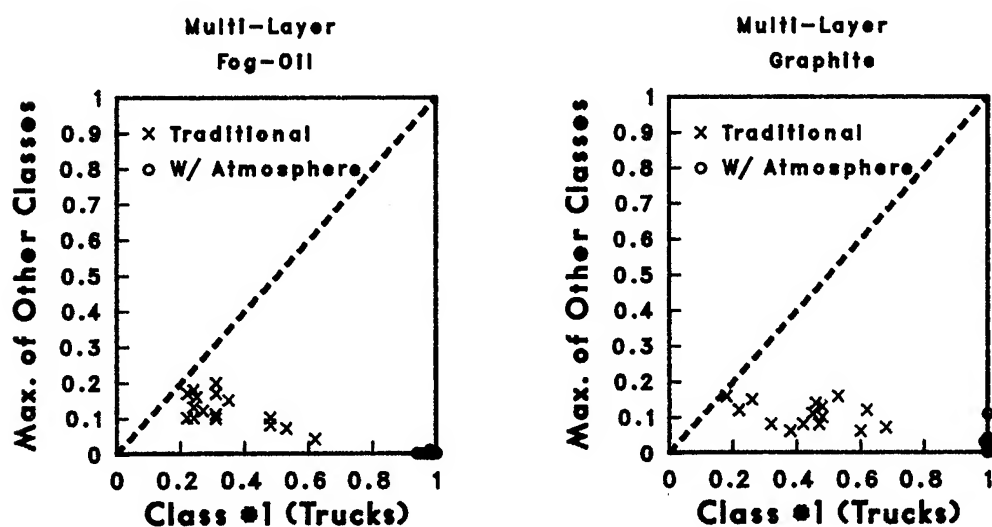


Figure 6. Multi-layer backpropagation performance for a 200 pixel, unsegmented (a) fog-oil and (b) graphite smoke-obscured truck image based on 3 target classes [truck, tank (front), and plane].

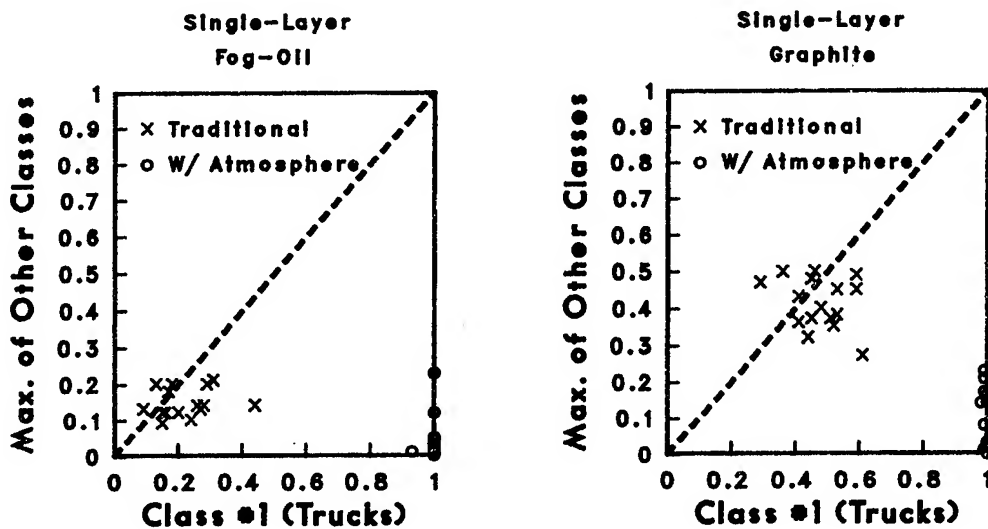


Figure 7. Single-layer backpropagation performance for an 800 pixel, unsegmented (a) fog-oil and (b) graphite smoke-obscured truck image based on 4 target classes [truck, tank (front), tank (side) and plane].

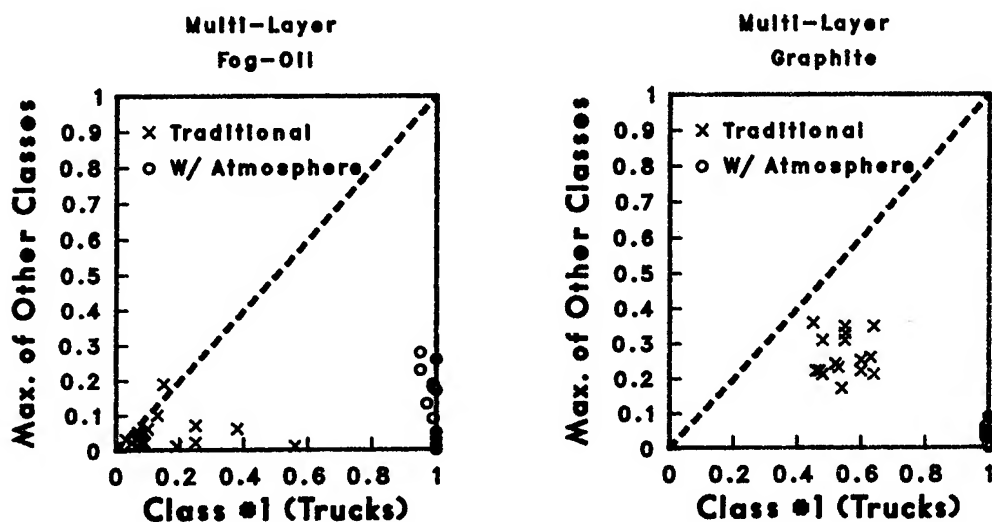


Figure 8. Multi-layer backpropagation performance for a 200 pixel, unsegmented (a) fog-oil and (b) graphite smoke-obscured truck image based on 4 target classes [truck, tank (front), tank (side), and plane].

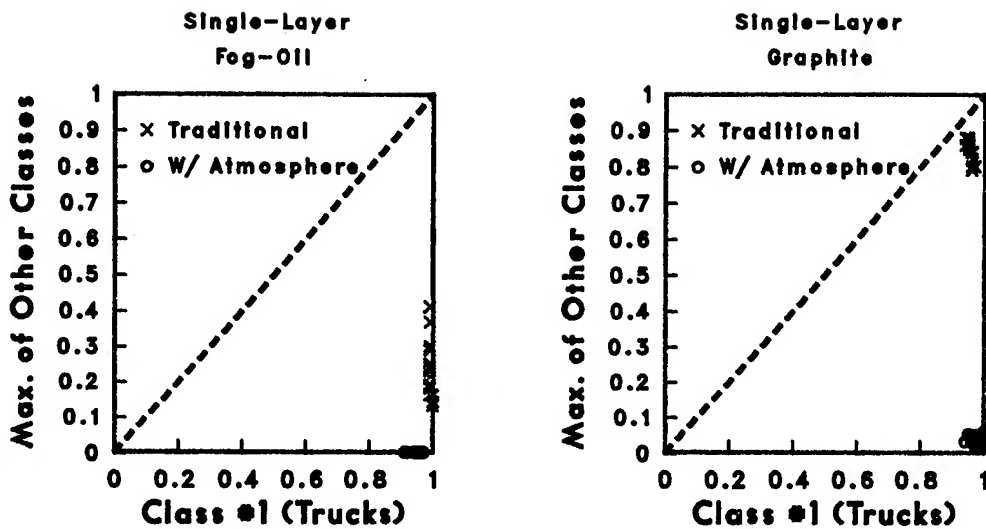


Figure 9. Single-layer backpropagation performance for an 800 pixel, perfectly segmented (a) fog-oil and (b) graphite smoke-obscured truck image based on 3 target classes [truck, tank (side), and plane].

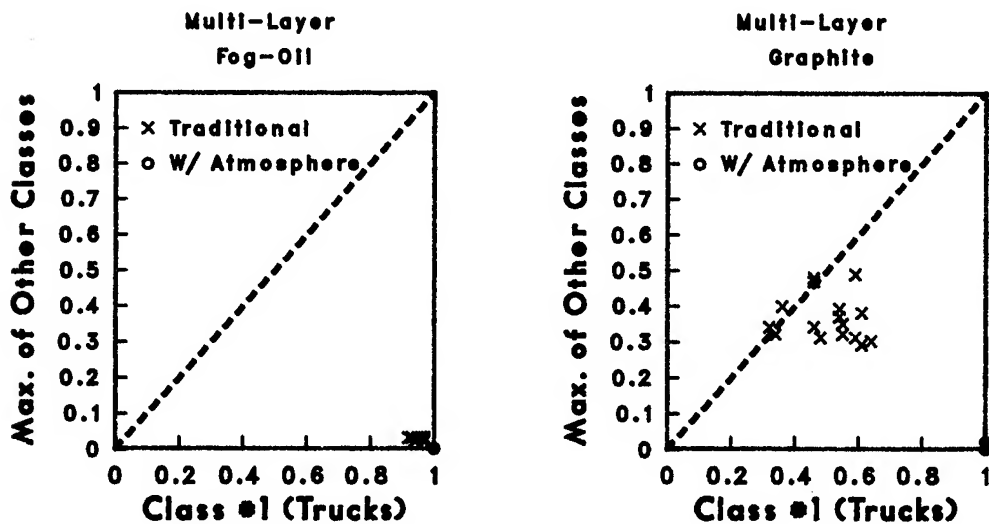


Figure 10. Multi-layer backpropagation performance for a 200 pixel, perfectly segmented (a) fog-oil and (b) graphite smoke-obscured truck image based on 3 target classes [truck, tank (side), and plane].

**CLOUD INFORMATION REFERENCE LIBRARY
AND ARCHIVE (CIRLA)**

by
Ronald J. Nelson and Kenneth P. Freeman

(The abstract for this paper was unavailable at press time.)



SPECTRALLY RESOLVED TRANSMITTANCE MEASUREMENTS AT SMOKE WEEK XIII

William A. Peterson and Dennis M. Garvey
U.S. Army Atmospheric Sciences Laboratory
White Sands Missile Range, New Mexico 88002-5501, USA

William M. Gutman
Physical Science Laboratory
New Mexico State University
Las Cruces, New Mexico 88003-0002, USA

ABSTRACT

The U. S. Army Atmospheric Sciences Laboratory Mobile Atmospheric Spectrometer (MAS) was used at Smoke Week XIII to obtain transmittance spectra of obscurant clouds. The spectral resolution was high enough to easily resolve molecular absorption bands and to begin to resolve some individual lines. The primary spectroscopic instrument in the MAS is a Fourier transform spectrometer. A broadband visible/infrared composite radiation source was used. The spectrometer was operated in two different configurations. The near-infrared configuration covered the transparent regions of the atmospheric spectrum between 6230 and 10,127 cm^{-1} (0.99–1.61 μm) at a spectral resolution of 8 cm^{-1} . The mid-infrared configuration covered the transparent regions between 800 and 5000 cm^{-1} (2.00–12.50 μm) at a spectral resolution of 4 cm^{-1} . Samples of the normalized transmittance spectra of several obscurant materials are presented. Pitfalls and problems associated with the measurements are also discussed. These include the small power per channel, interference by atmospheric attenuation, turbulence-induced intensity fluctuations, and relatively long measurement cycle times. The importance of spectrally resolved measurements is demonstrated by convolving measured transmittance spectra for several obscurants with typical broadband transmissometer response functions. Results from broadband instruments can be misleading when applied to discrete wavelengths or to broadband systems with different response functions.

1. INTRODUCTION

The U.S. Army Atmospheric Sciences Laboratory (ASL) Mobile Atmospheric Spectrometer (MAS) was used to measure transmittance spectra of obscurant materials during Smoke Week XIII (SW XIII) from 3–17 May 1991 at Eglin Air Force Base, Florida. The primary spectral instrument in the MAS is a Fourier transform spectrometer. Data were acquired for a wide variety of obscurant materials and test conditions. Two instrument configurations that provided different spectral coverage were used. These measurements provide new insight into the behavior of obscurant materials, and into the performance of broadband transmissometers and electro-optical devices. This work is discussed in greater detail by Peterson and Gutman (in preparation). The data will be available from the Atmospheric Aerosol and Optics Data Library (AAODL).

2. MEASUREMENT METHODOLOGY

2.1 BASIC CONCEPTS

A relative transmittance measurement of an obscurant material is quite simple in concept. For a fixed path through the unobscured atmosphere, the power as a function of spatial frequency, ν , recorded at the receiver can be written as

$$P_{Clear}(\nu) = S(\nu)R(\nu)T_{Atm}(\nu) \quad (1)$$

$S(\nu)$ is the source function, $R(\nu)$ is the system response function that includes the detector response and the transmittance of the system optics, and $T_{Atm}(\nu)$ is the transmittance of the path. With an obscurant present, the right-hand side of eq. (1) must be multiplied by the obscurant transmittance function.

$$P_{Obs}(\nu) = S(\nu)R(\nu)T_{Atm}(\nu)T_{Obs}(\nu) \quad (2)$$

The relative transmittance of the obscurant is found by dividing eq. (2) by eq. (1).

$$T_{Obs}(\nu) = \frac{P_{Obs}(\nu)}{P_{Clear}(\nu)} \quad (3)$$

It is apparent from eq. (3) that a measurement cannot be made when $P_{Clear}(\nu)$ is near zero.

When $P(\nu)$ is measured with an instrument that has a finite spectral resolution, the recorded signal is the convolution of the natural transmission spectrum (i.e., undegraded by instrument effects) with the line shape function of the spectrometer. Atmospheric features ratio out of eq. (3) along with the shape degradation effects, but the obscurant features remain, and the apparent resolution is limited by the line shape function.

2.2 PATH RADIANCE CONSIDERATIONS

Equations (1) and (2) neglect any contribution to the recorded signal by path and background radiance. Accurate transmittance measurements can only be made if these effects are removed. Path radiance results primarily from scattered sunlight, but it can also result from emission by excited molecular species that may be present in the cloud. Background radiation results from emission by objects other than the source that may be in the receiver field-of-view, and by the optics in the optical train. The signals that are actually recorded, $P_{Clear}(\nu)$ and $P_{Obs}(\nu)$, contain these contributions which will be denoted $P_{Clr-Pth}(\nu)$ and $P_{Obs-Pth}(\nu)$, respectively. The correct expression for the relative obscurant transmittance based on the actual recorded signals is

$$T_{Obs}(\nu) = \frac{P_{Obs}(\nu) - P_{Obs-Pth}(\nu)}{P_{Clear}(\nu) - P_{Clr-Pth}(\nu)} \quad (4)$$

Fixed-band transmissometers usually remove unwanted radiance contributions to the total signal by chopping at the source and employing synchronous detection, but this approach cannot be applied with a rapid scan Fourier spectrometer. The interferometer is a specialized beam modulator that also digitizes and records the modulated signal (the interferogram). The Fourier transformation process sorts this signal into spectral components. Additional modulation such as that resulting from a mechanical chopper cannot be accounted for by the Fourier transform. Intensity variation that results from atmospheric turbulence can also be thought of as unwanted beam modulation. The depth, however, is usually not severe, so the Fourier transform does a reasonable job of recovering the spectrum. The only significant effect is some reduction of the radiometric accuracy of the spectra; i.e., the uncertainties in the measured intensities result in uncertainty in the baseline of the transmittance spectra.

A different strategy must be used to remove path radiance from Fourier spectra. A good approach is to alternate data acquisition between obscurant transmittance spectra and path radiance spectra. The preferred method to measure the path radiance spectrum is to record the signal with the source blocked. By blocking and unblocking the source on alternate spectrometer scans, the background remains unchanged, and the obscurant and background data are in close temporal proximity. The blocking operation must be accurately synchronized with the spectrometer scanning, and so, a signal must be sent from the receiver to the transmitter. The MAS has a provision for such a signal, but it is based on a near-infrared optical link that cannot be used in an optically obscured environment. Therefore, a modified strategy was adopted. The telescope pointing was alternated between on-the-source to measure the transmitted power, and off-the-source to measure the path/background power. Manual control ensured that proper synchronization was maintained. The same method was used with the clear air path/background radiance. The data were reduced using eq. (4).

3. INSTRUMENTATION

3.1 FOURIER TRANSFORM SPECTROMETER

The MAS Fourier spectrometer is a Mattson Instruments, Inc., Nova Cygni model. It can be configured with several different beamsplitters and detectors for optimization in different spectral regions. Its maximum resolution is 0.04 cm^{-1} , but such high resolution is not practical for obscurant testing. The Smoke Week XIII measurements were conducted at a spectral resolution of 4 or 8 cm^{-1} . The primary optical component of every Fourier spectrometer is a Michelson interferometer. The Mattson spectrometer is particularly suited to field measurements because the interferometer is designed with corner-reflectors rather than the more common flat mirrors. Corner-reflector interferometers are inherently stable against thermally and mechanically induced misalignment that is the most common source of radiometric errors in Fourier spectroscopy. Longitudinal sampling errors can still occur, however, and these result in frequency scale errors. Frequency scale errors become a serious problem only at relatively high resolution, typically 0.5 cm^{-1} or greater.

Two distinct configurations of the Fourier spectrometer were used during the measurements. One of these covered the relatively near-infrared region from 0.99 to $1.61\text{ }\mu\text{m}$. The other covered a broad segment of the mid-infrared from 2.00 to $12.50\text{ }\mu\text{m}$. It should be noted that the use of the term "mid-infrared" in this paper is consistent with usage by infrared scientists. Obscurant specialists tend to use "mid-infrared" to refer to the $3\text{--}5\text{ }\mu\text{m}$ spectral region and "far-infrared" to refer to the $8\text{--}12\text{ }\mu\text{m}$ region. Infrared scientists refer to the region from about $2\text{ }\mu\text{m}$ to $50\text{ }\mu\text{m}$ as the mid-infrared, and the region from $50\text{ }\mu\text{m}$ to 1 mm as the far-infrared. In the near-infrared, the instrument resolution was about 8 cm^{-1} (point spacing of 4 cm^{-1}), and the instrument was configured with a quartz beamsplitter and liquid nitrogen-cooled germanium detector. In the mid-infrared, the resolution was about 4 cm^{-1} (point spacing of 2 cm^{-1}), and the instrument was configured with a potassium bromide beamsplitter and liquid nitrogen-cooled mercury-cadmium telluride detector. Triangular apodization was used in both cases, so the line shape was accurately described by the sinc^2 function. The resolution was sufficient to easily resolve molecular absorption bands. Both of these spectral regions have "holes" where the atmosphere is opaque. Table 1 summarizes the spectral regions covered during the measurements. As operated at SW XIII, the MAS Fourier spectrometer could acquire a single interferometer scan in $< 0.5\text{ s}$. In order to reduce noise and turbulence-related intensity errors, either 2 or, in some cases, 5 scans of the instrument were coadded, and the total acquisition time was either $\sim 1\text{ s}$ or $\sim 2\text{ s}$. Transfer of the data files to the control computer and storage on the disk required $\sim 10\text{ s}$. Therefore, the path/background radiance data were delayed by approximately 11 s with respect to the obscurant data, and the measurement repetition rate was about $2.7/\text{min}$. The transfer and storage time could only have been reduced by reducing the spectral bandwidth and/or resolution.

TABLE 1. SPECTRAL INTERVALS COVERED BY THE MAS DURING SMOKE WEEK XIII		
Wavenumber (cm ⁻¹)	Wavelength (μm)	Channels
Near-infrared Configuration		
6230–6694	1.493–1.606	121
7442–8637	1.158–1.344	309
8993–10,127	0.987–1.112	294
Mid-infrared Configuration		
800–1200	8.333–12.500	208
2100–2220	4.505–4.762	62
2400–2900	3.448–4.167	259
4050–5000	2.000–2.469	493

3.2 LARGE APERTURE TELESCOPE

The other major MAS component that was used during the measurements was the 0.8 m-Coudé-mounted Cassegrain telescope. The folded optical path of a Cassegrain optical system allows for a very compact telescope. The essential feature of the Coudé mount is that segments of the optical axis are coincident with both the azimuth and elevation rotational axes. This design is becoming increasingly popular in astronomical telescopes, but it is very unusual in field measurement systems. The primary benefit is that the beam position on the optical bench is invariant with respect to telescope pointing. The image rotates as the telescope slews, but that fact is of no consequence in non-imaging applications, provided that the sensitivity of the instrument is constant across its input aperture. The Coudé mount is particularly important in applications that require a moving target to be tracked. The main advantage at SW XIII was that it allowed rapid switching between different lines of sight. Using a Coudé telescope is not without disadvantages, however, the most important of which are: 1) great difficulty in satisfactorily achieving the Coudé condition; 2) need for a large number of mirrors in the optical train; and 3) slight sensitivity to polarization. None of these disadvantages played a significant role in the SW XIII testing.

3.3 RADIATION SOURCE

The radiation source for the measurements was either of two ASL Multipath Transmissometer/Radiometer (MPTR) sources. The large divergence of the sources made it possible to use them with both the MAS and MPTR receivers. A significant advantage of the MPTR source design is that it is a composite of infrared globars and visible quartz-halogen lamps, and thereby provides broader spectral content than most single sources. The large divergence of the MPTR sources limits the range over which they are useful with a spectroscopic instrument because the relatively small amount of radiant power in each measurement channel rapidly decreases with increasing range. The two ranges that were used with the MAS were approximately 0.8 km and 1.1 km. The 1.1 km distance is near the maximum practical range for operating the MAS with an MPTR source.

4. RESULTS

In total, 1471 usable obscurant spectra were acquired during 111 trials at SW XIII. There were 147 trials during the entire test. MAS data were not acquired during 36 of these, 31 because the materials were effective primarily outside the MAS spectral bandwidth, 1 because of a power outage, and 4 because of instrumentation problems.

4.1 EXAMPLE SPECTRA

Examples of obscurant transmission spectra for several materials are shown in figs. 1–6. Figures 1 and 2 contain spectra of fog oil and aluminum powder and cover the spectral region from 6230–10,127 cm^{-1} . Figures 3–6 contain spectra of fog oil, kaolin, white phosphorus, and graphite and cover the spectral region from 800–5000 cm^{-1} . Intervals in which the atmosphere was opaque were excluded from the plots.

The signal-to-noise ratio of the spectra is very good in some of the subintervals, but poorer than desired in others. Each final spectrum is a mathematical combination of four raw spectra, and thus contains a contribution to the noise from each. The main reason that some intervals are noisy is that they are outside the optimum response region of the specific beamsplitter and detector. One goal of the measurements was to cover as much spectral bandwidth as possible, and the alternative to a low signal-to-noise ratio in some regions was often no data at all in those regions.

4.2 DISCUSSION OF THE RESULTS

Even a superficial examination of the spectra reveals many interesting aspects. In the near-infrared, the materials exhibited either an essentially flat transmittance curve or transmittance that fell off gradually with decreasing wavelength. The mid-infrared spectra of many materials such as graphite and brass demonstrated similar behavior. The mid-infrared spectra of other materials, however, contained considerable structure. Kaolin, fog oil, and white phosphorus often, and somewhat surprisingly, exhibited lower transmittance in the 8–12 μm region than in the 3–5 μm region, and the transmittance in the subinterval from 4.505–4.762 μm was often higher than in the remainder of the 3–5 μm region. The latter effect may be an artifact of the low signal level in that subinterval that resulted from strong atmospheric water attenuation. Many fog oil spectra had a pronounced absorption feature at about 3.45 μm . Again because of water vapor absorption, this feature was on the edge of a usable spectral interval and so sometimes did not show up strongly. It resulted from the C–H stretch of the hydrocarbon vapors present in the smoke along with the particles (Pouchert, 1981). This absorption has been observed much more clearly in fog oil spectra collected through drier air. Both white phosphorus and kaolin exhibited pronounced band-like features in the 8–12 μm region. For kaolin, a particularly strong feature was centered at about 9.7 μm , and another weaker feature at about 9.0 μm . The stronger of these is of particular interest because of its proximity to the 9.6 μm CO_2 laser wavelength and the fact that kaolin is a common constituent of natural and man-made dust. The spectra presented here only hint at the wealth of information that becomes available with spectrally resolved measurements.

4.3 NOISE AND ERROR CONSIDERATIONS

Several factors contributed to the fact that the signal-to-noise ratio was not as high as desired in some spectral regions. For example, a broadband transmissometer covering the 8–12 μm spectral region effectively sums over 200 MAS Fourier spectrometer channels into a single channel. The spectrally resolved measurement must overcome this handicap in radiant power. This is the main reason that a large collecting aperture is used with the MAS. The design of the Coudé telescope itself reduces the optical throughput compared with other designs of similar aperture. Several additional reflecting surfaces are required, and each introduces some loss. The flexibility of the Coudé system outweighs this disadvantage, however. Steps taken to improve the signal-to-noise ratio of the spectra included keeping the optics as clean as possible, and coadding as many scans as possible within the constraint of maintaining high temporal resolution.

The large number of reflectors could also affect the baseline accuracy of the spectra. Even though the emissivity of a high reflector is small, the total thermal power emitted into the beam by all of the surfaces could be significant. Because this radiation was peaked near 10 μm , the potential errors were in the 8–12 μm spectral region. Although background emission was removed in the data

reduction process, it was important to collect clear air and background data in close temporal proximity and to minimize temperature changes of the optics during the measurement cycle. An important step was to minimize sunlight falling on the optics.

Atmospheric turbulence was another source of baseline errors. Atmospheric turbulence causes the phenomena of beam spread and wander. One observable effect of beam spread and wander is fluctuation of the apparent intensity of the source. This fluctuation takes place over a range of frequencies, but there is a significant component at frequencies under 1 Hz. Therefore, measurements conducted with an acquisition time on the order of 1 s can exhibit baseline variation because of this effect. Under high turbulence conditions, intensity fluctuations as high as ± 20 percent were observed during SW XIII, although ± 5 percent to ± 10 percent was more typical. If the clear air data were subject to the same level of turbulence-induced variation, even larger variation would be expected in the measured obscurant transmittance. There is a definite need to average the clear air data over a time period long enough to accurately approximate the mean apparent source intensity. The MAS clear air data were acquired over a period of approximately 50 s which was found to yield highly consistent spectra.

Background temperature variation was yet another source of spectral baseline errors. The methodology of slewing the telescope off the source to characterize the path and background radiance implicitly assumed that the scene selected to acquire these data was optically identical to the scene that included the source. The source itself obscured a part of the background and so this condition could not be met rigorously. In reality, the MPTR source at 1.1 km filled only about 2 percent of the field-of-view and so background obscuration was a small source of error. However, if the optical characteristics of the two scenes, i.e., temperature, reflectivity, emissivity, etc., were different, the path radiance subtraction could introduce errors. Although care was taken to ensure that the two regions were as close as possible in their characteristics, occasional baseline errors were noted that apparently originated in background variation. The main symptom of this effect was a large positive or negative slope of the transmittance curve at the long wavelength end of the spectrum. This effect occurred primarily during sunny periods, and it probably resulted from subtle differences in the topography and vegetation, which affected the rate of solar insolation, and ultimately, the ground temperature.

4.4 INTERFERENCE BY ATMOSPHERIC ATTENUATION

As noted above, useful transmittance information could not be derived for regions in which the atmosphere was opaque. The most important contributor to atmospheric infrared attenuation is water vapor, and in a low-lying, hot, humid area such as Eglin Air Force Base, the atmospheric water content can be very high. Therefore, the usable spectral intervals were significantly smaller compared with data collected through drier air. Using the shorter path whenever possible was the only available means to minimize atmospheric interference.

5. TRANSMISSOMETER SIMULATIONS

An important advantage of spectrally resolved measurements is that the data can be used to predict the performance of arbitrary transmissometer and electro-optical systems. One spectrum from each of the four sets of mid-infrared spectra in figs. 3–6 was used to simulate the performance of: 1) an actual broadband transmissometer; 2) a device whose response was flat across the entire 8–12 μm region; 3) a device whose response ramped up from 12 μm to 11.76 μm and then back down to 0 at 8 μm ; 4) a narrow band device centered at 10.6 μm ; and 5) a narrow band device centered at 9.6 μm . The transmissometer response curve was taken from Davis and Sutherland (1990), and corresponds to the "SMART" system. The curve was digitized at 0.1 μm intervals. A 1000 °C blackbody was assumed as the source for this system, for the device with the flat response, and for the device with the ramp response; and 10.6 μm and 9.6 μm lasers were assumed as the sources for the narrow band devices. The spectra that were used in the simulation are indicated in the figures.

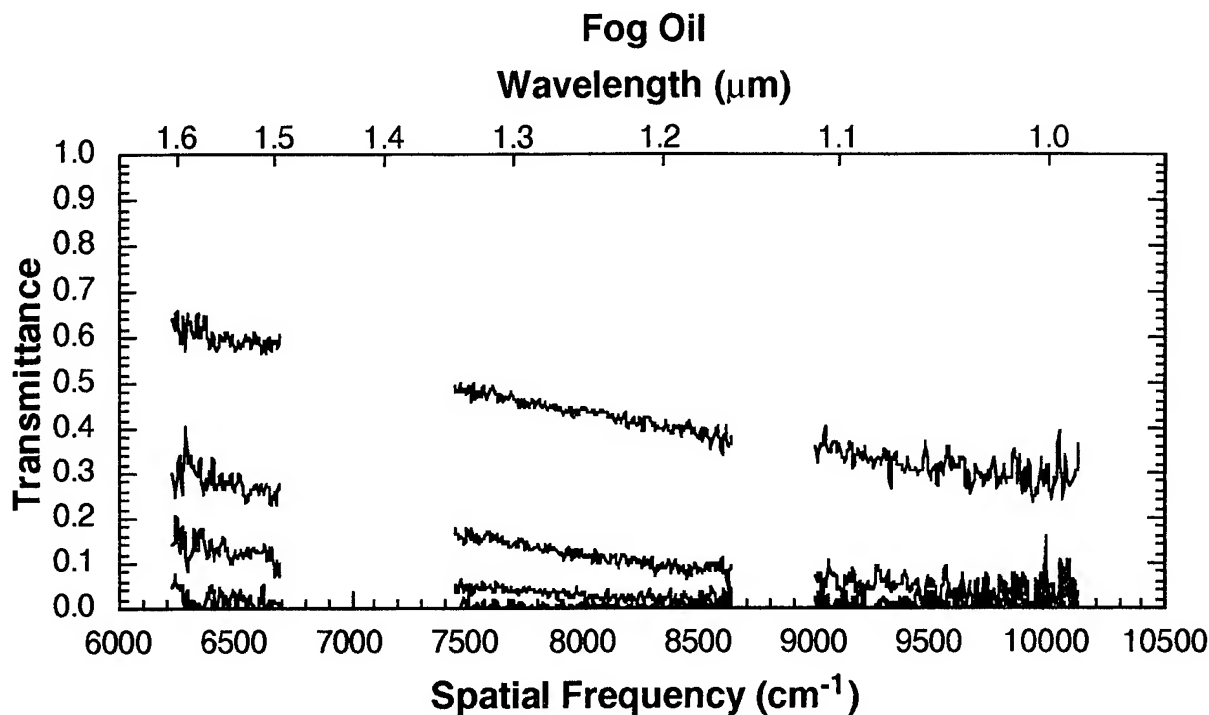


Figure 1. Near-infrared transmittance spectra of fog oil. Each spectrum represents the transmittance of the obscurant in a different one-second interval during Trial 01001.

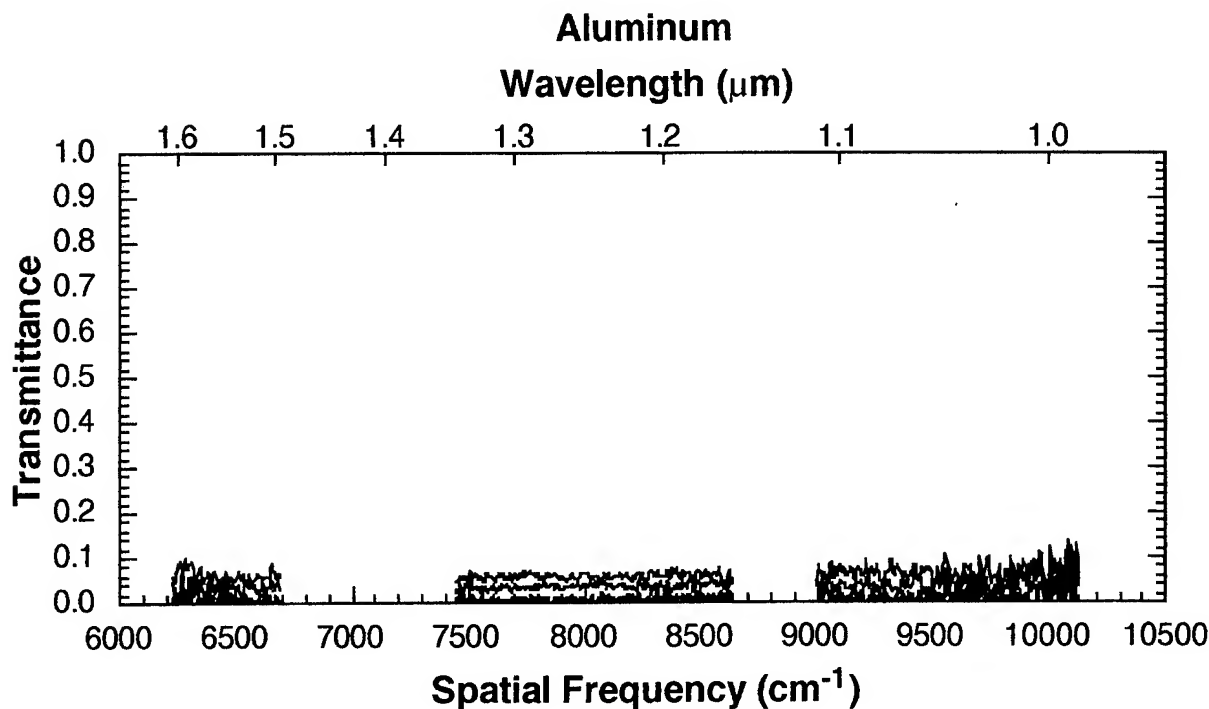


Figure 2. Near-infrared transmittance spectra of aluminum. Each spectrum represents the transmittance of the obscurant in a different one-second interval during Trial 14508.

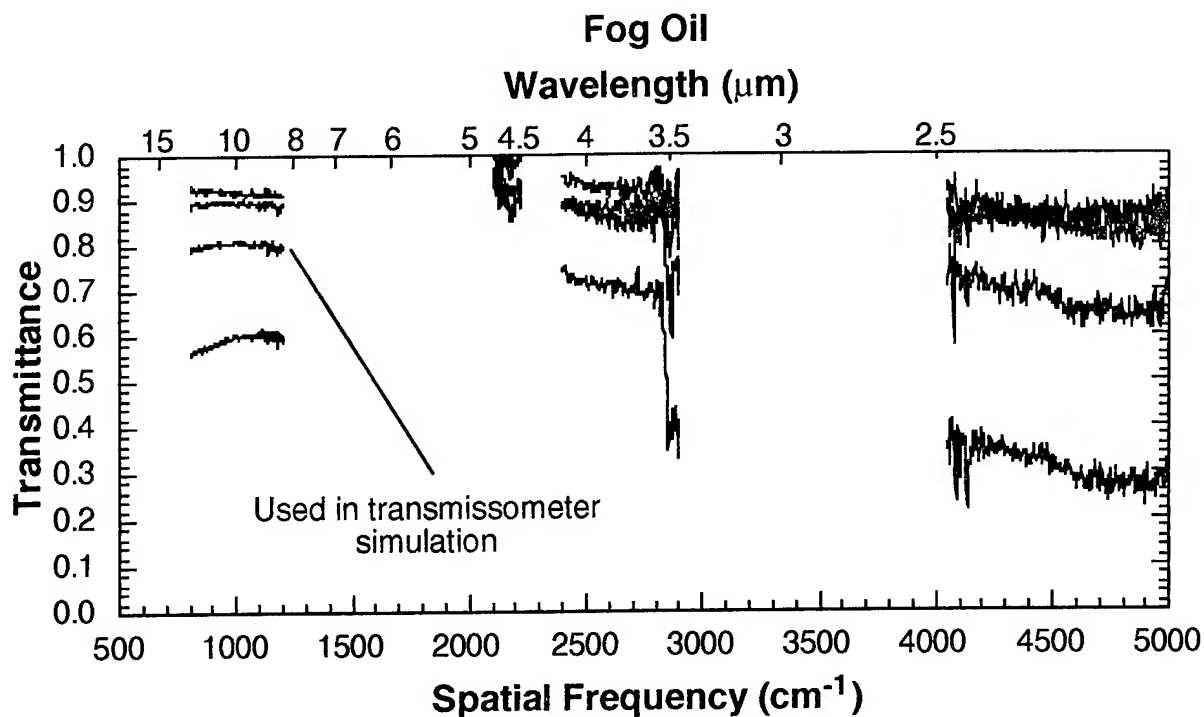


Figure 3. Mid-infrared transmittance spectra of fog oil. Each spectrum represents the transmittance of the obscurant in a different two-second interval during Trial 02701.

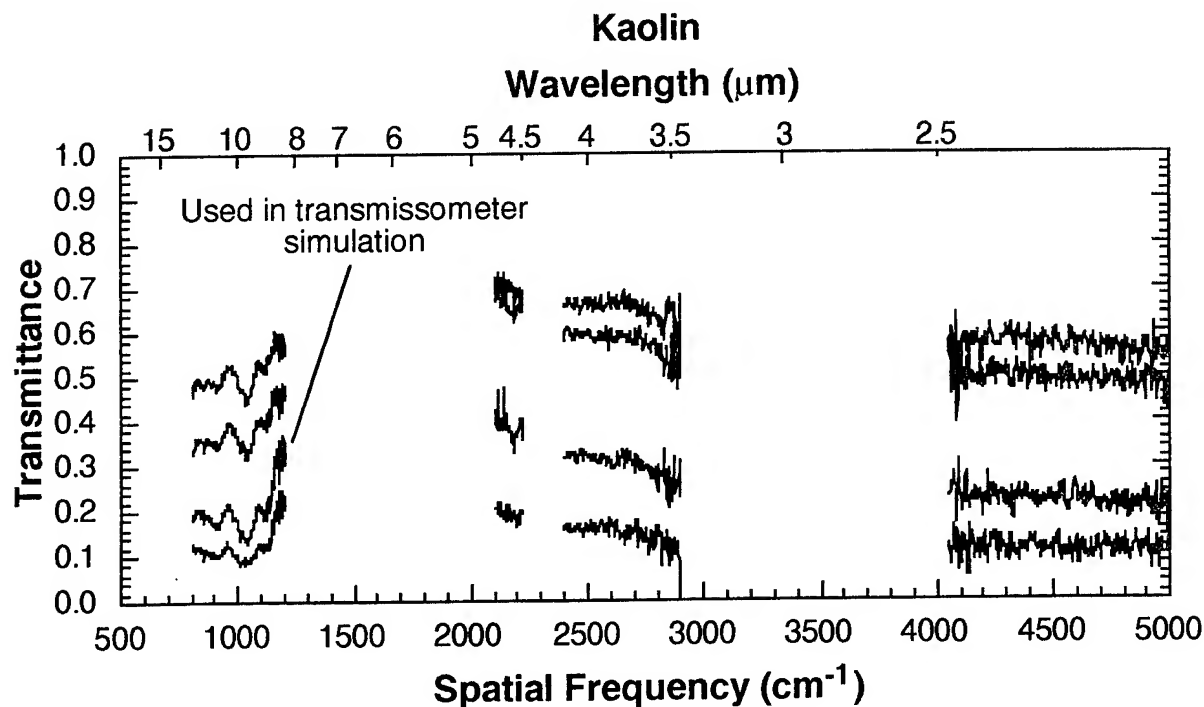


Figure 4. Mid-infrared transmittance spectra of kaolin. Each spectrum represents the transmittance of the obscurant in a different two-second interval during Trial 04109.

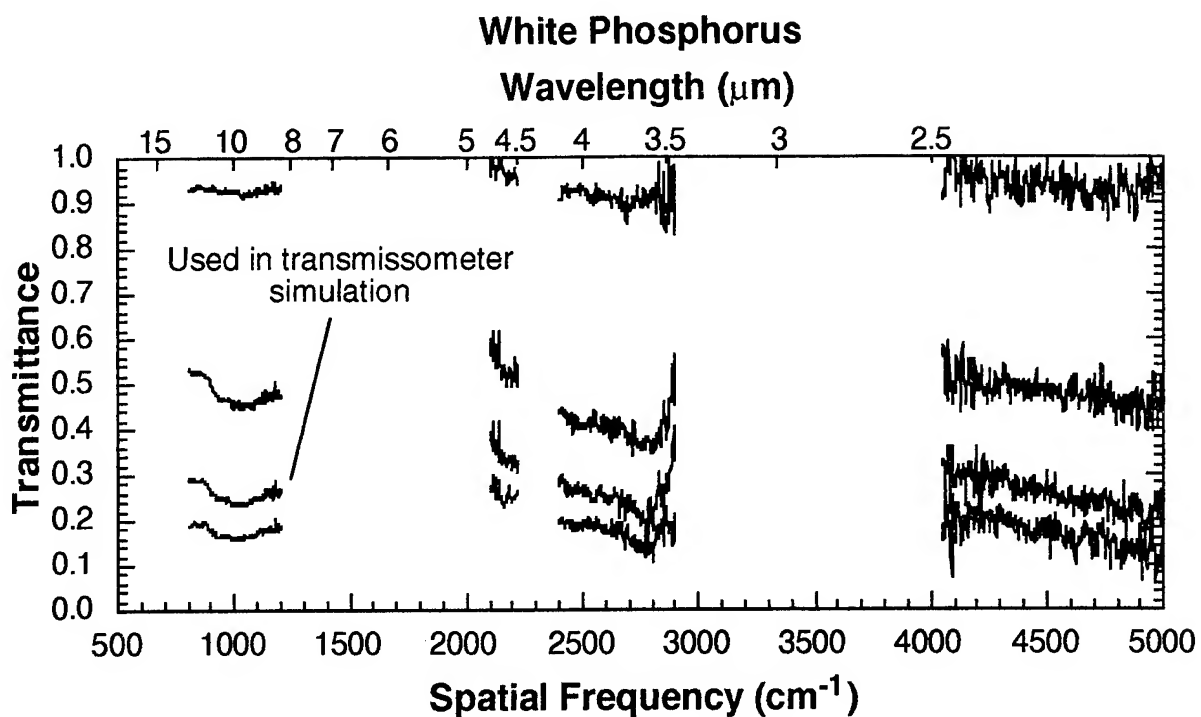


Figure 5. Mid-infrared transmittance spectra of white phosphorus. Each spectrum represents the transmittance of the obscurant in a different one-second interval during Trial 01712.

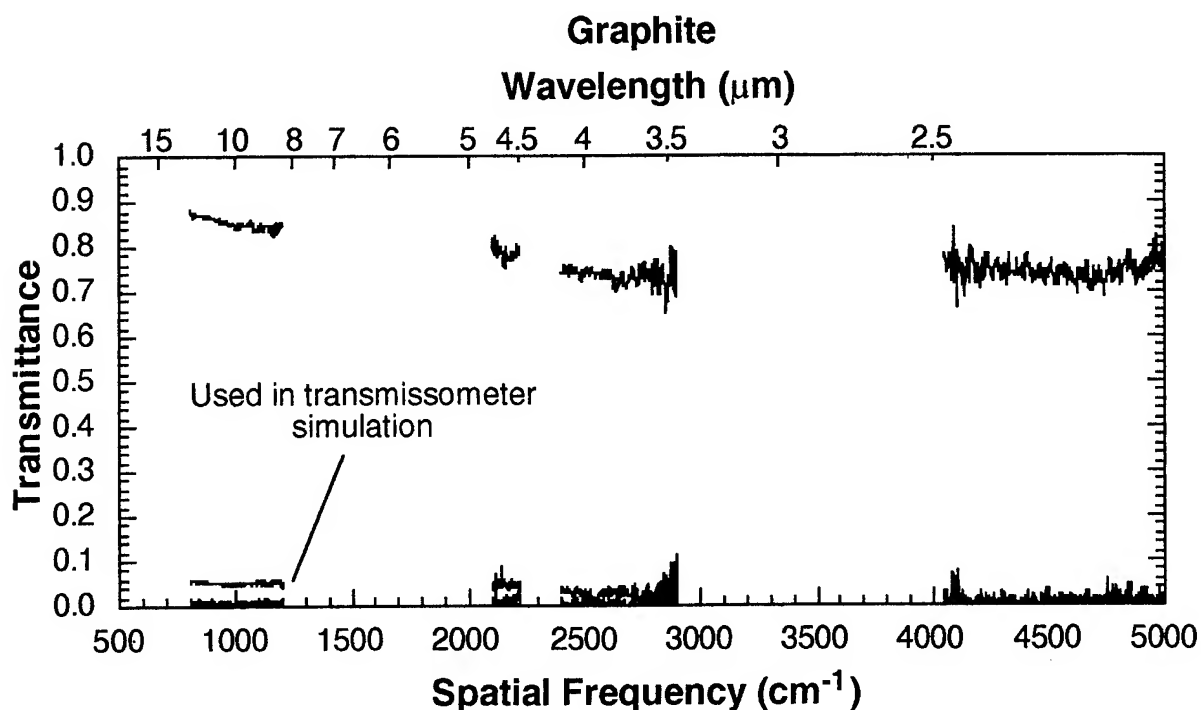


Figure 6. Mid-infrared transmittance spectra of graphite. Each spectrum represents the transmittance of the obscurant in a different two-second interval during Trial 02811.

The simulations were performed by convolving the measured transmittance function with the product of the response function and the source function. Because the instruments being simulated recorded only a single channel, the convolution reduced to a summation. It was assumed that the spectral resolution of the measured transmittance was sufficient to resolve any structure present because of the obscurant. In all cases, the transmittance that would have been measured with the specified device, had it been operating at the time of the spectral measurement, was computed. The results of these simulations are presented in table 2. From the results in this table, it is clear that the broadband transmissometer measurements can be misleading when applied to predictions of the performance of devices with different response functions. As expected, the results for the broadband transmissometer simulation were similar to those for the other systems when the transmittance of the material was nearly constant (fog oil and graphite). Likewise, the broadband system result agreed with the result for a flat response device. The broadband transmissometer simulation produced results significantly different from a laser transmissometer when the transmittance at the laser frequency deviated greatly from the mean value in the band. The large discrepancy between the SMART and the 9.6 μm laser values for kaolin illustrates this point. For broadband devices with much different response functions, discrepancies also appear. A methodology similar to this could be used to help resolve the inconsistencies between broadband transmissometers.

TABLE 2. COMPUTED TRANSMITTANCE VALUES FOR VARIOUS TRANSMISSOMETER AND OBSCURANTS				
	Fog Oil	Kaolin	White Phosphorus	Graphite
"SMART" response	0.80	0.21	0.26	0.05
Flat response	0.80	0.21	0.26	0.05
Ramp response	0.80	0.19	0.26	0.05
10.6 μm laser	0.81	0.20	0.25	0.05
9.6 μm laser	0.80	0.13	0.24	0.05

6. CONCLUSIONS

The measurements made with the Mobile Atmospheric Spectrometer at Smoke Week XIII clearly illustrate the advantages of spectrally resolved transmittance measurements in obscurant characterization tests. When the transmittance spectrum is known in detail, it is possible to simulate the performance of arbitrary electro-optical devices in the obscured environment. Spectrally resolved transmittance measurements can be used to more fully understand the basic physics of obscuration and to test and validate models of the underlying processes.

REFERENCES

- Davis, R. E., and R. A. Sutherland, 1990: The Effects of Instrumental Artifacts in AAODL Transmissometer Data. In Proceedings of the Smoke/Obscurant Symposium XIV, Volume I, Chemical Research, Development, and Engineering Command, Aberdeen Proving Ground, Maryland 21010-5423.
- Peterson, W. A., and W. M. Gutman, in preparation: Smoke Week XIII Test Support, Mobile Atmospheric Spectrometer, U. S. Army Atmospheric Sciences Laboratory, White Sands Missile Range, New Mexico 88002-5501.
- Pouchert, C. J., 1981: The Aldrich Library of Infrared Spectra, Edition III, Aldrich Chemical Company, Inc., Milwaukee, Wisconsin 53233.

**A SYNOPTIC TACTICAL SMOKE
COMBAT MODEL**

W. Michael Farmer
Bruce W. Kennedy
The Bionetics Corporation
Las Cruces, NM 88001

and

Van R. Jones
USA Chemical Research, Development, and
Engineering Center
Aberdeen Proving Ground, MD 21010

ABSTRACT

The Tactical Smoke Model (TACSMK) provides smoke/obscurant developers and users with a focused war game capability for the purpose of evaluating smoke and obscurant characteristics and effects on the results of combat. It combines combat power theory with practical knowledge of weapons and army structure to evaluate the effects of an obscured battlefield on force exchange ratios. The model, which is structured in spreadsheet format and compatible with desktop and laptop computers, allows the user to input 52 combat variables plus 63 smoke and electro-optical (EO) variables and graphically observe the results.

1. INTRODUCTION

This paper presents an overview of an ongoing effort to evaluate smoke screen effects using deterministic combat models developed from Lanchester's equations (Dolansky, et al 1962). The objective of this effort is to develop an easily accessible Tactical Smoke (TACSMK) engineering model which will provide smoke/obscurant developers with an understanding of the impact of smoke/obscurant material characteristics on combat. By using deterministic models of combat and relatively simple algebraic equations for specifying electro-optical sensor performance against smoke/obscurant countermeasures, the engineering model can be programmed using commercial spreadsheet software and run on personal computers. Spreadsheet software and personal computers are readily accessible to virtually all the smoke/obscurant development community.

The TACSMK model consists of three modules as shown in figure 1. The first, Tactical Force (TACFRC), computes the fraction force exchange ratio between opposing armies. Currently, the module

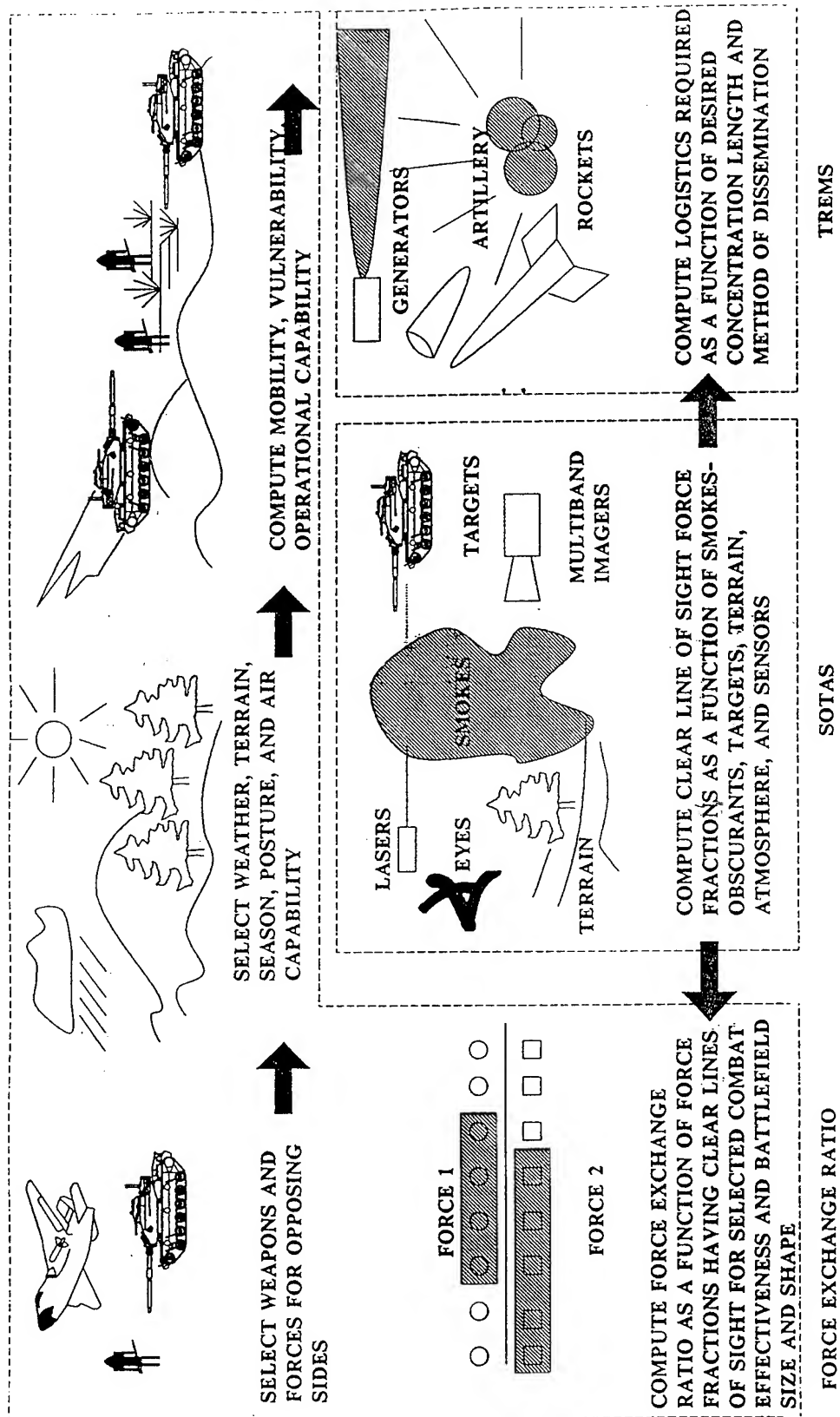


Figure 1. Computational logic for the TACSMK model.

has fifteen pre-selected scenarios ranging from corps to battalion level. However, the user can generate any arbitrary force structure desired. Factors such as force strength, weather, terrain, season, force posture, air capability, mobility, and operational capability are included as inputs. The second module is Smokes Obscurants Targets Atmospheres Sensors (SOTAS) which calculates fractional clear line-of-sight as a function of smoke concentration length, and considers smoke types, targets, terrain, atmospheric conditions, and electro-optical characteristics. The third module is Tactical Resources Evaluation Modeling System (TREMS) which computes logistics required as a function of desired concentration length and method of dissemination.

2. FORCE COMPARISON RATIO AND THE TACFRC MODULE

There are at least three classes of Lanchester equations which might be appropriate for smokes in combat: 1) linear law, 2) square law, and 3) combination linear and square law. Linear law Lanchester equations assume that combatants attack hidden targets. Square law equations assume combatants have clear targets; and, equations representing a combination of linear and square laws assume a mixture of clear and hidden targets. A set of Lanchester equations combining linear and square laws for clear/obscured target mixtures was developed after performing a literature review. The equations are used to compute the force exchange ratio for hidden and clear targets.

To maximize TACSMK accessibility and use, an unclassified method for computing casualty inflicting capability for combatants was sought. The method was found in the Quantified Judgement Model (QJM) (Dupuy 1985). The QJM computes force strength and weapon lethality for a wide range of combat factors including terrain, weather, season, and operational and behavioral variables. Rather than expressing force strength in simple numbers of combatants, as is normally done with the Lanchester equations, the QJM provides a method for computing force strength in terms of weapon lethality, troop dispersion, weapons type, numbers of troops, and force effects variables. Because the QJM uses tables of "combat multipliers" for the combat variables, it is particularly amenable to spreadsheet analysis. Use of the QJM method in TACSMK provides a broad base of potential combat scenarios in which smokes and obscurants can be used and evaluated.

The most reasonable forms of Lanchester's equations to use for smoke screen related battles are those which incorporate a combination of both linear and square law assumptions. The linear, square law, and guerilla warfare (one side completely hidden, opposing side exposed) forms of Lanchester's equations can be imagined to be special cases for the general forms of equations using smoke screens. For example, linear law

formulations would be expected if the smoke screen fully blinded both sides; the guerilla warfare form would correspond to the case where one side could see and the other could not; the square law formulation could represent the case where neither side was obscured.

Smoke effects on attrition rates are of at least two distinct classes. First, smoke affects the performance of weapons systems as an environmental force effects variable. Smoke should therefore appear as a parameter used to weight the aggregate weapon lethality, and it should be used as an environmental force variable. Second, smoke affects how a battle is fought and therefore determines the form of Lanchester's equations which should be applied to the analysis of the battle. Smokes are included in TACSMK as a weighting factor in the lethality and as a scaling parameter for determining the fractions of troops for which linear and square law assumptions will apply.

The following example illustrates the output of the TACFRC module. Figure 2 shows the exchange ratio results of a U.S. cavalry regiment under attack by a USSR motorized infantry regiment as a function of defender clear line of sight fraction for fixed attacker clear line of sight fractions. The Soviet side has a combined superior force strength based on types of weapons and operational lethality indices of approximately 2:1. Other inputs to the model for this output include terrain, weather, season, air strength, posture, mobility, vulnerability, combat effectiveness value, and size and shape of the battlefield. In this example, if both sides have unobscured vision, then the attacker/defender force exchange ratio is approximately 0.7. If the defender can reduce the attacker's clear view to sixty percent, then the attrition rate shifts in favor of the defender to about 1.2:1. In an extreme case where the defender has clear line-of-sight and the attacker is completely blinded the defender advantage changes dramatically to 40:1.

3. THE SOTAS MODULE

TACSMK also produces an evaluation of smoke and obscuration effects on vision and electro-optical sensors on the battlefield, and computes the clear line of sight fractions for opposing sides as a function of smoke/obscurant concentration length. This portion of the model is named Smokes Obscurants Targets Atmospheres Sensors (SOTAS). The inputs include meteorological conditions, visual and thermal contrast, luminance and sky/ground contrast ratio, target range and height, Johnson criteria, laser characteristics, smoke and obscuration type, extinction coefficients as a function of wavelength, and force strength distribution. Figure 3 shows the fractional clear line-of-sight as a function of smoke

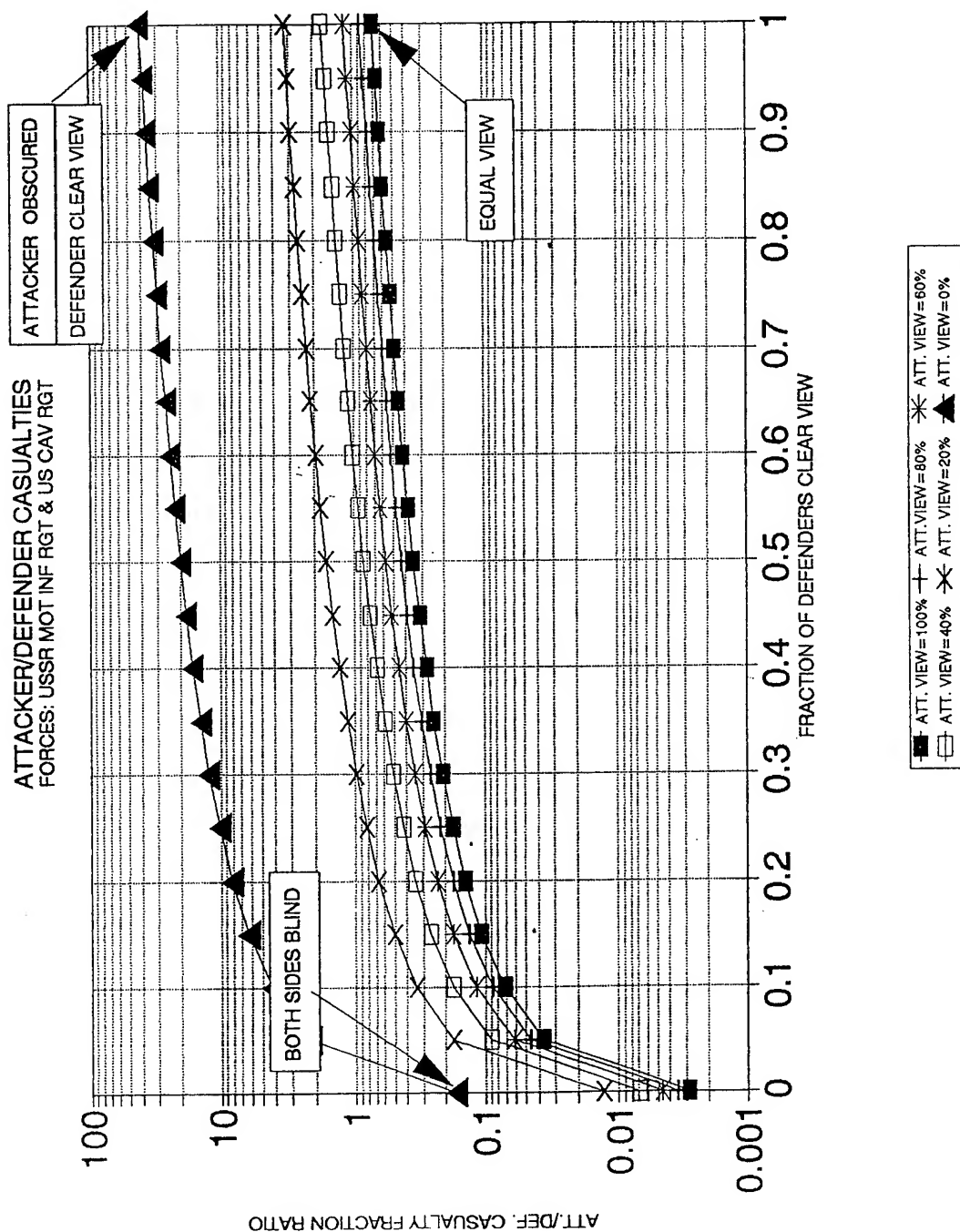


Figure 2. Exchange ratio for U.S. armored cavalry regiment versus a USSR motorized infantry regiment as a function of defender (U.S.) clear line of sight fraction for fixed values of attacker clear lines of sight fractions. This is the output of the TACSMK module.

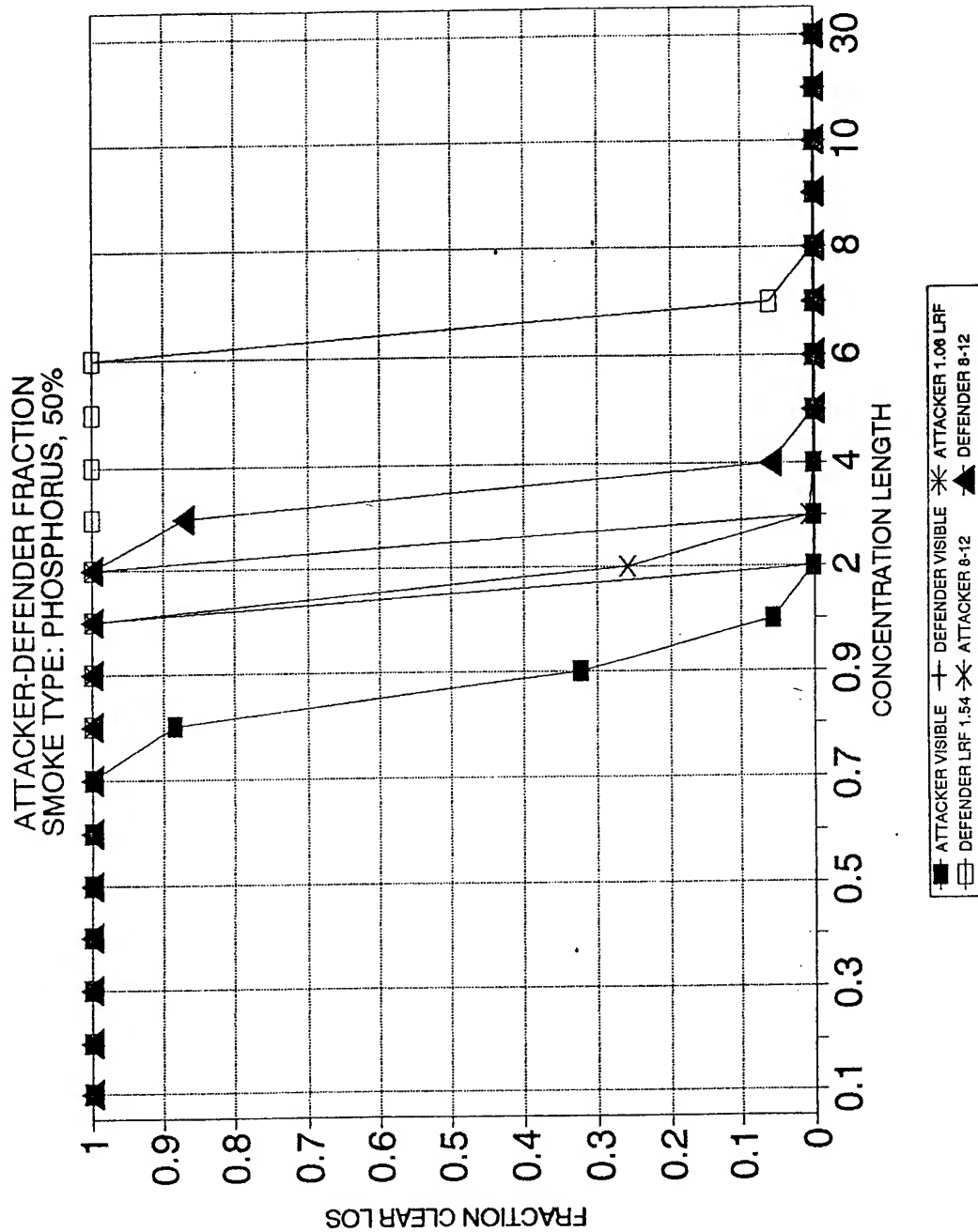


Figure 3. Clear line of sight fractions as a function of concentration length for U.S. armored cavalry regiment and USSR motorized infantry regiment utilizing electro-optical weapons systems in phosphorous smokes. This is the output of the SOTAS module.

concentration length for phosphorus smoke at 50 percent relative humidity. In this example the U.S. thermal imager has better minimum resolvable temperature (MRT) than an assumed Soviet counterpart, and the U.S. laser rangefinder operates at $1.54\mu\text{m}$ wavelength compared with an assumed USSR $1.06\mu\text{m}$ laser. Figure 3 shows equal attenuation of the visible wavelength but superior performance by the U.S. laser and thermal imager systems. It shows that if the defender can generate a smoke cloud with a concentration length of 3, then the attacker thermal imager would be virtually blind while the defender system would still have a clear view of the opposing side for approximately 90% of his force strength. Figure 2 shows that if this were the case, the exchange ratio would change from 0.7 where both sides have 100% clear lines of sight to opposing side targets and the attacker has a clear advantage to an exchange ratio of nearly 40 where the defender has a strong advantage.

4. THE TREMS MODULE

The Tactical Resources Evaluation Modeling System (TREMS) module of TACSMK permits the user to use the output of SOTAS (figure 3), to make an immediate assessment of smoke screen effectiveness. This module presently addresses production of smoke screens using both generators and munitions, including liquid obscurants such as fog oil, powder such as graphite or brass, rocket-dispensed phosphorus wedges, and puff clouds produced from grenades or other sources. Examples of the output are shown in figures 4(a)-4(d) for generated fog oil. User inputs include required visual threshold, material density, flow rate, generator efficiency, axial wind speed, required line-of-sight height, and material cost. Figure 4(a) plots the concentration length as a function of distance downrange from the generator for Pasquill stability categories A through F. Figure 4(b) calculates the cost per hour, figure 4(c) produces the gallons per hour required, and figure 4(d) indicates the number of generators needed to yield the desired screen.

5. CONCLUSION

TACSMK is an engineering tool. It is intended to provide insight into the results of battlefield engagements where smoke and obscurant are used. It does not large tactical wargame analysis; rather, TACSMK should be used as an expectation guide to scenarios and results from more exacting wargame models currently being used. TACSMK will also help the user to determine the parameters that most strongly affect smoke effectiveness in combat.

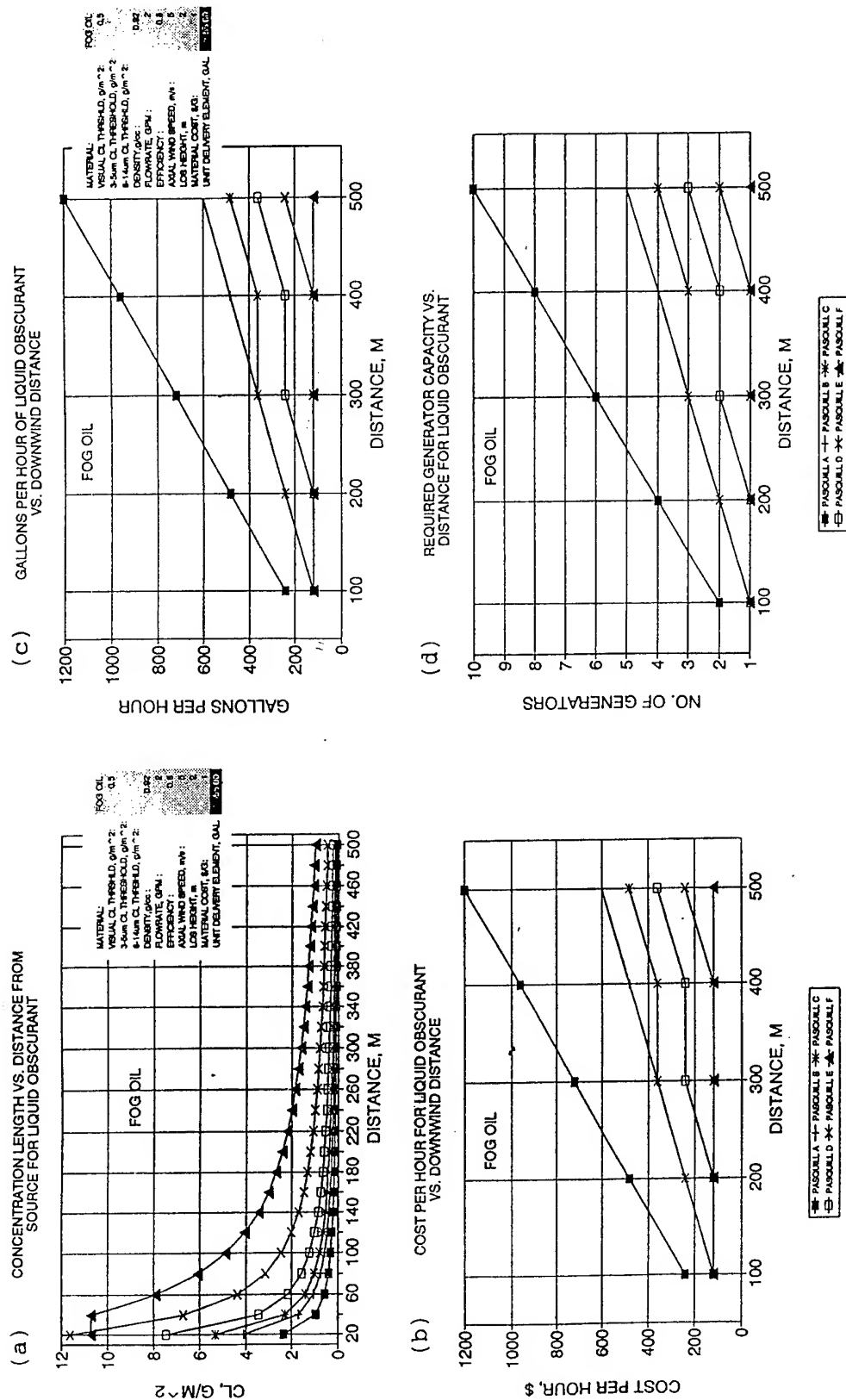


Figure 4. (a) Concentration length v. distance downrange from generators; (b) cost per hour of material v. distance; (c) gallons per hour v. distance; (d) number of generators v. distance for effective smoke screen.

REFERENCES

Dolansky, Ladislav, 1962: Present State of the Lanchester Theory of Combat, Operations Research, 12, pp. 344-358.

Dupuy, Col. Trevor N., 1985: Numbers, Predictions, and War, HERO Books, Fairfax VA, 1985 Revised Edition. . .

Farmer, W.M., and Kennedy, Bruce W., 1991, A Synoptic Tactical Smoke Combat Model for Conducting Survivability Studies, Proceedings of the Smoke/Obscurants Symposium.

VISUALIZATION AND QUANTITATIVE MEASURES OF SMOKE PLUME INTERMITTENCY

by

Charles L. Medler and Maureen E. Cianciolo
TASC
55 Walkers Book Drive
Reading, MA 01810

Models used by certain modules within EOSAEL predict mean-values of obscurant concentrations and estimates of line-of-sight (LOS) transmission under those mean-value conditions. However, because of turbulent motion in even relatively undisturbed environments, the spatial distributions of obscuring (i.e., energy absorbing and/or scattering) particles can be highly intermittent. Spatial regions within obscuring screens with reduced particle concentration can lead to LOS transmissivity above critical thresholds, exposing our forces to enemy threats. This poster paper will present models and visualizations of intermittent smoke plumes based on work done under contract to The Atmospheric Sciences Laboratory. The models merge the mean-value (Gaussian) models with outputs of a prefractal approximation of the intermittency function. We will include analysis results of data collected from both field tests and the model realizations that will demonstrate consistencies and inconsistencies between the model structure and the real-world observations. Important details of the prefractal algorithm used by the model will also be discussed.

(The full text of this paper was unavailable at press time.)

UVTRAN Demonstration

James B. Gillespie
U.S. Army Atmospheric Sciences Laboratory
White Sands Missile Range, NM 88002-5501

Edward M. Patterson
Georgia Institute of Technology
Atlanta, Georgia 30332-0800

UVTRAN , a program to model atmospheric propagation and lidar backscattering for the 200 nm to 700 nm spectral region, is demonstrated on a PC. This model combines a UV transmission code with a backscatter code for Mie and fluorescence lidar return calculations and a sky background radiance code into a modular, menu-driven, user-friendly FORTRAN program for an IBM PC compatible system. The model includes attenuation due to molecular scattering, molecular absorption, and aerosol extinction. The wavelength dependence of the aerosol attenuation is parameterized in terms of visual range. The molecular absorption includes oxygen, ozone, and several trace gases. The gaseous absorption is low resolution, but includes six high resolution UVVIS laser wavelengths that may be used for the backscatter calculations. User-changeable default parameters are included in the model.

(The full text of this paper was unavailable at press time.)

COMBIC 92: NEW AND IMPROVED

Scarlett D. Ayres
U.S. Army Atmospheric Sciences Laboratory
White Sands Missile Range, New Mexico 88002-5501, USA

ABSTRACT

The Combined Obscuration Model for Battlefield-Induced Contaminants (COMBIC) is part of the Electro-Optical Systems Atmospheric Effects Library (EOSAEL). COMBIC predicts the time-dependent transmission at seven different wavelengths through debris raised by high-energy explosives and vehicular movement, through smoke from phosphorus and hexachloroethane munitions, through smoke from diesel oil fires, through generator disseminated fog oil and diesel fuel oil, and other sources. Obscurant clouds are modeled as superpositions of Gaussian plumes and puffs transported and diffused over flat terrain by a wind field that does not vary horizontally. Several significant changes have been made to COMBIC92 that constitute a significant improvement of COMBIC87. This paper discusses these modifications and their effects on users. The modifications include (1) changing the methodology to increase computational speed integrating through plumes, (2) adding several new munitions to the default tables, and (3) modifying the printer-plot for easier readability.

1. INTRODUCTION

Significant amounts of airborne dust, smoke, and debris add to the battlefield environment. Resulting reduction in transmission of electromagnetic energy at visual, near-, mid-, and far-infrared (IR) wavelengths affects performance of many electro-optical (EO) systems. Even freshly produced high-explosive (HE) dust momentarily reduces millimeter wave (MMW) transmission. This results in a need to quantify the effects of obscurants on transmission of the visible through IR wavelengths for the realistic battlefield to determine the effectiveness of EO sensors. COMBIC was developed by the U.S. Army Atmospheric Sciences Laboratory (ASL) to meet this goal. COMBIC models the effects of reduction in electromagnetic energy (visible through IR wavelengths) by combining the munition characteristics with meteorological information of an idealized real world. It produces transmission histories at any of seven wavelength bands for a potentially unlimited number of sources and lines of

sight (LOS). The model was designed to be computationally fast without losing accuracy for wargame modeling applications. This was a very major concern in the early development of the model and had a big influence on the approach.

Execution speed, modeled cloud detail, and prediction accuracy are all competing design criteria in obscuration codes. COMBIC seeks a reasonable balance between these factors, but it has a greater emphasis on reducing computation time for large scenarios. This led to a separation of calculations into two parts or "phases." The first phase concentrates on accuracy and details of the physical processes acting on single obscurant clouds. The second phase is designed to be fast and to make efficient use of results from the first phase to simulate large obscuration scenarios.

In phase 1, a cloud history file is preprocessed "off-line" for one or more obscurant source types selected from a menu or defined through user inputs. Except for wind direction, all meteorological influences are included in these "phase 1" calculations of transport, rise, and diffusion of the obscurant clouds. Additional effects of the atmosphere on aerosol properties are also included. Four-dimension clouds (space and time) are compressed to tables of two-dimension subcloud profiles (about 370 values per subcloud). The total cloud for each user-selected source that goes into the history file can contain up to five subclouds.

In separate, "phase 2" calculations, COMBIC builds a user-defined scenario of smoke and dust sources. Table lookup and scaling of phase 1 histories are used to compute cloud concentrations at any given time. Path-integrated concentration is determined for each observer-target pair, and transmittance is computed at each of seven wavelength bands for (in principle) any scenario that is defined by multiple sources and active LOS. Phase 2 emphasizes computation speed. Efficient techniques are used to determine the path-integrated cloud concentrations over each LOS.

2. NEW MUNITIONS AND OBSCURANTS

Extensions to the obscurant sources in COMBIC for EOSAEL87 include the addition of extinction coefficients for graphite. Several new munitions have been added like the M76 IR grenade, L8A1 and L8A3 grenades. The characteristics of these munitions are stored in the model menus. The COMBIC model also now has the capability of modeling the dust produced by muzzle blasts.

2.1 M76 IR GRENADE

Table 1 shows the statistics for the M76 IR grenade based upon one trial. Spitznagel and Ayres (1989) describe the statistical methodology used to evaluate COMBIC. A data set of one hardly provides good statistics. However, several items can be noted from this one trial. Note the near identical values of the statistics across the spectrum due to the identical

extinction coefficients for all wavelengths. $M1$ is a measure of dispersion that denotes the average distance from the ideal line $COMBIC_i = DATA_i$. A variant $M1_a$ is defined that whenever COMBIC predicts greater than 90 percent transmission and greater than 90 percent transmission is measured, the data pair is discarded. The sharp decrease of $M1_a$ over $M1$ appears odd, but the M76 IR grenades have a very sharp decrease and increase in transmission, which is successfully modeled by COMBIC. The large negative time shift causes the COMBIC data to be almost completely out of phase with the measure values; that is, when COMBIC transmission is high, the measure data is low and vice versa. Eliminating the data of COMBIC and measured trial data that exceed 90 percent level transmission eliminates the only portions of the two curves that agree, causing the low $M1_a$. Note $M1 = .41$ improves to .71 when COMBIC is shifted 26 s to the right, causing the bias at shift to be miniscule. This one trial suggests that the agreement between model and data is very good.

TABLE 1. STATISTICS FOR M76 IR GRENADES

Wavelength	M1	$M1_a$	$M1_b$	Bias	Best M1	Shift	Bias At Shift
0.4 μ m-0.7 μ m(1)	.40	.04	-.06	.09	.70	-27.	.01
0.7 μ m-1.2 μ m(1)	.41	.13	-.03	.09	.69	-27.	.02
1.06 μ m(1)	.41	.13	-.03	.09	.69	-27.	.02
3.48 μ m(4)	.43	.18	.02	.06	.75	-22.	.00
8.0 μ m-12. μ m(1)	.39	.05	-.07	.09	.71	-28.	.01
10.6 μ m(1)	.40	-.04	-.10	.08	.72	-26.	.01
Combined(9)	.42	.11	-.02	.08	.73	-25.	.01

2.2 L8A1/L8A3 RP GRENADE

The L8A1/L8A3 RP GRENADE is modeled as a combination of three buoyant subclouds consisting of a puff, plume, and stem. The plume contains 92.5 percent of the mass and burns for 658 s. Total fill weight is .794 lb. Table 2 is a statistical evaluation of COMBIC modeling the grenade. Best $M1$ of table 2 is computed by shifting the COMBIC data by the time in seconds listed under the SHIFT column and then determining the measure. This measure was developed to identify trials in which a change in windspeed or wind direction caused the cloud mass to move across the LOS sooner or later than COMBIC predicts, or if the start time of the trial does not match COMBIC's start time. Best $M1$ demonstrates that most of the disagreements for these trials are caused by discrepancies in the start time. This time lead and/or lag could cause the range statistics seen in these trials for $M1_a$ and $M1_b$. Agreement between data and the COMBIC model is good, though the negative bias indicates the model overpredicts the CL.

TABLE 2. STATISTICS FOR L8A1 and L8A3 GRENADES

Wavelength	M1	M1 _a	M1 _b	Bias	Best M1	Shift	Bias At Shift
0.4 μ m-0.7 μ m(16)	.31	.28	.27	.06	.68	-17.	.04
0.7 μ m-1.2 μ m(13)	.23	.21	.11	-.27	.65	83.	-.13
1.06 μ m(13)	.28	.25	.16	-.23	.69	73.	-.10
3.48 μ m(19)	.67	.63	.58	-.02	.87	49.	.00
8.0 μ m-12. μ m(8)	.49	.48	.46	-.14	.80	119.	-.04
10.6 μ m(3)	.90	.87	.83	.02	.91	10.	.02
Combined(72)	.43	.40	.35	-.10	.75	51.	-.04

2.3 MUZZLE BLAST

Anyone who has seen large artillery fired knows that, in the process of firing, dust is lofted into the atmosphere. Questions arose in 1990 as to whether the dust produced by muzzle blasts can affect transmission of electromagnetic energy. The user community requested ASL to include muzzle blasts as a source of obscuration. Very little real data existed for muzzle blast. The only data available for muzzle blast was imagery. Virtually no transmittance data existed that could be utilized by COMBIC for comparison purposes. Therefore, the user should be aware that COMBIC models muzzle blast qualitatively. Muzzle blast is modeled as a single, instantaneous, nonbuoyant cloud of persistent dust. The initial cloud has a radius of 15 m x 10 m x 7 m and is treated as a buried, static charge.

3. CHANGES TO PRINTER-PLOT OPTIONS

EOSAEL84 COMBIC can also generate "pictures" of the clouds in the scenario by use of VIEW, GREY, and TPOS (table 3) input records. These records form pictures two ways. The first method creates a bundle of parallel LOS surrounding one of the specified target-observer pairs. All the LOS originate on a plane and end on a plane parallel to the first plane. The parallel default option provides an orthographic representation of the obscurant cloud. The second, new method creates a bundle of LOS surrounding one of the specified target-observer pairs. However, all the LOS originate with the specified observer. The LOS end normally on a plane. This provides a perspective representation of the obscurant cloud. For example, one's eye gives one a perspective representation of the visual world. These two types of viewing the battlefield can yield different values on the obscuration levels (Ayres and Randolph, 1991).

Alphanumerics are assigned for each LOS of the printer-plots to represent different values of transmittance or optical depth. The resultant printer-plot provides a crude but useful picture of transmittance or optical depth of the clouds. The GREY and TPOS records define the grey scale to be used to assign the alphanumerics with the obscuration levels. The

TABLE 3. THE TPOS CARD.

	1	2	3	4	5	6	7	8
	1234567890123456789012345678901234567890123456789012345678901234567890							
TPOS		HLOSP	VLOSP	PERSP	NEWGR			
TPOS		0.0	0.0	0.0	0.0			

Name	Units	Typically	Description
HLOSP		varies	Parameter that defines the centers of horizontal axes for the printer-plot. The labeling of the horizontal axis of the printer-plot is then labeled from HLOSP-.5*CLOSW to HLOSP+.5*CLOSW. CLOSW is a VIEW parameter that defines the horizontal extent of the printer-plot's viewport.
VLOSP		varies	Parameter that defines the centers of vertical axes for the printer-plot. The labeling of the vertical axis of the printer-plot is then labeled from VLOSP-.5*VLOSW to VLOSP+.5*VLOSW that defines the vertical extent of the printer-plot's viewport.
PERSP		0. or 1.	If PERSP = 1, then the perspective viewpoint is chosen for the printer-plot option and all LOS originate at the observer. If PERSP = 0, then the orthographic viewpoint is chosen and LOS for the printer-plot option are of equal length and parallel to an LOS defined by a OLOC-TLOC.
NEWGR		0. or 1.	0. = Grey scale interval equally spaced, 1= arithmetic grey scale separation. The new grey scale is more closely spaced for the densest part of the cloud where most researchers are interested.
<p>If NEWGR=1., then each grey scale value for transmission is a multiplicative factor times the previous grey scale value. The factor is determined from SMINV, SMAXV and DIVIS from the GREY record and is defined by the following equation:</p> $MULT = \left(\frac{SMINV}{SMAXV} \right)^{\frac{1}{DIVIS-1}}$ <p>Ex. SMINV=.05, SMAXV=.95, and DIVIS = 5, then $MULT = (.95/.05)^{1/4}$ or 2.088 This yields a grey scale at .05, .104, .218, .455 and .950.</p>			

* Modify grey scale density, revise printer-plot labeling and change from orthographic viewpoint.

user inputs a maximum and a minimum transmittance or optical depth and the number of divisions between the minimum and maximum that are to be assigned different characters on the listing. Previously, the grey scale was always evenly spaced. COMBIC92 allows the user the option of having the grey scale levels be equally spaced or varying with the density of the cloud. Most users like this new option that allows closely spaced grey scale levels during the most interesting part of the cloud—where it is most dense. Then the grey scale level's separations for the thin parts of the cloud are quite large. This new option allows the user to utilize a minimum number of grey scales to illustrate the obscurant.

TPOS also lets the user manipulate the "axis" of the printer-plot. In the previous version of COMBIC, the axes were always labeled so that the origin was at the center specified by the OLOC--TLOC used to define the center. This labeling may or may not correspond to the actual layout for the scenario. The new option is defined by the parameters HLOSP and VLOSP from the TPOS record. These parameters define the center of the printer-plot.

4. CHANGES IN INTEGRATING THROUGH PLUMES

The most significant change in COMBIC occurs in the methodology used to compute the concentration length (CL) integral of LOS-cloud pairs through plumes. The Romberg method of integration is used to increase the speed of the COMBIC runs. As many as ten thousand LOS-cloud pairs in a scenario are not unusual. To determine the reduction in transmission requires the computation of CL , the integral over the optical path of the mass concentration. Mathematical/computer models are available that describe CL quite accurately, but with many LOS-cloud pairs, the computation time can be prohibitive. COMBIC was designed to give the user a balance between speed and accuracy. This revision of COMBIC is designed to further increase the speed of computation of CL for plumes of aerosol concentration over EO paths that have nonnegligible downwind components. This revision provides the user with the option of specifying three values: the percentage of error that can be tolerated, a low threshold value, and a high threshold value beyond which further computation of CL is unnecessary for the user's application. These parameters are specified by the user on the TIME card (table 4). Each of these values is used by COMBIC to monitor the integration process for determining the point at which computation of CL can be terminated. Choice of these parameters for optimum speed and desired accuracy will require experimentation by the user.

Three features of the Romberg method make it nicely adaptable to approximating the CL for LOS not too nearly crosswind:

- a. Comparison of one step of the iterative method of Romberg with the previous step will yield an approximate percentage error of the latter step from the true value of CL . This fact allows the user to specify the maximum percentage error that can be tolerated. The number of iterations made is only the number required to achieve the necessary accuracy.

- b. After as few as two iterations, the approximation might be terminated because the anticipated CL value is small enough to be below a threshold value that the user has specified as negligible.
- c. Similarly, the approximation might be terminated if the CL is determined to be large enough to make the transmittance below some threshold value specified by the user.

TABLE 4. THE TIME CARD.

Name	Units	Typically	Description
BEGIN	s	0.	Time when updates begin.
ENDT	s	1. to 7200.	Time when updates end.
DELT	s	.1 to 10.	Time increment for cloud update.
CLIM	g/m^2	1. to 1000.	Minimum CL (g/m^2) that the calculation can be cut short since the cloud is so dense.
CLEND	g/m^2	.001 to .1	CL (g/m^2) cloud removal limit. When the maximum possible CL will always be less than CLEND, the cloud is removed from the active list.
CLACC	percent	0.00 to 100.	CLACC is the percentage of error that can be tolerated in the Romberg method of integration. Each succeeding step is compared with the previous step to check if the desired accuracy is reached.

* This card controls the times that the cloud positions are updated for cloud rejection calculations and the cloud removal criteria.

To approximate $\int_a^b f(x) dx$, the Romberg method requires the values of $f(x)$ at a and b and at certain equally spaced points between a and b . The method iterates through certain steps, each theoretically (and in some cases, dramatically), a better approximation of the integral than the previous step. Comparison with the previous step is used as an approximation of the accuracy of the current step. The user can set this accuracy by utilizing the CLACC parameter on the TIME card. It defaults to 10 percent.

4.1 THE CL INTEGRAL THROUGH PLUMES USING THE ROMBERG METHODOLOGY

To incorporate the Romberg method of integration, the user has to reformulate the CL path integral. Utilizing the LOS equations as given by $x = x_0 + \alpha r$, $y = y_0 + \beta r$, $z = z_0 + \gamma r$, evaluating \dot{m} at $t - t(x)$, and changing the usual variable of integration from r to the distance along the LOS, x , the downwind distance, the CL integral through plumes becomes

$$CL = \int_{x_1}^{x_2} \frac{\dot{m}/u}{2\pi\sigma_y\sigma_z\alpha} e^{-X^2/2} dx, \quad (1)$$

where

$$X^2 = \left[\frac{(x - x_0)\beta/\alpha + y_0 - y_c}{\sigma_y} \right]^2 + \left[\frac{(x - x_0)\gamma/\alpha + z_0 - z_c}{\sigma_z} \right]^2. \quad (2)$$

The cloud is assumed to have been rejected if it does not intersect the LOS. In eq. (1) the downwind coordinates, x_1 and x_2 , the limits of integration, are the points of intersection of the LOS with the cloud. Note that this transformation of coordinates cannot be made if $\alpha = 0$, that is, if the LOS is directly crosswind. If α is very small, eq. (1) will be ill-conditioned because CL would then be a quotient of two small values. However, if the LOS is nearly crosswind the CL integral is quickly and accurately approximated by the COMBIC87 usual integration method.

4.2 CONTRIBUTIONS FROM GROUND REFLECTION OF THE PLUME

This revision computes ground reflection of the Gaussian plume in a manner different from that of COMBIC87 (Hoock, Sutherland, and Clayton, 1987, pp 38-39). The method applied is the traditional one in which the reflection cloud is assumed to exist with centroid as far below (or above) ground as the centroid of the real cloud is above (or below) the ground. In COMBIC92 the amount of computation time and memory required to accomplish this modification is minimal.

By simply replacing z_c in eq. (2) with its negative, eq. (1) will result in the CL for the reflected cloud (assuming that 100 percent of the below-ground portion is reflected). By multiplying this by the reflection coefficient, R_e , and adding to eq. (1) we get the CL for the cloud, including the reflected portion:

$$CL = \int_{x_1}^{x_2} \frac{\dot{m}}{2\pi\sigma_y\sigma_z\alpha u} h(x) dx \quad (3)$$

$$h(x) = e^{-1/2 \left(\frac{(x-x_0)\beta/\alpha + y_0 - y_c}{\sigma_y} \right)^2} \left[e^{-1/2 \left(\frac{(x-x_0)\gamma/\alpha + z_0 - z_c}{\sigma_y} \right)^2} + R_e * e^{-1/2 \left(\frac{(x-x_0)\gamma/\alpha + z_0 + z_c}{\sigma_y} \right)^2} \right]. \quad (4)$$

COMBIC assumes the reflected mass has the same above-ground distributions as the real cloud. For clouds with centroids near ground level, COMBIC92 will compute somewhat higher values for CL than COMBIC87 in the lower portions of the cloud and lower values in the higher portions.

4.3 CORRECTION FOR AREA SOURCES EVAPORATION

COMBIC92 uses $\dot{m}(t)$ tables in ways quite similar to the way COMBIC87 uses m tables. The difficult corrections for area sources by COMBIC87 are made much simpler by averaging \dot{m} in phase 1 from $T - \Delta T$ to $T + \Delta T$. ΔT is the time the smoke takes to travel through the radius of the area source. $\dot{m}(t)$ varies linearly with $\dot{m}(\Delta T)$ in the diffuse leading edge of the plume. $\dot{m}(t)$, in the area source, varies quadratically with $\dot{m}(TM)$, where $TM = \text{minimum}(T - \Delta T, T_{burn} - \Delta T)$. T_{burn} is the total burn time of the munition.

Correction for evaporation is done by taking the time derivative of COMBIC87 eq. (76)

$$f_d \dot{m}(t) + (1 - f_d) e^{-\delta t} \left[-\delta \int_0^t e^{\delta t'} \dot{m}(t') dt' + e^{\delta t} \dot{m} \right],$$

which simplifies to

$$\dot{m}_{corrected} = \dot{m} - \delta(1 - f_d) e^{-\delta t} \int_0^t e^{\delta t'} \dot{m}(t') dt'. \quad (5)$$

This procedure requires that \dot{m} be stored in phase 1. To further save computation time, the tables of m , \dot{m} and the integral in eq. (5) known as XSIG in COMBIC (as a function of time after ignition) is incremented every second instead of every $\frac{T_{burn}}{55}$ s in COMBIC87. Then no searching is required and interpolation time is decreased by about 50 percent over the old method. Furthermore, since for some munitions the mass was stored up to every 20 s, this is more accurate.

5. INDEXING OF THE DOWNWIND DISTANCE

To apply the Romberg method, the code must tabulate the downwind distance x in each subcloud trajectory at values such that a simple transformation of the downwind distances will be equally spaced. The tabulated values in COMBIC87 (done in phase 1) satisfy this requirement for $x \geq 49.85$. The function is $x = (49.85)(1.123)^{n-10}$. But for $x < 49.85$ an exponential function will not approach 0 in a finite number of steps. What was required was a power function of the form n^p that would "spline" with the exponential function at the breakpoint; that is, both the power function and its first order derivative would agree with those of the exponential function at the breakpoint. This was best accomplished by

$$x = n^{1.508352871} \text{ for } n < 13. \quad (6)$$

$$x = (47.887223) \cdot (1.123026355)^{n-13} \text{ for } n \geq 13. \quad (7)$$

The first 15 tabulated values of the downwind distance by these formulas are 1.00, 2.84, 5.24, 8.09, 11.33, 14.92, 18.82, 23.02, 27.50, 32.24, 37.22, 42.44, 47.89, 53.78, and 60.39. The breakpoint is at $n = 13$ where $x = 47.89$. This modification required a minor change in the tabulation of subcloud trajectories in phase 1.

6. SUMMARY

In conclusion, COMBIC92 is a significant improvement over COMBIC87. The new version of COMBIC is faster and treats more munitions than ever before. Several of the new changes in COMBIC92 have been suggested by users who wanted improvements in the visualization of the output. Other users desired faster run times. As always, the developers of COMBIC92 have considered users requests when improving the model. Users will find that the input records have changed very little. Existing users will not need to modify their old input records. They will find that the readability of the printer-plots have been improved.

REFERENCES

- Ayres, S. D., and P. Randolph, 1991: Orthographic versus Perspective LOS for Battlefield Obscurants. In Proceedings of the Eleventh Annual EOSAEL/TWI Conference, U.S. Army Atmospheric Sciences Laboratory, White Sands Missile Range, New Mexico, 88002-5501, pp 341-350.
- Hook, D. W., R. Sutherland, and D. Clayton, 1984: EOSAEL 84, Volume 11, Combined Obscuration Model for Battlefield-Induced Contaminants, COMBIC, ASL-TR-0160-11, U.S. Army Atmospheric Sciences Laboratory, White Sands Missile Range, NM.
- Hook, D. W., R. Sutherland, and D. Clayton, 1987: EOSAEL 87, Volume 11, Combined Obscuration Model for Battlefield-Induced Contaminants, COMBIC, ASL-TR-0221-11, U.S. Army Atmospheric Sciences Laboratory, White Sands Missile Range, NM.
- Spitznagel, E., and S. D. Ayres, 1989: A Methodology for the Evaluation of COMBIC. In Proceedings of the Ninth Annual EOSAEL/TWI Conference, U.S. Army Atmospheric Sciences Laboratory, White Sands Missile Range, New Mexico, 88002-5501, pp 533-542.
- Walter, E., S. D. Ayres, and M. Munoz, 1990: Revised Obscuration Model for Battlefield-Induced Contaminants. In the Proceedings of the Tenth Annual EOSAEL/TWI Conference, U.S. Army Atmospheric Sciences Laboratory, White Sands Missile Range, New Mexico, 88002-5501, pp 608-617.

ELECTRO-OPTICAL CLIMATOLOGY VERSION 2.0

by

Major Robert L. Miller
USAF Environmental Technical Applications Center
Scott AFB, IL 62225

Electro-optical Climatology (EOCLIMO) microcomputer version 2.0 is nearly ready for release by the USAF Environmental Technical Applications Center. The menu-driven software program can be used to display site-specific transmittance (8-12 micron) and climatological data for precision guided munitions planning, training, and contingency support. Surface weather observations were used as input for the Low Spectral Resolution Transmission Code (LOWTRAN7) to provide three-hourly data. A sensor height of 125m with a 4km slant path to the target was used as standard geometry. The output includes graphs and tables of transmittance data, significant meteorological variables, and narratives explaining periods of low transmittance. A map depicting the user's region of interest with stations color coded based on cloud ceiling and transmittance thresholds is easy to evoke. The Southwest Asia/Northeast Africa theater will be released soon. Areas to follow include: Pacific, Central America, Northwest-Sub Saharan Africa, selected training ranges, and Europe.

The paper accompanying this demonstration appears in Session I, page 36.

Session II

WEATHER DECISION AIDS POSTERS AND DEMONSTRATIONS

**Chairperson
Mr. James Harris**

A MULTIPLE METEOROLOGICAL STATION VERSION OF THE BRL GENERAL TRAJECTORY MODEL

Abel J. Blanco

U.S. Army Atmospheric Sciences Laboratory
White Sands Missile Range, New Mexico 88002-5501, USA

Sherrill J.H. Edwards
electroMAGIC Tools

Organ, New Mexico 88052-0490, USA

ABSTRACT

The trajectory of an artillery projectile can rarely be characterized by a single set of meteorological measurements (MET Message). A composite model of multiple meteorological stations can provide enhanced target impact accuracy for indirect artillery fire. The Advanced Battlefield Environment Artillery Model (ABEAM) is a simulation program that utilizes the U.S. Army Ballistic Research Laboratory (BRL) General Trajectory (GTRAJ) model. ABEAM provides multiple MET Message handling capability to allow a more accurate modeling of the meteorological effects along the complete trajectory of the artillery projectile. This paper details the ABEAM software system and how it can be used for enhanced battlefield simulation such as smart munition dispersion. ABEAM will be useful in the development of an improved meteorological effects correction capability for more accurate targeting.

1. INTRODUCTION

The desire for artillery commanders to achieve tactical surprise with the indirect firing of their batteries forced the need for correction factors. The need to devise these correction factors for nonideal battlefield environments has driven the development of artillery ballistics models through the years. Early efforts concentrated on the aerodynamics and the physics of projectile flight. Later efforts added basic compensations for meteorological effects such as temperature, density, and winds.

The current model used by the U.S. Army Ballistic Research Laboratory (BRL) is the General Trajectory (GTRAJ) model. This model uses a single meteorological station report, known as a MET Message, to characterize the whole projectile flight. With current weapons systems able to achieve downrange impacts of greater than 15 km and future systems striving for even greater ranges, this model scenario presents an increasing uncertainty factor for the target impact accuracy as the range is extended.

For this reason, new approaches for handling the projectile flight meteorological effects are being proposed and evaluated. One such approach utilizes multiple meteorological stations. To determine the effectiveness of this and other approaches, the Advanced Battlefield Environment Artillery Model (ABEAM) is being developed. The ABEAM concept is to not only utilize the basic trajectory computation engine of the GTRAJ model, but to also provide flexibility in the handling of meteorological data and its effects. This flexibility is to include the various proposed approaches and the ability to utilize such data assets as the Project WIND (Wind In Non-uniform Domains) database (Cionco, 1989) and Project PASS (Proto-type Artillery Sub-System) database (D'Arcy, 1977).

With the advent of conventional long-range cannon capability, the U.S. Army Atmospheric Sciences Laboratory (ASL) is conducting applied research leading to improvement in the use of the artillery meteorological (met) messages. The lengthening flight time has significantly increased the unit met corrections. The current method of adjusting artillery fire with met data collected from a dedicated met station may no longer be valid for the new extended ranges. Since the atmospheric conditions are not homogeneous along the projectile trajectory, a composite met message, utilizing multiple met stations, has been derived to demonstrate the improvement of the first-round-hit probability.

The initial design defines the following four portions to a given trajectory: launch, preapogee, postapogee, and target area. ABEAM allows the operator to select the appropriate met data for these four portions. Statistical comparisons between simulated impacts can be derived from a single met station adjustment and multiple met station adjustments to demonstrate the bias error improvements afforded by the proposed composite met message. ABEAM is utilized to determine the met effect on munitions fired at these extended ranges. Demonstrating that these derived bias error differences are significant, the ABEAM methodology may be incorporated into fire control centers for use in aiming artillery.

2. MULTIPLE METEOROLOGICAL STATION THEORY

Approximately one-half of the extended range trajectory flight time is spent in the apogee portion (fig.1). Each 2 seconds of flight time is represented by a symbol. Using the standard munition aerodynamic coefficient tables extended to Mach 5 so as to represent future artillery capability, GTRAJ was utilized to compute four target ranges. The 35- and 45-km ranges are certainly future cannon ranges; and the 25- and 15-km ranges in the future will have a lower apogee. This means that the future met message will only be required up to 8 km to reach the current range of 25 km.

For a coasting shell, the most important met observations are required for the preapogee and postapogee portion. Normally, the windspeed is at a maximum for the trajectory during apogee; however, wind levels do fluctuate as higher altitudes are achieved. The trajectory apogee is where the projectile velocity is moving the slowest (a near zero vertical component and a high but decreasing horizontal component). When this susceptibility to deflection and displacement is combined with the time spent in this flight portion, the met has its best chance to deviate the projectile away from the initial aim point. Examination of available long-range firing tables such as FT 155-AO-0 (Firing Table FT 155-AO-0, 1978)

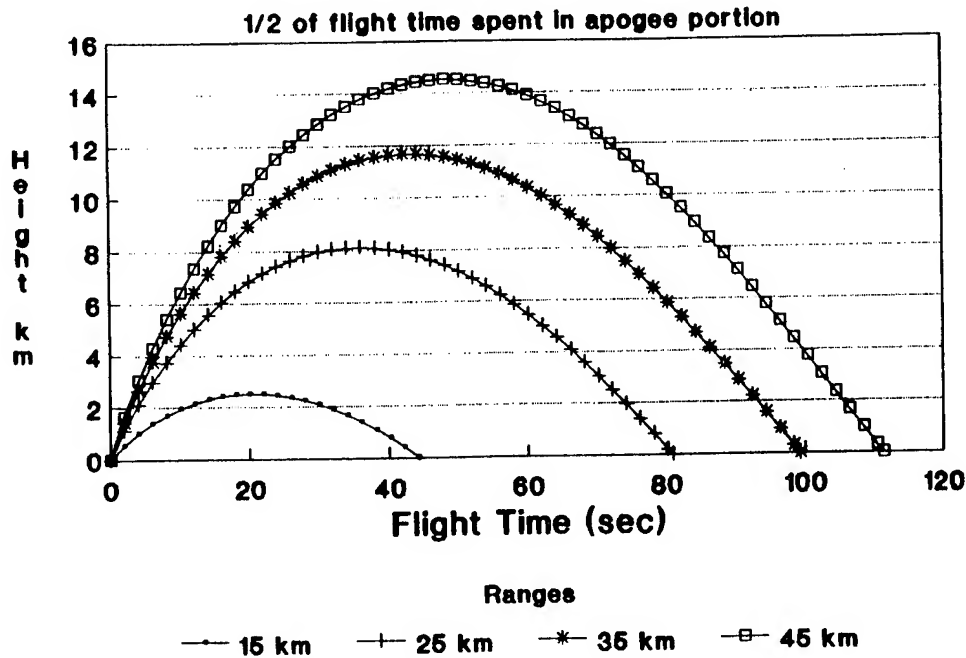


FIGURE 1. PROJECTILE FLIGHT PROFILE.

reveals wind, temperature, and density unit corrections that are significantly large. Since the current artillery met message used for aiming these long-range projectiles may not be representative of the actual experienced met data at the apogee of the trajectory, significant bias errors can be expected. ABEAM was developed to document the range of these expected errors. If the met error bias exceeds the lethal radius of the delivered munition, then a new aiming algorithm that contains a composite met message adjustment should be available for fire direction centers.

For the future rocket assisted rounds that utilize pop-out stabilizing fins, the launch area winds will be a major error source in aiming artillery fire. The wind causes a finned projectile to cox into the direction of the wind, deviating the flight path from the initial aiming direction. Once in the coast phase, the phenomenon will continue to have an effect, though not necessarily to the extent of the launch phase.

Figure 2 presents data from a controlled experiment conducted at White Sands Missile Range (WSMR), New Mexico (Blanco and Traylor, 1976). The experiment involved five met stations located across WSMR, simultaneously releasing rawinsonde balloons to achieve a multilocation model of the meteorological effects for an example battlefield environment. The stations — War Road (WAR), McGregor Range (MCG), Launch Complex 36 (TSX), Orogrande (ORO), and Small Missile Range (SMR) — all used the equipment and techniques of a field artillery met station (Field Manual FM 6-15, 1983). The displacement positions of the released balloons are diagrammed by the concatenated arrows. Each arrow represents the displacement that occurred in an atmospheric zone, which is a certain al-

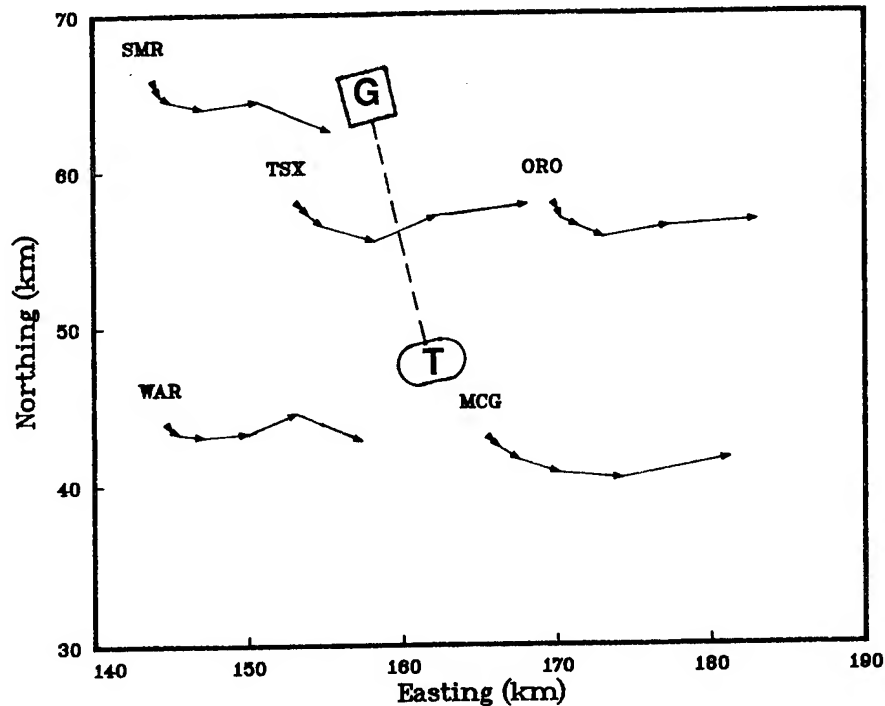


FIGURE 2. WIND DATA PROFILE, 1015, WSMR, NM.

titude range. The last arrow represents the wind conditions at zone 6 (2500 m), which corresponds to the apogee of a 15-km target range in fig. 1.

If a gun, shown in fig. 2 as a boxed *G*, were aimed using data from the SMR met station, the round would experience wind data from the TSX met station during apogee. In the target area, oval marked *T*, the round would be affected by winds characterized by the MCG met station. The difference between SMR and TSX/MCG determines the expected wind bias error at the impact location. For example, the SMR wind data at zone 6, used for aiming at the azimuth of fire, dictates a range and deflection adjustment; however, the projectile experiences only a deflection wind effect.

For delivery of bomblets, the target area met may not be a major concern in aiming artillery. However, if parachuted submunitions or smoke munitions are to be delivered, the target area met takes a more significant role. Winds in the target area may cause these submunitions to drift away from the target, and ABEAM will be used to predict these drifts.

3. MODEL IMPLEMENTATION

The GTRAJ model was written in a modular form using FORTRAN to implement the program logic. ABEAM adapted the original modules from GTRAJ to serve as the primary computation engine for the ballistics problems. The original modules were examined to determine the extent of involvement with meteorological effects that occurred within them. The variables and formulas affected were then identified and the interdependencies were charted to provide an overall understanding of how any one variable could influence

the projectile flight at any point along the trajectory. This provided a baseline for any modifications that might be attempted in trying to validate the new modeling scheme.

The multiple meteorological station approach required that the MET message data for several met stations (as implemented, up to 5 messages) be available as the data source at differing discrete portions of the projectile flight. These discrete portions could be broken down in terms of flight time, distance downrange, or physical coordinates. A new module handled the input of the meteorological profile established by the multiple met station data. This module established a MET message database with data keys to provide easy retrieval of the appropriate data for every portion of the projectile flight. This module also provided editing to the database and discrete portion parameters. Figure 3 diagrams the implementation.

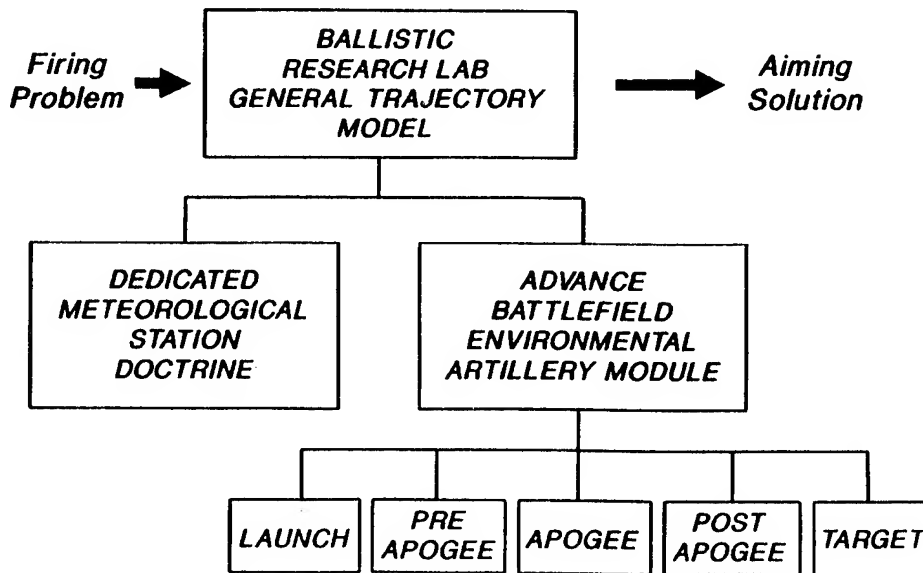


FIGURE 3. ABEAM IMPLEMENTATION.

With the met database to draw information from and the discrete portion parameters to determine the proper data drawn, the previously charted variables and formulas affected by meteorological effects were modified to utilize this database to get the appropriate values for calculating the projectile flight.

4. VALIDATION

The validation of the ABEAM modification was accomplished by using the same met message for the differing met areas and comparing the results with the single met message in a single met area. These results were then compared against the original GTRAJ results. In all comparisons the ABEAM results were validated.

5. MODEL UTILIZATION

ABEAM was used to simulate cannon artillery trajectories through different met scenarios. These scenarios were selected from the following met databases: Project WIND (Blanco and Solis, 1991) and Project PASS. Both projects were managed by ASL and the met data has been converted into the artillery computer met message format. Both databases contain simultaneous balloon releases. ABEAM is implemented in the following experiments designed to determine spacial wind effects, temporal wind effects, and criteria for selecting a best available met.

The operator selects a dedicated station to aim and simulate a trajectory that goes over another station and impacts near a third station. For example, the gun position in fig. 2 was aimed with the SMR computer met message and its simulated impact was then compared with the simulated impact derived from using a composite met message defined by: SMR at the launch area (zones 1-3), TSX at the preapogee and postapogee (zones 4-6), and MCG target area (zones 3-1). The difference between these simulated impacts represents the expected bias met improvement for the one replicate.

The experiment was designed to produce results that would reveal whether the dedicated met station concept is not appropriate for long-range applications because of met space variability. A more realistic design of experiment includes simulating the battlefield condition where the met is also stale (hours old). While obvious, it is important to understand that the aiming met is not necessarily representative of the actual round experienced met.

Figure 4 presents the scenario of firing with met messages that are 2 hours old versus new messages. Repeating the experiment with the paired difference for the simulated impact using "real time" versus 2 hour old data can present results that are more indicative of actual battlefield conditions. Comparing WAR and TSX at the apogee of the projectile (zone 6) shows that the wind direction and balloon displacement (speed) have changed significantly. A similar comparison for zone 1 between WAR and SMR reveals again a large difference between the direction of the launch and target winds.

Another reason for compiling these paired statistics is that the analysis of the results may provide a methodology for checking the availability of other met stations. In fig. 4, the commander who has WAR as the dedicated met station can be more effective in completing the mission at 1210 if he aims with the 1200 met data collected at the MCG met station. ABEAM will be used to derive results that may lead to rules that determine how old the dedicated met data can be before one should search for a more representative met message from other available artillery met stations.

By isolating a particular portion of the projectile trajectory, the significant role for each of the four portions defined in ABEAM can be determined. Once all the portions have been contrasted with the standard atmospheric effect, a percentage met error contribution can be associated with each portion of an artillery trajectory.

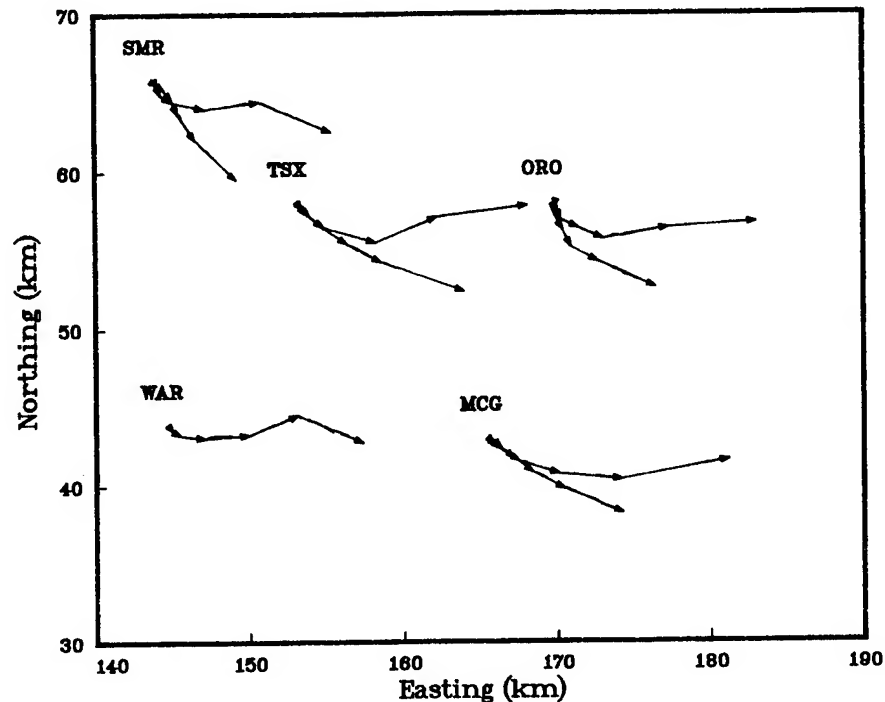


FIGURE 4. WIND DATA PROFILE, 1015 AND 1215, WSMR, NM.

6. RESULTS

Paired statistics from all possible replicates in the sample described in section 5 are available from the Authors. There is a significant difference in all experiments evaluating spacial, temporal, and best available met criteria. In general this difference may approach the lethal radius of a conventional round.

Table 1 lists the range statistical results for the bias and the percent contribution of the total met effect. Table 2 lists similar statistics for the deflection results.

Using the table data, the conventional round was most affected by the met effects during the coasting phase around the apogee of the trajectory. The target area contained the smallest met effect because the delivered munition was a 100-lb shell. Parachute delivered submunitions with a scan and search pattern, a chemical warhead burst, or wind gliding warheads would be much more affected by the meteorological effects in the target area.

An initial conclusion is that the bias errors associated with the dedicated met station can be larger than the lethal radius of the conventional high-explosive round.

These initial results indicate that the methodology of making final adjustments from met data collected at a dedicated met station is not necessarily appropriate for long-range fire.

TABLE 1. RANGE BIAS (m) AND PERCENT CONTRIBUTIONS OF THE TOTAL MET ERROR

	RANGE	LAUNCH	PRE APOGEE	POST APOGEE	TARGET	TOTAL
RESULTS FOR 10 KNOT DOWN RANGE (TAIL) DIRECTED WIND	15 km	37 19%	73 38%	50 26%	33 17%	193 100%
	25 km	60 17%	109 31%	110 31%	73 21%	352 100%
	35 km	62 13%	95 20%	134 28%	185 39%	476 100%
	45 km	111 19%	166 28%	121 20%	196 33%	594 100%
RESULTS FOR 10 KNOT UP RANGE (HEAD) DIRECTED WIND	15 km	39 21%	115 63%	22 12%	8 4%	184 100%
	25 km	70 20%	190 54%	69 20%	23 6%	352 100%
	35 km	65 14%	105 22%	231 49%	69 15%	470 100%
	45 km	104 19%	137 25%	185 33%	131 23%	557 100%
RESULTS FOR 1 PERCENT DECREASE IN PRESSURE	15 km	36 53%	22 32%	8 12%	2 3%	68 100%
	25 km	92 48%	81 42%	16 8%	4 2%	193 100%
	35 km	48 21%	101 44%	75 32%	8 3%	232 100%
	45 km	1018 71%	370 26%	27 2%	11 1%	1428 100%
RESULTS FOR 1 PERCENT INCREASE IN PRESSURE	15 km	38 54%	22 31%	8 12%	2 3%	70 100%
	25 km	62 41%	67 44%	20 13%	3 2%	152 100%
	35 km	67 34%	58 29%	66 33%	7 4%	198 100%
	45 km	292 58%	180 36%	16 3%	18 3%	506 100%
RESULTS FOR 1 PERCENT DECREASE IN TEMPERATURE	15 km	3 40%	4 45%	1 11%	0 4%	8 100%
	25 km	5 31%	8 50%	2 13%	1 6%	16 100%
	35 km	4 20%	7 39%	5 25%	3 16%	19 100%
	45 km	9 33%	8 31%	5 19%	4 13%	27 100%
RESULTS FOR 1 PERCENT INCREASE IN TEMPERATURE	15 km	3 36%	4 49%	1 11%	0 4%	8 100%
	25 km	4 31%	6 46%	2 16%	1 7%	13 100%
	35 km	4 25%	4 25%	6 32%	3 18%	17 100%
	45 km	53 70%	16 21%	5 6%	2 3%	76 100%

TABLE 2. DEFLECTION BIAS (m) AND PERCENT CONTRIBUTIONS OF THE TOTAL MET ERROR

	RANGE	LAUNCH	PRE APOGEE	POST APOGEE	TARGET	TOTAL
RESULTS FOR 10 KNOT CROSS-RANGE DIRECTED WIND	15 km	47 42%	42 38%	13 12%	9 8%	111 100%
	25 km	94 34%	108 40%	39 14%	32 12%	273 100%
	35 km	100 24%	133 32%	95 23%	83 21%	411 100%
	45 km	122 24%	149 30%	97 19%	136 27%	504 100%

7. FUTURE USE

ASL will continue compiling more replicate results for artillery munitions utilizing meteorological data from the two met databases. ABEAM will be the analysis tool utilized to perform the met effects comparison between the dedicated met station scheme and the proposed composite met station scheme. The results will be cataloged to determine the limits of spacial and temporal met effects that may lead to defining rules for the selection of a best available met message.

As a new version of GTRAJ has been released, GTRAJ3, future work will be done to incorporate the new version into the ABEAM scheme (BRL GTRAJ3, 1991). Further, the successful strategies developed through ABEAM will be examined for possible inclusion into the next generation GTRAJ.

Following further analysis of the new met effects handling approaches, the authors feel a field exercise would be a proper step in determining the "Battlefield" effectiveness and practicality of using these approaches.

ACKNOWLEDGMENTS

The authors express their appreciation to the following:

Mr. Jon Miller, U.S. Army Ballistic Research Laboratory, for providing the GTRAJ software for execution on the DEC VAX, modified aerodynamic coefficients that represent future artillery capabilities, and valuable comments on GTRAJ history and use.

Dr. Alan Wetmore, U.S. Army Atmospheric Sciences Laboratory, for providing the initial GTRAJ software conversion for execution on the HP 9000.

REFERENCES

- Cionco, Ronald M., 1989: Design and Execution of Project WIND. In *Proceedings of the 19th Conference on Agriculture and Forest Meteorology*. American Meteorological Society, Boston, MA, 156-159.

Blanco, Abel, and Saul Solis, 1991: *Computed Time and Space Meteorological Variability using Project WIND Phase I Upper-Air Data*. ASL-TR-0298, U.S. Army Atmospheric Sciences Laboratory, White Sands Missile Range, NM.

Blanco, Abel, and Larry Traylor, 1976: *Artillery Meteorological Analysis of Project PASS*. ECOM-5804, U.S. Army Atmospheric Sciences Laboratory, White Sands Missile Range, NM.

D'Arcy, Edward, 1977: *PASS 500 mb Rawinsonde Data Volume I and Volume II*. ECOM-DR-77-4, U.S. Army Atmospheric Sciences Laboratory, White Sands Missile Range, NM. (ADA046979)

Field Manual FM 6-15, August 1983: *Field Artillery Meteorology*. Headquarters, Department of the Army, Washington, DC.

Firing Table FT 155-AO-0, 1978: U.S. Army Ballistic Research Laboratory, Aberdeen, MD.

BRL GTRAJ3, May 1991: *User's Guide for the General Trajectory Program (GTRAJ3)*. U.S. Army Ballistic Research Laboratory, Aberdeen, MD.

INTEGRATING BATTLEFIELD WEATHER AND TERRAIN DATA FOR IPB
THROUGH AUTOMATED TECHNIQUES

Gary McWilliams
U.S. Army Atmospheric Sciences Laboratory
White Sands Missile Range, New Mexico 88002-5501, USA

ABSTRACT

Weather and terrain analyses are critical components for the intelligence preparation of the battlefield (IPB), which is performed as part of the command estimate process. IPB is a very labor-intensive and time-consuming procedure whose tactical utility can be significantly enhanced through automation. The U.S. Army Atmospheric Sciences Laboratory and the U.S. Army Topographic Engineering Center are engaged in a cooperative research program to develop automated techniques for IPB weather and terrain analysis. This paper describes those techniques, their requisite software architecture, and their potential application to other Army automated systems such as the force level control advisor.

1. INTRODUCTION

The four basic tenets of the Army's airland doctrine are: initiative--setting the terms of battle by action; agility--the ability of friendly forces to act faster; depth--extension of operations in space, time, and resources; and synchronization--arrangement of battlefield activities in time, space, and purpose to produce the maximum relative combat power at the decisive point (FM 100-5). One method the Army is using to enhance the successful execution of these tenets is the integration and automation of the command, control, communications, and intelligence (C3I) functions.

To further the Army's goal in this area, the U.S. Army Atmospheric Sciences Laboratory in cooperation with the U.S. Army Topographic Engineering Center and the U.S. Army Space Technology and Research Office is designing and developing techniques for automating the IPB analysis functions performed in support of the command estimate process (McWilliams, 1991).

2. BACKGROUND

IPB provides a basis for determining and evaluating enemy capabilities, vulnerabilities, and probable courses of action (FM 34-130). It is a very analytical process performed by the intelligence officer and his staff as part of the command estimate process. It is also a very labor-intensive and cyclic process comprised of the following: battlefield area evaluation, terrain analysis, weather analysis, threat evaluation, and threat integration. IPB basically involves integrating weather and terrain information with enemy doctrine and

is usually performed formally at the corps, division, and brigade echelons; with a planning horizon that cascades from 96 h at corps to 24 h at brigade.

IPB products are mostly graphic overlays (templates). The background for the template is usually a map of the region showing the relevant terrain elevation and feature information. An example of one such template resulting from the weather and terrain analysis is shown in fig. 1. This template is referred to as a modified combined obstacle overlay (MCOO) and shows the expected enemy and friendly division-level avenues of approach as determined from weather and terrain considerations. The nature of our research task is to develop a prototype software system that automates the generation of IPB products such as the MCOO.

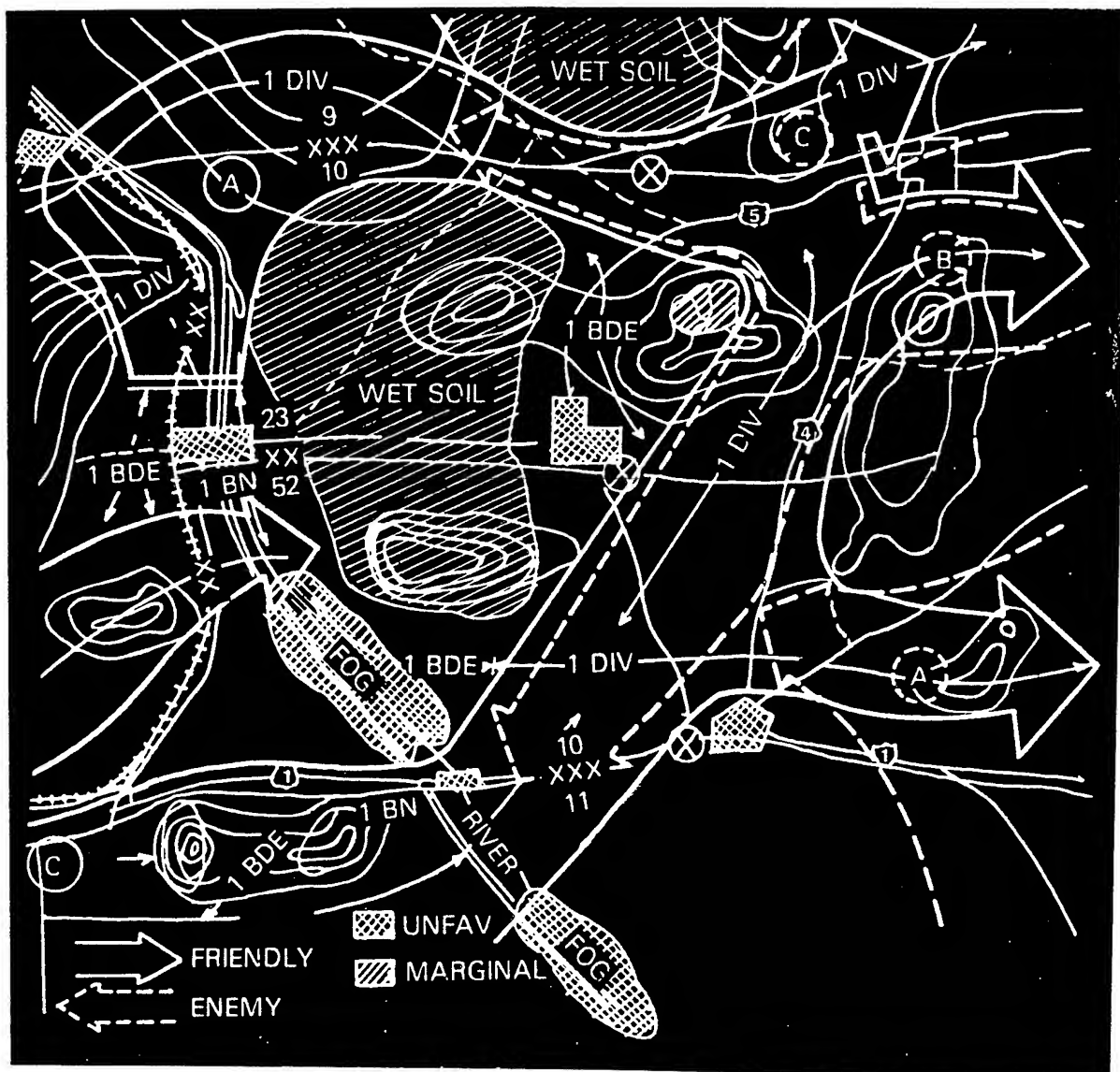


Figure 1. Division avenue of approach.

3. DESCRIPTION OF PROTOTYPE SYSTEM

3.1 OVERVIEW

The prototype system being developed is intended to complement other Army systems being developed for automating many of the battlefield C3I functions and is not intended to become a stand-alone tactical system. One candidate system for incorporating our software is the Airland Battle Management - Advanced Technology Transition Demonstration system, which is the forerunner of the force level control advisor (FLCA) (Reyenga, 1991). FLCA will assist with automating the battlefield tactical command and control under the battlefield functional area concept.

We have established several software development guidelines that we believe will facilitate the integration of our software into other Army C3I automated systems. These guidelines are generally very compatible with the Army Tactical Command and Control System common hardware and software standards. These guidelines include a modular software architecture (using the Unix operating system, X-windows graphics, and the motif user interface environment) and programming in the C language. A further description of the software architecture and the system requirements is presented in McWilliams et al. (1991).

Our system design is intended to capitalize on the strengths and reduce the liabilities that automation brings to the IPB process.

Included among the strengths are high-speed processing, large data storage, and three-dimensional representation of the battlefield. The high-speed processing will allow the revision of the IPB products with near real-time meteorological data and other environmental data. The large data storage will allow immediate access and cross referencing of a large volume of information that would have otherwise been impossible using the manual process. The three-dimensional representation of the IPB products such as the MCOO will allow the intelligence staff and commander to more accurately visualize the battlefield.

Two potential liabilities that automation introduces are the difference in skills required to operate the automated system as compared to the manual procedure and the present difficulty, if not impossibility, of having the system include abstract and other high-level forms of reasoning. The skills requirement is being addressed by developing a user-friendly interface, which to a degree is able to scale to the level of expertise of the user. The limited reasoning capability is addressed by incorporating some reasoning capacity through the use of rule-based expert system, case-based reasoning, and stochastic problem solving techniques. To a considerable degree this problem is mitigated by realizing the system is not intended to replace the user but instead to assist the user. Therefore, the user interface is being carefully engineered to allow the user to interject his/her experience, knowledge, and expertise when and where appropriate.

The IPB weather and terrain analysis prototype system currently exists as two separate modules. One module is for dealing with weather-related issues and the other module is for dealing with terrain-related issues. As the project

progresses, these two modules will be integrated into a single module with a common user interface. A more complete description of these two modules is provided below.

3.2 WEATHER ANALYSIS MODULE

The weather analysis module is being designed to perform several IPB functions, which to a large extent emulate many of the functions now performed manually. As in the manual procedure, the ultimate goal of the automated procedure is to determine how the weather affects the ability of the enemy to move, shoot, and communicate. The weather analysis module is referred to as the Weather and Doctrinal Information Fusion (WADIF) System (McWilliams et al., 1991). Remember that weather not only affects the terrain but also directly affects the weapons on board the various military assets.

WADIF begins by accessing a weather data base comprised of data from current observations, forecasts, and climatology. In a tactical situation we expect this data base to reside on a system such as the Integrated Meteorological System (IMETS) (Harris Corporation, 1987). During the development phase of WADIF, this data base (called Unidata) is being provided by a system developed at the University Corporation for Atmospheric Research (Campbell and Rew, 1988). Unidata emulates many of the data processing and analysis functions expected to be incorporated in IMETS. Since IPB is focused on the enemy (that is, a data denied area) and on planning, WADIF will use current weather information obtained from meteorological satellites and forecasted data provided by the staff weather officer and numerical prediction models extensively.

Once these data are available, WADIF next accesses the effect that the weather has or will have on various classes of military assets and activities over the battlefield area of interest. This assessment is performed via a rule-based expert system that rates the performance of an asset's target acquisition system and weapon systems according to the weather conditions. The expert system requires WADIF to represent the weather information in an object oriented-manner. A defined weather object such as a fog bank is then assigned properties and attributes that prescribe the effect of the object (here the fog bank) on the various military assets and missions.

The effect the weather has on the terrain, and hence on the mobility of an asset, is determined by a combination of an expert system and algorithmic program.

WADIF uses case-based reasoning to further examine the weather effect with regard to the nature of the mission in which the asset is engaged or activity is occurring.

After this assessment is completed, WADIF provides a graphic display of the information. WADIF will also display relevant collateral information specific to an asset or activity. This information may indicate crew size, vulnerabilities, etc.

When WADIF is combined with the terrain module, the integrated module will then use stochastic reasoning techniques to determine enemy intentions. These intentions can be expressed in several forms such as avenues of approach.

3.3 TERRAIN ANALYSIS MODULE

The mission of the terrain analysis is to determine how the terrain affects the enemy's ability to move, shoot, and communicate. The terrain analysis focuses on military aspects that are collectively referred to as OCOKA. These aspects include the following: O--observation and fields of fire, C--concealment and cover, O--obstacles, K--key terrain, and A--avenues of approach and mobility corridors. The automation of the OCOKA tasks is being pursued through a combination of expert system and algorithmic programs. The primary source for the terrain data is the Defense Mapping Agency.

Some inherent responsibilities assigned to this module include generating map backgrounds and updating the terrain elevation and cultural information data base by using satellite imagery and aerial photography. During conflict the updating of the cultural information, which includes lines of communication, will be paramount for bomb damage assessment and overall intelligence assessment. The subroutines generating map backgrounds will consist of a library of geographic information system utilities. There are several algorithms under development for importing and processing LANDSAT and SPOT satellite imagery and aerial photography data for updating the terrain elevation and cultural information data.

4. CONCLUSIONS

The technical challenge of automating IPB weather and terrain analysis lies to a large degree in the areas of automated data fusion and planning. The fusion process consists of integrating weather, terrain, and doctrinal information in both space and time to give an accurate and coherent view of the battlefield. Given this view of the battlefield it is then possible to more reliably infer the intentions of the enemy.

The automation of IPB weather and terrain analysis will make IPB a more effective tool because it will more readily integrate more current data into the intelligence process.

This project will also provide the framework for representing weather effects information consistent with the Army's other research and development programs related to automating C3I.

REFERENCES

- Campbell, D., and R. Rew, 1988: Design Issues in the Unidata Local Data Management System. In Preprints of the Fourth International Conference on Interactive Information and Processing Systems for Meteorology, Oceanography, and Hydrology, American Meteorological Society, Boston, MA, 208-212.
- FM 100-5, 1986: Operations. U.S. Army Headquarters, Washington, D.C.
- FM 34-130, 1989: Intelligence Preparation of the Battlefield, U.S. Army Headquarters, Washington, D.C.

Harris Corporation, 1987: Integrated Meteorological System (IMETS) Interface Control Document. Harris Corporation, Melbourne, FL.

McWilliams, Gary, 1991: Research and Development Plan: Real-Time Weather/Terrain Exploitation. In Proceedings of the 2nd Workshop on Weather and Terrain Templating, Computing Research Laboratory, New Mexico State University, Las Cruces, NM.

McWilliams, Gary, Steve Kirby, Tom Eskridge, and Jeff Newberry, 1991: An Expert System for Fusing Weather and Doctrinal Information Used in the Intelligence Preparation of the Battlefield. In Proceedings of the SPIE Conference on Applications of Artificial Intelligence IX, Society of Photo-Optical Instrumentation Engineers, Orlando, FL, 417-428.

Reyenga, Robert, 1991: AirLand Battle Management Advanced Technology Transition Demonstration Functional Description Requirements Specifications (ALBM ATTD FDRS). U.S. Army Combined Arms Command, Fort Leavenworth, KS.

METEOROLOGICAL OBSERVATIONS, INTERPOLATION, AND
TACTICAL DECISION AIDS

Robert R. Lee
U.S. Army Atmospheric Sciences Laboratory
White Sands Missile Range, New Mexico 88002-5501, USA

Philip Raihl and Sylvia Cossio
New Mexico State University
Las Cruces, New Mexico 88001, USA

ABSTRACT

This paper investigates the accuracy to which observations of meteorological parameters can be interpolated to a grid. The interpolation accuracy defines the accuracy that a tactical decision aid (TDA) will be able to achieve.

Observations of temperature, relative humidity, windspeed, and wind direction were interpolated to a grid from a set of very carefully chosen observation stations. Hypothetical chemical spill sites were selected at five different observation points. Four different experiments were performed in which comparisons of meteorological parameters were made between observations at the hypothetical spill sites and values from nearby, interpolated grid points.

Variations in the observed meteorological parameters caused by interpolation inaccuracies were applied to a heat stress casualty TDA. Sensitivity studies were performed to show the amount of variability in the TDA output.

1. INTRODUCTION

The U.S. Army needs weather information, in the form of observations and forecasts, so that it can plan for favorable or unfavorable conditions that may render tactical advantages or disadvantages. Tactical decision aids (TDA's) have been developed that use weather information to assess equipment and personnel performance, weapon system capability, chemical/nuclear hazards, aircraft operations, and so forth. The accuracy, timeliness, and availability of raw weather data defines how well the TDA's represent the real world environment in which military tactical strategies are performed.

The problem addressed in this paper concerns the collection and proper use of the weather data. The most comprehensive TDA in the world will produce useless results if its input weather data is out of date, incorrect, or not representative of the area where the TDA is being applied. The problem is illustrated throughout the paper with the following example.

A chemical spill has occurred and personnel must wear protective clothing to cleanup the disaster. Time is of the essence. The spill must be cleaned up as fast as possible. The number of cleanup personnel needs to be decided. A TDA must be consulted to determine how long personnel can stay in protective clothing (while performing heavy work) without rest or relief. The decisions are final and need to be made beforehand. Weather data is needed as input to a TDA to assess work rates for personnel in chemical protective clothing.

Surface weather observations are available and are collected every half hour from 10 stations scattered within the 100- by 100-km area where the disaster took place. This is the only available data from the area, and the chemicals did not spill on or near any of the meteorological sensors. This paper will not address the problem of sensor calibration, real-time communications between the observation sights and the centralized data collection platform, or the problem of archiving and managing all of the data as it flows into the central data depository. These concerns are not trivial and need serious consideration apart from this present study.

Weather observations taken at any of the 10 surface stations may not be representative of the conditions where the cleanup operation will be performed. Remember, there are only 10 observation points in a 10,000 km² area. Using nonrepresentative meteorological values to calculate work stress levels may result in erroneous estimates of work times and fatigue factors. Personnel could be jeopardized because of inaccurate weather data used by the TDA.

2. EXPERIMENTAL APPROACH

2.1 METEOROLOGICAL DATA

Several experiments were designed to test how accurately meteorological variables could be interpolated to specific points within an area of interest. Figure 1 shows an area of approximately 80 by 160 km in central New Mexico within the confines of the White Sands Missile Range.

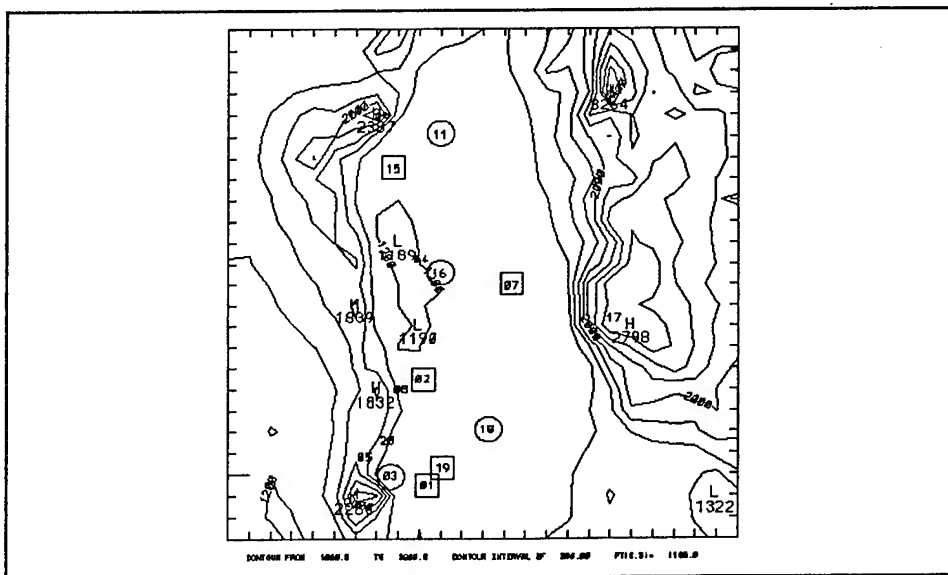


Figure 1. WSMR area and data collection stations.

Meteorological data was collected over 2 months at all of the stations that are numbered in fig. 1. An absolute best case scenario was developed for this study. Only the best data were used. Therefore, any stations that complicated the flat earth interpolation assumptions were eliminated. Any station that was known to have poorly calibrated sensors was eliminated. Any station that was positioned in such a location so that it was strongly influenced by the local terrain was also eliminated.

Based on Brock (1990), nine stations were selected that best satisfied all of the station selection criteria. The stations selected are all representative of the Tularosa Basin floor. Mountain sites and terrain influenced sites were eliminated. The following stations were selected: 1, 2, 3, 7, 11, 15, 16, 18, and 19. Brock (1990) also describes all of the stations and sensors shown in fig. 1 and the data that was collected during March and April 1990. Approximately 60 days X 24 hours/day X 4 reports/hour X 4 meteorological parameters X 9 stations = 207,360 numbers used in each of the interpolation evaluations. Because the stations were carefully chosen and the meteorological data had been edited by Brock to remove bad or questionable data, the authors felt that the data used in the interpolation evaluations represent an absolute best case scenario.

Because the meteorological data used in this study represents a best case scenario, the interpolation results will also reflect that fact. The results presented will show the best that can be done with meteorological measurements in the real world. Under different circumstances of meteorological data collection, inaccuracies would certainly be introduced due to data errors, missing data, sensor miscalibration, data collection delay times, terrain influences, and so forth. This study should be taken as a baseline point. Real world interpolations of meteorological data for TDA's will be much more inaccurate.

Data from nine observation stations was selected from within the 12,800 km² area. Since a hypothetical chemical spill could occur anywhere in the area defined by fig. 1, some of the data was needed to interpolate points to the grid and some of the data was needed as ground truth measurements to determine the accuracy of the interpolation.

At this point, the authors realized that the interpolation accuracy is going to depend on the configuration of the observation points. If all of the meteorological data were collected in one small corner or only on one side of the region, the resulting interpolations would be inaccurate. Stations should be selected (or positioned if possible) so that they are spread as evenly as possible over the entire area in order to achieve the greatest interpolation accuracy. Veazey and Tabor (1985), Motte (1986), Tabor et al. (1986), Motte (1987), Tabor and Motte (1987), Tabor and Hall (1987), Tabor et al. (1987), Tabor and Motte (1989), and Clark et al. (1990) have addressed the sensor placement problem; the results suggest that there is more to the problem than this simplistic rule of thumb. Interpolations that are made near to and between observational points are expected to be more accurate than interpolations made outside and far away from the grouping of observation points.

Considering all of the data constraints and the desire to develop a best case scenario, meteorological observations from stations 3, 11, 16, and 18 were interpolated to a grid. Locations 1, 2, 7, 15, and 19 were used as potential chemical spill sites. Note that for the most part, the ground truth observation sites (1, 2, 7, 15, and 19) are between the observation stations. The interpolation experiments reveal how well the grid point interpolated data agrees with ground truth observations at the hypothetical chemical spill locations.

2.2 INTERPOLATION AND STATISTICAL METHODS

Henmi (1989) evaluated seven different interpolation methods and their performance by comparing calculated and observed wind vectors. Results showed that no significant differences existed between the seven different interpolation methods that were compared. Barnes' interpolation method, one of the seven, was used in the present study to interpolate observed meteorological parameters to a grid.

Barnes (1964) describes an interpolation method that uses a Gaussian weight function and was developed specifically for two-dimensional meteorological fields. Henmi (1989) describes this approach in detail.

The interpolated values and observed ground truth values were compared by calculating the correlation coefficients for the various experiments. The accuracy of the interpolation was then assessed from the correlation coefficients.

3. DESCRIPTION OF INTERPOLATION EXPERIMENTS

Each experiment consisted of reading 60 days of data (March and April 1990) taken every 15 min from 4 observation stations located at 3, 11, 16, and 18 in fig. 1. Four meteorological parameters (temperature, relative humidity (RH), windspeed, and wind direction) were interpolated to a grid using the Barnes objective analysis. Interpolated values were then compared to ground truth values (possible chemical spill sites) located at 1, 2, 7, 15, and 19 in fig. 1. Correlation coefficients were then calculated for each of the comparisons.

The first experiment was designed as a baseline point from which all other experiments were varied. A 10 by 20 grid was fixed over the entire study area. The number of contributing stations, specified in the Barnes objective analysis, was set to three. The interpolated values from the nearest grid point to each of the potential spill sites were used for comparison.

The second experiment used the same 10 by 20 grid and nearest grid point data; but this time the number of contributing stations was reduced to two. This experiment seeks to determine how sensitive the Barnes analysis is to the number of contributing stations.

The third experiment tested the sensitivity of the interpolation to the number of contributing stations once again. This time the number was increased to six. All other parameters from the first baseline experiments remained the same. Only two of the five original possible spill sites were considered in order to have time to make additional experimental tests.

The fourth experiment tested the interpolation sensitivity to the grid resolution. The grid resolution was increased to 30 by 40 over the entire area. As in the baseline test, three contributing stations and data from the nearest grid point were used.

4. DISCUSSION OF INTERPOLATION RESULTS

The interpolation experiments show that temperature and relative humidity can be interpolated with a great degree of accuracy, while the interpolation of winds is poor. Correlation coefficients between observed and interpolated temperatures and relative humidities varied between 76 and 96 percent for all stations and all experiments. Correlation coefficients for windspeed ranged from 54 to 69 percent, and wind direction ranged from 7 to 34 percent (see figs. 2 through 4).

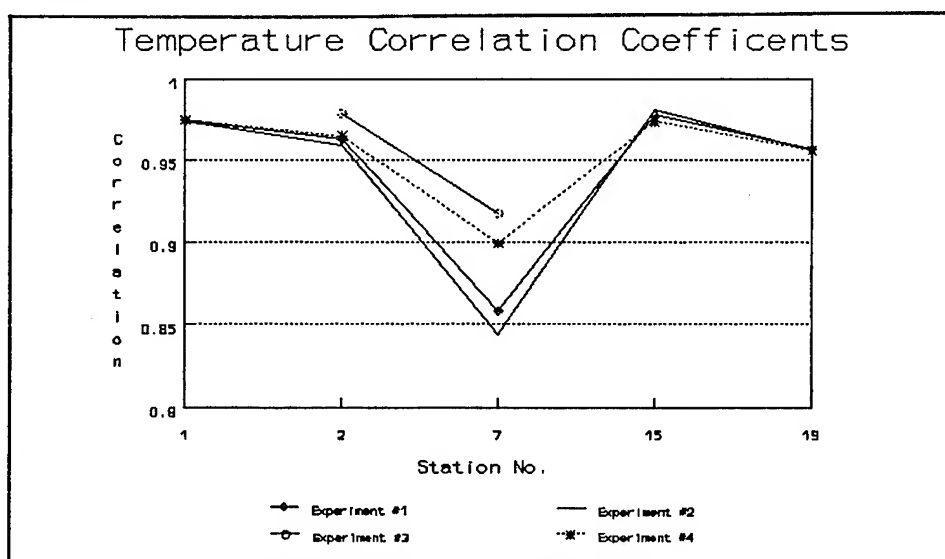


Figure 2. Correlation coefficients of temperature.

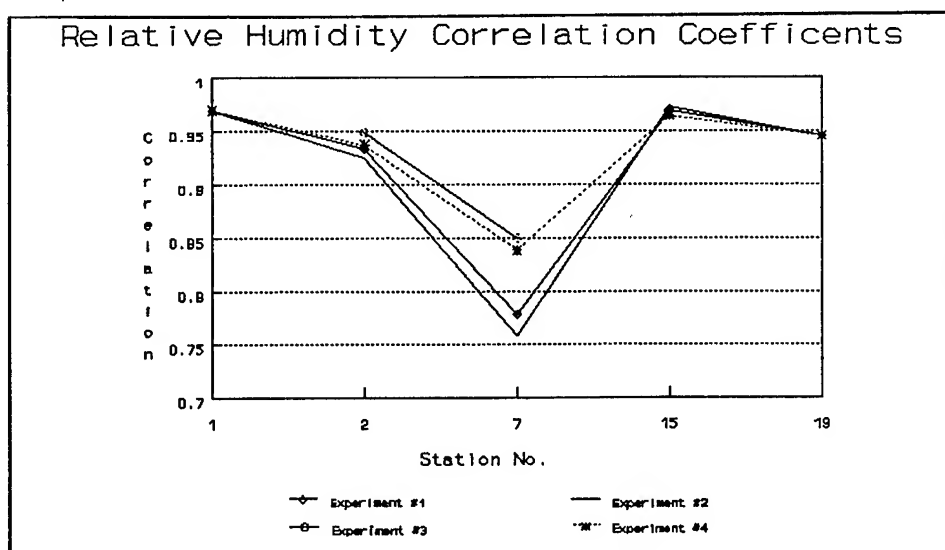


Figure 3. Relative humidity correlation coefficients.

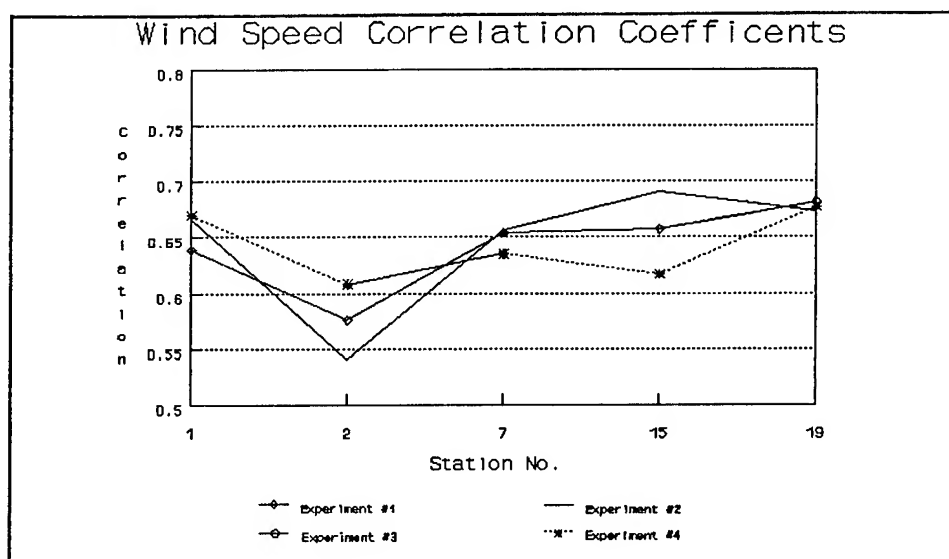


Figure 4. Windspeed correlation coefficients.

Correlation coefficients increased 10 percent or less by considering more stations in the interpolation and increasing the grid density. This improvement of 10 percent is expected to have little or no effect on the mission-oriented protective posture (MOPP) TDA recommendations.

5. DESCRIPTION OF THE TDA SENSITIVITY STUDY

5.1 DESCRIPTION OF THE MOPP TDA

The MOPP program estimates the probability of occurrence of heat stress casualties under given conditions of air temperature, relative humidity, windspeed for MOPP levels 1 to 4, and a variety of different forms of both sustained and intermittent activities. The program is based on the rise in body core temperature as predicted by the Ballistic Research Laboratory Program "TCORE."

The sensitivity study results do not account for errors inherent in the MOPP TDA calculations. We assume that the TDA calculations and recommendations are accurate. Whether this assumption is correct is unknown, and information concerning the absolute accuracy of this TDA is unavailable. The sensitivity studies define the error budget of the TDA but will not address its absolute accuracy.

5.2 METEOROLOGICAL DATA USED IN SENSITIVITY STUDY

Once all of the experiments were completed, sets of meteorological parameters used by the MOPP TDA that assesses heat stress casualties were generated. The question to be answered is "Can the interpolation algorithm be modified (either by increasing the number of contributing stations or increasing the grid density) to increase the correlation coefficients between the observed and interpolated values and will the MOPP TDA give more accurate recommendations?". Two cases were chosen from among the experiments to investigate this phenomena.

The first case consists of experiment #1, site #7, to represent a worst case scenario. The second case consists of experiment #3, site #7, to represent an increase of interpolation accuracy. For the second case, the number of contributing stations was increased and the resulting correlation coefficients between observed and interpolated values were improved. The meteorological values from these experiments are shown in table 1.

TABLE 1. CASE 1 AND CASE 2 VARIATIONS IN METEOROLOGICAL PARAMETERS

Trial Case (No.)	Temperature (°C)	RH (%)	Windspeed (m/s)
Case 1	15.0 +/- 4.5	38.3 +/- 15.7	4.2 +/- 2.5
Case 2	15.4 +/- 3.5	36.2 +/- 12.0	3.5 +/- 1.9

The meteorological values shown in table 2 were arrived at by applying the root-mean-square (rms) errors to the observed mean values of the interpolated data (shown in table 1) in such a way as to cause the TDA to predict maximum and minimum MOPP values. Temperatures were varied by adding the rms error to the mean. The RH was varied by adding the error to the mean. The windspeeds were varied by subtracting the error from the mean. Higher temperatures, higher RH, and lower windspeeds cause the person in MOPP to experience more severe heat stress. This is what is meant by "Most Strenuous" in table 2. The converse situation was implemented to achieve a situation that was "Least Strenuous" since lower temperatures, lower RH, and higher windspeeds ease heat stress.

TABLE 2. METEOROLOGICAL VALUES USED IN TDA SENSITIVITY STUDY

Experiment (No.)	Temperature (°C)	RH (%)	Windspeed (m/s)
Case 1 Most Strenuous	19.5	54.0	1.7
Case 1 Least Strenuous	10.5	22.6	6.7
Case 2 Most Strenuous	18.9	48.2	1.6
Case 2 Least Strenuous	11.9	24.2	5.4

6. DISCUSSION OF SENSITIVITY RESULTS

A comparison of the TDA results between the least strenuous Case 1 and least strenuous Case 2 revealed differences in probabilities on the order of 10 percent and differences in time to reach those probabilities on the order of 5 min. Recall that least strenuous Case 2 was generated from the more accurate interpolation results. This suggests that MOPP TDA results for least strenuous Case 2 are more accurate. However, the increased accuracy only affected the probabilities by 10 percent and the times by 5 min. An analyst would consider these differences insignificant. The absolute accuracy of the TDA calculations are unknown. The improvement of TDA accuracy due to increased accuracy of the meteorological interpolation is negligible.

If the interpolation accuracy were to increase to perfection, the rms error for each parameter would reduce to zero. Since perfect interpolation is not possible, each parameter still has an rms error due to the interpolation. By comparing TDA recommendations for least strenuous Case 2 and the most strenuous Case 2, we can see the variability of the TDA results due to the rms errors of each parameter. The inherent error left in each parameter, even after improving the interpolation scheme, still causes the TDA to produce wildly different results between its best and worst case scenarios. Probabilities of casualties vary plus or minus 36 percent, and times to reach those probabilities vary plus or minus 18 min.

An analyst would consider these differences in probabilities and times to reach those probabilities significant. Yet, this is the error that remains due to the interpolation, even though the measured data and interpolation has been optimized. These cases illustrate the greatest degree of accuracy that can be achieved from measured meteorological values. Many of the errors accounted for in this study would be much larger under normal data collection conditions, and the variation in the TDA output would be corresponding larger.

7. SUMMARY

This study has investigated the accuracy to which observations of meteorological parameters can be interpolated to a grid. Four different experiments were performed in which comparisons of meteorological parameters were made between observations at hypothetical chemical spill sites and values from nearby, interpolated grid points. The interpolation accuracy defines the accuracy of TDA recommendations.

The configuration of sensor placement has a large effect on the accuracy of the resulting interpolations. This study has chosen a best case scenario over relatively flat terrain with sensors spread out evenly over the area. Interpolations from data collected in time from operational sensors are expected to be less accurate than presented in this study.

Observations of temperature, RH, and windspeed were interpolated to grids from a set of very carefully chosen observation stations. The interpolation experiments show that temperature and RH can be interpolated with a great degree of accuracy, while the interpolation of winds is poor.

Variations in the observed meteorological parameters caused by interpolation inaccuracies were applied to a TDA. Sensitivity studies were performed to show the degree of variability of TDA output.

Interpolation errors in temperature and windspeed contribute more to MOPP TDA output variability than do errors in RH. Increasing the grid density and optimizing the objective analysis improved the correlation coefficients between the interpolated and observed values. However, these efforts did not have a significant effect on the TDA recommendations.

The inherent error left in each parameter, even after improving the interpolation scheme, caused the MOPP TDA to produce wildly different results between its best and worst case scenarios. Errors produced by the MOPP TDA due to the

inaccuracies left in the best achievable interpolations were plus or minus 36 percent probability of casualties and plus or minus 18 min to reach those probability of casualties.

All terrain effects were minimized. Erroneous data were discarded or adjusted. Poorly calibrated sensors were eliminated. The data used was timely and not stale from a data collection point of view. An ideal arrangement of sensors was chosen. The interpolation method was optimized by increasing the number of contributing stations and the grid density was increased. Still, the MOPP TDA provided recommendations that had a large degree of variability due to the interpolation inaccuracies and the inherent TDA sensitivities.

These experiments illustrate the greatest degree of accuracy that can be achieved from measured meteorological values. Many of the potential data acquisition problems accounted for in this study would be much larger under normal data collection conditions. The interpolation errors from real-time data acquisition would result in even larger variations in the TDA output.

The results presented here are specific to this particular data set and are not guaranteed to be the same if the time of year or the locations of observations and spill sites were changed. For this reason, this study should be considered as a baseline starting point. Other similar studies should be performed to verify these results. Time of year, station locations, and site locations should all be varied. A similar study should also be performed using real-time observations and verifications over terrain that is not quite so uniform.

REFERENCES

- Barnes, S. L., 1964: A Technique for Maximizing Details in Numerical Weather Map Analysis. J. Appl. Meteorol., 3:396-409.
- Brock, F. V., 1990: Analysis of the Surface Atmospheric Measurement System, Final Report, Contract Monitor: Teizi Henmi, U.S. Army Atmospheric Sciences Laboratory, White Sands Missile Range, NM 88002-5501 (unpublished).
- Clark, Pamela A., Richard Wade, John R. Elrick, and David L. Motte, 1990: A Tactical Decision Aid for Determining Meteorological Sensor Placement. In Proceedings of the Tenth Annual EOSAEL/TWI Conference. U.S. Army Atmospheric Sciences Laboratory, White Sands Missile Range, NM 88002-5501, 369-375.
- Henmi, T., 1989: Evaluation Study of Diagnostic Windflow Model over Complex Terrains - Interpolation Methods, ASL-TR-0241, U.S. Army Atmospheric Sciences Laboratory, White Sands Missile Range, NM, 42 pp.
- Motte, David L., 1986: Analytic Methods of Fitting Multidimensional Surfaces to Wind Fields Over Complex Terrain with Applications to the Sensor Density and Placement Problem. Final Report, DAAG29-81-D-0100, Battelle Columbus Laboratories, P.O. Box 12297, Research Triangle Park, NC 27709, 21 pp.

- Motte, David L., 1987: An Algorithm for Determining the Placement and Density of Meteorological Surface Sensors in Complex Wind Fields. Final Report, DAAL03-86-D-001, Battelle Columbus Laboratories, P.O. Box 12277, Research Triangle Park, NC 27709, 21 pp.
- Tabor, Pamela A., Don R. Veazey, and L. F. Hall, 1986: Meteorological Sensor Density on the Battlefield. In Proceedings of the Twenty-Fifth Annual Army Operations Research Symposium, Oct 8-9.
- Tabor, Pamela A., and L. F. Hall, 1987: Meteorological Sensor Density and Placement on the Battlefield. ASL Interim Report 87-2, U.S. Army Atmospheric Sciences Laboratory, White Sands Missile Range, NM 88002-5501.
- Tabor, Pamela A., Don R. Veazey, and L. F. Hall, 1987: Improvements in a Sensor Density and Placement Algorithm. In Proceedings of the Seventh Annual EOSAEL/TWI Conference, VOL I. U.S. Army Atmospheric Sciences Laboratory, White Sands Missile Range, NM 88002-5501, 229-240.
- Tabor, Pamela A., and David L. Motte, 1987: Optimal Placement of Meteorological Surface Sensors on the Battlefield. In Proceedings of the Eighth Annual EOSAEL/TWI Conference, VOL II. U.S. Army Atmospheric Sciences Laboratory, White Sands Missile Range, NM 88002-5501, 461-470.
- Tabor, Pamela A., and David L. Motte, 1989: Optimal Placement of Surface Sensors for Reconstruction of Wind Fields with Emphasis on Data Denied and Avoidance Areas. In Proceedings of the Ninth Annual EOSAEL/TWI Conference, VOL I. U.S. Army Atmospheric Sciences Laboratory, White Sands Missile Range, NM 88002-5501, 37-47.
- Veazey, Don R., and Pamela A. Tabor, 1985: Meteorological Sensor Density on the Battlefield. In Proceedings of the Sixth Annual EOSAEL/TWI Conference, VOL II. U.S. Army Atmospheric Sciences Laboratory, White Sands Missile Range, NM 88002-5501, 549-562.

TARGAC Demonstration

Patti Gillespie

**U.S. Army Atmospheric Sciences Laboratory
White Sands Missile Range, NM 88002-5501**

The capabilities of the latest version of the EOSAEL target acquisition model TARGAC are demonstrated on a 386 notebook PC. This model makes detection and recognition predictions for thermal devices, direct view optics, image intensifiers, silicon televisions, and user defined devices. The model has a molecular and aerosol extinction capability, uses sky-to-ground ratio calculations, incorporates smoke attenuation calculations when appropriate, and accesses three other EOSAEL routines for illumination, climatology, and extinction calculations. The new thermal contrast model, TCM2, will be demonstrated. TCM2 includes a slightly modified target menu with capabilities to include additional targets. Near future upgrades to TARGAC will be discussed during the demonstration including the merging of the ASL target acquisition tactical decision aid with TARGAC .

(The full text of this paper was unavailable at press time.)

PC BASED BETA SITE SYSTEM FOR AAODL APPLICATIONS

Young P. Yee
Robert A. Sutherland
U.S. Army Atmospheric Sciences Laboratory
White Sands Missile Range, NM 88002-5501

John Crain
Science Technology Corporation
Las Cruces, NM 88005

Liam McDaid
Physics Department, New Mexico State University
Las Cruces, NM 88003

ABSTRACT

The AAODL (Atmospheric Aerosol and Optics Data Library), which is sponsored by Chemical Research, Development and Engineering Center (CRDEC) and the Atmospheric Sciences Laboratory (ASL), is a database system to provide for the collection and management of the various Electro-Optical obscuration data reported from field tests such as the SMOKE WEEKS, Dusty Infrared Tests (DIRT), and SNOW. The mainframe AAODL site consists of relational database software, storage facility for tapes, reports and documentation, and output data retrieval facility for responding to user needs. A new user operated PC based beta site has been setup at ASL to facilitate sharing, dissemination, and modeling of field and laboratory data. The database format and language is compatible with the AAODL mainframe system, thus allowing easy data transfer. The user can tailor large data sets for individual requirements without the excessive overhead usually associated with large mainframe systems. The beta site gives users a stand alone capability to extract selected data from the mainframe system, to store and maintain on a smaller scale their own data of interest and to develop their own specific database applications for graphical display, analysis, and modeling. In this paper, the beta site system configuration is discussed and various hardware as well as software options are recommended. Graphical examples of SMOKE WEEK data and realtime computation and retrieval of data sets are demonstrated.

1. INTRODUCTION

The Atmospheric Aerosol and Optics Data Library (AAODL) is sponsored by the Chemical Research, Development and Engineering Center (CRDEC) and the Atmospheric Sciences Laboratory (ASL). The major function of the AAODL is to provide a system for the archival, retrieval, analysis, and quality control of data collected from laboratory experiments and field tests such as DIRT (Dusty Infrared Tests), BICT (Battlefield Induced Contamination Test), BEST (Battlefield Emissive Sources Test), and SMOKE WEEK tests. Currently, the AAODL mainframe hardware consists of a UNIX based SUN Microsystems network, 450 MByte fixed hard disks, 9-track tape drives, 3.5" and 5.25" floppy disk drives, a digitizing board, and graphics plotters (Crain, 1988). The primary computer software is the commercially available ORACLE Relational Database Management System (RDBMS). The main computer facility houses over 60 field tests with as many as 140 trials per field test.

Although gigabytes of data are available to the end users on the mainframe computer, the end users still must have some computer facility at his locale to accept selected data sets. In the remainder of this paper we describe the "beta site" concept that allows the user to set up their own scaled version of the AAODL database without the need for a larger mainframe.

2. AAODL DATA FLOW PROCESS

The conceptual AAODL data flow process is illustrated in Fig. 1 where the

measured field test and laboratory data are collected and then processed and stored in a relational database format. Once the data has been properly archived the end users extract pertinent data by using the powerful database tools available on the mainframe computer.

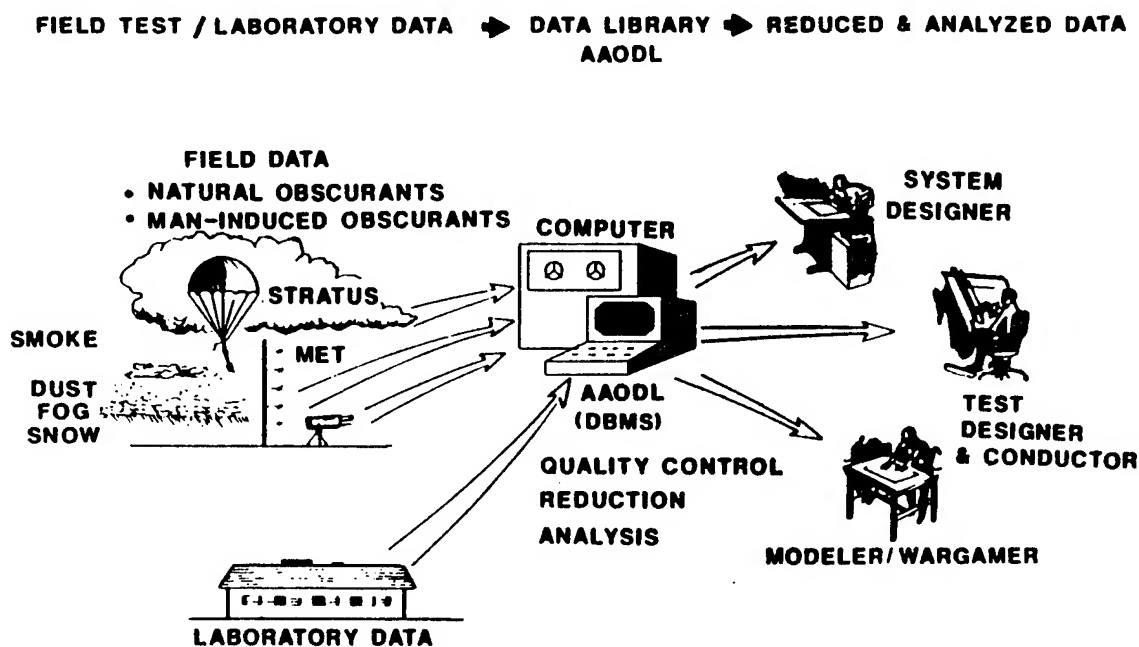


Figure 1. AAODL Date Flow Process.

The field experiments involve both naturally occurring obscurants such as wind blown dust, fog, rain, and snow and man-induced obscurants such as smokes, fire debris, and vehicular generated dust. The mainframe computer system resides on a SUN/UNIX Ethernet system implementing the ORACLE Relational Database Management System (Crain et al., 1991).

During initial entry into the AAODL database management system, the data is checked for bad data records, consistency, and data typing. Once the data has been loaded and formatted properly, the data can be averaged, reduced, quality controlled, and analyzed. At this stage, the end user can have access to the data either directly or through other transfer media (terminal, floppy disks, 9-track tapes, hardcopies). Supporting and supplementing the computerized data library is a collection of printed documentation and data, videotapes, and field test documentation. Possible applications of the data include system design, test design, modeling, wargaming, tactical decision aid development, training and education.

3. PC BETA SITE CONCEPT

Figure 2 is a schematic of the mainframe computer system containing gigabytes of field and laboratory data and a system of PC beta sites consisting of selected data for specific applications. These beta sites have the capability to load and manage as much as 100 megabytes of data depending on the end user's hardware configuration. The end users can then perform database functions on a local microsystem and develop tailored software for model analysis. Modem connections allow the users access to the mainframe database system and a means to directly issue database inquiries.

The primary hardware component of the PC-Beta site is a personal computer with a 386 microprocessor running at 33MHz and with 10MB RAM. With this configuration, the user can efficiently handle large subsets of data and perform database and graphical functions. The power of the software packages with this PC allows it to utilize full graphics (on screen and hardcopy) capability. For this demonstration, data on a variety of scattering agents was used.

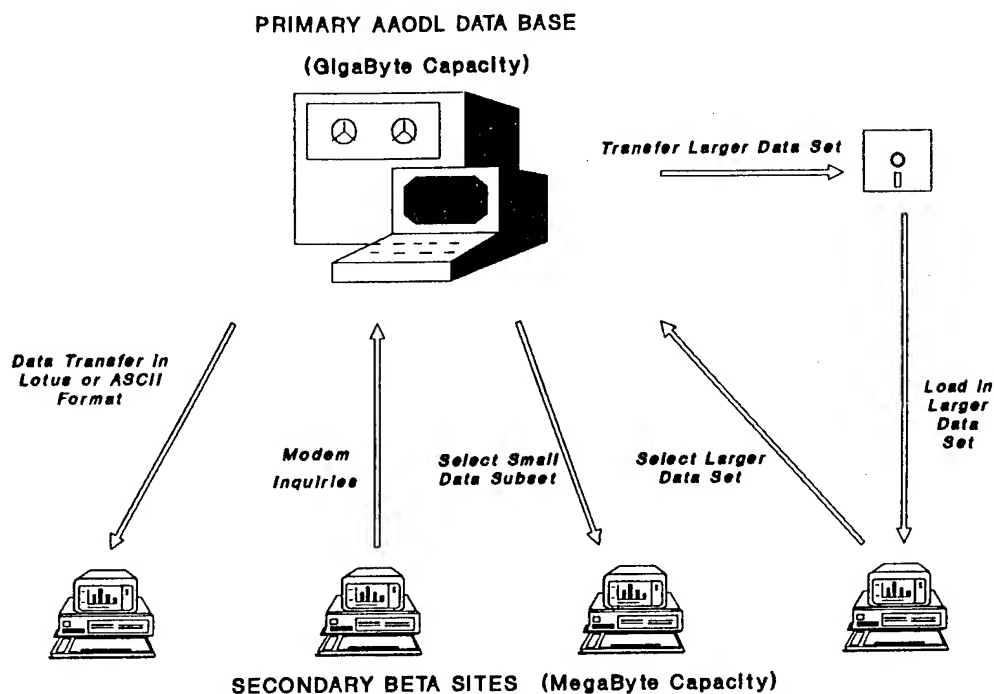


Figure 2. Primary AAODL mainframe computer and interactions with secondary PC-Beta site computer systems.

This machine also has a 600 Megabyte hard disk which is desirable when accessing large data sets on-line. An important consideration in choosing a hard disk is the user's data requirements and the overhead storage needed by the RDBMS to perform data backups. This gives a large level of latitude in holding and using large pieces of data.

The PC-Beta site has several graphics packages. Some software packages are interactive, stand alone executable code such as Grapher and Surfer while other packages such as Grafkit (NCAR graphics for the PC) contain callable FORTRAN graphical subroutines that must be integrated into the user's code and compiled. The latter allows for detailed user applications but the learning curve is higher than the former packages.

4. DATABASE FUNCTIONS

4.1 RELATIONAL DATABASE VERSUS CONVENTIONAL PROGRAMMING

A powerful feature of the PC based system is that the end user can perform full relational database functions under the ORACLE RDBMS. The advantage of a relational database system is that it is easy to learn and use. The heart of the relational system is the SQL (Structured Query Language) command language which is an English-like language defined by IBM and introduced into the commercial market in 1979. The American National Standards Institute (ANSI) has endorsed SQL as the standard relational database language. This standardization allows compatibility with the mainframe AAODL system as well as other SQL based systems such as INGRES and INFORMIX.

In the past, computer programmers expended extensive resources on procedural conventional programs to store, retrieve, sort, and combine and calculate data. These conventional programs quickly became complicated, redundant, and hard-to-debug as the number of data types and data entries increased. Also, these programs require expert programmers to tailor computer code that is often difficult to transport to other systems. On the other hand, relational programs are non-procedural and the user can retrieve pertinent data without extensive experience in data processing. Efficient data storage and quick data retrieval are already an integral part of the RDBMS.

In the relational database environment, the user does not need to know detailed data storage parameters, such as record length or the order of record storage, to access data. The database management system language allows the user to operate on any subset of a data table.

4.2 RELATIONAL DATABASE STRUCTURE

The basic unit of information in a RDBMS is a table. A table is made up of columns (vertical) and rows (horizontal). A row is made up of fields. Each field contains a data value at the intersection of a row and a column. In some respects, a table is very similar to a two dimensional electronic spreadsheet with data cells identified by rows and columns.

4.3 SQL COMMAND MANIPULATIONS

SQL functions allow the user to create tables in the database, store information in tables, select specific information from the database, make changes to the stored data, change the structure of a particular table such as adding or deleting columns, and combine and calculate data to generate the necessary information.

5. EXAMPLES OF DATA ANALYSIS ON BETA SITE SYSTEM

5.1 The PC-Beta system is also useful for generating data from computer models. Computer results from a white phosphorus model and fog oil model were calculated on the 386 PC computer system. There are a variety of codes available that can calculate such quantities as extinction coefficients as well as phase functions for a variety of shapes.

5.2 In the database, similar data are stored in one table. But the database allows the user to select data from two or more tables and combine the selected data in a single result. This feature can be illustrated by selecting a particular test trial and time interval and then extracting data from two tables. The correlation of transmittance and obscurant density of aluminum flakes can be seen in Fig. 3. The transmittance was taken from a multiple path transmissometer and the obscurant density was measured by a mass dosimeter. Graphical display of simultaneous measurements is an important part of data quality control and post analysis. This plot demonstrates the dependance of transmittance on the amount of material. It is also interesting to note the large fluctuations in transmittance over time.

5.3 Another method of presentation is to compare a measured quantity with the corresponding model calculated quantity. In this way, the assumptions leading to the calculated results can be evaluated and models can be validated. Figure 4 is an example of comparing measured smoke concentrations using mass dosimeters and calculated smoke concentrations from the simultaneous transmittance measurements. The relation between transmittance and the concentration of material generally follows an exponential function as predicted. These two independent measurements agree to a large degree although the calculated concentrations overestimate the measured density.

5.4 Laboratory data related to the physical properties of smokes are in the AAODL and can be easily accessed. In Fig. 5 the refraction indices for fog oil from 1 to 20 μm are plotted. There is correlation between the two indices as

is expected by the theorems of physical optics. The absorption peak in the region between 3 and 4 μm is due to hydrocarbon molecules that makes up fog oil and is often overlooked in field measurements. From the laboratory measurements, models can be developed and evaluated as shown in Fig. 6. The model used is a modified Mie scattering code for the extinction coefficients of fog oil. From model calculations with different particle sizes, the extinction coefficients computed from .4 μm particles showed the best fit to the laboratory data.

5.5 The PC-Beta site computer is capable of performing both spherical and non-spherical particle scattering calculations. Figure 7 shows some of the recent tests on phase functions. Phase functions for three different geometries: sphere, infinite cylinder, and finite cylinder, are shown. This data was generated from a computer code that was modified from Evans's (1990) scattering code. Tests like these give us insight toward understanding radiative transfer for non-spherical particles.

5.6 Relationships between two measurements taken at different wavelength regions can be investigated. The optical depth plot of test Trial #375 from SMOKE WEEK VIII (Fig. 8) shows two transmittance channels; one in the visible, one in the 3-5 μm range. It also shows the exponential relation of the transmittance of the two bands. In this plot, the maximum transmission is at the origin. The extinction coefficient ratio of the two bands, which determines the transmittance over wavelength, can be found from the slope of this line. In this case, it is 1.0.

5.7 Three dimensional display of data is a particularly useful tool in revealing surface features and patterns. Multiple arrays of data can be viewed in one graph. Figure 9 is a 3-D plot showing the concentration of brass flakes as measured by an array of nephelometers at Smoke Week XII. As the nephelometer axis is a measure of position, one can see that the smoke plume is physically drifting in space as the test progresses. At $t=250$ seconds, the plume seems to build up in concentration around the nephelometer sites 16-21. Nephelometer 4-6, 11-13, and 18-20 are above each other on the same pole. The pole spacings are approximately 20 meters apart.

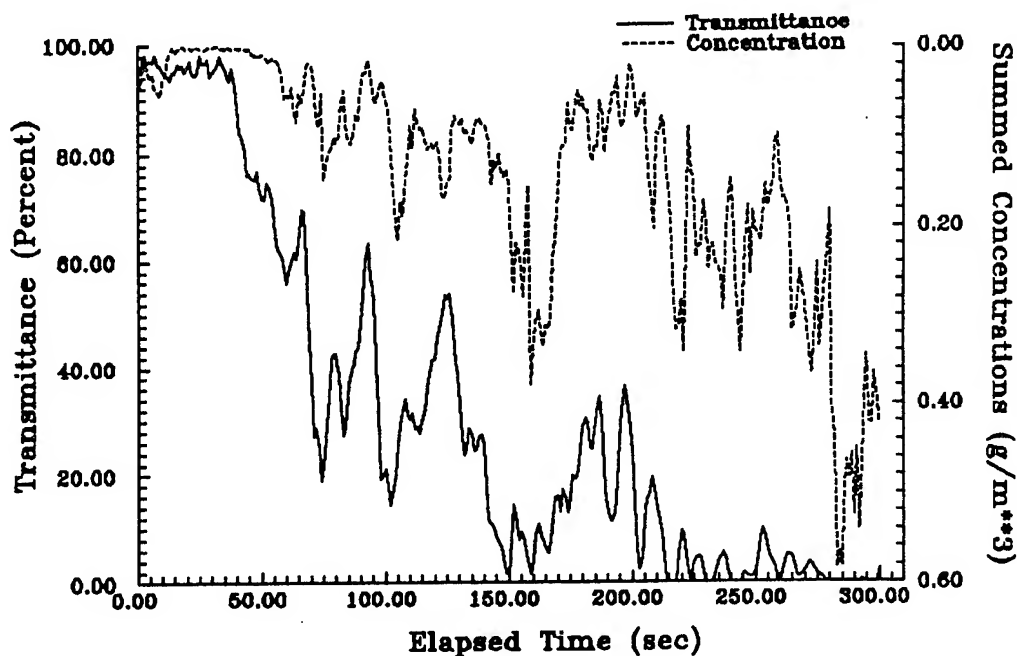


Figure 3. Transmittance and concentrations of Aluminum flakes from SMOKE WEEK XII, trial 8904.

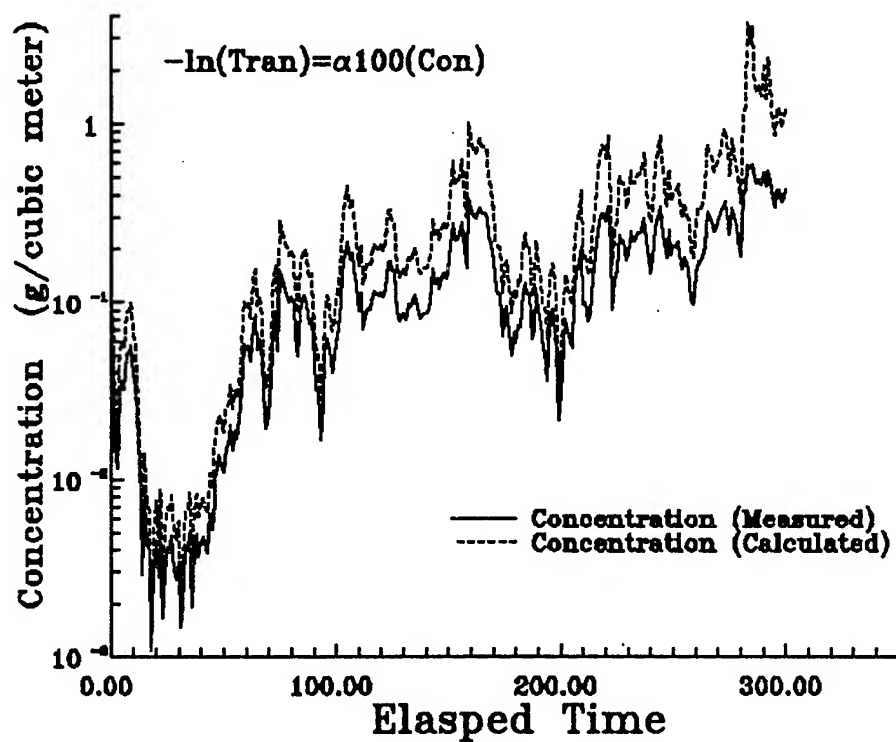


Figure 4. Comparison of mass dosimeter measured concentrations and derived concentrations from transmissometer measurements.

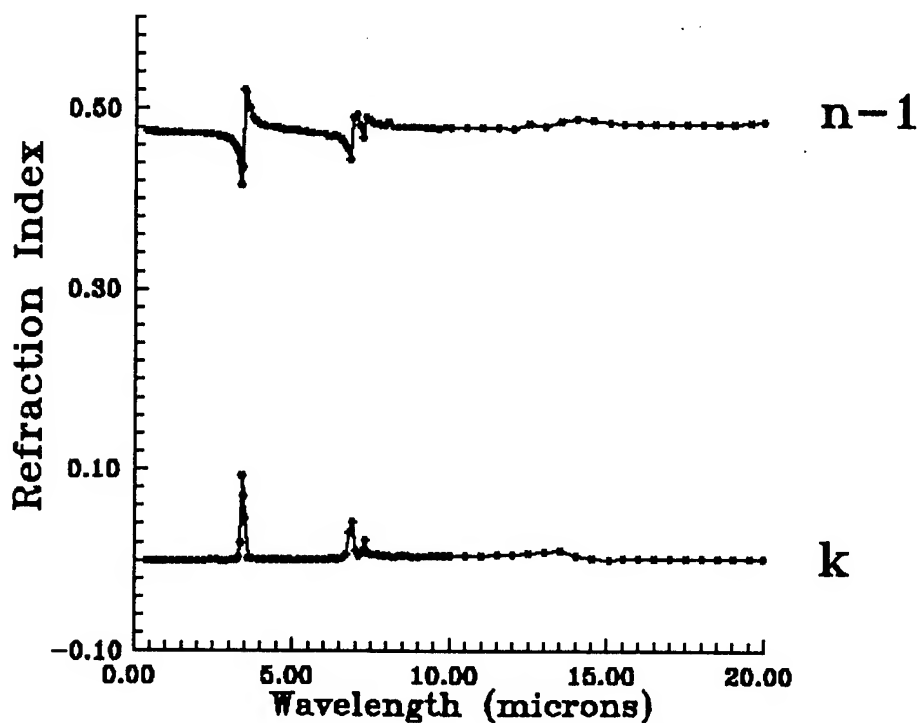


Figure 5. Refraction indices for fog oil.

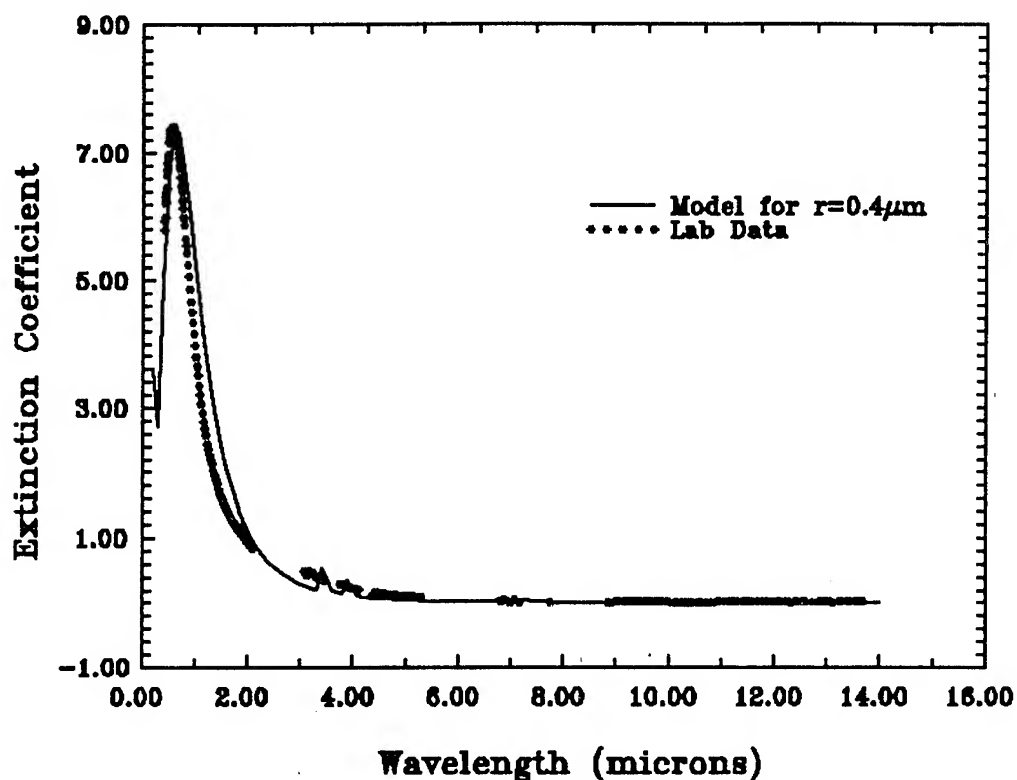


Figure 6. Comparison of model results assuming a monodisperse droplet distribution of $.4\mu\text{m}$ radius and measured fog oil data.

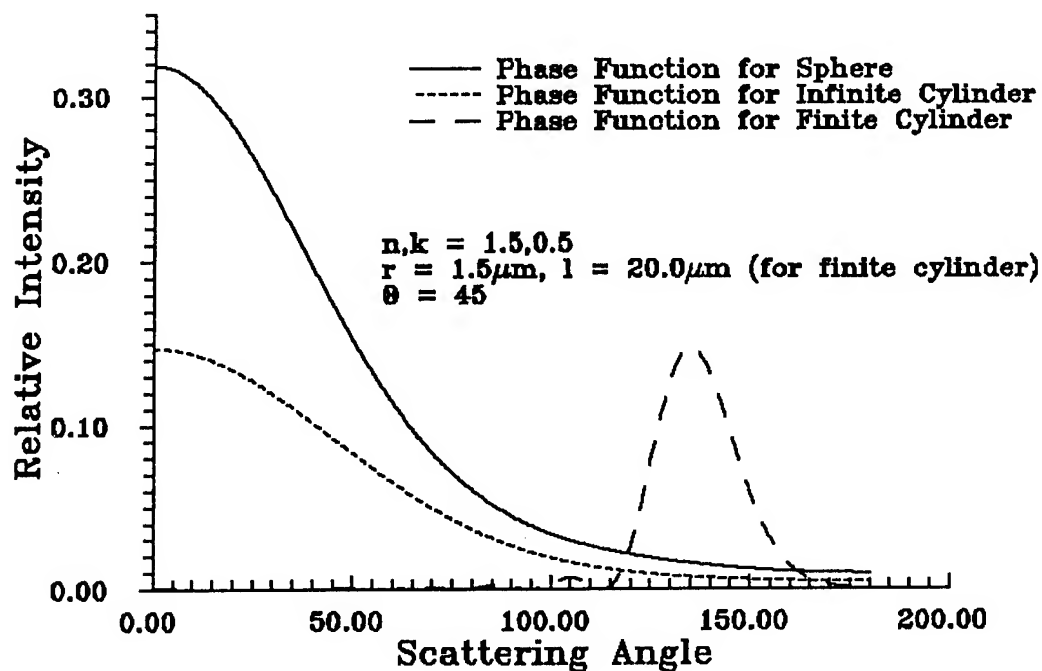


Figure 7. Calculated phase functions using the IPHASE scattering code for spheres and cylinders (Evans, 1990).

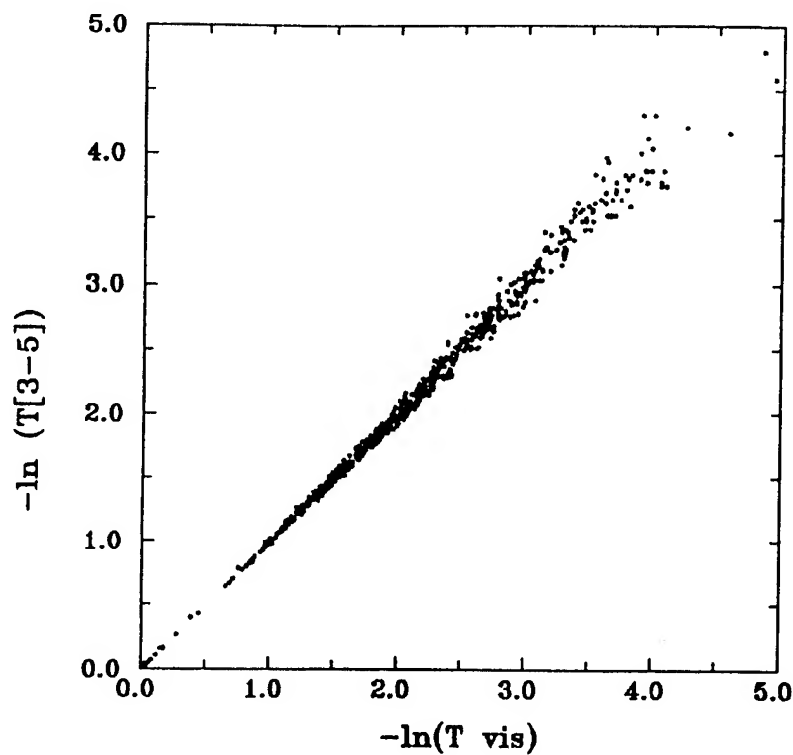


Figure 8. Optical depth plot from transmittance field data from SMOKE WEEK VIII, Trial 375 (AAODL Bulletin, 1991).

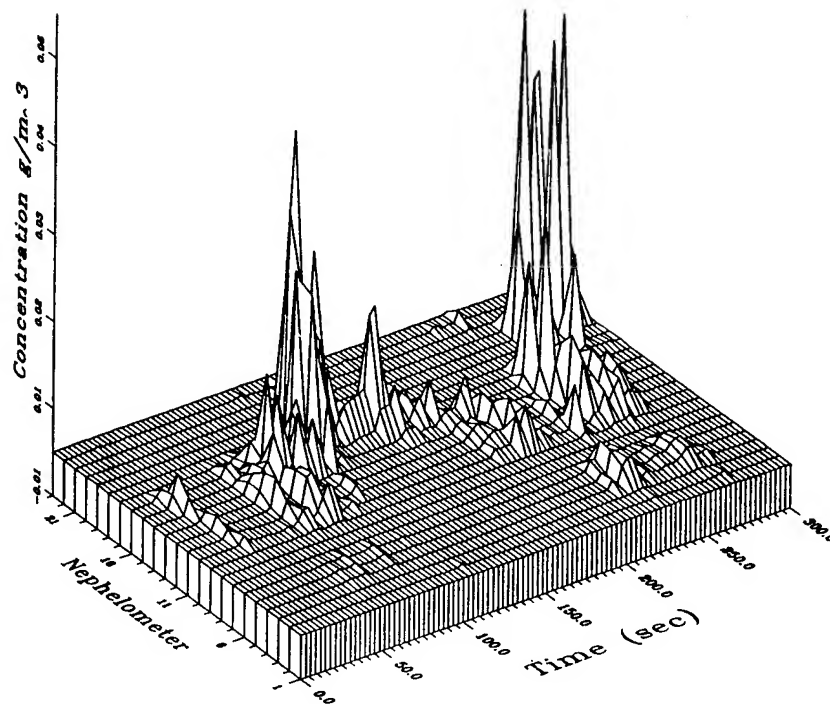


Figure 9. Three dimensional plot of brass concentrations versus time from an array of nephelometers at SMOKE WEEK XII, Trial 1703.

6. CONCLUSION

This paper describes the hardware and software characteristics of a 386 PC required to run a relational database management system for maintaining specific field data for the end user. A relational database system on a PC based environment is a powerful tool for end users. The end user has access to full relational database functions as well as well-tested commercial PC graphical software packages. These tools allow portability of large data sets as well as localized storage and maintenance of user specific data. The user can develop his own database applications and these applications can be run on the AAODL mainframe computer to process data from other field tests.

Graphical display of selected data sets demonstrate the variety of data types available, the time variability of a measurement, and the combination of data sets for analysis and quality control.

End users may request AAODL data in various formats (5.25-inch floppy diskettes, 3.5-inch diskettes, nine-track tape, and hardcopy printouts) via a user request form which can be obtained by contacting any of the authors of this paper.

REFERENCES

AAODL Bulletin sponsored by U.S. Army Atmospheric Sciences Laboratory (ASL) and Chemical Research, Development, and Engineering Center (CRDEC), September 1991 issue, Vol. 9, No. 1.

Crain, J., 1988: Atmospheric Aerosols and Optics Data Library (AAODL) System Upgrades. Proceedings for the Ninth Annual EOSAEL/TWI Conference, Sponsored by Atmospheric Sciences Laboratory, Held in Las Cruces, NM, 29 Nov-1 Dec 1988, p. 317-322.

Crain, J., R. Davis, and R.A. Sutherland, 1991: Accessing the Atmospheric Aerosols and Optics Data Library (AAODL). Proceedings of the SMOKE OBSCURANT SYMPOSIUM XV, Sponsored by the Chemical Research, Development and Engineering Center, Held in Laurel, Maryland, Apr 1991.

Evans, B.T.N., 1990: An Interactive Program for Estimating Extinction and Scattering Properties of Most Particulate Clouds. Department of Defence Materials Research Laboratory.

WADIF: A PROTOTYPE SOFTWARE
SYSTEM FOR FUSING WEATHER AND DOCTRINAL INFORMATION

Stephen Kirby
U.S. Army Atmospheric Sciences Laboratory
White Sands Missile Range, New Mexico 88002-5501, USA

ABSTRACT

The Weather and Doctrinal Information Fusion System (WADIF) is a prototype software system designed to automate the weather and terrain analysis component of the intelligence preparation of the battlefield process. It is undergoing continuing development and is in the initial stages of evaluation. This paper describes a demonstration of the WADIF system, using weather and terrain data for the Fort Hood and Fulda Gap regions. This demonstration highlights several features that are currently incorporated in the WADIF system. One such feature is its ability to categorize how the performance capability of a particular military asset varies over a region based upon available weather and terrain information. This performance categorization can be further refined by the context of a specified mission requirement.

1. INTRODUCTION

The task of the Weather and Doctrinal Information Fusion System (WADIF) "is to determine the acceptability of the performance of Army operation assets, such as tanks and helicopters, under different terrain, weather and mission constraints" (Eskridge, 1991). WADIF is a tool intended for use by either the intelligence officer or the staff weather officer (SWO) for intelligence preparation of the battlefield (IPB), which involves the integration of "enemy doctrine with the weather and terrain, the mission, and the specific battlefield environment" (U.S. Army, 1988). (For a complete description of the IPB process, see Field Manual (FM) 34-130, 1989.) While the user may simply want a synopsis of the current battlefield via current weather, terrain, and military asset information to perform IPB, he often will want the ability to ascertain hypothetical situations. For instance were an inch of rain to fall in the next 2 h how would vehicle mobility be affected. It is this ability to play out "what if" games from which the moniker WADIF is derived.

2. WADIF ARCHITECTURE

2.1 HARDWARE/SOFTWARE REQUIREMENTS

The current version of WADIF is running on a Sun SPARCstation IPX workstation under the UNIX and X-Windows environment, which are fast becoming Army standards. The software is written in C, which is intended to enhance its portability as well as to provide for fast execution.

2.2 METEOROLOGICAL DATA PROCESSING

The meteorological data that WADIF uses for IPB reasoning is preprocessed by the MERCURY subsystem. MERCURY creates a three-dimensional (3D) grid of data by fusing sources such as surface stations, rawinsonde, and satellite data. A set of heuristics guides MERCURY in its data processing and is intended to optimize the extrapolation of data from an observation point to a grid point. Before the heuristics can be called upon, the environmental data must be converted into a format more amenable to reasoning. Significant terrain and meteorological features are converted into individual, manipulable 3D objects, while land-use features are represented as two-dimensional (2D) objects, which like the 3D objects, are separate entities with attributes (McWilliams, 1991).

2.3 DATA AND KNOWLEDGE BASES

A key task for WADIF is to produce asset performance templates that are graphic representations of the varying degrees of an asset's ability to operate under a multitude of terrain and weather conditions. To facilitate the creation of these templates, two knowledge bases and two data bases are maintained by WADIF. The two knowledge bases are the weather effects matrix and the terrain effects matrix.

a. The weather effects matrix is conceptually a matrix with one axis containing all of the known assets and the other axis containing different combinations of meteorological variable values. Each cell contains a value representing the type and/or amount of performance lost or gained by the asset due to the weather conditions.

b. The terrain effects matrix is conceptually a matrix with one axis containing all relevant terrain types, and the other axis containing varying combinations of meteorological variable values. Each cell contains a value representing the type and/or amount of quality lost or gained by the terrain type due to the weather conditions. This module has not been implemented. For further discussion on these two modules, see McWilliams (1992).

The two data bases are the terrain and land use data and the meteorological variables data.

a. The terrain and land-use data base provides elevation and ground cover information, where ground cover refers to the type of area, such as urban, forest, or desert.

b. The meteorological variables data base allows WADIF to query for current or forecasted data by accessing the MERCURY mesoscale data fusion system (Eskridge, 1991).

To insure that WADIF provides an optimum solution, the user has the ability to edit any aspect of the system. For example, in a dynamic meteorological situation, an SWO may have more current data than MERCURY can provide so he could update the meteorological data base appropriately. Other updates might be to the terrain data base after battle damage or to information regarding asset

capabilities. This edit capability also allows the user to create various scenarios such as "worst case" enemy asset configuration or degraded weather conditions; that is, the user can ask the system "What if . . . ?"

Both WADIF and MERCURY are designed in a modular fashion to provide for ease of extensibility and do not contain region-specific heuristics, thus insuring portability.

3. THE WADIF REASONING PROCESS

When a user queries WADIF to produce an asset performance template, the user may ask how the asset will perform as a whole or he/she may ask what will happen given the state of certain components of an asset. This presents no problem to WADIF since it has the ability to reason at several levels. It can reason about an asset as a whole or in terms of its components.

For example, consider a company of tanks. One could construct an asset performance template for the company as a whole or could construct one based on the specific components of each tank. In this way a user can get a picture of an asset's capabilities, given the current conditions; or the user can determine which particular components degrade an asset's performance if any. Along the same vein an intelligence officer may want to create a particular weather/terrain scenario and then selectively disable particular asset components to determine mission feasibility, given a certain asset strength. As far as WADIF is concerned, there is no difference in an asset being a laser gun sight or a company of tanks. In either case a suite of rules applicable to the asset will be fired to determine performance predicated on current weather and terrain conditions (Eskridge, 1991).

4. CONCLUSIONS

WADIF is currently a benchmark demonstration system with the ability to combine weather, terrain, and doctrinal information to output asset performance templates. A limited asset inventory in conjunction with an Army weather factor analysis matrix has been incorporated into the knowledge base. WADIF can currently reason on five assets:

- airborne
- airmobile
- weapons sighting
- reconnaissance
- M1 tank

Clearly an upcoming task will be to expand this inventory. In addition WADIF presently lacks the capability to use mission objectives and constraints when determining the performance rating of an asset. The next version of WADIF will have the functionality to compute the performance of an asset by using mission objectives to determine which components of the asset are mission critical at

particular times during the mission. Also to be added to the knowledge base is a terrain effects matrix that quantifies the effect of weather on terrain. The knowledge base will be further enhanced by adding asset performance histories that will account for both crew and asset performance (Eskridge, 1991). These additions to the knowledge base should strengthen WADIF's reasoning capabilities significantly.

Furthermore, while MERCURY provides certain features of a geographic information system (GIS) to aid in WADIF's reasoning, more robust GISs are being considered. Among them are the Geographic Resources Analysis Support System written and supported by the Construction Engineers Research Laboratory and a GIS currently being developed by the Army. The Army GIS will likely be a synthesis of components of the TerraCAMMS GIS developed at the Waterways Experiment Station (WES) and the user interface module from the Maneuver Control System and is being designed with Army Tactical Command and Control System common hardware system compatibility in mind. TerraCAMMS itself is a merger of the TerraBase mapping system developed by the U.S. Military Academy and the Condensed Army Mobility Model System (CAMMS) written by WES.

To bring greater realism to WADIF, three-dimensional rendering is now being considered. This is not a simple problem and requires addressing the hardware and, in particular, the software requirements. The software package we are leaning toward for three-dimensional rendering is the Applications Visualization System (AVS). The initial demonstration will likely feature a fighter descending on an enemy headquarters passing through several weather types and then evading enemy radar, although the exact scenario configuration has not been definitively decided on. This effort will require considerable knowledge elicitation on asset capabilities as well as software development for the graphics rendering.

REFERENCES

- Eskridge, Thomas C., 1991: WADIF: An Expert System for Fusing Weather and Doctrinal Information Used in the Intelligence Preparation of the Battlefield, ASL contractor report, in preparation, U.S. Army Atmospheric Sciences Laboratory, White Sands Missile Range, NM.
- FM 34-30, 1989: Intelligence Preparation of the Battlefield, U.S. Army Headquarters, Washington, D.C.
- McWilliams, Gary, 1992: Integrating Battlefield Weather and Terrain Data for IPB Through Automated Techniques, In Proceedings of the 1991 Battlefield Atmospherics Conference, U.S. Army Atmospheric Sciences Laboratory, White Sands Missile Range, NM.
- U.S. Army, 1988: ST 100-9, The Command Estimate, U.S. Army Command and General Staff College, Fort Leavenworth, KS.

TACTICAL DECISION AID SOFTWARE DESIGN

ON THE ALBE TESTBED COMPUTER

John B. Spalding and Danforth C. Weems
Physical Science Laboratory
New Mexico State University
Las Cruces, NM 88003

ABSTRACT

The AirLand Battlefield Environment (ALBE) technology demonstration program has focused on the integration of terrain and weather information into Tactical Decision Aids (TDAs) for battlefield commanders. The implementation of ALBE, weather-oriented TDAs on graphics workstations has been ongoing since 1986, first on VAX/VMS platforms and more recently on Unix systems. TDAs developed are in the categories of Weapon System Performance; Nuclear, Biological and Chemical (NBC); Army Aviation; Weather Effects; and Meteorological Analyses. The current ALBE Testbed computer is a 486 PC with Unix and X Windows. In porting the VMS software to Unix, and in planning future changes, several concerns have guided the design of the Unix system. 1) TDA software must be highly modular, non-redundant, and easily maintainable. 2) Portability to future systems must be insured by minimizing and localizing all system-dependent elements of the software architecture. 3) Software libraries may change in the future, in particular those that support Geographical Information System (GIS), User Interface (UI), and graphics functions. A major design element of the current TDA software that reduces all three concerns is the use of high-level "shell" libraries for all GIS, UI, and graphics calls. This allows radical implementation changes in these areas to be made without having to make changes at the TDA level.

1. INTRODUCTION

Work in support of the Atmospheric Sciences Laboratory's participation in the AirLand Battlefield Environment (ALBE) technology demonstration program was begun in 1986. The ALBE program was designed to provide advanced technology in the form of Tactical Decision Aids (TDAs) based on environmental effects on the battlefield. TDAs were to be classed into two groups, terrain and weather, each running on their own ALBE Testbed (ATB) computer system. Products and data were to be shared between the two ATBs with the goal of "fusing" both types of environmental information into integrated TDAs.

After five years, many of these goals have been met. The ALBE Weather system is able to ingest current and forecast weather, produce 2- and 3-dimensional weather data grids and store them in a Geographical Information System (GIS), and supply these and terrain data to weather TDAs. These TDAs are in the categories of Weapon System Performance; Nuclear, Biological and Chemical (NBC); Army Aviation; Weather Effects; and Meteorological Analyses. The most complete references to the scope and use of these TDAs are in Spalding et al. (1990) and Spalding and Weems (1990).

The purpose of this paper is to discuss general aspects of the design of the ALBE weather TDA software from the point of view of maintaining an expandable and portable system. Rather than being well-defined in software and hardware from the beginning, the system has seen radical changes in support software (such as graphics and User Interface [UI]) and in the computer platform itself. In addition, the TDA software has been and will be required to run concurrently on different platforms with different types of support software. Furthermore, in 1990 the process of porting the software from the VAX/VMS to the Unix operating system was begun. Within this changing environment, the TDA software must continue to evolve and remain as system-independent as possible. This paper presents the most important design elements we have developed to meet these needs.

2. GENERAL SYSTEM DESIGN AND HISTORY

A simplified diagram of the TDA software system is shown in fig. 1. Current and forecast weather data are processed into grids and stored in the GIS by the weather software. Separate terrain software stores terrain data, such as land use, vegetation features, and elevation. A particular TDA program, such as NBC, obtains needed data through GIS functions and by directly accessing special TDA data files that are not part of the GIS.

The lower half of fig. 1 shows how information is passed between a TDA and the user. The three middle processes (GIS, UI, and graphics) are libraries of routines linked into the TDA program; these are support modules developed by system integrators. The core TDA code can be largely self contained except when it must communicate with the GIS or the user; in these cases, it must do so through the support modules. A final process shown in fig. 1 is the Map Server. Currently, this module is separate from the TDA program and interacts with the user to display and control the digital map background. In the first ATB, however, the Map Server was not supplied and instead was developed as part of the weather software.

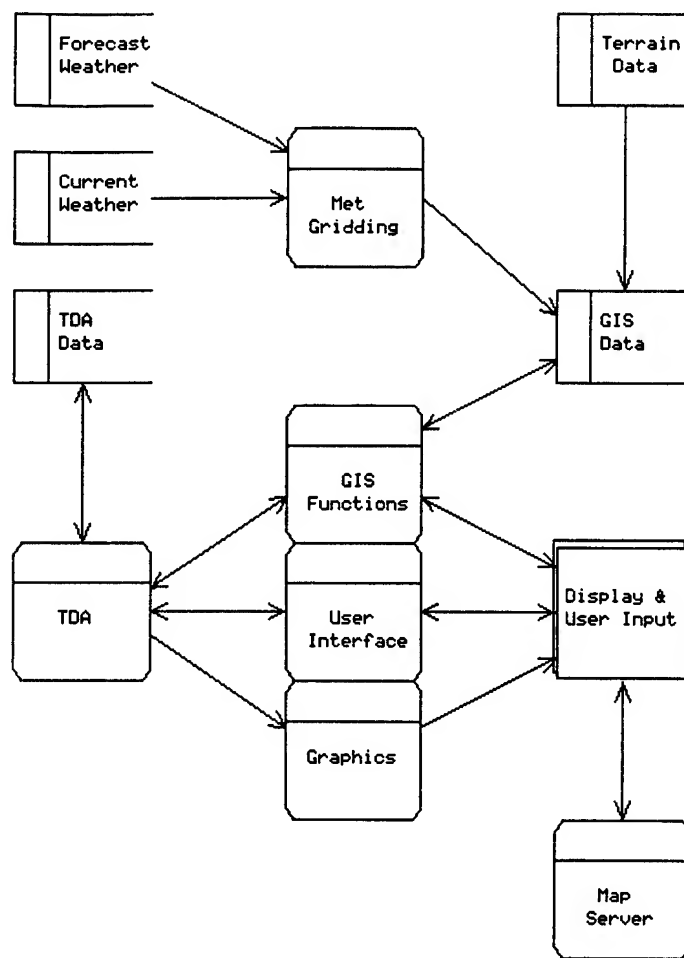


Figure 1. Simplified data flow diagram of the ALBE weather TDA software system. The open boxes represent data storage and the closed boxes represent processes, such as programs. The "TDA" process could be any of the weather TDAs.

Since starting work on the ALBE project, the number and capabilities of the weather TDAs have increased steadily. The support modules and computer platforms, however, have undergone several major changes, as outlined in table 1. The initial weather TDA software was built by porting sections of the Microfix software to VMS. By 1987 the first ATB (a MicroVax II with a graphics monitor) was available, with support modules developed by Battelle Pacific Northwest Laboratories. This ATB support software continued to evolve until 1990, when the decision was made to switch to a Unix/X Windows/Motif ATB, which is a 486 PC graphics workstation.

TABLE 1. HISTORY OF THE ALBE WEATHER TESTBED AND RELATED SYSTEMS

Functional Area	1986	1987	1988	1989	1990	1991	1992
Platform	ATB (VAX)		PAWS			ATB (PC)	ACCS
Operating System	VMS					Unix	
User Interface	Battelle		PAWS MMI			TCAMMS	?
GIS	Battelle					TCAMMS	?
Map Server	Battelle		PAWS Display Mgr.			TCAMMS	?
Graphics (Map)	Battelle GKS		PAWS Display Mgr.			TCAMMS	?
Graphics (Non-Map)	Battelle GKS		VAX GKS Window			TCAMMS	?

During this period, the support modules underwent a number of changes that required a TDA software design be developed insulated from these changes. The Battelle-developed UI and GIS modules increased in capabilities but also underwent several modifications of routine names and argument lists. In 1988, the ALBE software was ported to the Portable ASAS (All Source Analysis System) Workstation (PAWS), which was also a MicroVax II/VMS graphics workstation, but with a display managed through VaxStation Windows and with completely different support modules (except the GIS) developed by Martin Marietta. From 1988 to 1990 the same weather TDA software ran on both the ATB and the PAWS.

In late 1990, VMS development (on the original ATB and the PAWS) was frozen, so that the software could be ported to the second, Unix-based ATB. On this platform, all of the support modules are part of the TerraCAMMS software being developed by Waterways Experiment Station for the ALBE program. As a further complication for software design, the TDA software must be ported to the Army Command and Control System (ACCS) Common Hardware (Hewlett-Packard platforms) by the end of 1991. The question marks in table 1 for the ACCS development branch indicate that the support modules are not determined at this time.

Thus, the history and future of the ALBE weather TDA software puts severe demands on the development of a growing multi-platform system that must also be easily expandable and

maintainable. There are two main areas of design considerations: the TDA software and its interface to the support modules.

3. TDA DESIGN

Special design goals have been to make the TDA-specific code modular, non-redundant, and insulated from system-dependencies. By modular is meant that one TDA does not depend on the code in any other TDA. By non-redundant is meant that functions are not duplicated between TDAs. Any function that is needed by more than one TDA is generalized and maintained with the general purpose software. Finally, no code within a TDA (separate from the general purpose software) may be system dependent. This means that all system dependencies must be handled by lower level routines, which are discussed below.

The most important element that has contributed to meeting these goals has been the design of the general purpose software. The major areas of this software are listed in table 2. As defined in this table, three "modules" perform complex sets of functions not under direct control of the TDA, such as clearing all map graphics overlays. Each TDA calls these three modules to perform the basic set ups as well as the general map and meteorological operations; this allows the TDAs to be independent of how these modules are implemented.

TABLE 2. GENERAL PURPOSE TDA SOFTWARE TYPES AND DESCRIPTIONS

Software Area	Type	Description
General Setup	Module	Performs all setups and initializations
Map Operations	Module	Interactive management of map displays
	Library	Map-oriented I/O functions
Surface and Upper Air Meteorological Data	Module	Interactive met display and editing
	Library	Met I/O functions
User Interface	Library	Shell between TDAs and system UI
GIS	Library	Shell between TDAs and system GIS
Graphics	Library	Shell between TDAs and system graphics; high-level routines, contouring, NCAR
Coordinate Conversion	Library	All general conversion routines
Interpolation	Library	2- and 3-D gridding, interpolations
Mathematics	Library	Geometry, unit conversion, XSCALE
Miscellaneous	Library	Time, string, setup, sorting, operating system, and other functions
System Dependent	Library	Ada-FORTRAN interfaces, system calls

"Libraries" are groups of routines that perform specific functions and return to the calling TDA when done. The UI, GIS, and graphics libraries include special sets of routines we

call "shells", which are discussed in the next section. The remaining libraries listed in table 2 perform the wide range of functions required by all TDAs. The NCAR (National Center for Atmospheric Research) item listed in the graphics library includes special meteorological analysis and display software developed by that organization.

The System Dependent library is a special case. It contains all system-dependent code and is located in a directory with other system-dependent files, such as shell scripts and special data files. There is a different version of this directory for each supported system (at this time the ATB and ACCS). The only other system-dependent files are two special scripts that define environment variables used by the Unix "makefiles" that compile and link the code and programs. The system has been designed so that only a single, high-level environment variable "PLATFORM" need be defined for the software and shell scripts to define and use the correct system dependencies. Thus, to move the entire weather TDA software from the ATB to the ACCS platform requires only three steps: 1) copy all the TDA files, maintaining the same directory structures; 2) make sure that the "PLATFORM" variable is defined correctly; and 3) execute a top-level "Build" shell script to rebuild all the object and program executable files.

4. SHELL LIBRARIES

The areas of the TDA software system that are most system dependent are the three support modules (UI, graphics, and GIS). Table 1 lists the different versions of these modules that have been provided on the first and second ATBs, as well as on the PAWS; also, the versions to run on the ACCS platform are undecided at this time. Given this history, we have designed interfaces (or "shells") between the high-level TDA code and the support module routines.

As an example, to present a menu to the user a TDA would call the shell routine `UIT_MENU_SELECT`. Each system-specific version of the UI shell contains a routine of this name with the same arguments. Which version of the UI shell is accessed by the TDA is determined by linking in the correct version when building the program. Thus, the TDA code is insulated from how menus are implemented on a particular system.

The design of the shell libraries was driven by two considerations. First, the shells must be complete; that is, all needed functions must be provided by the shells. Second, the arguments passed to and from the routines must be such that they do not constrain the routines from using a particular version of a support module. An example of a design element that supports the latter is the definition of attribute arguments, such as text renditions and graphics drawing styles. These are all passed as externally defined symbolic constants (such as "GREEN") and are translated appropriately by the shells.

4.1 USER INTERFACE SHELL

Table 3 lists the routines in the UI shell library. These routines are oriented for text ("`UIT_`"), graphics ("`UIG_`"), or both ("`UITG_`"). A small set of graphics-oriented routines

that display messages and legends are not shown because they were used in only one version are not as well-defined.

TABLE 3. USER INTERFACE SHELL LIBRARY ROUTINES

Routine	Description
UITG_INIT	Initialize for use of text and graphics UI shell
UITG_TERM	Terminate the use of text and graphics UI shell
UIT_SHOW_MSG	Show a message of a particular type
UIT_CLEAR_MSG	Clear the last busy or prompt message
UIT_CLEAR_SCREEN	Clear the text screen (does nothing in X Windows)
UIT_PAUSE	Pause until user wishes to continue
UIT_GET_BOOL	Get a boolean (yes or no) value
UIT_GET_INT	Get an integer value
UIT_GET_REAL_4 / _8	Get a single / double precision real value
UIT_GET_STRING	Get a text string
UIG_GET_POINT	Get a graphics (map or non-map) point
UIG_GET_POINTS	Get multiple graphics (map or non-map) points
UIT_MENU_SELECT	Present a menu for selection
UIT_LIST_SELECT	Present a list for selection
UIT_FORM	Present a form for selection
UIT_OPEN_TEXT_WINDOW	Open the text window for output
UIT_CLOSE_TEXT_WINDOW	Close the text window
UIT_SHOW_TEXT	Show text in the text window
UIT_ERASE_TEXT	Erase text in the text window
UIT_CLEAR_TEXT	Clear the entire text window
UIT_TEXT_BROWSE	Display, print, save (in a file) long text output

4.2 GRAPHICS SHELL

Table 4 lists the routines in the graphics shell library. Not all of the "GS_SET_" routines are listed; for each attribute in the table description there is a separate routine, for example "GS_SET_LINE_COLOR." These routines are similar to the Graphics Kernel Standard (GKS) organization in that the attributes for the graphics primitives must be set before the primitives are drawn.

Graphics I/O occurs within two distinctly different graphics worlds. Map overlay graphics are drawn over the background map and use a longitude/latitude coordinate system. Non-

map (or "chart") graphics are drawn in a separate graphics window and use a normalized (0 - 1) coordinate system; these graphics include various graphs, plots, tables, and diagrams. Rather than have a separate library for each environment, each shell routine may use either. By default, the map graphics environment is used. A call to "GS_START_CHART", however, routes subsequent graphics to the non-map environment until "GS_END_CHART" is called.

TABLE 4. GRAPHICS SHELL LIBRARY ROUTINES

Routine	Description
GS_INIT	Initialize graphics shell for use
GS_CLEAR_ALL	Clear all graphics
GS_START_CHART	Start chart (non-map) graphics
GS_END_CHART	End chart (non-map) graphics
GS_DRAW_LINES	Draw lines between points
GS_DRAW_FILL_AREA	Fill an area bounded by points
GS_DRAW_MARKERS	Draw markers (symbols, icons)
GS_DRAW_TEXT	Draw text
GS_UPDATE	Update (flush) all graphics
GS_SET_LINE_?	Attributes: line color, type, width
GS_SET_FILL_AREA_?	Attributes: fill area color, style, hatch
GS_SET_MARKER_?	Attributes: marker color, size, type
GS_SET_TEXT_?	Attributes: text color, height, alignment, angle, font, precision
GS_GET_POINT	Get a mouse point
GS_GET_POINTS	Get multiple mouse points

4.3 GIS SHELL

Table 5 lists the routines in the GIS shell library. These routines are of two types: cell (or raster) for accessing gridded data and vector for data stored as nodes, lines, polygons, and text. Cell data may be categorical or continuous; the question marks in the cell routine names indicate that there are two versions, one for each of these types of data. The question marks in the vector read and write routine names indicate that there is a different version of each routine for each type of vector object.

TABLE 5. GIS SHELL LIBRARY ROUTINES

Routine	Description
GIS_CELL_COVERAGE	Returns coverage for specified feature
GIS_CELL?_READ_VALUE	Get a value from a 2-D grid
GIS_CELL?_READ_VECTOR	Get a vertical vector through a 3-D grid
GIS_CELL?_READ_GRID	Get a 2- or 3-D grid
GIS_CELL?_WRITE_GRID	Write a 2- or 3-d grid
GIS_VCTR_LIST	Get list of available vector products
GIS_VCTR_SELECT	User selects from list of vector products
GIS_VCTR_OPEN / _CLOSE	Open / close vector product for I/O
GIS_VCTR_READ_HEADER	Read header of open vector product
GIS_VCTR_READ_?	Read next vector object of type node, line, polygon, or text
GIS_VCTR_WRITE_HEADER	Write header of open vector product
GIS_VCTR_WRITE_?	Write next vector object as type node, line, polygon, or text
GIS_VCTR_PLOT	Plot specified vector product

5. DISCUSSION

The design decisions discussed in this paper were necessary because of the evolutionary nature of TDA software development and the changing and uncertain hardware/software systems on which the software runs. In order for TDA software to be easily expandable and maintainable, it was necessary to move all general purpose software into separate libraries. This not only removed redundant code from TDAs, but also made maintenance of the general purpose routines much easier — change in a common function need be made in only one place. More importantly, all system dependencies can be minimized and localized in this general software. The results are TDA modules that are cleaner, higher-level, and insulated from general purpose software changes and system dependencies.

Without the development of the UI, GIS, and graphics shell libraries, the migration of TDAs between computer systems would have required significant changes in code and certainly would have introduced errors. Moreover, the use of shells allowed the same body of software to run concurrently on two different systems, the first ATB and the PAWS. Because there have been only two versions of the GIS (table 1), the GIS shell as outlined in table 5 is immature and may change with more experience. The UI and graphics shells, however, have existed in several versions as the platforms and software support modules have changed. Two versions of the UI shell are in use now on the Unix ATB. One uses the X Windows/Motif interface supplied by TerraCAMMS and must be used on the

graphics monitor. The other uses standard Unix I/O methods and allows the TDAs to be run on text-only terminals by developers.

Although the use of shells offers the advantages outlined above, they do impose a certain rigidity on TDA software design. The use of the UI shell routines limits user interaction to the types and methods of those supported by the shell. The most complex type of interface in the shell, form specification and management, is constrained by how forms are implemented in TerraCAMMS and will be difficult to generalize to different UI support modules in the future. Certain highly customized interfaces may not be generalizable and may have to be system dependent. These types of limitations, however, have been greatly outweighed in the weather TDA software system by the maintainability advantages provided by using shells.

ACKNOWLEDGEMENTS

Arthur W. Dudenhoeffer, Steven J. LaMotte, and Gloria E. McCrary have made significant contributions to the design and development of the weather TDA software system and their efforts are genuinely appreciated. This work was supported by the U.S. Army Atmospheric Sciences Laboratory under contract numbers DAAD07-86-C-0034 and DAAD07-91-C-0139.

REFERENCES

- Spalding, J. B., D. C. Weems, G. E. McCrary, A. W. Dudenhoeffer, J. D. Brandt, D. Sauter, M. A. Seagraves, E. Avara, R. Dickenshied, J. Elrick, and D. Shoop, 1990: AirLand Battlefield Environment (ALBE) Weather Tactical Decision Aid User's Guide for the Portable All Source Analysis System Workstation (PAWS). PSL Report 90/76, Physical Science Laboratory, P. O. Box 30002, Las Cruces, NM 88003.
- Spalding, J. B. and D. C. Weems, 1990: Information on the Use of the ASL Weather Data on the ALBE Testbed Systems. PSL Report 90/43, Physical Science Laboratory, P. O. Box 30002, Las Cruces, NM 88003.

Session III

BATTLE SCALE WEATHER POSTERS AND DEMONSTRATIONS

**Chairperson
Col. Grant Aufderhaar**

MICROMETEOROLOGICAL SURFACE LAYER MEASUREMENTS
FOR CHARACTERIZATION AND MODEL EVALUATION

Ronald M. Cionco
U.S. Army Atmospheric Sciences Laboratory
White Sands Missile Range, New Mexico 88002-5501, USA

ABSTRACT

Micrometeorological measurements in the surface boundary layer are needed to provide a basis to characterize this scale of motion and to test and evaluate army-scale meteorological models. The micro-scale surface layer domain in high resolution is the battlefield environment for most of the field army's operations. The conduct of Project WIND (wind in non-uniform domains) by the U.S. Army Atmospheric Sciences Laboratory (ASL) provides a very large micrometeorological surface layer data base for both characterization and model evaluation. A significant portion of the Project WIND data base is composed of horizontal micrometeorological surface layer measurements as well as vertical measurements within and above vegetative canopy domains. Two major sites were established in canopy-covered/complex terrain domains of different characteristics. One site was located on "flat" terrain with geometrically-neat almond orchards in the domain. The other site was on mountainous slopes and had a complex coniferous forest prominently sited therein. To satisfy ASL's requirements, numerous automated surface meteorological stations were located outside of, near, and above each canopy site and identical sets of eight-level micrometeorological towers were located at three positions in the canopy domains. Micrometeorological measurements of wind, temperature, and humidity were collected in x, y, z, and t. Several examples of these data are presented for the surface layer's horizontal fields and vertical profiles of wind, temperature, and humidity in both time and space.

1. INTRODUCTION

Micrometeorological measurements in the surface boundary layer are needed to provide a basis to characterize this scale of motion and to test and evaluate army-scale meteorological models. The microscale surface layer domain in high resolution is the battlefield environment for most of the field army's operations. The conduct of Project WIND (wind in non-uniform domains) by the U.S. Army Atmospheric Sciences Laboratory (ASL) provides a very large micrometeorological surface layer data base for both characterization and model evaluation. Project WIND (Cionco, 1984 and 1989) is a cooperative field study conducted by ASL and the U.S. Forest Service (USFS). The objective of Project WIND was to collect a comprehensive meteorological, diffusion, and dispersion

data base over complex terrain, including land use such as vegetation domains for the purpose of evaluating and improving select mesometeorological, micrometeorological, deposition, diffusion, and dispersion models. A significant portion of the Project WIND data base is composed of horizontal micrometeorological surface layer measurements as well as vertical measurements near, within, and above vegetative canopy domains. Two major sites were established in canopy-covered/complex terrain domains of different characteristics. One site was located on "flat" terrain with geometrically neat almond orchards in the domain. The other site was on mountainous slopes and had a complex coniferous forest prominently sited therein. Four phases of Project WIND were successfully conducted in and about the Sacramento River Valley of northern California during June 1985 to October 1987. The result is a comprehensive data base documenting four different scenarios of meteorological physics that can be used for characterization of day, night, and diurnal periods and for model evaluation in a truly general sense.

2. FIELD STUDY DESIGN

The design of Project WIND (Cionco, 1989) is based on the multiple-scale data requirements of the ASL's hierarchical system of nested mesometeorological and micrometeorological models (Cionco, 1985 and 1987a). WIND was, therefore, designed with nested measurement domains to address scales ranging from meso-scale to boundary layer, surface layer, microscale, and canopy for nested physical domains of 200 km by 200 km by 8 km, 80 km by 80 km by 1 km, and 5 km by 5 km by 0.032 km. More than 54 measurement sites were established within the WIND domain. The two major sites that acquired data for all scales were established in canopy-terrain domains of different characteristics. One site was a geometrically neat almond orchard on the flat terrain of the Sacramento River Valley. The other site was a more complex coniferous forest on the west slopes of the Sierra Nevada Mountains. ASL was responsible for the acquisition of the micrometeorological data base along with the complimentary surface layer, boundary layer, and upper-air data sets for all phases of Project WIND.

Data was collected over a 2-week timespan for selected periods, resulting in two full sets of daytime, nighttime, and transition (sunrise and sunset) periods and two full 24-h diurnal periods as presented in table 1. Four phases of WIND were conducted during synoptic meteorological regimes (table 1) of weak marine incursion, cyclonic activity, shallow convection, and subsidence to provide data sets to test the generality of the models. In addition to ASL's meteorological data requirements, this data collection also supported other substudies simultaneously such as aerial spray/deposition, aircraft wake calibration, turbulence studies, and smoke trials within and about the two canopy domains. Of specific interest to Army meteorologists are the micrometeorological measurements of Project WIND.

3. MEASUREMENTS AND SITES

To satisfy the characterization and evaluation requirements of ASL's canopy and surface layer models, identical sets of eight-level micrometeorological towers were located at both orchard and forest sites at three positions, along with several surface meteorological stations located above and outside of each canopy. The orchard and forest areas are located within the WIND domain as shown in fig. 1.

TABLE 1. DATA COLLECTION SCHEDULE PER PHASE

Day	Data Period (Local Time) (h)
1	Day: 1000 to 1600
2/3	Night: 2200 to 0400
4/5	Diurnal: 1000 to 1000
6/7	No collection
8	Sunset: 1600 to 2200
9	Day: 1000 to 1600
10/11	Diurnal: 1000 to 1000
12	No collection
13/14	Night: 2200 to 0400
15	Sunrise: 0400 to 1000

Project WIND Field Study Phases

Jun-Jul 85	Marine Incursion	Summer
Jan-Feb 86	Cyclonic Activity	Winter
Apr-May 86	Convection	Spring
Sep-Oct 87	Subsidence	Fall

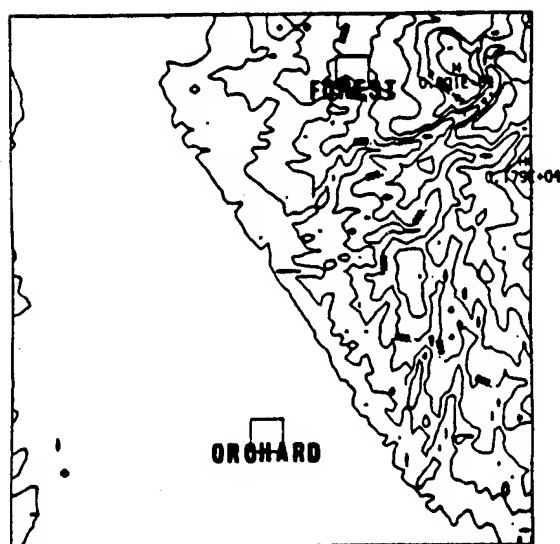


Figure 1. Locations of 5 km by 5 km orchard and forest domains in the mesogamma 80 km by 80 km domain of Project WIND.

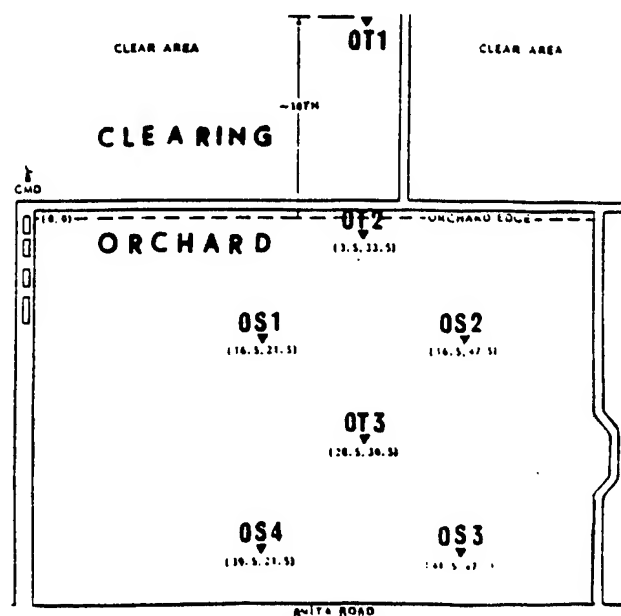


Figure 2. Orchard study area composed of almond orchard and clearing (to north) with OT-1, -2, and -3 micrometeorological towers and OS1-4 elevated surface stations.

The almond orchard was centered in a $(5 \text{ km})^2$ observational area located northwest of Chico, California (fig. 1). The study area was an extensive field of uniformly-cut grain stubble ($H \sim 30 \text{ cm}$) located adjacent (upwind) to the trees. The trees were 8 m in height and planted on 8 m centers in a square pattern. The trees uniformly had globe-like crowns with a vertical trunk space of about 1.3 m.

Figure 2 locates three 16 m towers of identical meteorological sensors that are sited with respect to the orchard's edge. The main tower (OT3) is positioned deep into the canopy (ZEF) more than 20 tree heights (TH) from the canopy's edge. The second tower (OT2) is placed just inside (3.5TH) the canopy's edge. The third tower (OT1) is established on the extensive and uniformly-cut grain field more than 20TH along wind from the canopy's edge in the clearing. Note that OT1 provides the reference profile of the ambient flow for this data set. Figure 3 displays the eight-level instrumented towers that define the canopy and ambient vertical profiles of wind (uvw), air temperature ($T/\Delta T$), and relative humidity (RH) along with special levels of ambient pressure (P), solar (R_s) and net (R_n) radiation, and soil heat flux (H_s). All sensors were sampled once per second exclusively for the schedule noted in table 1. Table 2 identifies the sensor height, variable, and tower location.

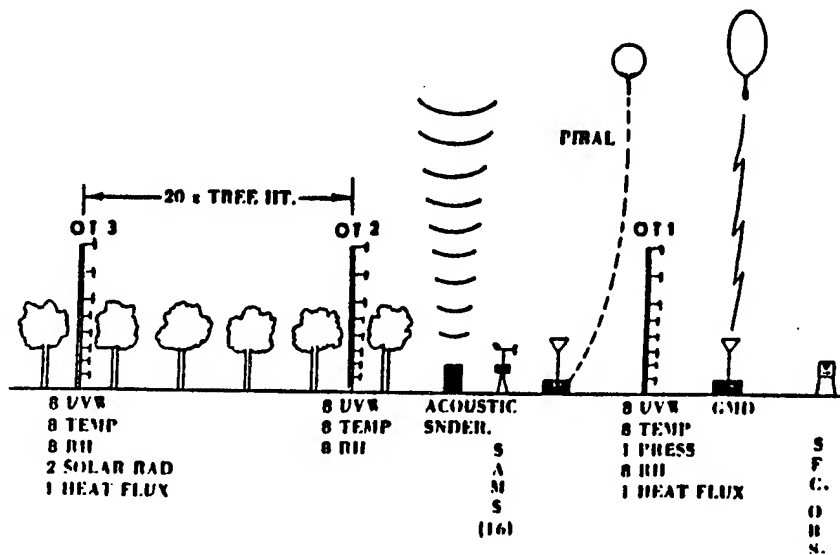


Figure 3. Schematic of the orchard area instrumentation including OT-1, -2, and -3 along with upper-air, boundary layer, and surface stations.

A forest of predominately coniferous trees was selected as the second study area. The forest is also located within a $(5 \text{ km})^2$ observational area in complex terrain some 48 km east of Red Bluff, California, on the slopes of the Sierra Nevada Mountains (fig. 1). The stand consisted of mainly ponderosa pine and incense cedar with some hardwood trees and bushes. Unlike the orchard canopy, the forest has an average height of 24 km with an irregular top. A large clearing (1000 by 700 m) is also present to the west of FT2 and the primary study area.

TABLE 2. ORCHARD TOWER INSTRUMENTATION

Sensor Hgt	OT1	OT2	OT3
2.0TH	uvw, T/ Δ T, RH	uvw, T/ Δ T, RH	uvw, T/ Δ T, RH
1.7	uvw, T/ Δ T	uvw, T/ Δ T, RH	uvw, T/ Δ T, RH
1.45	uvw, T/ Δ T	uvw, T/ Δ T, RH	uvw, T/ Δ T, RH, R _s
1.25	uvw, T/ Δ T	uvw, T/ Δ T, RH	uvw, T/ Δ T, RH
1.00	uvw, T/ Δ T	uvw, T/ Δ T, RH	uvw, T/ Δ T, RH
0.75	uvw, T/ Δ T	uvw, T/ Δ T, RH	uvw, T/ Δ T, RH
0.50	uvw, T/ Δ T, RH	uvw, T/ Δ T, RH	uvw, T/ Δ T, RH, R _s
0.18	uvw, T/ Rn.P	uvw, T/ RH	uvw, T/ RH
Below Sfc	Hs	-----	Hs

Figure 4 presents three 32 m towers of identical micrometeorological sensors that are located upwind and downwind of the forest's edge. The main tower (FT3) is located deep into the canopy (ZEF) more than 20TH from the canopy's edge. A second tower (FT2) is placed just inside (LE/TE) and 150 m from the forest's edge. The third tower (FT1) is established in the adjacent clearing of short, young "XMAS" trees some 20TH from the forest's edge. Tower FT1 provides the reference profile of the ambient flow. Similar to the orchard, fig. 5 displays the eight-level instrumented towers that define the canopy and ambient vertical profiles of wind, temperature and delta T, and humidity along with selected levels of pressure, solar and net radiation, and soil heat flux. The only change from the orchard configuration of table 2 is in the sensor location with respect to a 24-m canopy height. Different heights at which sensors are mounted are as follows for levels one through eight: 0.11, 0.2, 0.4, 0.6, 0.8, 1.0, 1.12, and 1.25TH level above the forest crown. All sensors were sampled and recorded at 1/s using the same schedule (table 1) that the orchard data collection followed.

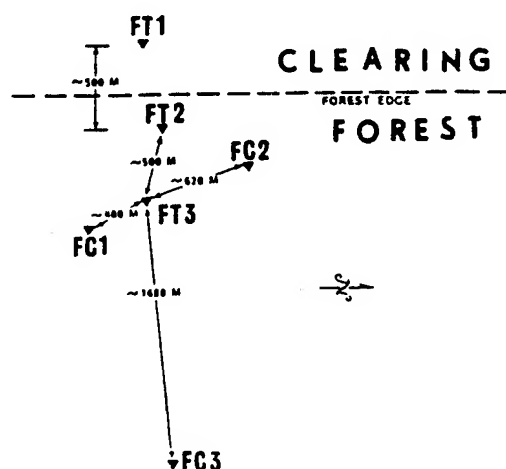


Figure 4. Forest study area composed of coniferous stand and "clearing" (to west) with FT-1, -2, and -3 micrometeorological towers and FC1-3 elevated surface stations.

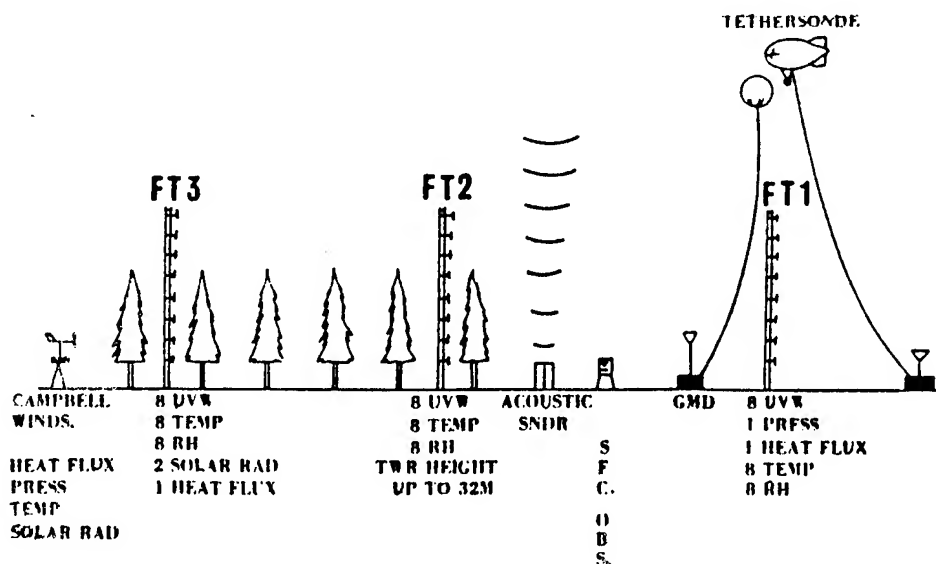


Figure 5. Schematic of the forest area instrumentation including FT-1, -2, and -3 along with upper-air boundary layer, and surface stations.

For both the forest and orchard, surface meteorological stations were elevated above the trees at 1.25TH and 2.0TH, respectively, to define the horizontal variations of the mean quantities above the canopy. Figure 4 locates FC1, 2, and 3 some 8 to 10 m above the forest centered on FT3 in the ZEF. Figure 2 locates OS1-4 10 m above the orchard centered on OT3 in the ZEF. Each tower measured windspeed, wind direction, and air temperature at the tower top and air temperature also 2 m above the canopy interface for a crude temperature difference. The orchard stations also measured humidity at the top of the tower, while atmospheric pressure was measured near the base of the FC and OS towers. All sensors were sampled 1/s and recorded as 1-min averages. Table 3 provides sensor locations of the elevated (OS1-4) and ground-based adjacent (BS1-12) surface stations for the orchard area and FC1-3 and BC1-6 stations for the forest, respectively.

TABLE 3. SURFACE STATION INFORMATION

Stations BS1-12		Stations OS1-4	
Sensor Hgt		Sensor Hgt	
(m)	Variables	(m)	Variables
10	WS,WD,T,RH	18	WS,WD,T,RH
10-2	T	18-10	T
1.5	P,Rn	1.5	P
Stations BC1-6		Stations FC1-3	
Sensor Hgt		Sensor Hgt	
(m)	Variables	(m)	Variables
11.0	WS,WD,T	31.0	WS,WD
		30.8	T

Figures 6 and 7 establish the locations of the surface stations bordering the orchard and forest areas under study as BS1-12 and BC1-6, respectively. Data collected at the BS and BC towers, of course, define the horizontal meteorological fields of the surface layer for the orchard and forest study areas.

4. EXAMPLES OF DATA COLLECTED

The following sets of data are presented as examples of Project WIND's canopy and surface layer data: (a) figs. 8 and 9 present wind vectors in time and space (that is, several locations) to evaluate the variation of wind in x, y, z, and t; (b) figs. 10 and 11 show vertical wind profiles as six consecutive 5-min profiles in time for stability, stratification, and structure; (c) figures 12 and 13 present lateral cross sections for a specific time in both the orchard and forest for towers OT1, 2, and 3 and FT1, 2, and 3 to denote flow structure with downwind distance; (d) figs. 14, 15, and 16 depict horizontal variations of the flow field for a cluster of stations in the orchard and forest areas. Space limitations permit only a few similar presentations of solar radiation for a surface station (fig. 17), forest (fig. 18) and orchard (fig. 19) micrometeorological temperature profiles, orchard (fig. 20) and forest (fig. 21) micrometeorological relative humidities, and orchard (fig. 22) and forest (fig. 23) micrometeorological wind w-components above and within canopy domains.

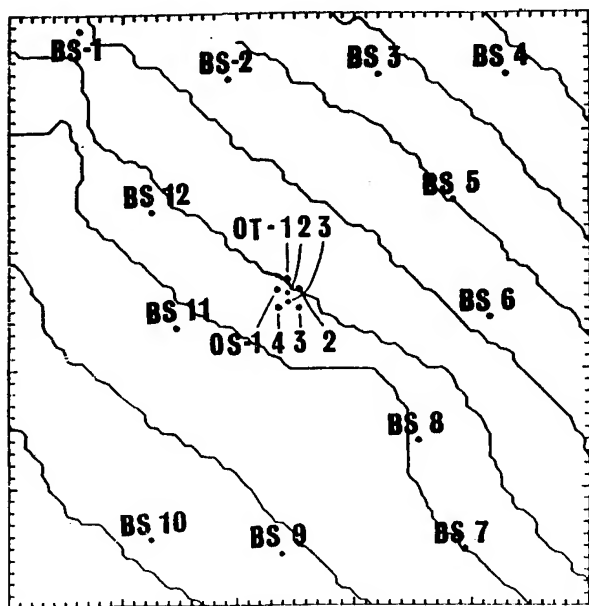


Figure 6. Locations of surface automated meteorological station sites BS1-12 and OS1-4 and micrometeorological towers OT-1, 2, and 3 established for the orchard canopy surface layer domain.

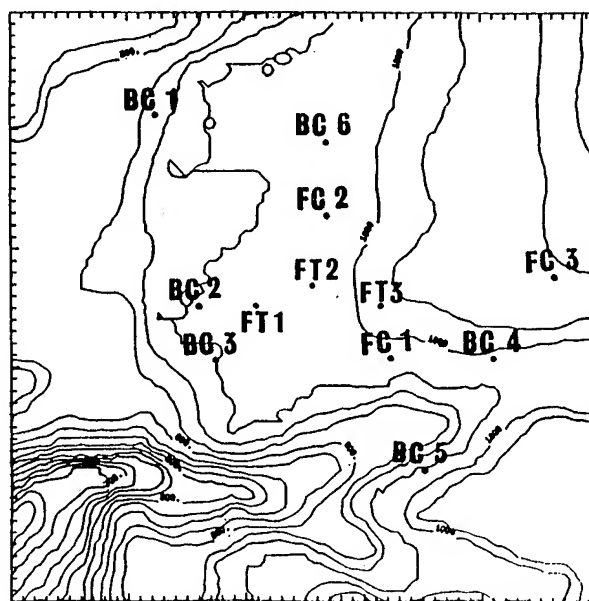


Figure 7. Locations of surface automated meteorological station sites BC1-6 and FC1-3 and micrometeorological towers FT-1, 2, and 3 established for the forest canopy surface layer domain.

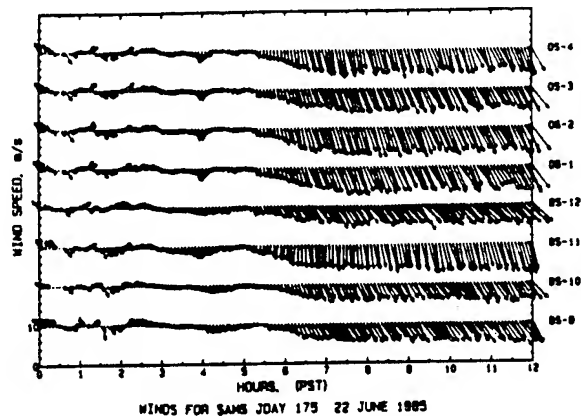


Figure 8. Time and space variations above (OS1-4) and around BS9-12) the almond orchard exposed to the ambient flow of the surface layer for JDAY 175, 1985 at 0000 to 1200 h, P.s.t.

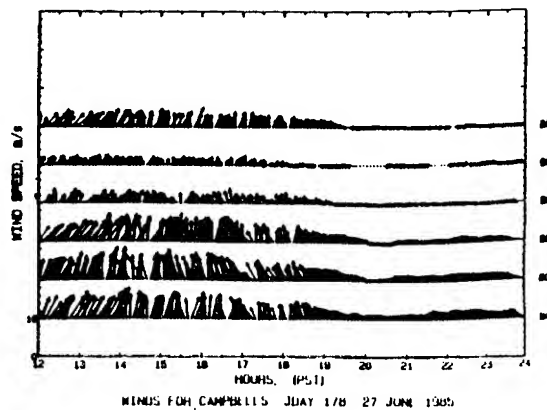


Figure 9. Time and space variations surrounding (BC1-6) the coniferous forest exposed to the ambient flow of the surface layer for JDAY 178, 1985 at 1200 to 2400 h, P.s.t.

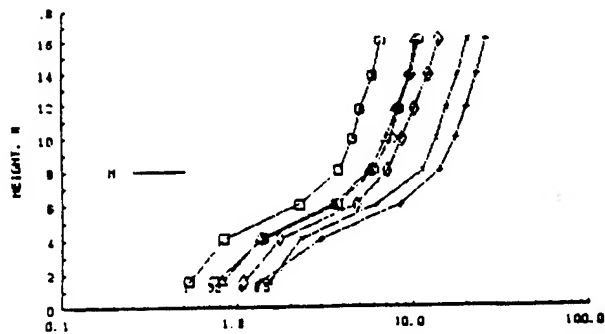


Figure 10. Daytime canopy and surface layer profiles ($\ln u$ vs z) for the almond orchard at OT-3, JDAY 173, 1985.

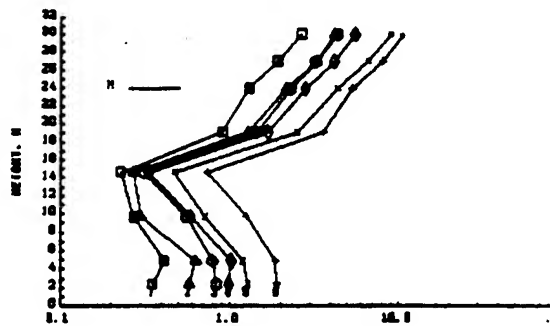


Figure 11. Nighttime canopy and surface layer profiles ($\ln u$ vs z) for the coniferous forest at FT-3, JDAY 177, 1985.

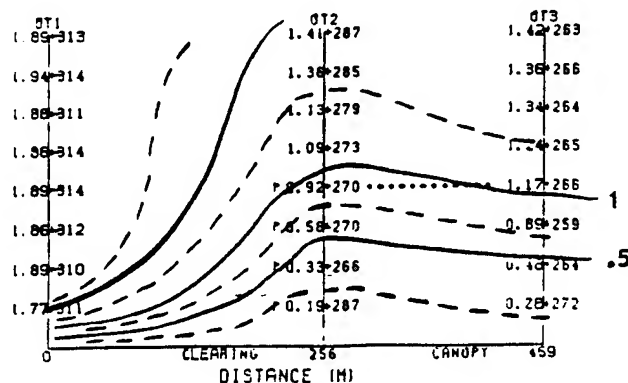


Figure 12. Isotach analysis of a cross section through the almond orchard edge using OT-1, -2, and -3 windspeed (and wind direction) data for JDAY 178, 1985 at 1000 h, P.s.t.

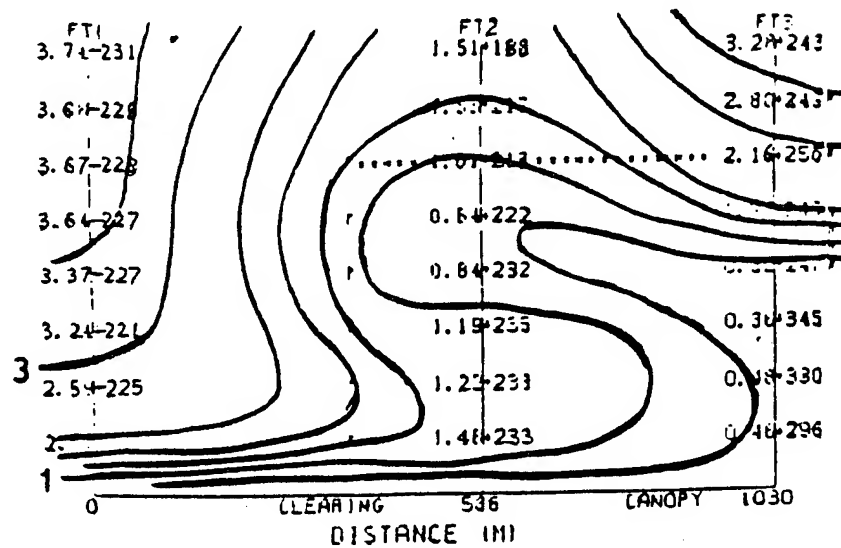


Figure 13. Isotach analysis of a cross section through the forest edge using FT-1, -2, and -3 windspeed (and wind direction) data for JDAY 184, 1985 at 1645 h, P.s.t.

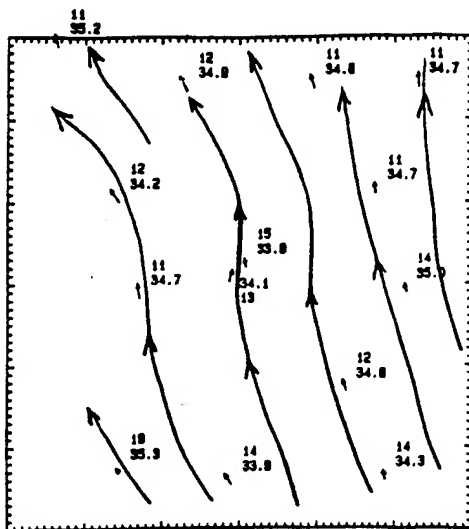


Figure 14. Surface layer wind streamline analysis (with temperature (TT.T) and humidity (HH) data) for the 5 km by 5 km forest domain JDAY 175, 1985 at 1415 h, P.s.t.

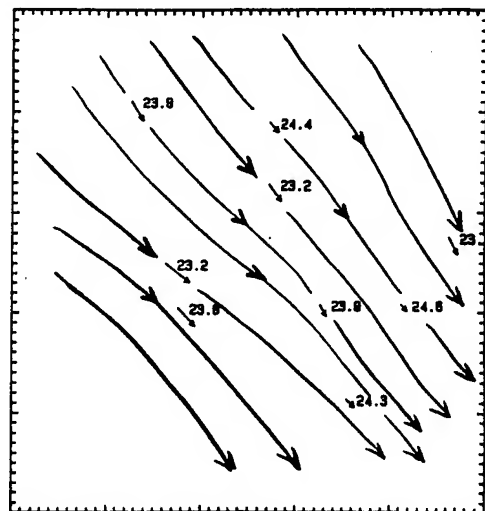


Figure 15. Surface layer wind streamline analysis (with temperature (TT.T) and humidity (HH) data) for the 5 km by 5 km forest domain JDAY 175, 1985 at 1500 h, P.s.t.

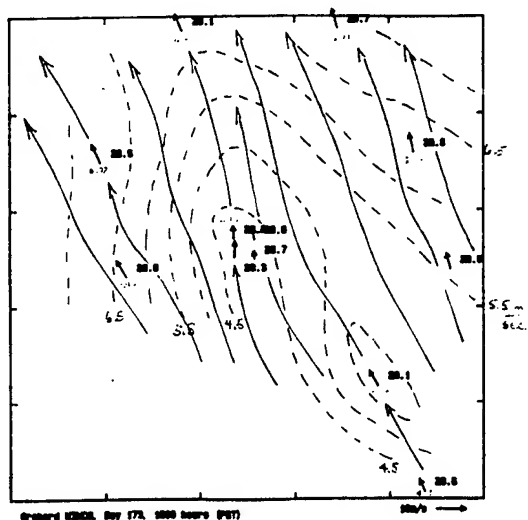


Figure 16. Surface layer wind streamline and isotach analysis (---) for the 5 km by 5 km orchard domain JDAY 173, 1985 at 1800 h, P.s.t.

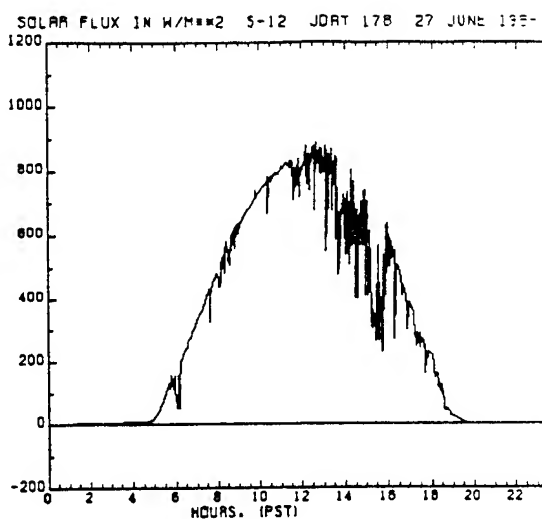


Figure 17. Time variation of incoming solar radiation for a surface automated meteorological station for JDAY 178, 0000 to 2400 h, P.s.t.

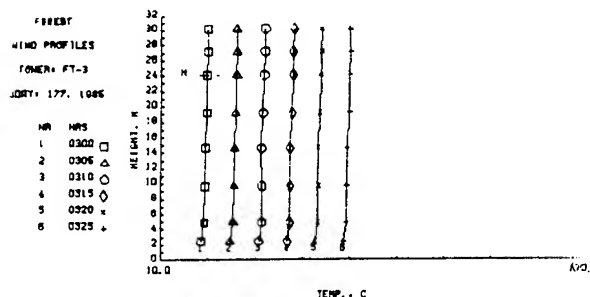


Figure 18. Nighttime canopy and surface layer profiles of temperature for the forest domain at FT-3, JDAY 177, 1985.

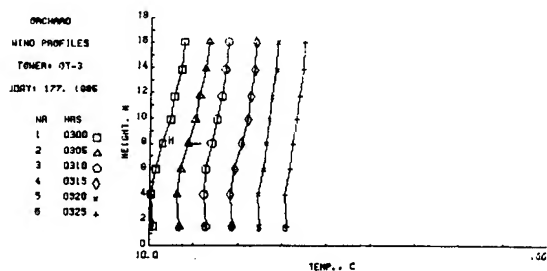


Figure 19. Nighttime canopy and surface layer profiles of temperature for orchard domain at OT-3, JDAY 177, 1985.

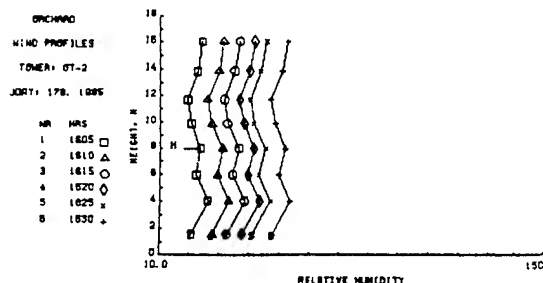


Figure 20. Daytime canopy and surface layer profiles of relative humidity for the orchard domain at OT-2, JDAY 178, 1985.

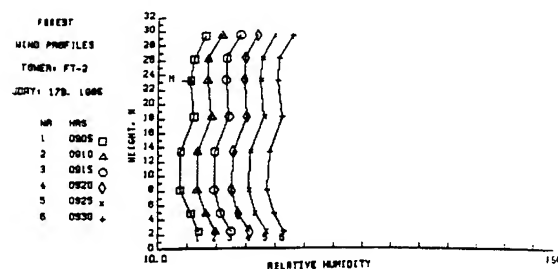


Figure 21. Daytime canopy and surface layer profiles of relative humidity for the forest domain at FT-2, JDAY 178, 1985.

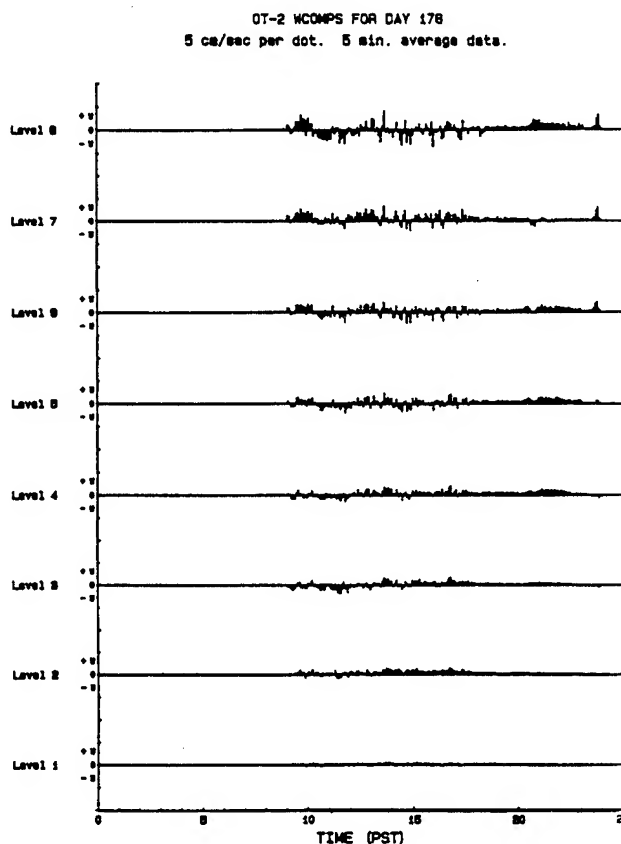


Figure 22. Time variations of vertical velocities (w component) for the orchard domain canopy layer (L1-4) and surface layer (LS-8) at OT-2, JDAY 178, 0900 to 2400 h, P.s.t.

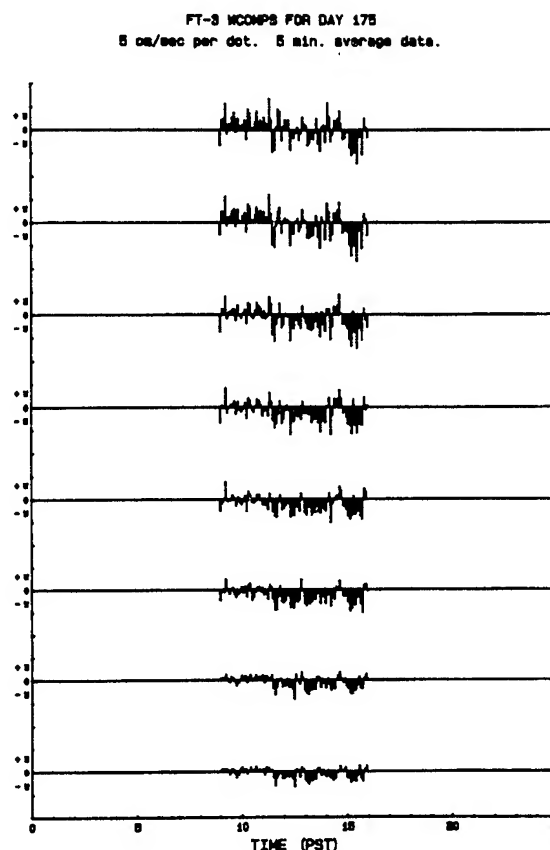


Figure 23. Time variations of vertical (w component) for the forest domain canopy layer (L1-6) and surface layer (L7-8) at FT-3, JDAY 175, 0900 to 1600 h, P.s.t.

5. PROPOSED USAGE OF THE DATA

Research-quality data is being used primarily for weather scenario characterization, simulation for model exercise or study input (Cionco, 1987b), and evaluation of models and codes (Cionco, 1987a and 1985). Numerous studies conducted by Army scientists require a characterization of the meteorology (Orndorff and Cionco, 1991) that may occur during those studies. Simulations in full-time and space domains can also enhance planning field activities such as wargaming exercises and combat simulations. Model evaluation requires data for initialization as well as comparison. Numerous data sets are also required to establish credibility of the evaluation results. The Project WIND data base provides exactly that capability for a variety of microscale/Army-scale problems that must be addressed.

REFERENCES

- Cionco, R. M., 1989: Design and Execution of Project WIND. In Proceedings of the 19th Conference of Agricultural and Forest Meteorology, Charleston, SC, American Meteorological Society, Boston, MA.
- Cionco, R. M., 1987a: Windfield Simulations from a Hierarchy of Nested Meso- and Micro-meteorological Models. In Proceedings of the Symposium of Mesoscale Analysis and Forecasting, IUGG, ESP SP-282 (Aug 1987), Vancouver, Canada.
- Cionco, R. M., 1987b: Field Measurements in Uniform and Non-uniform Canopies. In Proceedings of the 18th Conference of Agricultural and Forest Meteorology, American Meteorological Society, Boston, MA.
- Cionco, R. M., 1985: Modeling Windfields and Surface Layer Profiles Over Complex Terrain and Within Vegetative Canopies. Forest-Atmosphere Interactions, B. A. Hutchinson and B. B. Hicks, editors, D. Reidel Publishing Co., Holland.
- Cionco, R. M. 1984: Test Plan for Project WIND. Internal Report, U.S. Army Atmospheric Sciences Laboratory, White Sands Missile Range, NM.
- Orndorff, B. L., and R. M. Cionco, 1991: On the Characterization of Army-Scale Surface Layer Micrometeorology Using Field Measurements. In Proceedings of the Battlefield Atmospheric Conference, U.S. Army Atmospheric Sciences Laboratory, White Sands Missile Range, NM.

**EVALUATION OF A COUPLED KNOWLEDGE-BASED NOWCASTING
SYSTEM FOR U.S. ARMY FIELD OPERATIONS**

Montie Orgill
Science and Technology Corp.
White Sands Missile Range, NM 88002, USA

Robert Sutherland
U.S. Army Atmospheric Sciences Laboratory
White Sands Missile Range, NM 88002-5501, USA

John Kincheloe
New Mexico State University
Las Cruces, NM 88003, USA

ABSTRACT

An experimental weather classification, analysis, and nowcasting system, based upon a combination of artificial intelligence techniques and conventional numerical modeling techniques, and designed for use as a real-time range/field forecasting aid, is described. In particular, a computer-based prototype expert system, labeled PROCANS (PROtotype Classification, Analysis, and Nowcasting System), tailored for applications at the U.S. Army field testing range at Fort Hunter Liggett, California, is used as an example to demonstrate and evaluate the overall concept. The components of the system are: (a) a rule-based meteorological scenario evaluator for analysis and classification of existing weather scenarios; (b) a nowcaster that uses four rule-based and analogical expert subsystems for nowcasting radiation fog, wind gustiness, thunderstorms, and precipitation; (c) a numerical transport and diffusion module based upon either Gaussian or Monte Carlo particle trajectory models to simulate visual flow patterns; and (d) a master database for storing, retrieving, and comparing current weather scenarios with past scenarios for possible matching and analogical reasoning for future predictions. The capabilities of the system are described and evaluated, along with its advantages, disadvantages, and limitations in relation to field operations applications.

1. INTRODUCTION

The overall objective of this study is to explore and evaluate the concept of using a combination of modern artificial intelligence techniques and conventional numerical modeling techniques to develop a hybrid approach to meteorological nowcasting and forecasting. The major emphasis is on topographically complex geographical areas, where conventional numerical approaches are most difficult to implement, but where artificial intelligence techniques are most applicable. More specifically stated, the objectives are: (a) to investigate complex-terrain flow interactions in relation to transport and turbulent diffusion, (b) to investigate the coupled knowledge-based expert technique for developing a airflow-interaction knowledge base applicable in complex terrain, (c) to evaluate the knowledge-based technique for application to field operations, and (d) to determine the transferability of the technique to other geographic locations.

In this study, complex-terrain airflow interactions are defined as those physical processes, acting over all spatial and temporal scales, that influence the local meteorology of a terrain setting such as a valley, ridge, or basin. Our approach is to investigate the knowledge-based (expert) system (KBS) technique. In particular, the study involves experimentation with the development of a

prototype coupled knowledge-based system (C-KBS), a technique that has been utilized for analyzing difficult technical problems in hydrodynamics and other areas. C-KBSs are defined by Kitsmiller and Kowalik (1985) as any type of system linking both numerical and heuristic computing processes. Computer programs based upon these techniques have the objective of combining the explanation and problem-solving capabilities of heuristic reasoning with the precision of traditional numerical modeling.

In previous publications (Orgill et al., 1990; 1991), we have described the various stages of the PROCANS program as developed with the aid of synoptic-scale and micrometeorological data from Fort Hunter Liggett. One component of PROCANS, the meteorological scenario analysis and classification module (MSACM) was used to analyze and classify a selected weather scenario. In this paper, we report on the final research and development work on PROCANS, which includes a revised meteorological scenario evaluator, the addition of a nowcaster, and the development of a Monte Carlo particle transport and diffusion model.

2. COUPLED KNOWLEDGE-BASED SYSTEMS

A schematic example of a generic C-KBS is shown in fig. 1. The workstation represents the computer hardware and software; these elements function as an interface between the user and the KBS.

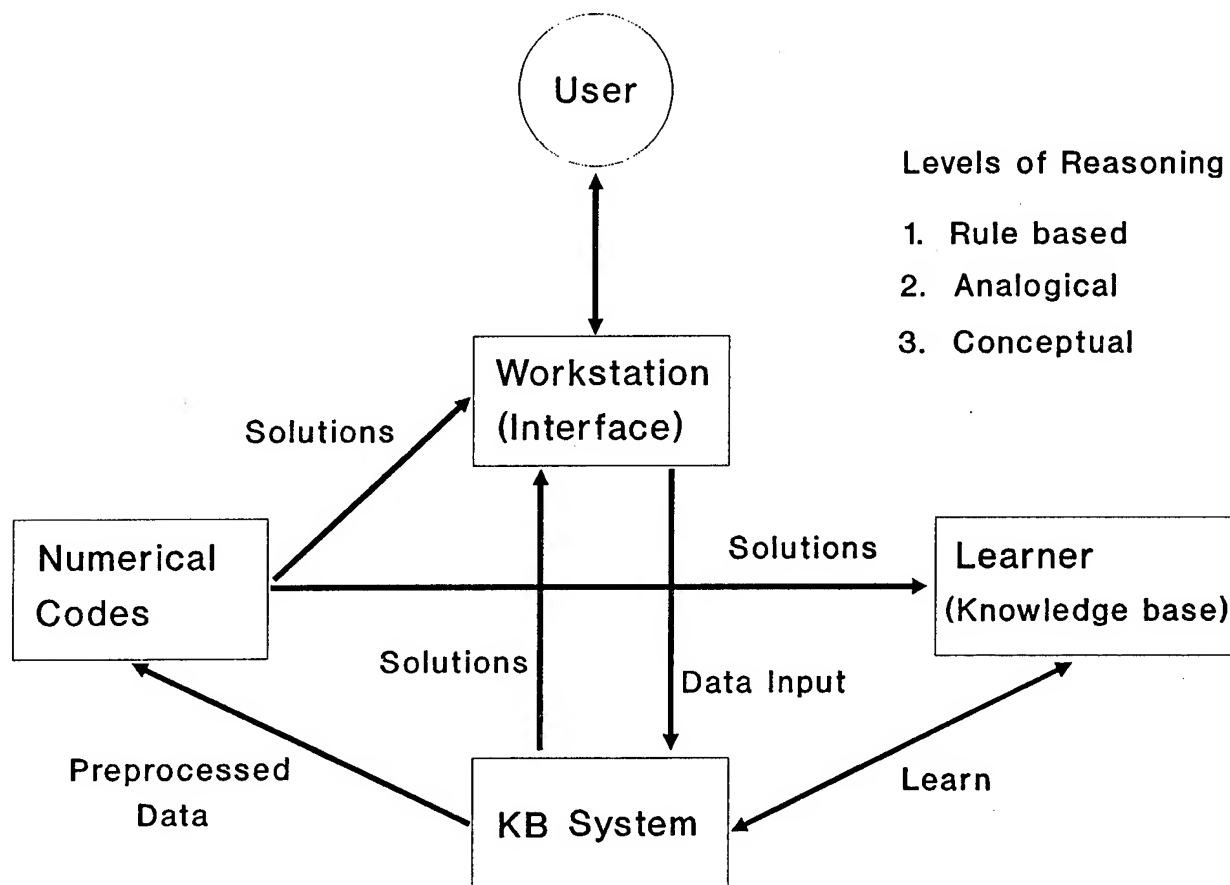


Figure 1. Example of a generic coupled knowledge-based expert system.

The work described here was performed with a SUN Microsystems 386i workstation equipped with extended graphics capabilities. The KBS acts as a symbolic interface to the numerical codes and the knowledge base. Solutions from numerical models are transported to the knowledge base, or Learner, where the KBS uses different levels of artificial reasoning to supply output data to the user through the workstation. Reasoning is done at three levels; the first and most elementary level is rule based, the second level uses analogy, and the third and deepest level is conceptual and involves the use of physical concepts. The goals of the C-KBS are to reason by rules, analogy, and concepts and to learn by experimentation. A system based mainly on rules is defined as a shallow-coupled system and a system based mainly on conceptual reasoning is defined as a deep-coupled system. In theory, as the KBS learns and enlarges the associated knowledge base, it tends to become less numerical and more symbolic. As the KBS becomes more symbolic, it operates a greater percentage of the time at the rule or analogical level. This mode of operation is usually faster and more efficient than working at the conceptual level, which may involve massive numerical calculations. The type of reasoning levels that a C-KBS may operate with depends upon the complexity of the problem and the user requirements, however.

3. THE FORT HUNTER LIGGETT PROTOTYPE SYSTEM

The Fort Hunter Liggett version of PROCANS is a prototype C-KBS that incorporates a variety of general meteorological concepts, or knowledge, along with rules and analogical levels of reasoning. The system is designed to provide decision-type information in support of field operations involving weather-dependent processes such as material transport and diffusion. Some of the meteorological concepts that are used in PROCANS are: (a) weather variables, features, events, and scenarios; (b) fair-weather climatology; (c) persistence; (d) continuity; and (e) meteorological spatial and temporal scales. In some cases the rules are developed from general meteorological principles, and in other cases from past data. In fact, one reason that the Fort Hunter Liggett area was chosen for the experiment was the availability of a large database obtained from a meteorological tower network routinely operated and maintained by the resident meteorological support team, which at the time was operated by ASL. A more complete description of how this database, along with synoptic data, is used to develop rules is given elsewhere (Orgill et al., 1990).

The prototype system consists of five basic software components, or modules, shown in fig. 2. These components are: (a) a data-processing module (DAPROM), (b) a meteorological scenario analysis and classification module (MSACM), (c) a nowcaster module (NOWCAM), (d) a transport and diffusion module (TADM), and (e) the master knowledge base (MDB). The knowledge-base management system (KBMS) handles the interfacing chores among the components.

In the operational mode, classification and transport/diffusion event databases are stored in the MDB as the main part of the knowledge base. The numerical component of PROCANS is the TADM, which for the present prototype uses an objective analysis model of Ludwig et al. (1990) to obtain wind fields and the random-walk Lagrangian particle diffusion model for transport and diffusion (Williams and Yamada, 1990). The main KBS components are the MSACM and NOWCAM. The MSACM consists of seven data- and rule-based analysis modules for providing current and past information on weather scenarios. These modules are used to analyze the scenario for seasonal aspects and climatology, weather systems, weather and cloudiness, mountain waves, convective systems, temperature inversions, and stability, winds, and turbulence in the lower boundary layer. The summarized parameter data are used for classifying the current weather scenario based upon the degree of correlation of various parameters with a fair-weather standard. The NOWCAM is a rule-based/analogical module consisting of four expert subsystems for nowcasting or forecasting radiation fog, wind gustiness, thunderstorms, and light/moderate precipitation episodes.

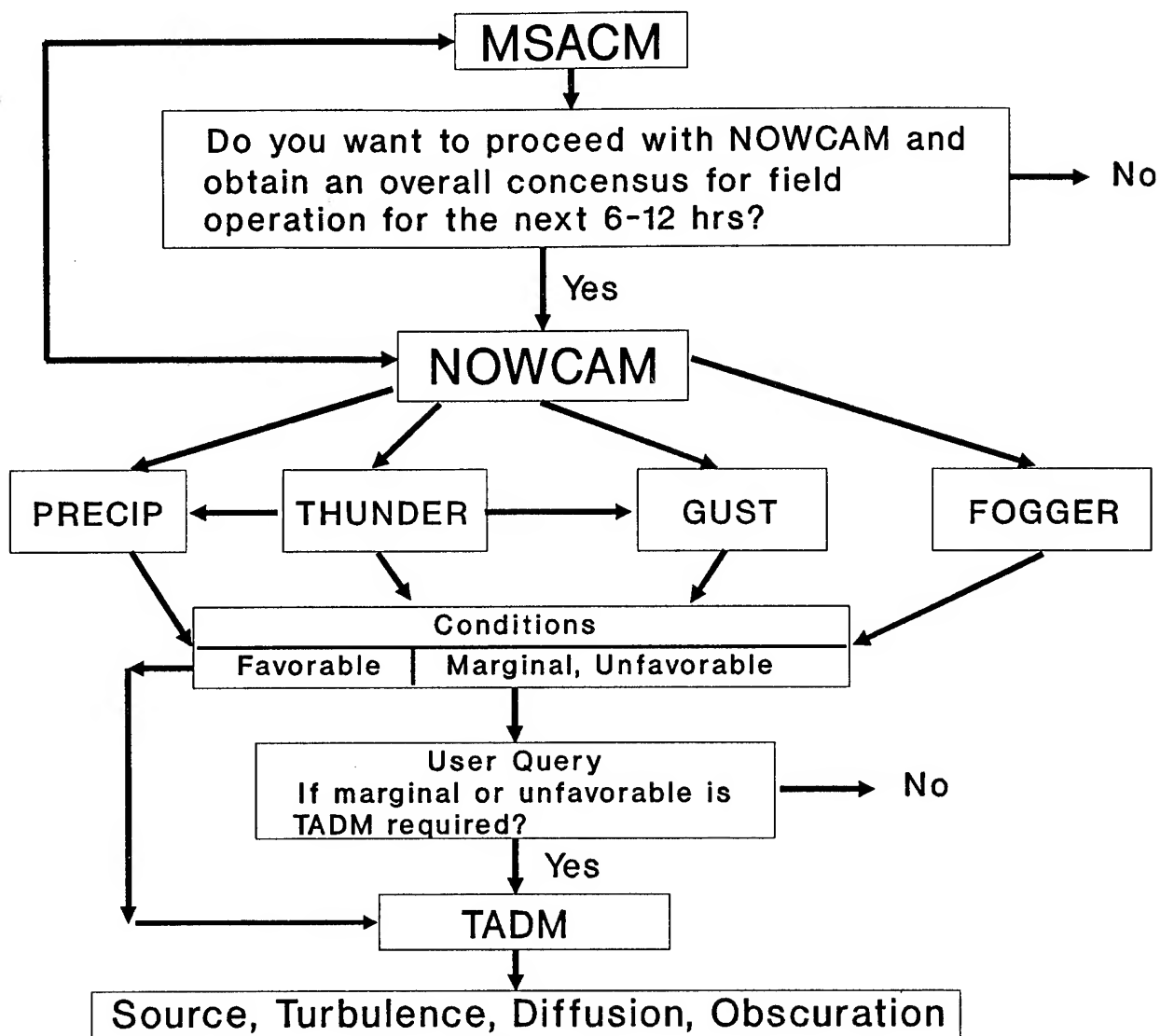


Figure 3. Operational flow chart of PROCANS.

4. PROCANS EXAMPLES

The original development of the Hunter Liggett prototype is based on a detailed analysis of four categories of weather episodes that occurred between October 1987 and December 1988 for which there was a nearly continuous record of data available from the surface meteorological network. The episodes under consideration involved precipitation, fog, gustiness, thunderstorms, and fair weather. There was some overlap among episodes because rain and fog occur together, as do thunderstorms and gustiness; however, these combinations did not occur often. The data associated with these weather episodes were used to help develop the rules for the four expert subsystems of the NOWCAM. The period over which the data used for PROCANS development were acquired did not contain any extremely severe weather events, such as heavy rain, snow, severe gustiness, or severe thunderstorms. Thus, the system utility is restricted to nonsevere events. During data acquisition, fog events did occur, but none persisted past 1100 PST.

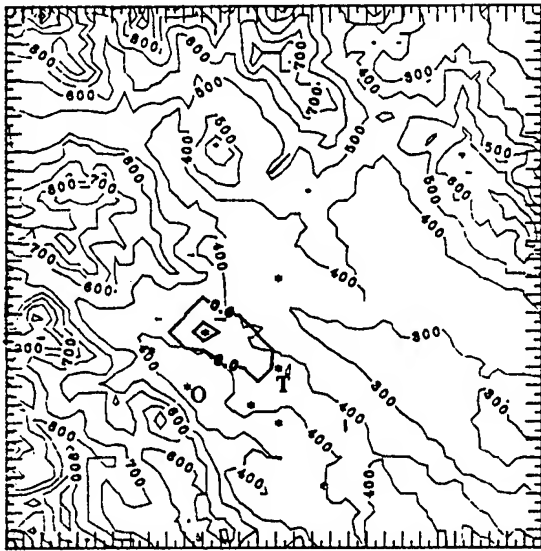
Normally, the Hunter Liggett area is characterized by a very strong nocturnal temperature inversion that causes a decoupling of the upper-level airflow from the local winds in the valley. This inversion creates a very stable situation that requires a strong storm or front to destabilize during the night. In the course of the research, however, it was found that during weaker storm episodes, when the ridge-top winds do not penetrate the strong nighttime inversion, these winds can eventually mix down into the valley during the day, as solar heating progresses, and valley stability becomes neutral or unstable. These events are very important in relation to diffusion of plumes, since the direction and spread of a plume may be significantly affected.

Data from one particularly interesting event are shown in the plots of fig. 4. This event was associated with a post-cold-frontal and cold-low-passage scenario that occurred during 4-5 May, 1988. The results of fig. 4 were generated with the TADM for the period 0600 PST to 1200 PST. As an aid to the analysis, a simulated smoke screen release was started at 0600 PST and the four plots of fig. 4, labeled a through d, show how the simulated plume responded to the simulated winds. As the morning progressed, a weak surface temperature inversion was dissipated by solar heating and the instability allowed the northwesterly synoptic winds to replace the valley drainage component and overpower the normal up-valley wind component. As a consequence of these winds, the plume moved generally to the southeast (fig. 4b), but portions of the plume were affected by westerly winds mixing down into the valley, as is most evident in fig. 4c. After 1200 PST, these westerly winds reached the valley surface, causing some gustiness.

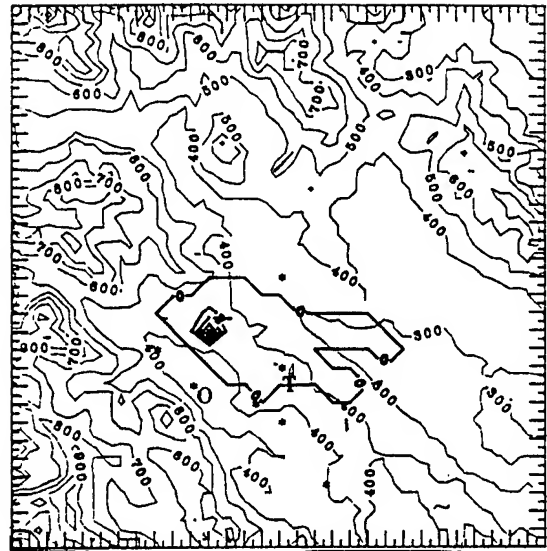
The foregoing event gives one example of the importance that above-valley winds can have on plume transport and diffusion. Other weather events such as a fog occurrence, an incipient thunderstorm, and wind gustiness have been analyzed using the various components of PROCANS and the results reported elsewhere (Orgill et al., 1991). The results of this preliminary evaluation, which is too involved to report in detail here, indicate that the fog nowcaster can successfully forecast morning fog and that the precipitation nowcaster can successfully forecast precipitation in terms of light, moderate, and none. The thunderstorm and gust nowcasters have been only partially successful, however, presumably because of the scarcity of these types of events during the experimental period. At any rate, we feel that a more refined set of rules based upon more data is needed for the Hunter Liggett thunderstorm nowcaster.

5. SUMMARY AND CONCLUSIONS

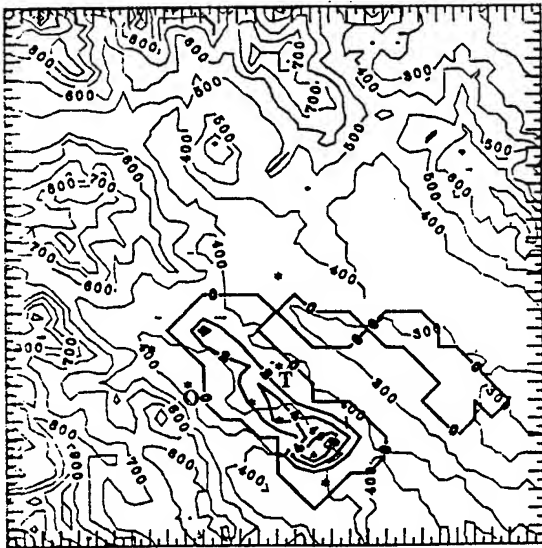
We have briefly described some aspects of the final development of a C-KBS for analyzing and nowcasting meteorological scenarios and events in support of weather-dependent field/range operations. The system requires consistent meteorological input to maintain continuity and requires occasional user inputs for all components. One major advantage of PROCANS is the systematic and step-by-step procedure used to integrate a variety of data sources and knowledge to arrive at a nowcast or forecast for making field decisions. Another advantage is the prospect of integrating heuristic-type knowledge with numerical techniques in order to obtain more knowledgeable assessments of meteorological scenarios. Although the basic techniques used in developing PROCANS are applicable in general, many of the rules are site specific and need to be redeveloped if the system is transferred to another location. Once developed, however, this hybrid technique offers a viable alternative to the more conventional modeling approaches to nowcasting and forecasting.



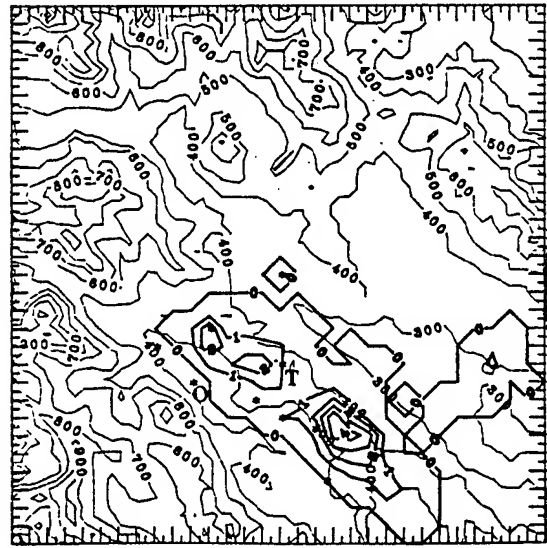
(a)



(b)



(c)



(d)

Figure 4. Simulated dispersion of a smoke-screen plume of pseudo-particles from a line source near Stony Valley using a Monte Carlo model technique. Plume history from 0600 to 1200 PST. (a) 0700 PST, (b) 0900 PST, (c) 1100 PST, and (d) 1200 PST.

REFERENCES

- Kitzmilller, C.T., and J.S. Kowalik, 1985: Symbolic and Numerical Computing in Knowledge-based Systems, Workshop on Coupling Symbolic and Numerical Computing in Expert Systems, Elsevier Science Publishers B.V. (North Holland), pp. 3-17.
- Ludwig, F.L., R.M. Endlich, and P. Lester, 1990: A Computer Code for Objective Analysis of Turbulence and Winds in the Lower Atmosphere, Report CR-90-0001/0680-1, SRI International, Menlo Park, CA, pp.150.
- Orgill, M.M., R.A. Sutherland, and J. Kincheloe, 1990: An Experiment to Determine the Feasibility of a Complex Terrain Effects Knowledge Base, Proceedings of the 10th Annual EOSAEL/TWI Conference, ASL, U.S. Army Laboratory Command, pp.217-227.
- Orgill, M.M., R.A. Sutherland, and J. Kincheloe, 1991: Further Experiments on the Feasibility of a Complex Terrain Effects Knowledge Base, Proceedings of the 11th Annual EOSAEL/TWI Conference, PSL 90/99, ASL, U.S. Army Laboratory Command, pp.307-314.
- Williams, M., and T. Yamada, 1990: A Microcomputer-based Forecasting Model: Potential Applications for Emergency Response Plans and Air Quality Studies., J. Air Waste Manage. Assoc., Vol. 40, pp. 1266-1274.

NOWCASTING AIRFLOWS AND TEMPERATURE OVER COMPLEX TERRAIN

BY FOUR-DIMENSIONAL DATA ASSIMILATION

Teizi Henmi

U.S. Army Atmospheric Sciences Laboratory
White Sands Missile Range, New Mexico 88002-5501, USA

ABSTRACT

A three-dimensional mesoscale forecast model, HOTMAC (Higher Order Turbulence Model for Atmospheric Circulation), was used to nowcast airflows and temperature over a complex terrain of the project WIND (wind in nonuniform domains) area (northern California). To nowcast three-dimensional fields of airflow and temperature by using a single upper-air sounding data, a four-dimensional data assimilation technique was used in HOTMAC, feeding the data into the model continually. Model simulations of temporal as well as spatial distributions of windspeed, wind direction, temperature, dew point, and pressure were compared with observational data. Statistical evaluation of model performance showed good nowcasting capability of the model.

1. INTRODUCTION

A mesoscale model, HOTMAC (Higher Order Turbulence Model for Atmospheric Circulation), simulated the evolution of locally forced circulations due to surface heating and cooling superimposed on weak synoptic flows when the model was initialized with data from a single upper-air sounding (Yamada, 1983). However, if a weather system is associated with local meteorological conditions that depart significantly from diurnal patterns, real-time observations need to be assimilated into the model to resolve the relevant phenomena.

This paper presents the results of the data assimilation study by HOTMAC in which upper-air sounding data taken at a station were assimilated by using a Newtonian nudging method (Anthes, 1974; Yamada et al., 1989; and Henmi, 1990). Simulated results were compared with observations, including both surface and upper-air data. Statistical comparisons between simulation and observation were also made, showing good nowcasting capability of the model.

2. DATA BASE AND MODEL DOMAIN

Data used for the study were from the Project WIND (wind in nonuniform domains) Phase I (Cionco, 1989). Phase I of the field study was conducted in June and July 1985 during a moderate-to-weak marine incursion regime. The study area was centered in the Sacramento River Valley north of Sacramento, California, extending eastward up the slopes of the Sierra Nevada Mountains and westward to the slopes of the coastal mountain range.

A meteorological data set (for a 24-h period starting at 0900 l.s.t. of day 178 in Julian date), consisting of upper-air sounding data at 5 locations every 2 h and surface data recorded at 21 stations every 15 min, was used in this study. Day 178 was characterized as a typical summer day. The most common flow regime in the Sacramento Valley during the summer is southerly flow during the day and northerly flow at night. The southerly flow was consistent with weak marine incursion resulting from wind that blows from the San Francisco Bay area, more than 200 km away, moves inland, and becomes diverted north and south by the Sierra Nevada Mountains along the Sacramento Valley.

Model calculation was conducted over terrain as shown in fig. 1. Latitude and longitude of the southwestern corner of the domain are 39.18 N and 123.99 W. The terrain heights were represented by grids of 81 by 81 with a unit grid distance of 2.5 km. The highest and lowest grid points are, respectively, 2477 m and 12 m above sea level. Meteorological parameters were calculated at every other grid point. In the figure, characters represent the locations of surface stations. Upper-air soundings were taken near BC3 (01), C7(02), S9(03), B1(04), and S3(05). Here, numbers in parentheses represent upper-air stations.

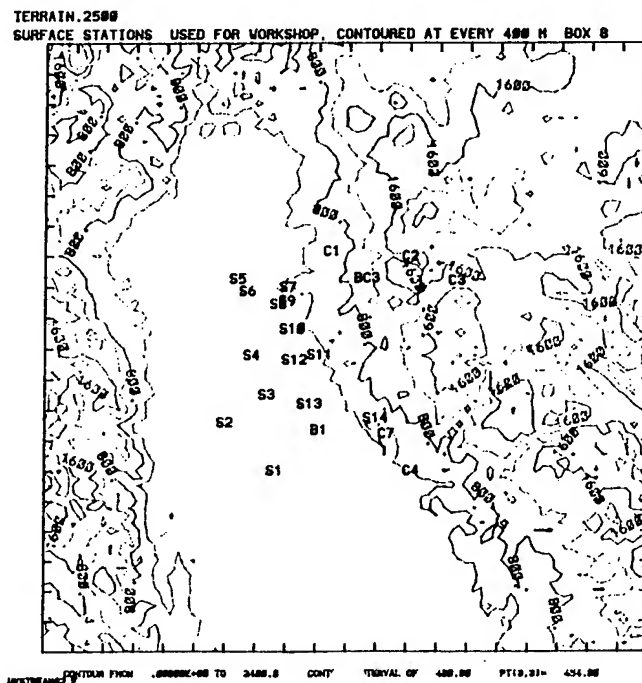


Figure 1. Project WIND terrain and station locations; contour lines are at every 400 m.

3. MODEL

Since Yamada and Bunker (1989) describe HOTMAC in detail, this paper presents only a brief review of the model's physics, assumptions, boundary conditions, and numerical procedures.

Prognostic equations for mean horizontal wind components, potential temperature, mixing ratio of water vapor, turbulence kinetic energy, and turbulence

length are solved in HOTMAC. A terrain-following vertical coordinate system is used to increase the accuracy in the treatment of surface boundary condition.

In terrain-following coordinates, a smoothing function averages the variables in the vertical as well as in the horizontal directions. For large potential temperature gradients, smoothing generates large horizontal temperature gradients and spurious pressure gradient forces. To alleviate the problem, Yamada and Bunker (1989) reformulated the conservation equation for potential temperature in a way that only the deviation from the horizontally averaged values was prognostically computed. Smoothing was applied to the perturbation potential temperatures.

Nudging terms $C_n(U_n - U)$ and $C_n(V_n - V)$ were added to the equations for mean horizontal wind components, where U and V are, respectively, x- and y- components of mean horizontal wind, C_n is a nudging coefficient, and (U_n, V_n) are the wind components that force (U, V) toward observed wind components (U_{obs}, V_{obs}) . The subject between (U_n, V_n) and (U_{obs}, V_{obs}) is given as

$$U_n = \frac{fC_n(V_{obs} - V_g) + f^2U_g + C_n^2U_{obs}}{C_n^2 + f^2} ;$$

$$V = \frac{-fC_n(U_{obs} - U_g) + f^2V_g + C_n^2V_{obs}}{C_n^2 + f^2} .$$

Derivations of the above equations are presented in Yamada and Bunker (1989).

The turbulence fluxes for momentum, heat, and water vapor are obtained from simplified turbulence-closure model equations (Yamada, 1983).

Surface boundary conditions were constructed from empirical formulas for non-dimensional wind and temperature profiles. The temperatures in soil layer were obtained by solving a heat conduction equation. Appropriate boundary conditions were the heat energy balance at the soil surface and specification of the soil temperature at a certain depth (30 cm in this study). Lateral boundary values were obtained by integrating the corresponding governing equations, except that variations in the horizontal directions were neglected.

The governing equations were integrated by using the alternating direction implicit method, and a time increment was chosen to satisfy the Courant-Friedrich-Lewy criteria.

To increase the accuracy of finite difference approximations, mean and turbulence variables were defined at grids that were staggered in both horizontal and vertical directions. To resolve great variations of mean winds, temperature, and mixing ratio of water vapor with height near the surface, nonuniform grid spacing, as shown in table 1, was used in the vertical direction.

TABLE 1. HEIGHTS OF THE VERTICAL GRID LEVELS IN THE TERRAIN FOLLOWING COORDINATE SYSTEM USED FOR ATMOSPHERIC AND SOIL LAYERS

Atmosphere			Soil		
Level number	Level grid (m)	Level Intermediate (m)	Level number	Level grid (m)	Level Intermediate (m)
16	5000.0	4559.0	1	0.0	0.0
15	4139.0	3739.0	2	0.009	0.003
14	3359.0	3000.0	3	0.054	0.024
13	2661.0	2342.0	4	0.159	0.100
12	2044.0	1767.0	5	0.300	0.228
11	1510.0	1273.0			
10	1057.0	861.0			
9	685.0	530.0			
8	395.0	281.0			
7	187.0	114.0			
6	61.0	28.0			
5	16.0	14.0			
4	12.0	10.0			
3	8.0	6.0			
2	4.0	2.0			
1	0.0	0.0			

4. INITIAL VALUES

An initial wind profile at station 04 (fig. 1) was first constructed by assuming a logarithmic variation (initially $u_g = 0.2$ m/s and $z_0 = 0.1$ m) from the ground up to the level where the windspeed reaches an ambient value (5 m/s). Initial wind profiles at other grid locations were obtained by multiplying the station 04 winds by $(H - z_g)_{04}/(H - z_g)$ to satisfy approximately the mass continuity. Wind directions were initially from SWS (210°) throughout the atmosphere.

The vertical profile of potential temperature was initialized based on upper-air sounding data taken at station 04 at 0900 l.s.t. of day 178:

$$\theta = 304.2 + 0.0015Z \text{ for } 0 < z < 1800 \text{ m,}$$

$$\theta = 306.9 + 0.0040Z \text{ for } z > 1800 \text{ m,}$$

where z is the height above mean sea level. Initial potential temperatures are assumed to be uniform in the horizontal directions. Initial values of water vapor are calculated by using the initial potential temperature profiles, pressure at the top of the domain, and observed relative humidity. The turbulence kinetic energy and length scale are initialized by using the initial wind and temperature profiles and the relationships determined by the level 2 model (Yamada, 1975).

5. ASSIMILATION

Cubic spline fitting of horizontal wind vector components was performed as a function of altitude on data from each upper-air sounding taken at station 04, and hourly wind profiles were generated by linear interpolation. Hourly wind data at 1 h ahead of simulation time were read in at the beginning of each

simulation hour. For example, wind at 1200 l.s.t. was read in at 1100 l.s.t. simulation time and used between 1100 and 1200 l.s.t. No time interpolation was made between hourly wind data. Wind profiles at other grid points were obtained by multiplying station 04 winds by $(H - z_g)/(H - z_s)$. Note that only horizontal wind components were assimilated.

Temperature and other prognostic variables were not assimilated. Calculation started at 0900 l.s.t. of day 178 and lasted till 0700 l.s.t. of day 179.

6. RESULTS AND EVALUATION

6.1 SURFACE PARAMETER COMPARISONS

As shown in fig. 1, surface observation points were located in the center area of the model domain. To make visual comparison easy, simulated horizontal wind vectors were plotted only for the center area. Simulated and observed surface (10 m level above the ground) horizontal wind vectors are plotted in (A) and (B), respectively, figs. 2 and 3. Daytime wind vectors (14 l.s.t.) are shown in fig. 2, and nighttime wind vectors (00 l.s.t.) are shown in fig. 3.

Southerly upvalley and southeasterly upslope wind conditions were well simulated during daytime. Development of downslope wind along the eastern slope of the Sierra-Nevada Mountain Range was also well simulated (See fig. 3). However, observed winds in the valley during the night showed unorganized patterns. For the present case, wind vectors were calculated at every 5 km distance. For calm nighttime conditions such as this case, grid distance may be too large to simulate localized effects.

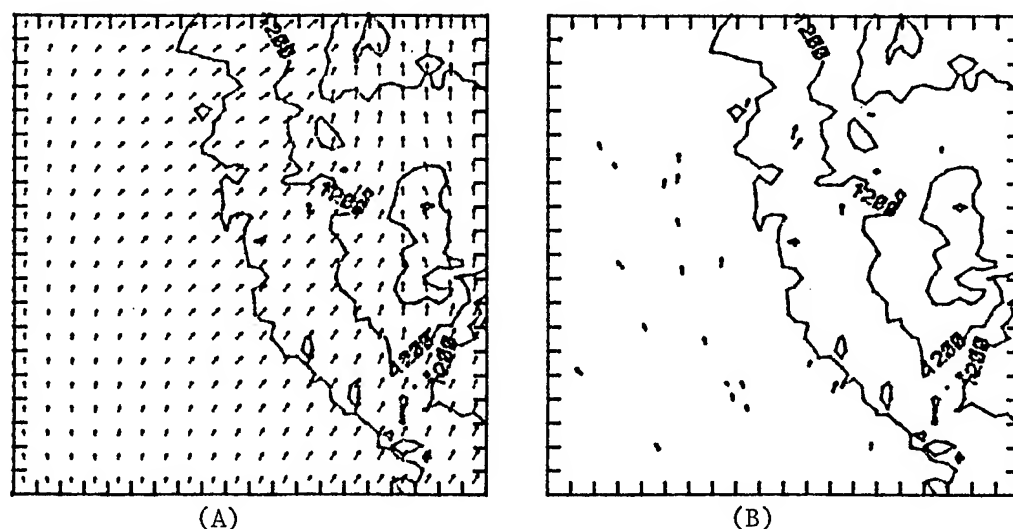


Figure 2. Surface (10 m level) wind vector distribution at 14 l.s.t. of day 178, A for calculated, and B for observed. Maximum wind vector = 7.6 m/s.

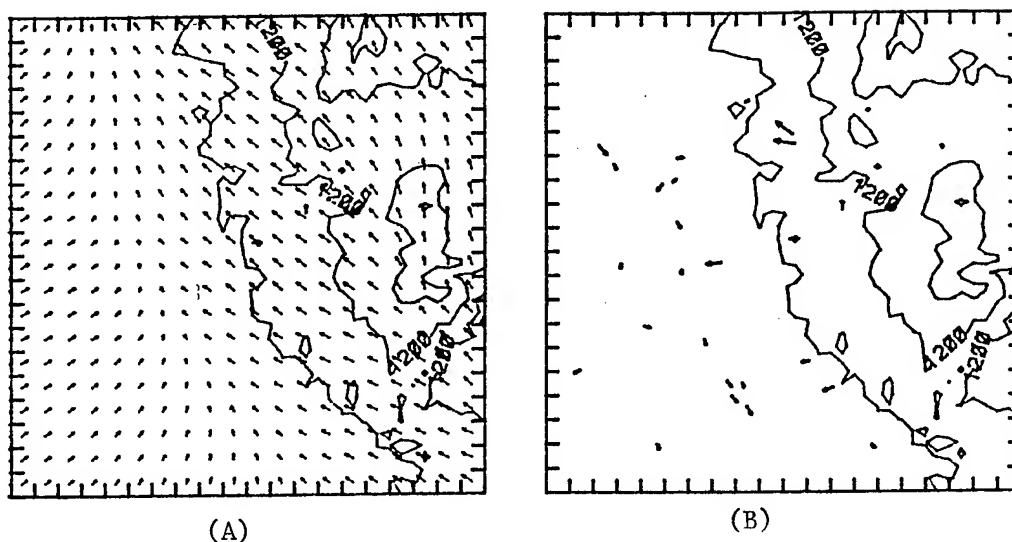


Figure 3. Same as fig. 2, except for 00 l.s.t. of day 179. Maximum wind vector = 3.85 m/s.

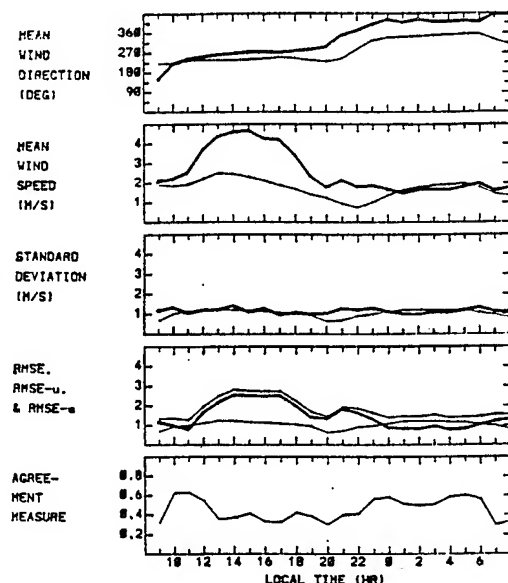
Since the locations of surface observation points do not generally correspond with model grid points, model output values at four grid points surrounding an observation point were interpolated, using inverse square distance weighting, to provide simulated values at observation points. Model performance on surface meteorological parameters was evaluated quantitatively by using the following parameters (Steyn and McKendy, 1988):

- Observed and modeled means and standard deviations (sd);
- Systematic and unsystematic components of the root-mean-squared errors (rmse-s; rmse-u) as well as the total rmse (σ_s , σ_u , and σ , respectively); and
- Agreement measure between the model and observations.

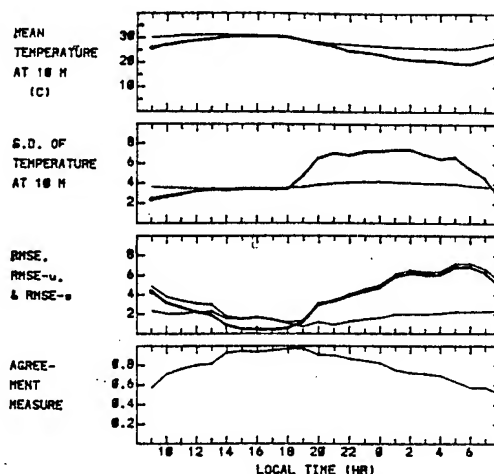
σ_s is an estimate of the model's bias, and σ_u is a measure of the nonlinear discrepancy between predictions and observations. Assuming no significant nonlinear biases, the more σ_u is, the better the model. Agreement measure is a dimensionless index that has a theoretical range of 1.0 (for perfect agreement) to 0.0 (for no agreement).

The above parameters were computed for surface wind and temperatures at every hour starting at 0900 l.s.t. of day 178 to 0800 l.s.t. of day 179. The results are shown in fig. 4, wind results on the left side and temperature results on the right side.

Mean wind direction was calculated from the means of horizontal wind components. Thin lines represent simulation, and dark lines represent observation in the top three portions of the figure. Agreement measure of windspeed was slightly lower during the day than during the night, as mean windspeed showed greater discrepancies during the day than during the night.



Time series of statistical parameters for wind.



Time series of statistical parameters for temperature.

Figure 4. Wind and temperature results, 0900 l.s.t. of day 178 to 0800 l.s.t. of day 179. Dark lines are for observation and thin lines are for model levels.

The figure shows good agreement between simulation and observation during the day. The diurnal variation of surface temperature calculated by the model was smaller than observations, resulting in poorer agreement during the night than during the day.

Generally the model showed good capability of simulation for surface wind and temperature.

6.2 UPPER-AIR PARAMETER COMPARISON

To compare upper-air parameters at certain levels, the author interpolated both model and observation as a function of height, using a bicubic spline interpolation method. Figure 5 shows evolutions of upper-air parameters (wind direction, windspeed, temperatures, and dew point) at four different height levels (700 and 850 mbar, and 100 and 10 m levels) for station 1. Station 1 is about 46 km from station 4. Note that upper-air data taken at station 4 were assimilated into the model. Agreements between model and observation were excellent throughout simulation at all the levels. The figure shows that diurnal variation of wind direction and temperature was greater near the surface than at high levels.

Figure 6 shows the evolutions of the mean of absolute difference between observation and simulation for horizontal wind components, windspeed, temperature, and dew point. The left side of the figure is for 200 m level, and the right side is for 2000 m level. Upper-air sounding data from five stations were used for calculation. At both levels, the means of absolute difference for all parameters did not show significant variations, indicating that the model simulated well the variation of meteorological conditions.

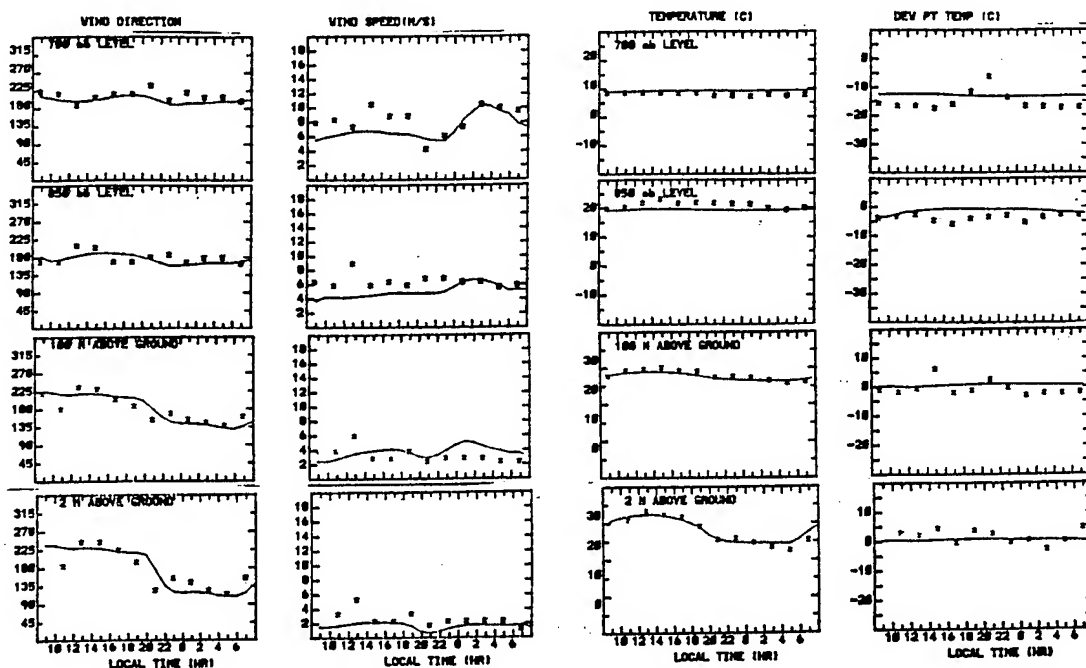


Figure 5. Time series of meteorological parameters (wind direction, windspeed, temperature, and dew point) at different levels (from the top, 700 mbar, 850 mbar, 100 m, and 2 m levels). Calculations are drawn by lines, and observations by *.

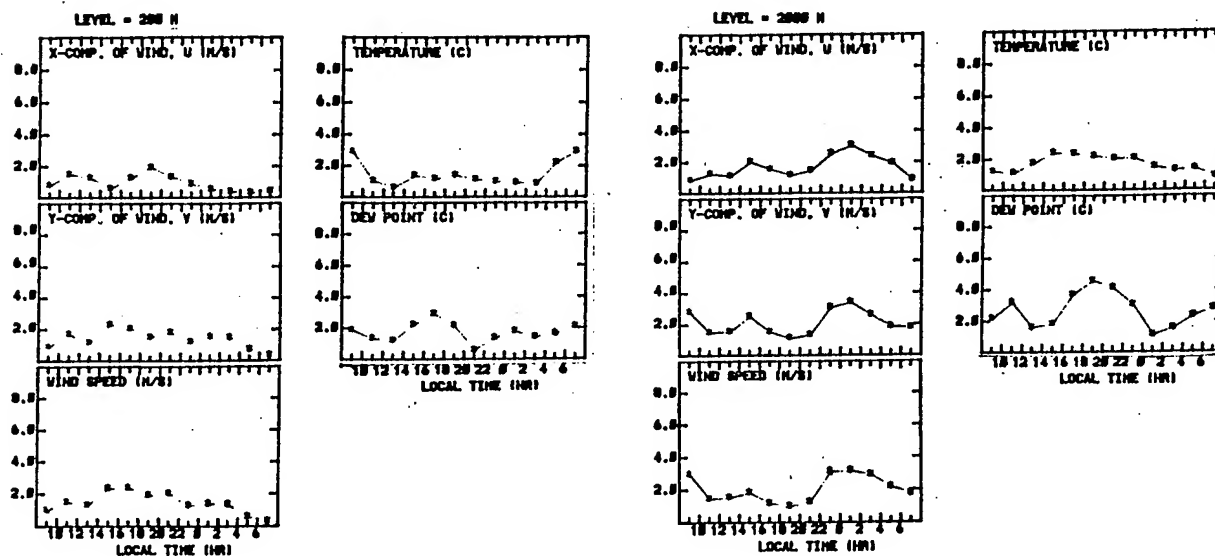


Figure 6. Time-series of means of absolute differences between model and observations for upper-air parameters (x and y components of wind, temperature, dew point, and pressure). Left side for 200 m level and right side for 2000 m level.

7. CONCLUDING REMARKS

Assimilation of upper-air wind data taken at one station into the HOTMAC model by the nudging method has resulted in good agreements between observation and simulation for both surface and upper-air meteorological parameters. Close examination of the simulated wind profiles revealed the following:

a. In the lower boundary layer, the wind field was dominated by model physics.

b. In the upper boundary layer, strong interactions between model physics and nudging of observed data occurred.

When large-scale wind flows are weak or steady, a good mesoscale model should be able to forecast wind and temperature fields accurately. However, when synoptic conditions are changing, the four-dimensional data assimilation technique should be employed for nowcasting or short-range forecasting.

REFERENCES

- Anthes, R. A., 1974: Data Assimilation and Initialization of Hurricane Prediction Models. J. Atmos. Sci., 31:702-710.
- Cionco, R. M., 1989: Design and Execution of Project WIND. Preprint Volume of the 19th Conference on Agriculture and Forest Meteorology and the 9th Conference on Biometeorology and Aerobiology, Charleston, American Meteorological Society, Boston, MA.
- Henmi, T., 1990: Assimilation of Wind Field Over Complex Terrain, Fifth Conference on Mountain Meteorology. Boulder, American Meteorological Society, Boston, MA, 118-124.
- Steyn, D. G., and I. G. Mckendry, 1988: Quantitative and Qualitative Evaluation of a Three-Dimensional Mesoscale Numerical Model Simulation of a Sea-breeze in Complex Terrain. Mon. Wea. Rev., 116:1914-1926.
- Yamada, T., 1983: Simulations of Nocturnal Drainage Flows by q^2 Turbulence Closure Model. J. Atmos. Sci., 40:91-106.
- Yamada, T., C-Y., J. Kao, and S. Bunker, 1989: Air Flow and Air Quality Simulations over the Western Intermountainous Region with a Four-Dimensional Data Assimilation Technique. J. Atmos. Environ., 23:539-554.
- Yamada, T., and S. Bunker, 1989: A Numerical Model Study of Nocturnal Drainage Flows with Strong Wind and Temperature Gradients. J. Appl. Meteorol., 28:545-554.

IMPLEMENTATION OF THE ARMY/NAVY MESOSCALE FORECAST

MODEL ON THE INTEGRATED METEOROLOGICAL SYSTEM

James E. Harris and Ronald E. Meyers
U.S. Army Atmospheric Sciences Laboratory
White Sands Missile Range, New Mexico 88002-5501, USA

ABSTRACT

The United States (U.S.) Army, in cooperation with the U.S. Air Force, is developing the Integrated Meteorological System (IMETS), a mobile automated weather data receiving, processing, and dissemination system. A major function of the IMETS will be to provide mesoscale four-dimensional (4-D) gridded meteorological data to the Army Tactical Command and Control System for use in battlefield planning and in generating weather effects decision aids. The U.S. Army Atmospheric Sciences Laboratory (ASL) conducts the basic and applied research to provide the Army with this capability. Discussed is ASL's plan to adapt the Naval Research Laboratory's (NRL) mesoscale forecast model for implementation on the IMETS. The plan involves a cooperative Army and Navy research program to evolve a joint Army/Navy model by increasing the resolution of the NRL model, adding multiple layers in the planetary boundary layer, improving the 4-D data assimilation techniques, and providing a nonhydrostatic capability. Longer term developmental goals are to evolve the Army/Navy model into an advanced mesoscale model incorporating advanced computer technology and programming practices, adaptive gridding, improved boundary layer physics, and nonlinear mathematics and discretization techniques. The NRL model is reviewed, adaptations are discussed, and developmental goals are presented.

1. INTRODUCTION

United States (U.S.) military policies and doctrine are undergoing major revisions as a result of a rapidly changing world. Until a few years ago, U.S. policy emphasized strategic nuclear forces over tactical general-purpose ones, and, because of the gravity of using nuclear weapons, the concept of centralized control and execution was necessarily employed. This policy of centralized control carried over into the military weather support concepts as well, with strong emphasis on centralized forecast facilities such as the Air Weather Service's Air Force Global Weather Central (AFGWC) and the Navy's Fleet Numerical Oceanography Center (FNOC). Computer processing power as we know it today was limited, and personal computers and high capacity workstations were nonexistent.

The era of "strategic deterrence" is now changing, computer technology is exploding, and military weather support concepts are changing as well. Lessons learned from Vietnam, Central America, and the political changes in Eastern Europe and the Soviet Union have contributed to forming more tactical, highly mobile, quick reaction forces. Modern weaponry, such as those used in Desert Storm, now cost orders of magnitude more and respond to much more subtle weather parameters than can be forecast by a distant military weather central. Computer technology now exists to exploit mesoscale forecasting technology on time and space scales of primary importance to the military, the battlefield scale. To keep pace with this changing environment, the Army and the Air Force are developing plans and equipment for a quasi-decentralized forecast capability. To prepare for this decentralized era, several systems are now being developed that will evolve mesoscale forecasting technology in the 1990's to the point where operational battlefield models become a reality. The U.S. Army, in coordination with the Air Force, is developing one such system called the Integrated Meteorological System (IMETS).

2. INTEGRATED METEOROLOGICAL SYSTEM

The IMETS will be the hub of Army weather support (see fig. 1). It will be a mobile automated weather data receiving, processing, and dissemination system operated by Air Force weather forecasters in support of Army operations. It will receive weather data from multiple sources to include the Air Force Automated Weather Distribution System (AWDS), the Automated Weather Network, meteorological satellites, remote surface sensors, unmanned aerial vehicles, artillery upper-air systems, and high-frequency radio intercept of indigenous sources. These data will be used to initialize a mesoscale forecast model that will provide four-dimensional (4-D) gridded meteorological data to the Army Command and Control System battlefield functional area nodes for use in battlefield planning and in generating weather effects decision aids.

The IMETS is on a fast development track and although the initial IMETS Block I, scheduled for fielding in fiscal year (FY) 93, does not call for a mesoscale forecasting capability, the IMETS Block II follow-on in late FY94 or early FY95 requires an operational mesoscale model for predicting battlefield scale target area weather. With this milestone in mind, the U.S. Army Atmospheric Sciences Laboratory (ASL) conducted a survey of available mesoscale modeling technology and concluded that by evolving the Naval Research Laboratory's (NRL's) Limited Area Dynamical Weather Prediction Model (LADWPM) (Madala et al., 1987) into a joint Army/Navy Model, an operational mesoscale forecasting capability could be achieved on the IMETS by FY94. The LADWPM has matured to the stage where it will be tested and evaluated for operational use by the Naval Oceanographic and Atmospheric Research Laboratory in Monterey, California, using FNOC data in FY92 (Madala, 1991). Therefore, ASL determined that a coordinated research effort with NRL would leverage NRL's expertise while adding ASL's finer scale expertise in complex terrain and boundary layer meteorology. Another more obvious benefit would result--a government owned state-of-the-art mesoscale model tailored specifically to each services applications and maintained and supported by a cadre of government scientists.

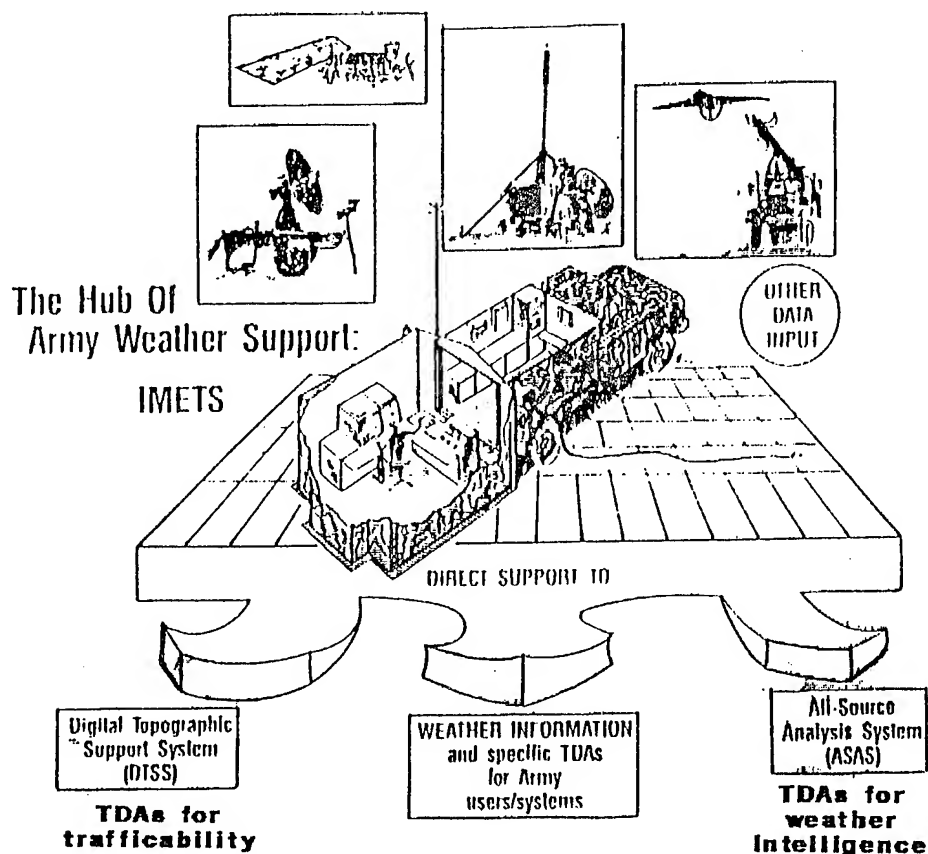


Figure 1. Integrated Meteorological System.

Therefore, ASL provided additional support to an on-going NRL research effort in 1991 to modify the LADWPM to be more useful for Army applications. NRL delivered the modified LADWPM (referred to in this paper as the Army/Navy Model) to ASL in August 1991. ASL meteorologists are now in the process of testing and evaluating the model with real-time operational data and integrating it into an IMETS prototype (IMETS/P). ASL will be working with NRL in FY92 to integrate a finer scale nest into the model to provide for the geographical scales of interest to the Army. The rest of this paper will describe the Army/Navy Model and discuss the modifications currently underway and programmed for the future.

3. ARMY/NAVY MODEL

As explained above, the Army/Navy Model evolved from the NRL LADWPM developed by Madala et al. (1987). It is a ten-layer primitive equation mesoscale, quasi-hydrostatic, baroclinic model in terrain-following coordinates having a one-way interacting three-level movable nested grid network. The continuous governing equations are written in flux form, and the model's time integration scheme is the split-explicit method. A staggered C-grid network is used for horizontal differencing. Lateral boundary conditions suggested by Davies (1976, 1983) are employed. The Monin-Obukhov similarity theory is used to determine the surface transfer of momentum, sensible heat, and latent heat. The cumulus convective parameterization scheme is the one suggested by Kuo (1974) and modified by Anthes (1977).

3.1 GOVERNING EQUATIONS

The vertical coordinate σ , defined as the ratio of pressure p to surface pressure p_s , is used because of its ease in handling changes in topography. The governing primitive equations are formulated in the flux form, that is, $p_s u$, $p_s v$, and so forth. The system of seven equations (five prognostic and two diagnostic) includes the u and v momentum equations $\left[\frac{\partial (p_s u)}{\partial t}, \frac{\partial (p_s v)}{\partial t} \right]$, the thermodynamic equation $\left[\frac{\partial (p_s T)}{\partial t} \right]$, the moisture continuity equation $\left[\frac{\partial (p_s q)}{\partial t} \right]$, the surface pressure tendency equation $\left[\frac{\partial p_s}{\partial t} \right]$, and the hydrostatic $\left[\frac{\partial \Phi}{\partial \sigma} \right]$ and continuity equations $\left[\frac{\partial (p_s \dot{\sigma})}{\partial \sigma} \right]$. The equations form a closed system for the seven dependent variables u , v , T , q , p_s , Φ , and $\dot{\sigma}$, where u , v are the zonal and meridional components of the wind, respectively, T the temperature, q the specific humidity, p_s the surface pressure, Φ the geopotential, and $\dot{\sigma}$ the vertical velocity defined as $\frac{d\sigma}{dt}$. The model equations are documented in detail by Madala et al. (1987).

3.2 PHYSICAL PROCESSES

The model physics include both convective and nonconvective precipitation, dry convective adjustment, and sensible heat and momentum exchange between boundary layer and the underlying surface using the surface similarity theory (Businger et al., 1971). A second-order diffusion for momentum on σ surfaces and for heat and water vapor on pressure surfaces is used to account for the cascading of the energy into unresolved subgrid-scale waves. The shortwave and longwave radiative transfer processes are not considered in the model (Alapati, 1991).

Precipitation and temperature distributions resulting from convective clouds are parameterized with a modified Kuo scheme (Kuo, 1974; Anthes, 1977). However, a recent study by Alapati et al. (1991) comparing the Kuo (1974) and Betts (1982, 1986) cumulus parameterization schemes indicates that the Betts scheme appears to do better than the Kuo scheme for orographically induced deep convection during an active monsoon period. Further research is being conducted by Madala (1991) to determine suitability of the Betts scheme for other meteorological conditions; we anticipate that Madala may replace the Kuo scheme with the Betts in the Army/Navy Model in FY92.

Nonconvective precipitation is determined using the Clausius-Clapeyron equation to compute excess moisture and isobaric heating. If supersaturation exists at any level, the excess moisture is assumed to precipitate into the next lower layer and evaporate or continue to fall, depending upon the state of saturation at that level (Chang et al., 1989; Alapati et al., 1991). Excess moisture of course precipitates to the surface.

The model has a simplified dry convective adjustment procedure to remove the dry convective instability in the model layers. Dry convective adjustment is activated when the static energy of a layer exceeds that of the adjacent higher

layer. The adjustment results in a slightly stable lapse rate while the total static energy is conserved. The adjustment can take place over several layers (Chang et al., 1989).

3.3 NUMERICS AND NESTING TECHNIQUES

The Army/Navy Model's time integration scheme uses the split-explicit method developed by Madala (1981). The split-explicit method allows larger time steps by effectively separating various terms in the prognostic equations into parts governing the slow-moving Rossby modes as opposed to the faster gravity modes. The split-explicit method has been found to be typically 3 to 5 times faster than conventional techniques used in other mesoscale models (Madala, 1991).

A staggered C-grid network is used for horizontal differencing (Arakawa and Lamb, 1977). On this grid, T , p_s , q , Φ , and $\dot{\sigma}$ are computed at mass points (i,j) while east-west velocity u is computed at the midpoint of mass points along the x-axis, and north-south component v is computed at midpoints along the y-axis. Vertical velocity $\dot{\sigma}$ is evaluated at half levels in the vertical. The finite difference technique used in the model is second-order accurate (Holt et al., 1990).

Originally the LADWPM had a two-level nested grid network, a coarse-grid mesh with approximately 180 km resolution, and a fine-grid mesh with approximately 60 km resolution. In evolving the Army/Navy Model, Madala has added a third nest with approximately a 20-km horizontal resolution. The two interior nests are movable. In the vertical, all three grids use 10 equally spaced sigma levels ($\Delta \sigma = 0.1$), with $\sigma = 1$ at the surface and $\sigma = 0$ at the model top.

3.4 ANALYSIS MODULE

A modified Barnes objective analysis scheme (Koch et al., 1981; Koch, 1983; Harms, 1985; Brehme, 1987) and a two-step successive corrections method using Gaussian weighting (Barnes, 1973) are currently used in the Army/Navy Model analysis module (Chang et al., 1989). The National Meteorological Center's (NMC) 2.5 degree analyses have been used routinely as the background field for model tests and specialized studies. Madala (1991) is conducting research to modify the analysis scheme using 3 hourly 4-D data assimilation techniques. The multivariate (geopotential inferred from observed wind) analysis module will use the model forecast fields as the background field, thereby providing a more accurate first guess and resolution compatible with the forecast model.

3.5 BOUNDARY CONDITIONS

The Army/Navy Model uses Davies' relaxation scheme (1976, 1983) to provide lateral boundary conditions. Model computed variables on nested grids are relaxed to boundary values in a boundary zone of 6 points. The NMC 2.5 degree analyses have been used routinely to provide the initial conditions and idealized boundary conditions for the coarse grid. At each time step, the boundary values are computed by linear interpolation in time from the 12 hourly NMC analyses. Lateral boundary conditions for each interior nest are obtained from the next higher level nest through a linear interpolation in time and space for each iteration. At the model top and bottom, the boundary condition

$\dot{\sigma} = 0$ is used (Alapati et al., 1991; Sashegyi and Madala, 1990; Madala, 1991). In testing and evaluating the Army/Navy Model for operational use, ASL will use uniform gridded data and surface and upper-air observations available from AFGWC through the AWDS to provide initial and boundary conditions.

3.6 INITIALIZATION

The Army/Navy Model currently uses the adiabatic nonlinear normal mode initialization (NNMI) procedure detailed by Sashegyi and Madala (1990). Adiabatic NNMI (ANNMI) has proven to be effective in controlling spurious large-amplitude gravity wave oscillations due to initial imbalances between the mass and wind fields in primitive equation models (Puri and Miller, 1990; Sashegyi and Madala, 1990). However, the use of ANNMI depletes divergent circulation associated with heat sources and does not alleviate the spinup problem when latent heat is excluded from the initialization process. Therefore, to provide more realistic initial conditions and to alleviate the spinup time of the LADWPM, Harms et al. (1991) have developed a diabatic NNMI (DNNMI). The results of their case study from the Genesis of Atlantic Lows Experiment (GALE) indicate that the spinup time of the vertical motion and rainfall, initially of the order of 3 to 5 h, could be reduced to almost zero. Madala (1991) expects the DNNMI to be integrated into the Army/Navy Model in FY92.

4. FUTURE IMPROVEMENTS

Modifications and improvements to the Army/Navy Model will be made through a coordinated research program between NRL and ASL. ASL has a strong basic research program in boundary layer meteorology, complex terrain, and numerical methods. As improvements in these areas evolve, they will be transitioned to ASL's applied researchers for incorporation into the IMETS. In the near term (FY92-93), ASL is most interested in increasing the vertical and horizontal resolution of the model to resolve more features of interest to the Army, integrating the model into the IMETS/P, optimizing run time, and conducting some rigorous tests and evaluations to meet IMETS development milestones. Data assimilation and initialization improvements discussed previously will also be incorporated during this time period as they become available. In the midterm (FY93-94), ASL research efforts will concentrate on achieving a multiresolution, nonhydrostatic multilevel two-way interactive nesting capability. In the long term (FY95 and beyond), as next generation computer systems find their way onto the battlefield, the Army/Navy Model will evolve into an advanced mesoscale model incorporating advanced computer technology and programming practices, multigridding and adaptive gridding techniques, and improved planetary boundary layer (PBL) physics.

4.1 INCREASED RESOLUTION

The Army mission requires detailed knowledge of that part of the atmosphere nearest the soldier, the PBL. Tests have shown (Holt et al., 1990) that forecasts significantly improve in the PBL when the number of layers and resolution in the model increases along with improved physics representations. Madala is testing a 16-layer version of the Army/Navy Model with six PBL layers and will transition this to ASL in the near term.

Since the LADWPM model is a quasi-hydrostatic model, its physics is limited in its ultimate grid size resolution over complex terrain and complex surface properties to keep it fast while covering a large domain. To resolve meteorological features in the PBL to 1 km in the horizontal, Ronald E. Meyers and other scientists at ASL are nesting its nonhydrostatic Air Flow Over Structures (AIRFLOS) model as the fourth nest in the Army/Navy Model. The AIRFLOS model is written in generalized curvilinear coordinates and has been successful in modeling flow over complex structures such as ships and complex terrain.

4.2 FOUR-DIMENSIONAL DATA ASSIMILATION

Madala and his colleagues have demonstrated that the incorporation of model output with new meteorological measurements initializes the model better and produces better forecasts than either ignoring the input of new measurements or of neglecting the inclusion of model forecast data in initialization. Such forecasts resolve terrain influences better. This argues strongly for assimilation of data as available. The Army/Navy Model will assimilate data every 3 h. These data will be added to forecast data and a new analysis field will be computed every 3 h. A new initialization and forecast will be performed using the analysis field from the combined data and forecast fields. This type of data assimilation is particularly useful for application to Army transport and diffusion problems where timely and accurate knowledge of PBL behavior is needed.

4.3 PBL PHYSICS

Models with the most detailed physics of the atmospheric PBL are called Large Eddy Simulation (LES) models. They are the forerunners of the advanced mesoscale models planned for the long term. Since it has been shown that forecasts significantly improve in the PBL as the number of layers and resolution increases and physics representation is improved (Holt et al., 1990), it is important to port LES physics to forecast models. This will be possible as computers become much faster. In the interim, faster parameterizations from LES experiments will be employed. Ronald E. Meyers and other scientists at ASL have used LES to model, in detail, the development and evolution of the PBL in all atmospheric stability conditions. This research will be incorporated into the Army/Navy Model as it evolves. The Navy is also working on improved PBL parameterizations over water and coastal areas.

4.4 NUMERICS

The numerical methods discretize the partial differential equations of the mesoscale model and render the model solvable by the computer. The three hydrostatic nests of the Army/Navy Model are accurately and quickly solved by Madala's split-explicit and eigenvalue solvers. With the inclusion of nonhydrostatic physics planned for the future, the computation greatly increases since the pressure deviations must be solved globally at each time step. Ronald E. Meyers (the second author of this paper) has been researching discretization techniques that optimize speed and accuracy. Multigrid numerical techniques, vectorization, and parallelization techniques will be used here to accelerate solutions.

It is nearly axiomatic, in mesoscale models, that the size of the spatial discretization error is many times larger than the size of the time discretization error. Adaptive numerical techniques with integral constraints will be used, in the fourth nest at first, to increase spatial resolution where needed to better resolve important meteorological features such as inversions, fronts, squall lines, and terrain influences. The Army/Navy Model is a large code with multiple nests and analysis. However, its modularity and good programming practices allow for maintainability and systematic upgrade of both the physics and the numerics.

5. SUMMARY

Military weather support is entering an era of "decentralization." Computer technology combined with mesoscale forecasting technology now makes it possible to conduct numerical forecasting operations on the tactical battlefield and provide 4-D meteorological parameters at the spatial and temporal resolutions required by modern weapon systems. This paper has presented a plan of how ASL, through a coordinated research effort with NRL, will evolve the NRL LADWPM into an operational mesoscale forecasting capability on the Army's IMETS by FY94. As the IMETS architecture matures so will an advanced mesoscale model incorporating advanced computer technology and programming practices, multigridding and adaptive gridding techniques, and improved PBL physics.

REFERENCES

- Alapati, K., R. V. Madala, S. Raman, and J. Baik, 1991: Numerical simulations of orographic-convective rainfall with Kuo and Betts cumulus parameterization schemes. Technical report available from R. Madala, Naval Research Laboratory, Washington, D.C. Submitted to Mon. Wea. Rev. in March 1991.
- Anthes, R. A., 1977: A cumulus parameterization scheme utilizing a one-dimensional cloud model. Mon. Wea. Rev., 105, 270-286.
- Arakawa, A., and V. R. Lamb, 1977: Computational design of the basic dynamic process of the UCLA general circulation model. Methods in Computational Physics, Academic Press, 17, 173-265.
- Barnes, S. L., 1973: Mesoscale objective map analysis using weighted time-series observations. NOAA Tech. Memo., ERL NSSL-62, Norman, OK, 60 pp.
- Betts, A. K., 1982: Saturation point analysis of moist convective overturning. J. Atmos. Sci., 39, 1484-1505.
- Betts, A. K., 1986: A new convective adjustment scheme. Part I: Observational and theoretical basis. Quart. J. Roy. Meteorol. Soc., 112, 677-691.
- Brehme, K. A., 1987: A method of objective analysis for meteorological fields for use in a numerical weather prediction model. M.S. thesis, North Carolina State University, Raleigh, NC, 123 pp.

- Businger, J. A., J. C. Wyngaard, Y. Izumi, and E. F. Bradley, 1971: Flux-profile relationship in the atmospheric surface layer. J. Atmos. Sci., 28, 181-189.
- Chang, S. W., K. Brehme, R. Madala, and K. Sashegyi, 1989: A numerical study of the East Coast snowstorm of 10-12 February 1983. Mon. Wea. Rev., 117, 1766-1776.
- Davies, H. C., 1976: A lateral boundary formulation for multi-level prediction models. Quart. J. Roy. Meteorol. Soc., 102, 405-418.
- Davies, H. C., 1983: Limitations of some common lateral boundary schemes used in regional NWP models. Mon. Wea. Rev., 111, 1002-1012.
- Harms, D. E., 1985: Application of an objective analysis scheme to mesoscale observational network design. M.S. thesis, North Carolina State University, Raleigh, NC, 91 pp.
- Harms, D. E., R. V. Madala, S. Raman, and K. D. Sashegyi, 1991: Diabatic initialization tests using the Naval Research Laboratory limited area numerical weather prediction model. Technical report available from R. Madala, Naval Research Laboratory, Washington, D.C.
- Holt, T., S. Chang, and S. Raman, 1990: A numerical study of the coastal cyclogenesis in GALE IOP 2: Sensitivity to PBL parameterizations. Mon. Wea. Rev., 118, 234-257.
- Koch, S. E., 1983: An interactive Barnes objective scheme for use with satellite and conventional data. J. Climate Appl. Meteorol., 22, 1487-1503.
- Koch, S. E., M. des Jardins, and P. J. Kocin, 1981: The Gempak Barnes objective analysis scheme. NASA Tech. Memo. 83851, NASA/GLAS, Greenbelt, MD, 56 pp.
- Kuo, H. L., 1974: Further studies of the parameterization of the influence of cumulus convection on large scale flow. J. Atmos. Sci., 31, 1232-1240.
- Madala, R. V., 1981: Efficient time integration schemes for atmosphere and ocean models. Finite Difference Techniques for Vectorized Fluid Dynamic Calculations, D. L. Book, Ed., Chap. 4, Springer-Verlag, New York, 56-74.
- Madala, R. V., Interview with author. Washington, D.C., 2 August 1991.
- Madala, R. V., S. W. Chang, U. C. Mohanty, S. C. Madan, R. K. Paliwal, V. B. Sarin, T. Holt, and S. Raman, 1987: Description of the Naval Research Laboratory Limited Area Dynamical Weather Prediction Model. NRL Memorandum Report, No. 5992, Naval Research Laboratory, Washington, D.C., 131 pp.

Puri, K., and M. J. Miller, 1990: The use of satellite data in the specification of convective heating for diabatic initialization and moisture adjustment in numerical weather prediction models. Mon. Wea. Rev., 118, 67-93.

Sashegyi, K. D., and R. V. Madala, 1990: Tests of initialization procedures with the NRL limited area numerical weather prediction model. NRL Memorandum Report 6648, Washington, D.C., 88 pp.

ON THE CHARACTERIZATION OF ARMY-SCALE SURFACE LAYER
MICROMETEOROLOGY USING FIELD MEASUREMENTS

Brian L. Orndorff and Ronald M. Cionco
U.S. Army Atmospheric Sciences Laboratory
White Sands Missile Range, New Mexico 88002-5501, USA

ABSTRACT

Characterization of the micrometeorology of the surface boundary layer is the basis for describing and analyzing the Army-scale of battlefield meteorology. Measurements from Project WIND provide a means to better understand the time and space behavior of the battlefield environment. This data base, the largest portion of which is micrometeorological, can be used to characterize the surface boundary layer. The WIND micrometeorological data base was collected in two major high-resolution domains. One was located on flat terrain with uniformly spaced almond tree orchards, and the other site was on complex terrain with a randomly spaced forest. For this initial study, characterization and analyses of the horizontal fields and vertical structure of the surface layer are performed for daytime and nighttime conditions. Methods developed for characterization and meteorological analysis include time sections of micrometeorological tower data, surface layer cross sections, horizontal windspeed gradient analysis, isotach analysis, and temperature and humidity gradient analyses. Vertical cross sections are constructed using data from the three micrometeorological towers located within the Orchard domain. Horizontal fields and contours also are constructed from 10 and 18 m high meteorological tower data. Composite fields and average profiles are then produced to define average daytime and nighttime conditions in the surface layer.

1. INTRODUCTION

Project WIND provided multiple scale meteorological measurements over differing domains in northern California (Cionco, 1989a). The majority of data was obtained over two 5 by 5 km micrometeorological domains. One micrometeorological site, called the Forest, was located on complex terrain with a randomly spaced forest. The other site, called the Orchard, was located on relatively flat terrain with orchards of uniformly spaced almond trees. This paper will characterize the micrometeorological data collected in the Orchard domain only. Although much of the domain consisted of orchards, the Orchard domain was not totally covered with trees. Much of the northern half of the Orchard domain was covered in grass and crops.

Numerous automated surface stations were used to document the horizontal fields of the surface layer in the Orchard domain. These stations measured windspeed,

wind direction, temperature, and relative humidity at the 10-m height in clearings and at the 18-m height in the almond orchard. The almond trees are 8 m in height. Figure 1 shows the locations of the stations that were used in the horizontal and vertical analyses. OS-1 and OS-3 were not used because of the close spacing.

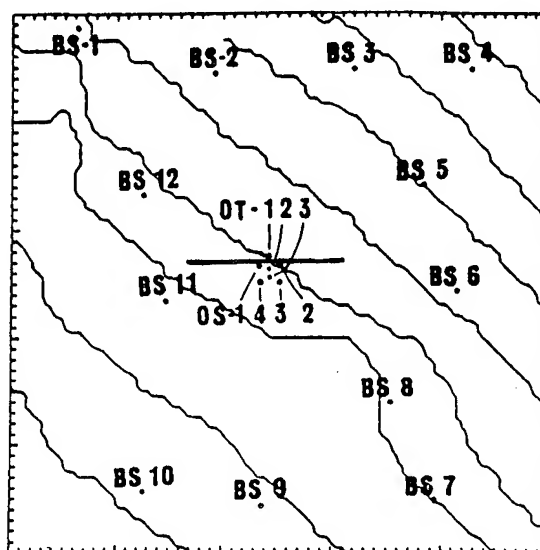


Figure 1. Orchard domain with 16 automatic surface stations and 3 micrometeorological towers. The line near the center denotes the transition from the orchard to the clearing.

The vertical structure of the surface layer was recorded at the Orchard site by three eight-level micrometeorological towers. One tower, OT-1, was located in a substantial clearing approximately 20 tree heights distance north of the almond orchard. Another tower, OT-2, was located just inside the orchard canopy edge south of OT-1. The third tower, OT-3, was located deep within the almond orchard south of OT-1 and OT-2. Vertical profiles of windspeed, wind direction, temperature, relative humidity with singular levels of solar and net radiation, soil heat flux, and pressure were recorded at the three tower locations (Cionco, 1989b).

Characterization and analyses of the horizontal fields and vertical structure of the surface layer were performed for daytime conditions from 0900 to 1700 P.s.t. and nighttime conditions from 2100 to 0400 P.s.t. during the summer of 1985. Methods used for characterization of the horizontal winds, temperature, and relative humidity were windspeed gradient analysis, isotach analysis, and temperature and relative humidity gradient analysis. The horizontal analyses used 10 m level data from stations BS-1 through BS-12 and 18 m level data (10 m above the trees) from stations OS-2 and OS-4. The vertical analyses included vertical cross sections of windspeed and wind direction. The resulting composite fields were derived from composite averages of horizontal parameters described above for daytime and nighttime conditions. Also, composite average vertical profiles of the windspeed, wind direction, temperature, and relative humidity are provided for daytime and nighttime conditions.

2. CHARACTERIZATION

Figure 2a shows a representative horizontal field of windspeed and wind direction over the Orchard domain during the day in the summer of 1985. The contours show the windspeed, and the streamlines with arrows indicate the wind direction. As expected, the general overall wind direction over this area is from the south-southeast, which is upvalley flow. However, a veering of the wind direction to a south to southwest direction can be seen at the transition from mainly orchard covered regions in the southern half of the domain to cleared land and grasslands in the northern half of the domain (Cionco, 1989c). This direction change is due to the wind flowing from a larger roughness length over the orchards to a smaller roughness length over the cleared land. Within less than 1 km distance downwind of the transition, the wind direction again becomes south-southeasterly. This statement is supported by a large percentage of negative vertical velocities above the orchard at station OT-2, which was located at the downwind edge of the canopy. The windspeed over the orchard covered region is in the range of 2 to 4 m/s, and over the clearing/grasslands region, it is about 4 to 5 m/s. This phenomenon is also due to the readjustment of the winds to the change in roughness and pressure gradient into the clearing.

Figure 2b shows a representative plot of temperature and relative humidity during daytime hours in northern California. Dashed lines are relative humidity. This plot shows that there were no significant temperature and relative humidity gradients over the Orchard domain during the day. The minor temperature changes that did occur were a slight temperature minimum near the center of the grid and a slight increase in relative humidity over the cooler, more moist orchards in the southern portion of the grid. These differences could be accounted for by the greater concentration of irrigated orchard areas in the southern half of the domain.

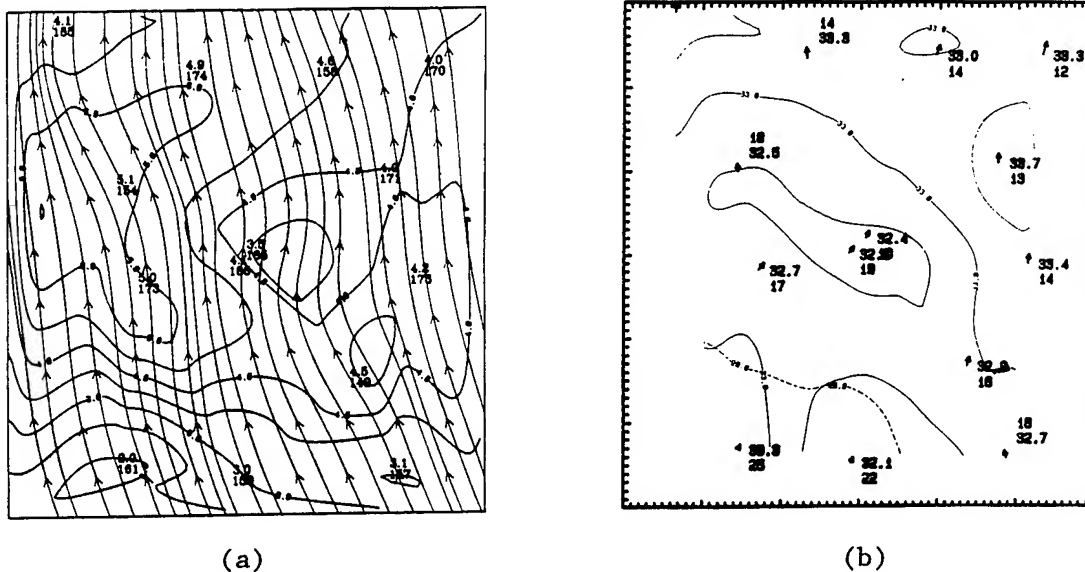


Figure 2. Analyzed horizontal (a) streamlines and isotachs (m/s) and (b) horizontal temperature (TT.T °C) and relative humidity (HH %) fields over the Orchard domain for Julian day 178 at 1200 P.s.t.

Figure 3 shows a representative cross section of vertical profiles from 16 m high micrometeorological stations OT-1, OT-2, and OT-3. This plot in conjunction with fig. 1 shows that the wind traveled nearly directly from OT-3 to OT-2 and then exited the orchard canopy toward OT-1, which was in a clearing. The wind direction did shift slightly upon exiting the canopy, but the windspeed change was much more dramatic. From within the canopy to the clearing, the 5-min averaged windspeed accelerated from about 0.5 m/s to about 3 m/s. Even at level 6, which is 4 m above the canopy, the windspeed accelerated from about 2.6 m/s directly above the orchard to about 3.7 m/s in the clearing. The windspeed at most levels showed a nominal 10 percent deceleration due to the continued loss of momentum from OT-3, deep within the canopy to OT-2, at the edge of the canopy.

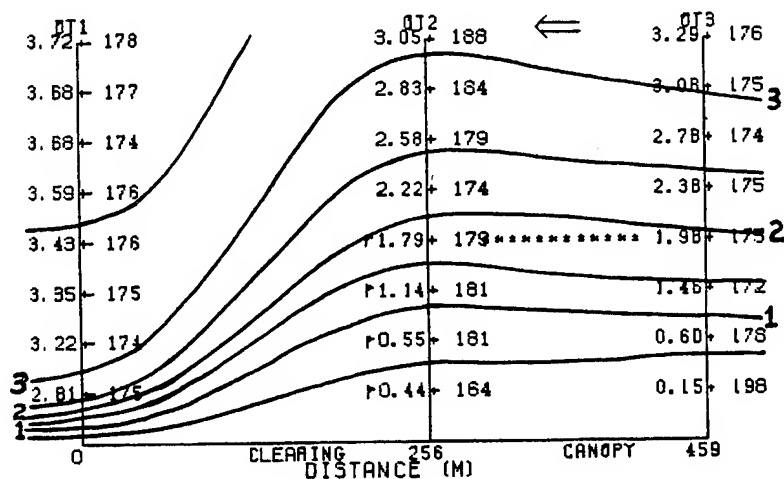
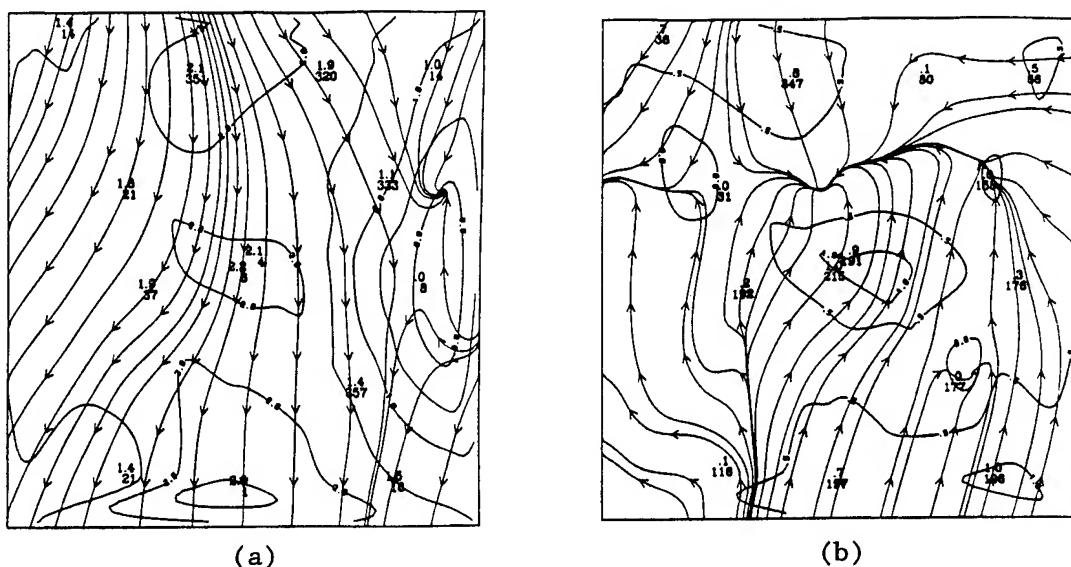


Figure 3. Isotach (m/s) analysis of a cross section through the almond orchard edge using OT-1, OT-2, and OT-3 windspeed and wind direction data for Julian day 178 at 1300 P.s.t. Arrow at the top indicates wind direction.

Figure 4a is an example of the nighttime horizontal windspeed and wind direction over the Orchard domain. The wind direction was generally from a northerly direction or down the valley. These northerly winds were due to drainage from the Coastal Mountain Range to the west and the Sierra Nevada Mountain Range to the east. A deflection of the wind direction as the wind flowed from open fields to tree orchards did exist. Horizontal windspeeds did not appear to change significantly due to the orchards; however, speeds did tend to be light.

Figure 4b shows an example of an anomalous situation that occurred between 0000 and 0200 P.s.t. when the expected downvalley drainage reversed itself to momentarily become upvalley. This is in contrast to the above examples. This wind flow also occurred well outside of the Orchard domain, indicating a possible mesoscale phenomenon.



A representative nighttime temperature and relative humidity pattern is shown in fig. 5. A significant temperature gradient can be seen between the clearing and orchard covered areas. There is approximately a 4 °C temperature difference mainly due to thermal storage within the almond orchard. Little change occurred in relative humidity between the clearing and orchard at night, although the clearing appeared to be nearly a factor of 2 drier.

Figure 6 shows a vertical cross section of windspeed and wind direction. This figure was chosen as a representative example of vertical wind profiles during nighttime conditions over northern California during the summer of 1985. Windspeeds within the canopy approached calm conditions much of the nighttime.

Windspeeds near the surface in the clearing were light (0.75 m/s) but significantly stronger than within the canopy. There was virtually no difference in windspeed at level 6 (12 m height) and at the same level in the clearing. Wind direction differences above the 12-m level were also not significant between the orchard covered region and the clearing. These observations indicate that during this nighttime case the canopy has little effect on the winds that are greater than 4 m above the canopy. However, this observation was not true during most daytime hours. During the day (see fig. 4) winds at 8 m above the orchard canopy were still affected by the canopy below. This difference between daytime and nighttime winds above the canopy can be explained by the typically greater stability and lighter windspeeds at night.

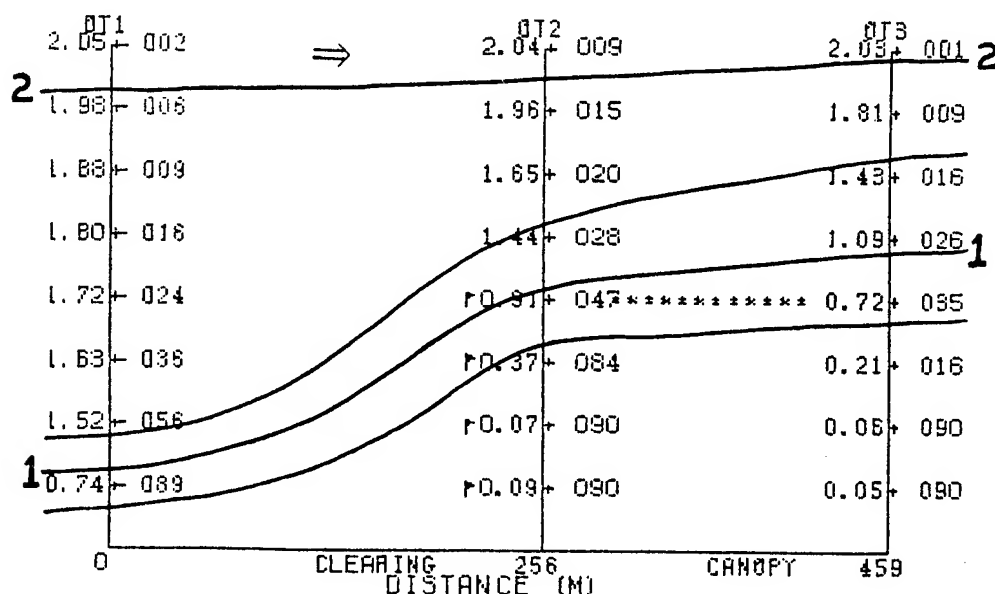


Figure 6. Isotach (m/s) analysis of a cross-section through the almond orchard edge using OT-1, OT-2, and OT-3 windspeed and wind direction data for Julian day 176 at 2300 P.s.t.

Figure 7 shows a daytime horizontal composite analysis of 5-min averaged wind-speed and wind direction data. This composite field indicates that the daytime horizontal wind flow over the Sacramento Valley was consistently from the south-southeast. Winds moving from mostly orchard covered regions in the southern half of the domain appeared to be affected by the transition to mostly open fields in the northern half of the domain. The wind direction veered by about 20 degrees over the orchard and the windspeed was reduced by about 0.5 to 1.0 m/s. Within 1 km after exiting the orchard regions, the windspeed and wind direction appeared to return back to the original speed and direction that occurred before entering the high density roughness of the orchards in the south-central area of the domain. The daytime composite temperature and relative humidity (not shown) did not show any significant changes over the Orchard domain.

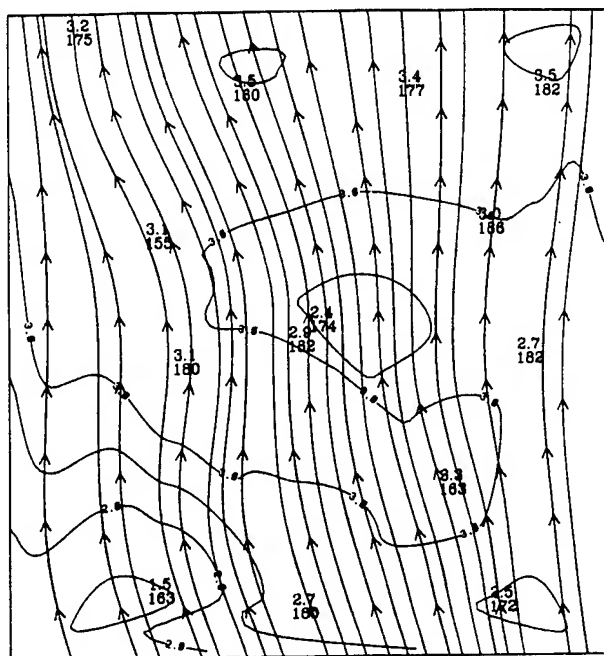


Figure 7. Composite horizontal streamlines and isotachs (m/s) over the Orchard domain for Julian day 178 at 0900 to 1700 P.s.t.

Figure 8a presents a nighttime horizontal composite of 5-min averaged windspeed and wind direction data. The wind direction appeared to be affected by the difference in roughness between the northern half of the domain and the southern half. Since the southern portion of the domain consists of mostly orchards, the wind appeared to veer toward the right shortly after entering the orchard regions, and then within about 2 km the wind direction returned back to a more northerly direction. During the nighttime, easterly winds occurred over the eastern third of the domain. The air in this region was coming from the drainage flow from the Sierra Nevada Mountains to the east merging with the downvalley flow.

Figure 8b presents the nighttime composite temperature and relative humidity over the Orchard domain, showing the drier air flowing over the open fields advecting into the orchard regions near the center of the domain. This figure also shows the warmer air over the almond orchard caused by the thermal storage of the trees.

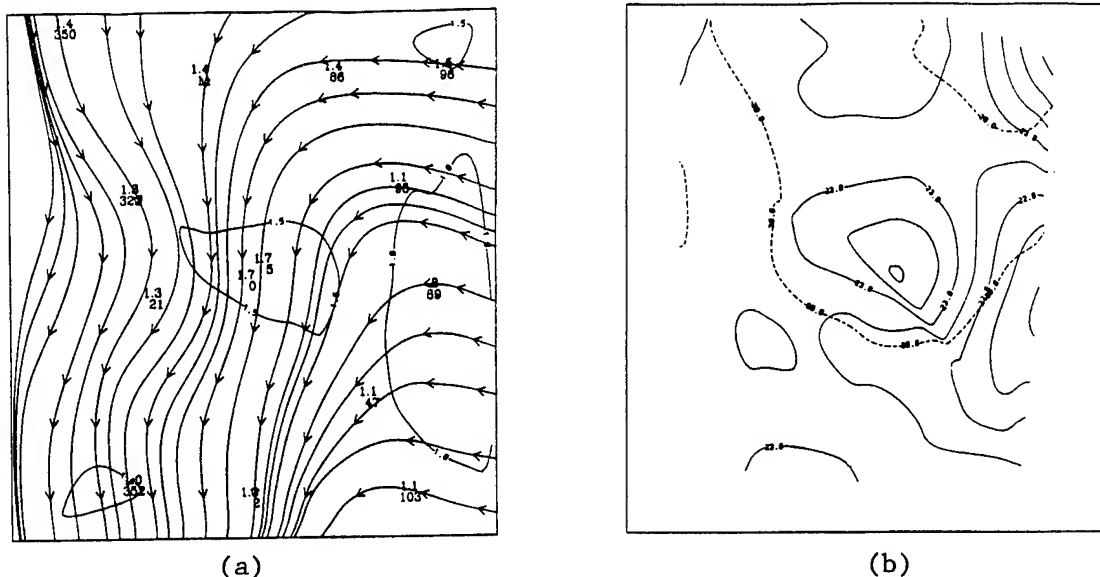


Figure 8. Composite horizontal (a) streamlines and isotachs (m/s) and (b) temperature (°C) and relative humidity (%) over the Orchard domain for Julian day 176 and 177 at 2100 to 0400 P.s.t.

Figure 9 shows the vertical composite windspeed and wind direction and the temperature and relative humidity for daytime conditions in the Orchard domain. Figure 10 shows similar composite profiles as in fig. 9, except nighttime conditions are presented. During the day, the wind flow was generally from the south-southeast at all levels within and outside of the orchard canopy. However a few levels deep within the canopy (OT-3) reported south-southwest flow. Windspeeds gradually increased with height outside of the canopy, but windspeeds increased dramatically above 4 m height within the orchard covered regions. Temperature and relative humidity vertical gradients were very small during the day within and outside of the canopy, though temperature did decrease gradually with height.

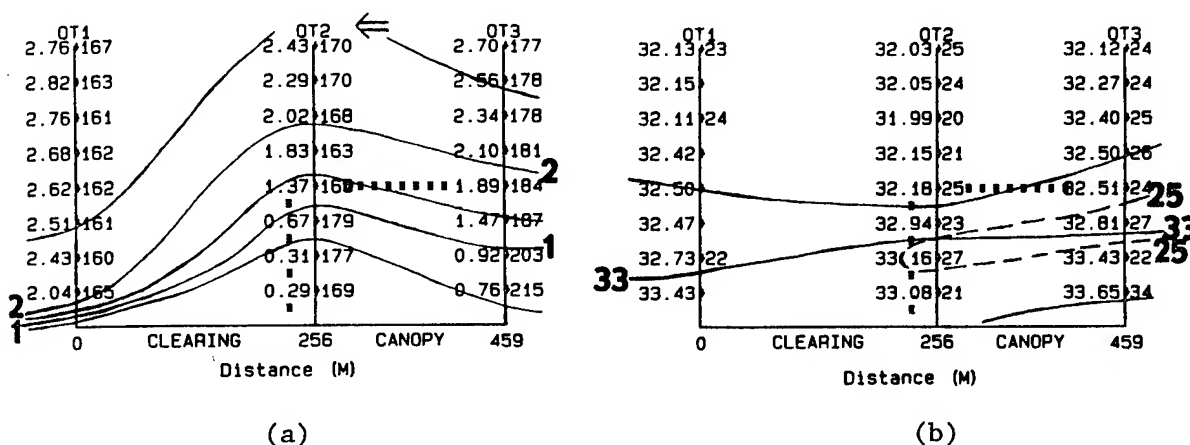


Figure 9. Composite (a) isotach and (b) temperature and relative humidity cross sections through the almond orchard edge using OT-1, OT-2, and OT-3 data for Julian day 178 at 0900 to 1700 P.s.t.

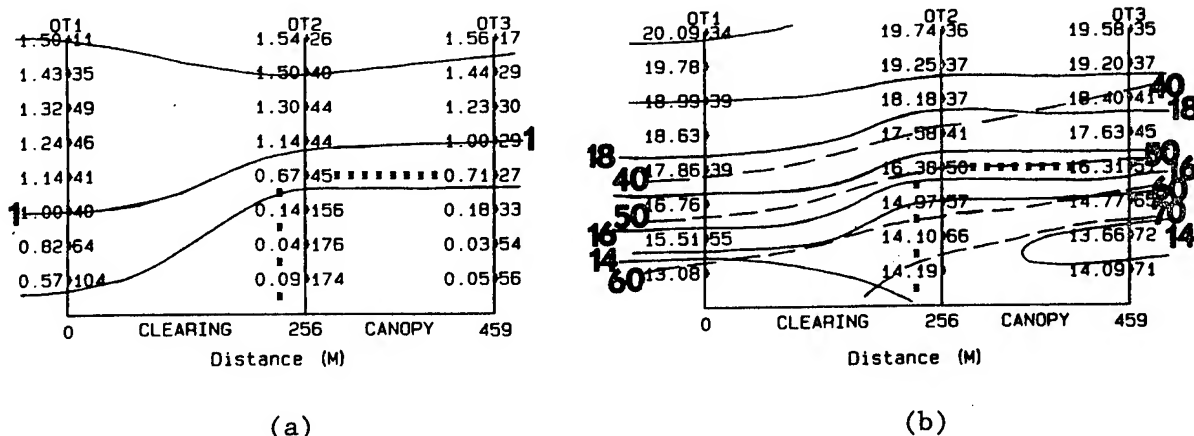


Figure 10. Composite (a) isotach and (b) temperature and relative humidity cross sections through the almond orchard edge using OT-1, OT-2, and OT-3 data for Julian day 176 to 177 at 2100 to 0400 P.s.t.

Nighttime windspeeds in figure 10a were generally much lighter than those during the day. The vertical gradients also tended to be less. However, the vertical gradient of wind direction was much greater at night even in the clearing. Nighttime vertical temperature gradients were also strong. The temperature at the top of the towers over the canopy was about 6 °C greater than at the near surface and was about 7 °C greater at the top of the tower than at the near surface in the clearing. Nighttime vertical relative humidity gradients were also significant, with a factor of 2 change from about 70 percent at 2 m to about 35 percent at 16 m height.

3. SUMMARY

Valley flow over northern California during the summer of 1985 exhibited a bimodal distribution changing from south-southeasterly during the daytime to north-northwesterly through the nighttime. Average daytime conditions over the study region consisted of winds predominantly from a south-southeasterly direction, with speeds of 1.5 to 3.5 m/s. Daytime temperatures generally averaged 31.5 to 32.5 °C, with relative humidities of about 15 to 20 percent. Within the surface layer, the vertical gradient of windspeed and wind direction was small during the daytime, but the windspeed gradient was large within the orchard canopy. The temperature decreased with height within and outside of the canopy, and the relative humidity changed very little with height during the day.

Average nighttime winds over northern California consisted of drainage winds generally from a northerly direction, except they were from an easterly direction over the eastern third of the Orchard domain. Although the wind direction shifted to a southerly flow during part of the night, the nighttime composite or predominant wind flow was from the north and east. Temperatures averaged about 22 to 24 °C, with relative humidities of about 20 percent over the cleared land and about 30 to 35 percent over more densely populated orchard regions. Within the surface layer, the vertical gradient of windspeed was moderate, especially within the orchard. The speed was nearly calm well below

the tree tops but was about 1.5 m/s at the top of the micrometeorological towers. The vertical gradient of wind direction was quite large within and outside of the orchard with up to a 148° change from the bottom to the top of OT-2. Nighttime vertical temperature and relative humidity gradients were also large with a 6 to 7 °C change in temperature and a 35 percent change in relative humidity from 2 to 16 m height.

During daytime and nighttime hours, the composite horizontal winds appeared to be affected by the transition from flowing out of or into predominantly orchard covered regions, even though measurements were taken above the orchard heights. The major change tended to be a slight wind direction shift that seemed to return back to the initial direction shortly after entering or exiting the orchard covered regions.

REFERENCES

- Cionco, R. M., 1989a: Design and Execution of Project WIND. In Proceedings of the 19th Conference of Agricultural and Forest Meteorology, Charleston, SC, American Meteorological Society, Boston, MA.
- Cionco, R. M., 1989b: Micrometeorological Measurements of Canopy Domains During Project WIND. In Proceedings of the 19th Conference of Agricultural and Forest Meteorology, Charleston, SC, American Meteorological Society, Boston, MA.
- Cionco, R. M., 1989c: Orchard Winds Coupled to Surface Layer Windfields. In Proceedings of the 19th Conference of Agricultural and Forest Meteorology, Charleston, SC, American Meteorological Society, Boston, MA.

CAMP GRAYLING WINTER SURFACE GIS MAPPING

by

Richard K. Haugen and Roy E. Bates
US Army Cold Regions Research and Engineering Laboratory
Hanover, NH 03755

This project was done in response to a task to be accomplished under SWOE Information Bases sponsorship i.e.; to provide a snow cover map representative of surface conditions for a winter Chicken Little Projects Office test during February - March 1990. Our approach was to use the GRASS Geographical Information System (GIS) to estimate snow-cover and temperature background characteristics for the Camp Grayling Michigan Winter Field Test Site, an area of approximately six km². A digital elevation model and related feature matrices were used to develop the GIS model on a Intergraphics Workstation. Based on digitized topographic and vegetation maps, a set of six surface background maps were developed. The interpreted scenes for two days during February 1990 were chosen to provide maximum background surface condition differences. Input data included an array of temperature and snow measurements from the Environmental Plot within the test site, and supplementary climatic data from the NOAA station at Grayling and Houghton Lake FAA. Solar azimuths and angle of incidence were calculated. The rules for the GIS input were based both on observational data from the above source, and our best estimate based on experience for parameters such as the temperature difference and snow cover depth and surface properties due to slope exposure, time of day, and vegetation type. The utilization of GIS technology provided a rational basis for the spatial extrapolation of limited on-site meteorological observations.

(The full text of this paper was unavailable at press time.)

Session IV

REMOTE SENSING POSTERS AND DEMONSTRATIONS

**Chairperson
Dr. Thomas Vonder Haar**

A SURVEY OF ARTIFICIAL INTELLIGENCE TECHNIQUES USED IN PROCESSING METEOROLOGICAL SATELLITE DATA

Donald D. Bustamante and Arthur W. Dudenhoeffer
Physical Science Laboratory, New Mexico State University
Las Cruces, NM 88003-0002, U.S.A.

ABSTRACT

Widespread interest exists in the application of artificial intelligence (AI) techniques to the processing and analysis of meteorological satellite data and related problems. The U.S. Army is particularly interested in AI applications involving the effects of weather on the realistic battlefield. This paper presents and reviews a number of current and potential AI approaches discussed in the literature. Emphasis is placed on the applications of knowledge-based systems and artificial neural networks to satellite data and selected meteorological products.

1. INTRODUCTION

Artificial intelligence (AI) has the potential to address problems considered difficult or intractable with conventional approaches. Indicative of the interest in this subject, the American Meteorological Society has established an AI Working Group. Also, the National Oceanic and Atmospheric Administration has formulated an initiative for Fiscal Year 1992 which will incorporate AI technologies to support and expand its capabilities (Moninger and Lynch, 1990). The U. S. Army is particularly interested in AI applications for the realistic battlefield, including weather and terrain effects, data merging techniques, and the man-machine interface (Try and Benton, 1989).

Problems in meeting Army requirements for meteorological satellite data may arise due to spatio-temporal resolution, accuracy, multi-spectral data fusion requirements, or processing time requirements (Hardy, 1989). Cogan (1989a, 1989b) has evaluated the ability of meteorological satellite data to meet the MJCS-154-86 (MJCS, 1986) requirements for defense environmental satellite data and has quantified deficiencies based on a modified Lickard scale. Miers (1989) has reviewed the capabilities of meteorological satellite environmental sensors and concluded that additional information needs to be incorporated in order to meet MJCS requirements. Hardy (1989) has identified three problem areas inherent in the processing and utilization of satellite meteorological data: availability of timely data, data merging capabilities, and limited computing capabilities of fielded tactical systems. It is expected that the application of AI technologies to these and related problems will improve the utilization of meteorological satellite data.

This paper presents a limited survey of representative AI applications found in the open literature, conference proceedings, and various government reports.

2. ARTIFICIAL INTELLIGENCE

Chabris (1987) draws a distinction between two broad concepts of AI. The first concept considers the creation of a complete artificial intelligence that actually thinks and understands in the same sense that a human being does. The second concept is concerned with the processes of human behavior and the development of computer applications based on these processes. In this survey only the second concept

noted here is considered. In particular we restrict our attention to the two different approaches represented by the knowledge-based system (KBS) and the artificial neural network.

A KBS is a computer program that offers advice or solves problems by using fairly simple algorithms to reason with a body of knowledge specific to a particular domain (Chabris, 1987). Knowledge-based software is directed primarily toward decision making rather than computation. It is used to address problems that can be narrowly defined and whose solutions frequently involve the selection of goals or predefined classes in the knowledge base. In order to solve a problem, a KBS performs inferences using knowledge existing in some appropriate representation, such as semantic networks, frames, facts, and rules. Knowledge-based systems can be categorized by the inferencing techniques and knowledge representations they employ. An expert system operates similarly to a KBS, and in this survey we treat the terms synonymously. Some authors draw a distinction, reserving the term "expert" for a KBS whose performance in some restricted problem domain is comparable to or exceeds that of human experts.

Neural networks employ a computational approach that utilizes principles of neurophysiology to develop an information processing system analogous to the human brain. "A neural network operates on inputs to extract information and produce outputs corresponding to the extracted information" (DARPA, 1988, p. 396). Like their biological models, neural networks are capable of adaptation and are massively parallel. Neural networks exhibit learning, generalization, and abstraction capabilities. Their intrinsic parallelism permits knowledge to reside within the neural interconnections, resulting in fault-tolerance and graceful degradation.

Knowledge-based systems often represent a top-down approach, while neural networks represent a bottom-up approach. The "knowledge" of a KBS is developed in coordination with a human domain expert. The "knowledge" of a neural network resides in the neural interconnection weights, which are computed from example cases. Nelson and Illingworth (1991) consider these approaches to the solution of a problem to be complementary in that neural networks can "identify what it is," KBSs can "identify what to do," and conventional algorithms describe "how to do it." Lupo (1989) argues for the continued use of KBSs and neural networks, using each approach's strengths to arrive at an optimal solution.

3. KNOWLEDGE-BASED APPLICATIONS

In recent years a number of domain-specific KBSs applicable to various meteorological problems have been reported. One forum for the presentation of such systems is the annual conference on Artificial Intelligence Research in Environmental Sciences (AIRIES). Moninger and Dyer (1988) and Moninger (1990) present summaries of KBSs described at different AIRIES conferences. Meteorology, climatology, natural-resource management, environmental-hazard response, and environmental protection are among the disciplines represented at the conferences. Individual KBSs applicable to forecasting, nowcasting, weather diagnosis, pattern classification, and meteorological data processing are reported.

3.1 IMAGE INTERPRETATION

There are numerous examples in the literature of the application of knowledge-based approaches to the interpretation of images derived from remotely sensed data. Taylor *et al.* (1986) present an overview of this area. Argialas and Harlow (1990) discuss the relevance of knowledge-based techniques to image analysis and how such techniques may be used in conjunction with conventional methods.

The feasibility of using a KBS to help automate the interpretation of meteorological satellite imagery has been investigated by Chance *et al.* (1987). This reference proposes to utilize preprocessed visible and infrared (IR) data to classify clouds and subsequently estimate significant weather parameters, where it is assumed that significant weather is most often present in well developed cloud systems, bands, and masses. Frontal systems, shear zones, vorticity maxima, upper level troughs, and tropical convergence zones are

mentioned as generating significant activity. The proposed system depends heavily on conventional methods for segmentation with knowledge-based techniques advising in feature extraction and classification.

The interpretation of mesoscale oceanographic features from satellite IR imagery is the subject of articles by Krishnakumar *et al.* (1989) and Thomason (1989). These references report systems that assist in the interpretation of North Atlantic Gulf Stream features, such as warm-core eddies and cold-core eddies. As is frequently the case, conventional techniques are used to extract feature descriptions, which are then matched against rule elements in the knowledge base. These papers illustrate the usefulness of location-specific expert knowledge in interpreting eddies north or south of the Gulf Stream.

A rule-based system for satellite derived winds (from cloud tracking) has been developed by Lampru and Atkinson (1989). This system, named CIRRUS I (Cloud Image Representation, Recognition, and Understanding Software I), was developed in LISP. Infrared imagery from the Geostationary Operational Environmental Satellite (GOES) imagery is used to identify regions of thermal homogeneity and derive displacement vectors for the leading edges of clouds. The CIRRUS I system is suggested as a possible candidate predictor for mesoscale forecasting.

Friedl *et al.* (1988) report on applications developed by several workers, as follows. Weinmann has developed a FORTRAN-based expert system running on a MacIdas mainframe which classifies satellite images of extra-tropical cyclones. A microcomputer-based system which locates fronts and cyclone centers has been developed based on knowledge acquired from this work. Garand and Weinmann have developed an expert system which classifies clouds and infers rainfall rates from GOES imagery using statistical analysis, cluster analysis and spatial correlation. Garand has developed a FORTRAN-based expert system running on a MacIdas mainframe which recognizes oceanic cloud patterns and infers meteorological parameters. Nowak has developed a system named Streamline Analyzer which determines wind direction from GOES water vapor images.

3.2 FORECASTING

Conway (1989) addresses some of the general issues involved in applying knowledge-based techniques to weather forecasting. This author envisages a multi-layered hybrid approach with a KBS (under the ultimate control of the end-user) querying and directing conventional programs that ingest current remotely sensed data from satellites and weather radars.

Moninger (1987) discusses a prototype system named ARCHER that was developed to investigate the problems and advantages associated with creating and using a KBS in the field of meteorology in general and weather forecasting in particular. This KBS uses a frame structure to encode meteorological knowledge for the purpose of identifying various weather phenomena from specific attributes associated with them. Examples of the archetypal phenomena to be identified are microburst, gust front, warm front, and cycles cold front. In ARCHER the knowledge was based primarily on radar signatures for various phenomena. However, it may be possible to encode knowledge derived from satellite data in a similar fashion.

The prediction of sea fog is the subject of a rule-based system named 4F (Tremant, 1989). It is programmed in Prolog and runs on a PC compatible computer. Tremant notes that Eyre *et al.* (1984) has demonstrated detection of nighttime fog using satellite imagery data from two IR channels of the Advanced Very High Resolution Radiometer (AVHRR). However, he does not indicate how the imagery data might be incorporated into the KBS.

3.3 DATA MERGING

The U. S. Army Integrated Meteorological System (IMETS) is a software system for weather data collection, preparation of products including forecasting and tactical decision aids, and the dissemination of these

products (Engebos *et al.*, 1988). This reference lists a number of areas in which knowledge-based methods are under consideration. One area is the management and merging of meteorological data from satellites and other remote sources.

McWilliams *et al.* (1988) address some of the issues involved in developing MERCURY, which is the prototype intelligent mesoscale meteorological data fusion system for IMETS. Many existing meteorological KBSs rely heavily on location-specific heuristics and are used to generate predictions of weather patterns for particular locations or types of locations (Fields *et al.*, 1988). This reference says that the use of such heuristics is impractical for a large-scale generalized data fusion system such as MERCURY. It also asserts that simulated neural networks are impractical for this task because extensive training would be required using historical data for specific locations.

Immense amounts of satellite data are projected to be available in the future. This is the motivation for the proposal of an Intelligent Information Fusion System (IIFS) that embodies knowledge of the users' domain-specific goals as well as automatically generating metaknowledge about objects or features of interest in near real time (Campbell and Crompton, 1990). For IIFS these authors envisage parallel processing and workstation environments with performance that rivals today's mainframes. The proposed IIFS would incorporate combinations of neural networks, KBSs, and object oriented environments with the capability to intercept satellite data streams in near real time and identify objects of interest.

4. NEURAL NETWORK APPLICATIONS

Neural networks have been applied to a variety of problems in many disciplines. Recent neural network bibliographies document the phenomenal growth in interest in neural networks. Neural network bibliographic entries have increased from approximately 1,500 in 1987 to approximately 4,000 in 1989 (Klimasaukas, 1989; Wasserman and Oetzel, 1990).

Applications have been studied in image interpretation, optimization, signal processing, data merging/fusion, and speech applications. DARPA (1988, pp. 195ff) notes that neural network applications have not been studied in sufficient depth so as to provide clear side-by-side comparisons with alternative approaches, due to the oversimplifications required by model systems. Recent advances have provided preliminary data on scalability and implementation issues.

4.1 IMAGE INTERPRETATION

The conventions of Marr (1982) are useful in dealing with the problem of image interpretation. Marr distinguishes between "low level" and "high level" vision. Low level vision consists of segmentation, feature extraction, and classification. High level vision controls the flow of low level vision information, and merges it with other knowledge to understand or interpret the image. Neural networks often blur the distinction between the various low level vision processes (Barrilleaux, 1990). Neural networks have been utilized to perform each of the low level vision processes individually or jointly. For example, some networks perform both segmentation and classification.

Lampru and Condon (1989) have utilized neural networks for the segmentation of multispectral imagery from the U.S. Earth Resources Satellite (LANDSAT). The approach utilized a neural network to segment imagery into land-use categories, followed by processing by an algorithm which converts the segmented image into a symbolic form capable of being processed by an image understanding algorithm. Accuracies of segmentation in excess of 90% using three spectral channels have been reported.

Key *et al.* (1990) have studied the application of backpropagation neural networks to extract surface and cloud classes from merged visible, IR, and microwave data from five AVHRR channels and two Scanning Multichannel Microwave Radiometer (SMMR) channels. Eight cloud classes (low level cloud over land,

water, and ice; mid level cloud over water and ice; and high level cloud over land, water and ice) and four surface classes (snow-free land, snow-covered land/ice cap, open water, and sea ice) were studied. Two networks were designed. One utilized spectral characteristics; the second incorporated local textural properties in order to classify cloudy regions. The results were compared with manual and supervised maximum likelihood method results. Maximum likelihood was unable to segment 10% of the image. Manually interpreted images differed from both maximum likelihood (agreement 68%) and the neural network (agreement 60%) results. Maximum likelihood and neural network segmentations were in reasonable agreement (80%). The difference between automated methods was attributed to the fact that the neural network was able to classify "indistinct" classes without being constrained by statistical assumptions.

Heermann and Khazenie (1990) have studied backpropagation neural networks and their ability to classify multi-spectral remote sensing data. The results were compared with those from piecewise linear classifiers, Markov random field unsupervised learning, and supervised contextual classification. The networks had an input layer (binary input), one hidden layer, and an output layer (output classes). Simulated and LANDSAT image data were used, including a series of temporal LANDSAT images to test the network's ability to generalize. The neural network was found to be ~60-65% accurate, with accuracy varying from image to image. This was lower than the corresponding alternative methods (statistical ~84%, linear ~68%); however, the difference may be due to the fact that the alternative methods had a larger training set. The high accuracy rate for the neural nets on the training image (~92%) may imply that the training sets were not sufficiently large to enable the network to generalize or perhaps that they did not have a sufficient number of examples in each classification category.

Maslanik *et al.* (1990) have developed model system neural networks for identification of sea ice seasons using SMMR data. Four separate neural networks (identifying winter, pre-melt, melt-onset, and false multiyear ice) were trained using six years of SMMR data. The authors are currently researching the development of a single network with multiple neurons in the output layer.

Lee *et al.* (1990) have studied neural network approaches to cloud classification. Drawing upon their previous work (Welch *et al.*, 1988, 1989; Chen *et al.*, 1989), they have developed a four-layer backpropagation feedforward neural network that utilizes textural features. This classifier achieved a classification accuracy of 93% using single channel visible LANDSAT multispectral scanner (MSS) imagery. Cirrus cloud classification was 96% accurate, while stratocumulus and cumulus accuracies were 92% and 90% respectively. The k-nearest neighbor technique had an accuracy of 85%, while linear discriminant accuracy was 84%. Two hidden layers were found to yield more accurate results.

Land-cover classification using a three-layer backpropagation neural network utilizing multispectral Thematic Mapper imagery consisting of bands 1, 2, and 3 (visible), and 4 (near IR) has been studied (Hepner *et al.*, 1990). Ground truth data from the Defense Mapping Agency was used to compare neural net and conventional classifier results. The neural network performance was superior to conventional supervised classifiers using identical training data. Neural network processed images were characterized by sharp boundaries, lack of speckle, and continuous features.

4.2 DATA MERGING

McClellan *et al.* (1990) have utilized three-layer backpropagation neural networks for multispectral pixel-by-pixel terrain classification using LANDSAT Thematic Mapper data. Bands 1 through 7 were utilized to generate false color maps of terrain. Initial studies utilized a two category classification which mapped land to green and water to red. Convergence was quickly obtained. A noteworthy result is that the neural network created a third category, which was not in the training set, with yellow representing shorelines.

Multisource classification of remotely sensed data using neural network and statistical classifiers has been studied (Benediktsson *et al.*, 1990). Topographic and LANDSAT MSS data were classified using statistical classifiers and neural networks trained with the generalized delta rule. The neural network was found to be superior to the statistical methods but was computationally complex. Multisource classification provided improved results over single source classification. Optimal results were obtained when the source inputs were weighted. Statistical classification methods were greatly dependent upon the selection of density functions, particularly since the input sources may have differing distributions. Improved results may be possible by increasing the number of classes in the training set, since only a limited number of examples of each class was used in the training set.

Hepner *et al.* (1990) have utilized neural networks in land cover classification of the Fort Lewis, Washington, region using Thematic Mapper imagery. A three-layer neural network consisting of 36 neurons in the input layer (3 by 3 pixel sample across visible bands 1, 2, and 3, and IR band 4), 10 in the hidden layer, and four in the output layer (water, grass, forest, urban) was developed. Backpropagation, Hopfield-like, Hebbian, and feedforward paradigms were studied. Ground truth information was obtained from the Defense Mapping Agency. Classification accuracy exceeded that of conventional classifiers. The network approach appeared to be more robust due to its data fusion capabilities. The training of the network was found to be computationally intensive.

4.3 MISCELLANEOUS APPLICATIONS

Jansson (1990) has utilized a higher order neural network, which uses neurons that operate on high-order products and powers of input variables as well as linear terms (DARPA, 1988), for the deconvolution of simulated absorption spectra. Deconvolution is a problem whose solution has been only partially successful utilizing conventional approaches. It was demonstrated that deconvolution with neural networks given physical realizability constraints is possible.

Measure and Balding (1989) have developed a two-layer (one input layer, one output layer) neural network for determining vertical profiles of atmospheric temperature utilizing microwave radiance, and surface temperature, pressure, and humidity data as inputs. Temperatures at various heights were the outputs of the network. The network utilized the delta rule for training. The neural network performance was found to be comparable or superior to those obtained using alternative methods.

5. HYBRID APPLICATIONS

Hybrid systems utilize a variety of AI techniques to solve applications problems. This approach utilizes the synergy obtained from applying the strengths of each of the component techniques to solving the applications problem. For example, a hybrid system is able to incorporate the classification skills of a neural network, the decision-making abilities of a KBS, and the numerical computation capabilities of conventional algorithms. Freundlich (1990) has noted the overlap of knowledge-based and database technologies, although their interests are still distinctly different. Current research focuses on hybrid systems. A variety of hybrid systems have been proposed or are currently under development.

Balasubramaniam *et al.* (1990), for example, developed an interactive knowledge-based approach for the selection of cluster algorithms applicable for a given situation. This system utilized a rule base to guide selection from thirteen algorithms (partitional, graph-theoretical, and hierarchical). The system uses forward chaining with backtracking. The system was tested using synthetic data sets, and found to yield good results. The system was easily extensible due to its design.

A hybrid approach using statistical signal processing and neural network approaches has been developed and tested (Eggers and Khuon, 1990). This system fuses data from two radar systems, then detects and classifies space object movements to assist in decision-making.

Smotroff (1990) and Smotroff *et al.* (1990) have been researching fusion of heterogeneous data with neural networks with the DATA FUNNEL (DATA Fusion Using Neural Network Learning) system. DATA FUNNEL accepts a variety of inputs ranging from point data to satellite imagery. Data are preprocessed by neural networks, which feed the data to a neural network classifier. The classifier system is trained with a variety of images to provide generalization over a variety of terrain, sun angle, and temperatures, and is controlled by a KBS. Initial qualitative results are reported to be promising.

6. CONCLUSION

Due to space limitations this survey is able to cite only a sampling of the publications involving the application of AI techniques to the processing of satellite data. Additional applications, including some that are subject to military critical technology restrictions, are discussed in Bustamante and Dudenhoeffer (1990). Most of the ongoing applications described in the literature are still in the stage of research and development. Commercial AI turn-key products whose primary purpose is the processing of meteorological satellite data are currently not readily available. Further development and eventual implementation of AI products required by the U. S. Army should build on existing research where appropriate. Products should operate on Army fielded tactical computing platforms, which are typically microcomputer or workstation based.

ACKNOWLEDGMENT

This work was supported by the U.S. Army Atmospheric Sciences Laboratory under contract number DAAD07-86-C-0034.

REFERENCES

- Argialas, D. P., and C. A. Harlow, 1990: Computational Image Interpretation Models: An Overview and a Perspective. Photogrammetric Engineering and Remote Sensing, 56:871-886.
- Balasubramaniam, A., G. Parthasarathy, and B. N. Chatterji, 1990: A Knowledge Based Approach to Cluster Algorithm Selection. Pattern Recognition Letters, 11:651-661.
- Barrilleaux, J. M., 1990: A Biologically Motivated Algorithm for Image Interpretation Based on Multi-Pass Multi-Resolution Techniques. In Proceedings of the International Joint Conference on Neural Networks 1990, San Diego, CA, II-813 - II-818.
- Benediktsson, J. A., P. H. Swain, and O. K. Ersoy, 1990: Neural Network Approaches Versus Statistical Methods in Classification of Multisource Remote Sensing Data. IEEE Transactions on Geoscience and Remote Sensing, 28:540-551.
- Bustamante, D. D., and A. W. Dudenhoeffer, 1990: A Survey of Artificial Intelligence Techniques for Processing Meteorological Satellite Data. Document PSL-90/102, Physical Science Laboratory, P. O. Box 30002, Las Cruces, NM 88003-0002.
- Campbell, W. J., and R. F. Crompt, 1990: Evolution of an Intelligent Information Fusion System. Photogrammetric Engineering and Remote Sensing, 56:867-880.
- Chabris, C. F., 1987: Artificial Intelligence and Turbo Pascal. Dow Jones-Irwin, Homewood, IL 60430.
- Chance, B. A., R. E. Introne Jr., and D. Izraelvitz, 1987: Automated Meteorological Satellite Image Interpretation: An Aid to Short-Range Weather Forecasting. SPIE 846 Digital Image Processing and Visual Communications Technologies in Meteorology (1987):13-17.

- Chen, D. W., S. K. Sengupta, and R. M. Welch, 1989: Cloud Field Classification Based Upon High Spatial Resolution Textural Features 2: Simplified Vector Approaches. Journal of Geophysical Research, 94(D12):14,749-14,765.
- Cogan, J. L., 1989a: Target Area Soundings in Near Real Time. In Proceedings of the Tenth Annual EOSAEL/TWI Conference, U. S. Army Atmospheric Sciences Laboratory, White Sands Missile Range, NM 88002-5501, 193-203.
- Cogan, J. L., 1989b: An Evaluation of Meteorological Satellite Data for Army Use, Part I: Stated Requirements, ASL-TR-0248, U. S. Army Atmospheric Sciences Laboratory, White Sands Missile Range, NM 88002-5501.
- Conway, B. J., 1989: Expert Systems and Weather Forecasting. Meteorological Magazine, 118:23-30.
- DARPA, 1988: DARPA Neural Network Study. AFCEA International Press, Fairfax, VA.
- Eggers, M., and T. Khuon, 1990: Neural Network Data Fusion Concepts and Applications. In Proceedings of the International Joint Conference on Neural Networks 1990, San Diego, CA, II-7 - II-16.
- Engelbos, B. F., R. R. Lee, and R. L. Scheinhart, 1988: Concept for Weather Related Decision Aids for the Tactical Commander. U. S. Army Symposium on Artificial Intelligence for Exploitation of the Battlefield Environment, J. R. Benton, Ed., 15-16 Nov., 1988, El Paso, TX, 58-61.
- Eyre, J. R., J. L. Brownscombe, and R. J. Allam, 1984: Detection of Fog at Night Using Advanced Very High Resolution Radiometer (AVHRR) Imagery. Meteorology Magazine, 113:266-271.
- Fields, C. A., M. J. Coombs, C. Cavendish, T. C. Eskridge, R. T. Hartley, H. D. Pfeiffer, C. A. Soderlund, S. Kirby, and G. McWilliams, 1988: MERCURY: A Mesoscale Meteorological Data Fusion System for Corp-Level Application. U. S. Army Symposium on Artificial Intelligence for Exploitation of the Battlefield Environment, J. R. Benton, Ed., 15-16 Nov., 1988, El Paso, TX, 143-157.
- Freundlich, Y., 1990: Knowledge Bases and Databases: Converging Technologies, Diverging Interests. IEEE Computer, November 1990:51-57.
- Friedl, M. A., J. E. Estes, and J. L. Star, 1988: Advanced Information-Extraction Tools in Remote Sensing for Earth Science Applications: AI and GIS. AI Applications in Natural Resource Management, 2:17-31.
- Hardy, K. R., Workshop Chairman, 1989: Satellite Remote Sensing of Mesoscale Phenomena Workshop Report. In Proceedings of the DoD Environmental Technical Exchange Conference on Mesoscale Phenomena (ETEC), Laurel, MD, 353-362.
- Heermann, P. D., and N. Khazenie, 1990: Application of Neural Networks for Classification of Multi-Source, Multi-Spectral Remote Sensing Data. 10th Annual International Geoscience & Remote Sensing Symposium: Remote Sensing Science for the Nineties (IGARSS-90), College Park, MD, 1273-1276.
- Hepner, G. F., T. Logan, N. Ritter, and N. Bryant, 1990: Artificial Neural Network Classification Using a Minimal Training Set: Comparison to Conventional Supervised Classification. Photogrammetric Engineering and Remote Sensing, 56:469-473.

- Jansson, P. A., 1990: Superresolving Neural Network for Deconvolution. In Proceedings of the International Joint Conference on Neural Networks 1990, Washington, DC, II-375 - II-378.
- Kadaba, N., K. E. Nygard, P. L. Juell, and L. Kangas, 1990: Modular Back-Propagation Neural Networks for Large Domain Pattern Classification. International Joint Conference on Neural Networks 1990, Washington, DC, II-551 - II-554.
- Key, J., J. A. Maslanik, and A. J. Schweiger, 1990: Neural-Network vs. Maximum Likelihood Classification of Spectral and Textural Features in Visible, Thermal, and Passive Microwave Data. 10th Annual International Geoscience & Remote Sensing Symposium: Remote Sensing for the Nineties (IGARSS-90), College Park, MD, 1277-1280.
- Klimasauskas, C., Ed., 1989: The 1989 Neuro-Computing Bibliography, MIT Press, Cambridge, MA.
- Krishnakumar, N., S. S. Iyengar, R. Holyer, and M. Lybanon, 1989: An Expert System for Interpreting Mesoscale Features in Oceanographic Satellite Images. SPIE 1095 Applications of Artificial Intelligence:184-194.
- Lampru, P. D. Jr., and L. A. Atkinson, 1989: Cloud-Tracked Winds Derived from Satellite Imagery Using an Image Understanding Approach. In Proceedings of the Tenth Annual EOSAEL/TWI Conference, U. S. Army Atmospheric Sciences Laboratory, White Sands Missile Range, NM 88002-5501, 454-461.
- Lampru, P. D. Jr., and M. D. Condon, 1989: Automated Recognition of Features in Multi-Spectral Imagery. In Proceedings of the Tenth Annual EOSAEL/TWI Conference, U. S. Army Atmospheric Sciences Laboratory, White Sands Missile Range, NM 88002-5501, 609-618.
- Lee, J., R. C. Weger, S. K. Sengupta, and R. M. Welch, 1990: A Neural Network Approach to Cloud Classification. IEEE Transactions on Geoscience and Remote Sensing, 28:846-855.
- Lupo, J. C., 1989: Defense Applications of Neural Networks. IEEE Communications Magazine, November 1989.
- Marr, D., 1982: Vision: A Computational Investigation into the Human Representation and Processing of Visual Information, W. H. Freeman & Co., San Francisco, CA.
- Maslanik, J., J. Key, and A. Schweiger, 1990: Neural-Network Identification of Sea-Ice Seasons in Passive Microwave Data. 10th Annual International Geoscience & Remote Sensing Symposium: Remote Sensing for the Nineties (IGARSS-90), College Park, MD, 1281-1284.
- McClellan, G. E., R. N. DeWitt, T. H. Hemmer, L. N. Matheson, and G. O. Moe, 1990: MultiSpectral Image-Processing With a Three-Layer Backpropagation Network. In Proceedings of the International Joint Conference on Neural Networks 1989, Washington, DC, I-151 - I-153.
- McWilliams, G., S. Kirby, C. Fields, C. Cavendish, M. Coombs, T. Eskridge, R. Hartley, H. Pfeiffer, and C. Soderland, 1988: Army Requirements for an Intelligent Interface to a Real-Time Meteorological Database. U. S. Army Symposium on Artificial Intelligence for Exploitation of the Battlefield Environment, John R. Benton, Ed., 15-16 Nov., 1988, El Paso, TX, 54-57.
- Measure, E. M., and J. M. Balding, 1989: A Neural Network Retrieval Algorithm. In Proceedings of the Tenth Annual EOSAEL/TWI Conference, U. S. Army Atmospheric Sciences Laboratory, White Sands Missile Range, NM 88002-5501, 271-278.

- Miers, B. T., 1989: Capabilities of Current and Future Meteorological Satellite Sensors to Meet Requirements for Environmental Data: A Review, ASL-TR-0244, U. S. Army Atmospheric Sciences Laboratory, White Sands Missile Range, NM 88002-5501.
- MJCS-154-86, 1986: Military Requirements for Defense Environmental Satellites. Memo - Joint Chiefs of Staff.
- Moninger, W. R., 1987: ARCHER: A Prototype Expert System for Identifying Some Meteorological Phenomena. Journal of Atmospheric and Oceanic Technology, 5:144-148.
- Moninger, W. R., 1990: Summary Report on the Third Workshop on Artificial-Intelligence Research in Environmental Science (AIRIES-89): 2-4 May 1989, Tysons Corner, Virginia. Bulletin American Meteorological Society, 71:672-679.
- Moninger, W. R., and R. M. Dyer, 1988: Survey of Past and Current AI Work in the Environmental Sciences. AI Applications in Natural Resource Management, 2, 48-52.
- Moninger, W. R., and J. L. Lynch, 1990: NOAA's Artificial Intelligence Initiative. In Abstracts of the AIRIES-90 Conference, Quebec, Canada.
- Nelson, M. M., and W. T. Illingworth, 1991: A Practical Guide to Neural Nets, Addison-Wesley, Reading, MA.
- Smotroff, I. G., 1990: Meteorological Classification of Satellite Imagery Using Neural Network Data Fusion. In Abstracts of the AIRIES-90 Conference, Quebec, Canada.
- Smotroff, I. G., T. P. Howells, and S. Lehar, 1990: Meteorological Classification Of Satellite Imagery Using Neural Network Data Fusion. In Proceedings of the International Joint Conference on Neural Networks 1990, San Diego, CA, II-23 - II-28.
- Taylor, A., A. Cross, D. C. Hogg, and D. C. Mason, 1986: Knowledge-Based Interpretation of Remotely Sensed Images. Image and Vision Computing, 4:67-83.
- Thomason, M. G., 1989: Knowledge-Based Analysis of Satellite Oceanographic Images. International Journal of Intelligent Systems, 4:143-154.
- Tremant, M., 1989: The Forecasting of Sea Fog. Meteorological Magazine, 118:69-75.
- Try, P. D., and J. R. Benton, Eds., 1989: Critical Investment Strategy Guidance for Artificial Intelligence Development in Support of the Realistic Battlefield, STC Technical Report 3087, Sept. 1989, Science and Technology Corporation, Hampton VA.
- Wasserman, P. D., and R. M. Oetzel, 1990: NeuralSource: The Bibliographic Guide to Artificial Neural Networks, Van-Nostrand Reinhold, New York, NY.
- Welch, R. M., M. S. Navar, and S. K. Sengupta, 1989: The Effect of Spatial Resolution Upon Texture-Based Cloud Field Classification. Journal of Geophysical Research, 94(D12):14,767-14,781.
- Welch, R. M., S. K. Sengupta, and D. W. Chen, 1988: Cloud Field Classification Based Upon High Spatial Resolution Textural Features I: Gray Level Co-Occurrence Matrix Approach. Journal of Geophysical Research, 93(D10):12,663-12,681.

A PRELIMINARY METHOD FOR COMPUTING INFRARED TRANSMITTANCES IN THE
TROPOSPHERE USING SATELLITE VALUES OF PRECIPITABLE WATER

James Cogan
U.S. Army Atmospheric Sciences Laboratory
White Sands Missile Range, New Mexico 88002-5501, USA

ABSTRACT

Transmittance in the thermal infrared (IR) may be estimated by using a variety of in-situ and remote techniques using ground-based or airborne sensors. However, estimating transmittance in the troposphere from data gathered by sensors on space platforms remains a problem, especially over land surfaces. This paper presents a preliminary method to compute thermal IR transmittance over a horizontal path that uses estimates of precipitable water from satellite data combined with sounding data from satellite or other sources. A brief description of the technique, along with a brief sensitivity analysis, provides a basic understanding of the method. Essentially, profiles of specific humidity are computed from actual atmospheric profiles or climatological data and then adjusted according to satellite estimates of total precipitable water. Temperature and humidity data at each pressure level provide input to equations of the type found in LOWTRN. These equations yield estimates of thermal IR transmittance for user-specified horizontal or vertical path lengths. Work is underway to extend the method to more complex cases. When completed, the expanded version of the method will be able to address a variety of slant paths in the atmosphere and allow extension to other spectral regions.

1. INTRODUCTION

A major problem for remote or inaccessible areas is the determination of atmospheric infrared (IR) transmittance in the troposphere, especially near the surface. Over remote areas, in-situ devices or remote sensing instruments may be carried by air or space-based platforms. However, methods to estimate IR transmittance by using data from space platforms remain a problem, especially over land surfaces. This paper presents a preliminary method to compute thermal IR transmittance over a horizontal path that uses estimates of precipitable water from satellite data, combined with sounding data from satellite or other sources. If sounding data are unavailable, or too distant in space or time from the time or area of interest, then climatological profile data may be used to provide an approximate estimate. A brief description of the technique, along with a brief sensitivity analysis, provides a basic understanding of the method. Essentially, profiles of specific humidity are computed from actual atmospheric profiles or climatological data and then adjusted according to satellite estimates of total precipitable water.

2. DESCRIPTION OF METHOD

2.1 OVERVIEW

The preliminary technique uses the relation between water vapor and IR extinction in the atmosphere. Algorithms of the type found in LOWTRN may be used to compute IR transmittance in a horizontally stratified atmosphere (Kneizys et al., 1980, 1983, 1988). Temperature and humidity data at each pressure level of an atmospheric sounding provide input to equations similar to those found in Kneizys et al. (1980). The older version was used since it uses standard type variables (for example, vapor pressure in atmospheres). The accuracy in the thermal IR is virtually the same as in Kneizys et al. (1983), and the algorithms are the same in Kneizys et al. (1988) and Kneizys et al. (1983). These equations yield estimates of thermal IR transmittance for user-specified horizontal path lengths. The preliminary version assumes horizontal homogeneity at a given pressure. The simple integration techniques of this approximate method assume constant or only slowly varying transmittance over spectral intervals of 20 cm^{-1} .

Atmospheric soundings from a variety of sources may be used in general; but for applications to remote areas, the primary sources would be satellite soundings, soundings derived from aircraft or unmanned aerial vehicle (UAV) data, dropsonde profiles, or a combination of the above (Cogan, 1990). The resultant sounding provides temperature (T) and humidity (h) values at given pressure levels, which may be used to compute specific humidity (q). From values of q one may compute precipitable water (PW) for layers or for the entire vertical extent of the sounding (total or integrated PW). Integrated values of PW may be compared to values derived from satellite imagery. The sounding amount (not the shape of the distribution curve) is adjusted according to the ratio of the estimate from satellite imagery (herein called satellite estimate or value) to the value computed from the sounding. If sounding data are not available for the time and area of interest, then climatological profiles for the most appropriate region and season may be used. The accuracy most likely will degrade, but useful gradient information may be possible.

Satellite estimates of PW may be obtained through techniques developed by a number of investigators using, for example, transmittance ratios (total through entire atmosphere). Split window radiances from the Visible Infrared Spin Scan Radiometer (VISSR) Atmospheric Sounder (VAS) carried on geostationary operational environmental satellites (GOES) were used by Chesters et al. (1983, 1987), while Jedlovic (1989) and Kleepsies and McMillin (1990) developed methods that used data from both the VAS and the Advanced Very High Resolution Radiometer (AVHRR) carried by National Oceanographic and Atmospheric Administration (NOAA) satellites. Jedlovic (1989) derived his method using aircraft data and then applied it to satellite values. Kleepsies and McMillin (1990) reported correlations as high as 0.85 (AVHRR) and 0.92 (VAS) relative to PW from radiosonde data. Ongoing work in this area by some of the above authors and others can be expected to lead to improved absolute accuracies.

2.2 TRANSMITTANCE ALGORITHMS

Actual sounding output is assumed to provide profiles of T (K), h (%), and z (m) at a number of pressure levels. Pressure (p) has units of hPa (= mbar).

Values of h are converted to values of absolute humidity q (g m^{-3}) through the standard equations found in references such as Ludlam (1980). First, vapor pressure (e) in hPa is computed

$$e = 6.108 \exp(17.27(T - 273.16)/(T - 35.86))h/100 \quad . \quad (1)$$

Then e is used in the computation of q by the standard formula

$$q = eh(10^6)/TR_v \quad . \quad (2)$$

Climatological profiles may include values of q , in which case the above equations are not required. From the q profile, PW for each layer (i) in units of g cm^{-2} is computed from

$$(PW)_i = 0.1(z_{i+1} - z_i)(q_{i+1} + q_i)/2 \quad . \quad (3)$$

The layer values of PW are summed to obtain the total PW. The ratio of the satellite measured value of PW to the total PW from the sounding is used to scale the values of q for each pressure level or height.

The resultant profile of q is used with equations of the type found in Kneizys et al. (1980) for the computation of transmittance. First, however, vapor pressure, e (in units of atm), is computed using a variation of eq. (2)

$$e = qTR_v(10^{-6})/P_0 \quad ,$$

where P_0 is standard atmospheric pressure ($= 1013.25$ hPa).

A LOWTRN water vapor parameter (w), the effective water vapor absorber amount per unit path length in $\text{g cm}^{-2} \text{ atm km}^{-1}$ at altitude z , is computed using the following

$$w = 0.1q[e(\exp[6.08(296/T - 1)]) + 0.002(p - e)] \quad . \quad (4)$$

where p is in units of atm. The water vapor attenuation coefficient (C_s) in $\text{g}^{-1} \text{ cm}^2 \text{ atm}^{-1}$, as defined in Kneizys et al. (1980) for a thermal IR wave number (ν) in the 8 to 14 μm wavelength region at a temperature of 296 K, is given by

$$C_s = 4.18 + 5578 \exp(-0.00787\nu) \quad . \quad (5)$$

Finally, the transmittance (t) over a horizontal path length (d_h) for a given thermal IR wave number is computed from a variation of the standard equation

$$t = \exp(-C_s w d_h) \quad (6)$$

This procedure is valid for a narrow wave number band to a useful accuracy. For example, t for the mean wave number of a 20 cm^{-1} band, as used in LOWTRN, provides a reasonable estimate of t for that interval. Transmittance is assumed to be constant or to vary only slowly and fairly smoothly over a 20 cm^{-1} interval. This assumption was supported through computation of t , using intervals of 20, 10, 5, and 1 cm^{-1} for channels 4 and 5 of the AVHRR, that is, $10.3\text{-}11.3$ and $11.5\text{-}12.5 \mu\text{m}$ ($885\text{-}971$ and $800\text{-}870 \text{ cm}^{-1}$). For a horizontal path of 5 km at the 1 km level in the Mid-Latitude Summer Atmosphere, the difference in t did not exceed 0.0002 relative to the value using an interval of 20 cm^{-1} . However, the use of LOWTRN, or this program, to compute monochromatic transmittances (as for a laser) may lead to serious errors (McClatchey, 1972).

The equations for carbon dioxide, ozone, and noncontinuum water vapor were derived from LOWTRN equations for "uniformly mixed gases" such as carbon dioxide, ozone, and water vapor (Kneizys et al., 1980). Transmittance over an interval of 20 cm^{-1} is computed from an equation of the form $t = f(C_n w^* \text{DS})$, where C_n is a wave number dependent absorption coefficient, w^* is an equivalent absorber density, and DS is the atmospheric path. For the parameter w^* ,

$$w^* = w \left[\frac{P(z)}{P_0} \int \frac{T_0}{T(z)} \right]^m, \quad (7)$$

where P_0 and T_0 correspond to standard pressure and temperature (1 atm and 273.16 K). m has values of 0.9, 0.75, and 0.4 for water vapor, carbon dioxide, and ozone, respectively. In LOWTRN the form of the function for t and the parameter m were determined empirically by using laboratory transmittance data and molecular line constants (Kneizys et al., 1980). Curves were computed based on these data and presented in Kneizys et al. (1980) for t (graphed as \log to the base 10 of t), C_n , and absorber concentrations. The curve of $\log_{10} t$ for ozone is different from that for water vapor (noncontinuum) and the uniform mixed gases, but the basic form is similar. The units for the C_n and concentrations differed, but can be converted to "standard" units through the use of relationships given in McClatchey et al. (1972).

The approach for aerosols was based on the technique of Kneizys et al. (1980). In this preliminary report only distributions for land aerosols is considered (rural and urban). Later, Kneizys et al. (1983) improved the distribution for the lowest 2 km over land through the use of routines based on Heaps (1982). More recent updates as noted in Kneizys et al. (1988) should improve matters further, but no documentation currently exists. However, the earlier approach should be sufficiently accurate for the needs of the research described in this paper.

Kneizys et al. (1980) presented aerosol profiles for a variety of situations, including the rural and urban curves, maritime distributions, and curves for after volcanic eruptions. Seasonal and high humidity differences were included. However, for the preliminary effort described herein the author felt that mean curves for the basic profiles for land, rural and urban, would be sufficient. Transmittance was then calculated through an equation of the form $t(\text{aerosol}) = \exp(-\text{extinction coef} * \text{haze scale factor value} * \text{distance})$.

In the program of this paper the several curves were approximated through piecewise linear or power law fits, or a combination of both. Other fits may produce a closer approximation, but the ones chosen gave a sufficiently good fit for the purposes of this initial investigation.

2.3 PRECIPITABLE WATER ADJUSTMENT

PW is calculated from q for layers determined by the sounding levels, and then summed to obtain a total integrated value for the sounding (PW_s). Values of PW may be calculated from satellite imagery (PW_i) by a method such as those developed by Chesters et al. (1983, 1987), Jedlovic (1989), and Kleepsies and McMillin (1990). Each layer value of q (q linearly related to PW) is then multiplied by the ratio PW_i/PW_s . The adjusted layer values of q are used in the computation of t by the method described above. If more than one sounding is close to a particular location, then appropriate mean values for computation of the ratio should be used. However, such a procedure had not been incorporated as of the date of this paper.

3. COMPARISONS AND SIMULATIONS

3.1 COMPARISONS

The approximate method of this paper for computation of thermal IR transmittances was compared with LOWTRAN 7 (PC version) for vertical paths from the surface to 14 km. In particular the spectral intervals covered by channels 4 and 5 of the AVHRR were chosen for the comparison (885-971 and 800-870 cm^{-1}). For this comparison the spectral responses of the actual instrument were not considered (that is, step function response used). For the LOWTRAN runs, a rural aerosol with a 23-km visibility was assumed. Table 1 shows the results of the comparison for a few of the "standard" atmospheres.

TABLE 1. RESULTS FROM TRANSMITTANCE COMPUTATIONS USING LOWTRAN 7 (L) AND THE APPROXIMATE METHOD (A) FOR THE INDICATED ATMOSPHERES AND AVHRR CHANNELS (CH). THE PC VERSION OF LOWTRAN WAS USED.

Atmosphere	Model	Transmittance	
		ch 4	ch 5
Tropical	L	0.516	0.368
	A	0.509	0.363
Mid-Latitude Summer	L	0.641	0.522
	A	0.662	0.541
Subarctic Winter	L	0.870	0.850
	A	0.941	0.927

The comparisons yielded small to moderate differences in t except for the much larger difference (over 0.07) for the Subarctic Winter atmosphere. For this preliminary study the differences were not broken down by individual absorbers. However, results from both LOWTRN and the program of this paper were compared to those from computations using a line-by-line method (GENLN2) as reported by Saunders and Edwards (1989). Table 2 compares values of t computed over a vertical path from 0 to 100 km for the U.S. Standard Atmosphere with an urban aerosol by the approximation program of this paper, the PC version of LOWTRN, and the GENLN2 line-by-line program. The GENLN2 values are listed as presented in Saunders and Edwards, that is, rounded to the nearest 0.01. As noted above, the calculations of this paper did not account for sensor response as did those for the GENLN2. However, sample computations with the U.S. Standard Atmosphere suggested that leaving out the response function (that is, constant response across the interval) only led to errors in the approximate and LOWTRN results that were about 0.002 too high and 0.005 too low in channels 4 and 5, respectively. Nevertheless, the closeness of the approximate method and GENLN2 results, with the possible "errors" taken into account, may be fortuitous. However, the method apparently can produce useful results for a cloud free line of sight.

TABLE 2. RESULTS FROM TRANSMITTANCE COMPUTATIONS USING GENLN2 (G) AS PRESENTED BY SAUNDERS AND EDWARDS (1989), LOWTRAN 7 (L) AND THE APPROXIMATE METHOD (A), FOR THE 1962 U.S. STANDARD ATMOSPHERE.

Model	Transmittance	
	ch 4	ch 5
G	0.85	0.80
L	0.792	0.737
A	0.851	0.792

Neither LOWTRN nor the approximate method produced values equal to the GENLN2 results, but the approximation values were closer. A comparison of the results shown in table 1 with those derived from values in Saunders and Edwards (1989) suggested that the approximation values were closer to the GENLN2 output (especially for the subarctic winter case), except for the tropical atmosphere. In all cases the line-by-line calculations led to higher values of t than either of the lower resolution programs. However, different line-by-line models may not yield the same values. Saunders and Edwards (1989) noted that Chedin et al. (1988) reported that for nadir paths in the 15 μm region various transmittance models agree to within 2 percent in t .

3.2 SIMULATIONS

A variety of simulations was run with the approximation program to obtain an idea of the likely errors in t that would be associated with typical errors in PW from satellite data. Chesters et al. (1983) reported an overall rms error in total PW computed from VAS data of about $\pm 1.0 \text{ g cm}^{-2}$ over a range of PW values from 1.7 to 5.5 g cm^{-2} . In a later paper by Chesters et al. (1987) the error was reduced to $\pm 0.6 \text{ g cm}^{-2}$. Kleepsies and McMillin (1990) found a

standard difference of around 0.44 g cm^{-2} when their technique was applied to AVHRR data and 0.39 g cm^{-2} for VAS data. For all of the above methods, single comparisons with individual radiosondes gave differences of up to around 2 or 3 g cm^{-2} . For this paper t values were calculated for the Tropical and Mid-Latitude Summer atmospheres where the total PW was changed by ± 0.5 and $\pm 1.0 \text{ g cm}^{-2}$. The results of those computations for the Mid-Latitude Summer are shown in table 3. Figure 1 shows the variation of t for horizontal paths of 3 km at each level up to 6 km for the same model atmosphere with a PW variation of $\pm 0.5 \text{ g cm}^{-2}$. As indicated in the figure, the differences in horizontal t at lower levels can be significant for the given uncertainty in PW.

TABLE 3. TRANSMITTANCES COMPUTED WITH THE APPROXIMATE METHOD USING THE MID-LATITUDE SUMMER ATMOSPHERE. PW IN g cm^{-2} WAS VARIED BY ± 0.5 AND $\pm 1.0 \text{ g cm}^{-2}$ RELATIVE TO THE NOMINAL MID-LATITUDE SUMMER VALUE OF 2.977 g cm^{-2} (TOTAL VALUE FROM 0 TO 14 km).

PW	Transmittance	
	ch 4	ch 5
1.977	0.796	0.718
2.477	0.732	0.631
2.977	0.663	0.545
3.477	0.592	0.458
3.977	0.520	0.377

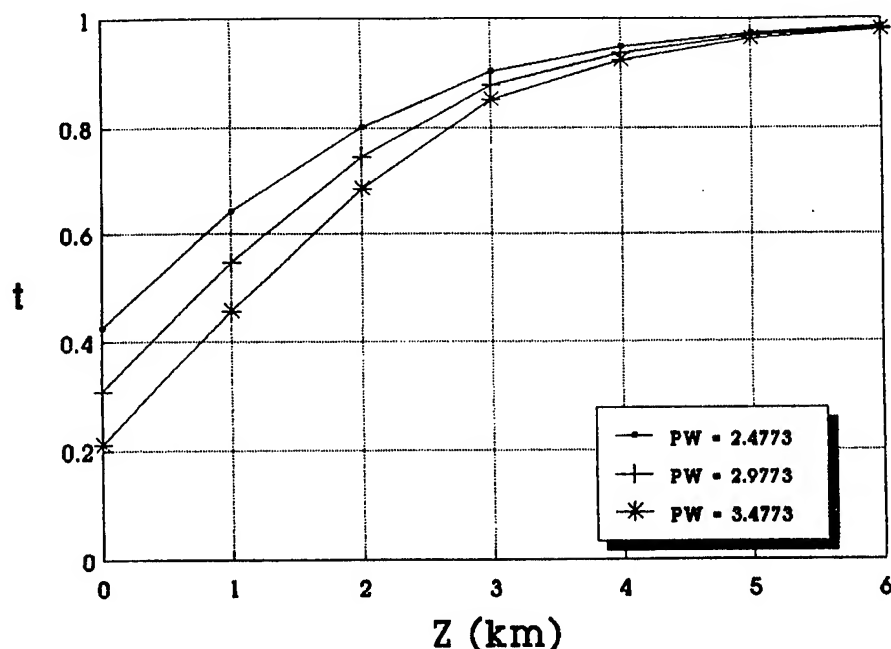


Figure 1. Transmittance (t) values computed using the approximate method for 3 km horizontal paths at the indicated heights (Z) for the listed values of PW in g cm^{-2} .

4. CONCLUSION

An initial version of a technique was developed for estimating transmittance in the thermal IR in the troposphere by using satellite-derived values of PW along with profile data that are not too distant in space or time. The computer model was written in the "C" computer language and easily runs on an 80286 based computer (with math coprocessor). Furthermore, Chesters et al. (1983) noted that relative accuracies in PW are very good relative to absolute accuracies. Consequently, adjustment of a coincident satellite-derived value of PW to that extracted from the profile data may allow a useful description of the surrounding moisture field and, therefore, better estimates.

The apparent accuracy of the approximate method for computing t seems reasonably useful for many cloud free atmospheres, although further refinement would be worthwhile. However, the primary source of error appears to be the quality of the satellite estimates of PW. Therefore, further work will concentrate mostly on improving the technique for estimating PW from satellite imagery.

REFERENCES

- Chedin, A., H. Fischer, K. Kunzi, D. Spankuch, and N. A. Scott, 1988: Report on the ITRA Campaign and Workshop. University of Maryland, College Park, MD, 12-14 March 1986.
- Chesters, D., W. D. Robinson, and L. W. Uccellini, 1987: Optimized Retrievals of Precipitable Water from the VAS "Split Window." J. Clim. Appl. Meteorol., 1059-1066.
- Chesters, D., L. W. Uccellini, and W. D. Robinson, 1983: Low-Level Water Vapor Fields from the VISSR Atmospheric Sounder (VAS) "Split Window" Channels. J. Clim. Appl. Meteorol., 725-743.
- Cogan, J., 1990: A Method for Obtaining Remote Area Meteorological Soundings in Near Real Time. Preprints of the Fifth Conference on Satellite Meteorology and Oceanography, London, England, published by the American Meteorological Society, Boston, MA, 98-103.
- Heaps, M. G., 1982: A Vertical Structure Algorithm for Low Visibility/Low Stratus Conditions. ASL-TR-0111, U.S. Army Atmospheric Sciences Laboratory, White Sands Missile Range, NM, 38 pp.
- Jedlovec, G. J., 1990: Precipitable Water Estimation from High Resolution Split Window Radiance Measurements. J. Appl. Meteorol., 863-877.
- Kneizys, F. X., E. P. Shettle, L. W. Abreu, J. T. Chetwynd, G. P. Anderson, W. O. Gallery, J. E. A. Selby, and S. A. Clough, 1988: Users Guide to LOWTRAN 7. AFGL-TR-88-0177, Air Force Geophysics Laboratory, Hanscom AFB, MA, 137 pp.
- Kneizys, F. X., E. P. Shettle, W. O. Gallery, J. T. Chetwynd, L. W. Abreu, J. E. A. Selby, S. A. Clough, and R. W. Fenn, 1983: Atmospheric Transmittance/Radiance: Computer Code LOWTRAN 5. AFGL-TR-83-0187, Air Force Geophysics Laboratory, Hanscom AFB, MA, 200 pp.

- Kneizys, F. X., E. P. Shettle, W. O. Gallery, J. T. Chetwynd, L. W. Abreu, J. E. A. Selby, R. W. Fenn, and R. A. McClatchey, 1980: Atmospheric Transmittance/Radiance: Computer Code LOWTRAN 5. AFGL-TR-80-0067, Air Force Geophysics Laboratory, Hanscom AFB, MA, 233 pp.
- Kleespies, T. J., and L. M. McMillin, 1989: Retrieval of Precipitable Water from Observations in the Split Window over Varying Surface Temperatures. J. Appl. Meteorol., 851-862.
- Ludlam, F. H., 1980: Clouds and Storms: The Behavior and Effect of Water in the Atmosphere. The Pennsylvania State University Press, University Park, PA, 468 pp.
- McClatchey, R. A., R. W. Fenn, J. E. A. Selby, F. E. Volz, and J. S. Garing, 1972: Optical [sic] Properties of the Atmosphere (Third Edition). AFCRL-72-0497, Air Force Cambridge Research Laboratories, L. G. Hanscom Field, Bedford, MA, 108 pp.
- Saunders, R. W., and D. P. Edwards, 1989: Atmospheric Transmittances for the AVHRR Channels. Appl. Opt., 4154-4160.

GROUND TRUTH FACILITIES AT THE U.S. ARMY ATMOSPHERIC SCIENCES LABORATORY
FOR SATELLITE ENVIRONMENTAL SENSORS

James Cogan, Richard Szymber, and Edward Measure
U.S. Army Atmospheric Sciences Laboratory
White Sands Missile Range, New Mexico 88002-5501, USA

ABSTRACT

The Atmospheric Sciences Laboratory (ASL) has the facilities and equipment for a proposed comprehensive facility for calibrating and evaluating satellite environmental sensors. The component facilities and equipment are located at White Sands Missile Range (WSMR), New Mexico, and are either operated by ASL or are available to ASL through cooperative agreements with relevant organizations at WSMR. The facilities include those for conventional measurements, such as radiosondes and meteorological towers, plus, for example, a rocketsonde facility and a Doppler weather radar. A set of radar profilers includes 50, 404, and 924 MHz units for wind and turbulence, each with its own radio acoustic sounding system for virtual temperature profiles. A variety of sodars, a 2.9 GHz sounder, and a passive, ground-based, microwave profiler can provide measurements of, for example, wind and temperature in the lower troposphere. Satellite data may be obtained through a small terminal that can process high-resolution imagery and sounding data from Defense Meteorological Satellite Program and National Oceanic and Atmospheric Administration polar orbiting satellites. Geostationary satellite data may be obtained through an on-site meteorological interactive data display system.

1. INTRODUCTION

The U.S. Army Atmospheric Sciences Laboratory (ASL) has the facilities and equipment for a comprehensive facility for calibrating and evaluating satellite environmental sensors, especially those of the National Aeronautics and Space Administration (NASA) Earth Observing System (EOS). The component facilities and equipment are located at White Sands Missile Range (WSMR), New Mexico, and are either operated by ASL or are available through cooperative agreements with relevant organizations at WSMR. The facilities include those for conventional measurements, such as radiosondes, automated surface stations, and meteorological towers, plus, for example, a rocketsonde facility, a lightning location detection network, and a Doppler weather radar. A set of radar profilers includes 50, 404, 924, and 2900 MHz units for wind and turbulence, each with its own radio acoustic sounding system (RASS) for virtual temperature profiles. A variety of sodars (for example, a minisodar and a phased array Doppler sodar) and a passive, ground-based, microwave profiler can provide measurements that include wind velocity, temperature, and integrated moisture in the lower

troposphere. Satellite data may be obtained through a small terminal that is capable of receiving and processing the complete high-resolution data streams (imagery and soundings) from National Oceanic and Atmospheric Administration (NOAA) and Defense Meteorological Satellite Program (DMSP) polar orbiting satellites. Geostationary satellite data may be obtained through an on-site meteorological interactive data display system (MIDDS). In the near future most of the ground-based data will be available on a data base at ASL through the use of a common data communication system.

2. FACILITY OVERVIEW

A detailed description of the wide range of facilities and equipment that may be used separately or as part of a coordinated system is beyond the scope of this paper. However, we can give a brief qualitative indication of what is available for the proposed comprehensive facility and the application of the various component systems. Table 1 lists most of the systems and instruments at ASL and WSMR, including fixed site facilities such as the only Army rocket-sonde launch facility and the large 50 MHz profiler, and transportable systems that include the mobile atmospheric spectrometer and laser Doppler velocimeter vans. As suggested by table 1, there is a capability for measurement of a large number of atmospheric variables; in many cases the same variable may be measured in more than one way (for example, temperature by the RASS, radio-sonde, and microwave radiometric sounder). Also the weather station at WSMR is staffed full time to provide operational weather support.

3. UNIVERSITY CONNECTIONS

The overall concept of a comprehensive ground truth facility includes expertise in the appropriate disciplines. Scientists and engineers of the University of Arizona (UA), Tucson, Arizona, can provide additional expertise as needed in the areas of data analysis and experiment design. Researchers from the UA have a long history in the area of satellite instrumentation and analysis of the resultant data. Furthermore, they are presently involved in EOS programs. Personnel from other nearby academic and related facilities can be called upon as required to assist ASL scientists and engineers. Those other institutions are New Mexico State University (NMSU) and the Physical Science Laboratory (PSL) located in Las Cruces, New Mexico, and the University of Texas at El Paso (UTEP) located in El Paso, Texas. The addition of the expertise from UA and the other institutions could make the proposed comprehensive facility a center of excellence in the field of calibration and validation of satellite environmental sensors.

4. POTENTIAL USERS

The primary potential users are NASA, the National Environmental Satellite Data Information Service (NESDIS) of NOAA, and the Space Systems Division (SSD) of the U.S. Air Force (USAF). Some of the relevant potential satellite instruments that could be evaluated at ASL/WSMR include the DMSP special sensor microwave-water vapor sounder (SSM/T-2), special sensor microwave imager sounder (SSMIS), and multispectral operational linescan system (MOLS); the future geostationary operational environmental satellite (GOES-Next) imager and sounder; and NASA mission to planet earth - EOS instruments. Table 2 lists

some of the EOS sensors that potentially could be calibrated and validated by using systems and instruments of the proposed comprehensive facility. A description of the listed EOS sensors may be found in NASA (1991). Heacock (1985) provides information on sensors carried on NOAA and DMSP polar orbiting satellites, and Bradley (1988) and McKenzie and Komajda (1988, 1987) present information on GOES sensors.

Table 3 presents a quick overview of the applicability of the ASL/WSMR systems and instruments listed in table 1 to the EOS sensors listed in table 2. For brevity, each item is indicated by the appropriate number (table 1) or letter (table 2). As shown by table 3, many of the satellite sensors could benefit from several systems or instruments. Although 4 of the 30 ASL/WSMR systems listed are not shown as providing direct support for 1 or more of the EOS instruments, they still may provide useful information for calibration and validation.

5. CONCLUSION

ASL has the facilities and equipment for a comprehensive "ground truth" facility at WSMR for calibrating and evaluating environmental satellite sensors. A large array of conventional and nonconventional atmospheric sensors and systems lie within the 4000-square-mile area of WSMR, much of it already operational. Some of these systems are mobile or portable, thereby permitting certain ground truth data to be obtained "off site." The scientists and engineers at ASL, UA, and the other institutions will provide a large and varied pool of appropriate skills. Since much of the overall facility already is in place, the start-up and fixed costs would be much less than if new facilities had to be constructed from scratch at other sites. The economies from avoiding redundant systems will significantly reduce operating costs. Consequently, the proposed ground truth facility would be unique in the combination of measurement systems, data analysis facilities, and expertise of personnel.

TABLE 1. SYSTEMS AND INSTRUMENTS AVAILABLE AT ASL OR WSMR

-
1. Atmospheric Profiling Research and Development Facility
 2. Surface Automated Meteorological System Stations and Network
 3. Integrated Upper Air System Radiosonde Stations and Network
 4. Doppler Weather Surveillance Radar (DWSR-88S)
 5. Lightning Detection and Location Network
 6. 500-foot and 100-foot Meteorological Tower Network
 7. LOKI Rocketsonde Launch Complex
 8. Phillips Laboratory Balloon Launch Facility
 9. Automatic Data Acquisition System Radiosonde Units
 10. Meteorological Tower Systems
 11. Tethered Balloon Systems
 12. Gas and Aerosol Sensing System I and II
 13. Transportable Atmospheric Characterization System and Mobile Meteorological Team
 14. Mobile Atmospheric Spectrometer Van
 15. Atmospheric Turbulence Measurement and Observation System
 16. Radiometric Atmospheric Profiler
 17. High Energy Laser Meteorological System
 18. Aerosol Characterization System
 19. Mobile Acoustic - Boundary Layer Sounding System
 20. Portable Atmospheric Measuring System
 21. High Speed Data Acquisition System
 22. Rent-A-MET Mobile Surface Automated Meteorological System
 23. Soil Moisture Sensors
 24. Present Weather Sensors
 25. Laser Doppler Velocimeter Mobile Laboratory
 26. Ultraviolet Lidar System
 27. Visioceilometers, Atmospheric Obscurant Lidars, and Laser Ceilometers
 28. SeaSpace/Terascan DMSP-RTD and NOAA-HRPT Transportable Terminal
 29. METSATPACK APT/WEFAX Transportable Terminals
-

TABLE 2. SATELLITE SENSORS THAT COULD USE ONE OR MORE OF THE SYSTEMS AND INSTRUMENTS IN TABLE 1

NASA EARTH OBSERVING SYSTEM INSTRUMENTS

- A. Atmospheric Infrared Sounder (AIRS)
- B. Advanced Microwave Sounding Unit-A (AMSU-A)
- C. Advanced Spaceborne Thermal Emission and Reflection Radiometer (ASTER)
- D. Clouds and Earth's Radiant Energy System (CERES)
- E. High-Resolution Dynamics Limb Sounder (HIRDLS)
- F. Laser Atmospheric Wind Sounder (LAWS)
- G. Lightning Imaging Sensor (LIS)
- H. Microwave Humidity Sounder (MHS)
- I. Multifrequency Imaging Microwave Radiometer (MIMR)
- J. Multi-Angle Imaging Spectro-Radiometer (MISR)
- K. Moderate-Resolution Imaging Spectrometer-Nadir (MODIS-N)
- L. Stratospheric Aerosol Gas Experiment III (SAGE III)
- M. Tropospheric Emission Spectrometer (TES)

TABLE 3. RELATION OF SATELLITE SENSORS TO GROUND TRUTH SYSTEMS AND INSTRUMENTS. NUMBERS AND LETTERS INDICATE ITEMS IN TABLE 1 AND 2 RESPECTIVELY

ASL/WSMR AND NASA-EOS INSTRUMENTS CAPABILITIES CROSS-CORRELATION MATRIX

INSTRUMENT	A	B	C	D	E	F	G	H	I	J	K	L	M
1.
2.
3.
4.					
5.							.						
6.
7.	
8.
9.
10.
11.
12.
13.
14.				
15.				
16.
17.
18.					
19.
20.
21.
22.		
23.									.		.		
24.									.				
25.						.							
26.						
27.	
28.	
29.													

REFERENCES

- Bradley, C., Ed., 1988: The GOES I-M System Functional Description, NOAA Technical Report NESDIS 40, NOAA, National Environmental Satellite, Data, and Information Service, Washington, DC, 126 pp.
- Heacock, E. L., Ed., 1985: ENVIROSAT-2000 Report, Comparison of the Defense Meteorological Satellite Program (DMSP) and the NOAA Polar-orbiting Operational Environmental Satellite (POES) Program, NOAA, National Environmental Satellite, Data, and Information Service, Washington, DC, 413 pp.
- McKenzie, K., and R. J. Komajda, 1988: The GVARs Users Compendium, Volume 1, NOAA Technical Memorandum NESDIS 21, NOAA, National Environmental Satellite, Data, and Information Service, Washington, DC, 194 pp.
- McKenzie, K., and R. J. Komajda, 1987: An Introduction to the GOES I-M Imager and Sounder Instruments and the GVAR Retransmission Format, NOAA Technical Report NESDIS 33, NOAA, National Environmental Satellite, Data, and Information Service, Washington, DC, 54 pp.
- NASA, 1991, May 1991 EOS Reference Handbook, Goddard Space Flight Center, MD, 147 pp.

VISIOCEILOMETER: A PROTOTYPE SYSTEM TO MAP ATMOSPHERIC AEROSOLS AND DETERMINE SLANT RANGE VISIBILITY

R. G. Steinhoff, A. E. Wade, R. G. Trujillo
U.S. Army Laboratory Command
Atmospheric Sciences Laboratory
White Sands Missile Range, New Mexico 88002-5501

ABSTRACT

The VISIOCEILOMETER (VISIO) is an eye-safe, handheld, erbium glass laser range finder. It is augmented with an internal signal processing unit (SPU) as well as an external personal computer that can be utilized in real time recording, displaying, post-processing, and analyzing of collected data. The system can be employed to determine background visibility in an homogeneous environment and may be able to determine slant range visibilities in non-homogeneous environments. The system may be used to map the height of a cloud base, a cloud's density and thickness, as well as to detect the presence of multiple cloud layers. Additional observations made with the VISIO include snow under clouds which does not extend to the surface and changes in background terrain surface reflectivity because of changes in surface wetness. Within limits of signal attenuation and path clutter, aerosols can remotely be mapped over a range of 80 meters to 9.6 kilometers along one line of sight.

1. INTRODUCTION

A continuing goal of lidar research is to devise an inversion method whereby atmospheric parameters such as attenuation and backscatter coefficients in an **inhomogeneous** atmospheric can be quickly and accurately deduced from the return signal of a monostatic, single wave length lidar system. Some of the difficulties which hinder a simple solution are caused by

limitations in lidar performance and associated data processing, while others follow from constraints peculiar to the inversion process. This paper begins by reviewing the classic lidar equation (1), which forms the basis for volumetric backscatter measurements. Second, the Beer's and Lambert's laws are reviewed since they form the basis of the lidar equation and facilitate the separation of the backscatter measurements of an aerosol into homogeneous and inhomogeneous components. Third, the author suggests refinements of terminology in equation (1) and an alternate method of solving its components. Fourth, several typical aerosol maps produced from visio data are examined, and comparisons are made of single shot returns at various visibilities in a freshwater, maritime environment.

2. THE MONOSTATIC LIDAR EQUATION

For a monostatic, single wavelength, pulsed lidar, the assumed basic governing form is the single-scattering lidar equation:

$$P(r) = P_0 \frac{c\tau}{2} \frac{A \beta(r)}{r^2} e^{-2 \int_0^r \sigma(r') dr'} \quad (1)$$

In this equation $P(r)$ is the instantaneous received power at time t ; P_0 the transmitted power at time t_0 ; $c\tau/2$ is the folded laser pulse length, where c is the velocity of light, τ is the pulse duration, A is the effective system receiver area, $r = c(t - t_0)/2$ is the range; $\beta(r)$ and $\sigma(r)$ are respectively the volume backscatter and the attenuation coefficients of the atmosphere; the exponential function is the total path integrated extinction $\exp[-2 \Delta r \sum_{r=1}^n \sigma(r)]$. Evans¹ refers to A/r^2 as "geometric attenuation". Evans also adds a term $F(r)$, referred to as a system function which includes factors such as system sensitivity and geometric crossover of the receiver and laser beam, to obtain the lidar equation:

$$P(r) = P_0 \frac{c\tau}{2} \frac{F(r) \beta(r)}{r^2} A e^{-2 \int_0^r \sigma(r') dr'} \quad (2)$$

Equations (1) and (2) refer to idealized systems. Working systems in contrast tend to be non-ideal, and therefore redefine $F(r)$ as the system power response function:

$$F(P(r)) = P_0 \frac{c\tau}{2} \beta(r) \frac{A}{r^2} e^{-2 \int_0^r \sigma(r') dr'} \quad (3)$$

which represents the power which is actually logged. Note that $P()$ is a function of range while $F()$ is a function of received power only. The exponential portion of the function representing total two way path extinction may be expressed as

$$\exp \left[-2\Delta r \sum_{r=1}^n \sigma(r) \right]. \quad (4)$$

To separate the atmosphere into its homogeneous and inhomogeneous components, let

$$\sigma(r) = \sigma_1(r) + \sigma_2(r) \quad (5)$$

Accounting for attenuation (i.e. extinction) by the contribution (i.e. concentration) of each aerosol type means that the backscatter must likewise be accounted for by species concentration. Let a species represent any ensemble of particles such that the ratio $\sigma_i : \beta_i$ is a constant. Therefore:

$$\beta(r) = \beta_1(r) + \beta_2(r) \quad (6)$$

Although σ_1 , the homogeneous component, is generally assumed to be a constant, it need not always be the case. One such example is the vertical structure profile of a "standard" atmosphere. The only restrictions of this function are $\sigma_1 > 0$ and σ_1 is integrable. It will be shown later in this paper that for a system having an effective sensitivity range of 80 dB, operating in an environment where both the extinction and backscatter are primarily caused by water vapor (including fog), that β_1 becomes negligible beyond about half a kilometer. In homogeneous regions $\sigma_2 = 0$. Inhomogeneous regions, such as clouds or obscurant smoke plumes, are accounted for with $\sigma_2 > 0$. It is assumed: 1) that σ_2 is locally homogeneous, and 2) that σ_1 and σ_2 are in dynamic equilibrium (that is, their partial pressures do not significantly alter each other).

As noted by Klett² small errors in the determination of σ_0 cause large perturbations in σ . This leads to the rationale for separating σ into $\sigma_1 + \sigma_2$. The total path attenuation to calculate σ_1 can be very accurately measured using a co-linear transmissometer. To ensure that the transmission measurements were both co-linear and at the same wavelength, sets of calibrated laser reflectors were placed at a distance of 0.7 and 1.7 kilometers respectively. Each set of reflectors consist of three corner reflectors¹ separated in range by one folded laser

¹ The corner reflectors (or corner cubes) are "Reflector Aiming Posts Model M1, M2, ..., Federal Stock No 665001x909599, 600, ... The reflectors are guyed atop 1.25 inch diameter antenna mast sections at a height adequate to avoid signal backscatter from intervening ground clutter. The guy wires and masts are

pulse length. This was done to insure both temporal and spatial stability of the measurements. Located just beyond the set of reflectors at 1.7k was a third set calibrated such that the return from the two sets was separated by about 70 dB. Thus total extinction along the 1.7 km path was measured on a dynamic range of approximately 140 dB. Measurements were made over a four week period in northern Michigan during October 1989. Measurements were made from predawn to postdusk, in clear weather, fog, rain, and snow conditions.

For a small fraction of these data, there are concurrent measurements of point—visibility, temperature, pressure, relative humidity, wind speed, and rain rate. The meteorological data were obtained from sensor packages located near the target line of sight at 0.2, 1.0, and 1.5 km. In addition, particle size distribution² and relative transmittance³ measurements were made at the 1.0 and 1.5 km sites. Note that no artificial obscurant were measured during this test.

The visio and met data are currently being combined to produce tables of 1) backscatter to extinction ratios (extinction is at 1.54 micron rather than in the visible band), and 2) extinction to visibility ratios under the various meteorological conditions (the meaning of met conditions is expanded to include met categories, aerosol types, and EOSAEL LOWTRAN like atmospheric profiles). Knowing the characteristics of the background aerosol (α_1, β_1) and the nature of obscurant plumes (α_2, β_2), two goals of the visio are to compute point to point visibility and obscurant density and depth. Obscurant are not limited to aerosol plumes, but may be any topographic features or natural occurring reflectors. Topographic targets can be employed to provide a convenient single—ended transmissometer system configuration.

painted flat black to minimize their reflectance. The reflectance of each corner cube is adjusted to the desired level by attaching appropriate neutral density filters to the front of each reflector.

² measured in 0.5 micron intervals, with sizes ranging from 0.5 to 40. microns

³ visibility is computed using the Koschmieder relationship from the measured relative transmittance in the visible spectrum for a 5% contrast ratio for the 1.0 and 1.5k sites.

3. The Beer—Lambert Law

Lambert in 1760 postulated that for a fixed path length through a given substance, the ratio of the intensities of the transmitted and incident light is independent of the intensity of incident light. This empirical law has been found experimentally to be accurately followed by practically all substances under extreme ranges of conditions.⁴ Lambert also pointed out that layers of the same thickness of the same substance **absorb** the same fraction of the incident light. If the mathematical statement of Lambert's laws is integrated, the law for the dependence of the absorption ratio on the path length can be derived:

$$P/P_0 = e^{-\sigma cl} \quad (7)$$

where P is the intensity of the transmitted light, P_0 is the intensity of the incident light, cl is the concentration—length of the substance and σ is the constant characteristic of the substance.

For most solutions (in this context, solution is synonymous for atmosphere and aerosol), the constant cl is approximately proportional to the mass of the solute in unit volume of solution; this is known as *Beer's law*. Thus, for practical purposes, the absorptivity of a substance, as defined below, is a constant with respect to changes in concentration and/or length of the light path, with the result that concentration may be determined *photometrically*.

Terminology—There is some nonuniformity of terminology; the following definitions and symbols are used herein:

Transmittance: P/P_0 . The ratio of the transmitted light intensity to the incident light intensity. Symbol **T**.

Absorbance: $-\log T$. The negative logarithm of the transmittance. Symbol: **A**.

Concentration: Concentrations are expressed in grams per cubic meter of solution. Symbol: **c**.

Absorptivity: The absorbance of a solution containing 1 gram per cubic meter contained in a cell having an absorption path length of 1 kilometer. Symbol: σ .

Lambert's law of absorption.³ Each layer of equal thickness absorbs an equal fraction of the light which traverses it.

⁴ Well understood from the point of Analytic Chemistry and Quantitative Analysis, in the authors view. The notation in this section reflects that bent. Whereas, the notation reflected in the prior sections is a reflection of Klett's style. The notation in the following sections reflects the style of the LIDAR documentation.

4. ANOTHER LOOK AT THE LIDAR EQUATION

Strictly speaking the r in the terms $P(r)$ and $\beta(r)$ are distinct from the r in as used in the exponential and r^2 terms. The former have discrete values with an interval equal to the folded pulse length, whereas the latter are determined by $t - t_0$. Let:

$$r_i = r / c\tau \quad (8)$$

Substituting Equations (4) and (8) into Equation (1) as appropriate produces:

$$P(r_n) = P_0 \frac{c\tau}{2} \frac{A \beta(r_n)}{r_n^2} \exp[-2\Delta r \sum_{i=0}^{n-1} \sigma(r_i)] \quad (9)$$

Recall that by definition $\sigma(r_j)/\beta(r_j)$ is a constant, and the unknown sigmas can be calculated by contrast with known values.

$$\begin{aligned} \frac{P_\theta(r_n)}{P(r_n)} &= \frac{P_0 \frac{c\tau}{2} \frac{A \beta_\theta(r_n)}{r^2} \exp[-2\Delta r \sum_{i=0}^{n-1} \sigma_\theta(r_i)]}{P_0 \frac{c\tau}{2} \frac{A \beta(r_n)}{r^2} \exp[-2\Delta r \sum_{i=0}^{n-1} \sigma(r_i)]} \\ &= \frac{\beta_\theta(r_n)}{\beta(r_n)} \\ &= \frac{\sigma(r_n)}{\sigma_\theta(r_n)} \\ \sigma(r_n) &= \frac{P_\theta(r_n) \sigma_\theta(r_n)}{P(r_n)} \text{ where } P, \beta, \text{ and } \sigma_\theta \text{ are known} \end{aligned} \quad (10)$$

By having a knowledge of the total path extinction, the weight of each $\sigma(r_i)$ can be adjusted such that their sum is reasonably close to that total. The intent of this exercise is to provide a means of converting the backscatter data β_i from a pulsed monostatic lidar into extinction values σ_i^* , where σ^* relates extinction to aerosol concentration at a given range.

An aid in determining total extinction to some point in the path can be accomplished by determining r_i where $P(r_i)$ first reaches the threshold of detection. This is done by range normalizing the data, $P_{rn}(r_i) = P(r_i) * r^{**2}$. At this range the aerosol backscatter just equals the total range extinction. Beyond the range of the detection threshold P_{rn} increases as a function of the range squared; that is the threshold occurs at the minima of this

function. Dividing each $P_{rn}(r_i)$ by the total path attenuation to that point creates an index value of the aerosol density at the respective point. When this calculation is performed for σ_1 and σ_2 instead of σ , then a density index is obtained for both the homogeneous background (a constant value) and for obscurant plumes. If the mass—extinction functions of the aerosols are known for both the laser wave length and in the visible then point to point visibility can be calculated along the laser line of sight. The mass—extinction functions will generally need to include terms of aerosol type and density, and atmospheric parameters of temperature, pressure, and absolute humidity.

5. Aerosol Mappings

Figures 1 through 4 depict typical single shot lidar returns. These four examples were selected because they are extreme examples of returns from a "near" homogenous background. In all four cases the visibility was determined to be less than 0.2 km using a Present Weather System, Model HSS 403, (PWS) located near the line of site. The path length (X-axis) in these figures is 1 km. The return signal (Y-axis) is logarithmic. Observe that in Figures 1 and 2 the target (located above the "↑") at 0.7 km is not apparent, while in Figures 3 and 4 the targets are not only apparent, but measure similar return signals. Also, observe that if Figures 1 and 2 are overlaid, the lines cross at several points before melting into the noise level.

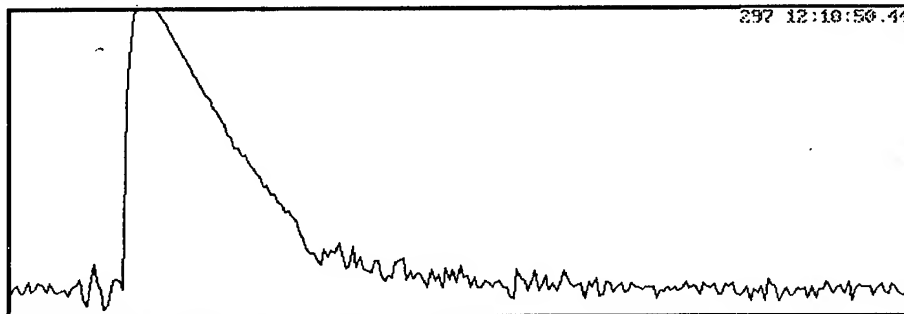


Figure 1 07:10 local time

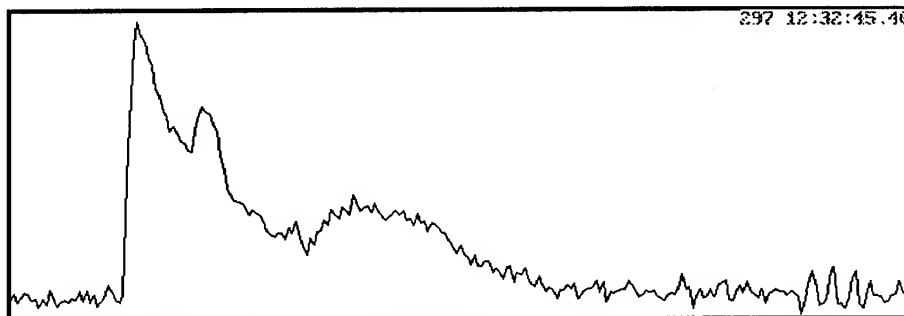


Figure 2 07:32 local time

This also occurs within figures 3 and 4.



Figure 3 07:37 local time

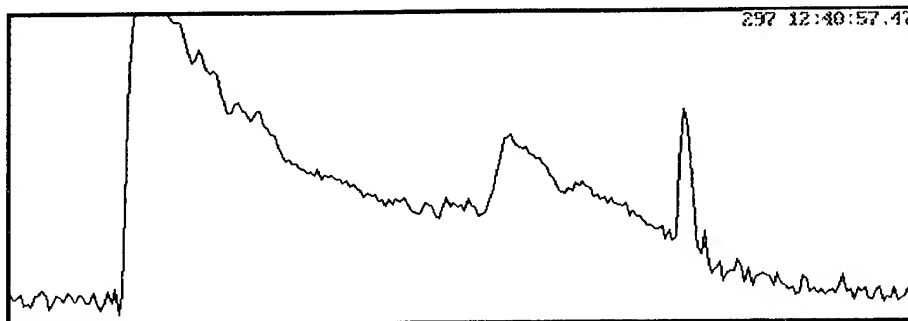


Figure 4 07:41 local time

Figure 1 and Figure 4 are extreme examples of the range where the signal fades into the background. The visibility in these cases is less than 0.2 km. Experience has shown that for cases of higher visibility in this environment that the signal drops into the background between these extremes.

Figure 5 through Figure 11 are typical time—line of sight aerosol mappings. These mappings depict regions where the local density is greater than the background density. In Figure 5 the observer is located inside the fog or cloud. While in Figure 6 to Figure 11 the observer is located outside of the cloud. Figure 5 is a 57 minute (X-axis) cloud map with a range (Y-axis) of 2 km. The PWS measured visibility at 7:35 am is 0.1 km when the target at .7 km is detected. The target at 1.7 km is detected at 7:51 am; the PWS visibility is 0.2 km. At 7:51 am the terrain located at 1.9 km is detected; the PWS measured visibility is

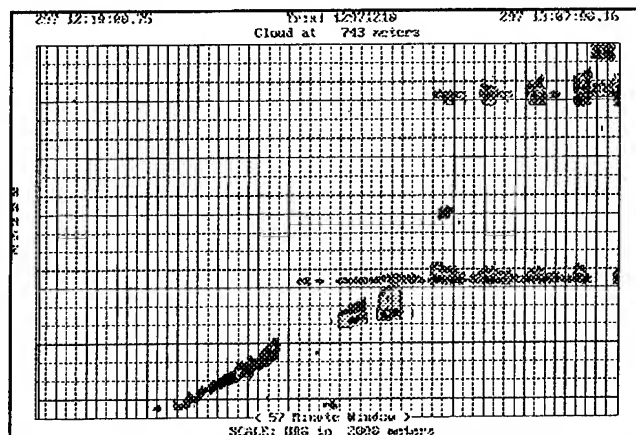


Figure 5 Local time 0710-0807

0.3 km. This may indicate that a VISIO type cloud mapper could be utilized to detect obstacles through fog at ranges well beyond the visible detection ranges.

The following six figures are simply to demonstrate the cloud mapping capability of the VISIO and the MAPPER software. Figure 6 shows a cloud base height at 1425 meters and cloud top at 1525 meters. Extending down from the cloud base to a height of 1000 to 800 meters are returns typical of vertical returns through snow. The frame starts at 6:30 am (sunrise occurred at 6:12 am) and lasts for 40 minutes. Figure 7 shows a cloud base height at 700 meters and cloud top at 100 meters. Extending down from the cloud base to a height of 150 meters are returns typical of vertical returns through snow. Horizontal returns through snow as well as vertical and horizontal returns through rain are generally lost in the system noise. The frame starts at 8:05 am and lasts for 42 minutes. The last 7 minutes of the frame show signal returns from the targets mentioned above.

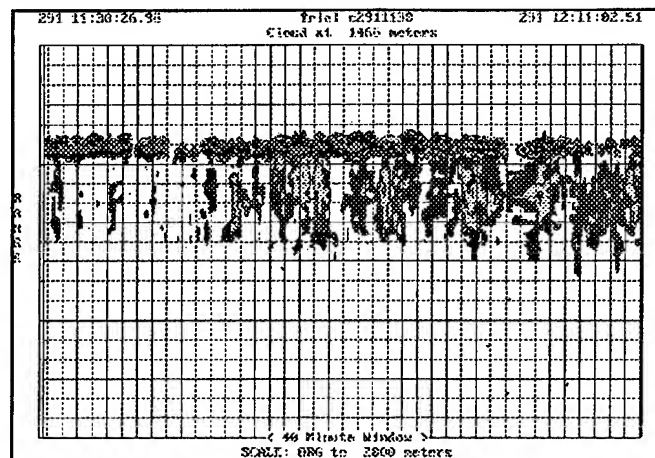


Figure 6 (Range 2000 meters)

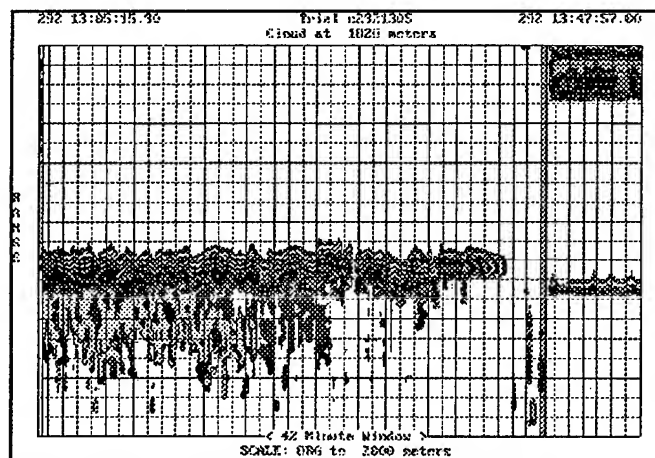


Figure 7 (Range 2000 meters)

Figure 8 and Figure 9 are typical of low lying clouds. The base of these clouds is 50 to several hundred meters from the observer.

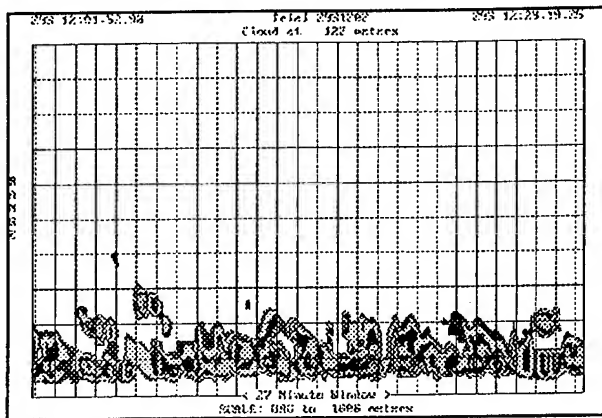


Figure 8 (Range 1000 meters)

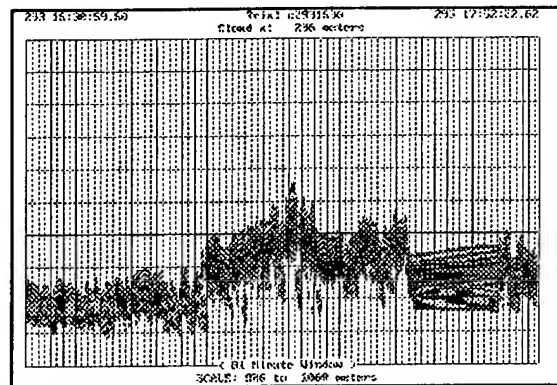


Figure 9 (Range 1000 meters)

Figure 10 and Figure 11 depict clouds located several kilometers from the observer.

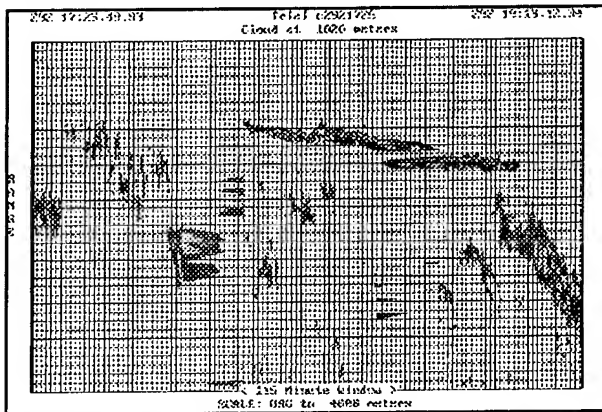


Figure 10 (Range 4000 meters)

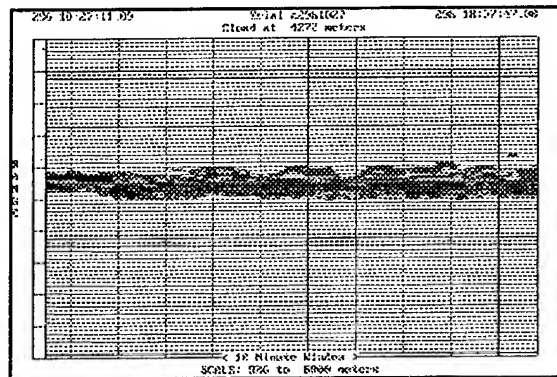


Figure 11 (Range 8000 meters)

6. REFERENCES

1. B.T.N. Evans, "ON THE INVERSION OF THE LIDAR EQUATION" Report, DREV R-4343/84 FILE: 3621B-005, Defence Research Establishment Valcartier, Québec, Canada.
2. James D. Klett, "ON THE ANALYTICAL INVERSION OF LIDAR RETURNS FROM AN INHOMOGENEOUS ATMOSPHERE", Contractor Report ASL-CR-80-0008-3, U.S. Army Atmospheric Sciences Laboratory (ASL), White Sands Missile Range, NM 88002-5501
3. Handbook of Chemistry and Physics, Forty-Eighth Edition, The Chemical Rubber Co., 18901 Cranwood Parkway, Cleveland, Ohio, 44128, pp F-77.

CLOUD MAPPING AND THE DETERMINATION OF AEROSOL DENSITIES ALONG A LINE OF SIGHT

by

**Ralph G Steinhoff
U.S. Army Atmospheric Sciences Laboratory
White Sands Missile Range, New Mexico 88002-5501**

The mapping of natural and artificially induced aerosols or smoke plumes continues to be a goal of lidar research which in the past has only achieved nebulous results in an inhomogeneous atmosphere. The determination of atmospheric parameters such as attenuation and backscatter coefficients in conjunction with determining the structure of such an aerosol using a monostatic, single wave length lidar system is the focus of this paper. Using a lidar to determine atmospheric stability and the structure of the boundary or surface layer in addition to mapping both the height of cloud base and the height cloud top are demonstrated. The ability to measure point visibility or the apparent visibility between to points along a line of site is examined.

(The full text of this paper was unavailable at press time.)

**STATISTICAL INVERSION OF TEMPERATURE PROFILES
FROM MICROWAVE RADIOMETRY MEASUREMENTS
WHEN THERE ARE INSTRUMENT ERRORS**

Dick Larson
Physical Science Laboratory
New Mexico State University
Las Cruces, NM 88003

ABSTRACT

Vertical temperature profiles can be retrieved from measurements of microwave radiation using the statistical technique of multiple linear regression. Balloon-measured temperature profiles are regressed against radiation "measurements." These are computed "measurements," by a radiative transfer model from the Balloon temperature, pressure and relative humidity profiles. Thus, sets of regression coefficients can be generated for any site for which there are archives of balloon sampled vertical profiles.

To derive as much information as possible from the radiometer measurements, they are made at several frequencies and at several angles of the Radiometer's antenna. This means that the regression will have many independent variables. Which is not normally a problem for the multiple regression technique but when all the independent variables are sampled from the same atmosphere at several frequencies and antenna angles then the variables are not truly independent. This situation can produce some very bad predictions of temperature profile.

Fortunately there is a solution to this problem that redeems the choice of the statistical retrieval technique and produces excellent predictions. This solution assumes that an estimate can be made of the instrument errors for each of the independent variables, i.e., the measurements made at each frequency and angle of the Radiometer. The squares of the error estimates are simply added to the diagonal of the covariance matrix (the computed sample variances of each of the independent variables). Then the multiple regression technique proceeds as usual, though with this modified covariance matrix, to produce sets of regression coefficients. These regression coefficients, then, predict excellent vertical temperature profiles from noisy Radiometer measurements.

1. INTRODUCTION

This work was done in support of a group at the U. S. Army Atmospheric Sciences Laboratory charged with remote atmospheric profiling using a Microwave Radiometer. This instrument is ground-based, as opposed to being flown on a satellite. A radiative transfer equation can be formulated which expresses the radiation detectable at the ground in terms of the total absorption contributed by a profile of atmospheric parameters above the Radiometer, e.g., temperature, pressure, relative humidity, cloud liquid water, etc. This equation is well known and, given sufficiently accurate input variables, it can produce the radiation values that a ground-based Radiometer should detect. The problem, for remote sensing, though, is to invert this equation, to find an atmospheric profile that would have produced the amount of radiation measured by the Radiometer. Unfortunately, the inversion problem is ill-posed and the solution is underconstrained. Thus, there are an infinity of solutions, e.g., temperature profiles, that could have produced the measured radiation.

The statistical approach to the remote sensing problem does not attempt to directly invert the radiative transfer equation. Instead, the equation and its problematic inverse is side-stepped. Linear least squares is utilized to establish the desired relationship between radiation detected at the ground and the generating atmospheric profile.

2. BACKGROUND

2.1 STATISTICAL INDEPENDENT AND DEPENDENT VARIABLES

The least squares technique requires a data history of radiation values and the atmospheric profile that produced those values. We've been using balloon-measured profiles, twice a day for about five years, from several sites in the U.S. for the atmospheric profiles. The corresponding values required for the technique are obtained by calculating them from the radiative transfer equation with, as input to the equation, the atmospheric parameters of each balloon profile. The radiation values have been calculated for four frequencies and, for each of those four frequencies, five elevation angles at which this Radiometer's antenna could be pointed. Thus, our least squares technique is a multiple linear regression with, potentially, more than 20 independent variables. We also use the surface temperature, pressure, and relative humidity as independent variables in the multiple regression.

2.2 THEORETICAL (NOISELESS) RADIATION VALUES; PROFILING ACCEPTABLE

We prepared for the arrival of a prototype Microwave Radiometer from Jet Propulsion Laboratory in California by studying the technique. We investigated the effectiveness of a set of regression coefficients formed over one year's history versus another set formed over five years. We investigated the effectiveness of a set of regression coefficients formed over profiles collected at sea level when utilized to infer

atmospheric parameters at a site with a high surface height above sea level, e.g., Denver, Colorado. Through all these studies we used our radiative transfer equation computed radiation "measurements" in place of the measurements that would be made when the Radiometer arrived.

2.3 MEASURED (NOISY) RADIATION VALUES; PROFILING UNACCEPTABLE

With the arrival of the JPL Radiometer we were able to measure the radiation received at the ground at the same time and the same place as a balloon was launched. But when we applied our regression coefficients to see how well we were able to infer a temperature profile from the radiation measurements we saw a very poor profile inference. That the measured values contained instrument error must have been the reason for the poor profiling. To obtain acceptable profiles from the Radiometer's measurements we obviously needed to account for instrument noise.

3. INFERRING AN ATMOSPHERIC PROFILE USING COMPUTED RADIATION "MEASUREMENTS"

Figure 1 shows a temperature profile, for Ft. Greely, Alaska, as measured by a balloon-borne instrument versus the temperature profile inferred statistically. The radiation "measurements" used as predictor variables with the regression coefficients were computed by the radiative transfer equation from the balloon profile; they were not measured by a Radiometer. The multiple regression coefficients utilized were formed over a data history of six January-February periods ('80 - '85) at Fairbanks, Alaska. (Fairbanks is about 100 miles Northwest of Ft. Greely. Fairbanks has an upper air sounding station the profiles from which are archived by the U.S. Air Force.) 12 radiation values computed from each of the profiles and the surface temperature, pressure and relative humidity were the independent variables for the multiple regression, and were the 15 predictor variables for the Ft. Greely temperature profile shown in fig. 1. As you can see, the inferred profile is acceptably close to the balloon-measured profile.

4. INFERRING AN ATMOSPHERIC PROFILE USING RADIOMETER MEASUREMENTS

Figure 2 shows the same Ft. Greely balloon-measured temperature profile as in fig 1. The inferred profile shown on the plot was computed with the same set of regression coefficients as in fig. 1. But the predictor variables were not computed. Instead they were measured by the Radiometer. The Radiometer measurements were taken one minute after launch at the balloon launch site.

5. WHY THE PROFILING FAILURE WHEN USING MEASURED RADIATION VALUES?

5.1 DIFFERENCE BETWEEN CALCULATED AND MEASURED RADIATION VALUES.

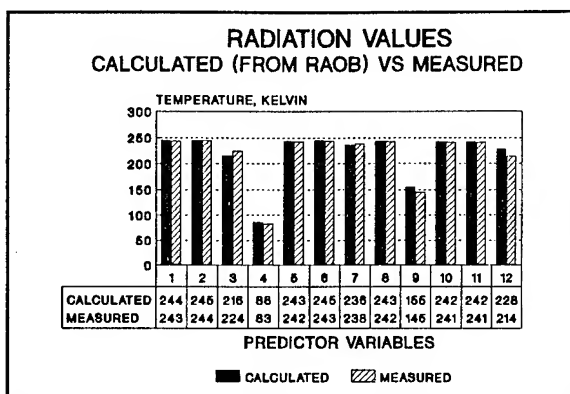


Figure 3. Radiation values computed by a radiative transfer model, with a 1 February '91 profile as the a priori atmospheric profile, versus radiation values measured by a ground-based radiometer.

Figure 3 shows that there is no substantial difference between calculated and measured predictor variables for the 1 February profile. Only the 12 radiance values, not the surface temperature, pressure and relative humidity, are shown on the bar chart. The surface predictor values are not shown because we have been using the same (Radiosonde's) surface values both when we use calculated predictor variables and when we use measured predictor variables. The 12 radiation values shown were either measured or calculated at the frequencies and the antenna pointing angles (90 Degrees means that the Radiometer's antenna was pointing straight up). The Radiometer has these frequency and pointing angle capabilities so, when calculating radiation values from the balloon-measured profile, we provided the radiative transfer model with these same frequency, angle parameters. That there is no substantial difference between the two sets of predictor variables indicates that we can not attribute the profiling failure to hardware error or some catastrophic lack of Radiometer calibration. (Figure 3 does show a general bias, for this 1 February profile, for the Radiometer to measure less radiation than that computed from the radiative transfer model. We have not yet investigated this slight bias.)

Table 1 shows the 20 frequency, angle Radiation measurements of which the Radiometer is capable. The 1 - 12 numbers placed in table 1 correspond to the 1 - 12 predictor variables along the x axis of the bar chart of fig. 3. This subset of 12 was selected because the regions where some of these measurements had most

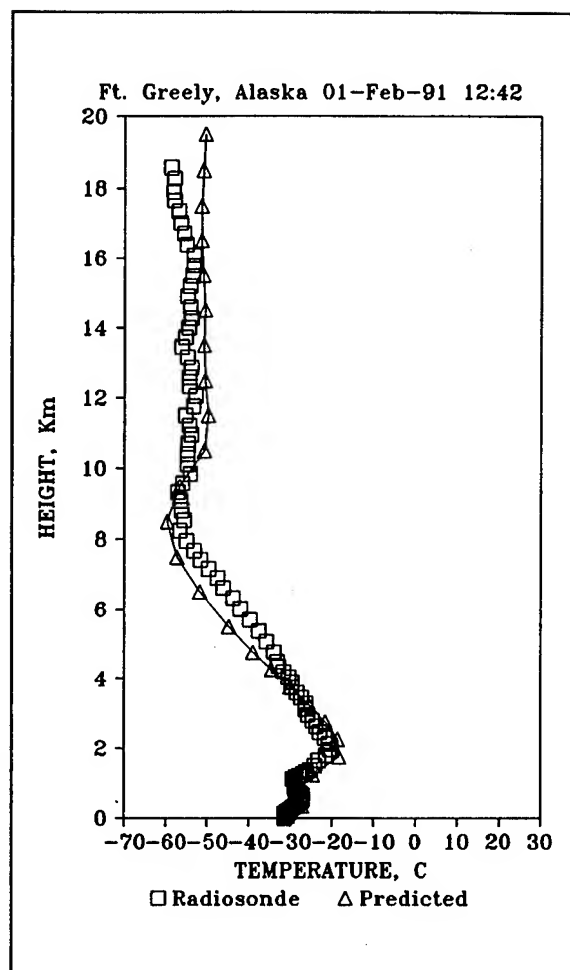


Figure 1. The regression did not account for instrument error. There was no error in the predictor variables; they were computed.

influence would have overlapped the influence of others so that no new information about the atmosphere to be sensed would have been provided, were all 20 measurements utilized in the multiple regression.

5.2 THE REGRESSION IS ILL-CONDITIONED

5.2.1 The independent variables are not truly independent

It must be admitted that the radiation values utilized as predictor variables in the multiple regression are not independent, as is required for proper use of the least squares technique. The four frequencies of this Radiometer all lie in the Oxygen absorption band, generally from 50 to 60 GHz. They differ in that the 57 GHz frequency "sees" only a little way up, while the 51 GHz frequency "sees" higher up in the atmosphere than any of the other channels. Still, as the 51 GHz frequency's radiation is measured at the ground it experiences an integrated contribution from all the atmospheric levels, between the top of the atmosphere and the ground, wherein the other three frequencies are most sensitive.

And that the Radiometer's antenna can be pointed at various elevation angles does gather more information from the atmosphere but, assuming a horizontally stratified atmosphere, elevations other than straight up are still probing the same atmosphere.

5.2.2 Exact solutions are highly sensitive to instrument noise

A regression that does not allow for instrument error in the predictor variables can be called an exact solution. The least squares technique, when no allowance is made for instrument error, requires that the sum of the squares of the difference between the predicted value and the dependent variable be a minimum. This Radiometer application, as are all remote sensing applications where the values to be measured are not truly independent, is highly sensitive to instrument noise. Intuitively you can see that, in order to make a good inference when the measured quantities have overlapping areas of sensitivity, you must amplify what distinctions there are. For

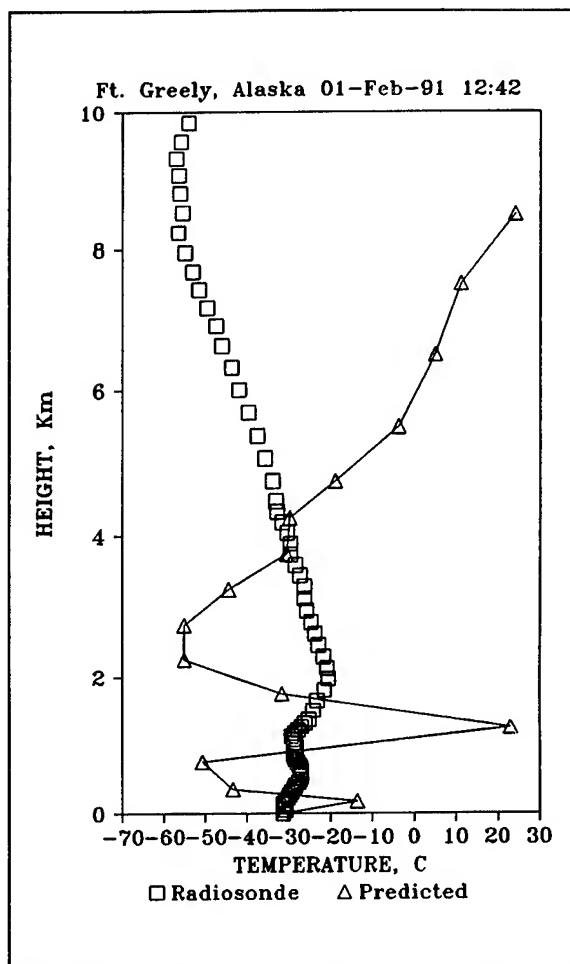


Figure 2. The regression did not account for instrument error. The predictor variables were measured, thus subject to instrument error.

Table 1. REGRESSION PREDICTOR VARIABLE NUMBER IN TERMS OF THE RADIOMETER'S FREQUENCY AND ANTENNA ANGLES

example, if the radiation calculated during the formation of the regression coefficients at the 19.5 Km altitude level, over a data history of Radiosonde profiles, for 51 GHz, 90 Degrees and for 51 GHz, 25 Degrees and for 53 GHz, 90 Degrees were all to correlate

FREQ (GHz)	ANTENNA ANGLE (Degrees)				
	90.00	40.03	25.11	14.92	9.00
57.45	1	5	8	10	11
55.29	2	6			
53.88	3	7			
51.07	4		9		12

quite well with the Radiosonde (balloon-measured) temperatures at the 19.5 Km level - then the regression coefficients must all be quite large to amplify what little difference there is between the three "independent" variables. That the regression coefficients are large (remember that these are coefficients for values that range from 80 to 300 Kelvin) can be seen in table 2 which shows the set of regression coefficients utilized to infer the 19.5 Km level's temperature for the profile of fig. 1.

Table 2. 19.5 Km REGRESSION COEFFICIENTS, NO INSTRUMENT ERROR

19	-44	41	-3	-22	-7	61	-85	4	-1	.4	-5
----	-----	----	----	-----	----	----	-----	---	----	----	----

In contrast, though to anticipate final results, table 3 shows the much smaller valued set of regression coefficients utilized to infer the 19.5 Km level's temperature for the profile of fig. 4. The profile of fig. 4 was inferred with a regression that did account for instrument error.

TABLE 3. 19.5 Km REGRESSION COEFFICIENTS, INSTRUMENT ERROR

0	-.1	-.2	-.3	-.2	.3	.3	.1	.2	-.1	-.1	-.01
---	-----	-----	-----	-----	----	----	----	----	-----	-----	------

You can see, given the large valued regression coefficients of table 2, that an instrument error, in one of the predictor variables, that varies from the mean more than the sample variance for that independent variable, would be highly amplified. This noise amplification is the cause of the profiling failure shown in fig. 2.

5.2.3 Interesting oscillations that occur in the profile failure

Rogers (Houghton, Taylor, Rogers, 1984:124) has noted the error sensitivity of exact solutions. Further, he has explained the interesting oscillations, seen in the lower part of the atmosphere, of the inferred profile in fig. 2. He says that

"..., it is difficult for the solution to follow noise in the observations without inducing oscillations, because if the solution has to be increased in the region of the peak of a weighting function in order to represent a positive error in the corresponding component of the measurements, there must be compensating decreases either side so that components due to the neighboring weighting functions are unaffected. This means that the original increase must be larger than it otherwise would, and very much larger if the weighting functions are closely spaced. The compensating decreases will also induce compensating increases in the next component, and so on."

By weighting functions he means the functions that describe the influence with height in the atmosphere of each of the Radiometer's measurements. That is, they describe the vertical atmospheric sensitivity of each of the 12 variables for our Radiometer application.

It is interesting to note about these oscillations that they occur over several of the levels of a profile at which we infer a temperature. That is, they swing out left of the Radiosonde profile that they fail to match for a couple of levels, getting progressively worse in their attempt to match the a priori profile. Then, for a couple of levels, they swing back toward the right and cross over the temperature value for the Radiosonde profile and then keep on going, swinging out right until the difference between inferred and a priori temperature is as much as 40 Degrees C. This trending over several levels is initially baffling because we utilize separate regressions for each level of the inferred profile (about 20 levels per profile in the case of figs. 1 and 2). If we have this amplified error effect, why doesn't the inferred temperature for one level go right of the a priori temperature for that level and then the inferred temperature for the next higher level go left and then the next higher above that go back right in some random pattern - rather than trending in its error as it does over several levels. The answer lies in that each of the radiation measurements has its length of influence in the atmosphere. And that, because we have an exact solution in the regression when no allowance is made for instrument error, we amplify the instrument error most at those heights a measurement has its greatest influence, and then less and less as you go up several levels, until the profile rises to a level dominated by another of the measurements.

6. SUCCESSFUL PROFILING WHEN USING MEASURED RADIOMETER VALUES

6.1 ONE SOLUTION

Remote measurements of the atmosphere, such as the 20 our Radiometer is capable of, will not be independent in the statistical sense. Thus, any statistical solution will be susceptible to ill-conditioning. And, as mentioned above, the ill-conditioning will worsen as more measurements are utilized for the regression. So one, not very good, solution is to reduce the number of measurements. Space does not allow the presentation of the results of this solution, but this does indeed solve the problem of the wild oscillations in the inferred temperature profile of fig. 2. (Using three of the radiation measurements plus the three surface values produces acceptable profile inference.) The obvious disadvantage of this solution is that it discards some of the

full spectrum of information measured about the atmosphere - simply to avoid ill-conditioning in the statistical approach.

6.2 ANOTHER SOLUTION

Another approach to a solution is throw out some of the measurements as in the above solution, but, instead of arbitrarily throwing out measurements until the profiling is finally acceptable, to make a more rigorous examination of the number of measurements that may be retained (Measure et al., 1989). This approach seeks to maximize the "information content" of the measurements retained for the regression.

6.3 PRESENT SOLUTION: INTRODUCE INSTRUMENT ERROR INTO THE REGRESSION

The instrument error to which an exact solution is so sensitive can be caused, for the Radiometer by receiver noise fluctuations, antenna side lobes, lossy wave guides, etc. The solution to successful temperature profiling with the statistical technique is to account for the instrument error in the regression. This solution was first proposed, for radiometry, by Westwater (1972) and was suggested to us by Steve Keihm (1991) of Jet Propulsion Laboratory.

6.3.1 Modification of the standard regression algorithm

First, this modification requires that the instrument error ϵ be a random variable that is uncorrelated with atmospheric fluctuations and that any bias present in the measurement can be removed experimentally so that ϵ has zero mean.

A common expression of the least squares estimate is:

$$y' = S_{xy} S_{xx}^{-1} x'$$

where

$$y' = t - \bar{t}$$

where t is the temperature for a particular level, e.g., 19.5 Km, that you wish to estimate, and

$$\bar{t} = \sum_{k=1}^n t_k$$

where n is the number of profiles in the data history, e.g., 531 Fairbanks profiles from January and February, 1980-1985, and where

$$\mathbf{x}' = [r_1 - \bar{r}_1 \quad r_2 - \bar{r}_2 \quad \dots \quad r_{12} - \bar{r}_{12} \quad s_t - \bar{s}_t \quad s_p - \bar{s}_p \quad s_{rh} - \bar{s}_{rh}]$$

where the r_i to r_{12} are, e.g., the 12 Radiometer measurements from which we wish to infer the temperature at the, e.g., 19.5 Km level, the s_t , s_p , and s_{rh} are the surface values measured at the same time and place as the as Radiometer measurements, and where the averages in the \mathbf{x}' vector are over the n , e.g., 531 values of Radiometer calculations and surface values derived from the data history.

The covariance matrix in the least squares estimate equation can be expanded thus:

$$S_{xx} = \begin{bmatrix} \frac{1}{n-1} \sum_{k=1}^n (x_{1k} - \bar{x}_1)(x_{1k} - \bar{x}_1) & \frac{1}{n-1} \sum_{k=1}^n (x_{1k} - \bar{x}_1)(x_{2k} - \bar{x}_2) & \dots & \frac{1}{n-1} \sum_{k=1}^n (x_{1k} - \bar{x}_1)(x_{15k} - \bar{x}_{15}) \\ \frac{1}{n-1} \sum_{k=1}^n (x_{2k} - \bar{x}_2)(x_{1k} - \bar{x}_1) & \dots & \dots & \dots \\ \dots & \dots & \dots & \dots \\ \frac{1}{n-1} \sum_{k=1}^n (x_{15k} - \bar{x}_{15})(x_{1k} - \bar{x}_1) & \dots & \dots & \frac{1}{n-1} \sum_{k=1}^n (x_{15k} - \bar{x}_{15})(x_{15k} - \bar{x}_{15}) \end{bmatrix}$$

Note that the diagonal elements of the covariance matrix are the sample variances, over the data history, of the independent variables, i.e., σ_i^2 , where $i = 1$ to 15. Mr. Keihm's suggestion was to determine an instrument error (random variable, no bias) for each of the Radiometer's measurements and the three surface values, express this error as a variance,

$$\sigma_e^2 = [\sigma_{e_{r_1}}^2 \quad \sigma_{e_{r_2}}^2 \quad \dots \quad \sigma_{e_{r_{12}}}^2 \quad \sigma_{e_{s_t}}^2 \quad \sigma_{e_{s_p}}^2 \quad \sigma_{e_{s_{rh}}}^2]$$

add the diagonal matrix (I is the identity matrix)

$$\sigma_e^2 I$$

to the covariance matrix, and proceed with the regression as usual, taking, of course, due caution to minimize problems caused computer calculations in the presence of ill-conditioning.

Figure 4 shows the same profile as in fig. 2, and utilizes the measured antenna temperatures as also in fig. 2, but the regression accounted for instrument error in the

above manner. As you can see in fig. 4, the temperature profile inference made in the presence of instrument error is almost as good as in fig. 1 when there were no errors in the calculated "measurements."

7. CONCLUSION

Introducing instrument error into the regression allows us to utilize all of the atmospheric information provided by the Radiometer but, at the same time, to avoid the ill-conditioning that results from non-independent measurements. Further, the errors can be tailored for each measurement (radiometry at some frequencies is more susceptible to error than at others and the surface *t*, *p*, and *rh* certainly have different error variances).

ACKNOWLEDGEMENTS

This work was supported by the U. S. Army Atmospheric Sciences Laboratory under contract number DAAD07-86-C-0034.

REFERENCES

- Keihm, Stephen J., 1991: Private Communication (Fax received 24 Jan. 1991).
- Houghton, J. T., Taylor, F. W., Rogers, C. D., 1984: Remote Sounding of Atmospheres. Cambridge University Press, New York, N. Y., 343 pp.
- Measure, E. M., Barber, T. L., Yee, Y. P., Larson, D. R., 1989: Number of Nonredundant Frequencies for Ground-Based Microwave Radiometric Temperature Profiling. J. Atmospheric and Oceanic Tech., Vol. 6, Num. 5:846-850.
- Westwater, E. R., 1972: Ground-Based Determination of Low-Altitude Temperature Profiles by Microwaves. Mon. Weather Review., Vol. 100:15-28.

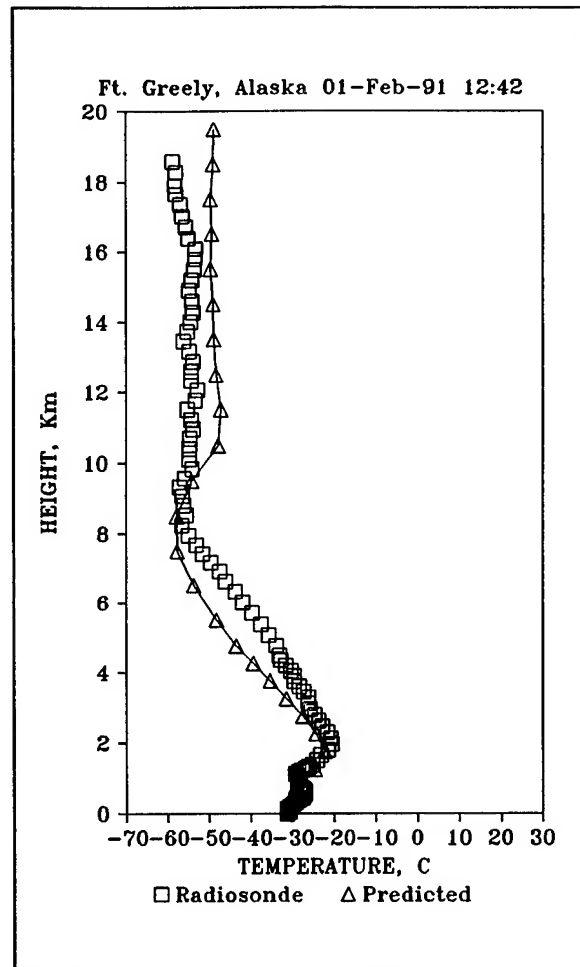


Figure 4. The regression utilized did account for instrument error. The predictor variables were measured, thus subject to error.

PERSONAL COMPUTER-BASED CODES FOR IDENTIFICATION BY FLUORESCENCE SIGNATURE

David Rosen
U.S. Army Atmospheric Sciences Laboratory
White Sands Missile Range, New Mexico 88002-5501, USA

James Klett
PAR Associates
Las Cruces, New Mexico 88001, USA

James Gillespie
U.S. Army Atmospheric Sciences Laboratory
White Sands Missile Range, New Mexico 88002-5501, USA

ABSTRACT

The authors are developing laser-induced fluorescence as a tool for the remote sensing of various objects. Identification of a target from a fluorescence signature requires sophisticated methods of spectral discrimination. A personal computer-based, spectral discrimination code, FARA1.FOR, that can be used to analyze fluorescence data from field experiments is presented. FARA1.FOR uses factor analysis-rank annihilation to analyze spectra. The authors discuss the requirements of factor analysis-rank annihilation on computer memory and speed.

1. INTRODUCTION

Laser-induced fluorescence (LIF) has great potential for target identification because it contains chemical information. Certain types of chemicals, skin oils, and other objects all have distinctive fluorescence spectra. However, few investigators use LIF for remote sensing because fluorescence spectra are broad and without line structure. Natural environments are mixtures of components with fluorescence spectra broad enough to overlap each other. Vibrational states, inhomogenous broadening, and molecular collisions both quench and broaden the narrow spectral lines of solids, liquids, and tropospheric gases. Although these materials lack narrow spectral lines, they often have broad emission bands.

Investigators have considered various algorithms for interpreting broad LIF spectra in remote sensing. Factor analysis-rank annihilation (FARA) is a set of algorithms for interpreting fluorescence intensity when measured as a function of two variables. The two variables are usually excitation wavelength and emission wavelength. FARA analyzes this data in the form of excitation-emission matrices (EEM). The major limitation of FARA is the requirement that

both the number of excitation wavelengths and the number of emission wavelengths must be greater than the number of simple components, called fluorescence centers, in the sample. The wavelength tunability of the laser used to induce fluorescence limits the number of excitation wavelengths. This limitation is discussed further in a later section.

The authors have theoretically analyzed FARA for application in remote sensing (Rosen and Gillespie, 1989a; 1990). These studies have revealed the potential and the limitations of FARA as applied to fluorescence lidar. However, these codes are not applicable to analysis of real experimental data either in the laboratory or in field measurements because previous codes have been mainframe based, not personal computer (PC)-based. Also, their protocol has not been user friendly.

In this paper, the authors describe a preliminary code, FARAl.FOR, for using FARA in a laboratory or lidar module. An earlier version of the code is described by Klett (1990). The code will only discriminate between a fluorescence signal and a fluorescence background. It does not currently include corrections for atmospheric effects or scattered light. Future modifications will address these issues. In this paper, we describe how to use the code and hardware limitations to the code.

2. USE OF FARAl.FOR

FARA techniques require a sequence of calculations. The goal of an FARA calculation is the concentration of a specific compound in the sample of unknown composition. An investigator must measure the EEM of the specific compound from a laboratory standard and store this EEM in a reference data base. This compound will be called the standard. The sample of unknown composition will be called either the unknown or the mixture. In a lidar situation, the unknown is the sample volume interrogated by the lidar. The user enters the dimensions of the EEM, for both standard and unknown, from the keyboard.

The flowchart in fig. 1 shows a complete FARA code. The investigator enters the EEM of an unknown, D , from a laboratory measurement, a fluorescence lidar return, or computer simulation. The EEM can be corrected at this point for various interferants that cannot be filtered out by FARA, including elastic scatter, Raman scatter, and random noise. A numerical algorithm then decomposes the unknown EEM into eigenvalues and eigenvectors of DD^T and D^TD . The eigenvalues of DD^T are the same as those of D^TD . The fastest algorithm for decomposing a matrix is singular value decomposition (SVD).

The program calculates the effective rank, r , of the unknown EEM. The effective rank is the number of types of fluorescence centers in the unknown. A fluorescence center is the part of the molecule that emits a photon. Without distortion, the number of nonzero eigenvalues of DD^T is equal to the number of different types of fluorescence centers in the unknown. Distortion of the EEM, such as noise or atmospheric effects, creates insignificant nonzero eigenvalues. SVD automatically avoids calculation of zero eigenvalues and their eigenvectors. SVD calculates a singular value and two eigenvectors for each nonzero eigenvalue, whether or not distortion generated them. A singular value

of D is the square root of a nonzero eigenvalue of DD^T . Accurate FARA calculations require the removal of eigenvalues and their eigenvectors created by distortion. This step is the hardest part of FARA analysis because the choice of methods for recognizing insignificant eigenvalues is often sensitive to specific experimental conditions. All calculations that follow use the effective rank.

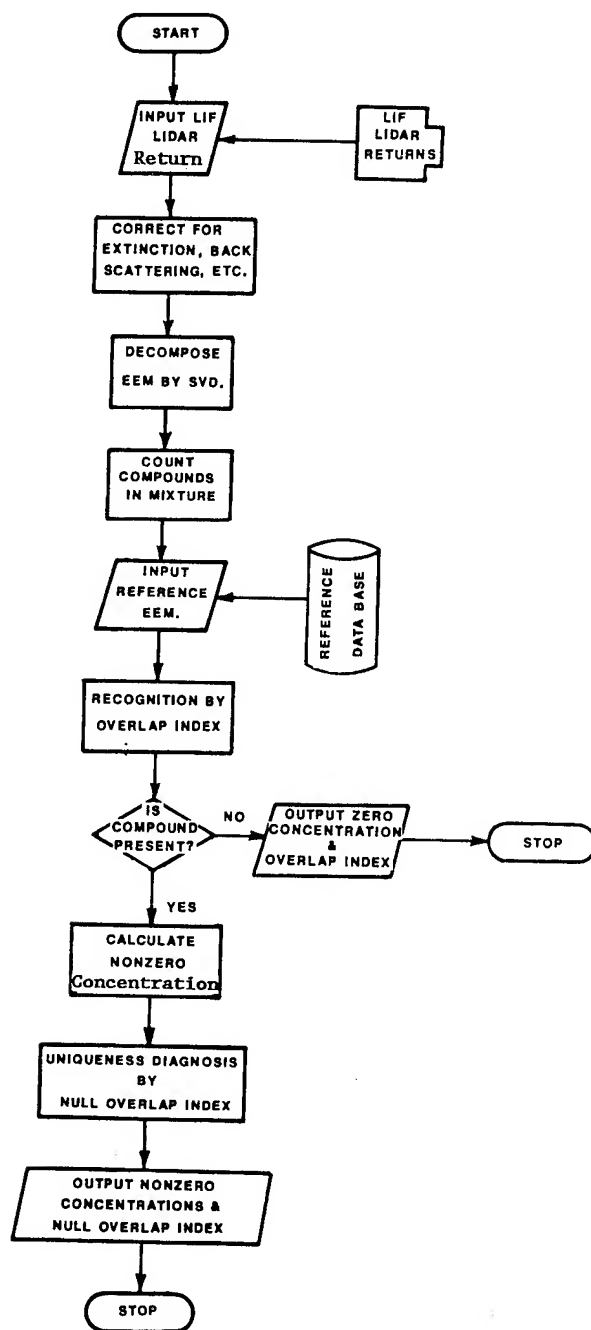


Figure 1: Flowchart of a complete program for factor analysis-rank annihilation.

Program FARAL.FOR calculates an effective rank by using the following ratio algorithm developed by Rosen and Gillespie (1989b). Let s_i be a singular value of D . The index, i , is ordered so that as i increases, s_i decreases. Let Q_i be the ratio s_{i+1}/s_i . According to the ratio algorithm, Q_r is the maximum of Q_i . If two Q_i are equal, FARAL.FOR chooses the smallest possible r . This value of r is a default.

The ratio algorithm assumes both that significant eigenvalues are much larger than insignificant errors and that the insignificant eigenvalues are nearly constant. The first assumption is true when the fluorescence signal is much larger than the noise, while the second assumption is true if the noise is independent of signal intensity (that is, additive noise). The program lists both s_i and Q_i so that the user can judge the validity of the assumptions. If the user decides that these assumptions are not valid, FARAL.FOR permits the user to choose any value of r .

The user then enters an EEM, N , of the standard from an input file. Detection of the standard requires only one emission spectrum and one excitation spectrum from N . FARAL.FOR picks the excitation and emission spectra containing the peak value of N as default spectra. The user can choose any other spectra from N if necessary. If there is no noise, all nonzero excitation and emission spectra are equivalent for detection. However, the program chooses the vectors as large as possible because choosing the largest vector eliminates the possibility of choosing excitation and emission spectra with zero intensity and also reduces the signal-to-noise ratio of the standard EEM.

The overlap index method now determines the presence or absence of the standard compound in the unknown (Ho et al., 1978; 1980). The presence of the standard compound (that is, a nonzero concentration) must be determined before any further quantitative calculation. The algorithm described later for calculating nonzero concentrations does not converge correctly if the concentration is zero.

The overlap index, p , is defined as

$$p = \sum_{i=1}^r |u_i \cdot x|^2 \sum_{j=1}^r |v_j \cdot y|^2 \quad , \quad (1)$$

where x and y are normalized vectors corresponding to the excitation and emission spectra of the standard, u_i and v_j are normalized eigenvectors of DD^T and D^TD , i and j are the indices designating the singular values to which the eigenvector belongs, and r is the effective rank calculated previously. In this paper, the column vectors of an EEM are excitation spectra and the row vectors of an EEM are emission spectra. The overlap index is always between 0 and 1, inclusive, as one can easily derive from eq. (1).

The program outputs the overlap index to the user. The user determines the presence or absence of the standard compound in the unknown as follows. Without noise, error, or linear dependence the compound is present if and only

if p is 1. Linear dependence means that insufficient information is available to determine the absence or presence of a compound, such as when two compounds have identical EEM. In the presence of noise and error, a threshold must be set. The compound would then be present if the overlap index is above a certain threshold between 0 and 1. The overlap index test only works if N is bilinear (that is, if the standard contains only one type of fluorescence center). The overlap index is used in a manner very similar to a correlation function (Beer and Norton, 1988). The correlation function method does not work if a reference EEM is not available for any background component in the unknown.

The program can then determine the concentration of the reference compound in the mixture. If the compound is not present, the concentration is obviously zero. If the compound is present, another algorithm determines the nonzero concentration. Lorber (1984; 1985) developed the following direct method of determining nonzero concentrations. One can easily derive the following equation (Rosen and Gillespie, 1991a) from the original equations by Lorber.

$$c = q/\text{tr}(U^T N V S^{-1}) \quad , \quad (2)$$

where N is the EEM of the standard EEM, q is the effective rank of N , U is a matrix whose column vectors are the eigenvectors, u_i , V is a matrix whose column vectors are the eigenvectors, v_j , and S is a diagonal matrix containing the significant singular values of D . The program pads matrices with zeroes to make the dimensions of the matrices consistent with matrix multiplication in eq. (2). Equation (2) works even if N is nonbilinear (that is, q is greater than 1).

Diagnostics are algorithms for determining the possibility of an incorrect calculation. Sometimes the value for concentration is not correct because of linear dependence, noise, or other interferants. FARA uses both the overlap index and the null overlap index as diagnostics. The overlap index can be used as a diagnostic by comparing the value from the EEM of the unknown to the value obtained from the EEM of a hypothetical background (Rosen and Gillespie, 1991b). The current version of FARAl.FOR does not include the null overlap index. However, some references describe the null overlap index in detail (Ho et al., 1978; 1980). Future versions of FARAl.FOR will include more diagnostics.

FARAl.FOR is more user friendly than previous FARA programs developed by the authors; for example, FARAl.FOR is one main program calling on modular subroutines. Previously, separate main programs executed every algorithm. Also, the input/output files for the EEM are in a simple three-column format. The three columns are for emission wavelength, excitation wavelength, and signal intensity. The file formats used by FARAl.FOR are compatible with SURFER, a commercially available software package for drafting three-dimensional plots. Previously, the authors designed the file formats for flexibility rather than simplicity. The FARAl.FOR file format is easier for beginners to understand than the previous file format.

3. LIMITATIONS OF FARAl.FOR

This section discusses limitations due to the computer hardware. Limitations of the FARA algorithms will not be discussed here, but are discussed in the references. The authors found many of these limitations on computer hardware while developing FARAl.FOR.

A fundamental condition of FARA is the requirement that both dimensions of the EEM be larger than the effective rank in the unknown. In terms of computer limitations, the largest possible effective rank of a lidar return determines the minimum dimensions of the array that stores an EEM. If the EEM of the unknown does not satisfy this condition, there is a problem with linear dependence (that is, an intrinsic ambiguity in the FARA calculations). Therefore, the measurement must use more excitation wavelengths and more emission wavelengths than fluorescing centers in the unknown. The lidar designer must choose wavelengths to avoid redundant information. The range of wavelengths must cover a significant fraction of the standard spectra. Many more excitation wavelengths than fluorescing centers may be necessary. However, the laser used in the experiment generally limits the number of excitation wavelengths. The powerful lasers used in lidar are currently nontunable. However, the use of new laser sources and nonlinear crystals that change laser beam wavelengths may soon provide excitation sources with sufficient tunability. An upper limit to the effective rank of the lidar return may exist in some applications where only a few materials in the environment fluoresce intensely. For example, lidar returns from vegetation usually have only one or two emission bands. Therefore, one can assume a maximum effective rank of two from vegetation under most conditions.

The computer hardware and compiler limit the maximum dimensions of the array that stores an EEM. First, the random access memory (RAM) limits the size of an array in a computer. The total number of elements in an array (that is, the product of the number of excitation wavelengths and the number of emission wavelengths) must be less than a certain number determined by the size of the RAM. Second, the time required for FARA analysis increases dramatically with the size of the EEM. Assuming SVD is the slowest step and that the EEM is very noisy, the amount of time for analyzing an m by n EEM is proportional to $(m + n) \min(m, n)$. Lidar returns are often noisy because of sky radiance (Rosen and Gillespie, 1991b). Therefore, both m and n must be limited for any real-time calculation.

The authors observed the following example of computer limits on EEM size. A PC with 1 MB RAM and a Fortran Microsoft compiler ran FARAl.FOR. On this PC, the FARAl.FOR analyzed EEM with 32 emission wavelengths and 16 excitation wavelengths. The program would not run with arrays of more than 2^{17} elements. Analyzing EEM this size required about a second. However, another program running on a mainframe with a virtual memory (about 30 MB) was able to analyze EEM with 512 emission wavelengths and 512 excitation wavelengths. This required arrays with 2^{34} elements. Analyzing noisy EEM this size took a few minutes. The dimensions of the EEM were chosen as powers of 2 because computers store arrays most efficiently if the dimensions are powers of 2.

The requirements on RAM are important because the computing power on a mobile lidar system may be limited. The EEM should be kept as small as possible, but

no smaller than necessary. The investigator could limit the number of emission wavelengths to be nearly the same as the number of excitation wavelengths. Some photodiode arrays could record data from 512 emission wavelengths. However, the laser source usually limits the number of excitation wavelengths more than the photodiode limits the number of emission wavelengths. If the investigator uses far more emission wavelengths than excitation wavelengths, the measurement is redundant for the purposes of FARA. Wavelengths should be carefully chosen over a section of the reference EEM, to reduce the amount of redundant information. However, the EEM should not have fewer excitation or fewer emission wavelengths than types of fluorescence centers in the target volume.

For example, consider an unknown with two overlapping emission bands each 50 nm wide. A nonlinear crystal could easily provide 16 excitation wavelengths. A photodiode array could provide 512 emission wavelengths. The unknown EEM has an effective rank of 2. A 2 by 2 EEM could be analyzed in theory, and a 16 by 8 EEM probably could work in practice. A small PC could store and analyze a 16 by 8 EEM much better than a 512 by 16 EEM.

In summation, the authors have started work on a PC-based FARA program. The initial work has shown important computer limits of the FARA algorithms.

REFERENCES

- Beer, R., and R. H. Norton, 1988: Analysis of Spectra Using Correlation Functions. Appl. Opt., 27:1255.
- Ho, C. N., G. D. Christian, and E. R. Davidson, 1978: Application of the Method of Rank Annihilation to Quantitative Analysis of Multicomponent Fluorescence Data from a Video Fluorometer. Anal. Chem. 50:1108.
- Ho, C. N., G. D. Christian, and E. R. Davidson, 1980: Application of the Method of Rank Annihilation Factor Analysis to Fluorescent Multicomponent Mixtures of Polynuclear Aromatic Hydrocarbons. Anal. Chem. 52:1071.
- Klett, J. D., 1990: Laser Induced Fluorescence Signal Analysis Algorithms. PAR SBIR Report, Contract DAAD07-89-C-0201, PAR Associates, Las Cruces, NM 88001.
- Lorber, A., 1984: Quantifying Chemical Composition from Two-Dimensional Data Arrays. Anal. Chim. Acta. 164:293.
- Lorber, A., 1985: Features of Quantifying Chemical Composition from Two-Dimensional Data Array by Rank Annihilation-Factor Analysis Method. Anal. Chem., 57:2395.
- Rosen, D. L., and J. B. Gillespie, 1989a: Atmospheric Extinction Effect on Analysis of UV Fluorescence Signatures. ASL-TR-0276, U.S. Army Atmospheric Sciences Laboratory, White Sands Missile Range, NM 88002-5501.

- Rosen, D. L., and J. B. Gillespie, 1989b: Algorithms for Analyzing Laser-Induced Fluorescence Spectra. ASL-TR-0240, U.S. Army Atmospheric Sciences Laboratory, White Sands Missile Range, NM 88002-5501.
- Rosen, D. L., and J. B. Gillespie, 1991a: Algorithms for Spectral Discrimination of Fluorescence Lidar Returns Degraded by Atmospheric Attenuation. ASL-TR-0297, U.S. Army Atmospheric Sciences Laboratory, White Sands Missile Range, NM 88002-5501.
- Rosen, D. L., and J. B. Gillespie, 1991b: Detection Algorithms for Fluorescence LIDAR with Photon Noise and Sky Radiance. In Proceedings of the Eleventh Annual EOSAEL/TWI Conference, U.S. Army Atmospheric Sciences Laboratory, White Sands Missile Range, NM 88002-5501.

**IMPROVING ATMOSPHERIC CHARACTERIZATION
AT THE
HIGH-ENERGY LASER SYSTEMS TEST FACILITY**

**Kenneth P. Freeman
Science and Technology Corporation
White Sands Missile Range, NM 88002**

**Robert W. Endlich
U.S. Army Atmospheric Sciences Laboratory
White Sands Missile Range, NM 88002-5501**

ABSTRACT

Meteorological information is used at the High-Energy Laser Systems Test Facility (HELSTF) to determine whether conditions are favorable for a specific laser mission, and as a post-mission analysis tool for experimenters. The atmosphere is characterized with an array of standard meteorological instruments, along with scintillometers and a tethered aerostat system. A workshop, convened in December 1990, examined system problems and proposed research and engineering efforts to improve the characterization of the atmosphere at HELSTF. These efforts were to focus on the meteorological elements critical to high-energy laser propagation: beam ventilation (cross winds), absorption (primarily by water vapor), and optical turbulence. This paper includes a description of the problems observed and an outline of the research and engineering efforts to mitigate those problems.

1. INTRODUCTION

The High-Energy Laser System Test Facility (HELSTF) at the White Sands Missile Range is dedicated to testing and experimentation with high-energy lasers, specifically the Mid-Infrared Advanced Chemical Laser (MIRACL), which is a deuterium fluoride laser operating at a wavelength of about 3.8 μm . Meteorological support for the HELSTF is provided by the Beam Weapons Assessment Section of the U.S. Army Atmospheric Sciences Laboratory. The critical meteorological elements measured and predicted include cross winds, water vapor, and optical turbulence. Water vapor is the primary absorber in the beam's spectral range and contributes to thermal blooming, a nonlinear effect that is a complex function of the absorption and beam ventilation for a given beam power and shape. Cross-wind measurements are crucial for assessments of beam ventilation, which is a determining factor in preventing thermal blooming. Optical turbulence, primarily due to temperature inhomogeneities in the atmosphere along the beam path, contributes to scintillation of the beam, beam spreading, and beam wander.

Before a free-atmosphere laser test, these and other parameters are used to predict the atmospheric impact upon the laser beam. Go/no-go decisions about proceeding with a laser test depend, in part, on atmospheric conditions. The MIRACL laser depends upon chemical reactions involving toxic materials; therefore the possibility of an inadvertent release of toxic gases is present, and real-time meteorological information is essential to predicting the behavior and movement of a possible toxic cloud. Many tests conducted with the MIRACL depend upon reliable assessments of the actual laser energy delivered to a target. Thermal blooming, scintillation, and beam spreading will all affect the results. Following a laser test, therefore, a detailed assessment of the atmosphere is provided to laser experimenters to assist their post-mission analyses.

All lasers can be adversely affected by the traditional meteorological obstacles, such as clouds and precipitation, and by linear effects such as scattering, absorption, and turbulence. High-energy lasers are subject to all these effects, as well as to nonlinear effects such as thermal blooming. Thus, the lessons learned in the highly instrumented environment of the HELSTF about the need for accurate characterization of the atmosphere to support laser operations may be applicable to predicting the probability of success of laser operations on a future battlefield. In addition, lessons learned from the work at HELSTF may have application to other test ranges, which need increasingly sophisticated measurements of atmospheric parameters in order to specify completely the performance of new weapons systems.

2. MEASUREMENTS OF ATMOSPHERIC PARAMETERS

A variety of sensors has been used to measure parameters that are important to high-energy laser propagation. The following paragraphs describe the current methods and instrumentation.

2.1 CROSS WINDS

The high-energy laser community uses the distortion parameter, α/v , to help assess whether nonlinear propagation is likely, where

α = total absorption (molecular + aerosol)

v = cross-beam component of the wind.

Cross-wind measurements are critical for assessments of beam ventilation. A significant cross wind is required to provide sufficient beam ventilation to prevent thermal blooming. Greater absorption requires greater ventilation, so absorption of 0.045 km^{-1} (approximately the mean annual absorption at 100% MIRACL power) needs about 1.5 m s^{-1} ventilation to prevent significant thermal blooming. Winds at HELSTF are measured by three-component anemometers mounted at heights of 2, 4, 8, and 16 m above ground on three towers located approximately 100 m southwest of the endpoints and middle of the beam path. The beam path is about 1 km long, so the towers are referred to as the 0-, 0.5-, and 1-km towers. The 0- and 1-km towers also have anemometers located at 32 m. Readings from these anemometers are normally averaged over the time required for the wind to travel 500 m, the distance between sensors. The output from these instruments is collected, processed, and displayed in the meteorological office by an automated data processing system called HELMET I. The beam path and instrument locations are shown in fig. 1.

Two additional anemometers, termed the "near" and "far" cross-wind anemometers, are mounted along the beam path. These two anemometers are oriented to measure the horizontal wind component perpendicular to the beam, at the beam height of 8 m. Output from these instruments is presented on an analog strip chart in the meteorological office.

2.2 WATER VAPOR

Water vapor is a major absorber of radiation in the spectral range of the MIRACL laser, and is responsible for approximately 95% of the beam absorption in free atmosphere tests. Such absorption is a contributor to the phenomenon of thermal blooming, which affects the size, shape, and resultant power of the high-energy laser beam as it traverses the atmosphere and interacts with a target. Although White Sands Missile Range is a desert environment, atmospheric water vapor can be highly variable, particularly in the summer thunderstorm season. For these reasons, accurate, precise, and high-density measurements of atmospheric water vapor are essential. Current instrumentation includes dew-point hygrometers of

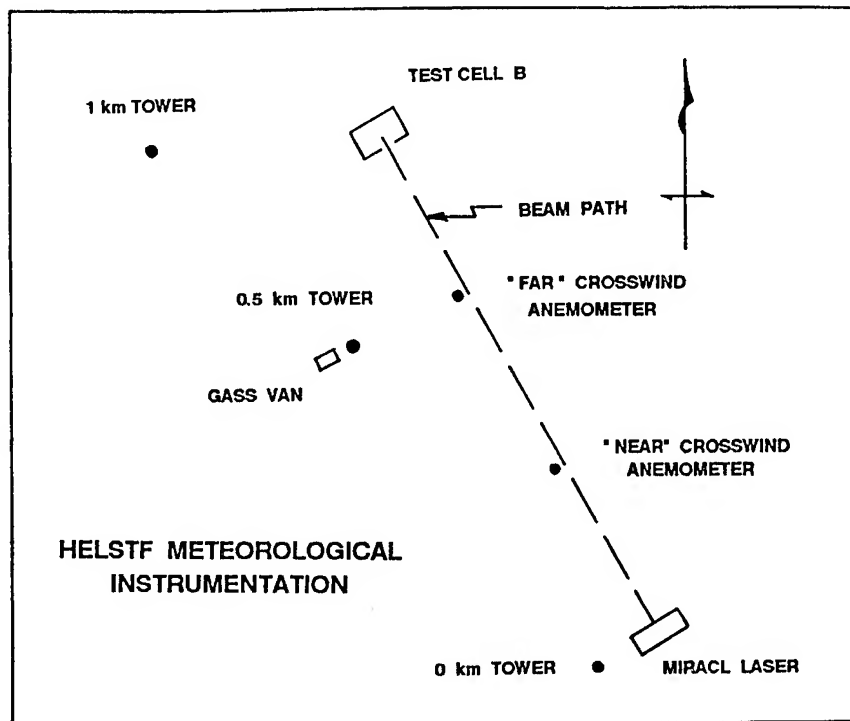


Figure 1. HELSTF site plan, showing locations of primary meteorological instruments.

the cooled-mirror type, mounted on each of the three towers at a height of 2 m. Temperature measurements are made coincident with the dew points. This information is collected, processed, and displayed in the meteorological office by the HELMET I system.

2.3 OPTICAL TURBULENCE

Optical turbulence is a complex phenomenon, generally caused by temperature inhomogeneities in the atmosphere along the beam path. Optical turbulence may cause scintillation of the laser beam, beam spreading, and beam wander. A working assumption at HELSTF is that the critical threshold value of the turbulence structure parameter C_n^2 is $1.0 \times 10^{-13} \text{ m}^{-2/3}$. Without detailed information about the phase and amplitude structure of the beam as it emerges from the laser, it cannot be determined whether this is a realistic threshold. Optical turbulence is measured by optical scintillometers along horizontal paths between the 0- and 1-km towers at heights of 8 and 32 m. An acoustic sounder, near the 1-km tower, and a tethered aerostat, near the 0.5-km tower, have also been used to measure the temperature structure parameter, C_t^2 , from which optical turbulence can be calculated. So far, these latter two instruments have met with only limited success. Again, output from the scintillometers and other instruments is processed and displayed in the meteorological office.

2.4 OTHER MEASUREMENTS

Other atmospheric parameters measured at the HELSTF include aerosol content, measured with Knollenberg probes, and gaseous minor constituents, all measured near the 0.5-km tower with instruments contained in a van, called the Gas Aerosol Sampling System (GASS) van. In addition, other standard surface meteorological instrumentation is installed close to the HELSTF and read out in the meteorological office.

3. PROBLEMS WITH ATMOSPHERIC CHARACTERIZATION

After several years of experience with collecting and analyzing meteorological data in support of laser tests, the meteorologists at HELSTF found reasons to question the adequacy of the data they were collecting to support the stringent requirements of high-energy laser testing. In some cases, the validity of the data was called into question. A number of case studies were performed and documented wherein the atmosphere at HELSTF did not seem to conform to expectations. For example, cross winds deduced from the tower-mounted anemometers differed significantly among themselves and when compared to the cross winds measured by the "near" and "far" cross-wind anemometers. Even the "near" and "far" anemometers differed significantly, occasionally even exhibiting different signs. In several cases studied, extending the averaging time for wind speeds and direction from two minutes or less out to an hour or more did not produce convergence of the measurements from different instruments, as would be expected. Figure 2 illustrates a typical example of this problem.

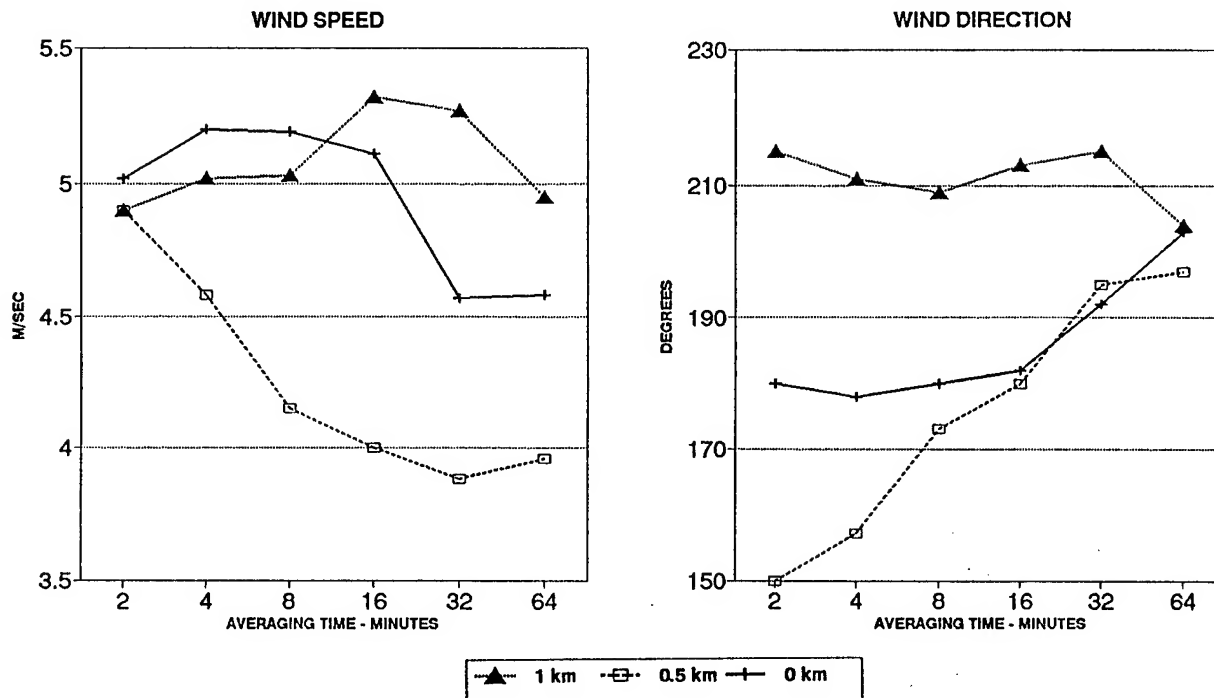


Figure 2. Average 8-m wind speed and direction for three meteorological towers, 14 August 1990. Averaging times 2 to 64 min (Endlich, 1990).

These measurements are unacceptable because, in marginal cross winds, they do not permit confident prediction of the beam ventilation to be expected in the next five minutes, which is the time required to start the laser and complete a test. Furthermore, such measurements do not provide a reliable post-mission assessment of beam ventilation.

Present water vapor measurements were unsatisfactory primarily because the five available dew-point hygrometers disagreed among themselves (at times by as much as 5 to 6 °C) and attempts to calibrate them in the field, using sling psychrometers, were unconvincing.

Optical turbulence measurements were a source of concern primarily because of the large variability of measured values of C_n^2 . Minute-to-minute differences on the order of a factor of two were regularly measured, and the scintillometers mounted at a height of 32 m often showed variability exceeding a factor of 10. The instruments produce a path-averaged value of C_n^2 and the values given by the oppositely pointed instruments track well, but such large variability raised doubts about whether the scintillometer paths are sufficiently close to the laser beam path and whether the path-weighting function of the measurements is close enough to that required to predict atmospheric optical effects on the beam.

4. WORKSHOP RESULTS

A workshop of government and private industry scientists was convened in December 1990 to review the critical requirements for meteorological support at HELSTF, to examine known and suspected shortfalls in capabilities to provide that support, and to develop an effective approach to resolving those shortfalls. The workshop systematically examined each of the critical parameters, assessed the requirements and capabilities for measuring each, and proposed further study, theoretical development, and engineering where appropriate to mitigate the problems. The workshop proposed five approaches to solving the problems: theoretical work to determine the critical values for each parameter and the accuracy to which each must be specified; analysis of existing meteorological data to augment and validate the theoretical studies; improvements to measurements attainable with current instruments and data collection systems; improvements possible with upgraded or new-technology instruments; and improved presentation of meteorological data to customers at HELSTF.

4.1 THEORY

The stringent requirements for real-time measurements of atmospheric parameters at HELSTF mean that the common description of variations in atmospheric variables in terms of their spectra and probability distributions are inadequate. The intermittent nature of such variables near the ground in the vicinity of obstacles is real, and probably responsible for many of the anomalies observed in measurements at HELSTF. The response of a laser beam to these short-term fluctuations in the atmosphere can best be described by an integral equation addressing beam propagation through an inhomogeneous medium. For low-power lasers, where nonlinear effects may be unimportant, such equations are well known. It is assumed that such relations also exist for the nonlinear propagation effects of thermal blooming and thermal bending. Further development of the theory will permit answers to such questions as how large a region of calm air can exist along an otherwise well-ventilated beam before unacceptable thermal blooming will occur.

Information about the phase and amplitude distribution of the laser beam wave front will enable us to assess the accuracy required of meteorological measurements. The threshold for acceptable optical turbulence varies with different experiments, but one commonly used criterion is that C_n^2 not exceed a value of $1.0 \times 10^{-13} \text{ m}^{-2/3}$. The origin and validity of this value is uncertain, but suitable information about the beam as it enters the atmosphere may make it possible to verify or refine that value.

4.2 ANALYSIS OF EXISTING METEOROLOGICAL DATA

Despite the unknowns surrounding the interactions of the beam with the atmosphere, it is obvious that the large discrepancies among the cross winds derived from the various sensors point to the need for improvements in wind measurements, or for explanations for the observed phenomena. The workshop recommended that a correlation analysis of the available data be performed to answer such questions as whether the statistics at the various locations are similar or whether obstacles and terrain features dominate the velocity field at the beam height. Other questions involve determining whether the statistics for the various instruments differ significantly depending upon direction and speed

of the wind, and whether the tower anemometers enhance the knowledge of beam ventilation deduced from the cross-beam anemometers. The goal of such an analysis was to be to determine how many anemometers would be needed to provide an acceptably small probability of missing a calm region that would cause thermal blooming, and where such sensors should be placed.

If theoretical studies show that optical turbulence imposes a major limitation on the quality of the beam, further analysis would be required to match the optical path and weighting function of the optical turbulence data to the weighting function of the MIRACL-atmosphere system. Turbulence occurs in organized spatial structures; convective plumes during the day and stratified layers at night. This point is underscored by the wide fluctuations seen in existing turbulence data. Previous measurements show approximately a 100-m autocorrelation length for thermal plumes 8 to 16 m above the ground. Separations between the measurements and the MIRACL beam beyond that distance will be uncorrelated. Thus, a careful analysis is essential to determining the proper location of sensors along the beam path.

4.3 IMPROVED MEASUREMENTS WITH CURRENT INSTRUMENTS

The current instruments are located as they are for historical reasons, but there is no evidence that they are being misapplied in any way. Sampling rates were felt to be adequate and the calibration and maintenance of the instruments generally seemed to be sound. Sampling rates will increase in conjunction with the implementation of a new data collection, processing, and display system, called HELMET II, now being installed. These sampling rates should be more than adequate. With the possible exception of the readings from the dew-point hygrometers, most of the variations recorded by the different instruments probably represent real effects of the atmosphere at the site. The theoretical studies and data analysis outlined above should confirm this view and provide estimates of the density and placement of sensors needed to do the job. Finally, correlation measurements with a tightly packed array of sensors along the most critical portion of the beam (near the source) would confirm the results.

4.3.1 Calibration and Intercomparison of Wind Sensors

Despite confidence that the anemometer calibrations are essentially correct and that maintenance is adequate, an independent quality-control assessment was felt to be necessary through calibration and intercomparison of the anemometers, under strictly controlled circumstances. Calibration curves for each separate instrument and propeller set were generated. This calibration and intercomparison is the subject of another paper in this conference (Vaucher and Endlich, 1991) and of a technical report (Vaucher and Endlich, 1991b).

4.3.2 Calibration and Intercomparison of Dew-Point Hygrometers

Two instruments were taken to the National Institute of Standards and Technology in Maryland for primary calibration. This procedure and the results are also described in the paper by Vaucher and Endlich (1991) and in a technical report (Vaucher and Endlich, 1991a). Generally, however, the differences between the instruments were reduced considerably by the calibration process, and now these instruments are being intercompared with others to improve the overall system accuracy and confidence. Comprehensive revisions to the standard calibration procedures at HELSTF have improved the precision and repeatability of the measurements.

4.3.3 Improving Optical Turbulence Measurements

The workshop participants included several with extensive experience with optical scintillometers and other optical turbulence measurement systems. A fairly simple comparison, between a two-scintillometer system mounted on the existing towers and a two-scintillometer system mounted along and very near the beam path, should demonstrate the validity of C_n^2 measurements made from the meteorological towers as a measure of optical turbulence at the beam itself. Furthermore, the

path weighting functions for the scintillometers and the laser beam should be calculated. If they are found to differ significantly, the scintillometer function can be adjusted to improve the match. This adjustment should improve the relevance of the optical turbulence measurements to the impact on the beam. Finally, locating the scintillometers at 500-m intervals along the beam path would allow for forward weighting of the path closest to the beam source, where turbulence has the greatest impact on the beam.

4.4 IMPROVED MEASUREMENTS WITH NEW OR UPGRADED SENSORS

It is possible, with adequate funds, to improve the spatial resolution, time resolution, and accuracy of many of the atmospheric observations at HELSTF with new sensors. For determining cross winds, an optical cross-wind sensor or profiler was recommended. For humidity, new technology hygrometers are available, and the best solution might be an optical transmissometer to directly measure absorption in the spectral range of interest. This latter choice would be expensive, if suitable commercial instruments become available. Finally, if optical turbulence is felt to be a critical parameter, a profiling scintillometer located near the beam will provide adequate measurements of C_n^2 .

4.5 IMPROVED DATA PRESENTATION

At present, a one-page summary of the meteorological conditions during a test is provided to customers. This Atmospheric Test Report will be examined carefully in light of what is determined about the observations, and appropriate changes will be recommended. For example, it may be possible to provide more detailed and informative descriptions of the cross wind and optical turbulence during each test.

5. CURRENT STATUS OF THE EFFORT

Following the workshop, a detailed plan was developed to implement approximately 20 specific recommendations made by members of the panel. This plan has been altered somewhat, to account for availability of funds and appropriate personnel to perform the work, but essentially the program has proceeded on track. The theoretical studies and modeling of the beam are being performed under several task orders, and are not included here.

The various meteorological parameters of interest at HELSTF were prioritized and work was directed toward those priorities. The first priority was felt to be cross-wind analysis, since beam ventilation is a critical parameter. While the specific requirements for characterizing the ventilation of the beam remain unknown, much work has been done in an attempt to improve the response and accuracy of the wind measurements through calibration and intercomparison. At the same time, an effort has been underway to examine and explain the apparently anomalous behavior of the wind data observed on several occasions. Results of this wind variability study are presented in another paper included in this volume (Vaucher and Endlich, 1991).

The parameter next on the list of priorities is water vapor, not only because of its importance in absorbing the beam energy, but because of the great uncertainties associated with the measurements of water vapor at HELSTF. Results are presented in the paper by Vaucher and Endlich.

Work on the optical turbulence measurements has just begun, and no results are yet available. Aerosol measurements will be considered following the optical turbulence measurements, and the final effort will focus on the presentation of the meteorological data, both in the meteorological office and to experimenters after the fact.

6. CONCLUSIONS

The problem of characterizing the atmosphere at the HELSTF, in sufficient detail and with sufficient accuracy to support operational testing of the MIRACL high-energy laser, is really two-fold. The first problem is to determine the requirements for accuracy and precision of the measurements. This effort calls for detailed knowledge of the effects of the atmosphere upon the beam. The second problem is to achieve those standards of accuracy and precision, either with the instruments at hand or with new and improved instruments. Primarily because of financial limitations, the efforts at HELSTF thus far have concentrated on the more obvious and basic tasks of examining the current instruments and their calibrations. Highly detailed calibrations have been performed on the wind and water vapor measurement systems. The results of this early work point to increased confidence in the measurements. The next step in the process is to perform intercomparisons of the calibrated instruments, and this effort is now ongoing. The final step in the process will be to implement the results and new calibration procedures into the operational support system at the HELSTF. When this work with the instruments is completed, the goal of improving the atmospheric characterization at the HELSTF will be realized, at least within the limitations of the existing instruments. Hopefully, additional insight will also have been gained into the real variability of the atmosphere at this site. Further research into the interactions between the laser beam and the atmosphere will ultimately reveal the detailed requirements for such measurements, and a final assessment can then be made about the adequacy of the present instruments.

REFERENCES

- Dowling, J.A., and J.L. Manning, eds, 1983: High Energy Laser Propagation Handbook, Vol I, Phenomenological Basis, Optimetrix, Inc., for U.S. Army Atmospheric Sciences Laboratory, White Sands Missile Range, NM 88002-5501.
- Endlich, Robert W., 1990: Presentation to the Workshop on Improving Atmospheric Characterizations at the High-Energy Laser Systems Test Facility. U.S. Army Atmospheric Sciences Laboratory, White Sands Missile Range, NM 88002-5501.
- Lawrence, R.S., Paul Try, Donald Walters, and Gerald R. Ochs, 1991: Workshop on Improving Atmospheric Characterizations at the High-Energy Laser Systems Test Facility, Science and Technology Corporation, P.O. Drawer 250, White Sands Missile Range, NM 88002.
- Vaucher, Gail T., and Robert W. Endlich, 1991: Improving Atmospheric Characterizations at HELSTF: Winds and Humidity, Proceedings of the 1991 Battlefield Atmospherics Conference, U.S. Army Atmospheric Sciences Laboratory, White Sands Missile Range, NM 88002-5501.
- Vaucher, Gail T., and Robert W. Endlich, 1991a: Improving Atmospheric Characterizations at HELSTF: Humidity Analysis; Phase I--Calibrating the General Eastern Dew-Point Hygrometers, STC Technical Report 6216, Science and Technology Corp., P.O. Box 7390, Hampton, VA 23666.
- Vaucher, Gail T., and Robert W. Endlich, 1991b: Improving Atmospheric Characterizations at HELSTF: Wind Analysis; Phase I--Calibrating the R.M. Young Gill UVW Anemometers, STC Technical Report 6217, Science and Technology Corp., P.O. Box 7390, Hampton, VA 23666.

An Insitu Soil Moisture Sensor for Soil Sensing and Modeling Applications

Robert Olsen, Atmospheric Sciences Laboratory, White Sands Missile Range, NM 88002

Rene' Klein, New Mexico State University, Las Cruces, NM 88003

Harold Ballard, **Claude Tate**, **Robert Hootman**, University of Texas at El Paso, El Paso, TX 79903

Ronald Atkins, **Roy Bates**, Cold Regions Research and Engineering Laboratory, Hanover, NH 03755

Requirements exist for measurements of soil moisture in meteorological modeling, acoustical modeling as well as estimating trafficability under various road conditions. For these purposes an insitu soil moisture sensor for continuous measurements of moisture was tested and results are described. The sensor measures soil moisture by using the dielectric constant of water within the soil. The sensor was located at a test area at the Dirt Site, White Sands Missile Range. There were a number of rain storms, resulting in an appreciable increase in the soil moisture. Ground truth measurements were performed by on-site desiccation of the soil sample. These were done on an hourly basis during particular test periods. The insitu probe measurements agree with the ground truth measurement showing diurnal moisture increases coinciding with the diurnal variability in soil temperature. These tests were conducted using sandy soil, further testing in other types of soil is recommended to fully realize the sensor's capability.

(The full text of this paper was unavailable at press time.)

AN ALGORITHM FOR THE RETRIEVAL OF
ATMOSPHERIC CONSTITUENT CONCENTRATIONS

Frank T. Kantrowitz
Daniel R. Billingsley, Fernando R. Palacios, and Wendell R. Watkins
U.S. Army Atmospheric Sciences Laboratory
White Sands Missile Range, New Mexico 88002-5501, USA

ABSTRACT

On 17 January 1991, hostilities began what was to become known as the Persian Gulf War. The effects of the oil fires that engulf the region have both military and environmental ramifications. The military has become reliant on sophisticated electro-optical systems. Such systems enhance the effectiveness of decision makers in obtaining data upon which to formulate and execute operations. Adverse atmospheric conditions can degrade the ability of systems to operate reliably. Design of such systems requires the capability to monitor the factors affecting the path over which they operate. Among the factors affecting atmospheric propagation are the atmospheric constituent concentrations.

With the end of the conflict, the damage the planet has suffered is of great environmental concern. Although some oil fires were ignited as the result of military action, it is believed that this war gave rise to the use of government sponsored environmental terrorism as a weapon of warfare. In the aftermath of the war, the long-term consequences on a planetary scale must be assessed. For the inhabitants of the American Southwest, the question here is whether pollutants from the Persian Gulf War have reached the American Southwest.

This paper presents a methodology for the analysis of trace gases by Fourier transform spectroscopy (FTS). Through the application of spectral least squares methods, the concentration of a trace gas may be determined. With the addition of toxic gas libraries, this algorithm may be utilized to monitor gases that could impact human lives during military operations.

1. INTRODUCTION

In the present study a horizontal scenario algorithm will be addressed. To validate this algorithm for low concentration gases, the Air Force Phillips Laboratory HITRAN database is utilized. The researchers are specifically investigating if there is an increase in the levels of carbon dioxide (CO_2) and carbon monoxide (CO) in the American Southwest that might be due to the Gulf

oil fires or the recent volcanic activity in the Philippines. Figure 1 presents a view from the Earth orbiting Space Shuttle Discovery (STS-39) during the late April 1991 mission. In the aftermath of Iraqi occupation, smoke from burning oil well fires is visible north of the Bay of Kuwait and south of Kuwait City. To initiate our study, we begin with some historical background on selected molecular species.

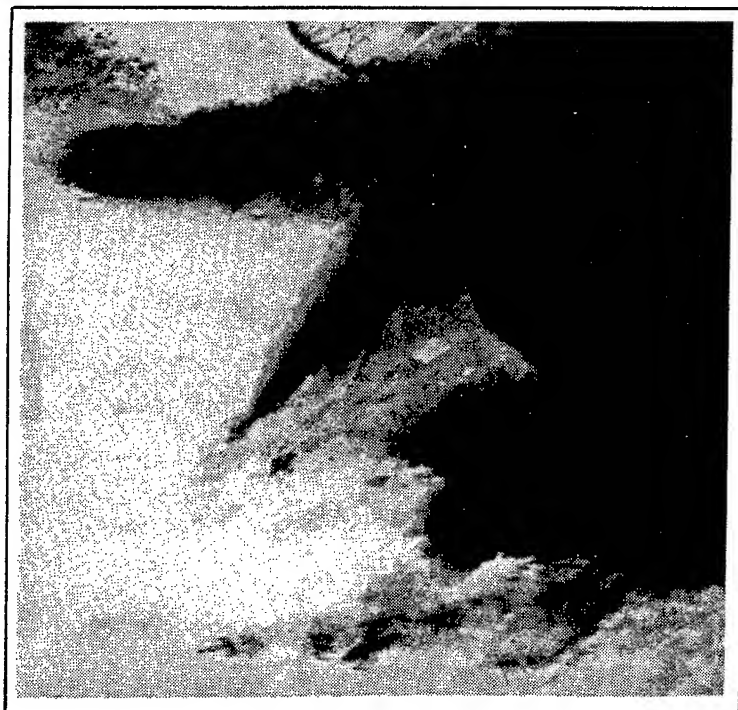


Figure 1. A view from the Earth orbiting Space Shuttle Discovery (STS-39) during the late April 1991 mission. Smoke from oil well fires is visible in the aftermath of Iraqi occupation.

2. SELECTED MOLECULAR SPECIES--HISTORICAL BACKGROUND

2.1 Overview

The atmosphere has long been known to have one major reactive component, oxygen, and one rather inert one, nitrogen. Analytical capabilities have moved forward rapidly over the last 40 yr, and each increase in sensitivity has revealed the existence of an even larger number of chemical compounds in the atmosphere. With a sensitivity to 0.01 percent, air has only a few additional molecular types: water (H_2O), CO_2 , and argon (Ar). At the parts per million level, methane (CH_4), neon (Ne), and krypton (Kr) join the list. At the parts per billion level, hundreds of compounds have been identified and some are measurable at the parts per trillion level. As the precision of the analysis increased, the concept of a static atmosphere has been replaced with the knowledge that many of the trace chemical species are increasing in concentration. Clear evidence now exists that the amounts of a large number of trace species in the atmosphere are changing on a global scale. Many of these species are important climate gases because they absorb thermal infrared (IR) radiation emitted by the Sun and the Earth and thus control the temperature at the Earth's surface (Rowland and Isaksen, 1988).

2.2 ATMOSPHERIC WATER VAPOR

It is difficult to generalize about atmospheric water vapor because of its large diurnal and seasonal variations. The amount observed in the White Sands region ranges from a low value of about 2 torr during the winter to about 18 torr during the summer thunderstorm season (High Energy Laser Propagation Handbook, 1984).

2.3 ATMOSPHERIC CARBON DIOXIDE

During the last glaciation, the atmospheric CO_2 concentration was only about 66 percent of the preindustrial level. In Antarctica, in a joint U.S.-Swiss operation, an ice core was drilled upon which a reconstruction of the atmospheric CO_2 increase since 1800 has been possible (fig. 2) (Neftel et al., 1985). The results indicate a preindustrial atmospheric CO_2 concentration near 280 ppmv before about 1800 A.D. The main natural source is from biospheric activity while the main anthropogenic source is from the combustion of fossil fuels (fig. 3). The natural sources and sinks produce a diurnal and seasonal variability in the CO_2 level while the anthropogenic sources contribute to a slow increase in the total atmospheric burden (Oeschger and Siegenthaler, 1988).

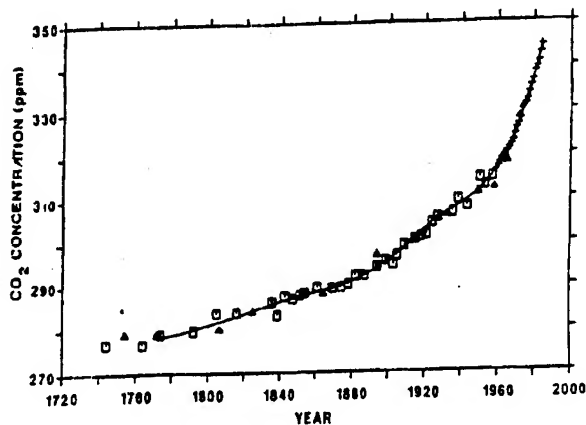


Figure 2. Increase in atmospheric CO_2 since 1750.

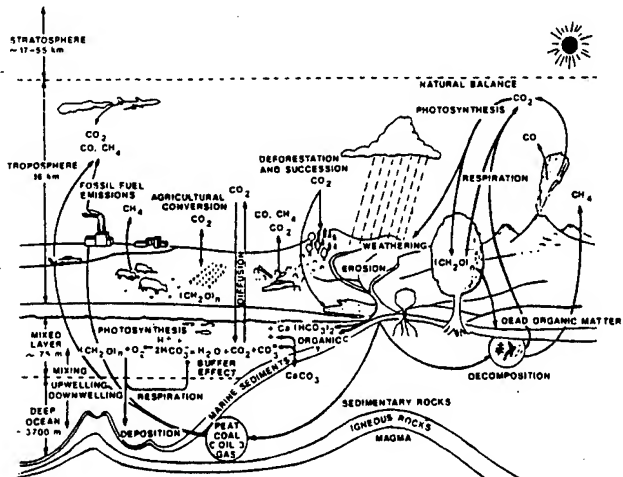


Figure 3. Carbon cycle.

2.4 ATMOSPHERIC METHANE

There is general agreement that the atmospheric concentration of CH_4 is on the increase. As fig. 4 indicates, the CH_4 increase began early in the last century, starting from a steady state value of 0.7 ppm, and is increasing at the rate of 1 percent per year (Blake and Rowland, 1987). Analysis of the emission inventory of atmospheric CH_4 points to the reason for the increase. The various sources and their estimated source strength are summarized in fig. 5 (Blake and Rowland, 1987). Although the uncertainties are great, this figure demonstrates that man may control more than 50 percent of today's sources of atmospheric CH_4 mainly through his agricultural practices (Bingemer and Crutzen, 1987). Apparently the observed increase in atmospheric CH_4 is largely due to an increase in man-made sources and is coupled to the increase in world population (Ehhalt, 1988).

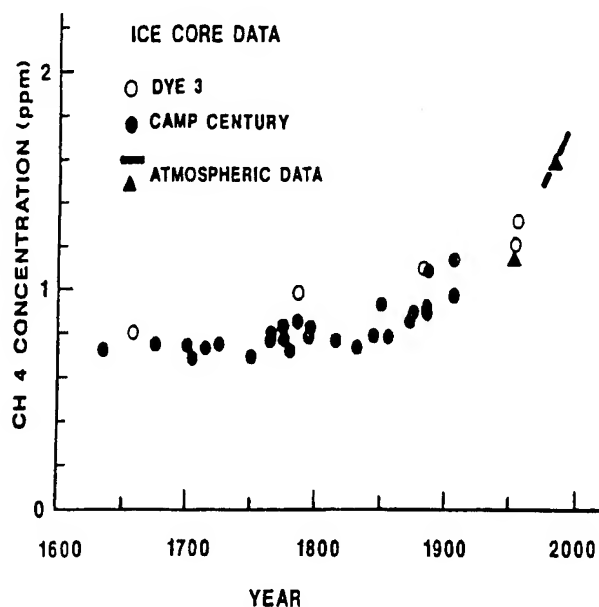


Figure 4. Increase in atmospheric CH_4 .

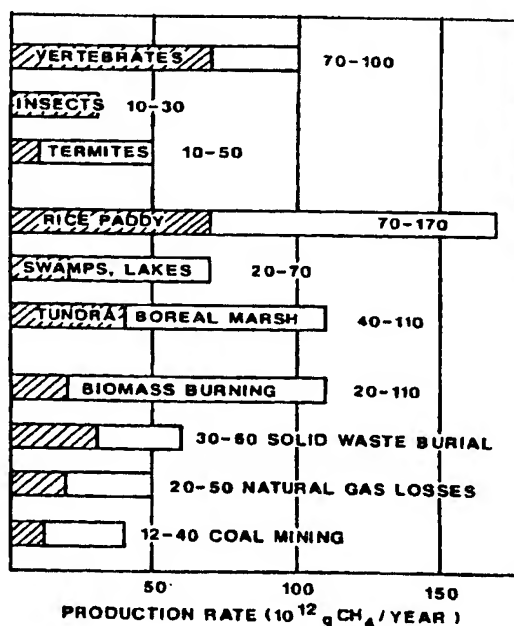


Figure 5. Sources for CH_4 .

2.5 ATMOSPHERIC NITROUS OXIDE

Nitrous oxide, N_2O , is the most important molecular absorber other than H_2O for deuterium fluoride (DF) lasers. The 1984 mean global concentration in "clean" air was 307 ppbv, and it is increasing at a rate of about 0.8 ppbv per year. N_2O influences the climate through the greenhouse effect and also affects the ozone chemistry of the stratosphere. Natural sources include microbiological processes. Anthropogenic sources arise from the burning of fossil fuel and the use of nitrogen fertilizers. The most important sinks are processes in the stratosphere (Prinn, 1988).

2.6 ATMOSPHERIC CARBON MONOXIDE

In polluted regions such as urban centers, elevated CO concentrations can be dangerous to human health, and they are taken as key indications of other kinds of pollution. In the presence of nitrogen oxides, the atmospheric oxidation of CO generates ozone. In clean air, where there are subcritical amounts of nitrogen oxides, the oxidation of CO to CO_2 consumes ozone. Thus, CO exerts control over tropospheric ozone, an important oxidant and a potent climatic greenhouse gas. The latitudinal distribution of CO is presented in fig. 6. A useful compilation of CO budgets is summarized in table 1 (Logan et al., 1981). Data seem to indicate that atmospheric CO has increased in the northern hemispheric troposphere since 1950. The data suggest no positive trend in the Southern Hemisphere (Cicerone, 1988; Heidt et al., 1980).

The question arises as to whether atmospheric gases can be accurately modeled. Section 3 shows that researchers at the Air Force Phillips Laboratory Geophysics Directorate have developed a sophisticated atmospheric transmittance model.

TABLE 1. CO BUDGET

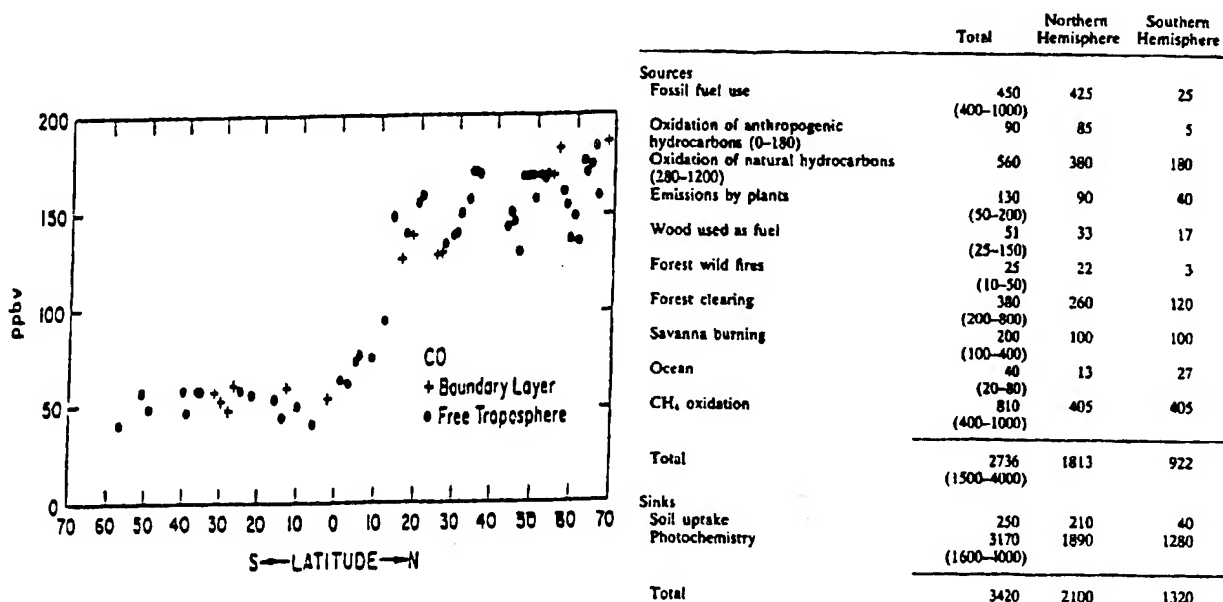


Figure 6. Latitudinal distribution of CO.

3. FASCODE

The Fast Atmospheric Signature Code (FASCODE) is a line-by-line spectral transmittance and radiance model for atmospheric scenarios developed at the Air Force Phillips Laboratory Geophysics Directorate, Hanscom Air Force Base, Massachusetts (Clough, 1986; Kantrowitz, 1990). The program is applicable to investigations in the spectral regions from the microwave to the near ultraviolet. The source of the spectral line information is the high-resolution molecular absorption database known as HITRAN. This database covers 348,043 transitions of 28 molecular species over a region from the millimeter through the visible portion of the spectrum (Rothman et al., 1987).

4. METHODOLOGY

The horizontal path algorithm employed in the data analysis was suggested by Matise (1988) after development by Haaland et al. (1985). Reference spectra are generated for water vapor, CO₂, CH₄, CO, and N₂O using FASCODE 2 and the 1986 HITRAN compilation. The transmittance spectra are converted into absorbance spectra, and the area under selected spectral lines is measured for each reference species and each concentration. By relating all of the spectral information present in the reference spectra of a trace gas to that of the unknown sample and by appropriately fitting the baseline, trace gases can be detected. Four least squares methods incorporating different baseline assumptions are utilized. Table 2 displays the symbols used in the least squares analysis.

TABLE 2. SYMBOLS UTILIZED IN LEAST SQUARES ANALYSIS

A_{si}	=	sample absorbance at frequency i
A_{ri}	=	reference absorbance at frequency i
k	=	ratio of sample and reference concentration
v_i	=	frequency
a, b	=	terms pertaining to linear baseline assumption
e_{si}	=	noise at frequency i
p	=	subscript indicating values pertaining to a particular peak

4.1 METHOD 1: BASELINE OF SPECTRA ZERO OR KNOWN

In this case the assumed relationship is

$$A_{si} = kA_{ri} + e_{si} .$$

4.2 METHOD 2: LINEAR BASELINE

In this case the assumed relationship is

$$A_{si} = a + bv_i + kA_{ri} + e_{si} .$$

4.3 METHOD 3: DIFFERENT LINEAR BASELINE OVER EACH PEAK

In this case the assumed relationship is

$$A_{spi} = a_p + b_p v_{pi} + kA_{rpi} + e_{spi} .$$

Thus, the assumption made is of possibly different linear baselines within each peak.

4.4 METHOD 4: NEGLIGIBLE BASELINE SHIFT BETWEEN SUCCESSIVE DATA POINTS

In this case the assumed relationship is

$$\Delta A_{si} = k\Delta A_{ri} + e_{si} .$$

The differences considered are only those within a peak. This model is of the same form as that for method 1, so the least squares estimate of k is identical, but with ΔA 's replacing the A 's.

5. TRIAL 1: RETRIEVAL FROM SYNTHETIC SPECTRA

Before field measurements were undertaken, the algorithm was tested against synthetic spectra that were generated with FASCODE. These data have a spectral bandpass of 2000.0 cm^{-1} to 3000.0 cm^{-1} and a resolution of 0.0300 cm^{-1} . The simulated pathlength is 1.5 km. The output is shown in table 3. A favorable comparison is given in table 4. Sample spectral lines are displayed in fig. 7.

6. TRIAL 2: RETRIEVAL FROM FIELD SPECTRA

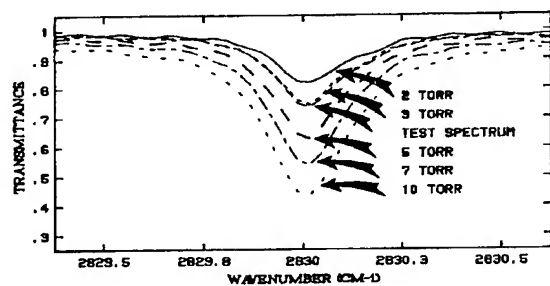
FTS transmittance measurements were made over a 1.115-km path at Dirt Site, White Sands Missile Range, during August and September 1991. A Bomem Inc., Model DA02 high-resolution field spectrometer was utilized in this experiment (Kantrowitz, 1987). Data sets 7, 8, 10, and 12 have a spectral resolution of 0.0593 cm^{-1} . The remaining data have 0.0386 cm^{-1} resolution. The IR source for this test was a $1,400^\circ\text{C}$ blackbody. The transmitting optics utilized a 0.9-m Cassegrain telescope. In fig. 8a, a measured H_2O line is compared with a FASCODE waterline with 10.0 torr partial pressure. In fig. 8b, a measured CO_2 line is weighed against a FASCODE CO_2 line for a concentration of 330.0 ppm. Figure 8c displays both a measured CH_4 and a 1.7-ppm synthetic line. An N_2O line is presented in fig. 8d. The synthetic line is for a concentration of 0.320 ppm. Finally, in fig. 8e, a measured CO line is compared with a 0.150-ppm synthetic line. The results of the retrievals are displayed in table 5. With the exception of data sets 11 and 12, the spectroscopically measured H_2O concentrations (column 1) are in good agreement with the dew-point sensor data. A vehicle engine was in operation near the source during data acquisition for data sets 5, 6, 9, and 12. As a result, the CO_2 concentrations were elevated at those times. It is unknown why the CO concentrations did not appear to increase or why the N_2O concentrations are somewhat higher than expected. The data were obtained in a desert environment and are reflected in the low average CH_4 concentrations.

TABLE 3. CONCENTRATIONS RETRIEVED FROM SYNTHETIC SPECTRUM FOR THE INDIVIDUAL FITTING ROUTINES

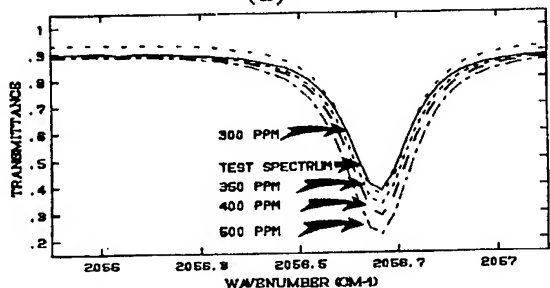
Species	Fit 2	Fit 3	Fit 4
H_2O	3.0496E+00	3.0496E+00	2.8743E+00
CO_2	3.3768E+02	3.3768E+02	3.3598E+02
N_2O	3.1203E-01	3.1203E-01	2.6359E-01
CO	1.3500E-01	1.3500E-01	1.5400E-01
CH_4	1.6607E+00	1.6607E+00	1.6620E+00

TABLE 4. COMPARISON OF SYNTHETIC INPUT CONCENTRATIONS AND RETRIEVED CONCENTRATIONS

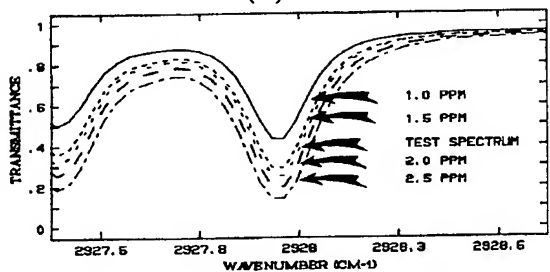
Species	Input Concentration	Retrieved Concentration	Delta (%)
H_2O	3.000 torr	2.991 torr	-0.003
CO_2	330.000 ppmv	337.110 ppmv	+2.150
CO	0.150 ppmv	0.141 ppmv	-6.0
N_2O	0.320 ppmv	0.296 ppmv	-7.5
CH_4	1.700 ppmv	1.661 ppmv	-2.3



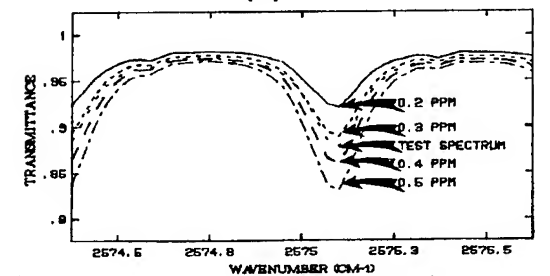
(a)



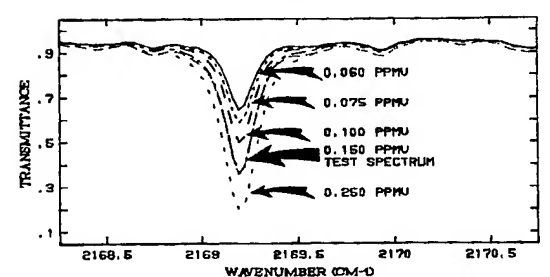
(b)



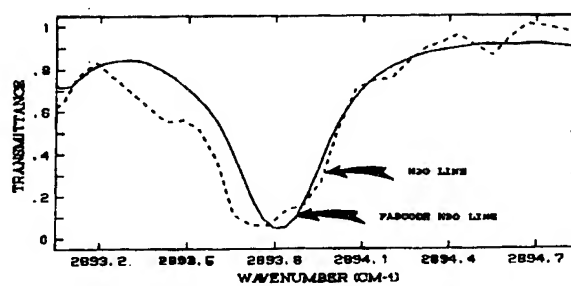
(c)



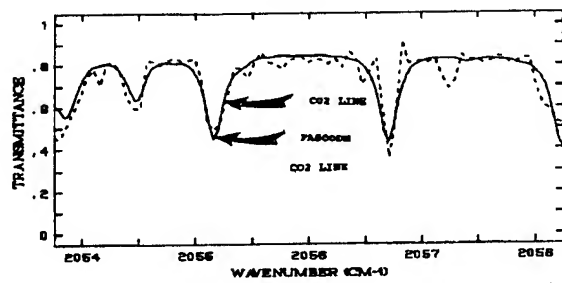
(d)



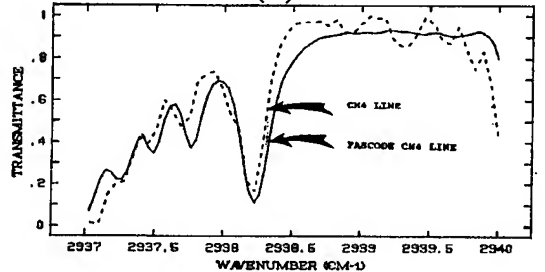
(e)



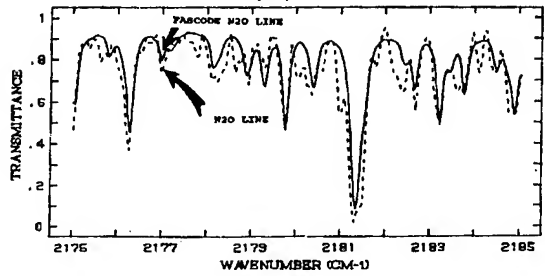
(a)



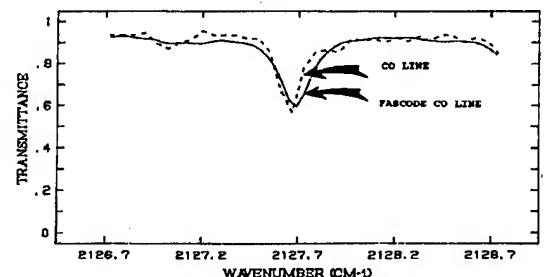
(b)



(c)



(d)



(e)

Figure 7. Synthetic spectra for H_2O , CO_2 , CH_4 , N_2O , and CO .

Figure 8. Measured versus synthetic spectra for H_2O , CO_2 , CH_4 , N_2O , and CO .

TABLE 5. RETRIEVAL OF ATMOSPHERIC CONSTITUENTS FROM FIELD DATA

Data Set	H ₂ O* (torr)	H ₂ O† (torr)	CO ₂ (ppmv)	CO (ppmv)	N ₂ O (ppmv)	CH ₄ (ppmv)
1.	9.38	9.23	322.7	0.104	0.480	0.976
2.	----	8.56	478.3‡	0.157	0.517	1.198
3.	9.79	9.58	332.5	0.179	0.420	1.396
4.	8.09	8.56	337.0	0.086	0.667	1.100
5.	7.83	7.64	510.4‡	0.136	0.573	1.119
6.	14.88	13.82	486.8‡	0.161	0.459	1.156
7.	12.38	13.34	374.9	0.196	0.341	0.840
8.	10.31	12.86	330.6	0.163	0.473	1.100
9.	10.80	11.96	495.4‡	0.133	0.570	1.083
10.	10.04	11.53	335.2	0.176	0.487	1.221
11.	8.39	11.11	364.6	0.177	0.660	1.243
12.	7.63	11.11	441.5‡	0.156	0.351	1.052

*Determined from spectral data. †Determined from dew-point sensor.

‡Indicates that a vehicle engine was running near the source.

7. CONCLUSIONS

The long-term effects of the Persian Gulf oil fires are beyond the scope of this report. This investigation is meant as a snapshot of what is possible with an FTS and a horizontal path retrieval algorithm. For the present, it appears that the levels of CO₂ and CO have not increased in the American Southwest Desert.

We hope that with the addition of toxic gas libraries, this algorithm may be utilized to monitor gases that could impact human lives during military operations. The work presented is part of a greater effort in research into the effectiveness of new state-of-the-art retrieval algorithms for thermal and constituent characterization over horizontal and vertical paths. Testing of a vertical path algorithm with synthetic spectra will begin this fall. The acquisition of vertical path spectral data will commence in early 1992. Results of this investigation will be reported shortly thereafter.

REFERENCES

- Bingemer, H. G., and P. J. Crutzen, 1987: The Production of Methane from Solid Wastes. J. Geophys. Res., 92:2181-2187.
- Blake, D., and S. Rowland, 1987: Increasing Global Concentrations and Tropospheric Methane. Symposium on Atmospheric Methane: Formation of Fluxes from the Biosphere and Geosphere, American Chemical Society, Denver, CO.
- Cicerone, R. J., 1988: How Has the Atmospheric Concentration of CO Changed? Report of the Dahlem Workshop on the Changing Atmosphere, Berlin, Germany.
- Clough, S. A., F. X. Kneizys, E. P. Shettle, and G. P. Anderson, 1986: Atmospheric Radiance and Transmittance: FASCOD2, Sixth Conference on Atmospheric Radiation, Williamsburg, VA.

- Ehhalt, D. H., 1988: How Has the Atmospheric Concentration of CH₄ Changed? Report of the Dahlem Workshop on the Changing Atmosphere, Berlin, Germany.
- Haaland, D. M., and R. G. Easterling, 1980: Improved Sensitivity of Infrared Spectroscopy by the Application of Least Squares Methods. Appl. Spectros., 34:(5):539-548.
- Haaland, D. M., R. G. Easterling, and D. A. Vopicka, 1985: Multivariate Least-Squares Methods Applied to the Quantitative Spectral Analysis of Multicomponent Samples. Appl. Spectros., 39:(1):73-84.
- Heidt, L. E., J. P. Krasnec, R. A. Lueb, W. H. Pollack, B. E. Henry, and P. J. Crutzen, 1980: Latitudinal Distributions of CO and CH₄ Over the Pacific. J. Geophys. Res., 85:7329-7336.
- High Energy Laser Propagation Handbook, Volume I, Phenomenological Basis, 1984: ASL-TR-0148, U.S. Army Atmospheric Sciences Laboratory, White Sands Missile Range, NM.
- Kantrowitz, F., 1987: Fourier Transform Spectrometer and Mobile Spectroscopy Laboratory. Technical Memorandum: U.S. Army Atmospheric Sciences Laboratory, White Sands Missile Range, NM.
- Kantrowitz, F. T., 1990: A VAX/VMS/GKS Format Version of the Fast Atmospheric Signature Code (FASCODE 2) with Comparisons to ASL Field Spectroscopic Data. ASL-TR-0269, U.S. Army Atmospheric Sciences Laboratory, White Sands Missile Range, NM.
- Logan, J. A., M. J. Prather, S. C. Wofsy, and M. B. McElroy, 1981: Tropospheric Chemistry: A Global Perspective. J. Geophys. Res., 86:7210-7254.
- Matise, B., 1988, private communication, OptiMetrics, Inc.
- Neftel, A., E. Moor, H. Oeschger, U. Siegenthaler, and B. Stauffer, 1985: Evidence from Polar Ice Core Record for the Increase in Atmospheric CO₂. Nature, 315:45-47.
- Oeschger, H., and U. Siegenthaler, 1988: How has the Atmospheric Concentration of CO₂ Changed? Report of the Dahlem Workshop on the Changing Atmosphere, Berlin, Germany.
- Prinn, R. G., 1988: How Has the Atmospheric Concentration of the Halocarbons Changed? Report of the Dahlem Workshop on the Changing Atmosphere, Berlin, Germany.
- Rothman, L. S., et. al., 1987: The HITRAN Database: 1986 Edition. Appl Opt., 26:(19):4058-4096.
- Rowland, F. S., and I. S. A. Isaksen, 1988: Introduction, Report of the Dahlem Workshop on the Changing Atmosphere, Berlin, Germany.

PORTABLE WEATHER TESTBED

John R. Elrick

U.S. Army Atmospheric Sciences Laboratory
White Sands Missile Range, New Mexico 88002-5501, USA

ABSTRACT

The U.S. Army has a continuing need for accurate, real-time weather support. This is true for peacetime exercises and in times of conflict to ensure that operations are successful or that logical alternatives can be exploited. Advances in satellite meteorology and meteorological sensors have made this real-time support to day-to-day operations possible. The U.S. Army Atmospheric Sciences Laboratory (ASL) has procured a portable weather workstation that can fulfill the Army's needs. The system is lightweight and can be carried by two people in a backpack configuration. The unit will gather satellite data from both polar-orbiting and geostationary satellites as well as high-frequency radio data. The data that is collected includes satellite imagery and analyzed weather facsimile charts as well as data from local sensors and forecasts and weather observations. Messages may also be received and transmitted by this system by means of a built-in transceiver. Valuable information in the form of tactical decision aids are included on the system to aid battlefield decision makers in making valid decisions based on current or projected weather. The unit is completely redundant in its satellite reception capability, having two identical satellite receivers. The system is currently being tested by ASL scientists for its utility in supporting U.S. Army operations.

1. INTRODUCTION

The U.S. Army Atmospheric Sciences Laboratory (ASL) has procured a second-generation portable weather workstation that will receive and process automatic picture transmission (APT), weather facsimile (WEFAX), high-frequency facsimile (HFFAX), and HF broadcasts of weather observations and forecasts. This unit's primary function is to provide the field meteorologist with an autonomous weather support workstation. The equipment has been designated the portable weather testbed (PWTB). The workstation will process satellite imagery with enhancements, colors, text, labels, and symbols. Additional computer software consisting of weather forecaster aids and tactical decision aids (TDAs) has been added to the workstation for assessing the effect of weather on day-to-day operations and to aid in meteorological data analysis and management.

The PWTB has two primary components: the antenna assembly and the 386-based computer workstation. One person can easily assemble or disassemble and pack the entire system in 1 h or less. All components of the system are packed in

two "backpacks" for easy handling and transportability for use by very mobile U.S. Army units.

2. HARDWARE

2.1 ANTENNA ASSEMBLY

The antenna group consists of three separate antennas: a long-wire, HF radio antenna; a dual-boom loop Yagi antenna; and an omnidirectional quadrifilar antenna. These antennas will be discussed here.

The long-wire, HF antenna consists of two 50-ft lengths of copper wire erected in an inverted "V" configuration. It is used to receive HFFAX charts, HF regional broadcast system weather observations and forecasts, and WWV timing signals for accurately setting the computer system clock. The new dual boom loop Yagi antenna is made of two 6-ft rods with circular focusing elements along the length of the antenna with a final focusing element at the rear of each antenna. The two antennas each separate into three 2-ft segments that can be meshed together for easy handling. This antenna assembly replaces the normal 3- to 4-ft dish that is commonly used. This antenna receives transmissions of WEFAX information from geostationary satellites. Data received come from U.S. National Oceanic and Atmospheric Administration (NOAA), European Meteosat, and Japanese Geostationary Meteorological Satellite (GMS) satellites. NOAA data is received directly after processing, and the data from the other two sources are relayed by the NOAA Geostationary Operational Environmental Satellite (GOES).

The quadrifilar antenna is a finely tuned, omnidirectional antenna used to receive real-time APT imagery from low-earth, polar-orbiting satellites. Real-time imagery is received from U.S., Soviet, and Chinese satellites. The antenna assembly consists of a ground anchored tripod, a number of antenna extensions, stabilizing guy-ropes, and ground stakes. The antenna group can be used up to 100 ft from the PWTB computer workstation.

2.2 WORKSTATION UNIT

The system workstation is made up of a 386-based IBM compatible personal computer with a 387-math coprocessor operating under PC-MOS. Keyboard, mouse, and video interfaces are available. The primary display is video graphics array (VGA) compatible with a 640- by 480-pixel resolution, included is a 5-in TV monitor for the rapid deployment mode of operation. Satellite reception is accomplished through redundant QUORUM satellite receivers. An uninterruptible power supply allows the system to operate for up to 1 h under full load and much longer if usage is limited. It is capable of working on a set of system solar cells or commercial power anywhere in the world. The unit has hardcopy printout capability with a Kodak Diconic 150-ink jet printer. A transceiver is installed on the system to receive and transmit data at the workstation. A Digital weather sensor is included to make local observations of temperature, relative humidity, pressure, wind, and rainfall accumulation.

3. WEATHER EFFECTS DECISION AIDS AND FORECASTER TOOLS

Weather effects decision aids and forecaster tools are installed on the PWTB's computer workstation in an attempt to help the field commander and his staff understand and solve some of their weather problems. These tools are specifically designed to be flexible and user-friendly and are structured as a software package composed of a series of utility and applications programs. TDAs are available in the following categories:

- meteorological analysis
- weather effects
- weapon system performance
- refractive index analysis

Other TDA categories will be added as they become available to ASL.

4. SUMMARY

ASL has obtained a second-generation, portable weather testbed that is two-man portable in a backpack configuration. It can receive polar-orbiting APT imagery, geostationary WEFAX imagery and charts, and HFFAX charts and HF text broadcasts. It is also equipped with a transceiver to collect and transmit data at the workstation. A sensor is included in the package for automated local weather observations. The PWTB is capable of autonomous operation and can be used with commercial power worldwide or solar cells. Forecaster tools and TDA software have been added to the PWTB to aid personnel in assessing the effects of weather on specific operations, personnel, or equipment. TDAs can be used by the field commander or his staff to account for adverse effects that the weather may have on current activities or future plans.

THE KUWAIT SMOKE PLUME AS A SOURCE OF BATTLEFIELD OBSCURATION

Howard Holt, Robert Sutherland, and John Grace
U.S. Army Atmospheric Sciences Laboratory
White Sands Missile Range, New Mexico 88002-5501, USA

S. A. Luces
Physical Science Laboratory
New Mexico State University, Las Cruces, New Mexico 88003, USA

William Ohmstede
Wm Ohmstede, CCM
Las Cruces, New Mexico 88001, USA

John Barnes
Computer Sciences Corporation
White Sands Missile Range, New Mexico 88002-5501, USA

Kenneth Chin-Purcell
Army High Performance Computing Research Center
Minneapolis, Minnesota 55454, USA

ABSTRACT

The Kuwait oil fire disaster is an opportunity to evaluate the concepts implicit in the Army Regional Aerosol Transport Simulation (ARATS). This simulation describes the transport of clouds of particles in the atmosphere on a battlefield scale. The Kuwait smoke plume is an example of battlefield obscuration that produced a cloud of particles of sufficient concentration to be readily visible over distances of several hundred kilometers. This plume is under surveillance from a geostationary satellite (METEOSAT) and several polar orbiters so that the verification of the ARATS predictions can be precise and rigorous. The ARATS includes a meteorological code and a particle code. These codes, together with codes describing the source function and particle concentrations, are run on the supercomputers of the Army High-Performance Computing Research Center. Results are displayed by three-dimensional, multicolor, dynamic video techniques simulating 24 h of plume development. Emphasis is being placed on the inter-comparison of meteorological codes, which is enabled by our modular concept.

1. INTRODUCTION

The Army must fight effectively in the degraded environment of the realistic battlefield. One feature of this degradation is the enhanced aerosol content of the atmosphere due to battlefield activities. This enhanced content reduces the range of laser rangefinders, blurs the images of targets, modifies the

PURPOSE

This project was started with the intent of studying the long-range aerosol effects due to battlefield and other atmospheric particles.

The project involves examining Army problems with a modular collection of off-the-shelf models.

The research focusses on the effects of the changing surface, boundary layer, atmospheric thermal structure, and wind field on the long-range transport and diffusion of obscurant particles.

This study takes advantage of an existing tracer to help verify models and techniques.

APPROACH

A system was developed called the Army Regional Aerosol Transport Simulation (ARATS). Conceptually, it includes identifying the influence of the source, synoptics, dispersion, and effect of resultant concentration.

Source

Initial concentration, temperature, etc.

Synoptics

Observations/climatology and forecasts

Dispersion

Models for cloud spread

Results

Visibility, toxicity, or optical depth

behavior of both biological and chemical toxic clouds, and degrades the performance of high-energy laser systems. The local effects of battlefield obscurants and clouds of toxic and radioactive products are well understood. However, if under certain meteorological conditions these effects may be felt at extended ranges, it is important to be able to predict when this may occur and to calculate the magnitude of the effects. The Army payoff is the reduction in surprise and the opportunity to mitigate the severity of the effects.

The accompanying inserts describe the purpose and approach taken in the work. Long-range aerosol effects are known to occur in the troposphere, particularly in the planetary boundary layer, so the research is focused in this area. The approach taken is described in terms of the Army Regional Aerosol Transport Simulation (ARATS) concept of the simulation of long-range aerosol effects in the atmosphere.

The remainder of the paper discusses the evaluation of this concept by applying it to the Kuwait smoke plume--a spectacular example of battlefield obscuration.

2. THE ARATS MODULES AND PRELIMINARY STUDIES

The modeling system selected for the study of long-range aerosol transport and diffusion includes a meteorological prediction model with sufficient physics to depict the dynamics of the planetary boundary layer, a Monte Carlo particle transport and diffusion model (driven by the winds and turbulence predicted by the meteorological model), and a concentration model based on particle location and statistics.

The initial meteorological model chosen for use in ARATS was called SIG1D--a one-dimensional version of the ASL SIGMET mesoscale model derived from the model of Anthes and Warner (1974). This model was subsequently replaced by the more comprehensive Regional Atmospheric Modeling System (RAMS) developed at Colorado State University (Tripoli and Cotton, 1982). The Monte Carlo particle model was developed by Ohmstede (1991) based on the work of Gifford (1982). In this model the particle locations are found by integrating the advecting effect of the wind and adding Monte Carlo velocity components that are scaled by the size of the turbulence. Significant features include a variable integration time step based on the size of the turbulence and the vertical wind shear. Ohmstede also provided the concentration model that was based on probability distribution functions assumed around each simulated particle location.

Using the SIG1D model, Holt et al. (1990) investigated the influence of initial windspeed and the strength of the temperature inversion on the transport of battlefield dust. They (Holt et al., 1991) followed this investigation with investigations in one and two dimensions, using the RAMS model to study the effects of vertical wind shear, soil moisture, and cloud cover. The vertical wind shear results showed that a wind profile that veered with height (which corresponds to warm air advection) produced a concentration pattern that spread extensively and had no areas of high concentration. On the other hand, a wind backing with altitude (typical of cold air advection) resulted in a long, thin plume pattern with high particle concentration. This result may bear on a question that arose in the course of the CAPTEX (Cross-Appalachian Tracer Experiment) study (Kao and Yamada, 1988); namely, why was the CAPTEX grid able to detect particles when the release was from the west but not for releases from Canada after cold front passage? Our suggestion is that the sensor grid was too widely spaced to detect this plume in this case.

3. MODEL IMPLEMENTATION ON THE ARMY HIGH-PERFORMANCE COMPUTING RESEARCH CENTER COMPUTERS

The modules of ARATS have been implemented on the Cray computers of the Army High-Performance Computing Research Center (AHPCRC). Four independently executable modules are used for the implementation. The modules are kept as independent entities to give the researcher flexibility in choosing meteorological models, particle motion models, analysis schemes, visualization options, and a rich variety of machine architectures upon which to implement the modules. Generation of the modules is controlled by UNIX makefiles--the CF77 compiling system for three of the modules and a C compiler for the fourth. Module execution is controlled by the researcher using UNIX shell scripts and the network queuing system job control facility. The four modules are the following:

RAMS--an executable binary to produce meteorological data, specifically wind fields. The binary is named for the Regional Atmospheric Modeling System. RAMS is initialized with weather information and produces an ASCII file for input to the ANALYSIS binary. RAMS source code is written in FORTRAN 77.

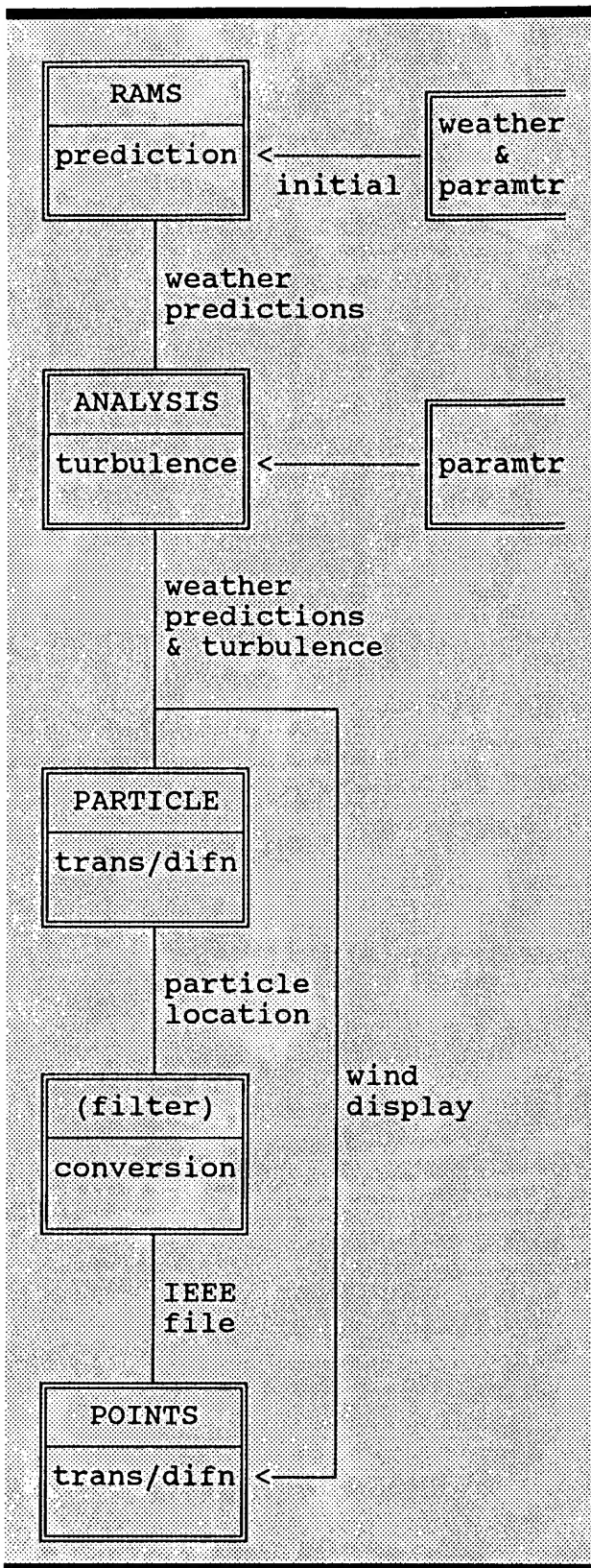


Figure 1. ARATS flowchart.

ANALYSIS--an executable binary to analyze meteorological data from the RAMS binary and to produce turbulence statistics from the wind field data. ANALYSIS reads the ASCII file from RAMS and produces an unformatted binary data file for input to the PRATICLE binary. ANALYSIS source code is written in FORTRAN 77.

PARTICLE--an executable binary of a Lagrangian force model. It produces particle transport by using the wind data from the ANALYSIS binary and Monte Carlo location increments related to the turbulence strength. PARTICLE reads the unformatted binary file from ANALYSIS and produces an unformatted binary data file for input to various post-processing routines, but specifically as input for scientific visualization. PARTICLE source code is written in FORTRAN 77 and also in FORTRAN 90 (8X).

A filter program was written to convert the particle and wind data from Cray to IEEE (Institute of Electrical and Electronic Engineers) floating point format for use on the Silicon Graphics 4D workstation.

POINTS--an executable binary to produce visualization of particle transport from data produced by the PARTICLE binary. This module is written in C, specifically for Silicon Graphics, Incorporated, workstations using the standard AVS graphics package.

The above modules are linked together by data files and by software filters that convert the files into specific internal formats for various machine architectures.

A typical production run of the combined modules and linking data files consists of particle movement

across a 30 by 30 grid with 30 km spacing between grid points. Vertically, 34 levels are used with atmospheric parameters calculated for each level. Motion for approximately 10,000 particles (100 every 15 min) is calculated over the grid for a 24-h modeling period. Under the above initial conditions, table 1 shows an approximate usage of computer resources.

The first column lists the four executable binaries that are combined to produce the visualization of the particle movement.

The second column lists the three data files that link the four modules together.

The third column indicates the amount of machine time required for a typical production run.

Columns 4 and 5 are self-explanatory.

TABLE 1. COMPUTER RESOURCE USAGE

Module	Data file format	CPU time (min)	File size (Mbytes)	Module size (Mbytes)
RAMS*		83		1.8
	ASCII		85	
ANALYSIS*		8		1 +
	binary		252	
PARTICLE*		21		1.7
	binary		188	
POINTS**		***		small

*Machine architecture is a CRAY Research, Inc., CRAY-2.

**Machine architecture is a Silicon Graphics, Inc., 4D/320.

***CPU time depends on visualization required.

4. MODEL EVALUATION AND THE KUWAIT SMOKE PLUME--TARGET OF OPPORTUNITY

The evaluation of mesoscale and regional scale meteorological models requires extensive field data. This data may consist of meteorological data (that is, windspeed, wind direction, temperature, humidity, and pressure) gathered over the volume and time scales appropriate to mesoscale and regional scale regimes. Or it may consist of a combination of meteorological and tracer observations in the same four-dimensional matrix. The potential advantage of the latter approach is that the tracer depicts the wind field with a precision that cannot be equalled by direct measurement, due to the costs involved. We observe that an adequate tracer experiment itself may also be unaffordable!

The Kuwait smoke plume can be looked upon as a tracer experiment on the meso-scale and regional scale. This is not to belittle the ecological disaster or the human and economic costs this tragedy represents.

For the same reasons the Kuwait smoke plume is the subject of intense interest and of a determined effort by the worldwide meteorological community to build a comprehensive data base describing its characteristics. ASL is contributing to the acquisition of this data base.

The Kuwait smoke plume data base consists of meteorological observations, satellite images, and various specialized ground-based and aircraft measurements. It is being made available to scientific investigators. Whatever its inadequacies turn out to be, it represents an incomparable collection of data for the purpose of evaluating mesoscale and regional scale meteorological models.

5. VISUALIZATION OF PARTICLE LOCATIONS USING THE SILICON GRAPHICS WORKSTATION

Visualizing the result of the particle simulation proved to be useful for both verifying and interpreting the data. When the plume was animated, all of the data could be quickly viewed, different runs compared, critical regions inspected, and insight gained into the interactions between the particles and the wind field.

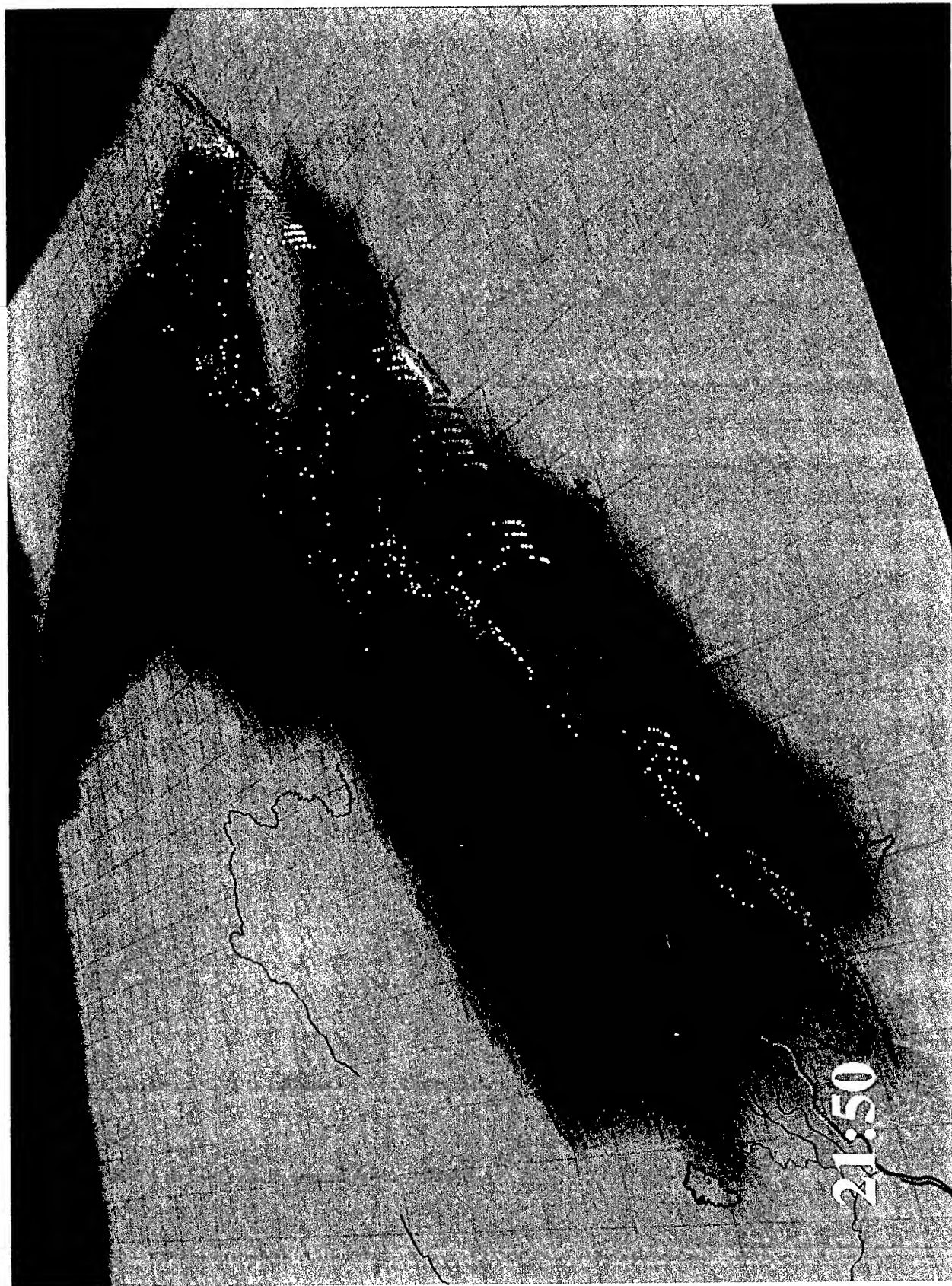
A computer workstation with high-speed graphics hardware was used to portray the particle data in three dimensions, over a terrain map of the Persian Gulf. The scene was continuously redrawn to animate the progress of the particles downwind.

A custom graphics program was written to integrate the particles, wind velocities, terrain, and political borders into a common scene. The program can orient the scene. Either a mouse or a script file can be used. The final visualization was recorded by running the program from a script with the computer output being converted in real time to video. Several frames were also digitally captured and sent to a color printer.

6. STUDIES WITH THE KUWAIT SMOKE PLUME

A realistic representation of the source of the Kuwait smoke plume must account for the buoyancy due to the heat energy of the oil fires. This was done by using the work of Cogan (1985) and Weil (1982) to develop buoyancy equations. The resulting model was tuned by using the results of previous studies of battlefield fires and the plume altitude measurements made by the United Kingdom (UK) Meteorology Office aircraft in March-April 1991 (Maryon, 1991).

A grid of 30 by 30 grid points in the horizontal and 34 grid points in the vertical was used. The horizontal grid spacing was 30 km. This grid encompassed the Persian Gulf region from Kuwait to the Strait of Hormuz. The prediction model (RAMS) and the transport and diffusion model (PARTICLE) were run on the Cray computers at the AHPCRC, and visualizations (using a computer code called POINTS) were produced on the Silicon Graphics workstations of the Visualization and Graphics Laboratory of the AHPCRC.



The first simulation used a single climatological wind profile representative of the entire region to initialize the meteorological model. The effects of varying the strength of the turbulence factor were investigated. The second simulation was initialized with the 00Z 2 March 1991 upper-air sounding taken at Dharhan. The sounding had much stronger windspeeds and more structure in the lowest levels than the climatological wind profile. In both cases the model produced a ground cloud which, in the climatological case, rose in the afternoon and became caught up in the land/sea breeze produced by the model. In the Dharhan initialization, the ground cloud was rapidly driven across the Gulf after being caught in the strong westerly low-level flow.

The following page shows a frame from the visualization of the plume using the upper-air sounding from Dharhan for 2 March 1991 to initialize the RAMS code. The number in the lower left corner, 21:50, indicates the time in hours and minutes into the 24-h simulation. The simulation is initiated at 0600. The particles are represented by spheres and are color coded, with a different color used every hour. The particles are released in the simulation every 15 min. The particle flow shows the effect of the strong westerly wind at the lower altitudes. At the higher altitudes the flow is predominantly to the south.

7. FUTURE STUDIES

At Colorado State University, these simulations are being expanded to include terrain elevation and full initialization using all available data for the case of 2-3 March 1991. The grid is also being nested to permit greater resolution in the source region. At New Mexico State University, LANDSAT (land remote sensing satellite) imagery is being analyzed to determine the location and concentration of the plume. At the UK Meteorological Office, simulations for this same case have been made by using both regional and mesoscale meteorological models.

These various simulations will be intercompared and analyzed with reference to the satellite imagery in an attempt to develop criteria for evaluating the attributes of different models.

ACKNOWLEDGMENTS

A grant from the University of Minnesota AHPARC is gratefully acknowledged. The unfailing cooperation and assistance of the AHPARC staff greatly contributed to our success. Outstanding help in running the RAMS code from Dr. Robert Walko, Atmospheric Science Department, Colorado State University, was an essential to this investigation. We are also thankful for the Kuwait surface and upper-air data provided by the U.S. Air Force Environmental Technical Applications Center.

REFERENCES

- Anthes, R. A., and T. T. Warner, 1974: Prediction of Mesoscale Flow over Complex Terrain. ECOM-5532, U.S. Army Atmospheric Sciences Laboratory, White Sands Missile Range, NM 88002-5501.
- Cogan, J., 1985: Monte Carlo Simulation of Buoyant Dispersion. Atmos. Envir., 19:867-878.
- Gifford, F. A., 1982: Horizontal Diffusion in the Atmosphere: Lagrangian-Dynamical Theory. Atmos. Envir., 16:505-512.
- Holt, E. H., S. A. Luces, and W. D. Ohmstede, 1990: Regional Visibility Degradation: Application to Conventional Warfare Scenarios. In Proceedings SPIE, Propagation Engineering, 1312:2-13.
- Holt, E. H., R. A. Pielke, R. L. Walko, S. A. Luces, and W. D. Ohmstede, 1991: Methodology for Modeling Extreme Effects of Aerosol Particles Transported on a Regional Scale. In preprint volume for The Seventh Joint Conference on Applications of Air Pollution Meteorology with AWMA, January 14-18, 1991, New Orleans, LA, American Meteorological Society, Boston, MA.
- Kao, C-Y. J., and T. Yamada, 1988: Use of the CAPTEX Data for Evaluations of a Long-Range Transport Numerical Model with a Four-Dimensional Data Assimilation Technique. Mon. Wea. Rev., 116:293-306.
- Maryon, R., 1991: Meteorological Office, United Kingdom, private communication.
- Ohmstede, W. D., 1991: A Novel Application of a "Particle" Model to the Problem of Long-Range Transport and Diffusion. In preprint volume for The Seventh Joint Conference on Applications of Air Pollution Meteorology with AWMA, January 14-18, 1991, New Orleans, LA, American Meteorological Society, Boston, MA.
- Tripoli, G. J., and W. R. Cotton, 1982: The Colorado State University Three-Dimensional Cloud/Mesoscale Model - 1982. J. Res. Atmos., 16:185-219.
- Weil, J. C., 1982: Source Buoyancy Effects in Boundary Layer Diffusion. In Proceedings of the Workshop on the Parameterization of Mixed Layer Diffusion, Physical Science Laboratory, New Mexico State University, Las Cruces, NM 88003.

RAPID DEPLOYMENT IMAGERY TERMINAL (RDIT) USING DMSP SPECIAL SENSOR DATA

Presented by
Thomas L. Harris
Harris Corporation (Omaha Operations)
Bellevue, NE 68005

ABSTRACT

Recently, Harris Corporation developed a Rapid Deployment Imagery Terminal (RDIT) which the Government deployed in support of Desert Shield/Desert Storm operations. This small, lightweight, and rapidly deployed terminal can ingest, process, and display the Defense Meteorological Satellite Program (DMSP) visual and infrared imagery which was used to identify clouds, bodies of water, fires, and pollution. However, DMSP special sensors also have the ability to remotely sense additional information which can help identify cloud type and height, land and water surface temperatures, water currents, ocean features, ice and snow, and vertical temperature/moisture profiles of the atmosphere. Harris IR&D effort have now made it possible, using only DMSP data, to create, in real-time, most of the meteorological analyses needed to support deployed combat forces. This presentation will provide an overview of the RDIT system, the applications of DMSP special sensor data, and an approach to providing these technologies to deployed IMETS.

The paper accompanying this demonstration appears in Session IV, page 202.

Session V

PBL ENERGY BUDGET POSTERS AND DEMONSTRATIONS

**Chairperson
Dr. Austin Hogan**

EVAPOTRANSPIRATION AND LATENT HEAT FLUX

IN THE SURFACE BOUNDARY LAYER

Frank V. Hansen, Henry Rachele, and Arnold Tunick
U.S. Army Atmospheric Sciences Laboratory
White Sands Missile Range, New Mexico 88002-5501, USA

ABSTRACT

Viable solutions for the turbulent kinetic energy budget, the surface energy balance, and the dynamic and thermodynamic characteristics of the atmosphere's Ekman layer are categorically dependent on, and highly susceptible to, the vagaries of evapotranspiration and the associated latent heat fluxes into the lowest portions of the atmosphere. The vertical flux of latent heat, particularly into the surface boundary layer, will reduce both the ambient temperature and the sensible heat flux, resulting in a more dynamically stable layer immediately above the air-earth interface. Other immediate effects include modification to the index of refraction and the propagation of electromagnetic energy through the atmosphere. Evapotranspiration rates can be shown to be functions of the soil water content, insolation and net radiation, season of the year, and soil types; all with respect to precipitation amounts and the time since rainfall ended. Actual evapotranspiration can be related to potential evapotranspiration through a moisture availability coefficient that is unity at field capacity and approaches zero under extreme stress conditions.

Experimental evapotranspiration data as a function of temporal distribution is used to semiempirically evaluate the availability coefficient. The effects of evaporative cooling upon the surface layer are demonstrated as well as the dramatic effects of water vapor deficits on the sensible heat flux, surface temperatures, refractive indices, and stability.

1. INTRODUCTION

Water vapor in the atmosphere at any point or time may be considered as originating from two sources: local evaporation from the surface and the advection of moist air from regions outside the immediate area of interest. The increase of humidity from advection must be considered when dealing with atmospheric processes involving the turbulent kinetic energy budget or the surface energy balance. Specifically, when dealing with buoyant heat fluxes in the surface boundary layer, the portion of the energy contributed by the latent heat flux can be in error if the atmospheric water vapor is assumed to originate entirely from evaporation.

Evaporation from a bare surface or evapotranspiration from a vegetated surface is a function of soil physics, soil heat fluxes, net radiation, volumetric water content of the soil, and the time since natural or artificial irrigation ended. Natural irrigation may be defined as precipitation.

Parameterization of the dynamic or thermodynamic structure of the surface boundary layer of the atmosphere can be accomplished by using semiempirical or engineering estimate approaches. These techniques can be based upon much simplified and modified forms of the Penman (1948) or Monteith (1965) evaporation schemes, when combined with the dynamic similarity of flow theory of Obukhov (1946).

2. MISCELLANY AND POTPOURRI

Semiempirical parameterization and amplification of any scheme leading to practical engineering estimates of atmospheric surface boundary layer processes require some clarification and the tying together of some seemingly unrelated principles. A primary assumption, based upon the work of Brunner (1977), is that the relative humidity is constant in the first 100 or so meters of the atmosphere. This premise allows specific humidity and vapor pressure profiles to be established from wet- and dry-bulb temperature measurements at one level above the surface.

The saturation vapor pressure e_s can be calculated for any temperature T at any height Z using Tetens' (1930) formula

$$e_s = 6.11 \left(10^{\frac{aT}{T+b}} \right) , \quad (1)$$

where T is in degrees Celsius and

over ice, $a = 9.5$, $b = 265.5$

over water, $a = 7.5$, $b = 237.3$.

If the relative humidity is known, then the ambient vapor pressure is found from

$$e = e_s (RH) , \quad (2)$$

where RH is the relative humidity in percent. Specific humidities are determined from

$$q = 0.621 \frac{e}{p - 0.379e} , \quad (3)$$

where p is the atmospheric pressure.

The density of moist air may be found from

$$\rho_w = \frac{p}{R\theta_v} , \quad (4)$$

where R is the gas constant and θ_v the virtual potential temperature given by

$$\theta_v = \frac{\theta}{1 - 0.379e/p} \quad (5)$$

Establishment of evaporation rates and their influences upon latent heat fluxes and buoyancy are related to the specific humidity profile in the surface layer. In similarity theory form

$$q_* = \frac{k(q - q_o)}{\ln z/z_o + \psi_H(z/L)} \quad (6)$$

where q_* is a scaling humidity, k , Karman's constant, $\psi_H(z/L)$ the temperature diabatic influence function, and q_o the specific humidity at the surface roughness length Z_o . According to Myrup's (1969) semiempirical results,

$$q_o = \frac{RH}{1000} \left[3.74 + 2.64 \left(\frac{T_o}{10} \right)^2 \right] \quad (7)$$

where T_o is temperature at Z_o in degrees Celsius.

The surface energy balance is typically written in the form

$$R_N = H + LE + G \quad (8)$$

where G is the soil heat flux and given by

$$G = -\lambda \frac{\partial T_s}{\partial z_s} \quad (9)$$

where λ is the soil thermal conductivity and $\partial T_s / \partial z_s$ is the temperature gradient with respect to soil depth. Empirical micrometeorological solutions will sometimes assume that

$$G = 0.1 R_N \quad (10)$$

where R_N is the net radiation. Typically, soil heat fluxes will vary over the range $0.05 < R_N < 0.35$, depending upon soil characteristics.

The sensible heat flux with respect to the eddy diffusivity K_H is given by

$$H = -C_p \rho K_H \frac{\partial \theta}{\partial z} \quad (11)$$

where C_p is the specific heat of air at constant pressure, ρ density, and θ the potential temperature. Latent heat fluxes may be determined from

$$L E = -\rho L K_w \frac{\partial q}{\partial z} , \quad (12)$$

where L is the latent heat of vaporization, E the evaporation rate, and K_w the eddy diffusivity for water vapor, usually set equal to K_H . The buoyant heat flux can be shown to be

$$H = (H + 0.07 L E) \quad (13)$$

and is presumed to be dependent upon both evapotranspiration and horizontal advection of water vapor.

3. EVAPORATION

The release of water vapor from the soil to the atmosphere can be thought of as bare surface evaporation and evapotranspiration from vegetated surfaces and is a most complex boundary layer phenomenon. According to Penman (1948), the potential latent heat flux can be shown to be

$$L E = \frac{S}{S + \gamma} (R_n - G) + \frac{\gamma}{S + \gamma} (e_a - e_d) f(\bar{v}) , \quad (14)$$

where S is the slope of the saturation specific humidity curve versus temperature, γ is the psychrometric constant, e_a the saturation vapor pressure for ambient air, e_d the saturation vapor pressure at the dew point, and $f(v)$ given by

$$f(\bar{v}) = 0.35 \left(1 + \frac{\bar{v}}{100} \right) \quad (15)$$

over a grassy surface. \bar{v} is the mean horizontal windspeed.

To establish the actual evaporation, a moisture availability coefficient, such as suggested by Nappo (1975), may be expressed as

$$M = E/E_p . \quad (16)$$

Jackson, Idso, and Reginato (1976) were able to express M in terms of the increasing albedo of drying soils, as

$$M = (\alpha_d - \alpha) / (\alpha_d - \alpha_w) , \quad (17)$$

where α_d is dry soil albedo, α_w is wet soil albedo, and α is the albedo for a particular time. Albedo measurements were also found to be an ideal mechanism of integrating various drying ratios and partitioning the portions contributing to the energy limiting, or potential evaporation, and the soil limiting phases of the process. The coefficient M will vary from unity for a soil at field capacity to zero for a dry surface. The potential evaporation rate can be combined with the soil limiting rate E_s to obtain the actual evaporation or evapotranspiration rate:

$$E = ME_p + (1 - M) E_s. \quad (18)$$

The soil limiting rate was found by Ritchie (1972) to be

$$E_s = C t^{-1/2}, \quad (19)$$

where t is time in days and C varies with soil type and season of the year. Seasonal dependencies are a function of temperature and will vary by about a factor of 2 from winter to summer as shown in fig. 1. Moisture availability coefficients extracted from Jackson et al. (1976) are given in fig. 2.

The complexity of the evaporation process requires that the energy limiting and soil limiting phases be partitioned according to the starting times of the soil limiting fraction. Thus, eq. (17) must be rewritten as

$$E = ME_p + C \sum (M_{t-1} - M_t) (n - i + 1)^{-1/2}, \quad (20)$$

where n is the number of days after evaporation began.

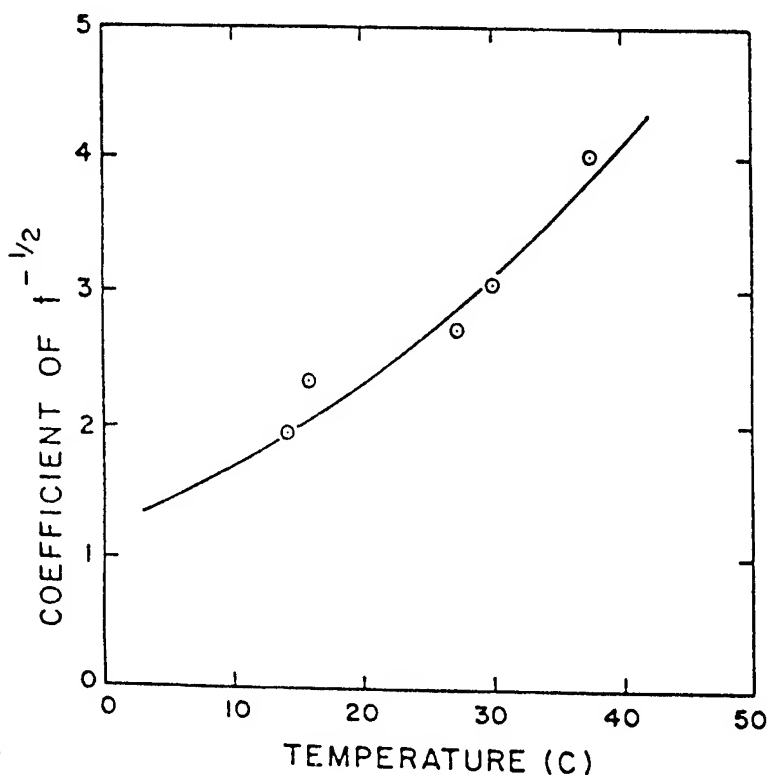


Figure 1. The temperature dependence of the square root of time coefficient (open circles) and of the water vapor diffusion in soil (line).

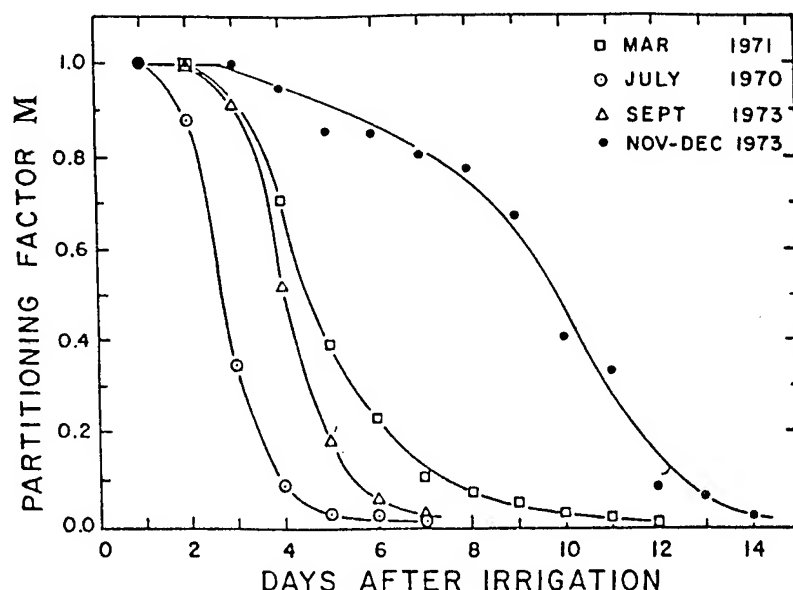


Figure 2. The moisture availability coefficient M as a function of days after irrigation for four experiments at different seasons of the year.

Dugdale (1989) empirically determined that daily evaporation could be represented by

$$E = 0.7 (E_p t^{-1}) \quad , \quad (21)$$

where again t is the number of days after rainfall ended.

The moisture availability coefficient M , based upon cumulative evaporation rate data, as extracted from Dugdale (1989), Jackson et al. (1976), Nappo (1975), Wilson and Rouse (1972), Jackson (1972) and Ritchie (1972) is presented in fig. 3.

4. POTENTIAL, APPARENT, AND ACTUAL LATENT HEAT FLUXES

The contribution of the latent heat flux to buoyancy in the surface boundary layer may be considered enigmatic. Potential evaporation or latent heat flux may be estimated by using eqs. (12) and (14). Apparent or actual latent heat fluxes may be found from eqs. (20) and (21). Latent heat flux estimates may also be formed by first considering the gradient Richardson (1920) number.

This number was initially formulated by using ambient potential temperatures rather than the concept of virtual potential temperature, which apparently was not perceived until the 1930's by Rossby (1932).

The Richardson number is given by

$$R_i = \frac{g}{\theta} \frac{\partial \theta / \partial z}{(\partial \bar{V} / \partial z)^2} \quad , \quad (22)$$

where g is the gravitational acceleration and \bar{V} the mean horizontal windspeed.

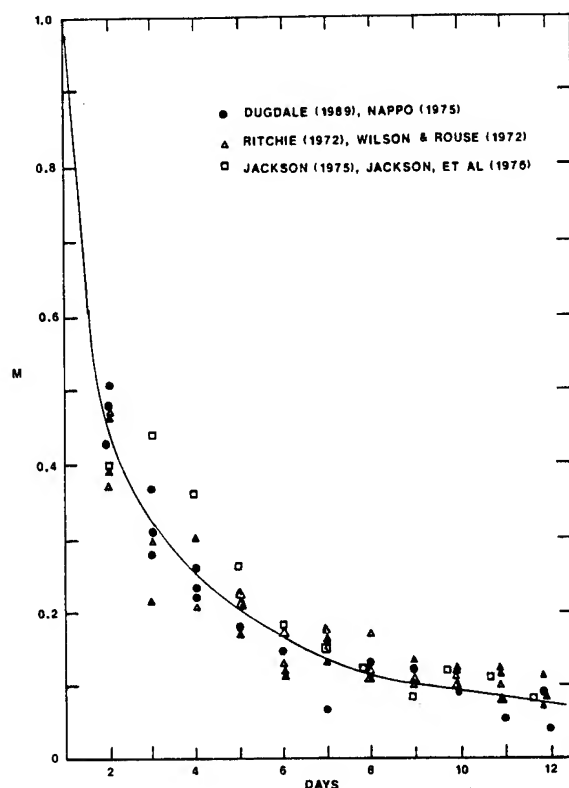


Figure 3. The moisture availability coefficient based upon cumulative evaporation over a 12-day period.

R_i is related to the Obukhov (1946) scaling length L by

$$\frac{z}{L} = R_i \Phi_m \frac{K_H}{K_M} = R_i \frac{\Phi_H}{\Phi_M^2} , \quad (23)$$

where $\frac{k_H}{k_M}$ is the ratio of the exchange coefficients for heat and momentum. The parameters Φ_M and Φ_H are the dimensionless winds shear and lapse rate, respectively.

The Monin and Obukhov (1954) scaling ratio z/L is then given by

$$\frac{z}{L} = - \frac{kgz (H + 0.07 L E)}{u_*^3 C_p \rho_w \theta} , \quad (24)$$

where k is Karman's constant and u_* the scaling or friction velocity.

In a thermally stratified unstable temperature regime, $z/L \equiv R_i$. This allows eq. (24) to be rewritten as

$$L E = 14.29 \left[R_i \frac{u_*^3 C_p \rho \theta}{kgz} - H \right] . \quad (25)$$

We will presume that eq. (25) represents the actual contribution of the latent heat flux to buoyancy to include advected water vapor.

Additional parameters required to evaluate atmospheric moisture effects upon the various physical processes include the friction velocity u_* , which may be obtained from the similarity wind profile

$$u_* = \frac{k\bar{v}}{\ln z/z_o + \Psi_m(z/L)} \quad , \quad (26)$$

where $\Psi_m(z/L)$ is a diabatic influence function. The wind and temperature influence functions, based upon regression fits by Zhang and Antes (1982), may be found from

$$\Psi_m(z/L) = - \left[0.0954 - 1.86 \left(\frac{z}{L} \right) - 1.07 \left(\frac{z}{L} \right)^2 - 0.249 \left(\frac{z}{L} \right)^3 \right] ; \quad (27)$$

$$\Psi_m(z/L) = - \left[0.201 - 3.23 \left(\frac{z}{L} \right) - 1.999 \left(\frac{z}{L} \right)^2 - 0.474 \left(\frac{z}{L} \right)^3 \right]. \quad (28)$$

To properly evaluate q_* from eq. (6) and q_o , eq. (7), one needs to know the temperatures θ_o and T_o at z_o . The temperature profile can be written as

$$\theta - \theta_o = \frac{T^*}{K} [\ln z/z_o + \Psi_H(z/L)] \quad , \quad (29)$$

and, of course, $T_o = \theta_o - 273.15$ in degrees Celsius. The scaling temperature T^* is easily determined for unstable conditions from

$$T^* = R_i \frac{\theta}{g} \frac{u_*^2}{kz} \quad (30)$$

The sensible heat flux as given by eq. (11) can be rewritten as

$$H = -C_p \rho T^* u_* \quad (31)$$

and the potential latent heat flux as

$$L E = - \rho L u_* q_* \quad . \quad (32)$$

The right-hand side of eq. (32) must be multiplied by M to yield the apparent latent heat flux.

The surface roughness length z_o , referred to in eqs. (6), (26), and (29) should be considered as an area-wide, or effective, roughness length. For practical applications in the surface layer, z_o is typically assumed to be representative of the tallest roughness elements in about the first three upwind kilometers from an observational site. Typical roughness lengths for rural and urban terrain have been tabulated by Hansen (1990).

Analysis of profile data is based upon forming temporal averages for each level above the surface for all entities of interest. In addition, to insure that the best estimate of the statistical properties is available, the surface layer stability parameters must also be smoothed in the vertical so that some measure of stationarity may be assumed. Vertical smoothing is by the methodology of Lettau (1957) using an approximation of the height derivative of R_i , where

$$L^{-1} = \frac{\sum (R_i) z}{\sum (z)_i}, \quad i = 1, 2, 3, \dots \quad (33)$$

5. EVALUATION OF THE SEMIEMPIRICAL PARAMETERIZATION

Table 1 lists a smoothed set of profile variables extracted from the Project Prairie Grass (see Barad, 1958) data set. These data were observed on 29 July 1956 for 20 min following 1505 CST. Richardson (1920) numbers were calculated for each height from

$$R_i = \frac{g}{\theta} \frac{\Delta\theta + \Gamma\Delta z}{(\Delta V)^2} z_g \Delta \ln z \quad (34)$$

and then smoothed in the vertical by using eq. (33). The atmospheric and bulk aerodynamic parameters are also listed in table 1.

TABLE 1. MICROMETEOROLOGICAL PROFILE DATA FOR 24 JULY 1956, 1505 CST EXTRACTED FROM PROJECT PRAIRIE GRASS (BARAD 1958)

Ht m	\bar{V} m/s	ΔV m/s	\bar{T} °C	$\bar{\theta}$ °K	$\Delta\theta$	$\bar{\theta}_v$ °K	e_s mbar	e mbar	R_i	z/L	F
z_0	0	-	38.41	311.56	-	313.82	67.74	18.97	-	-	0.0119
0.25	4.34	-	33.08	306.23	-	307.88	50.54	14.15	-	-	0.0088
0.50	5.07	1.40	32.23	305.38	-1.64	306.95	48.18	13.49	-0.0185	-0.0182	0.0084
1.00	5.74	1.34	31.44	304.59	-1.49	306.09	46.08	12.90	-0.0367	-0.0363	0.0081
2.00	6.41	1.30	30.74	303.89	-1.37	305.32	44.28	12.40	-0.0710	-0.0726	0.0077
4.00	7.04	1.27	30.07	303.22	-1.35	304.60	42.60	11.93	-0.1436	-0.1452	0.0074
8.00	7.68	1.21	29.39	302.54	-1.31	303.86	40.98	11.47	-0.2929	-0.2904	.00072
16.0	8.25	-	28.76	301.91	-	303.18	39.51	11.06	-	-	0.0069
0											

Note: The following constants apply:

$$z_0 = 0.006 \text{ m}, \quad L = -27.55 \text{ m}, \quad u_* = 0.4587 \text{ m/s}, \quad T^* = -0.5723, \quad RH = 28\%$$

$$\rho = 1153 \text{ g/m}^3, \quad \rho_v = 1144 \text{ g/m}^3, \quad p = 1000 \text{ mbar}, \quad g^* = -0.00051$$

The sensible heat flux was determined, using eq. (31), to be

$$H = 302 \text{ W m}^{-2} ,$$

and the latent heat flux using the indicated equations.

$$LE_p = 656 \text{ W m}^{-2} \text{ eq. (14)}$$

$$LE_p = 669 \text{ W m}^{-2} \text{ eq. (32)}$$

$$LE = 133 \text{ W m}^{-2} \text{ eq. (20)}$$

$$LE = 141 \text{ W m}^{-2} \text{ eq. (25)}$$

$$LE = 134 \text{ W m}^{-2} \text{ eq. (32) plus (16)}$$

The agreement between eqs. (14) and (32) is considered excellent. The potential evaporation E_p must be operated upon by the moisture availability coefficient M to determine the actual evaporation. The results using eq. (20) were determined by using an arbitrary moisture availability coefficient of $M = 0.2$ for 5 days after precipitation ended. A similar value of actual latent heat flux for eq. (32) operated upon by the coefficient M resulted in a miniscule difference. The use of eq. (25) and the calculated profile Richardson number resulted in a difference of 8 W m^{-2} .

A nonadvective case was arbitrarily selected. Undoubtedly, if the relative humidities were higher, advection would be revealed. The effect of evaporation on ambient air temperature was estimated to be approximately 1.2 to about 1.5 °C decrease. This estimate is based upon the differences between the actual air temperatures and the virtual potential temperature.

6. WATER VAPOR EFFECTS UPON STABILITY

Rachele and Tunick (1991) have developed a surface energy balance model for estimating the effects of surface boundary layer phenomena upon imagery and electromagnetic propagation through the atmosphere. This highly versatile scheme may be used to show the effects of water vapor upon atmospheric stability.

The surface energy balance, as given by eq. (8), is also dramatically modified by an increase in atmospheric water vapor. Two simulated cases are given in table 2 for relative humidities of 25 and 75 percent. Initial conditions are presumed to be identical with the exception of the relative humidity. Tripling the relative humidity drastically alters the surface energy balance as a function of incoming solar radiation reaching the earth's surface. Insolation is reduced by 33 W m^{-2} or about 4 percent, while the net radiation increases by approximately 4 percent. The most significant modification to the surface boundary layer occurs in the stability parameters L and z/L , both of which decrease by 37 percent. This decrease is attributed to the approximately 17 percent increase in the latent heat flux and an extremely large, 43 percent, decrease in buoyant heat flux. The results show that atmospheric water vapor, evapotranspiration, or advective processes cannot be ignored in the surface boundary layer.

TABLE 2. THE SURFACE ENERGY BALANCE AND ATMOSPHERIC STABILITY AS A FUNCTION OF RELATIVE HUMIDITY

Parameter	RH = 25%	RH = 75%
Height	2 m	2 m
Roughness length	0.0065 m	0.0065 m
Temperature	27 °C	27 °C
Windspeed	4 m s ⁻¹	4 m s ⁻¹
Insolation	875 W m ⁻²	842 W m ⁻²
Net radiation	675 W m ⁻²	740 W m ⁻²
Soil heat flux	66 W m ⁻²	141 W m ⁻²
Sensible heat flux	249 W m ⁻²	127 W m ⁻²
Latent heat flux	363 W m ⁻²	436 W m ⁻²
Buoyant heat flux	275 W m ⁻²	158 W m ⁻²
Scaling temperature	-0.9664	-0.5078
Virtual scaling temperature	-1.07	-0.635
Obukhov length	-3.52 m	-5.63 m
Scaling ratio	-0.5683	-0.3551

7. WATER VAPOR EFFECTS UPON INDICES OF REFRACTION

Tunick and Rachele (1991) have investigated the effects of temperature and atmospheric water vapor on the index of refraction for electromagnetic radiation for the visible, infrared, microwave, and millimeter portions of the spectrum.

Two data sets from field experiments conducted at Davis, California, and at Tempe, Arizona, were used for a very comprehensive analysis. For a complete description of the analysis, see Tunick and Rachele (1991). The results for the Arizona data are given in table 3 for three soil moisture and evaporation regimes, that is, water-covered soil, wet soil, and dry soil. The atmospheric water vapor effects upon the C_n^2 values are quite striking in that moisture appears to be a major factor in determining the indices of refraction across the electromagnetic spectrum.

These results are reinforced when contributions to refraction by moisture at Davis is considered as illustrated in fig. 4. Percent of contribution versus time is shown. Note that during the afternoon hours, the moisture effect predominates as would be expected since the latent heat contribution to the energy balance is greatest during this time of day.

8. CONCLUSIONS

Water vapor effects upon atmospheric processes in the surface boundary layer are still not totally understood. The complexities of turbulent flow near the earth's surface are usually investigated in terms of wind and temperature fluctuations, while humidity is partially ignored. Of particular interest are the large changes in stability as humidity increases. Neglecting the latent heat flux contribution to the buoyant heat flux in the surface layer can lead to considerable error in projected values of the Richardson number of the Obukhov length.

Advection of moisture into a region can easily upset the determination of actual and potential evaporation rates and lead to false conclusions concerning ambient processes. Advective ramifications can introduce uncertainties into the evaporative processes, producing sometimes invalid interpretation of both the energy balance and turbulent kinetic energy budget. Most certainly, additional investigation of water vapor advection is necessary.

TABLE 3. TOTAL AND PORTIONED VALUES OF REFERENCE LEVEL C_n^2 FOR THE SALT RIVER VALLEY, ARIZONA

		Total C_n^2	Percent Temperature Effect	Moisture Effect
<u>Water Covered Soil</u>				
T = 17.1 °C	Visible	3.12×10^{-13}	77	23
V(m/s) = 2.1	IR	4.37×10^{-13}	53	47
RH = 18.0 %	Radio	4.53×10^{-11}	0.5	99.5
	mm	5.50×10^{-11}	0.4	99.6
<u>Wet Soil</u>				
T = 23.9 °C	Visible	4.48×10^{-14}	2	98
V(m/s) = 1.8	IR	2.58×10^{-13}	0.3	99.7
RH = 15.5%	Radio	3.49×10^{-10}	-0	-100
	mm	3.63×10^{-10}	-0	-100
<u>Dry Soil</u>				
T = 25.9 °C	Visible	2.43×10^{-13}	80	20
V(m/s) = 2.3	IR	3.25×10^{-13}	57	43
RH = 15.8%	Radio	2.45×10^{-11}	0.8	99.2
	mm	3.11×10^{-11}	0.6	99.4

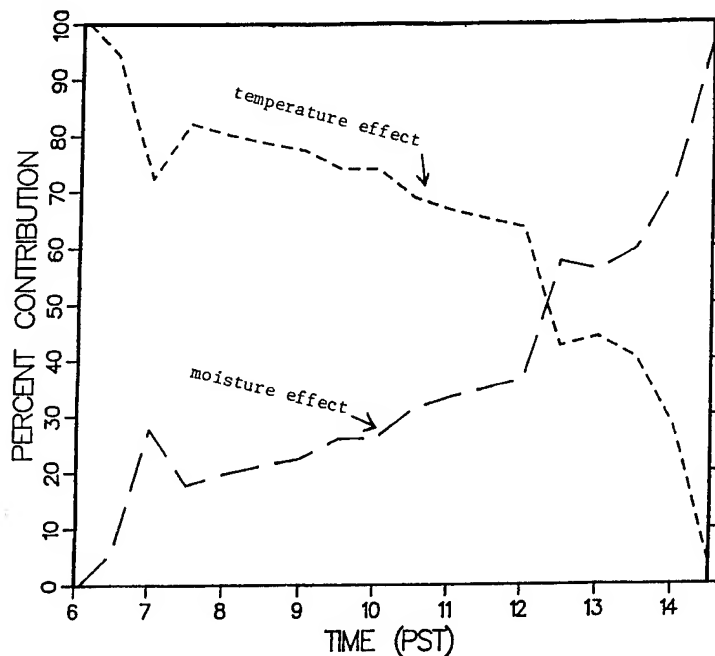


Figure 4. Percent contribution of temperature and moisture effect upon the index of refraction with respect to time (Davis, CA data, 7-13-66 IR).

REFERENCES

- Barad, M. L., 1958: Project Prairie Grass, A Field Program in Diffusion, Vol II. AFCRL-TR-58-235 (II), Air Force Cambridge Research Center, Bedford, MA.
- Brunner, F. K., 1977: On the Refraction Coefficient of Microwaves, Bull Geol. 51:257-264.
- Dugdale, G., 1989: The Influence of Variability of Rainfall and Soil Moisture on Evaporation From Semi-arid Areas. University of Reading, Reading, U.K.
- Hansen, F. V., 1990: A Fractional Stability Category Scheme. ASL-TR-0275, U.S. Army Atmospheric Sciences Laboratory, White Sands Missile Range, NM.
- Jackson, R. D., 1973: Diurnal Changes in Soil Water Content During Drying. Field Water Regime Special Pub No. 5, In Proceedings, Soil Science Society of America.
- Jackson, R. D., S. B. Idso, and R. J. Reginato, 1976: Calculation of Evaporation Rates During the Transition from Energy Limiting to Soil-limiting Phases Using Albedo Data. Water Res. Resch. 12:(1):23-26.
- Lettau, H. H., 1957: Computation of Richardson Numbers, Classification of Wind Profiles and Determination of Roughness Parameters. In Exploring the Atmosphere's First Mile, Vol 1, H. H. Lettau and B. Davidson, eds., Pergamon Press, New York, pp 328-336.
- Monteith, J. L., 1965: Radiation and Crops. Exp. Agril. 1:241.
- Myrup, L. O., 1969: A Numerical Model of the Urban Heat Island. J. Appl. Meteorol., 8:908-918.
- Nappo, C. J., Jr., 1975: Parameterization of Surface Moisture and Evaporation Rate in a Planetary Boundary Layer Model. J. Appl. Meteorol., 14:289-296.
- Obukhov, A. M., 1946: Turbulence in an Atmosphere of Nonhomogeneous Temperature. Trans Inst Theort Geophys USSR. 1:95.
- Penman, H. L., 1948: Natural Evaporation from Open Water Bare Soil and Grass. Proc. Roy. Soc. London. A 193, 120-145.
- Rachele, H., and A. Tunick, 1991: Estimating Effects of Temperature and Moisture on C_n^2 in the Damp Unstable Boundary Layer for Visible, Infrared, Radio, and MM Wavelengths. In Proceedings of 1991 Battlefield Atmospheric Conference, El Paso, TX, 3-6 December 1991.
- Ritchie, J., 1972: Model for Predicting Evaporation from a Row Crop with Incomplete Cover. Water Res. Resch. 8:(5):1204-1213.
- Richardson, L. F., 1920: The Supply of Energy from and to Atmospheric Eddies. Proc. Roy. Soc., A97, 354.

- Rossby, C. G., 1932: Thermodynamics Applied to Air-Mass Analysis. M.I.T. Meteorol. Papers, Massachusetts Institute of Technology, Cambridge, MA., 1(3).
- Tetens, O., 1930: Über Einige Meteorologische Begriffe. Z. Geophysik, 6:297-309.
- Wilson, R. G., and W. R. Rouse, 1972: Moisture and Temperature Limits of the Equilibrium Evapotranspiration Model. J. Appl. Meteorol., 11:436-442.
- Zhang, D., and R. A. Anthes, 1982: A High-Resolution Model of the Planetary Boundary Layer - Sensitivity Tests and Comparison with SESAME-79 Data. J. Appl. Meteorol., 21:1594-1609.

Prediction of Surface and Subsurface Temperatures Using a Two-Dimensional Model of Coupled Surface Energy Balance

Michael D. DeAntonio
New Mexico State University
Las Cruces, NM 88003, U.S.A.

ABSTRACT

The Coupled Surface Energy Balance (CSEB) model is used to predict temperature both on and below the surface of various terrain. The model will aid in the prediction of thermal contrast between a target and its background. It can also be used to verify theoretical models of energy balance at the surface of the terrain. CSEB is an extension of another model called VEGIE, created by the U.S. Army Engineer Waterways Experiment Station. This paper will discuss the differences between CSEB and VEGIE, as well as present a brief description of the present model. Testing, verification and uses of the model will also be discussed.

1. INTRODUCTION

The purpose of the program CSEB (Coupled Surface Energy Balance) is to predict temperature both on and below the surface of various terrain. These temperatures are given in the output for each grid point at time intervals of one hour over the course of a single day.

The program is based on the FORTRAN code, VEGIE, written by Balick, Scoggins, and Link. VEGIE is described in the technical report *Inclusion of a Simple Vegetation Layer in Terrain Temperature Models for Thermal Infrared (IR) Signature Prediction* [Balick et al., 1981a]. Further information is contained in another report entitled *Thermal Modeling of Terrain Surface Elements* [Balick et al., 1981b].

The program CSEB is divided into modules in such a way that the code for various processes may be modified without affecting other parts of the program. This also gives the program greater readability. At this time, the program includes modules for the various boundary conditions, atmospheric thermal infrared energy, ground radiative emittance, sensible and latent heat transfer, insolation, and the effects of vegetation.

The inputs to the program characterize the terrain by giving the necessary parameters for the soil and vegetation and by defining an initial temperature profile for the grid. The inputs also characterize the day by specifying atmospheric weather conditions, Julian day, etc. We will discuss each of these inputs in more detail in section 2.

The temperature at each grid point, for the first time step, is calculated using the initial temperature profile and the characteristics of the day given in the inputs. For each new time

step, the temperatures are calculated from those of the previous time step using the heat flow equation with the proper boundary conditions. The temperatures at 24 hours then replace those for the first time step, and the process is repeated. This is continued until the conditions for steady state convergence are met.

CSEB is an update of VEGIE in that it is a two-dimensional model. Whereas VEGIE accounts only for changes which occur with depth, CSEB accounts for changes which occur with width as well.

2. INPUTS

The inputs to the program are separated into the following categories: control specifications, atmospheric specifications, surface orientation specifications, initial temperature profile, top surface constants, layer specifications, section specifications, block specifications, bottom boundary data, left boundary data, right boundary data, and vegetation parameters.

The control specifications allow the user to choose the number of layers and sections, the minimum number of 24 hour iterations, the time step, and the maximum temperature difference.

The number of layers is the number of soil layers. A new layer begins at the horizontal plane where the values of thermal diffusivity or heat conductivity are discontinuous. The number of sections is the number of soil sections. A new section begins at the vertical plane where the values of thermal diffusivity or heat conductivity are discontinuous. The program allows for a maximum of six layers and six sections.

The minimum number of 24 hour iterations is also specified. This requires the program to repeat a 24 hour iteration a minimum number of times. After this minimum number of iterations the program will begin to check for convergence in the temperatures. In this way the user may be sure that the program proceeds to a point where the information from a given boundary has propagated completely throughout the grid. This is especially helpful when one of the boundaries is a heat source.

The time step is given in units of minutes. This is the time step which will be used for the numerical solution of the differential heat equation.

The maximum temperature difference has units of degrees Celsius. The program checks the difference between the temperatures, for each time step and for each grid point, as it proceeds from one iteration to the next. If all of these temperature differences are smaller than the maximum temperature difference then steady state convergence has occurred.

The atmospheric specifications allow the user to input the atmospheric pressure, cloud type, and shelter height. The hourly weather information includes the air temperature, relative humidity, cloud cover, wind speed, and insolation.

The atmospheric pressure has units of millibars. The cloud type is a number which specifies one of the following eight classifications of clouds: cirrus, cirrostratus, altocumulus, altostratus, stratocumulus, stratus, nimbostratus, and fog. This number is used to determine a pair of empirical coefficients used in the calculation of insolation. The shelter height is the height above the surface in centimeters at which the weather data is recorded.

Information about the weather is measured at periods of one hour during the course of a single day. The information should begin at hour 0 (midnight) and proceed to hour 24 (midnight).

the following day), so that 25 measurements are taken. Hour 0 need not be included. In this case, the code will substitute the data from hour 24 into hour 0.

The weather information is input as 25 (or 24) cards consisting of the hour, the air temperature in degrees Celsius, the relative humidity as a percentage, the cloud cover as a fraction (0=clear sky, 1=completely overcast), the wind speed in meters per second and the insolation in watts per squared meter.

Note that the program converts the units on some of these variables immediately after they are input. The air temperature is converted to degrees Kelvin, the relative humidity to a fraction, the wind speed to centimeters per second, and the insolation to calories per squared centimeter per minute.

The user also specifies the Julian day, and the latitude in radians. The surface orientation card specifies the angles at which the surface of a section deviates from level. The surface slope is the angle between the plane of the surface and horizontal. The surface azimuth specifies the angle between the projection of the surface normal and south (with positive angles increasing from south to west). Both of these angles are input in degrees and changed by the program to radians.

The initial temperature profile is used as the temperature grid for the first iteration in the temperature calculations. Temperatures are specified for any number of depths into the soil. Values for the other depths used in the calculation are interpolated from these values.

The inputs are the the depths and the temperatures for each coordinate. The depth is given in units of centimeters and the temperature in degrees Celsius. The temperature is then converted by the program to degrees Kelvin. Note that the bottom profile coordinate must lie within the bottom soil layer.

The top surface constants include the emissivity, absorptivity, and moisture content for a given section on the surface. The emissivity is the thermal infrared emissivity and ranges from 0.0 to 1.0. The absorptivity is the visible wavelength absorptivity and also ranges from 0.0 to 1.0. Finally, the moisture content specifies the amount of moisture in the soil (0.0=dry, 1.0=wet/saturated).

The layer and section specifications describe the properties of the grid with respect to depth or width. For each layer or section the user inputs the layer or section number, the thickness of the layer or section in centimeters, and the grid spacing, also in centimeters. The grid spacing determines the depth or width between grid points within a layer or section. The total number of grid points can be no greater than 40 in either direction.

The block specifications determine the thermal properties of the soil within a block. For each block, the user inputs the block number (the layer number followed by the section number), the thermal diffusivity in squared centimeters per minute, and the thermal conductivity in calories per minute per centimeter per degree Kelvin.

In the boundary data, the user has a choice for each section of three boundary conditions determined by the first input variable IBND. Each of these choices requires different inputs. The three conditions are as follows: (1) IBND equal to zero specifies a constant temperature at the boundary. The user is then required to input the temperature in degrees Celsius. The program will convert this to degrees Kelvin. (2) IBND less than zero specifies a constant heat flux through the boundary. The user is then required to input the heat flux in units of calories per squared centimeter per minute. (3) IBND greater than zero specifies a constant heat flux at the boundary and an additional constant temperature radiating surface near this boundary.

The inputs are then the heat flux in calories per squared centimeter per minute, the bottom boundary emissivity, (0.0 to 1.0), the bottom boundary geometric shape factor, (0.0 to 1.0), the radiating surface emissivity, (0.0 to 1.0), the radiating surface geometric shape factor, (0.0 to 1.0), and radiating surface temperature in degrees Celsius (converted by the program to degrees Kelvin). The geometric shape factor accounts for changes in thermal infrared emittance and absorption efficiency due to shape.

One set of vegetation parameters is given for each section and includes the index, coverage, state, emissivity, absorptivity, and foliage height.

The index indicates whether vegetation is present or not. The coverage, is the area average shielding factor and measures the fraction of shortwave radiation which does not reach the ground. The state is a multiplier which affects the stomatal resistance function for typical unstressed plants. It allows the user to account for adjustments due to moisture stress, senescence or various other factors. The emissivity is the grey body thermal infrared emissivity of the foliage. Absorptivity is the fraction of visible solar radiation absorbed by the foliage. Finally, the foliage height is the average height of the top of the foliage.

3. MATHEMATICS

As we have already stated, the purpose of the program is to predict the temperature of the terrain both on and below the surface. The output will be a three-dimensional grid, which has as its coordinates depth (x), width (y), and time (t). The temperature $[T(x, y, t)]$ is then calculated for each coordinate point. This calculation begins with the heat equation [Zemansky, 1968, pg.91],

$$\frac{\partial T(x, y, t)}{\partial t} = \alpha(x, y) \left[\frac{\partial^2 T(x, y, t)}{\partial x^2} + \frac{\partial^2 T(x, y, t)}{\partial y^2} \right], \quad (1)$$

subject to boundary conditions at the surface, the bottom of the grid, on the left and right sides of the grid and at the vertical and horizontal discontinuities of the diffusivity or thermal conductivity within the grid. Here, $\alpha(x, y)$ is the diffusivity of the soil.

3.1 General solution of the heat equation

For any point on the grid which is not part of a boundary or discontinuity in thermal diffusivity or conductivity, the heat equation may be solved directly to yield the new temperature. Numerically, it is solved using the Crank-Nicolson (or finite-difference) method [Cheney and Kincaid, 1985, pp.429-437].

$$T(x, y, t) = T(x, y, t - \Delta t) + A_x \delta T_x^2 + A_y \delta T_y^2, \quad (2)$$

where

$$\delta T_x^2 = [T(x + \Delta x, y, t - \Delta t) - 2T(x, y, t - \Delta t) + T(x - \Delta x, y, t - \Delta t)], \quad (3)$$

$$\delta T_y^2 = [T(x, y + \Delta y, t - \Delta t) - 2T(x, y, t - \Delta t) + T(x, y - \Delta y, t - \Delta t)], \quad (4)$$

$$A_x = \frac{\alpha(x, y)\Delta t}{\Delta x^2}, \quad (5)$$

and

$$A_y = \frac{\alpha(x, y)\Delta t}{\Delta y^2}. \quad (6)$$

3.2 Left, right and bottom boundaries

Since the left, right and bottom boundaries are treated similarly, we will discuss only the bottom boundary conditions in detail.

The equations for the bottom boundary depend upon the value of the variable IBND (see section 2.) and may be different for each section. If $\text{IBND} = 0$, we insert the given value of the temperature at the boundary. However, if $\text{IBND} \neq 0$, then the temperature (T'_B) is governed by conservation of heat flux through the boundary [Balick *et al.*, 1981b],

$$I_\downarrow - G_R - I_\uparrow - G_B = 0, \quad (7)$$

where I_\downarrow is the radiative energy lost through the bottom boundary, G_R is the heat flux into the lower radiating surface, I_\uparrow is the radiative energy from the lower radiating surface, and G_B is the heat flux through the bottom boundary. Equation 7 is solved for the new boundary temperature, T'_B , using the Newton-Raphson iteration method for finding the roots of an equation.

The above treatment accounts for the change in the temperature at the boundary due to the vertical heat flow through it. We must, however, still consider the conduction of heat along the boundary itself. For this, we use the one-dimensional heat equation,

$$\frac{\partial T(x, y, t)}{\partial t} = \alpha(x, y) \left[\frac{\partial^2 T(x, y, t)}{\partial y^2} \right], \quad (8)$$

which may be solved numerically by the Crank-Nicolson equation,

$$T_B(x, y, t) = T'_B(x, y, t) + A_y \delta T_{By}^2. \quad (9)$$

where $T_B(x, y, t)$ is the new temperature at the point (x, y) on the boundary. An exception is made if we are at the point of a vertical discontinuity. In that case, we use the vertical equivalent of equation 10 in the next section.

3.3 Vertical and horizontal discontinuities

There are vertical and horizontal discontinuities of thermal diffusivity and conductivity. The mathematical models for these vertical and horizontal discontinuities are equivalent. Therefore, only the horizontal equation is shown here.

$$T(x, t) = T(x, t - \Delta t) + \frac{1}{A} [BT(x - \Delta x_1, t - \Delta t) - CT(x, t - \Delta t) + DT(x + \Delta x_2, t - \Delta t)], \quad (10)$$

where the factors are

$$B = \frac{k_1}{\Delta x_1}, \quad (11)$$

$$D = \frac{k_2}{\Delta x_2}, \quad (12)$$

$$C = B + D, \quad (13)$$

and

$$A = \frac{B\Delta x_1^2}{2\alpha_1\Delta t} + \frac{D\Delta x_2^2}{2\alpha_2\Delta t} = \frac{B}{2A_{x1}} + \frac{D}{2A_{x2}}. \quad (14)$$

In the case where a vertical and an horizontal boundary intersect, the values of the conductivity and diffusivity are uncertain. Therefore, we simply take the average of the *new* temperatures just above and just to the left of the point of intersection. That is,

$$T(x, y, t) = \frac{1}{2} [T(x - \Delta x, y, t) + T(x, y - \Delta y, t)]. \quad (15)$$

3.4 Surface boundary

The surface boundary temperature can be found by considering the conservation of total heat flux. That is, it must be a root of the equation [Balick *et al.*, 1981b]

$$\alpha_g S + I_l - H - E - I_f - G = 0, \quad (16)$$

where α_g is the absorptivity of the ground S is the incident solar insolation, I_l is the atmospheric and cloud infrared energy, H is the conductive and convective sensible heat transfer, E is the latent heat exchange, I_f is the ground radiative emittance, and G is the heat flux out of the surface. The root of this equation is found using the Newton-Raphson method. Each of these processes is described in detail in a report by the author entitled *A Two-Dimensional Model of Coupled Surface Energy Balance* [DeAntonio, 1991]. The equations for each process are taken from VEGIE [Balick *et al.*, 1981b].

3.5 The effects of vegetation

When vegetation is included as part of the surface for a given section, two heat flux conservation equations must be satisfied. One of these equations models the heat transfer through the top of the vegetation, the other between the vegetation and the surface.

Due to the presence of the vegetation, the heat transfer at the surface, equation 16 will change significantly. The new equation is [Balick *et al.*, 1981a]

$$S_g + I_{g\downarrow} - H_g - E_g - I_{g\uparrow} - G = 0. \quad (17)$$

Again, this equation is solved for T_g using the Newton-Raphson method.

We must also solve for the temperature at the top of the vegetation, T_f . This is found by using conservation of heat flux between the vegetation and the air [Balick *et al.*, 1981a],

$$S_f + I_{f\downarrow} - H_f - E_f + I_n = 0, \quad (18)$$

where I_n denotes a net thermal infrared interaction between the vegetation, ground, and the atmosphere. Again the equations for each process are those which were used in VEGIE [Balick *et al.*, 1981a]. A detailed description of each process is given in the aforementioned report [DeAntonio, 1991].

3.6 Steady state convergence

An initial grid file is created using the inputs in the cards INIT and interpolating to create a one-dimensional grid. That is, only values for depth (x) and time (t) are given initially. We then calculate a new temperature grid based on only one-dimension. In other words, we ignore the vertical boundaries and discontinuities for this first series of iterations. The reason for this additional step, instead of beginning directly with a two-dimensional grid, is that the total number of iterations necessary to reach convergence is decreased. Only after we have reached convergence on the one-dimensional grid do we begin the iterations using two-dimensions.

The day specified by the initial temperature grid is usually not in steady state. By this we mean that, if the following day retained the same conditions (which includes being identified by the same Julian day) and heat is allowed to flow through the soil, then the temperature grid of this second day would be significantly different than the first.

The purpose of the program CSEB is to allow the heat to flow during each new day, which we shall call one iteration, and continue until the temperature grids of the two days are not significantly different. That is, we have reached convergence.

There are several criteria which must be fulfilled in order for a particular day to be considered in steady state. First A_x and A_y , calculated in equations 5 and 6, must both be less than 0.5 [Balick *et al.*, 1981b]. If this condition is not met, the temperature grid of each successive iteration will diverge from the previous grid. This condition is checked immediately after the calculation of A_x and A_y . If it is not fulfilled, the program stops and an error message is given.

The second criteria is input by the user as the minimum number of iterations. The program will iterate both the one-dimensional and two-dimensional grids at least this number of times each.

The third criteria involves the maximum temperature difference also given by the user. The program checks the difference between the temperatures of each grid point and time step for this day and the previous one. This difference we call DTEMPN. If the temperature difference for all of the grid points is smaller than the maximum temperature difference then the temperature grid is in steady state and the program terminates normally.

The final criteria for convergence involves the change in DTEMPN. The difference between the temperature after a given iteration and the true temperature is given by the sum of all the temperature changes in all subsequent iterations.

$$\Delta T_{\text{act}} = \Delta T_0 + \Delta T_1 + \Delta T_2 + \dots \quad (19)$$

If the each temperature change in the series is related to the previous change by a multiplicative constant, β , then we have the geometric sum [Arfken, 1985]

$$\Delta T_{\text{act}} = \sum_{n=1}^{\infty} \beta^n \Delta T_0 = \frac{\Delta T_0}{1-\beta}. \quad (20)$$

Now, we want the total difference in temperature after an iteration to be less than the change in temperature during the iteration or

$$\Delta T_{\text{act}} - \Delta T_0 < \Delta T_0. \quad (21)$$

This would assure convergence.

Substituting equation 20 and solving for β , we find that the condition for convergence is

$$\beta < \frac{1}{2}. \quad (22)$$

And so, each change in temperature must be less than $\frac{1}{2}$ the previous change if we wish the previous temperature change to be the maximum possible error in temperature. In other words, to have convergence.

At first, this argument may seem somewhat artificial since β was assumed the same for all iterations. However, after careful examination, it can be seen that, even if β changes after each iteration, relation 21 will remain valid if all the values of β are less than $\frac{1}{2}$.

Additionally, if the changes in temperature oscillate between positive and negative values, then the absolute value of the new temperature change must be less than the absolute value of the old change in temperature, or convergence is not attained. And so, we must have

$$-1 < \beta < \frac{1}{2} \quad (23)$$

for convergence.

4. OUTPUT

The output of CSEB consists of an output to screen and an output to a file which is named by the user.

The output file contains the same header as the input file (followed by the name of the program (CSEB), the date and the time at which the output was completed if we are using the non-ANSI standard code). After this the screen output is duplicated in the file.

Lastly the output file contains a table labeled FINAL TEMPERATURE GRID. This contains the grid points for each hour. First, we have the TIME, then the LAYER number. Also, given

is the INSOLation for each TIME. Following these is a list of temperatures which are given at each point along the width of the layer, beginning with the left boundary and proceeding to the right.

5. VERIFICATION

A series of studies, done by the U.S. Army Engineer Waterways Experiment Station in 1980, served to confirm the calculations of the program TSTM (a forerunner of VEGIE). [Balick *et al.*, 1981b] These same studies can serve as a preliminary test of CSEB. More comprehensive tests are being planned by the Atmospheric Sciences Laboratory located at White Sands Missile Range, NM.

5.1 Concrete Pad, Vicksburg, August 1980

The first test was a measurement of the surface temperature of a concrete pad using a thermistor attached to the concrete's surface. Atmospheric and hourly data were recorded on Campbell Scientific Model CR21 Microloggers, with the exception of cloud cover and cloud type. Observations of the clouds were made periodically during daylight hours and assumed to be constant. Values of conductivity, diffusivity and absorptivity were determined using a report given by Link. [Link, 1979]

Figure 1 plots the temperature calculated by CSEB against the actual measurements. In this calculation, the measured values of the insolation at the surface were used.

5.2 Bare Soil, Vicksburg, August 1980

Another test was performed near the same location and on the same day as the first test. In this case the temperature of a bare soil patch within a grass covered area was measured using a thermistor located approximately one centimeter beneath the surface. All other parameters were determined in the same way as in the first test.

Figure 2 plots the temperature calculated by CSEB against the actual measurements. In this calculation, the measured values of the insolation at the surface were used.

5.3 Bare Soil, Vicksburg, July 1980

The last test is the same as the second; however, the measurements were taken on July 31, 1980 instead of August 5.

Figure 3 plots the temperature calculated by CSEB against the actual measurements. In this calculation, the measured values of the insolation at the surface were used.

6. CONCLUSIONS AND RECOMMENDATIONS

Two major improvements have been made to the original program (VEGIE). The first is that the CSEB model includes two spatial dimensions instead of one. The increased number of

FIGURE 1. Comparison of output file to actual data taken from a concrete pad in Vicksburg, MS on August 5, 1980. The solid line is the surface temperature calculated by CSEB, and the dashed line is the measured data.

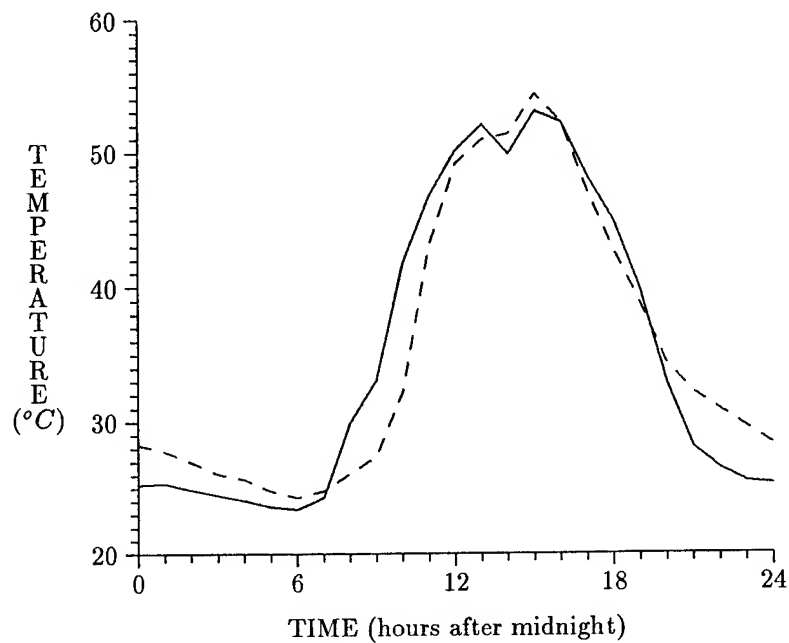


FIGURE 2. Comparison of output file to actual data taken from a bare soil patch in Vicksburg, MS on August 5, 1980. The solid line is the ground temperature calculated by CSEB, and the dashed line is the measured data.

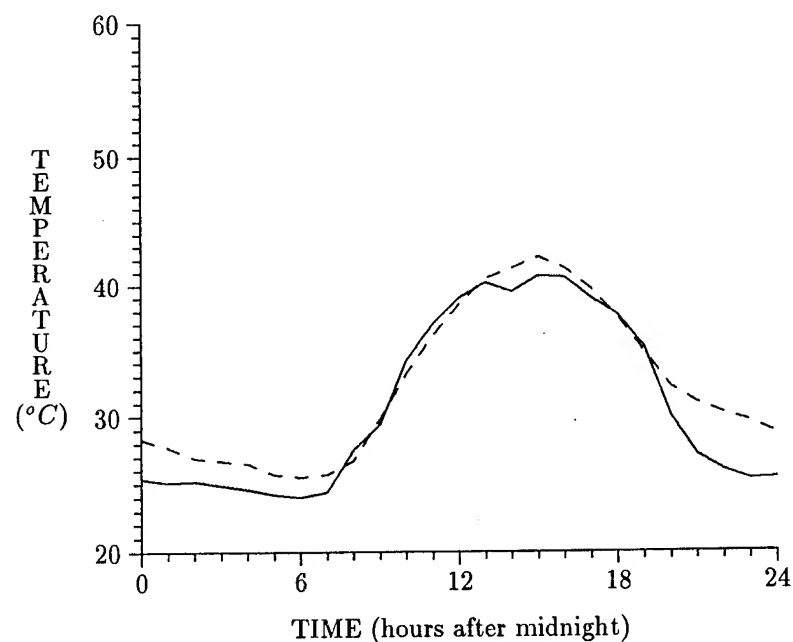
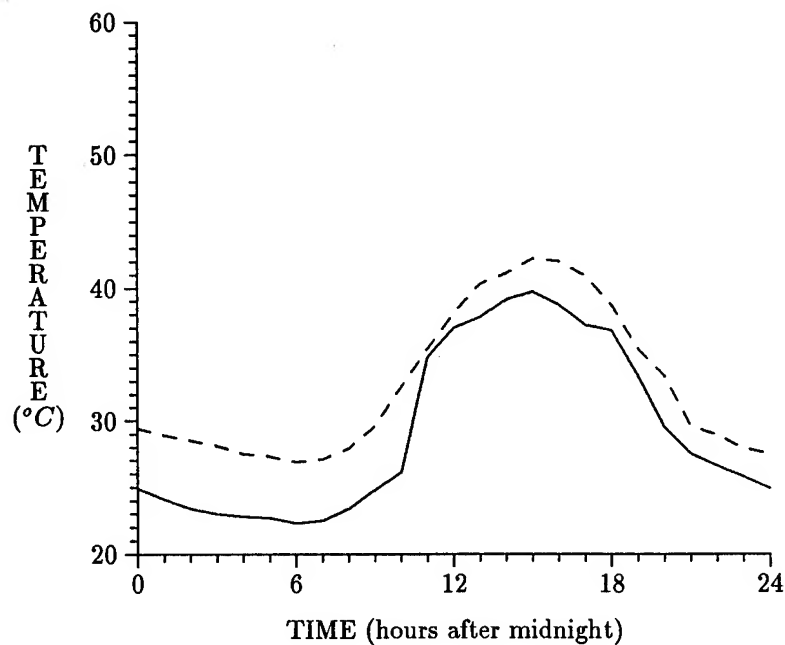


FIGURE 3. Comparison of output file to actual data taken from a bare soil patch in Vicksburg, MS on July 31, 1980. The solid line is the ground temperature calculated by CSEB, and the dashed line is the measured data.



dimensions should allow for more accurate treatment of various boundary conditions. Still it is not complete. A true two-dimensional model should account for reflections from heavily inclined surfaces. It should also account for shadows from these same surfaces. Also, although rectangular blocks should be a sufficient approximation under most conditions, many objects will be found both on and below the surface which are irregular in shape. Finally, a three-dimensional model may be necessary to take into account all of the effects which contribute to a change in temperature both on and below the surface of the terrain.

The second improvement to VEGIE is that CSEB has been divided into modules which handle each process used to calculate the temperature. Most of the models, however, have never been changed from those used in VEGIE. Many of the modules are empirical in nature or contain assumptions which may limit their validity. Much work needs to be done to determine the accuracy of the equations which are used here, and to recommend new ones when these are found to be insufficient. We hope that these investigations will have been made easier by the changes to the program format.

Although much can be done with the current version of CSEB, its main purpose is to allow the user freedom to change the model of any process easily and efficiently. With this in mind, many changes will be made to the program in the future. Yet it is hoped that the current version of CSEB will provide a good framework from which these changes can be made.

REFERENCES

[Arfken, 1985] Arfken, George, 1985: *Mathematical Methods for Physicists*. Academic Press,

third edition.

- [Balick *et al.*, 1981a] Balick, Lee K., Lewis E. Link, Jr., and Randy K. Scoggins, 1981: *Inclusion of a Simple Vegetation Layer in Terrain Temperature Models for Thermal Infrared (IR) Signature Prediction*. EL-81-4, U.S. Army Engineer Waterways Experiment Station, P.O. Box 631, Vicksburg, Miss. 39180.
- [Balick *et al.*, 1981b] Balick, Lee K., Lewis E. Link, Jr., and Randy K. Scoggins, 1981: *Thermal Modeling of Terrain Surface Elements*. EL-81-2, Department of Mathematics, Mississippi State University, Starkville, Miss. 39762.
- [Cheney and Kincaid, 1985] Cheney, Ward, and David Kincaid, 1985: *Numerical Mathematics and Computing*. Brooks/Cole, second edition.
- [DeAntonio, 1991] DeAntonio, M. D., 1991: *A Two-Dimensional Model of Couple Surface Energy Balance*. , U.S. Army Atmospheric Sciences Laboratory, White Sands Missile Range, NM 88002-5501. This report is available through the EOSAEL work unit at ASL.
- [Link, 1979] Link, L. E., 1979: *Thermal Modeling of Battlefield Scene Components*. EL-79-5, U.S. Army Engineer Waterways Experiment Station, P.O. Box 631, Vicksburg, Miss. 39180.
- [Zemansky, 1968] Zemansky, Mark W., 1968: *Heat and Thermodynamics*. McGraw-Hill, fifth edition.

Session VI

BEST TWO POSTER

**Chairperson
Ir. J. Rogge**

**THE BATTLEFIELD EMISSIVE SOURCE TRIALS (BEST) DATABASE:
STATUS AND UPDATE**

Roger E. Davis
Science and Technology Corporation
Las Cruces, NM 88001, USA

Patti S. Gillespie
U.S. Army Atmospheric Sciences Laboratory
White Sands Missile Range, NM 88002, USA

ABSTRACT

Under the sponsorship of Research Study Group (RSG) 15, Panel 4, NATO AC/243, two field tests have been conducted. The Battlefield Emissive Sources Trials at Oldebroek, the Netherlands (BEST ONE) was held September 1985 in the Netherlands; the Battlefield Emissive Sources Trials under European Theater Weather and Obscurants (BEST TWO) was held July/August 1990 in France. Archive data acquired at these tests have been submitted to the Atmospheric Aerosols and Optics Data Library (AAODL) for storage. This paper describes BEST data categories, data forms, and data types. Data retrieval procedures are discussed and database points of contact are identified. A topical summary of papers using BEST data is presented.

1. INTRODUCTION

The concern of Research Study Group 15 (RSG 15), Panel 4, NATO AC/243 (NATO AC/243.P04.RSG.15) is the characterization of battlefield effects and related measurement techniques. Members of RSG.15 are Denmark (DK), France (FR), Germany (GE), the Netherlands (NE), SHAPE Technical Center (STC), United Kingdom (UK), and the United States (US). The Group is chaired by Ir. Jaap Rogge (NE). Mr. Tim Pentecost (UK) is the secretary.

Under the sponsorship and direction of RSG.15, two field tests have been performed. The Battlefield Emissive Sources Trials at Oldebroek, the Netherlands (BEST ONE) was held September 1985 in the Netherlands; the Battlefield Emissive Sources Trials under European Theater Weather and Obscurants (BEST TWO) was held July/August 1990 in France. In order to centralize field test information, RSG.15 has submitted trial data to the Atmospheric Aerosols and Optics Data Library (AAODL). This paper describes these data, the BEST AAODL archive, and the procedures for obtaining data from the archive.

1.1 BEST ONE

All RSG.15 member nations participated in BEST ONE. The primary objectives of BEST ONE were to quantify characteristics of emissive sources that may affect electro-optical (EO) systems, to determine how these sources affect EO system performance, and to determine how observer performance (static field of view) is affected in laboratory experiments using trial imagery (Rogge, 1986). Secondary objectives and goals are described by Rogge (1986).

BEST ONE was divided into two weeks. The first week of the trials was devoted to source characterization and source effects on EO systems. The second week's measurements concentrated on observer performance, viewing EO sensor imagery of targets with emissive sources present. Most of the experiments focused on thermal imagery.

For additional information describing BEST ONE, see Niles (1987, 1989) and Rogge (1986, 1990). Information concerning data reviews and analyses can be found in papers and publications cited in the BEST bibliography discussed in Section 3.0.

1.2 BEST TWO

As with BEST ONE, all RSG.15 member nations participated in BEST TWO. The objectives of BEST TWO were the following:

1. To determine the effectiveness of EO systems under adverse European atmospheric conditions with and without battlefield events
2. To examine the effects in the near and far fields of single and multiple emissive sources
3. To obtain data on target acquisition of static and moving ground vehicles in clutter
4. To evaluate target acquisition models and models that characterize battlefield events and their effects
5. To establish a database for the evaluation of aided target recognition (ATR) systems and smart weapons (Niles, 1990)

Four scenarios were utilized at BEST TWO. Scenarios 2, 3, and 4 were broken into subsets. Table 1 identifies the scenarios.

For additional information describing BEST TWO see Niles (1990, 1991) and Rogge (1990). Information concerning data reviews and analyses can be found in papers and publications cited in the BEST bibliography.

TABLE 1. BEST TWO SCENARIOS

Scenario	Type
1	Single static vehicles
2	Single moving vehicles
2A	Without simulated battlefield effects
2B	With fire events
2C	With simulated artillery barrages
3	Vehicles in column
3A	Without simulated battlefield events
3B	With fires
4	Vehicles in attack formation
4A	Without simulated battlefield events
4B	With simulated artillery barrage near the vehicles
4C	With simulated artillery barrage near observers
4D	With white phosphorus smoke near the observers
4E	With both simulated artillery barrage and WP smoke near the observers

2. DATA ARCHIVE

In this section we present an overview of the BEST AAODL electronic database. The BEST AAODL archive includes not only electronically stored information, but also videotape and hard copy data.

Data from BEST are submitted to the archive through the RSG.15 U.S. representatives. After receiving the data, AAODL personnel perform a quality assurance review. Any questions pertaining to data quality, completeness, or validity are referred back to the submitting member country for clarification. If possible, data acquisition and reduction procedures are kept in the archive, as well as instrument descriptions. BEST data are archived under the ORACLE relational database management system (DBMS) in tabular format. Data may be retrieved as ORACLE files or ASCII files.

2.1 BEST ONE ARCHIVE

Table 2 summarizes the BEST ONE data sets by data classification and country. Table 3 provides a current summary of the computerized BEST ONE data tables.

TABLE 2. BEST ONE DATA SETS

COUNTRY	DATA CLASSIFICATION		
	NATURAL ENVIRONMENT	CHARACTERIZATION	IMAGE DATA
DA	None	MTF degradation (limited trials)	Digitized video (AN/TAS-4 on IBM PC)
FR	Met: 6-min intervals	T(max), cloud size (cumulative area)	Digital cal. AGA for scheduled tests; SECAM SiTV
GE	Met: (at fire location) 100-s & 4-min intervals	T(max), cloud size C_n^2 , CO_2 , transmission	Digital cal. AGA VTR CCIR, TICH II 2 TVs
NL	Met, vis., C_n^2 from He-Ne Scint.	Aerosol/gas sampler spectral emission from fifth-wheel spectrometer	VTR CCIR, IR-AT
UK	Met, C_n^2 5-min interval	Thermocouple data (100-s interval) Nd:YAG laser and video imager viewing target board for beam spread and wander	VTR, 2-IR18s visual TV
US	Met data (1-s intervals); C_n^2 (15-min avg); Transmittance	MIDAS (cloud sizes) Radiance Pyrometer He-Ne beam wander	Video SiTV AN/TAS-4, AN/TAS-6 SMART: digitized & calibrated

TABLE 3. BEST ONE DATABASE TABLES

Table Name	Description
SMART	ASL SMART transmittance data
SMTMET	ASL SMART supporting meteorological data
AME10	AME-10 Site meteorological Data
FWS2	TNO filter wheel spectrometer II data
FWS3	TNO filter wheel spectrometer III data
CHEMISS	TNO smoke plume chemical emissions measurements
VAPCON	TNO total organic vapor concentrations by compound type
MIDAS	ASL cloud imagery characterization data
GENINFO	Summarized general trial information
ABBREV	Definitions of BEST ONE database abbreviations

2.2 BEST TWO ARCHIVE

Table 4 presents an overview of the data acquired at BEST TWO by data category and country. The BEST TWO field experiments were more varied and greater in number than those in BEST ONE. A number of national experiments were performed by several countries. Data from these experiments will probably not be included in the BEST AAODL.

TABLE 4. BEST TWO DATA SETS

COUNTRY	DATA CLASSIFICATION		
	ENVIRONMENT	CHARACTERIZATION	IMAGE DATA
DA	None	Target signatures (3-5, 8, 12 μ m) with DuDa	AN/TAS-4 video analog and digital
FR	Met, target positions & site survey	Radar, laser, and IR system performance	Visible, mid and far IR video system
GE	Met; camouflage	TICM II, FLIR, radiometry, video, staring array	Analog & digital: visible, mid and far IR systems

TABLE 4. BEST TWO DATA SETS (CONTINUED)

COUNTRY	DATA CLASSIFICATION		
	ENVIRONMENT	CHARACTERIZATION	IMAGE DATA
NL	Met; transmittance	AN/TAS-4, IR systems; observer performance; laser performance	Analog & digital: visible, near IR, far IR
UK	None	Acoustic array; TICM II and imager performance	Analog & digital: visible, mid and far IR
US	Met; GPS; transmittance	MIDAS (cloud sizes); target contrast; acoustic arrays;	Analog visible, near IR, mid IR, and far IR

Table 5 provides the current status of the BEST TWO electronic archive loaded under the ORACLE DBMS. This archive continues to expand as trial participants complete their initial data reviews and analyses and submit reduced data and results to the AAODL.

TABLE 5. BEST TWO DATABASE TABLES

Table Name	Description
DDTEMP	DuDa target IR characterization
DUSTBIN	ASL MIDAS dust cloud dimensions
EXPDIM	ASL MIDAS explosive cloud dimensions
GERMET	German 5-min meteorological data
LOWTRAN_US	LOWTRAN model transmittances for clear air (from U.S. meteorological data)
MET FRN	French meteorological data
MPTRFIR	TNO transmittance data (7.9-12.3 μm)
MPTRMIR	TNO transmittance data (3.5-4.8 μm)
MPTRNIR1	TNO transmittance data (0.7-1.0 μm)
MPTRNIR2	TNO transmittance data (1.0-1.4 μm)
MPTRNIR3	TNO transmittance data (2.0-2.2 μm)
MPTRVIS	TNO transmittance data (0.4-0.7 μm)
PATHLEN	MIDAS LOS path lengths through clouds
RASIT4	French ETCA vehicle radar positions
REVIRT	ASL REVIRT transmittance data

TABLE 5. BEST TWO DATABASE TABLES (CONTINUED)

Table Name	Description
REVNOTES	REVIRT transmissometer operating parameters
SCENDEF	Scenario descriptions/definitions
SITE2_US	Site 2 meteorological data
SITE4_US	Site 3 meteorological data
TNOMET10S	TNO 10-s meteorological data
TNOMET15M	TNO 15-min averaged meteorological data

Additional electronic information not yet loaded into the ORACLE DBMS is kept in spreadsheet or word processing files. These data, which concern data location/loading status, points of contact for the data acquisition efforts, video logs, and bibliography material, will be loaded into ORACLE as they become more complete.

3. BEST PAPERS AND REPORTS

A bibliography of documents, papers, and reports concerning BEST ONE and BEST TWO trial descriptions, data acquisition, the data archive, and data analyses is maintained in the BEST AAODL archive. Information stored for each item in the bibliography is: author, co-author(s), title, publication source, publication identification, year of publication, and security classification.

This is an active bibliography that continues to grow. Currently 40 BEST-related documents, papers, and reports have been logged in the bibliography. Copies of many of the documents contained in the bibliography are kept at the AAODL facility and are readily available to requestors. Documents not kept in the archive can be obtained from the originating agencies.

Participants in BEST reside on two separate continents. Consequently, communication with authors is difficult, which in turn makes it difficult to compile a comprehensive bibliography. Readers are urged to submit information on or copies of documents concerning BEST either to this paper's authors or to U.S. RSG.15 delegates. A current copy of the bibliography can be obtained by filling out an AAODL data request (see Section 4).

4. BEST DATA RETRIEVAL

To acquire BEST ONE and BEST TWO data from the AAODL, the user must complete the AAODL BEST Data Request Form given in Appendix A. This form requires the user's name, address, phone number, identification of data required, data specifications, and the data transfer medium. The AAODL BEST data request form should be submitted to Dr. Patti Gillespie at the address appearing on the form.

Upon review and approval of the request, Dr. Gillespie will forward BEST data requests to AAODL personnel. Dr. Gillespie will also notify the user that the request has been received and that action to fill the request has been initiated. No data can be released from the AAODL BEST archive until the designated ASL representative (Dr. Gillespie) has approved the user request. Distribution of data is restricted to RSG.15 member nations.

Should any questions arise concerning user requirements, AAODL personnel will contact the requestor for clarification. The data will be sent directly to the user on whatever media the user requests.

5. SUMMARY

RSG.15, Panel 4, NATO AC/243 member nations have sponsored and directed the BEST ONE and BEST TWO field experiments. Data collected at these trials have been submitted to a central repository, the BEST AAODL archive, for organization, documentation, storage, and distribution. Data forms include electronic files (primarily in the ORACLE DBMS), video, and hard copy (data and publications). Video logs and a BEST bibliography are also maintained by the AAODL staff.

The BEST TWO portion of the database is increasing in size and scope as participants continue to send contributions for archive. Points of contact for BEST participants are maintained by AAODL personnel. These individuals can be consulted concerning data not yet submitted to the database.

Data in the repository can be accessed by submitting a User Request Form (Appendix). Access and distribution of BEST data must be approved by the designated U.S. delegate (Dr. Patti Gillespie). Data distribution is restricted to RSG.15 member nations.

REFERENCES

- Niles, F.E., 1987: Battlefield Obscuration Tests Nato AC/243 PANEL IV, Proceedings of Smoke/Obscurants Symposium XI, Vol II, AMCPM-SMK-001-87, Office of the Project Manger, Smoke/Obscurants, Aberdeen Proving Ground, MD.
- Niles, F.E., 1989: BEST ONE and BEST TWO, Proceedings of Smoke/Obscurants Symposium XIII, Secret Nofor, AMCPM-SMK-003-89, Office of the Project Manager, Smoke/Obscurants, Aberdeen Proving Ground, MD.
- Niles, F.E., 1990: Battlefield Emissive Sources Trials Under European Weather and Obscurants (BEST TWO), Proceedings of Smoke/Obscurants Symposium XIV, Vol II, CRDEC-CR-09, Chemical Research Development & Engineering Center, Aberdeen Proving Ground, MD.
- Niles, F.E., 1991: Preliminary Observations from BEST TWO, Proceedings of Eleventh Annual EOSAEL/TWI Conference, U.S. Army Atmospheric Sciences Laboratory, NM.
- Rogge, J., 1986: The Battlefield Emissive Sources Trial (BEST ONE), Proceedings of Smoke/Obscurants Symposium X, Vol I, AMCPM-SMK-001-86, Office of the Project Manager, Smoke/Obscurants, Aberdeen Proving Ground, MD.
- Rogge, J., 1990: The NATO Tests "BEST ONE" and "BEST TWO" Target Acquisition in the Presence of Battlefield Effects, Proceedings of Tenth Annual EOSAEL/TWI Conference, U.S. Army Atmospheric Sciences Laboratory, NM.

AAODL BEST DATA REQUEST

Mail this form to:

Commander/Director
U.S. Army Atmospheric Sciences Laboratory
ATTN: SLCAS-AE-T (Dr. Patti Gillespie)
White Sands Missile Range, New Mexico
88002-5501 USA

Requester: _____

Address: _____

Telephone: _____

Description of data requested (please use additional pages if necessary):

Required delivery date: _____

Data transfer specifications (ASCII only):

Operating system: ☐ DOS ☐ UNIX Other _____

Medium/Format: ☐ Hardcopy

 3 1/2-inch Diskette ☐ 1.44 M ☐ 720 K

 5 1/4-inch Diskette ☐ 1.2 M ☐ 360 K

 Magnetic tape (9-track) ☐ 6250 bpi ☐ 1600 bpi

 Video ☐ PAL ☐ SECAM ☐ NTSC

☐ 3/4-inch ☐ 1/2-inch ☐ 8-mm

(To be completed by AAODL personnel)

Authorized by: _____ Signature: _____ Date: _____

Completed by: _____ Date: _____

Attendees

1991 Battlefield Atmospheric Conference

Attendee List

Commander
Geophysics Directorate
Phillips Laboratories
ATTN: OPS (Mr. Leonard Abreu)
Hanscom AFB, MA 01731
(617) 377-2337

DSN 478-2337

•
MR. D. NEIL ALLEN
METSAT, Incorporated
Colorado State University
515 South Howes Street
Fort Collins, CO 80521-0000
(303) 221-5420

•
Commander
U.S. Army Atmospheric Sciences Lab
ATTN: SLCAS-BA-C (C. Amacker)
White Sands Missile Range, NM 88002-5501
(505) 678-7453

DSN 258-7453

•
COL GRANT AUFDERHAAR
Mil Asst for Environmental Science
Office of Under Secretary of Defense
(R&AT) ELS, Room 3D129
The Pentagon
Washington, DC 20301-3080
(703) 695-9604

DSN 225-9604

•
Commander/Director
U.S. Army Atmospheric Sciences Lab
ATTN: SLCAS-AM-A (Dr. Harry Auvermann)
White Sands Missile Range, NM 88002-5501
(505) 678-4224

DSN 258-4224

•
Commander/Director
U.S. Army Atmospheric Sciences Lab
ATTN: SLCAS-AM-T (Mr. Elton P. Avara)
White Sands Missile Range, NM 88002-5501
(505) 678-1570

DSN 258-1570

•
Commander/Director
U.S. Army Atmospheric Sciences Lab
ATTN: SLCAS-AM-T (Ms. Scarlett Ayres)
White Sands Missile Range, NM 88002-5501
(505) 678-4350

DSN 258-4350

•
Commander/Director
U.S. Army Atmospheric Sciences Lab
ATTN: SLCAS-AM-A (Mr. Jeff M. Balding)
White Sands Missile Range, NM 88002-5501
(505) 678-8301

DSN 258-8301

•
Commander/Director
U.S. Army Atmospheric Sciences Lab
ATTN: SLCAS-BW-R (Mr. Teddy L. Barber)
White Sands Missile Range, NM 88002-5501
(505) 678-2542

DSN 258-2542

•
PHILIPPE BATAILLE
Université De Rennes I
Laboratoire Radiocommunication
Campus de Beaulieu
Rennes 35042
FRANCE
99-42-90-44

•
Commander
U.S. Army Cold Regions Research and
Engineering Laboratory
ATTN: CECRL-RG (Mr. Roy B. Bates)
72 Lyme Road
Hanover, NH 03755-1290
(603) 646-4262

•
MR. JAN L. BEHUNEK
METSAT, Incorporated
Colorado State University
515 South Howes Street
Fort Collins, CO 80521
(303) 221-5420

•
DR. AMI BEN-SHALOM
Electro-Optics Research Center
EORD/Technion
Technion City, Haifa 32000
ISRAEL
972-4-321058

•
MR. STEPHEN W. BERRICK
Science and Technology Corporation
555 Telshor Blvd., Suite 200
Las Cruces, NM 88001
(505) 521-4353

•
Commander/Director
U.S. Army Atmospheric Sciences Lab
ATTN: SLCAS-AM-T (Mr. D. Billingsley)
White Sands Missile Range, NM 88002-5501
(505) 678-4313

DSN 258-4313

Commander/Director
U.S. Army Atmospheric Sciences Lab
ATTN: SLCAS-AM-A (Mr. Abel J. Blanco)
White Sands Missile Range, NM 88002-5501
(505) 678-3924 DSN 258-3924

•
Commander/Director
U.S. Army Atmospheric Sciences Lab
ATTN: SLCAS-AA-F (Mr. Max P Bleiweiss)
White Sands Missile Range, NM 88002-5501
(505) 678-3504 DSN 258-3504

•
Commander
Combat Vehicles Team
Ground Systems Division
ATTN: Mr. Thomas R. Bowman
Ft. Belvoir, VA 22060-5677
(505) 678-3504 DSN 258-3504

•
Commander
3246 TESTW (Weather Flight)
ATTN: Mr. Harry L Brano
Eglin AFB, FL 32542-5000
(904) 882-5960 DSN 872-5960

•
Commander
U.S. Army Space Technology and Research
Office (Federal Regional Center)
ATTN: SLCSP-ASTRO (Ms. B L Brathwaite)
5321 Riggs Road
Gaithersburg, MD 20882-0000
(301) 926-5483 DSN 393-5483

•
Commander/Director
U.S. Army Atmospheric Sciences Lab
ATTN: SLCAS-BA (Dr. Douglas R. Brown)
White Sands Missile Range, NM 88002-5501
(505) 678-2412 DSN 258-2412

•
Commander/Director
U.S. Army Atmospheric Sciences Lab
ATTN: SLCAS-BA-M (Mr. Robert C. Brown)
White Sands Missile Range, NM 88002-5501
(505) 678-4301 DSN 258-4301

•
Commander/Director
U.S. Army Atmospheric Sciences Lab
ATTN: SLCAS-AM-T (Dr. Dorothy Bruce)
White Sands Missile Range, NM 88002-5501
(505) 678-5524 DSN 258-5524

DR. EDWARD J. BURLBAW
Physical Science Laboratory
P.O. Box 30002
Las Cruces, NM 88003-0002
(505) 522-9350

•
Commander
U.S. Army Atmospheric Sciences Lab
ATTN: SLCAS-AM-A (Ms. Sue Bussells)
White Sands Missile Range, NM 88002-5501
(505) 678-2461 DSN 258-2461

•
MR. DONALD D. BUSTAMANTE
Physical Science Laboratory
New Mexico State University
Box 30002
Las Cruces, NM 88003-0002
(505) 522-9209

•
Commander
U.S. Army Atmospheric Sciences Lab
ATTN: SLCAS-AA-F (J. Butterfield)
White Sands Missile Range, NM 88002-5501
(505) 678-5713 DSN 258-5713

•
Commander/Director
U.S. Army Atmospheric Sciences Lab
ATTN: SLCAS-BA-M (Mr. John H. Byers)
White Sands Missile Range, NM 88002-5501
(505) 678-3951 DSN 258-3951

•
COL William H. Campbell
HQ USAF/XOWO, Directorate of Weather
Chief, Program Evaluation Division
Washington, DC 20330-1000
(703) 614-9023 DSN 224-9023

•
MR. MOGENS CASPERSEN
DDRE VED INDRAETSPARKEN 4
P.O. Box 2715
DK2100 Copenhagen
DENMARK
01 425707

•
Commander/Director
U.S. Army Atmospheric Sciences Lab
ATTN: SLCAS-AM-A (Ms. Thelma Chenault)
White Sands Missile Range, NM 88002-5501
(505) 678-6579 DSN 258-6579

MR. PRASAN CHINTAWONGVANICH

New Mexico State University
Physical Science Laboratory
P.O. Box 30002

ATTN: Mr. Prasan Chintawongvanich
Las Cruces, NM 88003-0002
(505) 522-9142

MR. HUGH W. CHURCH

Sandia National Laboratories
Organization 6321
Albuquerque, NM 87185-5800
(505) 845-8705

Commander/Director

U.S. Army Atmospheric Sciences Lab
ATTN: SLCAS-BA-M (Mr. Ronald Cionco)
White Sands Missile Range, NM 88002-5501
(505) 678-5210 DSN 258-5210

Commander

U.S. Army Laboratory Command
ATTN: AMSLC-AT (Pamela A. Clark)
2800 Powder Mill Road
Adelphi, MD 20783-1145
(301) 394-2135 DSN 290-2135

Commander/Director

U.S. Army Atmospheric Sciences Lab
ATTN: SLCAS-BW-W (Dr. James L. Cogan)
White Sands Missile Range, NM 88002-5501
(505) 678-2094 DSN 258-2094

U.S. Army RD&S - United Kingdom
ATTN: USARD5G-UK (Mr. Comati)
Box 65
FPO, New York 09510-1500
UK
1-402-8490 DSN 225-9490

Commander

Air Force Technical Applications Center
AFTAC/DOW
ATTN: (Thomas D. Corey)
Patrick AFB, FL 32925-0000
(407) 494-4531 DSN 854-4531

MR. JOHN N. CRAIN

Science and Technology Corporation
555 Telshor Boulevard, Suite 200
Las Cruces, NM 88001-0000
(505) 521-4353

Commander/Director

U.S. Army Atmospheric Sciences Lab
ATTN: SLCAS-AA-A (Mr. Edward Creegan)
White Sands Missile Range, NM 88002-5501
(505) 678-4684 DSN 258-4684

Commander/Director

U.S. Army Atmospheric Sciences Lab
ATTN: SLCAS-AM-T (Mr. Samuel B. Crow)
White Sands Missile Range, NM 88002-5501
(505) 678-4313 DSN 258-4313

MR. FRANCIS DANIELIAN

Section d'Etudes et Fabrications des
Telecommunications (SEFT)
18, Rue du Docteur Zamenhof
92131 ISSY-LES-MOULINEAUX CEDEX
FRANCE
1.40.95.35.51

DR. ROGER E. DAVIS

Science and Technology Corporation
555 Telshor Boulevard, Suite 200
Las Cruces, NM 88001-0000
(505) 521-4353

MR. MICHAEL D. DEANTONIO

NMSU
Physics Department
Dept 3D, Box 30001
Las Cruces, NM 88003
(505) 646-4446

DR. ADARSH DEEPAK

Science and Technology Corporation
101 Research Drive
Hampton, VA 23666-1340
(804) 865-1894

Commander/Director

U.S. Army Atmospheric Sciences Lab
ATTN: SLCAS-BA-C (Mr. R DeKinder, Jr.)
White Sands Missile Range, NM 88002-5501
(505) 678-7371 DSN 258-7371

Commander/Director

U.S. Army Atmospheric Sciences Lab
ATTN: SLCAS-BW-W (Mr. R. Dickenshied)
White Sands Missile Range, NM 88002-5501
(505) 678-1153 DSN 258-1153

Commander/Director
U.S. Army Atmospheric Sciences Lab
ATTN: SLCAS-BW-W (Mr. Marvin H Dubbin)
White Sands Missile Range, NM 88002-5501
(505) 678-3335 DSN 258-3335

•
DR. ARTHUR W. DUDENHOEFFER
Physical Science Laboratory
Applied Analysis
P.O. Box 30002
New Mexico State University
Las Cruces, NM 88003-0002
(505) 522-9343

•
Commander/Director
U.S. Army Atmospheric Sciences Lab
ATTN: SLCAS-BA-M (Mr. R E Dumais, Jr.)
White Sands Missile Range, NM 88002-5501
(505) 678-4650 DSN 258-4650

•
HQ, Air Weather Service/XTX
ATTN: CPT Clifton E. Dungey
Bldg 1521
Scott AFB, IL 62225-5008
618-256-4598 DSN 576-4598

•
Commander/Director
U.S. Army Atmospheric Sciences Lab
ATTN: SLCAS-BW-R (Dr. Frank D. Eaton)
White Sands Missile Range, NM 88002-5501
(505) 678-3956 DSN 258-3956

•
Commander
SHERRILL J. EDWARDS
U.S. Army Atmospheric Sciences Lab
ATTN: SLCAS-AM-A (S. Edwards)
White Sands Missile Range, NM 88002-5501
(505) 678-4232 DSN 258-4232

•
Commander/Director
U.S. Army Atmospheric Sciences Lab
ATTN: SLCAS-BW-W (Mr. John R. Elrick)
White Sands Missile Range, NM 88002-5501
(505) 678-3691 DSN 258-3691

•
Commander/Director
U.S. Army Atmospheric Sciences Lab
ATTN: SLCAS-AA-AB (Mr. Robert Endlich)
White Sands Missile Range, NM 88002-5501
(505) 679-5187 DSN 349-5187

MS. JOANNE M. ESPARZA
Physical Science Laboratory
Applied Analysis
P.O. Box 30002
New Mexico State University
Las Cruces, NM 88003-0002
(505) 522-9117

•
DR. OSKAR M. ESSENWANGER
C/o Mathematics Department
The Univ of Alabama in Huntsville
Huntsville, AL 35899-0000
(205) 895-6296

•
Commander/Director
U.S. Army Atmospheric Sciences Lab
ATTN: SLCAS-D (COL Ronald L. Evans)
White Sands Missile Range, NM 88002-5501
(505) 678-1225 DSN 258-1225

•
DR. MICHAEL W. FARMER
The Bionetics Corporation
500 S. Main, FNB #900
Las Cruces, NM 88004-0000
(505) 527-5623

•
Commander/Director
U.S. Army Atmospheric Sciences Lab
ATTN: SLCAS-AM-T (Dr. Robert Fiegel)
White Sands Missile Range, NM 88002-5501
(505) 678-3756 DSN 258-3756

•
Headquarters, Air Weather Service
Technical Development
ATTN: HQ AWS/XTR (MAJ Jeffrey Fink)
Scott AFB, IL 62225-5008
(618) 256-5731 DSN 576-5731

•
Commander
U.S. Army Research Office
ATTN: DRXRO-GS (Dr. W. A. Flood)
Research Triangle Park, NC 27709-0000
(919) 549-4246 DSN 832-4246

•
MR. RICHARD M. FRED A
TRW Inc.
P.O. Box 6213, MS DH5/2483
Carson, CA 90746-6213
(213) 764-9197

•
DR. K. PATRICK FREEMAN
Science and Technology Corporation
BLDG. 1418; PO Drawer 250
White Sands Missile Range, NM 88002-0250
(505) 678-8013

•
Commander/Director
U.S. Army Atmospheric Sciences Lab
ATTN: SLCAS-BW-W (Mrs. Nancy Fudge)
White Sands Missile Range, NM 88002-5501
(505) 678-4450 DSN 258-4450

•
Commander
U.S. Naval Training Systems Center
ATTN: Mr. Jerrold M. Gans
12350 Research Parkway, Code 242
Orlando, FL 32826-3224
(407) 380-4753 DSN 960-4753

•
MR. GEOFFREY Y. GARDNER
Grumman Data Systems Corporation
MS D12-237
1000 Woodbury Road
Woodbury, NY 11797-0000
(516) 682-8417

•
Commander/Director
U.S. Army Atmospheric Sciences Lab
ATTN: SLCAS-AA-A (Dr. Dennis Garvey)
White Sands Missile Range, NM 88002-5501
(505) 678-5677 DSN 258-5677

•
MR. JOHN C. GIEVER
Physical Science Laboratory
New Mexico State University
P.O. Box 30002
Las Cruces, NM 88003-0002
(505) 678-6826

•
Commander/Director
U.S. Army Atmospheric Sciences Lab
ATTN: SLCAS-BW-R (Dr. James Gillespie)
White Sands Missile Range, NM 88002-5501
(505) 678-6609 DSN 258-6609

•
Commander/Director
U.S. Army Atmospheric Sciences Lab
ATTN: SLCAS-AM-T (Dr. Patti Gillespie)
White Sands Missile Range, NM 88002-5501
(505) 678-1817 DSN 258-1817

•
MR. PAUL J. GRAF
TRW
One Federal Systems Park Drive
Fairfax, VA 22033-0000
(703) 803-5177

•
MR. WILLIAM G. GREENLEAF
Computer Sciences Corporation
200 Sparkman Drive
Huntsville, AL 35805
(205) 876-8487

•
MRS. SHLOMIT GROSSMAN
Hancal Systems Engineering Israeli
Military Industries
P.O. Box 1044/45
Ramat Hashazom 47100
ISRAEL
03-5484265/252

•
MR. KEITH S. GROVES
Defesne Services Division
Meteorological Office
London Road
Bracknell, Berkshire RG12 2SZ
UK
344-85-6297

•
Commander/Director
U.S. Army Atmospheric Sciences Lab
ATTN: SLCAS-DP-P (MAJ Grunwald)
White Sands Missile Range, NM 88002-5501
(505) 678-5236 DSN 258-5236

•
DR. WILLIAM M. GUTMAN
Physical Science Laboratory
New Mexico State University
P.O. Box 30002
Las Cruces, NM 88003-0002
(505) 522-9291

•
Commander
D/Geography & Environ. Engineering
U.S. Military Academy
ATTN: CPT Bruce L. Gwilliam
West Point, NY 10996-0000
(914) 938-2472 DSN 688-2472

•
Geophysics Laboratory
Phillips Laboratory, Atmos. Science Div
ATTN: PL/GPAA (MAJ J. K. Hancock)
Hanscom AFB, MA 01731-5000
(617) 377-4871 DSN 478-4871

•
Commander/Director
U.S. Army Topographic Engineering Cent.
ATTN: CETEC-GL-VA (Mr. Hardaway)
Bldg. 2592, 7701 Telegraph Rd.
Fort Belvoir, VA 22060-5546
(703) 355-3852 DSN 345-3852

Commander/Director
U.S. Army Atmospheric Sciences Lab
ATTN: SLCAS-BW-W (Mr. James E. Harris)
White Sands Missile Range, NM 88002-5501
(505) 678-5424 DSN 258-5424

•
MR. THOMAS L. HARRIS
Harris Corporation
Omaha Operations
301 N. Washington Street
Bellevue, NE 68005-0000
(402) 293-3412

•
Commander/Director
U.S. Army Atmospheric Sciences Lab
ATTN: SLCAS-BW-R (Mr. William H Hatch)
White Sands Missile Range, NM 88002-5501
(505) 678-1561 DSN 258-1561

•
Commander
U.S. Army Cold Regions Research and
Engineering Laboratory
ATTN: CECRL (Mr. Richard K. Haugen)
72 Lyme Road
Hanover, NH 03755-1209
(603) 646-4407

•
Office of the Federal Coordinator for
Met Services & Supporting Research
ATTN: (COL Floyd F. Hauth)
6010 Executive Blvd., Suite 900
Rockville, MD 20852-0000
(301) 443-8704 DSN 851-1460

•
Commander/Director
U.S. Army Atmospheric Sciences Lab
ATTN: SLCAS-BA-M (Dr. Teizi Henmi)
White Sands Missile Range, NM 88002-5501
(505) 678-3519 DSN 258-3519

•
DR. DONALD B. HODGES
HUGHES STX
109 Massachusetts Avenue
Lexington, MA 02173-0000
(617) 862-0713 FAX 863-2357

•
Commander
U.S. Army Corps of Engineers Cold
Regions Research & Engineering Lab.
ATTN: CECRL-RC (Dr. A. W. Hogan)
72 Lyme Road
Hanover, NH 03755-1290
(603) 646-4364 DSN 561-4100

Commander/Director
U.S. Army Atmospheric Sciences Lab
ATTN: SLCAS-MT-S (Mr. B. Holberg)
White Sands Missile Range, NM 88002-5501
(505) 678-5733 DSN 258-5733

•
Commander/Director
U.S. Army Atmospheric Sciences Lab
ATTN: SLCAS-BA-C (Dr. Howard E. Holt)
White Sands Missile Range, NM 88002-5501
(505) 678-4242 DSN 258-4242

•
Commander/Director
U.S. Army Atmospheric Sciences Lab
ATTN: SLCAS-AM-T (Dr. Donald W. Hoock)
White Sands Missile Range, NM 88002-5501
(505) 678-5430 DSN 258-5430

•
MS. KAREN L. HUTCHISON
Physical Science Laboratory
Applied Analysis
P.O. Box 30002
Las Cruces, NM 88003-0002
(505) 522-9412

•
MR. ROBERT E. INTRONE, JR.
The Analytic Sciences Corporation (TASC)
55 Walkers Brook Drive
Reading, MA 01867-0000
(617) 942-2000

•
Commander/Director
U.S. Army Atmospheric Sciences Lab
ATTN: SLCAS-AA-A (Mr. Jeffrey Johnson)
White Sands Missile Range, NM 88002-5501
(505) 678-3569 DSN 258-3569

•
Commander/Director
U.S. Army Atmospheric Sciences Lab
ATTN: SLCAS-DP-P (Mr. Odell M Johnson)
White Sands Missile Range, NM 88002-5501
(505) 678-5236 DSN 258-5236

•
MR. ANDREW S. JONES
METSAT, Inc.
515 South Howes Street
Fort Collins, CO 80521-0000
(303) 221-5420

•
MS. FRANCES J. JONES-LORY
Science and Technology Corporation
P.O. Drawer 250
White Sands Missile Range, NM 88002-0250
(505) 678-8303

MR. JON P. KAHLER

OptiMetrics, Incorporated
106 E. Idaho, Suite G
Las Cruces, NM 88005-0000
(505) 523-4986

•
Commander/Director

U.S. Army Atmospheric Sciences Lab
ATTN: SLCAS-AA-A (Mr Frank Kantrowitz)
White Sands Missile Range, NM 88002-5501
(505) 678-1526 DSN 258-1526

•
MR. DENNIS D. KASPAREK

Science and Technology Corporation
555 Telshor Blvd, Suite 200
Las Cruces, NM 88001
(505) 521-4353

•
DR. NEAL H. KILMER

Physical Science Laboratory
Applied Analysis
P.O. Box 30002
New Mexico State University
Las Cruces, NM 88003-0002
(505) 522-9495

•
Commander/Director

U.S. Army Atmospheric Sciences Lab
ATTN: SLCAS-BW-W (Mr. Steve F. Kirby)
White Sands Missile Range, NM 88002-5501
(505) 678-4329 DSN 258-4329

•
MR. FRANK J. KLEIN

Science and Technology Corporation
2140 Broken Circle Road
Colorado Springs, CO 80915-0000
(719) 550-1178

•
Commander

Geophysics Directorate
Phillips Laboratory
ATTN: PL/GPOS (Francis X. Kneizys)
Hanscom AFB, MA 01731-5000
(617) 377-3654 DSN 478-3654

•
MR. STEVEN J. LAMOTTE

Physical Science Laboratory
New Mexico State University
P.O. Box 30002
Las Cruces, NM 88003-0002
(505) 522-9322

MR. DICK R. LARSON

Physical Science Laboratory
Applied Analysis
P.O. Box 30002
New Mexico State University
Las Cruces, NM 88003-0002
(505) 522-9383

•
Commander/Director

U.S. Army Atmospheric Sciences Lab
ATTN: SLCAS-BW-W (Mr Patrick V. Laybe)
White Sands Missile Range, NM 88002-5501
(505) 678-1618 DSN 258-1618

•
MR. ALAIN LE DORTZ

DGA/DAT/SEFT
18 rue du Docteur Zamenhof
92131 Issy-les-Moulineaux
FRANCE
(1) 40-95-34-42

•
Commander/Director

U.S. Army Atmospheric Sciences Lab
ATTN: SLCAS-BA-C (Mr. Martin E. Lee)
White Sands Missile Range, NM 88002-5501
(505) 678-5593 DSN 258-5593

•
Commander/Director

U.S. Army Atmospheric Sciences Lab
ATTN: SLCAS-AM-A (Mr. Robert R. Lee)
White Sands Missile Range, NM 88002-5501
(505) 678-4006 DSN 258-4006

•
Commander

U.S. Army Missile Command
ATTN: AMSMI-RD-WS-CM (Mr. L Levitt)
Redstone Arsenal, AL 35898-5248
(205) 876-4328 DSN 746-4328

•
MR. LUIS C. LINGGI

Physical Science Laboratory
New Mexico State University
Box 30002
Las Cruces, NM 88003-0002
(505) 522-9226

•
MR. BRIAN A. LOCKE

Science and Technology Corporation
555 Telshor Boulevard, Suite 200
Las Cruces, NM 88001-0000
(505) 521-4353

MR. SABA A. LUCES
Physical Science Laboratory
New Mexico State University
P.O. Box 30002
Las Cruces, NM 88003-0002
(505) 522-9480

MR. FRANCIS L. LUDWIG
SRI International
333 Ravenswood Avenue
Menlo Park, CA 94025-0000
(415) 859-2915

Commander/Director
U.S. Army Atmospheric Sciences Lab
ATTN: SLCAS-BA-M (Mr. Dave Marlin)
White Sands Missile Range, NM 88002-5501
(505) 678-5447 DSN 258-5447

Commander
U.S. Army Research Institute of
Environmental Medicine
ATTN: SGRD-UE-EMB (Mr William Matthew)
Kansas Street
Natick, MA 01760-5007
(508) 651-5140 DSN 256-5140

Director
U.S. Army Materiel Systems
Analysis Activity
ATTN: AMXSY-GC (Mr. Jeffrey Matthews)
Aberdeen Proving Grnd, MD 21005-5071
(301) 278-7287 DSN 298-7287

MR. STEVE J. MCGEE
Physical Science Laboratory
New Mexico State University
P.O. Box 30002
Las Cruces, NM 88003-0002
(505) 522-9374

Commander/Director
U.S. Army Atmospheric Sciences Lab
ATTN: SLCAS-AM-A (Mr. Robert E McPeck)
White Sands Missile Range, NM 88002-5501
(505) 678-4382 DSN 258-4382

Commander/Director
U.S. Army Atmospheric Sciences Lab
ATTN: SLCAS-BW-W (Mr. Gary McWilliams)
White Sands Missile Range, NM 88002-5501
(505) 678-4388 DSN 258-4388

Commander
U.S. Army Atmospheric Sciences Lab
ATTN: SLCAS-AA-A (Ms. Meade)
White Sands Missile Range, NM 88002-5501
(505) 678-2926 DSN 258-2926

Commander/Director
U.S. Army Atmospheric Sciences Lab
ATTN: SLCAS-BW-R (Dr. Edward Measure)
White Sands Missile Range, NM 88002-5501
(505) 678-3307 DSN 258-3307

DR. ROBERT E. MEREDITH
Optimetrics, Incorporated
3115 Professional Drive
Ann Arbor, MI 48104-5131
(313) 973-1177

Commander/Director
U.S. Army Atmospheric Sciences Lab
ATTN: SLCAS-BW-W (Mr. Bruce T. Miers)
White Sands Missile Range, NM 88002-5501
(505) 678-4501 DSN 258-4501

Commander/Director
U.S. Army Atmospheric Sciences Lab
ATTN: SLCAS-TD (Mr. James E. Morris)
White Sands Missile Range, NM 88002-5501
(505) 678-1227 DSN 258-1227

Commander
U.S. Air Force Environmental
Technical Applications Center
ATTN: ADG (CAPT Jeffrey S. Morrison)
Scott AFB, IL 62225-5438
(618) 256-5211 DSN 576-5211

Defense Nuclear Agency
ATTN: NANF (MAJ Robert F. Mull)
6801 Telegraph Road
Alexandria, VA 22310-0000
(703) 325-0918 DSN 221-0918

MR. RONALD NELSON
Science and Technology Corporation
12452 Towner N.E.
Albuquerque, NM 87112
(505) 275-6663

Commander/Director
U.S. Army Atmospheric Sciences Lab
ATTN: SLCAS-AM (Dr. Franklin E. Niles)
White Sands Missile Range, NM 88002-5501
(505) 678-3721 DSN 258-3721

Commander/Director
U.S. Army Atmospheric Sciences Lab
ATTN: SLCAS-AM-A (Dr. John M. Noble)
White Sands Missile Range, NM 88002-5501
(505) 678-3751 DSN 258-3751

•
DR. SEAN G. O'BRIEN
Las Cruces Scientific Consulting
3373 Solar Ridge St.
Las Cruces, NM 88005-0000
(505) 382-0285

•
MR. RICHARD J. OKRASINSKI
Physical Science Laboratory
Applied Analysis
P.O. Box 30002
Las Cruces, NM 88003-0002
(505) 522-9496

•
DR. MONTIE M. ORGILL
Science and Technology Corporation
P.O. Drawer 250
White Sands Missile Range, NM 88002-0250
(505) 678-8303

•
Commander/Director
U.S. Army Atmospheric Sciences Lab
ATTN: SLCAS-BA-M (Mr. Brian Orndorff)
White Sands Missile Range, NM 88002-5501
(505) 678-1803 DSN 258-1803

•
Commander
U.S. Army Atmospheric Sciences Lab
ATTN: SLCAS-AA (Ms. Ortega)
White Sands Missile Range, NM 88002-5501
(505) 678-5232 DSN 258-5232

•
Commander
U.S. Army Defense Nuclear Agency
ATTN: NANF (MAJ Paul A. Oswald)
6801 Telegraph Road
Alexandria, VA 22310-0000
(703) 325-1228 DSN 221-1228

•
MR. CLEM OTA
Science and Technology Corporation
555 Telshor Blvd., Suite 200
Las Cruces, NM 88001-0000
(505) 521-4353

Commander/Director
Defense Nuclear Agency
RARP
ATTN: Dr. Muhammad Owais
6801 Telegraph Rd
Alexandria, VA 22310-3398
(703) 325-7744

•
HQDA
ATTN: DAMI-POI (Mr. L. Page)
Washington, DC 20310-1067
(202) 695-5509 DSN 225-5509

•
Commander/Director
U.S. Army Atmospheric Sciences Lab
ATTN: SLCAS-BW-W (Mr. Jeffrey Passner)
White Sands Missile Range, NM 88002-5501
(505) 678-3193 DSN 258-3193

•
Commander/Director
U.S. Army Atmospheric Sciences Lab
ATTN: SLCAS-AA-A (Dr David Pendleton)
White Sands Missile Range, NM 88002-5501
(505) 678-5634 DSN 258-5634

•
DR. H.T.A. PENTECOST
Defence Research Agency Military Div
RARDE, Fort Halstead
Sevenoaks, KENT TN14 7BP
UNITED KINGDOM
0959 32222-2798

•
Commander/Director
U.S. Army Atmospheric Sciences Lab
ATTN: SLCAS-AA-A (Dr. W. A. Peterson)
White Sands Missile Range, NM 88002-5501
(505) 678-1465 DSN 258-1465

•
Commander/Director
U.S. Army Atmospheric Sciences Lab
ATTN: SLCAS-AA-A (Dr. Ronald Pinnick)
White Sands Missile Range, NM 88002-5501
(505) 678-5634 DSN 258-5634

•
Commander/Director
U.S. Army Atmospheric Sciences Lab
ATTN: SLCAS-AA-AB (Mr. John W. Raby)
White Sands Missile Range, NM 88002-5501
(505) 679-5187 DSN 349-5187

•
Commander/Director
U.S. Army Atmospheric Sciences Lab
ATTN: SLCAS-BA-M (Dr. Henry Rachele)
White Sands Missile Range, NM 88002-5501
(505) 678-6687 DSN 258-6687

•
 Commander
 NATO School (SHAPE)
 ATTN: LTC Jerry A. Rankin
 Box 44
 APO AE 09172-4251
 49-8822-6051/x355

•
 MR. DONALD L. REINKE
 METSAT, Incorporated
 515 South Howes Street
 Fort Collins, CO 80521-0000
 (303) 221-5420

•
 Commander
 USAR, FA
 ATTN: SLCAS-AM-T (LTC Reynolds)
 White Sands Missile Range, NM 88002-5501
 (505) 678-5430 DSN 258-5430

•
 Commander
 WL/DOW
 Wright Laboratory
 ATTN: (MAJ John R. Roadcap)
 Wright Patterson AFB, OH 45433-6543
 (513) 255-1978 DSN 785-1978

•
 MR. JAAP ROGGE
 Royal Military Academy
 P.O. Box 90154
 4800 Rg Breda
 The NETHERLANDS
 (31) 76 273172 FAX 273534

•
 Commander/Director
 U.S. Army Atmospheric Sciences Lab
 ATTN: SLCAS-BW-R (Dr. David L. Rosen)
 White Sands Missile Range, NM 88002-5501
 (505) 678-4488 DSN 258-4488

•
 Commander/Director
 U.S. Army Atmospheric Sciences Lab
 ATTN: SLCAS-AA-A (Mr. Robert Rubio)
 White Sands Missile Range, NM 88002-5501
 (505) 678-2926 DSN 258-2926

•
 Commander
 U.S. Army Research Institute of
 Environmental Medicine
 ATTN: SGRD-VE-EMB (Dr. W. Santee)
 Kansas Street
 Natick, MA 01760-5007
 (508) 651-4878 DSN 256-4878

•

Commander/Director
 U.S. Army Atmospheric Sciences Lab
 ATTN: SLCAS-DP-P (Mrs. Barbara Sauter)
 White Sands Missile Range, NM 88002-5501
 (505) 678-2840 DSN 258-2840

•
 Commander/Director
 U.S. Army Atmospheric Sciences Lab
 ATTN: SLCAS-AM-A (Mr. David P. Sauter)
 White Sands Missile Range, NM 88002-5501
 (505) 678-2078 DSN 258-2078

•
 Commander/Director
 U.S. Army Atmospheric Sciences Lab
 ATTN: SLCAS-BW-W (Dr. M. A. Seagraves)
 White Sands Missile Range, NM 88002-5501
 (505) 678-4207 DSN 258-4207

•
 MR. JOSE M. SERNA
 Physical Science Laboratory
 Applied Analysis
 P.O. Box 30002
 Las Cruces, NM 88003-0002
 (505) 522-9333

•
 Commander/Director
 U.S. Army Atmospheric Sciences Lab
 ATTN: SLCAS-AM-T (Dr. Rick Shirkey)
 White Sands Missile Range, NM 88002-5501
 (505) 678-5470 DSN 258-5470

•
 Commander/Director
 U.S. Army Atmospheric Sciences Lab
 ATTN: SLCAS-BW-W (Douglas Shoop)
 White Sands Missile Range, NM 88002-5501
 (505) 678-5861 DSN 258-5861

•
 Commander/Director
 U.S. Army Atmospheric Sciences Lab
 ATTN: SLCAS-MT (Mrs. Marsha Smith)
 White Sands Missile Range, NM 88002-5501
 (505) 678-3515 DSN 258-3515

•
 Director
 U.S. Army CECOM Center for Night Vision
 and Electro Optics
 ATTN: AMSTE-TC-AM/BE (Mr. R. W. Smith)
 Fort Belvoir, VA 22060-5677
 703-664-1188 DSN 354-1188

•
 Commander
 U.S. Army Atmospheric Sciences Lab
 ATTN: SLCAS-DP-P (Mrs. S. Soto)
 White Sands Missile Range, NM 88002-5501
 (505) 678-5236 DSN 258-5236

•
DR. JOHN B. SPALDING
Physical Science Laboratory
Applied Analysis
P.O. Box 30002
Las Cruces, NM 88003-0002
(505) 522-9298

•
Commander/Director
U.S. Army Atmospheric Sciences Lab
Director, Managment & Tech Spt Office
ATTN: SLCAS-MT (Mrs. Sharon Steffey)
White Sands Missile Range, NM 88002-5501
(505) 678-2811 DSN 258-2811

•
Commander/Director
U.S. Army Atmospheric Sciences Lab
ATTN: SLCAS-AA-F (Mr. Ralph Steinhoff)
White Sands Missile Range, NM 88002-5501
(505) 678-4481 DSN 258-4481

•
Commander
Headquarters, Space Division/MIA
ATTN: (CPT Wayne G. Strang)
P.O. Box 92960
Los Angeles AFB
Los Angeles, CA 90009-2960
(310) 336-4458 DSN 833-4458

•
Commander
CECOM Night Vision Laboratory
and Electro-Optics
ATTN: AMSEL-RD-NV-GSID (Susan Strohl)
Fort Belvoir, VA 22060-5677
(703) 664-4837 DSN 354-6792

•
DR. THOMAS J. SULLIVAN
Lawrence Livermore National Laboratory
P.O. Box 808, L-262
Livermore, CA 94551-0808
(510) 422-1838

•
Commander/Director
U.S. Army Atmospheric Sciences Lab
ATTN: SLCAS-BA-M (Dr. R. Sutherland)
White Sands Missile Range, NM 88002-5501
(505) 678-4520 DSN 258-4520

•
MR. CARY D. SUTTON
Harris Corporation - GISD
(Omaha Operations)
301 N. Washington Street
Bellevue, NE 68005-0000
(402) 293-3447

•
Commander
Geophysics Laboratory
Phillips Laboratory
ATTN: (Mr. Paul Tattelman)
Hanscom AFB, MA 01731-0000
(617) 377-5956 DSN 478-5956

•
MR. DAVID D. TELLES
Physical Science Laboratory
New Mexico State University
P.O. Box 30002
Las Cruces, NM 88003-0002
(505) 522-9371

•
DR. FRIEDRICH THEUNERT
German Military Geophysical Office
Mont Royal
D5580 Traben-Trarbach
GERMANY
49-6541-18-341

•
Commander/Director
U.S. Army Atmospheric Sciences Lab
ATTN: SLCAS-AA-F (Mr Fidel Tibuni, Jr)
White Sands Missile Range, NM 88002-5501
(505) 678-1801 DSN 258-1801

•
Commander/Director
U.S. Army Atmospheric Sciences Lab
ATTN: SLCAS-AM-T (Mr David H. Tofsted)
White Sands Missile Range, NM 88002-5501
(505) 678-3039 DSN 258-3039

•
MR. ANDREW R. TOOTH
British Aerospace PLC
Sowerby Research Centre
FPC 267, P.O. Box 5
Filton, Bristol
UNITED KINGDOM
0272 36 3095

•
Commander
HQ AFSC/WE
ATTN: CPT Jason P. Tuell
Andrews Air Foce Base, DC 20334-5000
301-981-6929 DSN 858-6929

•
Commander/Director
U.S. Army Atmospheric Sciences Lab
ATTN: SLCAS-BA-M (Mr Arnold D. Tunick)
White Sands Missile Range, NM 88002-5501
(505) 678-4832 DSN 258-4832

MR. J. M. VALETON

TNO Institute for Perception

PO BOX 23

3769 ZG Soesterverg

The NETHERLANDS

(505) 678-4832

DSN 258-4832

GAIL T. VAUCHER

Science and Technology Corporation

P.O. Drawer 250

White Sands Missile Range, NM 88002-0250

(505) 678-4832

DSN 258-4832

Commander/Director

U.S. Army Atmospheric Sciences Lab

ATTN: SLCAS-AA (Mr. Don R. Veazey)

White Sands Missile Range, NM 88002-5501

(505) 678-5232

DSN 258-5232

DR. THOMAS H. VONDER HAAR

Colorado State University

Fort Collins, CO 80523-0000

(303) 491-8566

Commander/Director

U.S. Army Atmospheric Sciences Lab

ATTN: SLCAS-AA-F (Arnold Wade)

White Sands Missile Range, NM 88002-5501

(505) 678-1761

DSN 258-1761

Commander

U.S. Army Intelligence Center & School

ATTN: ATSI-CDC-S (Mr. Charles Warnick)

Fort Huachuca, AZ 85613-6000

(602) 538-7216

DSN 879-7216/17

Commander/Director

U.S. Army Atmospheric Sciences Lab

ATTN: SLCAS-AM-T (Mr. Wendell Watkins)

White Sands Missile Range, NM 88002-5501

(505) 678-4313

DSN 258-4313

MR. DANFORTH C. WEEMS

Physical Science Laboratory

Applied Analysis

P.O. Box 30002

New Mexico State University

Las Cruces, NM 88003-0002

(505) 522-9406

Commander/Director

U.S. Army Atmospheric Sciences Lab

ATTN: SLCAS-AA-A (Dr. Alan E. Wetmore)

White Sands Missile Range, NM 88002-5501

(505) 678-5563

DSN 258-5563

Commander/Director

U.S. Army Atmospheric Sciences Lab

ATTN: SLCAS-AA-A (Mr. J. Williams)

White Sands Missile Range, NM 88002-5501

(505) 678-3684

DSN 258-3684

Commander/Director

U.S. Army Atmospheric Sciences Lab

ATTN: SLCAS-BA-M (Mr. Young P. Yee)

White Sands Missile Range, NM 88002-5501

(505) 678-1589

DSN 258-1589

DR DOUGLAS C. YOON

Logicon R&D Associates

P.O. Box 92500

Los Angeles, CA 90009-0000

(213) 645-1122/342

Commander

U.S. Army Laboratory Command

ATTN: AMSLC-DL-TC (Mr. D. Youngberg)

Aberdeen Proving Ground, MD 21005-5066

(410) 278-9798

DSN 298-9798

DR. BERNARD D. ZAK

Sandia National Labs

Org 6321

Albuquerque, NM 87185

(505) 845-8631

DR. ANDREW ZARDECKI

Los Alamos National Laboratory

N-4, E541 (Dr. A. Zardecki)

Los Alamos, NM 87545-0000

(505) 665-2812

***INDEX
BY FIRST AUTHOR***

Index by First Author

ABREU, L. W., F. X. Kneizys, G. P. Anderson, J. H. Chetwynd, A. Berk, L. S. Bernstein, and D. C. Robertson	7
AYRES, Scarlett D.	382
BATAILLE, Philippe	316
BEHUNEK, J. L., and T. H. Vonder Haar	197
BERRICK, Stephen W., and Patti S. Gillespie	75
BLANCO, Abel J., and Sherrill J. H. Edwards	395
BODEN, J. A., and R. J. L. Lerou	315
BRUCE, Dorothy	349
BUSTAMANTE, Donald, D., and Arthur W. Dudenhoeffer	499
CAMPBELL, Colonel William H.	3
CASPERSEN, Mogens	317
CHENAULT, Thelma, John Fox, and Don Foiani	217
CIONCO, Ronald M.	447
COGAN, James	509
COGAN, James, Richard Szymber, and Edward Measure	518
CREEGAN, Edward D.	341
DAVIS, Roger E., John Crain, and Robert A. Sutherland	103
DAVIS, Roger E., and Patti S. Gillespie	619
DEANTONIO, Michael D.	605
DUMAIS, Robert E. Jr., and Jeffrey E. Passner	176
ELRICK, John R.	573

ESSENWANGER, Oskar	166
FARMER, W. Michael, Bruce W. Kennedy, and Van R. Jones	371
FIEGEL, Robert P.	15
FINK, J. D., and P. B. Roohr	142
FREEMAN, Kenneth P., and Robert W. Endlich	554
GARDNER, Geoffrey Y., and G. Michael Hardaway	56
GILLESPIE, James B., and Edward M. Patterson	381
GILLESPIE, Patti	421
GROSSMAN, S., A. Katz, and D. Elial	35
GROVES, Keith S., Ian D. Todd, and Jonathan D. Turton	156
HANSEN, Frank V., Henry Rachele, and Arnold Tunick	591
HARRIS, James E., and Ronald E. Meyers	476
HARRIS, Thomas L.	587
HARRIS, Thomas L., and Jimmy A. Jensen	202
HAUGEN, Richard K., Roy E. Bates, and Andrew J. Bruzewicz	496
HAUTH, Col. Floyd F.	141
HENMI, Teizi	467
HOGAN, A., and D. Leggett	149
HOLT, Howard, Robert Sutherland, John Grace, S. A. Lucas, William Ohmstede, John Barnes, and Kenneth Chin-Purcell	576
HOOCK, Donald W.	46
HOOCK, Donald W., and John C. Giever	350
de JONG, A. N.	292
KANTROWITZ, Frank T., Daniel R. Billingsley, Fernando R. Palacios, and Wendell R. Watkins	563

KILMER, Neal H., and Henry Rachele	25
KIRBY, Stephen	431
LARSON, Dick	536
LE DORTZ, Alain	313
LEE, Martin E., and Steven J. LaMotte	94
LEE, Robert R., Philip Raihl, and Sylvia Cossio	411
LEROU, R. J. L.	318
LEVITT, Larry J., and Dorathy A. Stewart	113
LOCKE, Brian A., Stephen W. Berrick, Lori Fuentes, Ronald A. Catherson, and Patti Gillespie	84
McWILLIAMS, Gary	405
MEASURE, Edward M., Teddy L. Barber, Randall J. Hulsey, and Dick R. Larson	223
MEDLER, Charles L., and Maureen E. Cianciolo	380
MILLER, Maj. Robert L.	392
MILLER, R. L., and B. T. Regan	36
NELSON, Ronald J., and Kenneth P. Freeman	360
NOBLE, John M.	66
OLSEN, Robert, René Klein, Harold Ballard, Claude Tate, Robert Hootman, Ronald Atkins, and Roy Bates	562
ORGILL, Montie, Robert Sutherland, and John Kincheloe	459
ORNDORFF, Brian L., and Ronald M. Cionco	486
PETERSON, William A., Dennis M. Garvey, and William M. Gutman	361
RACHELE, Henry, and Arnold Tunick	251
REINKE, D. L., C. L. Combs, and T. H. Vonder Haar	212
ROGGE, J.	302

ROGGE, J., and LCol D. M. Vonhof	314
ROSEN, David, James Klett, and James Gillespie	546
SAUTER, David	123
SMITH, Robert W., and Ted Corbin	282
SPALDING, John B., and Danforth C. Weems	435
STEINHOFF, Ralph G.	535
STEINHOFF, R. G., A. E. Wade, and R. G. Trujillo	525
SUTHERLAND, Robert A., Young P. Yee, Frank D. Eaton,	185
William A. Peterson, Miklos Z. Kiss, and Craig E. Foster	
TOFSTED, David H., and James B. Gillespie	268
TOOTH, A. R.	319
TUNICK, Arnold, and Henry Rachele	241
VALETON, J. M., and P. Bijl	328
VAUCHER, Gail Tirrell, and Robert W. Endlich	228
VESQUE, Jacques	281
VONDER HAAR, T. H., and J. L. Behunek	131
WATKINS, Wendell R., Samuel B. Crow, Daniel R. Billingsley,	303
Fernando R. Palacios, and Richard W. Dutro	
WILLIAMS, James, Robert Fiegel, and Alan Wetmore	331
YEE, Young P., Robert A. Sutherland, John Crain, and Liam McDaid	422
ZARDECKI, Andrew, and Alan E. Wetmore	261